Mathematical Problems in Engineering

Trends in Analysis and Design of Nonlinear Control Systems with Applications to Engineering Problems

Lead Guest Editor: Raúl Villafuerte-Segura
Guest Editors: Víctor Estrada-Manzo, Baltazar Aguirre-Hernández, Rosalba Galván-Guerra, and José Antonio Rosales Martínez

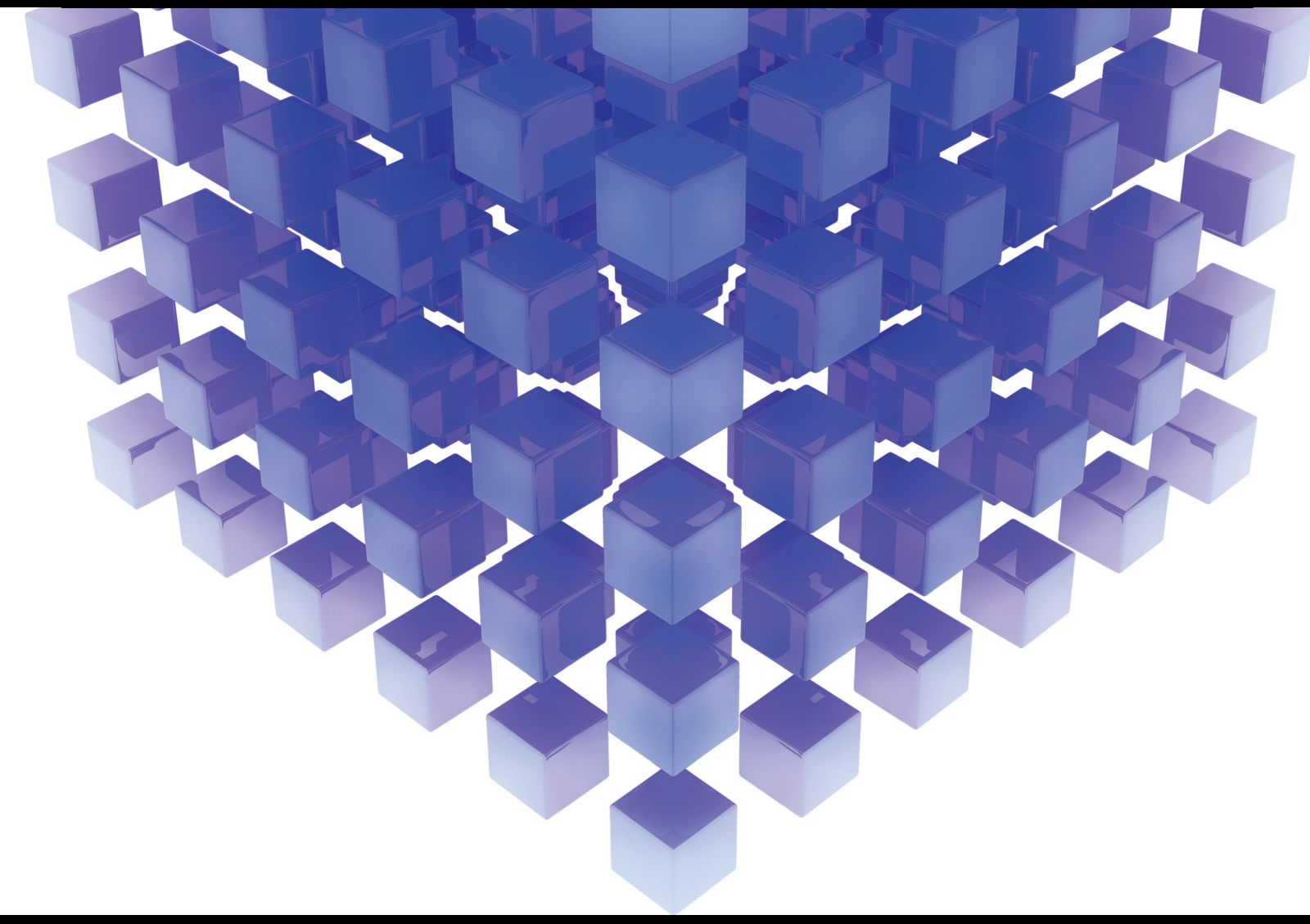

Trends in Analysis and Design of Nonlinear Control Systems with Applications to Engineering Problems

Mathematical Problems in Engineering

Trends in Analysis and Design of Nonlinear Control Systems with Applications to Engineering Problems

Lead Guest Editor: Raúl Villafuerte-Segura
Guest Editors: Víctor Estrada-Manzo, Baltazar Aguirre-Hernández, Rosalba Galván-Guerra, and José Antonio Rosales Martínez

Chief Editor

Academic Editors

Contents

Hindawi
Mathematical Problems in Engineering
Volume 2021, Article ID 8825609, 16 pages
https://doi.org/10.1155/2021/8825609

Research Article

Actuator Fault Detection for Discrete-Time Descriptor Systems via a Convex Unknown Input Observer with Unknown Scheduling Variables

Javier Martinez,[1] **Braulio Aguiar**,[2] **Víctor Estrada-Manzo**,[1] **and Miguel Bernal**[2]

[1]*Dept. of Mechatronics, Universidad Politécnica de Pachuca, C.P. 43830 Zempoala, Mexico*
[2]*Dept. of Electrical and Electronics Engineering, Sonora Institute of Technology, 5 de Febrero 818 Sur, C.P. 85000 Cd Obregon, Mexico*

Correspondence should be addressed to Víctor Estrada-Manzo; victor_estrada@upp.edu.mx

Received 11 December 2020; Revised 13 February 2021; Accepted 20 February 2021; Published 30 March 2021

Academic Editor: Zhifeng Dai

This paper presents actuator fault detection of discrete-time nonlinear descriptor systems by means of nonlinear unknown input observers. The approach is based on the exact factorization of the estimation error in order to overcome the well-known problem of unmeasurable scheduling variables within the observation of convex models, thus avoiding the use of Lipschitz constants, differential mean value theorem, or robust techniques. As a result, the designing conditions are cast in terms of linear matrix inequalities and efficiently solved via commercially available software. Numerical as well as academic setups are provided to illustrate the advantages and performance of the proposal.

1. Introduction

The use of state observers [1] is important for many tasks within control theory. In particular, unknown input (UI) observers whose task is to estimate both the state and unknown inputs (they may be disturbances) have been developed in [2], and they are of particular interest also for fault detection and isolation [3, 4] or fault tolerant control schemes [5, 6]; they can be also applied in other fields [7]. For linear systems, there are several UI observers, e.g., [8–10]; for nonlinear systems, linear methods are mostly chosen because of its simplicity [11]. Nonlinear techniques such as sliding mode [12], adaptive schemes [13], Lipschitz approaches [14], high-gain observers [15], or combinations of them require certain structure of the model or performing nonlinear transformations.

On the other hand, convex models (a convex model is a collection of linear models interconnected by scalar functions (also known as scheduling functions), which are nonlinear and hold the convex sum property in a region [16, 17]. If the convex model is the result of the sector nonlinearity [18], it is an exact representation of the nonlinear system) [19, 20] have been directly combined with the direct Lyapunov method; thus obtaining conditions in terms of linear matrix inequalities (LMIs) [21]. Conditions in the form of LMIs are preferred since they are numerically solvable via convex optimization techniques [22]. Within this context, there exist several state observers for both continuous [23, 24] and discrete-time systems [25–27]. In the case of UI observers, there are some works concerning proportional-integral setups [28, 29] or non-Luenberger forms [30–34].

Nevertheless, within the convex framework, the observer design presents an open problem: if the scheduling variables do not exclusively depend on measurable/available signals, the designing conditions get involve and difficult to cast as LMIs. Recent works have intended to tackle this issue by employing Lipschitz constraints [24, 35], the differential mean value theorem (DMVT) [36, 37], and robust H_∞ approaches to mitigate the influence of the unknown scheduling parameters [38]; more recently, in [39, 40], a transformation that enlarges the size of the state is proposed.

In this work, we follow the ideas of [41] for solving this problem: algebraic rearrangements in order to properly factorize the error signal.

A generalized representation for standard state-space models is given by descriptor systems [42]; within this setup, a special case considers that the descriptor matrix is invertible [43]. For this class of descriptor systems, in [27], a convex observer design has been developed, and it considers only available scheduling variables; in [44, 45], an UI observer has been proposed, and it can handle unmeasurable scheduling variables by robust argumentations.

The estimation of the states and parameters makes possible the fault diagnosis, which is divided into fault detection, fault isolation, and fault identification [46, 47]. The fault detection (FD) is used to identify when there is a malfunction in the system and determine the moment when the fault occurs [48]. In FD, there exist some results using the UI observer for actuator fault, for example, [13] where an adaptive approach is developed for an aircraft actuator fault. In [49], UI observers are employed for fault detection and isolation.

Contributions: a novel convex UI observer scheme is used for discrete-time descriptor models with unmeasurable scheduling variables; the scheme makes use of algebraic manipulations instead of Lipschitz constraints, the differential mean value theorem, or robust techniques in order to obtain an adequate estimation error dynamics, thus relaxing the results. Actuator fault detection and estimation is performed by means of the proposed UI observer.

The rest of the paper is organized as follows: Section 2 provides the background for further developments and notation. Section 3 states the LMI conditions for the nonlinear UI observer design via convex models. In Section 4, the UI observer is applied to actuator fault detection and estimation of nonlinear systems. Section 5 illustrates the proposal via the numerical example and train system. Section 6 concludes the paper by giving some final remarks.

2. Problem Statement

Consider the following discrete-time nonlinear descriptor model:

$$E(y_k)x_{k+1} = A(x_k)x_k + B(y_k)u_k + D(y_k)d_k, \quad y_k = C(x_k)x_k, \tag{1}$$

where $x_k \in \mathbb{R}^n$ is the state vector, $u_k \in \mathbb{R}^m$ is the input vector, and $d_k \in \mathbb{R}^q$ is the unknown input vector, $y_k \in \mathbb{R}^o$ is the output vector; $A(x_k)$, $B(y_k)$, $C(x_k)$, $D(y_k)$, and $E(y_k)$ are matrix functions whose entries are smooth and bounded in a region $\Omega_x \subset \mathbb{R}^n$ including the origin. This work only considers the particular case when $E(\cdot)$ is full rank (the case when descriptor matrix is not invertible has been recently treated in [50, 51], this case is also referred as differential-algebraic-equation (DAE) systems or singular ones [52], and it is out of the scope of this work. Fault diagnosis schemes for this type of systems have been addressed in [53]) for $x_k \in \Omega_x$; that is, from (1), it is always possible to obtain a standard state-space representation:

$$\begin{aligned} x_{k+1} &= E^{-1}(y_k)\left(A(x_k)x_k + B(y_k)u_k + D(y_k)d_k\right) \\ &= f(x_k, u_k, d_k). \end{aligned} \tag{2}$$

In what follows, arguments will be omitted when their meaning can be inferred from the context.

The approach is based on designing an observer for the estimation of both the state x_k and the unknown input d_k; to this end, an augmented vector is employed [29, 44], that is, $\chi_k = \left[\, x_k^T \;\; \mathbf{d}_k^T \,\right]^T$, $\mathbf{d}_k = \left[\, d_k^T \;\; d_{k+1}^T \;\; \cdots \;\; d_{k+p}^T \,\right]^T \in \mathbb{R}^{(p+1)q}$, where p is such that $(z-1)^{p+1} d_k \approx 0$ as proposed in [45]; for instance, for $p = 1$, we have

$$\mathbf{d_{k+1}} = S\mathbf{d}_k, \text{ with } \mathbf{d_{k+1}} = \begin{bmatrix} d_{k+1} \\ d_{k+2} \end{bmatrix}, S = \begin{bmatrix} 0 & 1 \\ -1 & 2 \end{bmatrix}. \tag{3}$$

Hence, an augmented system yields

$$\mathscr{E}(y_k)\chi_{k+1} = \mathscr{A}(x_k, y_k)\chi_k + \mathscr{B}(y_k)u_k, \quad y_k = \mathscr{C}(x_k)\chi_k, \tag{4}$$

where $\chi \in \mathbb{R}^{n+(p+1)q}$, $S \in \mathbb{R}^{(pq+q)\times(pq+q)}$ is a known matrix, and

$$\begin{aligned} \mathscr{E}(y_k) &= \begin{bmatrix} E(y_k) & 0 \\ 0 & I \end{bmatrix}, \\ \mathscr{A}(x_k, y_k) &= \left[\begin{array}{c|c} A(x_k) & D(y_k)0_{n\times pq} \\ \hline 0 & S \end{array}\right], \\ \mathscr{B}(y_k) &= \begin{bmatrix} B(y_k) \\ 0 \end{bmatrix}, \\ \mathscr{C}(x_k) &= \begin{bmatrix} C(x_k) & 0 \end{bmatrix}. \end{aligned} \tag{5}$$

In the literature, most of the observer design approaches deal with systems in standard form (2); for instance, without the unknown input, $x_{k+1} = f(x_k, u_k)$ and $y_k = Cx_k$; they consider special cases $x_{k+1} = Ax_k + Bf(y_k, u_k) + \phi(x_k)$; thus, the task is to stabilize an error system with the form $e_{k+1} = (A - LC)e_k + \phi(x_k) - \phi(\hat{x}_k)$, where $e_k = x_k - \hat{x}_k$ is the estimation error, $\hat{x}_k$ is the estimated state vector, L is the observer gain to be designed, and the function $\phi(\cdot)$ is assumed to hold Lipschitz bounds, i.e., $\|\phi(x) - \phi(\hat{x})\| \leq \|\mathscr{L}x - \hat{x}\|$, $\mathscr{L} > 0$ being a Lipschitz constant [54, 55]. In the context of convex models, most of the works only consider that the scheduling variables are available and then $\phi(x_k) - \phi(\hat{x}_k) = 0$ [25], which, in practice, is not realistic. For the general case, when $\phi(x_k) - \phi(\hat{x}_k) \neq 0$, this expression is treated by means for Lipschitz bounds [24], as a perturbation via H_∞ approach [38], as an uncertainty via robust approaches [56]; other works employ the differential mean value theorem [37], Jacobian [57], or transformations that enlarge the size of the state [40]. Nevertheless, these approaches are conservative approximations, or increase the computational complexity of the problem, or are only valid for particular cases [58]; additionally, none of them consider observers for systems of form (1). Next section presents a methodology that avoids the use of previous ones.

2.1. An Amenable Descriptor Error Form. In order to obtain an amenable error system for Lyapunov analysis, in [41], a methodology that avoids the use of Lipschitz-like bounds has been presented; it is based on algebraic operations in order to factorize the estimation error at the left side of error dynamic difference equation. Thus, the variation of the Lyapunov function along the trajectories of the error system can be written as $\Delta V(e) = e_k^T Q(\cdot) e_k$ and $\Delta V(e) < 0$ if $Q(\cdot) < 0$, and the latter is guaranteed via convex models and linear matrix inequalities. Motivated by these ideas, the following observer structure is adopted:

$$\mathscr{E}(y_k)\widehat{\chi}_{k+1} = \mathscr{A}(\widehat{x}_k, y_k)\widehat{\chi}_k + \mathscr{B}(y_k)u_k + L(\widehat{x}_k, y_k)(y_k - \widehat{y}_k), \quad \widehat{y}_k = \mathscr{C}(\widehat{x}_k)\widehat{\chi}_k. \tag{6}$$

with

$$\widehat{\chi}_k = \begin{bmatrix} \widehat{x}_k \\ \widehat{\mathbf{d}}_{\mathbf{k}} \end{bmatrix},$$
$$\mathscr{A}(\widehat{x}_k, y_k) = \left[\begin{array}{c|c} A(\widehat{x}_k) & D(y_k)0_{n\times pq} \\ \hline 0 & S \end{array}\right], \tag{7}$$
$$\mathscr{C}(\widehat{x}_k) = [\, C(\widehat{x}_k) \;\; 0 \,],$$

and the nonlinear observer gain $L(\widehat{x}_k, y_k) \in \mathbb{R}^{(n+pq+q)\times o}$ depending only on all the available signals; it should be designed such that the estimation error

$$e_k = \chi_k - \widehat{\chi}_k = \begin{bmatrix} x_k - \widehat{x}_k \\ \mathbf{d}_{\mathbf{k}} - \widehat{d}_{\mathbf{k}} \end{bmatrix} \tag{8}$$

satisfies $\lim_{k\to\infty} e_k = 0$. Thus, in [41], it has been proven that, under mild assumptions, it is always possible to write the error dynamics as

$$\mathscr{E}(y_k)e_{k+1} = \left(\overline{\mathscr{A}}(x_k, \widehat{x}_k) - L(\widehat{x}_k, y_k)\overline{\mathscr{C}}(x_k, \widehat{x}_k)\right)e_k, \tag{9}$$

where $\overline{\mathscr{A}}(x_k, \widehat{x}_k)e_k = \mathscr{A}(x_k, y_k)\chi_k - \mathscr{A}(\widehat{x}_k, y_k)\widehat{\chi}_k$ and $\overline{\mathscr{C}}(x_k, \widehat{x}_k)e_k = \mathscr{C}(x)\chi_k - \mathscr{C}(\widehat{x})\widehat{\chi}_k$ have bounded entries in $\Omega_x \times \Omega_{\widehat{x}}$. For instance, consider a polynomial expression $p(x) - p(\widehat{x})$ with $p(x) = x_1x_2$ and $p(\widehat{x}) = \widehat{x}_1\widehat{x}_2$; following [41], we have $p(x) - p(\widehat{x}) = 0.5(x_2 + \widehat{x}_2)e_1 + 0.5(x_1 + \widehat{x}_1)e_2$, $e_1 = x_1 - \widehat{x}_1$, $e_2 = x_2 - \widehat{x}_2$. Now, consider a nonpolynomial expression $\widetilde{p}(x) - \widetilde{p}(\widehat{x})$, with $\widetilde{p}(x) = \sin x_1$ and $\widetilde{p}(\widehat{x}) = \sin \widehat{x}_1$; a third-order Taylor approximation will give $\widetilde{p}(x) - \widetilde{p}(\widehat{x}) \approx x_1 - (x_1^3/6) - \widehat{x}_1 + (\widehat{x}_1^3/6)$, and then we can apply similar procedure as before.

Now, error system (9) has an amenable form for Lyapunov-based analysis. However, if the aim is to obtain LMI conditions, (9) should be expressed as an exact convex model, and this is the matter of the following section.

2.2. Convex Expressions. The sector nonlinearity [18] is employed to express bounded nonconstant terms $z(\cdot) \in [z^0, z^1]$ as a convex sums of its bounds, that is, $z(\cdot) = w_0(z)z^0 + w_1(z)z^1$, where z^0 and z^1 are the minimum and maximum of $z(\cdot)$ in a region; the functions $w_0 = (z^1 - z(\cdot))/(z^1 - z^0)$ and $w_1 = 1 - w_0$ hold the convex sum property in the same modeling region, i.e., $w_0(z) + w_1(z) = 1$ and $w_0, w_1 \in [0, 1]$.

Note that, in (9), matrices $\mathscr{E}(y_k)$, $\overline{\mathscr{A}}(x_k, \widehat{x}_k)$, and $\overline{\mathscr{C}}(x_k, \widehat{x}_k)$ contain nonconstant terms depending on x_k, $\widehat{x}_k$, and y_k; clearly, all the state variables are not fully available; thus, a useful convex rewriting must take this into account. The following steps extend the sector nonlinearity to our case:

Step 1: identify all the nonconstant terms, also known as scheduling variables, in $\mathscr{E}(y_k)$, $\overline{\mathscr{A}}(x_k, \widehat{x}_k)$, and $\overline{\mathscr{C}}(x_k, \widehat{x}_k)$ depending exclusively on available signals, and capture them in the vector $z(\widehat{x}_k, y_k) \in \mathbb{R}^s$ while all the rest of the terms should be grouped in $\zeta(x_k, \widehat{x}_k, y_k) \in \mathbb{R}^\sigma$. Each entry is assumed to be bounded in $\Omega_x \times \Omega_{\widehat{x}}$, i.e., $z_i(\widehat{x}_k, y_k) \in [z_i^0, z_i^1]$, $i \in \{1, 2, \ldots, s\}$, and $\zeta_j(x_k, \widehat{x}_k, y_k) \in [\zeta_j^0, \zeta_j^1]$, $j \in \{1, 2, \ldots, \sigma\}$.

Step 2: construct, for each $z_i(\widehat{x}_k, y_k)$, $i \in \{1, 2, \ldots, s\}$, and $\zeta_j(x_k, \widehat{x}_k, y_k)$, $j \in \{1, 2, \ldots, \sigma\}$ a pair of scalar convex functions as follows:

$$w_0^i(\widehat{x}, y) = \frac{z_i^1 - z_i(\widehat{x}, y)}{z_i^1 - z_i^0},$$
$$w_1^i(\widehat{x}, y) = 1 - w_0^i(\widehat{x}, y),$$
$$\omega_0^j(x, \widehat{x}, y) = \frac{\zeta_j^1 - \zeta_j(x, \widehat{x}, y)}{\zeta_j^1 - \zeta_j^0}, \tag{10}$$
$$\omega_1^j(x, \widehat{x}, y) = 1 - \omega_0^j(x, \widehat{x}, y);$$

by construction, these functions hold the convex sum property in $\Omega_x \times \Omega_{\widehat{x}}$, i.e., $w_0^i(\widehat{x}, y) + w_1^i(\widehat{x}, y) = 1$, $w_0^i(\widehat{x}, y), w_1^i(\widehat{x}, y) \in [0, 1]$, $\omega_0^j(x, \widehat{x}, y) + \omega_1^j(x, \widehat{x}, y) = 1$, $\omega_0^j(x, \widehat{x}, y), \omega_1^j(x, \widehat{x}, y) \in [0, 1]$.

Step 3: define the scheduling functions as

$$\mathbf{w}_i(z) = w_{i_1}^j(z_1)w_{i_2}^2(z_2), \ldots, w_{i_s}^s(z_s),$$
$$\boldsymbol{\omega}_j(\zeta) = \omega_{j_1}^1(\zeta_1)\omega_{j_2}^2(\zeta_2), \ldots, \omega_{j_\sigma}^\sigma(\zeta_\sigma), \tag{11}$$

with $i \in \{1, 2, \ldots, r\}$, $j \in \{1, 2, \ldots, \rho\} i_j \in \{0, 1\}$, $r = 2^s$, $\rho = 2^\sigma$; moreover, the sets of indexes $[i_1 i_2, \ldots, i_s]$ and $[j_1 j_2, \ldots, j_\sigma]$ are a s-digit and σ-digit binary representation of $(i-1)$ and $(j-1)$, respectively. The scheduling functions also hold the convex sum property in $\Omega_x \times \Omega_{\widehat{x}}$, that is, $\sum_{i=1}^r \mathbf{w}_i(z) = 1$, $\mathbf{w}_i(z) \in [0, 1]$, $\sum_{j=1}^\rho \omega_j(\zeta) = 1$, and $\omega_j(\zeta) \in [0, 1]$.

Step 4: compute the vertex models $\mathscr{E}_i = \mathscr{E}(y_k)|_{\mathbf{w}_i=1}$, $\overline{\mathscr{A}}_{ij} = \overline{\mathscr{A}}(x_k, \widehat{x}_k)|_{\mathbf{w}_i\omega_j=1}$, $\overline{\mathscr{C}}_{ij} = \overline{\mathscr{C}}(x_k, \widehat{x}_k)|_{\mathbf{w}_i\omega_j=1}$, $i \in \{1, 2, \ldots, r\}$, $j \in \{1, 2, \ldots, \rho\}$.

Thus, an exact convex representation of (9) is

$$\sum_{i=1}^{r} \mathbf{w}_i(z_k)\mathscr{E}_i e_{k+1} = \sum_{i=1}^{r}\sum_{j=1}^{\rho} \mathbf{w}_i(z_k)\boldsymbol{\omega}_j(\zeta_k)\left(\overline{\mathscr{A}}_{ij} - L(\hat{x}_k, y_k)\overline{\mathscr{C}}_{ij}\right)e_k. \tag{12}$$

The nonlinear observer gain is $L(\hat{x}_k, y_k)$ and will be defined later on.

2.2.1. Notation. For convex expressions, the following shorthand notation will be employed throughout the manuscript: single convex sums $\Upsilon_{\mathbf{w}(z_k)} = \sum_{i=1}^{r} \mathbf{w}_i(z_k)\Upsilon_i$ and its inverse $\Upsilon^{-1}_{\mathbf{w}(z_k)} = (\sum_{i=1}^{r} \mathbf{w}_i(z_k)\Upsilon_i)^{-1}$, with delayed scheduling functions $\Upsilon_{\mathbf{w}(z_{k+1})} = \sum_{m=1}^{r} \mathbf{w}_m(z_{k+1})\Upsilon_m$, or depending on nonavailable variables $\Upsilon_{\omega(\zeta_k)} = \sum_{j=1}^{\rho} \omega_j(\zeta_k)\Upsilon_j$, and so on. Additionally, $A > 0\,(<0)$ means that $A \in \mathbb{R}^{n\times n}$ is positive (negative) definite. An asterisk $(*)$ will be used in matrix expressions to denote the transpose of the symmetric element; for in-line expressions, it will denote the transpose of the terms on its left side:

$$\begin{bmatrix} A & B^T \\ B & C \end{bmatrix} = \begin{bmatrix} A & (*) \\ B & C \end{bmatrix} \text{ and } A + B + A^T + B^T + C = A + B + (*) + C. \tag{13}$$

Hence, system (12) is shortly written as

$$\mathscr{E}_{\mathbf{w}(z_k)})e_{k+1} = \left(\overline{\mathscr{A}}_{\mathbf{w}(z_k)\boldsymbol{\omega}(\zeta_k)} - L(\hat{x}_k, y_k)\overline{\mathscr{C}}_{\mathbf{w}(z_k)\boldsymbol{\omega}(\zeta_k)}\right)e_k. \tag{14}$$

The following lemmas are useful in order to derive LMI conditions for the design of $L(\hat{x}_k, y_k)$. The first one concerns a sum-relaxation scheme based on [59]; the second one allows avoiding the computation of $\mathscr{E}^{-1}(y_k)$ while adding slack variables [27].

Lemma 1 (see [59]). *Let $\Upsilon^{jm}_{il} = (\Upsilon^{jm}_{il})^T$, $(i,l,m) \in \{1,2,\ldots,r\}^3$, $j \in \{1,2,\ldots,\rho\}$, be matrices of adequate dimensions. Then, $\Upsilon_{\mathbf{w}(z_k)\mathbf{w}(z_k)\mathbf{w}(z_{k+1})\omega(\zeta_k)} < 0$ holds if*

$$\frac{2}{r-1}\Upsilon^{jm}_{ii} + \Upsilon^{jm}_{il} + \Upsilon^{jm}_{li} < 0, \tag{15}$$

for all $(i,l,m) \in \{1,2,\ldots,r\}^3$, $j \in \{1,2,\ldots,\rho\}$.

Lemma 2 (see [60]). *Let $\xi \in \mathbb{R}^n$, $\mathscr{Q} = \mathscr{Q}^T \in \mathbb{R}^{n\times n}$, and $\mathscr{B} \in \mathbb{R}^{m\times n}$, $rank(\mathscr{B}) < n$; then, the following statements are equivalent:*

(i) $\xi^T\mathscr{Q}\xi < 0$, $\forall \mathscr{B}\xi = 0$, $\xi \neq 0$

(ii) $\exists \mathscr{Z} \in \mathbb{R}^{n\times m}$: $\mathscr{Q} + \mathscr{Z}\mathscr{B} + \mathscr{B}^T\mathscr{Z}^T < 0$

Now, we are ready to establish LMI conditions for the stabilization of error system (9) at the origin $e = 0$ via its exact convex representation (12).

3. LMI-Based Stabilization of the Error System

This section provides LMI conditions to compute $L(\hat{x}_k, y_k)$. The developments are based on a convex Lyapunov function candidate (in the context of TS models, it has been introduced as nonquadratic Lyapunov function [61], in the context of fuzzy systems as fuzzy Lyapunov functions [62], in the context of LPV models, as parameter dependent Lyapunov functions [63]. Here, the name convex Lyapunov function is adopted due to its dependence on the convex functions $\mathbf{w}_i(z_k)$):

$$V(e) = e_k^T P_{\mathbf{w}(z_k)} e_k, \quad P_{\mathbf{w}(z_k)} = \sum_{i=1}^{r} \mathbf{w}_i(z_k)P_i, \tag{16}$$

with $P_i \in \mathbb{R}^{(n+pq+q)\times(n+pq+q)}$: $P_i > 0$, $i \in \{1,2,\ldots,r\}$; its variation is

$$\Delta V(e) = e_{k+1}^T P_{\mathbf{w}(z_{k+1})} e_{k+1} - e_k^T P_{\mathbf{w}(z_k)} e_k, \tag{17}$$

which can be expressed as follows (without substituting the dynamics of estimation error (9)):

$$\Delta V(e) = \begin{bmatrix} e_k \\ e_{k+1} \end{bmatrix}^T \begin{bmatrix} -P_{\mathbf{w}(z_k)} & 0 \\ 0 & P_{\mathbf{w}(z_{k+1})} \end{bmatrix} \begin{bmatrix} e_k \\ e_{k+1} \end{bmatrix}. \tag{18}$$

Note that function (16) is convex and it only depends on available signals. With this in mind, the following result states LMI conditions for the design of the nonlinear gain $L(\hat{x}_k, y_k)$.

Theorem 1. *The origin $e = 0$ of error system (9), with an exact convex representation (12), is asymptotically stable if there exist matrices $P_l \in \mathbb{R}^{(n+pq+q)\times(n+pq+q)}$, $N_l \in \mathbb{R}^{(n+pq+q)\times o}$, and $G_l \in \mathbb{R}^{(n+pq+q)\times(n+pq+q)}$, $l \in \{1,2,\ldots,r\}$ such that $P_l > 0$ and the LMIs in (15) are satisfied with*

$$\Upsilon^{jm}_{il} := \begin{bmatrix} -P_l & (*) \\ G_l\overline{\mathscr{A}}_{ij} - N_l\overline{\mathscr{C}}_{ij} & -G_l\mathscr{E}_i - \mathscr{E}_i^T G_l^T + P_m \end{bmatrix}, \tag{19}$$

for all $(i,l,m) \in \{1,2,\ldots,r\}^3$, $j \in \{1,2,\ldots,\rho\}$. Then, the observer gain is computed as $L(\hat{x}_k, y_k) = G^{-1}_{\mathbf{w}(z_k)}N_{\mathbf{w}(z_k)}$. Moreover, any trajectory e_k starting in the outermost Lyapunov level set $\{e\colon V(e_k) \le c\} \subset \Omega_x \times \Omega_{\tilde{x}}$, $c > 0$ goes to zero as time goes to infinity.

Proof. Recall the variation of the Lyapunov function expressed as in (18); thus, error system (9), with exact convex representation (12), is also expressed as

$$\left[\overline{\mathscr{A}}_{\mathbf{w}(z_k)\boldsymbol{\omega}(\zeta_k)} - L(\hat{x}_k, y_k)\overline{\mathscr{C}}_{\mathbf{w}(z_k)\boldsymbol{\omega}(\zeta_k)} \;\; -\mathscr{E}_{\mathbf{w}(z_k)}\right]\begin{bmatrix} e_k \\ e_{k+1} \end{bmatrix} = 0. \tag{20}$$

By Lemma 2, (18) and (20) can be written together:

$$\begin{bmatrix} Z_1 \\ Z_2 \end{bmatrix}\left[\overline{\mathscr{A}}_{\mathbf{w}(z_k)\boldsymbol{\omega}(\zeta_k)} - L(\hat{x}_k, y_k)\overline{\mathscr{C}}_{\mathbf{w}(z_k)\boldsymbol{\omega}(\zeta_k)} - \mathscr{E}_{\mathbf{w}(z_k)}\right] + (*) + \begin{bmatrix} -P_{\mathbf{w}(z_k)} & 0 \\ 0 & P_{\mathbf{w}(z_{k+1})} \end{bmatrix} < 0. \tag{21}$$

Hence, by choosing $Z_1 = 0$ and $Z_2 = G_{\mathbf{w}(z_k)}$ and the definition $L(\hat{x}_k, y_k) = G^{-1}_{\mathbf{w}(z_k)}N_{\mathbf{w}(z_k)}$, $G_{\mathbf{w}(z_k)} \in \mathbb{R}^{(pq+q+n)\times(pq+q+n)}$, $N_{\mathbf{w}(z_k)} \in \mathbb{R}^{(pq+q+n)\times o}$, and we have

$$\Upsilon_{\mathbf{w}(z_k)\mathbf{w}(z_k)\mathbf{w}(z_{k+1})\boldsymbol{\omega}(\zeta_k)} \coloneqq \begin{bmatrix} -P_{\mathbf{w}(z_k)} & (*) \\ G_{\mathbf{w}(z_k)}\overline{\mathscr{A}}_{\mathbf{w}(z_k)\boldsymbol{\omega}(\zeta_k)} - N_{\mathbf{w}(z_k)}\overline{\mathscr{C}}_{\mathbf{w}(z_k)\boldsymbol{\omega}(\zeta_k)} & -G_{\mathbf{w}(z_k)}\mathscr{C}_{\mathbf{w}(z_k)} + (*) + P_{\mathbf{w}(z_{k+1})} \end{bmatrix} < 0. \tag{22}$$

Finally, by means of relaxation Lemma 1, the desired result yields. □

Remark 1. The speed convergence of observer (6) can be increased if the following condition is verified $\Delta V(e) \leq (\alpha^2 - 1)V(e)$, $0 < \alpha \leq 1$ which can be translated into LMIs, that is, solving the LMIs in (15) with

$$\Upsilon_{il}^{jm} \coloneqq \begin{bmatrix} -\alpha^2 P_l & (*) \\ G_l\overline{\mathscr{A}}_{ij} - \overline{N}_{lij} & -G_l\mathscr{E}_i - \mathscr{E}_i^T G_l^T + P_m \end{bmatrix}, \tag{23}$$

for all $(i,l,m) \in \{1,2,\ldots,r\}^3$, $j \in \{1,2,\ldots,\rho\}$.

The following result provides LMI conditions for standard systems and its corresponding observer, i.e., (6) with $E(y_k) = I_n$, where I_n is the identity matrix. Hence, the next result follows directly from Theorem 1.

Corollary 1. *The origin of error system (9), with $E(y_k) = I_n$, is asymptotically stable if there exist $P_l \in \mathbb{R}^{(n+pq+q)\times(n+pq+q)}$, $N_l \in \mathbb{R}^{(n+pq+q)\times o}$, and $G_l \in \mathbb{R}^{(n+pq+q)\times(n+pq+q)}$, $l \in \{1,2,\ldots,r\}$ such that $P_l > 0$ and LMIs in (15) hold with*

$$\Upsilon_{il}^{jm} = \begin{bmatrix} -P_l & (*) \\ G_l\overline{A}_{ij} - N_l\overline{C}_{ij} & -G_l - G_l^T + P_m \end{bmatrix}, \tag{24}$$

for all $(i,l,m) \in \{1,2,\ldots,r\}^3$, $j \in \{1,2,\ldots,\rho\}$. The nonlinear observer gain $L(\widehat{x}_k, y_k) = G_{\mathbf{w}(z_k)}^{-1} N_{\mathbf{w}(z_k)}$. Moreover, any trajectory e_k starting in the outermost Lyapunov level set $\{e\colon V(e) \leq c\} \subset \Omega_x \times \Omega_{\widehat{x}}, c > 0$ goes to zero as time goes to infinity.

Proof. It follows directly by considering $E(y_k) = I_n$ from the developments in Theorem 1. □

Remark 2. The methodology in previous approaches starts by computing a convex model of the given nonlinear one (standard or descriptor), and then, the estimation error is computed; if the problem involves unmeasurable scheduling variables, it is solved by considering the already defined scheduling functions. In contrast with those works, the methodology hereby presented begins by obtaining the nonlinear estimation error dynamics via factorizations; then, it employs the sector nonlinearity approach for writing an equivalent convex representation; thus, a fitter convex model is employed and the observer gain includes all the available signals.

Remark 3. In this work, a convex Lyapunov function such as the one introduced in [61] is employed; naturally delayed scheduling functions can be included similar to [25] or to the generalization [27]. For instance, following [25], the Lyapunov function candidate would be $V(e) = e_k^T P_{\mathbf{w}(z_{k-1})} e_k$, $P_{\mathbf{w}(z_{k-1})} = \sum_{m=1}^{r} \mathbf{w}_m(z_{k-1}) P_m$ together with the observer gain $L(\widehat{x}_k, \widehat{x}_{k-1}, y_k, y_{k-1}) = G_{\mathbf{w}(z_k)\mathbf{w}(z_{k-1})}^{-1} N_{\mathbf{w}(z_k)\mathbf{w}(z_{k-1})}$.

Remark 4. The numerical complexity of Theorem 1 can be approximated by $\log_{10}(n_d^3 n_l)$ where $n_d = r(n+pq+q)(0.5(n+pq+q+1)+n+pq+q+o)$ is the number of decision variables and $n_l = 2r^3\rho(n+pq+q)$ is the number of LMI rows [64]. Moreover, if the number LMI conditions in Theorem 1 is large, one can reduce its complexity by "judiciously eliminating" some convex functions either from the Lyapunov function or the observer gain.

In the case without unknown inputs ($d_k = 0$) in (1), the states of the resulting system can be estimated by the following nonlinear observer:

$$E(y_k)\widehat{x}_{k+1} = A(\widehat{x}_k, y_k)\widehat{x}_k + B(y_k)u_k + L(\widehat{x}_k, y_k)(y_k - \widehat{y}_k), \quad \widehat{y}_k = C(\widehat{x}_k, y_k)\widehat{x}_k, \tag{25}$$

where $\widehat{x}_k \in \mathbb{R}^n$ is the observer state and $L(\widehat{x}_k, y_k) \in \mathbb{R}^{n\times o}$ is the observer gain to be designed. Following the methodology previously presented, the error dynamics is

$$E(y_k)e_{k+1} = (\overline{A}(x_k, \widehat{x}_k) - L(\widehat{x}_k, y_k)\overline{C}(x_k, \widehat{x}_k))e_k, \tag{26}$$

where $\overline{A}(x_k, \widehat{x}_k)e_k = A(x_k)x_k - A(\widehat{x}_k, y_k)\widehat{x}_k$ and $\overline{C}(x_k, \widehat{x}_k)e_k = C(x_k)x_k - C(\widehat{x}_k, y_k)\widehat{x}_k$. Thus, we have the next result.

Corollary 2. *The origin of error system (26) is asymptotically stable if there exist $P_l \in \mathbb{R}^{n\times n}$, $N_l \in \mathbb{R}^{n\times o}$, and $G_l \in \mathbb{R}^{n\times n}$, $l \in \{1,2,\ldots,r\}$ such that $P_l > 0$ and LMIs in (15) hold with*

$$\Upsilon_{il}^{jm} = \begin{bmatrix} -P_l & (*) \\ G_l\overline{A}_{ij} - N_l\overline{C}_{ij} & -G_lE_i - E_i^T G_l^T + P_m \end{bmatrix}, \tag{27}$$

for all $(i,l,m) \in \{1,2,\ldots,r\}^3$, $j \in \{1,2,\ldots,\rho\}$. The nonlinear observer gain $L(\widehat{x}_k, y_k) = G_{\mathbf{w}(z_k)}^{-1} N_{\mathbf{w}(z_k)}$. Moreover, any trajectory e_k starting in the outermost Lyapunov level set $\{e\colon V(e) \leq c\} \subset \Omega_x \times \Omega_{\widehat{x}}, c > 0$ goes to zero as time goes to infinity.

Proof. The proof follows a similar path than the one for Theorem 1, with a Lyapunov function candidate $V(e) = e_k^T P_{\mathbf{w}(z_k)} e_k$, $P_i > 0$, $P_i \in \mathbb{R}^{n\times n}$, $i \in \{1,2,\ldots,r\}$, and the nonlinear error dynamics (26) expressed in a convex form as

$$\left[\overline{A}_{\mathbf{w}(z_k)\boldsymbol{\omega}(\zeta_k)} - L(\widehat{x}_k, y_k)\overline{C}_{\mathbf{w}(z_k)\boldsymbol{\omega}(\zeta_k)} \quad -E_{\mathbf{w}(z_k)}\right]\begin{bmatrix} e_k \\ e_{k+1}\end{bmatrix} = 0, \tag{28}$$

and by the use of Finsler's lemma, with $L(\widehat{x}_k, y_k) = G^{-1}_{\mathbf{w}(z_k)}N_{\mathbf{w}(z_k)}$, $Z_1 = 0$, and $Z_2 = G_{\mathbf{w}(z_k)}$, we have

$$\Upsilon_{\mathbf{w}(z_k)\mathbf{w}(z_k)\mathbf{w}(z_{k+1})\boldsymbol{\omega}(\zeta_k)} \coloneqq \begin{bmatrix} -P_{\mathbf{w}(z_k)} & (*) \\ G_{\mathbf{w}(z_k)}\overline{A}_{\mathbf{w}(z_k)\boldsymbol{\omega}(\zeta_k)} - N_{\mathbf{w}(z_k)}\overline{C}_{\mathbf{w}(z_k)\boldsymbol{\omega}(\zeta_k)} & -G_{\mathbf{w}(z_k)}E_{\mathbf{w}(z_k)} + (*) + P_{\mathbf{w}(z_{k+1})}\end{bmatrix} < 0. \tag{29}$$

Finally, by means of relaxation Lemma 1, we conclude the proof.

Recall that most of the previous works do not consider scheduling functions depending on unmeasurable variables [25, 27] nor descriptor systems of form (1) [25]. □

4. Actuator Fault Detection and Estimation

In this section, an application of the UI observer developed above is employed in order to estimate and detect actuator faults [46, 47]. Thus, let us now consider nonlinear discrete-time descriptor system (1) with an actuator fault:

$$E(y_k)x_{k+1} = A(x_k)x_k + B(y_k)u_k + f_a(u_k, y_k) + D(y_k)d_k, \quad y_k = C(x_k)x_k, \tag{30}$$

where $f_a(u_k, y_k) \in \mathbb{R}^m$ represents the actuator fault vector; if it can be included inside of the unknown input, then (30) can be expressed as (1); in this case, conditions in Theorem 1 can be used. As customary in fault detection schemes, a residual signal based on the observer estimation of the unknown input is generated [65, 66]:

$$r_k = \left\|\widehat{d}_k\right\|. \tag{31}$$

The residual can be filtered to get a clear signal. The estimation of the fault can be done once the fault is considered as an unknown input [67].

Remark 5. It is possible to apply a mix of H_∞ and H_- performances, for instance, H_∞ attenuation in order to make residual (31) robust to uncertainties, noise, and the fault and the index H_- index in order to make more sensitive the detection of the fault [68, 69].

5. Examples

In this section, two examples are presented. The first one is intended to compare the performance of our proposal in contrast with recent approaches while the second one illustrates the estimation of actuator faults in the train system. The LMI conditions have been implemented in YALMIP [70] with SeDuMi [71], while simulations have been run in Simulink for MATLAB2019b.

Example 1. Consider descriptor system (1) with matrices

$$\begin{aligned} E(y_k) &= \begin{bmatrix} 2 & -\left(1+x_1^2\right)^{-1} \\ \left(1+x_1^2\right)^{-1} & 1\end{bmatrix}, \\ A(x_k) &= \begin{bmatrix} x_2^2 & -0.5\beta \\ 0.7 & \sin x_1\end{bmatrix}, \\ B &= \begin{bmatrix} 0.1 \\ 0.1\end{bmatrix}, \\ D &= \begin{bmatrix} 0.2 \\ 0.2\end{bmatrix}, \\ C &= \begin{bmatrix} 1 \\ 0\end{bmatrix}^T, \end{aligned} \tag{32}$$

with $\beta > 0$ is a known parameter. It is assumed that the unknown input has dynamics such as $(z-1)^2 d_k \approx 0$, i.e., $\mathbf{d}_{k+1} = S\mathbf{d}_k$ with $S = \begin{bmatrix} 0 & 1 \\ -1 & 2\end{bmatrix}$. In order to estimate both the state x_k and the unknown input d_k, an extended system of form (4) and its corresponding observer (6) are constructed. Thus, the error dynamics $e_k = \chi_k - \widehat{\chi}_k$ can be computed as

$$\mathscr{E}(y_k)e_{k+1} = \begin{bmatrix} x_1x_2^2 - 0.5\beta x_2 + 0.2d_1 \\ 0.7x_1 + x_2\sin x_1 + 0.2d_1 \\ d_2 \\ -d_1 + 2d_2\end{bmatrix} - \begin{bmatrix} \widehat{x}_1\widehat{x}_2^2 - 0.5\beta\widehat{x}_2 + 0.2\widehat{d}_1 \\ 0.7\widehat{x}_1 + \widehat{x}_2\sin\widehat{x}_1 + 0.2\widehat{d}_1 \\ \widehat{d}_2 \\ -\widehat{d}_1 + 2\widehat{d}_2\end{bmatrix} - L(\cdot)(y - \widehat{y}). \tag{33}$$

Applying the factorization methodology in [41] and considering that $y = x_1$, we have $x_2^2 - \widehat{x}_2^2 = (x_2 + \widehat{x}_2)(x_2 - \widehat{x}_2) = (x_2 + \widehat{x}_2)e_2$ leading to final error dynamics

$$\underbrace{\begin{bmatrix} 2 & -(1+x_1^2)^{-1} & 0 & 0 \\ (1+x_1^2)^{-1} & 1 & 0 & 0 \\ 0 & 0 & 1 & 0 \\ 0 & 0 & 0 & 1 \end{bmatrix}}_{\mathscr{E}(y_k)} e_{k+1} = \left(\underbrace{\begin{bmatrix} 0 & x_1(x_2+\widehat{x}_2) - 0.5\beta & 0.2 & 0 \\ 0.7 & \sin x_1 & 0.2 & 0 \\ 0 & 0 & 0 & 1 \\ 0 & 0 & -1 & 2 \end{bmatrix}}_{\overline{\mathscr{A}}(x_k, \widehat{x}_k)} - L(\cdot) \underbrace{\begin{bmatrix} 1 & 0 & 0 & 0 \end{bmatrix}}_{\overline{\mathscr{C}}} \right) e_k. \tag{34}$$

In order to synthesize the nonlinear observer gain via LMIs, it is necessary to express (34) in a convex form (12); to this end, let us consider the compact sets $\Omega_x = \{|x_1| \le 0.5, |x_2| \le 0.8\}$ and $\Omega_{\widehat{x}} = \{|\widehat{x}_2| \le 0.8\}$. Thus, the nonconstant terms and their bounds are $z_1 = (1+x_1^2)^{-1} \in [0.8, 1]$, $z_2 = \sin x_1 \in [-0.4794, 0.4794]$, $z_3 = x_1 \in [-0.5, 0.5]$, $z_4 = \widehat{x}_2 \in [-0.8, 0.8]$, and $\zeta_1 = x_2 \in [-0.8, 0.8]$ (nonavailable signals). The scalar convex functions are $\mathbf{w}_i(z) = w_{i_1}^1(z_1) w_{i_2}^2(z_2) w_{i_3}^3(z_3) w_{i_4}^4(z_4)$, $w_0^i(z_i) = (z_i^1 - z_i)/(z_i^1 - z_i^0)$, $w_1^i(z_i) = 1 - w_0^i(z_i)$, $i \in \{1, 2, 3, 4\}$, and $\omega_j(\zeta) = \omega_{j_1}^1(\zeta_1)$, $\omega_0^1(\zeta_1) = (\zeta_1^1 - \zeta_1)/(\zeta_1^1 - \zeta_1^0)$, $\omega_1^1 = 1 - \omega_0^1$. The vertex matrices are

$$\begin{aligned} \mathscr{E}_i &= \begin{bmatrix} 2 & -z_1^{i_1} & 0 & 0 \\ z_1^{i_1} & 1 & 0 & 0 \\ 0 & 0 & 1 & 0 \\ 0 & 0 & 0 & 1 \end{bmatrix}, \\ \overline{\mathscr{A}}_{ij} &= \begin{bmatrix} 0 & z_3^{i_3}\left(\zeta_1^{j_1} + z_4^{i_4}\right) - 0.5\beta & 0.2 & 0 \\ 0.7 & z_2^{i_2} & 0.2 & 0 \\ 0 & 0 & 0 & 1 \\ 0 & 0 & -1 & 2 \end{bmatrix}. \end{aligned} \tag{35}$$

For example, if $i = 6$ and $j = 1$, we have $\mathbf{w}_6(z) = w_0^1(z_1) w_1^2(z_2) w_0^3(z_3) w_1^4(z_4)$, $\omega_1(\zeta) = \omega_0^1(\zeta_1)$, and

$$\begin{aligned} \mathscr{E}_6 &= \begin{bmatrix} 2 & -z_1^0 & 0 & 0 \\ z_1^0 & 1 & 0 & 0 \\ 0 & 0 & 1 & 0 \\ 0 & 0 & 0 & 1 \end{bmatrix} = \begin{bmatrix} 2 & -0.8 & 0 & 0 \\ 0.8 & 1 & 0 & 0 \\ 0 & 0 & 1 & 0 \\ 0 & 0 & 0 & 1 \end{bmatrix}, \\ \overline{\mathscr{A}}_{6,1} &= \begin{bmatrix} 0 & z_3^0\left(\zeta_1^0 + z_4^1\right) - 0.5\beta & 0.2 & 0 \\ 0.7 & z_2^1 & 0.2 & 0 \\ 0 & 0 & 0 & 1 \\ 0 & 0 & -1 & 2 \end{bmatrix} = \begin{bmatrix} 0 & -0.5\beta & 0.2 & 0 \\ 0.7 & 0.4794 & 0.2 & 0 \\ 0 & 0 & 0 & 1 \\ 0 & 0 & -1 & 2 \end{bmatrix}. \end{aligned} \tag{36}$$

Several numerical tests have been performed in order to show the effectiveness of the proposal in contrast with recent works:

(i) LMIs in Theorem 1 have been run as well as the ones in [45], Theorem 2, with a Lyapunov function candidate (16) and decay rate $\alpha = 0.95$ (see Remark 1), seeking feasibility for the largest $\beta > 0$. It results that our proposal is feasible up to $\beta = 0.863$, while the one in [45], Theorem 2, is only up to $\beta = 0.794$. Comparisons have been done with the same Lyapunov function (16) and under the same relaxation scheme.

(ii) In terms of the number of decision variables, for this example, we have that numerical complexity for Theorem 1 is 12.86 while for [45] is 10.24.

(iii) A UI observer uses the generalization in [27], and although it is for discrete-time descriptor systems, it cannot be applied as it only considers available scheduling variables.

(iv) If UI observer schemes for standard state-space models are to be applied [33, 39], then the inverse of the matrix $E(y_k)$ has to be computed. For instance, using conditions in Corollary 1 yields numerical problems because 65568 LMIs have to be solved.

For illustration purposes, the LMI conditions in form (1) have been found feasible for $\beta = 0.85$ and a decay rate $\alpha = 0.95$, and some of the computed matrices are

$$N_1 = 1 \times 10^{-4} \begin{bmatrix} 0.3502 \\ 0.4455 \\ 0.0786 \\ -0.0245 \end{bmatrix},$$

$$G_1 = 1 \times 10^{-4} \begin{bmatrix} 0.4528 & 0.4482 & -0.1117 & -0.0147 \\ -0.4197 & 0.6839 & 0.0704 & -0.0772 \\ 0.0656 & -0.3033 & 0.7189 & -0.5508 \\ -0.0796 & 0.1505 & -0.5751 & 0.4700 \end{bmatrix},$$

$$N_5 = 1 \times 10^{-4} \begin{bmatrix} 0.4936 \\ 0.5295 \\ 0.0875 \\ -0.0429 \end{bmatrix},$$

$$G_5 = 1 \times 10^{-4} \begin{bmatrix} 0.3710 & 0.5399 & -0.2236 & 0.0594 \\ -0.4458 & 0.6316 & 0.0105 & -0.0417 \\ 0.0960 & -0.2168 & 0.6811 & -0.5264 \\ -0.0961 & 0.0893 & -0.5422 & 0.4492 \end{bmatrix},$$

$$N_{16} = 1 \times 10^{-4} \begin{bmatrix} -0.1330 \\ 0.7569 \\ 0.1866 \\ -0.0911 \end{bmatrix},$$

$$G_{16} = 1 \times 10^{-4} \begin{bmatrix} 0.8122 & -0.3260 & 0.0464 & -0.0970 \\ -0.0814 & 0.9592 & -0.2018 & 0.0460 \\ -0.0773 & -0.1013 & 0.6744 & -0.5174 \\ -0.0047 & 0.0364 & -0.5419 & 0.4463 \end{bmatrix}. \tag{37}$$

A first simulation has been performed without unknown inputs, i.e., $d_k = 0$ and the known input $u_k = 0.4 \sin(0.6k)$. Figure 1 shows evolution of the error signals converging asymptotically to the origin. A second simulation considers $u_k = 0$, and the unknown input is defined as

$$d_k = \begin{cases} 0.4k, & \text{if } 3 \le k < 5, \\ 0.8, & \text{if } 5 \le k < 12, \\ 0, & \text{otherwise}, \end{cases} \tag{38}$$

and initial conditions $x(0) = [0.4 - 0.6]^T$, $\mathbf{d}(0) = \begin{bmatrix} 0 & 0 \end{bmatrix}^T$, $\widehat{x}(0) = \begin{bmatrix} 0 & 0 \end{bmatrix}^T$, and $\widehat{d}(0) = \begin{bmatrix} 0 & 0 \end{bmatrix}^T$. Figure 2 shows the state x_2 being adequately estimated while in Figure 3, it can be seen that the observer effectively reconstructs the unknown input.

The next example provides an application of the UI observer hereby proposed for the task of actuator fault detection in a train system.

Example 2. This example provides a fault detection scheme via the proposed UI observer for a train system, and see Figure 4 for a diagram. Let us consider first the fault-free case, and thus, a continuous-time model is [72–74]

$$\begin{aligned} M\dot{v}(t) &= b_T(v(t))u_T(t) - b_B(v(t))u_B(t) - w(v(t)) - g(\theta(p)), \\ \dot{p}(t) &= v(t), \end{aligned} \tag{39}$$

where $v(t)$ is the speed of the train, $p(t)$ is the position of the train, $b_B(v)$ is the maximum coefficient of the braking force, $u_B(t)$ is the relative braking force, $b_T(v)$ is the maximum coefficient of the traction force, $u_T(t)$ is the relative traction force, $g(\theta)$ is the force of declivity or external force, $w(v)$ is the friction force, and M is the mass of the train. In practical cases, the declivity force is considered as $g(\theta(p)) = Mg\sin(\theta(p))$, where $\theta(p)$ is the slope angle on the position $p(t)$ and g is the gravity force [75]. In [76], the friction force $w(v)$ can be estimated via David's equation:

$$w(v) = w_0 + w_1 v + w_2 v^2, \tag{40}$$

where w_0, w_1, and w_2 are real coefficients that depend on the train characteristics and rail type; their values are unknown in the practice, but there exist some methods for their estimation [76]. By means of the Euler approximation $\dot{x}(t) \approx (x_{k+1} - x_k)/T_s$, where T_s is the sampling time. Therefore, a discrete-time train system of (23) is

$$\begin{aligned} Mv_{k+1} = &\left(b_T(v_k)u_{T_k} - b_B(v_k)u_{B_k} - w(v_k)\right. \\ &\left. - g(\theta(p_k))\right)T_s + Mv_k, \quad p_{k+1} = v_k T_s + p_k. \end{aligned} \tag{41}$$

The fault studied in this example is the jamming fault, and it may occur only during the braking. This fault depends on the adherence conditions between the wheel and the track, producing that when the brake locks the wheel, the wheel slides on the track [68, 74]; in the real setup, the fault can occur depending on weather conditions. The main issue of a jamming fault is the impact directly on the measurements, producing a wrong estimate of both position and speed of the train. In Figure 5, it

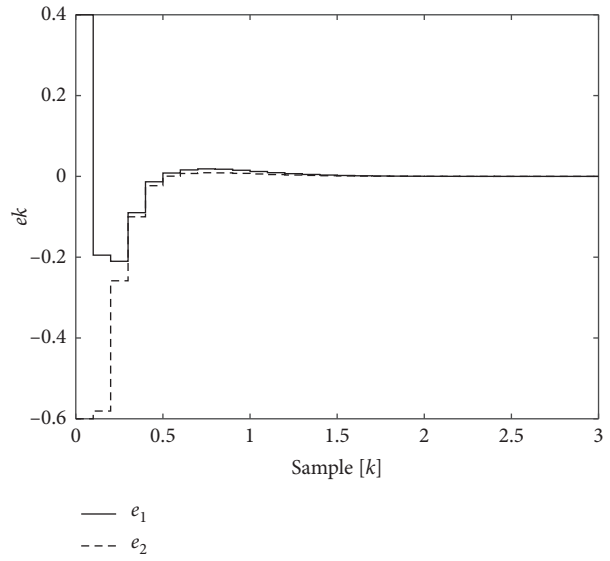

Figure 1: Error signal e_k in the absence of unknown inputs.

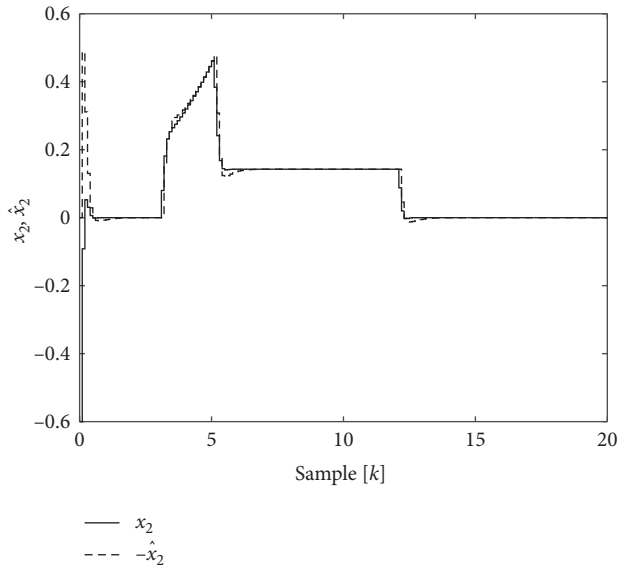

Figure 2: State x_2 and its estimation $\widehat{x}_2$.

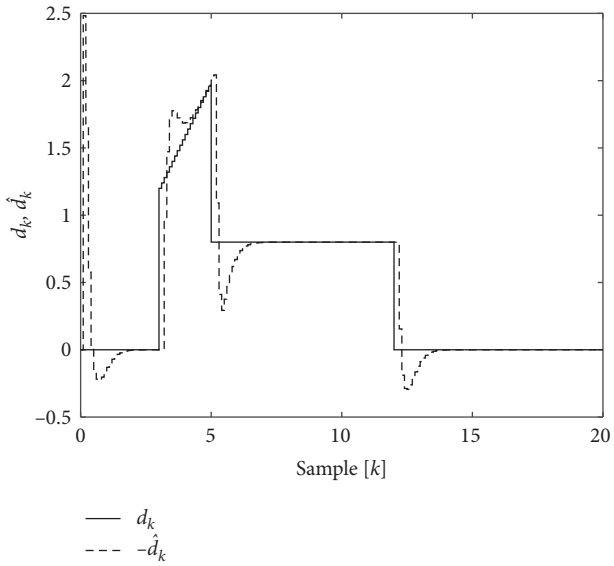

Figure 3: Unknown input d_k and its estimation $\widehat{d}_k$.

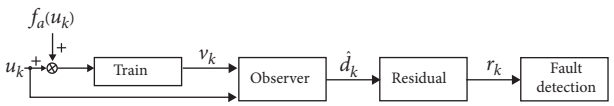

Figure 4: Fault detection scheme.

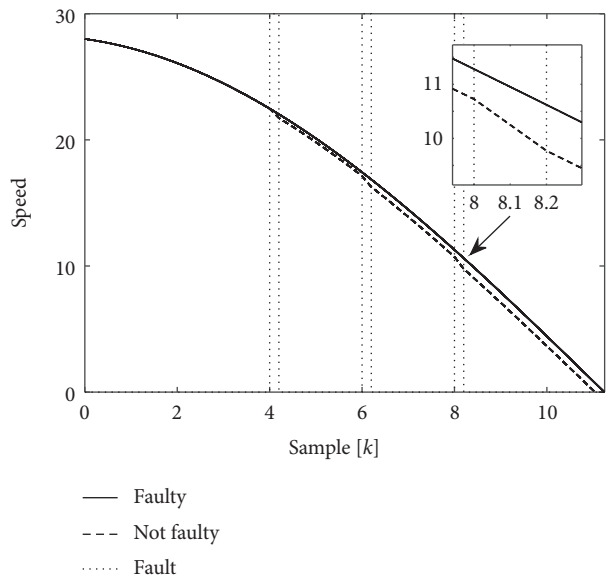

Figure 5: Comparison between the time evolution of the speed v_k with fault and without fault.

can be seen that the speed v_k under the fault is lower, and this is because the wheel is locked during the fault and the sensor is not able to provide the right measure and thus both the speed and position are erroneous; for example, the measured position differs 4.10 meters from the real position, see Figure 6. Therefore, this fault can be considered as an actuator fault or exogenous input, when it occurs, the control is inhibited [72–74]. The actuator fault to be considered is

$$f_a\left(u_{T_k}, u_{B_k}\right) = -\left(b_T\left(v_k\right)u_{T_k} - b_B\left(v_k\right)u_{B_k} + \xi_k\right)f_k, \qquad (42)$$

where $f_k \in [0, 1]$ represents the grade of the fault; if $f_k = 0$, then the system is fault-free; if $f_k = 1$, a total fault occurs and the control is inhibited. The term $\xi_k \in \mathbb{R}$ represents a resistive force produced by the fault, and it is unknown [74].

As the previous examples, the unknown input is assumed to comply with $\mathbf{d}_{k+1} = S\mathbf{d}_k$; therefore, we have an augmented system of form (3) with $\chi = \left[\begin{array}{cccc} v_k & p_k & d_k & d_{k+1} \end{array}\right]^T$ and matrices

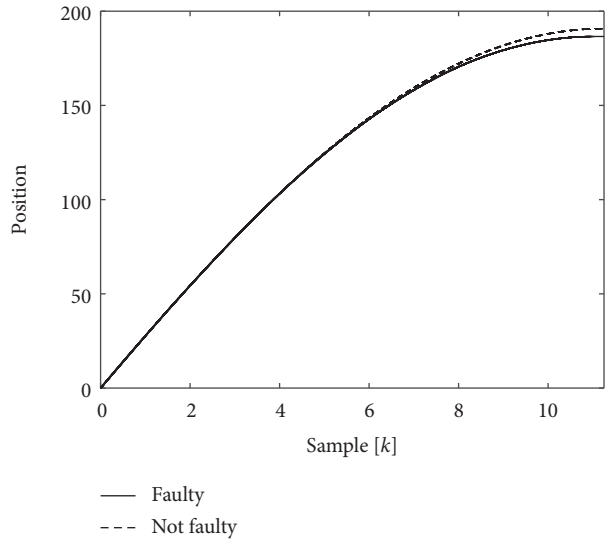

Figure 6: Comparison between the time evolution of the position p_k with fault and without fault.

$$\mathscr{E} = \begin{bmatrix} M & 0 & 0 & 0 \\ 0 & 1 & 0 & 0 \\ 0 & 0 & 1 & 0 \\ 0 & 0 & 0 & 1 \end{bmatrix},$$

$$\mathscr{A}(y_k) = \begin{bmatrix} (-w_1 - w_2 v_k)T_s + M & T_s g \dfrac{(\theta(p_k))}{p_k} & T_s & 0 \\ T_s & 1 & 0 & 0 \\ 0 & 0 & 0 & 1 \\ 0 & 0 & -1 & 2 \end{bmatrix},$$

$$\mathscr{B} = \begin{bmatrix} b \\ 0 \\ 0 \\ 0 \end{bmatrix},$$

$$\mathscr{C} = \begin{bmatrix} 1 \\ 0 \\ 0 \\ 0 \end{bmatrix}^T, \tag{43}$$

and the parameter b is a constant value for $b_B(v)$ and $b_T(v)$, producing a unique control signal u_k, where $u_k > 0$ and $u_k < 0$ correspond to u_{T_k} and u_{B_k}, respectively. Let us consider the braking period, i.e., when the train is arriving to the station and there are no big slopes, we have $g(\theta(p_k)) = Mg\sin(\theta(p_k))$, with $\theta(p_k) = \beta p_k \in [-1, 1]$, where β is a constant.

Thus, with UI observer (4), the error dynamics $e_k = \chi_k - \widehat{\chi}_k$ is

$$\begin{aligned} \mathscr{E}e_{k+1} = & \begin{bmatrix} \left(-w_1 v_k - w_2 v_k^2 + d_k\right)T_s + M v_k - T_s M g \sin(\beta p_k) \\ T_s v_k + p_k \\ d_{k+1} \\ -d_k + 2d_{k+1} \end{bmatrix} \\ & - \begin{bmatrix} \left(-w_1 \widehat{v}_k - w_2 \widehat{v}_k^2 + \widehat{d}_k\right)T_s + M\widehat{v}_k - T_s M g \sin(\beta \widehat{p}_k) \\ T_s \widehat{v}_k + \widehat{p}_k \\ \widehat{d}_{k+1} \\ -\widehat{d}_k + 2\widehat{d}_{k+1} \end{bmatrix} \\ & - L(\cdot)(y - \widehat{y}). \end{aligned} \tag{44}$$

Applying the factorization in [41] and considering that $y_k = v_k$ (the only available signal is the velocity v_k), we have $v_k^2 - \widehat{v}_k^2 = (v_k + \widehat{v}_k)e_1 = 2y_k e_1$, $e_1 = v_k - \widehat{v}_k$, as for $\sin(\beta p_k) - \sin(\beta \widehat{p}_k)$, two terms of the series Taylor are taken; then, the error dynamics yields:

$$\mathscr{E}e_{k+1} = \left(\overline{\mathscr{A}}(y_k, \chi_k, \widehat{\chi}_k) - L(y_k)\overline{\mathscr{C}}\right)e_k, \tag{45}$$

with matrices

$$\overline{\mathscr{A}}(y_k,\chi_k,\widehat{\chi}_k)=\begin{bmatrix}-(w_1+2w_2y_k)T_s+M & T_sMg\left(-1-\dfrac{\beta^3}{6}\left(p_k^2+p_k\widehat{p}_k+\widehat{p}_k^2\right)\right) & T_s & 0\\ T_s & 1 & 0 & 0\\ 0 & 0 & 0 & 1\\ 0 & 0 & -1 & 2\end{bmatrix},$$
$$\overline{\mathscr{C}}=\begin{bmatrix}1\\0\\0\\0\end{bmatrix}^T. \tag{46}$$

Therefore, considering that $v_k \in [0,30]$ (m/s) and $p_k, \widehat{p}_k \in [0,600]$ (m), we have that the nonconstant terms are $z = v_k \in [0,30]$ (available), $\zeta_1 = p_k^2 \in [0,360000]$, $\zeta_2 = p_k \in [0,600]$, $\zeta_3 = \widehat{p}_k \in [0,600]$, and $\zeta_4 = \widehat{p}_k^2 \in [0,360000]$ (nonavailable signals). The scheduling functions are defined as $\omega_j(\zeta) = \omega_{j_1}^1(\zeta_1)\omega_{j_2}^2(\zeta_2)\omega_{j_3}^3(\zeta_3)\omega_{j_4}^4(\zeta_4)$, $\omega_0^j(\zeta_j) = (\zeta_j^1 - \zeta_j)/(\zeta_j^1 - \zeta_j^0)$, $\omega_1^j = 1 - \omega_0^j(\zeta_j)$, and $\mathbf{w}_1(z) = (z^1 - z)/(z^1 - z^0)$, $\mathbf{w}_2(z) = 1 - \mathbf{w}_1(z)$. The vertex matrices are

$$\overline{\mathscr{A}}_{i,j}=\begin{bmatrix}-\left(w_1+2w_2z^i\right)T_s+M & T_sMg\left(-1-\dfrac{\beta^3}{6}\left(\zeta_1^{j_1}+\zeta_2^{j_2}\zeta_3^{j_3}+\zeta_4^{j_4}\right)\right) & T_s & 0\\ T_s & 1 & 0 & 0\\ 0 & 0 & 1 & 0\\ 0 & 0 & -1 & 2\end{bmatrix}, \tag{47}$$

where $i = \{1,2\}$ and $j = \{1,2,3,4\}$. The LMI conditions in Theorem 1 have been found feasible with a decay rate $\alpha = 0.7$ (see Remark 1), and the parameters are $M = 408.5$ tons, $w_0 = 3.525$(N), $w_1 = 2.98 \times 10^{-}3$(N/m), $w_2 = 4.575 \times 10^{-}4$(N^2/m^2), and $T_s = 0.001$(s). The computed matrices are

$$
N_1 = 1 \times 10^{-5} \begin{bmatrix} 139.52295 \\ 0.00157 \\ -0.00023 \\ 0.00003 \end{bmatrix},
$$

$$
N_2 = 1 \times 10^{-5} \begin{bmatrix} 151.49720 \\ 0.00172 \\ -0.00022 \\ 0.00003 \end{bmatrix},
$$

$$
G_1 = 1 \times 10^{-5} \begin{bmatrix} 0.34152 & 0.00284 & -0.00070 & 0.00035 \\ 0.000007 & 0.0000001 & -0.00000003 & 0.00000002 \\ -0.000001 & -0.00000003 & 0.00000001 & -0.00000001 \\ 0.0000008 & 0.00000002 & -0.00000001 & 0.000000008 \end{bmatrix},
$$

$$
G_2 = 1 \times 10^{-5} \begin{bmatrix} 0.36992 & 0.00305 & -0.00071 & 0.00035 \\ 0.000007 & 0.0000001 & -0.00000003 & 0.00000002 \\ -0.000001 & -0.00000003 & 0.00000001 & -0.00000001 \\ 0.0000008 & 0.00000002 & -0.00000001 & 0.000000008 \end{bmatrix},
$$

$$
P_1 = 1 \times 10^{-5} \begin{bmatrix} 125.55422 & 0.00267 & -0.00065 & 0.00033 \\ 0.00267 & 0.00000009 & -0.00000003 & 0.00000002 \\ -0.00065 & -0.00000003 & 0.00000001 & -0.00000001 \\ 0.00033 & 0.00000002 & -0.00000001 & 0.0000000075 \end{bmatrix},
$$

$$
P_2 = 1 \times 10^{-5} \begin{bmatrix} 129.30379 & 0.00278 & -0.00068 & 0.00035 \\ 0.00278 & 0.0000001 & -0.00000003 & 0.00000002 \\ -0.00068 & -0.00000003 & 0.00000001 & -0.00000001 \\ 0.00035 & 0.00000002 & -0.00000001 & 0.000000007 \end{bmatrix}. \tag{48}
$$

A simulation has been performed for initial conditions $v(0) = 28$, $p(0) = 0$, $\mathbf{d}(0) = \begin{bmatrix} 0 & 0 \end{bmatrix}^T$, $\widehat{v}(0) = 27.9$, $\widehat{p}(0) = 0.05$, and $\widehat{\mathbf{d}}(0) = \begin{bmatrix} 0.05 & 0.01 \end{bmatrix}^T$, with a constant braking force $u_k = -0.5$, $\beta = 0.0016$, and the unknown input $d_k = f_a(u_k)$, with $\xi_k = 2M$ and the fault occurrence

$$
f_k = \begin{cases} 1, & \text{if } 4 \le k \le 4.2, \\ 1, & \text{if } 6 \le k \le 6.2, \\ 1, & \text{if } 8 \le k \le 8.2, \\ 0, & \text{otherwise.} \end{cases} \tag{49}
$$

As the previous example, first simulation has been performed without unknown inputs, i.e., $d_k = 0$. Figure 7 shows the speed being adequately estimated while Figure 8 plots the Lyapunov function, whose signal is always positive and monotonously decreases to zero.

In the case where $d_k = f_a(u_k)$, in order to detect the fault, the unknown input estimation is used as residual $r_k = |\widehat{d}_k|$ with a single threshold of $\epsilon = M/2$. If the residual r_k is bigger than ϵ, then the fault is occurring; otherwise, the fault has finished. Thus, we obtain a delay average of 0.003 seconds to detect when the fault begins and 0.006 to detect when the fault ends. As we can see from Figure 9, our proposal is enough to detect when the fault occurs.

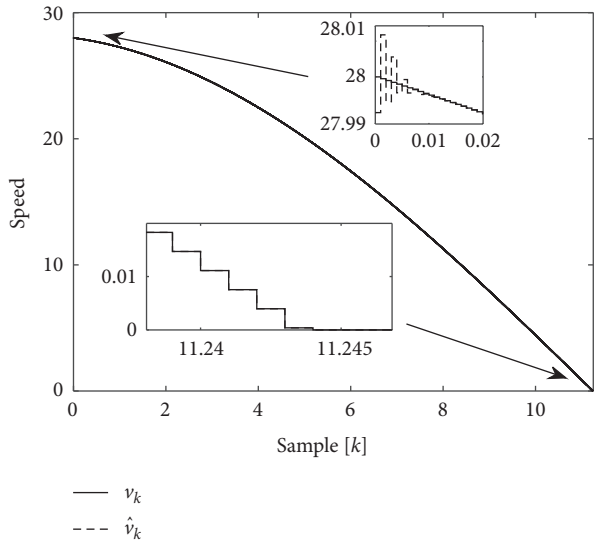

Figure 7: The time evolution of the speed v_k and its estimation $\hat{v}_k$.

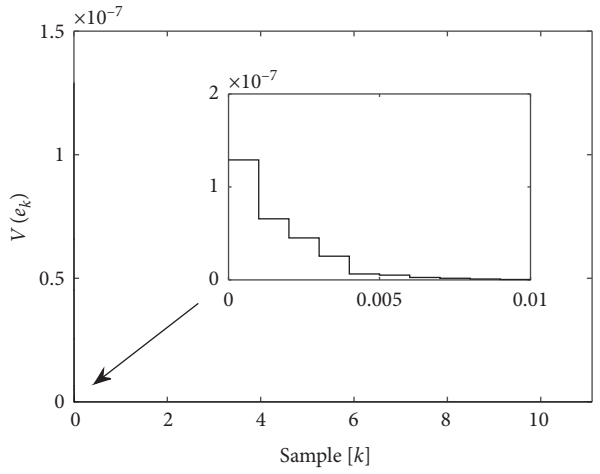

Figure 8: The time evolution of the Lyapunov function $V(e)$.

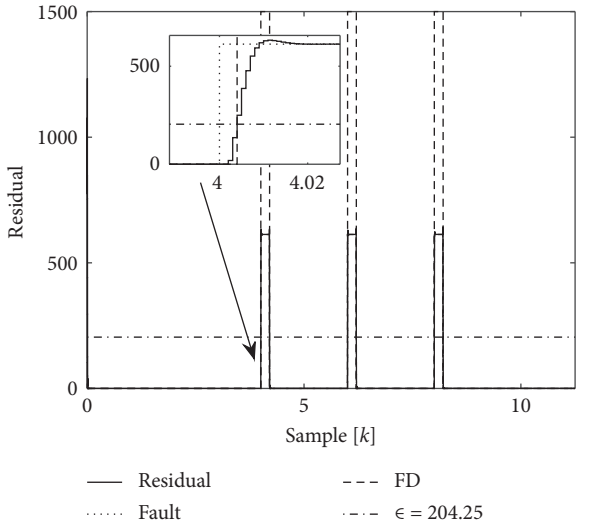

Figure 9: The time evolution of the residual r_k and the fault detection.

6. Conclusions

It has been presented a methodology for the design of unknown input observers for discrete-time nonlinear descriptor systems. It is based on algebraic rearrangements and allows overcoming the problem of unmeasurable premise variables as to get a compatible error dynamic system with the direct Lyapunov method; thus, sufficient conditions in terms of LMIs have been obtained. The resulting UI observer is proven to be less conservative than those in the literature. Moreover, the proposed scheme has been employed to solve the detection and estimation of actuator faults. The advantages of the proposal have been illustrated via numerical example and applied to the fault detection in train systems.

Data Availability

No data were used to support this study. All the values to reproduce the results are included within the article.

Conflicts of Interest

The authors declare that there are no conflicts of interest regarding the publication of this paper.

Acknowledgments

This work was supported by CONACYT via the scholarship number 930683, the laboratory LANAVEX from the Universidad Politécnica de Pachuca, the Project ITSON-PROFAPI CA-18 2020-0038, and the postdoctoral fellowship PRODEP CA-18.

References

[1] D. Luenberger, "An introduction to observers," *IEEE Transactions on Automatic Control*, vol. 16, no. 6, pp. 596–602, 1971.

[2] Y. Guan and M. Saif, "A novel approach to the design of unknown input observers," *IEEE Transactions on Automatic Control*, vol. 36, no. 5, pp. 632–635, 1991.

[3] P. M. Frank, "Fault diagnosis in dynamic systems using analytical and knowledge-based redundancy," *Automatica*, vol. 26, no. 3, pp. 459–474, 1990.

[4] G.-R. Duan and R. J. Patton, "Robust fault detection using Luenberger-type unknown input observers-a parametric approach," *International Journal of Systems Science*, vol. 32, no. 4, pp. 533–540, 2001.

[5] R. Isermann, *Fault-diagnosis Systems: An Introduction from Fault Detection to Fault Tolerance*, Springer Science & Business Media, Berlin, Germany, 2006.

[6] D. Ichalal, B. Marx, J. Ragot, and D. Maquin, "New fault tolerant control strategies for nonlinear Takagi-Sugeno systems," *International Journal of Applied Mathematics and Computer Science*, vol. 22, no. 1, pp. 197–210, 2012.

[7] Z. Dai, H. Zhou, J. Kang, and F. Wen, "The skewness of oil price returns and equity premium predictability," *Energy Economics*, vol. 94, Article ID 105069, 2021.

[8] N. Kobayashi and T. Nakamizo, "An observer design for linear systems with unknown inputs," *International Journal of Control*, vol. 35, no. 4, pp. 605–619, 1982.

[9] M. Darouach, M. Zasadzinski, and S. J. Xu, "Full-order observers for linear systems with unknown inputs," *IEEE Transactions on Automatic Control*, vol. 39, no. 3, pp. 606–609, 1994.

[10] C.-C. Tsui, "A new design approach to unknown input observers," *IEEE Transactions on Automatic Control*, vol. 41, pp. 464–468, 1996.

[11] H. Khalil, *Nonlinear Systems*, Prentice Hall, Upper Saddle River, NJ, USA, 3rd edition, 2002.

[12] C. Edwards and C. P. Tan, "A comparison of sliding mode and unknown input observers for fault reconstruction," *European Journal of Control*, vol. 12, no. 3, pp. 245–260, 2006.

[13] D. Wang and K.-Y. Lum, "Adaptive unknown input observer approach for aircraft actuator fault detection and isolation," *International Journal of Adaptive Control and Signal Processing*, vol. 21, no. 1, pp. 31–48, 2007.

[14] W. Chen and M. Saif, "Unknown input observer design for a class of nonlinear systems: an LMI approach," in *Proceedings of the 2006 American Control Conference*, p. 5, IEEE, Minneapolis, MN, USA, June 2006.

[15] G. Besançon, "High-gain observation with disturbance attenuation and application to robust fault detection," *Automatica*, vol. 39, no. 6, pp. 1095–1102, 2003.

[16] K. Tanaka and H. Wang, *Fuzzy Control Systems Design and Analysis: A Linear Matrix Inequality Approach*, John Wiley & Sons, New York, NY, USA, 2001.

[17] Z. Lendek, T. M. Guerra, R. Babuška, and B. De-Schutter, *Stability Analysis and Nonlinear Observer Design Using Takagi-Sugeno Fuzzy Models*, Springer-Verlag, Dordrecht, Netherlands, 2010.

[18] H. Ohtake, K. Tanaka, and H. O. Wang, "Fuzzy modeling via sector nonlinearity concept," in *Proceedings of the Joint 9th IFSA World Congress and 20th NAFIPS International Conference*, vol. 1, pp. 127–132, Vancouver, Canada, July 2001.

[19] T. Takagi and M. Sugeno, "Fuzzy identification of systems and its applications to modeling and control," *IEEE Transactions on Systems, Man, and Cybernetics*, vol. SMC-15, no. 1, pp. 116–132, 1985.

[20] J. S. Shamma, "An overview of lpv systems," in *Control of Linear Parameter Varying Systems with Applications*, pp. 3–26, Springer, Berlin, Germany, 2012.

[21] S. Boyd, L. E. Ghaoui, E. Feron, and V. Belakrishnan, "Linear matrix inequalities in system and control theory," *SIAM: Studies In Applied Mathematics*, vol. 15Philadelphia, PA, USA, 1994.

[22] C. Scherer, *Linear Matrix Inequalities in Control Theory*, Delf University, Delf, The Netherlands, 2004.

[23] K. Tanaka, T. Ikeda, and H. O. Wang, "Fuzzy regulators and fuzzy observers: relaxed stability conditions and LMI-based designs," *IEEE Transactions on Fuzzy Systems*, vol. 6, no. 2, pp. 250–265, 1998.

[24] P. Bergsten, R. Palm, and D. Driankov, "Observers for Takagi-Sugeno fuzzy systems," *IEEE Transactions on Systems, Man and Cybernetics, Part B (Cybernetics)*, vol. 32, no. 1, pp. 114–121, 2002.

[25] T. M. Guerra, H. Kerkeni, J. Lauber, and L. Vermeiren, "An efficient Lyapunov function for discrete T-S models: observer design," *IEEE Transactions on Fuzzy Systems*, vol. 20, no. 1, pp. 187–192, 2012.

[26] T. Lei, Q. Song, and Y. Liu, "State estimation for discrete-time Takagi-Sugeno fuzzy systems with time-varying delays," *Mathematical Problems in Engineering*, vol. 2015, 2015.

[27] V. Estrada-Manzo, Z. Lendek, and T. M. Guerra, "Generalized LMI observer design for discrete-time nonlinear descriptor models," *Neurocomputing*, vol. 182, pp. 210–220, 2016.

[28] G.-P. Jiang, S.-P. Wang, and W.-Z. Song, "Design of observer with integrators for linear systems with unknown input disturbances," *Electronics Letters*, vol. 36, no. 13, pp. 1168-1169, 2000.

[29] D. Koenig and S. Mammar, "Design of proportional-integral observer for unknown input descriptor systems," *IEEE Transactions on Automatic Control*, vol. 47, no. 12, pp. 2057–2062, 2002.

[30] Z. Gao, X. Liu, and M. Z. Chen, "Unknown input observer-based robust fault estimation for systems corrupted by partially decoupled disturbances," *IEEE Transactions on Industrial Electronics*, vol. 63, pp. 2537–2547, 2015.

[31] D. Ichalal and S. Mammar, "On unknown input observers for LPV systems," *IEEE Transactions on Industrial Electronics*, vol. 62, no. 9, pp. 5870–5880, 2015.

[32] F. Xu, J. Tan, Y. Wang et al., "Generalized set-theoretic unknown input observer for LPV systems with application to state estimation and robust fault detection," *International Journal of Robust and Nonlinear Control*, vol. 27, pp. 3812–3832, 2017.

[33] B. Marx, D. Ichalal, J. Ragot, D. Maquin, and S. Mammar, "Unknown input observer for LPV systems," *Automatica*, vol. 100, pp. 67–74, 2019.

[34] H. R. Karimi and M. Chadli, "Robust observer design for Takagi-Sugeno fuzzy systems with mixed neutral and discrete delays and unknown inputs," *Mathematical Problems in Engineering*, vol. 2012, 2012.

[35] D. Ichalal, B. Marx, J. Ragot, and D. Maquin, "State estimation of Takagi-Sugeno systems with unmeasurable premise variables," *IET Control Theory & Applications*, vol. 4, no. 5, pp. 897–908, 2010.

[36] A. Zemouche, M. Boutayeb, and G. I. Bara, "Observer design for nonlinear systems: an approach based on the differential mean value theorem," in *Proceedings of the 44th IEEE Conference on Decision and Control and 2005 European Control Conference. CDC-ECC'05*, pp. 6353–6358, IEEE, Seville, Spain, December 2005.

[37] T. M. Guerra, R. Márquez, A. Kruszewski, and M. Bernal, "H_∞ LMI-based observer design for nonlinear systems via takagi-sugeno models with unmeasured premise variables," *IEEE Transactions on Fuzzy Systems*, vol. 26, no. 3, pp. 1498–1509, 2018.

[38] D. Ichalal, B. Marx, J. Ragot, and D. Maquin, "Design of observers for Takagi-Sugeno systems with immeasurable premise variables: an L_2 approach," in *Proceedings of the 17th IFAC World Congress*, pp. 2768–2773, Seoul, South Korea, July 2008.

[39] D. Ichalal, B. Marx, D. Maquin, and J. Ragot, "A method to avoid the unmeasurable premise variables in observer design for discrete time TS systems," in *Proceedings of the 2016 IEEE International Conference on Fuzzy Systems (FUZZ-IEEE)*, pp. 2343–2348, Vancouver, Canada, July 2016.

[40] D. Ichalal, B. Marx, S. Mammar, D. Maquin, and J. Ragot, "How to cope with unmeasurable premise variables in Takagi-Sugeno observer design: dynamic extension approach," *Engineering Applications of Artificial Intelligence*, vol. 67, pp. 430–435, 2018.

[41] D. Quintana, V. Estrada-Manzo, and M. Bernal, "An exact handling of the gradient for overcoming persistent problems in nonlinear observer design via convex optimization techniques," *Fuzzy Sets and Systems*, 2020.

[42] D. Luenberger, "Dynamic equations in descriptor form," *IEEE Transactions on Automatic Control*, vol. 22, no. 3, pp. 312–321, 1977.

[43] F. Lewis, D. Dawson, and C. Abdallah, *Robot Manipulator Control: Theory and Practice*, CRC Press, Boca Raton, FL, USA, 2003.

[44] M. Blandeau, V. Estrada-Manzo, T. M. Guerra, P. Pudlo, and F. Gabrielli, "Fuzzy unknown input observer for understanding sitting control of persons living with spinal cord injury," *Engineering Applications of Artificial Intelligence*, vol. 67, pp. 381–389, 2018.

[45] M. Blandeau, T.-M. Guerra, and P. Pudlo, "Application of a TS unknown input observer for studying sitting control for people living with spinal cord injury," in *Control Applications for Biomedical Engineering Systems, Chap. 7*, A. T. Azar, Ed., pp. 169–195, Elsevier, Amsterdam, Netherlands, 2020.

[46] J. Chen and H. Zhang, "Robust detection of faulty actuators via unknown input observers," *International Journal of Systems Science*, vol. 22, no. 10, pp. 1829–1839, 1991.

[47] J. Chen, R. J. Patton, and H.-Y. Zhang, "Design of unknown input observers and robust fault detection filters," *International Journal of Control*, vol. 63, no. 1, pp. 85–105, 1996.

[48] Z. Gao, C. Cecati, and S. X. Ding, "A survey of fault diagnosis and fault-tolerant techniques-Part I: fault Diagnosis with model-based and signal-based approaches," *IEEE Transactions on Industrial Electronics*, vol. 62, no. 6, pp. 3757–3767, 2015.

[49] W. Chen and M. Saif, "Fault detection and isolation based on novel unknown input observer design," in *Proceedings of the 2006 American Control Conference*, vol. 6–, Minneapolis, MN, USA, June 2006.

[50] P. Di Franco, G. Scarciotti, and A. Astolfi, "A globally stable algorithm for the integration of high-index differential-algebraic systems," *IEEE Transactions on Automatic Control*, vol. 65, no. 5, pp. 2107–2122, 2019.

[51] J. Arceo, M. Sánchez, V. Estrada-Manzo, and M. Bernal, "Convex stability analysis of nonlinear singular systems via linear matrix inequalities," *IEEE Transactions on Automatic Control*, vol. 64, pp. 1740–1745, 2018.

[52] L. Dai, *Singular Control Systems*, Vol. 118, Springer, Berlin, Germany, 1989.

[53] F. R. López-Estrada, D. Theilliol, C. M. Astorga-Zaragoza, J. C. Ponsart, G. Valencia-Palomo, and J. Camas-Anzueto, "Fault diagnosis observer for descriptor takagi-sugeno systems," *Neurocomputing*, vol. 331, pp. 10–17, 2019.

[54] S. Raghavan and J. K. Hedrick, "Observer design for a class of nonlinear systems," *International Journal of Control*, vol. 59, no. 2, pp. 515–528, 1994.

[55] A. Zemouche, M. Boutayeb, and G. I. Bara, "Observers for a class of Lipschitz systems with extension to performance analysis," *Systems & Control Letters*, vol. 57, no. 1, pp. 18–27, 2008.

[56] M. Chadli and H. R. Karimi, "Robust observer design for unknown inputs Takagi–Sugeno models," *IEEE Transactions on Fuzzy Systems*, vol. 21, pp. 158–164, 2012.

[57] G. Phanomchoeng, R. Rajamani, and D. Piyabongkarn, "Nonlinear observer for bounded Jacobian systems, with applications to automotive slip angle estimation," *IEEE Transactions on Automatic Control*, vol. 56, no. 5, pp. 1163–1170, 2011.

[58] G. Wood and B. Zhang, "Estimation of the Lipschitz constant of a function," *Journal of Global Optimization*, vol. 8, pp. 91–103, 1996.

[59] H. D. Tuan, P. Apkarian, T. Narikiyo, and Y. Yamamoto, "Parameterized linear matrix inequality techniques in fuzzy control system design," *IEEE Transactions on Fuzzy Systems*, vol. 9, no. 2, pp. 324–332, 2001.

[60] M. Oliveira and R. Skelton, "Stability tests for constrained linear systems," in *Perspectives in robust control, vol. 268 of Lecture Notes in Control and Information Sciences*, pp. 241–257, Springer-Verlag, Berlin, Germany, 2001.

[61] T. M. Guerra and L. Vermeiren, "LMI-based relaxed nonquadratic stabilization conditions for nonlinear systems in the Takagi-Sugeno's form," *Automatica*, vol. 40, no. 5, pp. 823–829, 2004.

[62] K. Tanaka, T. Hori, and H. O. Wang, "A multiple Lyapunov function approach to stabilization of fuzzy control systems," *IEEE Transactions on Fuzzy Systems*, vol. 11, no. 4, pp. 582–589, 2003.

[63] J. Daafouz and J. Bernussou, "Parameter dependent Lyapunov functions for discrete time systems with time varying parametric uncertainties," *Systems & Control Letters*, vol. 43, no. 5, pp. 355–359, 2001.

[64] X. Xie, D. Yue, T. Ma, and X. Zhu, "Further studies on control synthesis of discrete-time T-S fuzzy systems via augmented multi-indexed matrix approach," *IEEE Transactions on Cybernetics*, vol. 44, no. 12, pp. 2784–2791, 2014.

[65] P. M. Frank and X. Ding, "Survey of robust residual generation and evaluation methods in observer-based fault detection systems," *Journal of Process Control*, vol. 7, no. 6, pp. 403–424, 1997.

[66] V. Krishnaswami and G. Rizzoni, "A survey of observer based residual generation for FDI," *IFAC Proceedings Volumes*, vol. 27, no. 5, pp. 35–40, 1994.

[67] S. Li, H. Wang, A. Aitouche, Y. Tian, and N. Christov, "Active fault tolerance control of a wind turbine system using an unknown input observer with an actuator fault," *International Journal of Applied Mathematics and Computer Science*, vol. 28, no. 1, pp. 69–81, 2018.

[68] B. Aguiar, D. Berdjag, T.-M. Guerra, and B. Demaya, "Improving train position accuracy in case of wheel jamming faults," in *Proceedings of the 2nd IFAC Workshop on Linear Parameter Varying Systems LPVS 2018*, vol. 51, pp. 25–30, Florianópolis, Brazil, September 2018.

[69] J. L. Wang, G.-H. Yang, and J. Liu, "An LMI approach to $H_$index and mixed/$H\_$ H_∞ofault detection observer design," *Automatica*, vol. 43, pp. 1656–1665, 2007.

[70] J. Y. A. L. M. I. P. Lofberg, "A toolbox for modeling and optimization in MATLAB," in *Proceedings of the 2004 IEEE International Symposium on Computer Aided Control Systems Design*, pp. 284–289, Taipei, Taiwan, September 2004.

[71] J. F. Sturm, "Using SeDuMi 1.02, a MATLAB toolbox for optimization over symmetric cones," *Optimization Methods and Software*, vol. 11, no. 1-4, pp. 625–653, 1999.

[72] Z. Mao, G. Tao, B. Jiang, and X.-G. Yan, "Adaptive compensation of traction system actuator failures for high-speed trains," *IEEE Transactions on Intelligent Transportation Systems*, vol. 18, no. 11, pp. 2950–2963, 2017.

[73] S. Liu, B. Jiang, Z. Mao, and S. X. Ding, "Adaptive backstepping based fault-tolerant control for high-speed trains with actuator faults," *International Journal of Control, Automation and Systems*, vol. 17, no. 6, pp. 1408–1420, 2019.

[74] B. Aguiar, D. Berdjag, B. Demaya, and T.-M. Guerra, "A robust and fault tolerant approach for automatic train stop control system design," in *Proceedings of the 20th IFAC-PapersOnLine*, vol. 50, no. 1, pp. 8549–8554, Toulouse, France, October 2017.

[75] P. G. Howlett, I. P. Milroy, and P. J. Pudney, "Energy-efficient train control," *Control Engineering Practice*, vol. 2, no. 2, pp. 193–200, 1994.

[76] B. P. Rochard and F. Schmid, "A review of methods to measure and calculate train resistances," *Proceedings of the Institution of Mechanical Engineers, Part F: Journal of Rail and Rapid Transit*, vol. 214, no. 4, pp. 185–199, 2000.

Hindawi
Mathematical Problems in Engineering
Volume 2021, Article ID 6697838, 9 pages
https://doi.org/10.1155/2021/6697838

Research Article

Fault-Tolerant Control with Control Allocation for Time-Varying Linear Systems by Using Continuous Integral Sliding Modes

Oziel Hernández-Durán,[1] **Rosalba Galván-Guerra**,[2] **Juan Eduardo Velázquez-Velázquez**,[2] **and Benjamín A. Itzá-Ortiz**[1]

[1]*Universidad Autónoma del Estado de Hidalgo, Pachuca, Hidalgo 42184, Mexico*
[2]*Instituto Politécnico Nacional, Unidad Profesional Interdisciplinaria de Ingeniería Campus Hidalgo, San Agustín Tlaxiaca, Hidalgo 42162, Mexico*

Correspondence should be addressed to Juan Eduardo Velázquez-Velázquez; jvelazquezv@ipn.mx

Received 12 December 2020; Revised 21 January 2021; Accepted 13 February 2021; Published 10 March 2021

Academic Editor: Erivelton Geraldo Nepomuceno

A fault-tolerant control algorithm based on sliding modes is proposed to ensure the tracking of the desired trajectory for time-varying systems even in the presence of actuator faults. The proposed algorithm uses a continuous integral sliding mode and a linear quadratic regulator, together with control allocation and system inversion techniques, resulting in both a finite-time exact compensation of the faults and the exponential tracking of the reference.

1. Introduction

In general, linear and nonlinear systems are vulnerable or susceptible to failure. A fault changes the behavior of a system so that the system can no longer fulfill its objective. Faults are usually classified as system parameter faults, sensor faults, and actuator faults [1]. As airplanes or aerospace systems, there are many applications that for safety require fault-tolerant control (FTC) schemes that guarantee the fulfillment of the control objective in the presence of faults.

This work only considers actuator faults, which can be partial or total, and it is assumed that the system has redundancy in the actuators. This redundancy allows the control signal in the actuators to be reconfigured to the fault. Therefore, satisfactory performance can be maintained even with critical main actuator faults.

Fault tolerance cannot be achieved by typical state feedback control [1]. However, this problem can be addressed in several ways, such as robust control (passive fault tolerance) [2, 3], adaptive control (active fault tolerance) [4], detection and isolation of faults, or by combinations of these techniques [5]. Furthermore, faults may be seen as a disturbance, so if a robust closed-loop control is designed, the effects of any of these disturbances can be minimized.

One way to make the system robust is through sliding mode control [6, 7]. Methodologies based on sliding modes make the system insensitive to the matched effects of faults during the sliding phase, allowing fault detection and isolation [8–10].

If the faults are present from the initial time, the conventional integral sliding modes (ISMs) [11, 12] can be used due to the absence of the reaching phase. In [13], a fault control strategy for linear time-invariant (LTI) systems is proposed. It uses an ISM control law to compensate for the matched effects of the faults right after the initial time. For nonlinear systems, the ISM is used for a flexible spacecraft in [14]. However, in [15], an FTC approach based on ISM is given for linear parameter-varying (LPV) systems. In [16], this scheme is extended for linear time-varying (LTV) systems. Unfortunately, the ISM has the disadvantage of producing a high level of chattering, limiting its application.

To decrease the chattering, for relative degree one systems, the continuous sliding modes based on the

supertwisting algorithm (STA) [17, 18] are a good option since they generate a continuous control law. On the contrary, the continuous integral sliding modes (CISM) combine the ISM with the STA [19, 20], ensuring the system's nominal behavior using a continuous control signal, thus reducing the chattering. In [21], an FTC scheme based on CISM for LTI systems is proposed, guaranteeing convergence right after the initial time by assuming the absence of faults until the controller has converged. However, this assumption is quite restrictive since the system may present faults at the initial time.

This paper aims to design a fault-tolerant control algorithm against actuator faults, based on continuous integral sliding modes with online control allocation for time-varying linear systems, with redundancy in the actuators. This algorithm can be applied to nonlinear systems if tracking linearization is used, turning the tracking problem into a stabilization one. The designed algorithm ensures the theoretically exact compensation of actuator faults in finite time and ensures that the system affected by the failures behaves as the nominal system in finite time using a continuous control signal. The effectiveness of the proposed algorithm is shown by simulating the longitudinal movement of an airplane in MATLAB.

This paper is organized as follows. Some preliminary results and the problem formulation are described in Section 2. The controller design that stabilizes in finite time the tracking error is given in Section 3. Section 4 gives the simulation results and the performed analysis. Finally, Section 5 contains the conclusions of the paper.

2. Preliminaries and Problem Formulation

In this section, we introduce some preliminary results used throughout the paper and establish the formulation of the problem.

2.1. Supertwisting Algorithm. Consider a relative degree one-scalar system:

$$\dot{s}(t) = u(t) + \psi(t), \tag{1}$$

where $\psi(t)$ is a Lipschitz uncertainty/perturbation, i.e., $\|\dot{\psi}(t)\| \le L$. The STA [15] is a second-order sliding mode control that drives the sliding variable s and its derivatives to zero in finite time. It generates a continuous control and attenuates the chattering effect by hiding the switching term under an integral. In general, the STA controller is given by

$$\begin{aligned} u(t) &= -k_1 \lfloor s(t) \rceil^{1/2} + w(t), \\ \dot{w}(t) &= -k_2 \lfloor s(t) \rceil^{0}, \end{aligned} \tag{2}$$

where $\lfloor \cdot \rceil^p = |\cdot|^p \operatorname{sign}(\cdot)$ and k_1 and k_2 are designed to guarantee the finite-time convergence of s and $\dot{s}$ to the origin in finite time. This controller compensates in finite-time Lipschitz uncertainties/perturbations.

Theorem 1 (see [17, 18]). *System (1) is finite-time stable if the parameters of the system (2) satisfy*

$$\begin{aligned} &k_2 > L; \\ &k_1 > \sqrt{k_2 + L}. \end{aligned} \tag{3}$$

2.2. Problem Formulation. Consider a nonlinear system:

$$\begin{aligned} \dot{x}(t) &= f(t, x(t)) + g(t, x(t))u(t); \\ x(t_0) &= x_o, \end{aligned} \tag{4}$$

where $f(t, x(t))$, $g(t, x(t))$ are smooth vector fields, defined on an open set $D \subset R^n$, $u(t) \in R^m$ is the control input, and $x(t) \in R^n$ is the state vector, and it is fully known. For simplicity, assume that the previous system has been transformed to its normal form and linearized around a trajectory so that the dynamics of the error are represented by the following LTV system, which is subject to actuator fault:

$$\begin{aligned} \dot{\tilde{z}}(t) &= A(t)\tilde{z}(t) + B_u(t)W(t)u(t); \\ \tilde{z}(t_0) &= \tilde{z}_o, \end{aligned} \tag{5}$$

where $A(t) \in R^{n\times n}$ and $B_u(t) \in R^{n\times m}$ are known matrices, $W(t) = \operatorname{diag}(w_1(t), \ldots, w_m(t)) \in R^{m\times m}$ is the fault matrix, and $\tilde{z}(t) \in R^n$ is the tracking error. Assume that the range of the matrix $B_u(t) = l < m$ for all t; i.e., there is redundancy in the actuators. So, the matrix $B_u(t)$ can be factorized using the range factorization [22] as

$$B_u(t) = B_v(t)B(t), \tag{6}$$

where $B_v(t) \in R^{n\times l}$ and $B(t) \in R^{l\times m}$, both with rank l. Hence, the faulty system (5) has been transformed into

$$\dot{\tilde{z}}(t) = A(t)\tilde{z}(t) + B_v(t)B(t)W(t)u(t). \tag{7}$$

The fault matrix $W(t)$ denotes the possible actuators faults; if $w_i(t) = 1$ for $i = 1, \ldots, m$, there is no fault in the i-actuator, while $w_i(t) = 0$ denotes its complete failure. If $0 < w_i(t) < 1$, there is a partial fault in the actuator. Note that if $w_i(t) = 0$ for all t, the system loses controllability, so it is required to establish the characteristics of the faults that the system can withstand without losing controllability.

A strategy that takes the system to a free-redundancy form is presented, where the faults are seen as disturbances. Such a strategy allows designing a control law that compensates the matched faults' effects in finite time and exponentially stabilizes the error.

3. Control Design

Consider the LTV system subject to actuator fault (7), and assume the following:

(1) System (1) is controllable.

(2) The matrix $B_v(t)$ is a function that can be differentiated at least once. Also, both $B_v(t)$ and $\dot{B}_v(t)$ are bounded and known.

Since system (7) has redundancy in the actuators, it is necessary to distribute the full control signal in the actuators.

A strategy to achieve this is through the control allocation allowing to calculate the control input $u(t)$. To carry out the control allocation, assume that no fault is affecting the system (5), that is, $W(t) = I_m$. Then,

$$\dot{\tilde{z}}(t) = A(t)\tilde{z}(t) + B_\nu(t)B(t)u(t). \tag{8}$$

Let $\tilde{\nu}(t) = B(t)u(t)$, then $u(t)$ can be reconstructed, solving the minimization problem:

$$\begin{aligned} &\min u^T(t)u(t) \\ &\text{subject to } B(t)u(t) = \tilde{\nu}(t). \end{aligned} \tag{9}$$

The solution to this optimization problem [23] is

$$u(t) = B^+(t)\tilde{\nu}(t), \tag{10}$$

where $B^+(t) = B^T(t)(B(t)B^T(t))^{-1}$.

Now that the $u(t)$ control has been calculated, system (8) is rewritten, and the actuator faults can be considered as follows:

$$\dot{\tilde{z}}(t) = A(t)\tilde{z}(t) + B_\nu(t)B(t)W(t)B^+(t)\tilde{\nu}(t). \tag{11}$$

The set of possible actuator faults is defined as

$$\begin{aligned} \mathbf{W} = W(t) = \{&\operatorname{diag}\left(w_{1(t)}, w_{2(t)}, \ldots, w_{m(t)}\right) | \det(\Gamma(t)) \\ &\neq 0 \wedge \|W(t)\| \geq w_{\min} > 0,\} \end{aligned} \tag{12}$$

where $\Gamma(t) = B(t)W(t)B^+(t)$.

Because $l < m$, the det $(\Gamma(t)) \neq 0$ even if $m - l$ actuators have a total failure. If more than $m - l$ actuators fail, system stability cannot be ensured [13].

In the case of a fault-free system, that is, $W(t) = I$, the system (11) reduces to

$$\dot{\tilde{z}}_n(t) = A(t)\tilde{z}_n(t) + B_\nu(t)\nu_n(t). \tag{13}$$

This nominal fault-free system is used to design the nominal control. Hence, assume that the pair $(A(t), B_\nu(t))$ is controllable. Therefore, it is possible to design a state feedback control law $\nu_n(t) = -K(t)\tilde{z}_n(t)$ such that the closed-loop system is exponentially stable.

To compensate for the effects of the actuator faults, let us define a time-varying integral sliding surface:

$$s(\tilde{z}(t)) = G(t)\left(\tilde{z}(t) - \tilde{z}(t_0)\right) - \int_{t_0}^{t} \left(G(\tau)\left(A(\tau)\tilde{z}(\tau) + B_\nu(\tau)\nu_n(\tau)\right) + \dot{G}(\tau)\left(\tilde{z}(\tau) - \tilde{z}(t_0)\right)\right)\mathrm{d}\tau, \tag{14}$$

where $\tilde{z}(t_0) = \tilde{z}_o$ and $G(t)$ is a design matrix such that det $(G(t)B_\nu(t)) \neq 0$.

The derivative of the sliding surface along the trajectories of (8) is given by

$$\dot{s}(\tilde{z}(t)) = G(t)B_\nu(t)\Gamma(t)\tilde{\nu}(t) - G(t)B_\nu(t)\nu_n(t). \tag{15}$$

Assume that $\tilde{\nu}(t) = \nu_n(t) + \nu_I(t)$ and $G(t) = B_\nu^+(t)$, where $B_\nu^+(t) = (B_\nu^T(t)B_\nu(t))^{-1}B_\nu^T(t)$, then

$$\dot{s}(\tilde{z}(t)) = \Gamma(t)\nu_I(t) + \left(\Gamma(t) - I_l\right)\nu_n(t). \tag{16}$$

The equivalent control that maintains the trajectories of system (11) in the sliding mode is

$$\nu_{\mathrm{eq}}(t) = -(\Gamma(t))^{-1}\left(\Gamma(t) - I_l\right)\nu_n(t). \tag{17}$$

During the sliding phase, the system (11) takes the following form:

$$\dot{\tilde{z}}(t) = A(t)\tilde{z}(t) + B_\nu(t)\nu_n(t). \tag{18}$$

Observe that, on the sliding mode, system (18) is equivalent to system (13).

Remark 1. Note that the proposed sliding variable (14) contains the nominal dynamics of the LTV system. Hence, if the sliding mode is guaranteed, the actuator faults' matched effects are wholly compensated.

The controller is designed, so system (11) in the sliding mode reaches and remains on the origin. Therefore, the proposed controller has the following form:

$$\nu_I(t) = (\hat{\Gamma}(t))^{-1}\underbrace{\left(-k_1\lfloor s(\tilde{z}(t))\rceil^{1/2} - k_2\int_{t_0}^{t}\lfloor s(\tilde{z}(t))\rceil^0\mathrm{d}\tau\right)}_{\nu_b(t)}, \tag{19}$$

where $\hat{\Gamma}(t)$ is a numerical approximation of the matrix $\Gamma(t)$. The computation procedure to obtain this approximation is given in the next section, k_1, k_2 are designed constants, and the function $\lfloor s(\tilde{z}(t))\rceil^q$ is defined as

$$\lfloor s(\tilde{z}(t))\rceil^q = \begin{bmatrix} \left(|s_1(\tilde{z}(t))|^q \operatorname{sign}\left(s_1(\tilde{z}(t))\right)\right) \\ \vdots \\ |s_l(\tilde{z}(t))|^q \operatorname{sign}\left(s_l(\tilde{z}(t))\right) \end{bmatrix}. \tag{20}$$

Therefore, equation (16) can be rewritten as

$$\begin{aligned} \dot{s}(\tilde{z}(t)) &= -k_1\lfloor s(\tilde{z}(t))\rceil^{1/2} + \Omega(t), \\ \dot{\Omega}(t) &= -k_2\lfloor s(\tilde{z}(t))\rceil^0 + \dot{\overline{W}}(t), \end{aligned} \tag{21}$$

where $\overline{W}(t) = (\Gamma(t) - I_l)\nu_n(t)$ and $\|\dot{\overline{W}}(t)\| \leq L$.

According to the previous construction development and if we choose $k_1 = 1.5\sqrt{L}$ and $k_2 = 1.1L$ as in [17], it can be seen that the system (21) complies with Theorem 1, so stability can be ensured, and it can be concluded that the sliding variable $s(\tilde{z}(t))$ converges to zero in finite time, and therefore, system (11) in sliding mode will behave like system (13).

Remark 2. The convergence velocity of the proposed approach can be improved by increasing the parameters k_1 and k_2. Moreover, a specific reaching time can be guarantee by

following the scheme proposed in [24]. However, the greater the parameters, the bigger the chattering.

3.1. Fault Matrix Approximation. The proposed controller (19) uses $\Gamma(t)$, so an approximation is necessary. Let $\widehat{\Gamma}(t)$ be an approximation of $\Gamma(t)$ obtained by a fault-identification algorithm as in [13]. Consider the nonlinear system (4); for simplicity, assume that the system (4) has been transformed to its normal form. Hence, it can be represented as

$$\dot{z}(t) = f(z(t), t) + B_\nu(t)\Gamma(t)\widetilde{\nu}(t), \tag{22}$$

where $\widetilde{\nu}(t) = \nu_n(t) + \nu_I(t)$. Since the state $z(t)$ is completely known, $\dot{z}(t)$ can be calculated in finite time by using the Levant differentiator [25]. To obtain $\widehat{\Gamma}(t)$, the following residual is defined: $r = \dot{z}(t) - \dot{z}_n(t)$, where $\dot{z}_n(t)$ is the nominal system; therefore,

$$r = B_\nu(t)\Gamma(t)\left(\nu_I(t) + \nu_n(t)\right) - B_\nu(t)\nu_n(t). \tag{23}$$

Let $\nu_I(t) = \widehat{\Gamma}^{-1}(t)\nu_b(t)$, then

$$\Gamma(t) = \left(B_\nu^+(t)r + \nu_n(t)\right)\left(\widehat{\Gamma}^{-1}(t)\nu_b(t) + \nu_n(t)\right)^{-1}. \tag{24}$$

Note that, with this method, it is not possible to know the value of the faults $w_i; i = 1, \ldots, m$. Moreover, the proposed approach may be affected by the used identification algorithm.

4. Simulation Results

Some MATLAB simulations are presented to validate the above results. Consider the longitudinal motion of an aircraft [26]:

$$\begin{bmatrix} \dot{\gamma} \\ \dot{\theta} \\ \dot{q} \end{bmatrix} = \begin{bmatrix} \frac{1}{mV_t}\left(\overline{q}SC_L(x) + T_n\sin(\alpha + \sigma_t) - mg\cos(\gamma)\right) \\ q \\ \frac{1}{I_y}\left(\overline{q}S\overline{c}C_m(x) + T_n\iota_{tz}\cos(\sigma_t)\right) \end{bmatrix} + \begin{bmatrix} 0 & 0 \\ 0 & 0 \\ \frac{1}{I_y}\overline{q}S\overline{c}\frac{dC_m}{d\delta_e} & \frac{1}{I_y}\overline{q}S\overline{c}\frac{dC_m}{d\delta_{ih}} \end{bmatrix}\begin{bmatrix} \delta_e \\ \delta_{ih} \end{bmatrix}, \tag{25}$$

where θ, q, γ, δ_e, and δ_{ih} represent pitch angle, pitch rate, flight path angle, elevator, and horizontal stabilizer, respectively. The other parameters are V_t, α, m, g, I_y, T_n, ι_{tz}, and σ_t which represent true airspeed, angle of attack, mass, gravity, the body axis moment of inertia, total engine thrust, the distance from the engine centerline to the fuselage reference line, and engine inclination angle, respectively. These parameters are available in [27].

The desired trajectory is shown in Figure 1, and the simulations were made considering that the plane is at 6100 meters above sea level and with a speed of 0.8 Mach. The system is linearized along the desired trajectory to obtain an LTV model. The nominal controller is composed of an auxiliary control that maintains the system on the desired trajectory and a linear quadratic regulator (LQR). The auxiliary control law is obtained by using a typical inversion technique. In the following sections, the following 2 cases will be analyzed:

(i) In the first case, the simulation begins considering that there are no faults in the actuators, and after some time, it introduces a partial fault in the horizontal stabilizer, which will become a total fault over time and finally add a partial failure in the elevator.

(ii) In the second case, a time-varying fault is simulated in the horizontal stabilizer.

In both cases, the CISM controller is designed following the proposed approach and considering a perturbation bound $L = 3$.

4.1. Piecewise Continuous Fault. For this simulation, in the initial moment, neither the elevator nor the horizontal stabilizer has failures. After 300s, a partial failure of 50% is introduced in the horizontal stabilizer. From the second 600, the partial failure of the horizontal stabilizer becomes a total failure. Finally, after 900s, a partial failure of 70% is added to the elevator, i.e.,

$$w_1 = \begin{cases} 1, & \text{if } t \in [0, 900), \\ 0.7, & \text{if } t \in [900, 1200], \end{cases}$$
$$w_2 = \begin{cases} 1, & \text{if } t \in [0, 300), \\ 0.5, & \text{if } t \in [300, 600), \\ 0, & \text{if } t \in [600, 1200], \end{cases} \tag{26}$$

where t is the simulation time.

In Figure 2, we can see that, from the first moment, the value of $\Gamma(t)$ is known, i.e., $\widehat{\Gamma}(t) = \Gamma(t)$. Observe that, with the considered faults, the inverse of $\Gamma(t)$ always exists.

In Figure 3, it can be noted that the error is zero in all state variables. The proposed fault is not Lipschitz in all t,

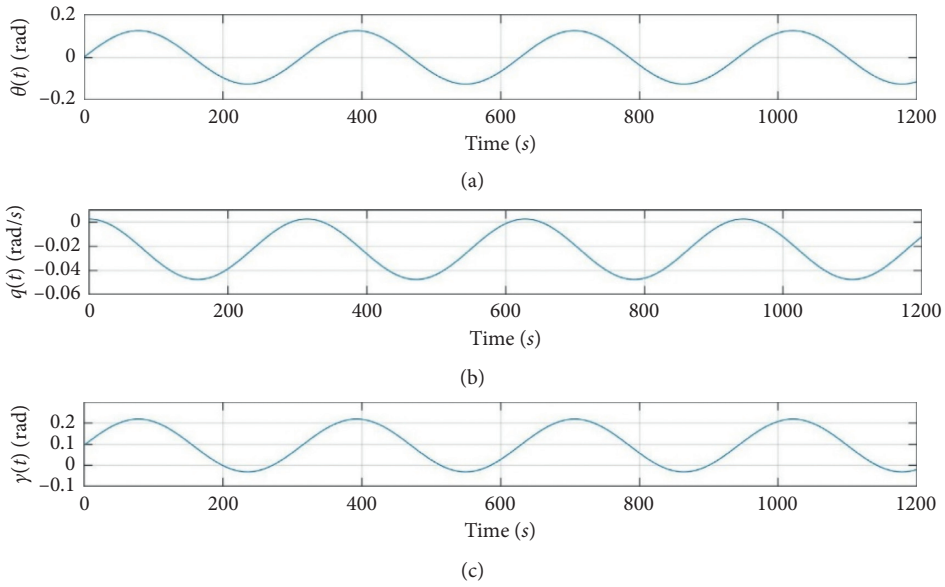

Figure 1: Desired trajectory: (a) pitch angle; (b) pitch rate; (c) flight path angle.

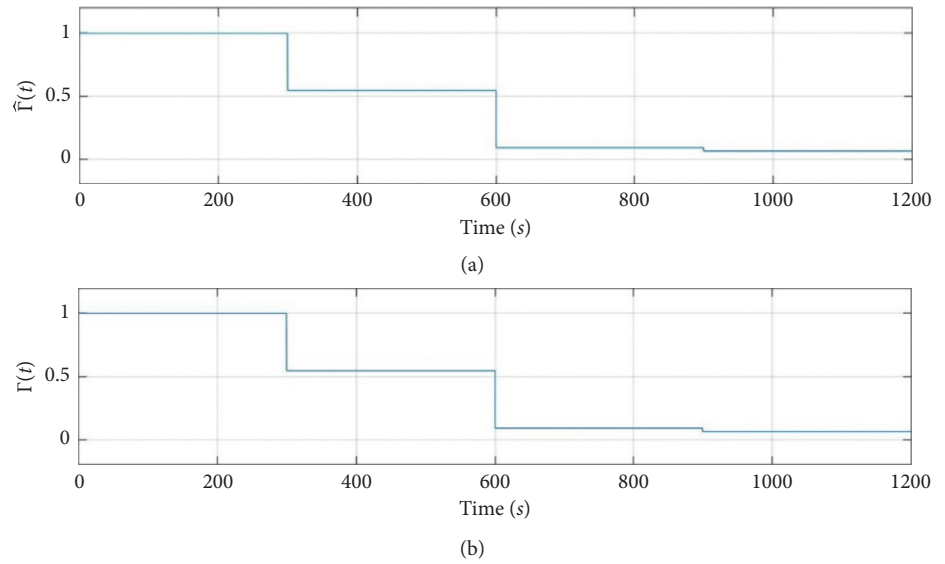

Figure 2: (a) $\widehat{\Gamma}(\mathbf{t})$ and (b) $\Gamma(\mathbf{t})$ of the case 1.

which causes the controller to lose its convergence in the points where the faults are non-Lipschitz. This effect can be seen as peaks in the pitch rate error in the seconds 300 s, 600 s, and 900 s.

Figure 4 shows the control signal made up of the LQR and the CISM, introduced into the elevator and the horizontal stabilizer, respectively. Observe how the control signal increases in the seconds where the fault is introduced. The sliding variable remains at zero, but as expected, the variable ceases to be zero in the seconds where the fault is not Lipschitz and re-converges in finite time.

4.2. Time-Varying Fault. For simulation purposes, a time-varying fault in the horizontal stabilizer is considered, i.e., $w_1 = 1, w_2 = (1/2)\cos((\pi/21)t) + 0.5$, where t is the simulation time.

In Figure 5, we can see that, as in Figure 2, from the first moment, $\widehat{\Gamma}(t) = \Gamma(t)$. Note that, with the considered fault, $\Gamma(t)$ is always invertible.

As shown in Figure 6, the error converges to zero in finite time in all the state variables, so it can be concluded that the desired trajectory is followed in the same manner. Note that, in comparison with the first case, since the considered faults fulfill the Lipschitz condition for all t, the controller never loses its convergence.

As seen in Figure 7, the elevator control signal and the horizontal stabilizer have several peaks. This behavior is caused by the shape of $\widehat{\Gamma}(t)$. At those times, $\widehat{\Gamma}(t)$ is close to zero; i.e., the failure is near to be total. The value of the faults

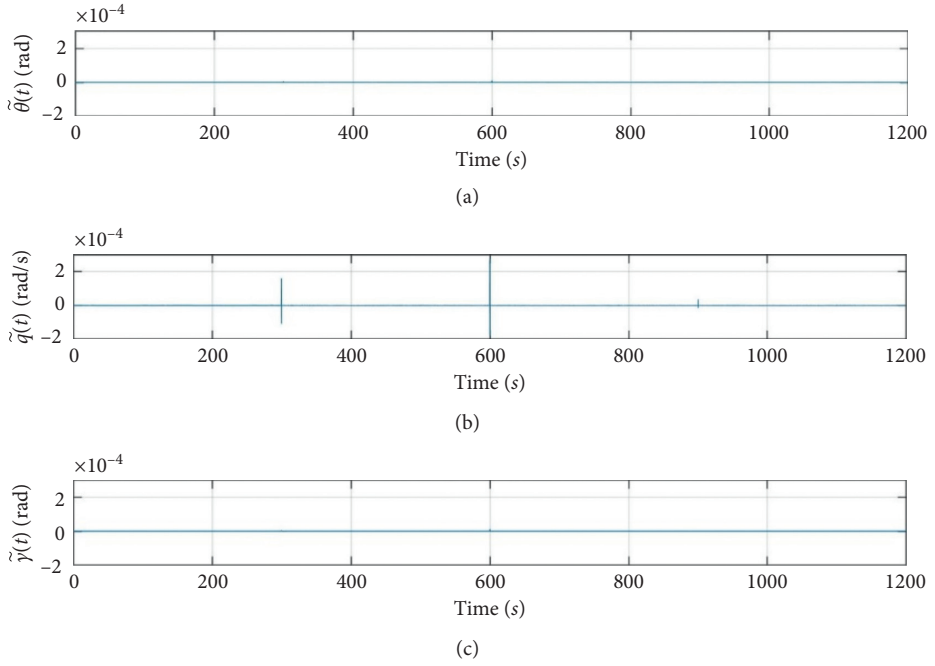

Figure 3: Tracking error case 1: (a) pitch angle error; (b) pitch rate error; (c) flight path angle error.

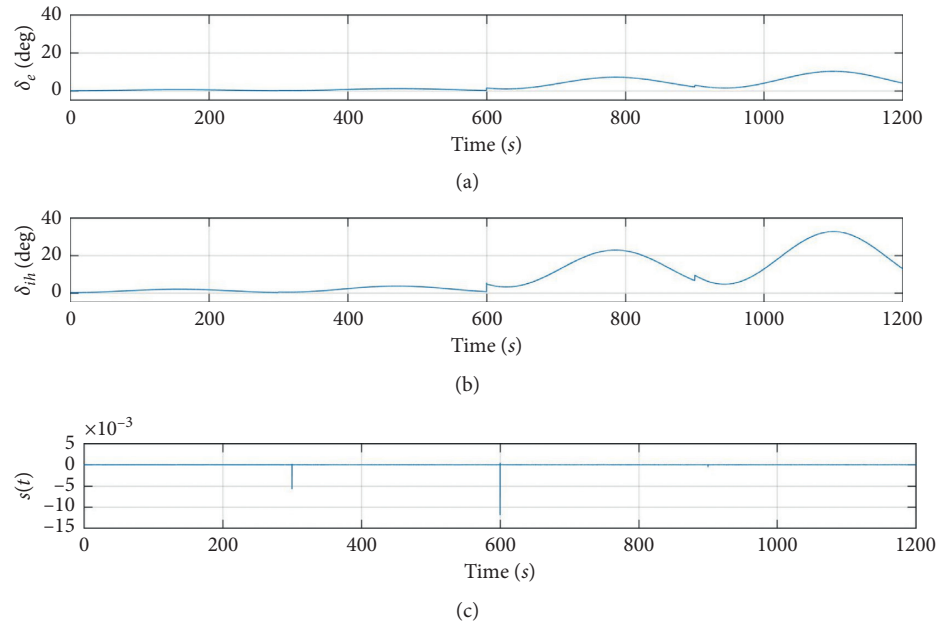

Figure 4: Control signal and the sliding surface of case 1: (a) elevator; (b) horizontal stabilizer; (c) sliding surface.

may increase the control signal necessary to maintain the system on the surface. Hence, the more severe the fault is, the bigger the necessary control signal will be.

The simulations show that, in the presence of actuator faults in both cases, the trajectory tracking is assured exponentially by compensating the faults' effects in finite time.

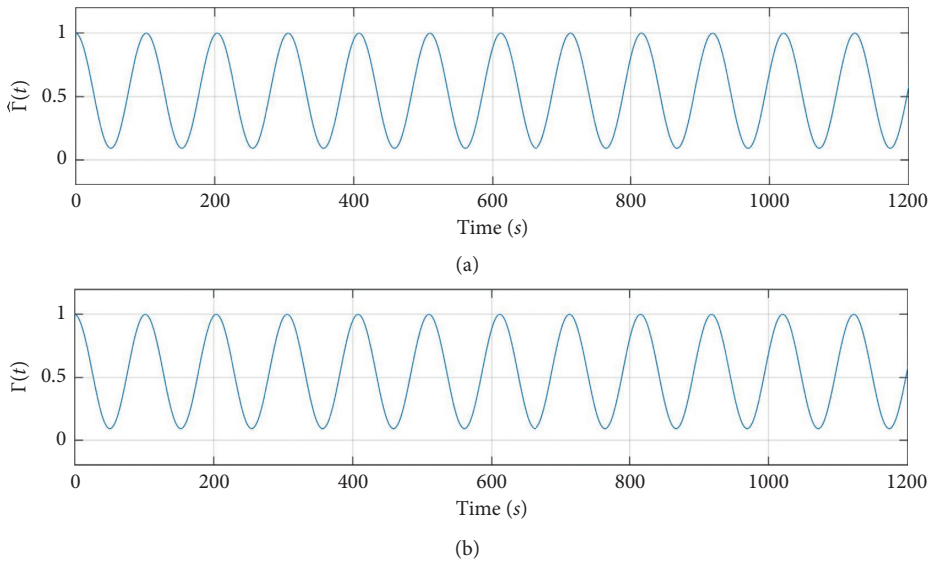

Figure 5: (a) $\widehat{\Gamma}(\mathbf{t})$ and (b) $\Gamma(\mathbf{t})$ of the case 2.

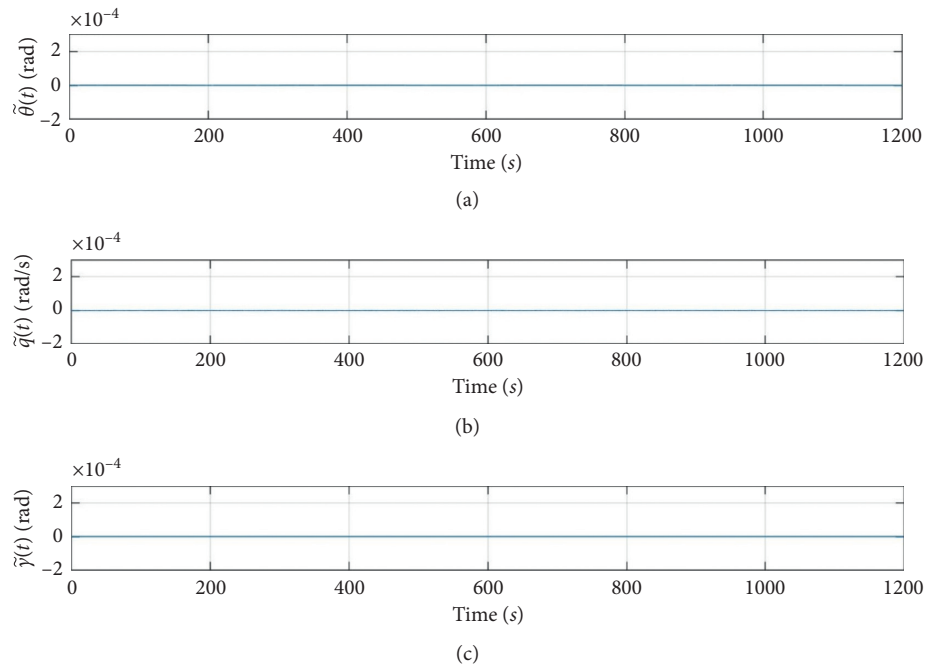

Figure 6: Tracking error case 2: (a) pitch angle error; (b) pitch rate error; (c) flight path angle error.

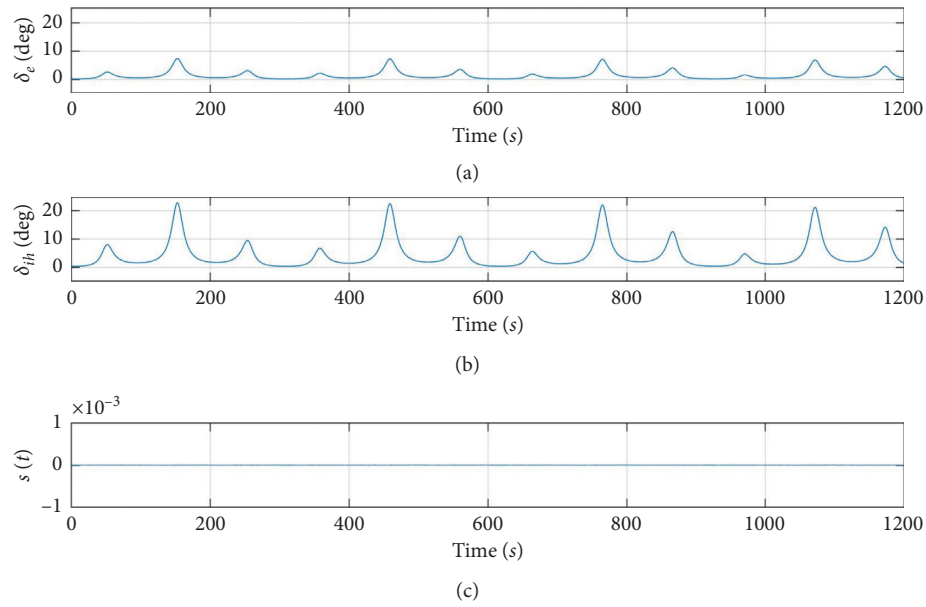

Figure 7: Control signal and the sliding behavior of the case 2: (a) elevator; (b) horizontal stabilizer; (c) sliding surface.

5. Conclusions

A fault-tolerant control scheme for time-varying linear systems is presented. The proposed scheme uses the LQR to stabilize the nominal system so that when an actuator fault occurs, the integral sliding mode makes the faulty system behave as the nominal system in finite time. On the contrary, the control allocation is responsible for distributing the control signal, ensuring that the faulty system performs like the nominal system in finite time. An application to the longitudinal motion of an aircraft is included. Simulations are included showing the effectiveness of the proposed fault-tolerant control scheme.

Data Availability

The data used to support the findings of this study are included in the article.

Conflicts of Interest

The authors declare that there are no conflicts of interest regarding the publication of this paper.

Acknowledgments

This work was supported in part by the Secretaría de Investigación y Posgrado of the Instituto Politécnico Nacional (Grant nos. 20210595, 20202256, and 20211316) and Consejo Nacional de Ciencia y Tecnología Becas Nacionales (Grant no. CVU 921369).

References

[1] M. Blanke, M. Kinnaert, J. Lunze, and M. Staroswiecki, *Diagnosis and Fault-Tolerant Control*, Springer, Berlin, Germany, 2006.

[2] R. F. Stengel, "Intelligent failure-tolerant control," *IEEE Control Systems Magazine*, vol. 11, no. 4, pp. 14–23, 1991.

[3] R. J. Patton, "Robustness issues in fault-tolerant control," in *Proceeding of the IEEE Colloquium on Fault Diagnosis and Control System Reconfiguration*, p. 1, IET, London, UK, May 1993.

[4] A. Bondavalli, J. Stankovic, and L. Strigini, "Adaptable fault tolerance for real-time systems," in *Responsive Computer Systems: Steps toward Fault-Tolerant Real-Time Systems*, pp. 187–208, Springer, Berlin, Germany, 1995.

[5] R. J. Patton, "Fault-Tolerant control: the 1997 situation," *IFAC Proceedings Volumes*, vol. 30, no. 18, pp. 1029–1051, 1997.

[6] Y. Wang, X. Xie, M. Chadli, S. Xie, and Y. Peng, "Sliding mode control of fuzzy singularly perturbed descriptor systems," IEEE Transactions on Fuzzy Systems, 2020.

[7] Y. Wang, Y. Xia, H. Li, and P. Zhou, "A new integral sliding mode design method for nonlinear stochastic systems," *Automatica*, vol. 90, pp. 304–309, 2018.

[8] R. J. Patton, "fault-tolerant control," in *Encyclopedia of Systems and Control*, J. Baillieul and T. Samad, Eds., pp. 422–428, Springer, Berlin, Germany, 2015.

[9] L.-Y. Hao, J. H. Park, and D. Ye, "Integral sliding mode fault-tolerant control for uncertain linear systems over networks with signals quantization," *IEEE Transactions on Neural Networks and Learning Systems*, vol. 28, no. 9, pp. 2088–2100, 2017.

[10] H. Alwi and C. Edwards, "Fault tolerant control using sliding modes with on-line control allocation," in *Fault Tolerant Flight Control*, pp. 247–272, Springer, Berlin, Germany, 2010.

[11] F. J. Bejarano, L. Fridman, and A. Poznyak, "Output integral sliding mode control based on algebraic hierarchical observer," *International Journal of Control*, vol. 80, no. 3, pp. 443–453, 2007.

[12] V. Utkin and J. Shi, "Integral sliding mode in systems operating under uncertainty conditions," *35th IEEE Conference on Decision and Control*, , Kobe, Japan, December 1996.

[13] M. T. Hamayun, C. Edwards, and H. Alwi, "Design and analysis of an integral sliding mode fault-tolerant control

scheme," *IEEE Transactions on Automatic Control*, vol. 57, no. 7, pp. 1783–1789, 2011.

[14] Q. Hu and B. Xiao, "Adaptive fault tolerant control using integral sliding mode strategy with application to flexible spacecraft," *International Journal of Systems Science*, vol. 44, no. 12, pp. 2273–2286, 2013.

[15] M. T. Hamayun, H. Alwi, and C. Edwards, "An lpv fault tolerant control scheme using integral sliding modes," in *Proceedings of the 51st IEEE Conference on Decision and Control (CDC)*, Maui, China, December 2012.

[16] R. Galván-Guerra, X. Liu, S. Laghrouche, L. Fridman, and M. Wack, "Fault-tolerant control with control allocation for linear time varying systems: an output integral sliding mode approach," *IET Control Theory and Applications*, vol. 11, no. 2, pp. 245–253, 2017.

[17] A. Levant, "Sliding order and sliding accuracy in sliding mode control," *International Journal of Control*, vol. 58, no. 6, pp. 1247–1263, 1993.

[18] R. Seeber and M. Horn, "Stability proof for a well-established super-twisting parameter setting," *Automatica*, vol. 84, no. 1, pp. 241–243, 2017.

[19] R. Galván-Guerra, L. Fridman, J. E. Velázquez-Velázquez, S. Kamal, and B. Bandyopadhyay, "Continuous output integral sliding mode control for switched linear systems," *Nonlinear Analysis: Hybrid Systems*, vol. 22, pp. 284–305, 2016.

[20] A. Chalanga, S. Kamal, and B. Bandyopadhyay, "Continuous integral sliding mode control: a chattering free approach," in *Proceedings of the IEEE International Symposium on Industrial Electronics*, Taipei, China, May 2013.

[21] H. Ríos, S. Kamal, L. M. Fridman, and A. Zolghadri, "Fault tolerant control allocation via continuous integral sliding-modes: a hosm-observer approach," *Automatica*, vol. 51, pp. 318–325, 2015.

[22] S. Banerjee and A. Roy, *Linear Algebra and Matrix Analysis for Statistics*, CRC Press, Boca Raton, FL, USA,, 2014.

[23] O. Härkegård and S. Glad, "Resolving actuator redundancy-optimal control vs. control allocation☆," *Automatica*, vol. 41, no. 1, pp. 137–144, 2005.

[24] R. Seeber, M. Horn, and L. Fridman, "A novel method to estimate the reaching time of the super-twisting algorithm," *IEEE Transactions on Automatic Control*, vol. 63, no. 12, pp. 4301–4308, 2018.

[25] A. Levant, "Robust exact differentiation via sliding mode technique," *Automatica*, vol. 34, no. 3, pp. 379–384, 1998.

[26] H. Alwi, C. Edwards, and M. T. Hamayun, "Non-linear integral sliding mode fault tolerant longitudinal aircraft control," in *Proceedings of the IEEE International Conference on Control Applications (CCA)*, Denver, CO, USA, September 2011.

[27] C. Hanke and D. Nordwall, *The Simulation of a Jumbo Jet Transport Aircraft*, NASA, Washington, DC, USA, 1970.

Hindawi
Mathematical Problems in Engineering
Volume 2021, Article ID 6646231, 19 pages
https://doi.org/10.1155/2021/6646231

Research Article

LMI-Based Analysis and Stabilization of Nonlinear Descriptors with Multiple Delays via Delayed Nonlinear Controller Schemes

Javier Adrián Romero-Vega,[1] **Raúl Villafuerte-Segura**,[1] **and Víctor Estrada-Manzo**[2]

[1]*Research Center on Information Technology and Systems, Hidalgo State University, Pachuca-Hidalgo C. P. 42184, Mexico*
[2]*Department of Mechatronics of the Universidad Politécnica de Pachuca, Zempoala, C.P 43830, Mexico*

Correspondence should be addressed to Raúl Villafuerte-Segura; villafuerte@uaeh.edu.mx

Received 17 December 2020; Revised 31 January 2021; Accepted 10 February 2021; Published 8 March 2021

Academic Editor: Maria Patrizia Pera

This paper presents a convex approach for nonlinear descriptor systems with multiple delays; it allows designing delayed nonlinear controllers such that the closed-loop system holds exponential estimates for convergence. The proposal takes advantage of an equivalent convex representation of the given descriptor model together with Lyapunov-Krasovskii functionals; thus, the conditions are in the form of linear matrix inequalities, which can be efficiently solved by commercially available software. To avoid possible saturation in the actuators, conditions for bounding the control input are also given. Numerical and academic examples illustrate the performance of the proposal.

1. Introduction

In the last decades, a large number of results concerning the analysis and stabilization of systems by means of the direct Lyapunov method [1], since the publication of the book [2], linear matrix inequalities (LMIs) have become a preferred solution to many control problems [3, 4], as they can be effectively solved by means of convex optimization techniques already implemented in commercially available software [5, 6]. These ideas have been extended to the analysis of time-delay systems (TDSs) via LyapunovKrasovskii (L-K) functionals [7] or LyapunovRazumikhin (L-R) functions [8]. In this context, there are several results that provide sufficient stability conditions using LMI-based approaches for different classes of TDS, such as linear time-delay systems [9–13], uncertain linear time-delay systems [14–16], neutral linear systems [17–20], systems with uncertain time-invariant delays [21], descriptor system approach for TDS [22], linear parameter-varying (LPV) time-delay systems [23], systems with time-varying delays [24–29], exponential estimates for TDS [30, 31], systems with polytopic-type uncertainties [32], singular systems [33], neural networks with time delay [34, 35], and genetic regulatory networks with probabilistic time delays [36]. Recently, in [37] convex approaches are employed to provide robust stability conditions based on quasi-polynomials.

In general, delays are undesirable phenomena, because they can destabilize or produce a poor performance in the system response. However, in recent years, it has been shown that delays can also stabilize and improve the close-loop performance of a system. Moreover, the deliberate induction of delays by means of the control law is an efficient alternative to stabilize systems [38, 39]; these types of controllers are known as delayed ones. For example, in [40–42], a proportional control with an appropriate delay replaces a traditional proportional-derivative one; thus, the system response is fast and insensitive to high-frequency noise. In [43], a scheme called time-delayed feedback control (TDFC) is proposed, originating different investigations [44–55].

As mentioned above, LMI-based approaches have become important in the control community; however, in the context of TDS, there is an inherent conservatism for

stability and stabilization conditions even for linear setups [37]; this leaves room for improvements. Moreover, a problem little explored by the community is obtaining stability conditions for nonlinear TDS. Although, originally, LMI-based stability conditions were given for linear time-invariant (LTI) systems, these have also been used on LPV [3] and nonlinear setups via exact Takagi-Sugeno (TS) [56]. The latter case employs the sector of no linearity approach [57] which allows rewriting the original nonlinear model as a convex one by means of scalar convex functions that capture uncertainties and nonlinearities. This technique has also been applied to a class of nonlinear TDS; for instance, in [58, 59], sufficient LMI conditions are proposed; in [60], uncertain TS systems are considered; in [61], sufficient LMI conditions have been given for a class of nonlinear systems. A larger family of functionals is explored in [62]. Nonetheless, none of these previous works deal with nonlinear descriptor systems; they appear when using the EulerLagrange formalism for modeling plants [63]. In the context of convex descriptor models without delays, there are some recent works [64, 65]; time-delay nonlinear descriptor systems are a few works in the literature; for instance, in [66], LMI stability and stabilization conditions have been developed for systems with only one time-delay.

Contribution: this paper proposes an LMI methodology for analysis and stability of nonlinear descriptor systems with multiple delays, thus overcoming recent results in the literature. For example, the work [4] only considers linear in standard form systems with multiple delays, [52] only studies nonlinear systems in standard form, and [66] treats nonlinear systems in descriptor with one delay. Additionally, to avoid possible saturation in the actuators, LMI conditions for bounding the control signal are established. Numerical and academic examples illustrate that including delays in the controller can reduce noise in the control signal, which increases the useful life of the actuators.

The paper is organized as follows: the problem statement and preliminary results are shown in Section 2. LMI-based stability analysis and delayed nonlinear controller design conditions for a class of nonlinear descriptors systems with multiple delays are given in Section 3, and additionally conditions for input constraints are also given. In Section 4, the implementation and numerical validation of the previous theoretical results are provided. Concluding remarks are stated in Section 5.

2. Problem Statement and Preliminary Results

2.1. Problem Statement. Let us consider a nonlinear descriptor system under multiple delays of the following form:

$$E(x)\dot{x}(t) = A(x)x(t) + \sum_{h=1}^{d} A_{\tau_h}(x)x\left(t-\tau_h\right) + B(x)u,$$
$$x(\theta) = \phi(\theta), \quad \theta \in [-\tau, 0], \tag{1}$$

where $x \in \mathbb{R}^n$ is the state vector, $u \in \mathbb{R}^m$ is the input vector, $E(x)$, $A(x)$, $B(x)$, and $A_{\tau_h}(x)$ are matrix functions assumed to be smooth and bounded, $0 < \tau_1 < \tau_2 < \cdots < \tau_d = \tau$ are time delays, and $\phi \in \mathscr{C}([-\tau, 0], \mathbb{R}^n)$ are the initial functions, where $\mathscr{C}([-\tau, 0], \mathbb{R}^n)$ is the Banach space of real continuous functions on the intervals $[-\tau, 0]$ with the following norm:

$$\|\phi\|_\tau = \max_{\theta\in[-\tau,0]} \|\phi(\theta)\|, \tag{2}$$

where $\|\cdot\|$ stands for the Euclidean norm in $\mathbb{R}^n$. It is assumed that for each initial condition $\phi \in \mathscr{C}([-\tau, 0], \mathbb{R}^n)$, $t > 0$ there exists a unique solution $x(t, \phi)$ of the system; moreover, $x_t(\phi) = \{x(t+\theta, \phi)\colon \theta \in [-\tau, 0]\}$. In this work, matrix $E(x)$ is assumed to be invertible, at least in a region including the origin; this is a common assumption when studying systems (1) derived from the EulerLagrange formalism [63, 65].

In order to obtain LMI conditions, the sector nonlinearity approach [57] is employed to compute an exact convex representation of (1). This methodology begins by defining a premise vector $z(x) \in \mathbb{R}^p$ whose entries are different nonconstant terms in $A(x)$, $A_{\tau_h}(x)$, $B(x)$, $h \in \{1, 2, \ldots, d\}$; similarly, $\zeta(x) \in \mathbb{R}^q$ is the premise vector with nonconstant terms in $E(x)$. It is assumed that each entry of the vectors $z(x)$ and $\zeta(x)$ is bounded in the compact set Ω_x that includes the origin, that is, $z_i(x) \in [z_i^0, z_i^1]$ and $\zeta_k(x) \in [\zeta_k^0, \zeta_k^1]$. Thus, each of them can be expressed as convex sums of their bounds:

$$z_i(x) = z_i^0 w_0^i(x) + z_i^1 w_1^i(x), \quad i \in \{1, 2, \ldots, p\},$$
$$\zeta_k(x) = \zeta_k^0 \omega_0^k(x) + \zeta_k^1 \omega_1^k(x), \quad k \in \{1, 2, \ldots, q\}, \tag{3}$$

where

$$w_0^i(z) = \frac{z_i^1 - z_i(x)}{z_i^1 - z_i^0},$$
$$w_1^i(x) = 1 - w_0^i(z),$$
$$\omega_0^k(\zeta) = \frac{\zeta_k^1 - \zeta_k(x)}{\zeta_k^1 - \zeta_k^0}, \tag{4}$$
$$\omega_1^k(\zeta) = 1 - \omega_0^k(\zeta),$$

are scalar convex functions holding the convex sum property for all $x \in \Omega_x$, i.e., $0 \le w_i(z) \le 1$, $w_1^i + w_0^i = 1$, $0 \le \omega_k(\zeta) \le 1$, and $\omega_1^k + \omega_0^k = 1$. Then, the so-called scheduling (membership) functions can be computed:

$$\mathbf{w}_i(z) = w_{i_1}^1(x) w_{i_2}^2(x) \cdots w_{i_r}^p(x), \quad i_j \in \{0, 1\},$$
$$\boldsymbol{\omega}_k(\zeta) = \omega_{k_1}^1(x) \omega_{k_2}^2(x) \cdots \omega_{k_\rho}^q(x), \quad k_j \in \{0, 1\}, \tag{5}$$

where $i \in \{1, 2, \ldots, r\}$, $r = 2^p$, and indexes $[i_1 i_2 \cdots i_p]$ are chosen as a p-digit binary representation of $(i-1)$; similarly, $k \in \{1, 2, \ldots, \rho\}$, $i_j \in \{0, 1\}$, $\rho = 2^q$; and the set $[k_1 k_2 \cdots k_q]$ is a q-digit binary representation of $(k-1)$. The scheduling functions also hold the convex sum property in Ω_x. Finally, an equivalent convex representation of (1) is [67]

$$\sum_{k=1}^{\rho} \boldsymbol{\omega}_k(\zeta) E_k \dot{x}(t) = \sum_{i=1}^{r} \mathbf{w}_i(z) \cdot \left(A_i x(t) + \sum_{h=1}^{d} A_{\tau_h i} x(t-\tau_h) + B_i u \right), \tag{6}$$

where $E_k = E(x)|_{\omega_k(\zeta)=1}$, $A_i = A(x)|_{\mathbf{w}_i(z)=1}$, $A_{\tau_h i} = A_{\tau_h}(x)|_{w_i(z)=1}$, $h \in \{1, 2, \ldots, d\}$, and $B_i = B(x)|_{w_i(z)=1}$ are constants matrices; $r = 2^p$ and $\rho = 2^q$ are the number of vertices for the right and left side of (6), respectively. It is important to notice that (6) is a convex rewriting of (1); thus, all the conclusions derived from the former directly apply to the latter.

2.2. Notation and Properties. In the following, convex sums of matrices will be shortly represented by

$$\Upsilon_{\mathbf{w}} = \sum_{i=1}^{r} \mathbf{w}_i(z) \Upsilon_i, \Upsilon_{\boldsymbol{\omega}} = \sum_{k=1}^{\rho} \boldsymbol{\omega}_k(\zeta) \Upsilon_k, \Upsilon_{\mathbf{w}}^{-1} = \left(\sum_{i=1}^{r} \mathbf{w}_i(z) \Upsilon_i \right)^{-1},$$
$$\Upsilon_{\mathbf{ww\omega}} = \sum_{i=1}^{r} \sum_{j=1}^{r} \sum_{k=1}^{\rho} \mathbf{w}_i(z) \mathbf{w}_j(z) \boldsymbol{\omega}_k(\zeta) \Upsilon_{ijk}. \tag{7}$$

Thus, (6) is expressed as $E_\omega \dot{x}(t) = A_{\mathbf{w}} x(t) + \sum_{h=1}^{m} A_{\tau_h \mathbf{w}} x(t-\tau_h) + B_{\mathbf{w}} u(t)$. Additionally, an asterisk $(*)$ will be employed in matrix expressions to denote the transpose of the symmetric element; for in-line ones, it indicates the transpose of the terms in its left-hand side, that is, $A + B + A^T + B^T + C = A + B + (*) + C$.

Usually, when deriving LMI conditions for convex descriptor models, the designer is faced to inequalities of the form $\Upsilon_{\mathbf{ww}\omega} < 0$; the scheduling functions are dropped off by means of the following relaxation lemma:

Lemma 1 (see [68]). *Let $\Upsilon_{ijk} = \Upsilon_{ijk}^T$, $(i, j) = \{1, 2, \ldots, r\}^2$, and $k \in \{1, 2, \ldots, \rho\}$ be matrices of adequate sizes. Then,*

$$\sum_{i=1}^{r} \sum_{j=1}^{r} \sum_{k=1}^{\rho} \mathbf{w}_i(z) \mathbf{w}_j(z) \boldsymbol{\omega}_k(\zeta) \Upsilon_{ijk} < 0, \tag{8}$$

holds if the following LMIs,

$$\frac{2}{r-1} \Upsilon_{iik} + \Upsilon_{ijk} + \Upsilon_{jik} < 0, \tag{9}$$

are satisfied for all $(i, j) = \{1, 2, \ldots, r\}^2$, $k \in \{1, 2, \ldots, \rho\}$.

The following results establish the exponential estimates for time-delay nonlinear systems:

Lemma 2 (see [30]). *Consider system (1). If there exists a functional $V(\cdot)$ and positive constants c_1, c_2, and α, such that*

(1) $c_1 \|x\|^2 \leq V(x_t) \leq c_2 \|x_t\|_\tau^2$,

(2) $\dot{V}(x_t) + 2\alpha V(x_t) < 0$,

then, the solutions $x(t, \phi)$ of the system (1) satisfy the exponential estimates:

$$\|x(t, \phi)\| \leq \sqrt{\frac{c_2}{c_1}} e^{-\alpha t} \|\phi\|_\tau. \tag{10}$$

As customary, for the analysis and design of convex descriptor models, the so-called descriptor redundancy is employed [69]; in our case, the augmented vectors $\overline{x}(t) = \left[x^T(t) \;\; \dot{x}^T(t) \right]^T$ and $\overline{x}(t-\tau_h) = \left[x^T(t-\tau_h) \;\; \dot{x}^T(t-\tau_h) \right]^T$, $h \in \{1, 2, \ldots, d\}$, are employed to rewrite (6) as follows:

$$\overline{E} \dot{\overline{x}}(t) = \overline{A}_{\mathbf{w}\boldsymbol{\omega}} \overline{x}(t) + \sum_{h=1}^{d} \overline{A}_{\tau_h \mathbf{w}} \overline{x}(t-\tau_h) + \overline{B}_{\mathbf{w}} u, \tag{11}$$

with

$$\overline{E} = \begin{bmatrix} I & 0 \\ 0 & 0 \end{bmatrix}, \quad \overline{A}_{\mathbf{w}\boldsymbol{\omega}} = \begin{bmatrix} 0 & I \\ A_{\mathbf{w}} & -E_{\boldsymbol{\omega}} \end{bmatrix}, \quad \overline{A}_{\tau_h \mathbf{w}} = \begin{bmatrix} 0 & 0 \\ A_{\tau_h \mathbf{w}} & 0 \end{bmatrix}, \quad \overline{B}_{\mathbf{w}} = \begin{bmatrix} 0 \\ B_{\mathbf{w}} \end{bmatrix}, \quad h \in \{1, 2, \ldots, d\}. \tag{12}$$

In what follows, the stability and stabilization conditions are derived from the augmented system (11); nevertheless, it is important to stress that the system under study has the form (1).

Let us recall previous works on the subject. The work [66] studies the stability and stabilization of a nonlinear descriptor system with only one delay, that is (1) with $d = 1$. For stabilization purposes, the following control law is proposed:

$$u = K_{\mathbf{w}\boldsymbol{\omega}} x(t) + F_{\mathbf{w}\boldsymbol{\omega}} x(t-\tau), \tag{13}$$

with $K_{\mathbf{w}\omega} x(t) = \sum_{j=1}^{r} \sum_{k=1}^{\rho} \mathbf{w}_j(z(x)) \omega_k(\zeta(x)) K_{jk}$ and $F_{\mathbf{w}\omega} = \sum_{j=1}^{r} \sum_{k=1}^{\rho} \mathbf{w}_j(z(x)) \omega_k(\zeta(x)) F_{jk}$; it is a nonlinear control law with nonlinearities of both sides of the nonlinear descriptor model. In the Section 3, a generalization of this controller will be presented.

3. LMI Conditions for Descriptor Systems with Multiple Delays

In this section, the developments are based on the following LyapunovKrasovskii functional candidate:

$$V(x_\tau) = \overline{x}^T(t) \overline{E}^T \overline{P}_{\mathbf{w}} \overline{x}(t) + \sum_{h=1}^{d} \int_{-\tau_h}^{0} \overline{x}^T(t+\theta) \overline{E}^T \overline{Q}_h e^{2\alpha\theta} \overline{x}(t+\theta) \mathrm{d}\theta, \tag{14}$$

with

$$\overline{P}_{\mathbf{w}} = \begin{bmatrix} P_1 & 0 \\ P_{2\mathbf{w}} & P_{3\mathbf{w}} \end{bmatrix},$$
$$\overline{Q}_h = \begin{bmatrix} Q_h & 0 \\ 0 & 0 \end{bmatrix},$$
$$\overline{E}^T \overline{P}_{\mathbf{w}} = \overline{P}_{\mathbf{w}}^T \overline{E} \geq 0, \quad \alpha > 0, P_1 > 0, Q_h > 0, h \in \{1, 2, \ldots, d\}. \tag{15}$$

Note that, the functional (14) is a valid L-K functional candidate as it reduces to

$$V(x_\tau) = x^T(t) P_1 x(t) + \sum_{h=1}^{d} \int_{-\tau_h}^{0} x^T(t+\theta) Q_h e^{2\alpha\theta} x(t+\theta) \mathrm{d}\theta, \tag{16}$$

which is clearly positive definite and bounded by $c_1 \|x\|^2 \leq V(x_t) \leq c_2 \|x_t\|_\tau^2$, with $c_1 = \lambda_{\min}(P_1)$ and $c_2 = \lambda_{\max}(P_1) + \sum_{h=1}^{d} \tau_h \lambda_{\max}(Q_h)$, thus fulfilling conditions (1) in Lemma 2.

For the analysis of system (1), i.e., when $u = 0$, we have the following result.

Theorem 1. *The origin of system (1), with $u = 0$ and an exact convex representation (6), is exponentially stable if the exist matrices $P_1 > 0$, P_{2j}, P_{3j}, $Q_h > 0$ with $h \in \{1, 2, \ldots, d\}$, $j \in \{1, 2, \ldots, r\}$, and a scalar $\alpha > 0$ such that LMIs (9) hold with*

$$\Upsilon_{ijk} := \begin{bmatrix} P_{2j}^T A_i + A_i^T P_{2j} + 2\alpha P_1 + \sum_{h=1}^{d} Q_h & (*) & (*) & (*) & (*) \\ P_1 - E_k^T P_{2j} + P_{3j}^T A_i & -E_k^T P_{3j} - P_{3j}^T E_k & \cdots & (*) & (*) \\ P_{2j}^T A_{\tau_1 i} & A_{\tau_1 i}^T P_{3j} & -e^{-2\alpha\tau_1} Q_1 & \cdots & (*) \\ \vdots & \vdots & \cdots & \ddots & (*) \\ P_{2j}^T A_{\tau_d i} & A_{\tau_d i}^T P_{3j} & 0 & \cdots & -e^{-2\alpha\tau_d} Q_d \end{bmatrix}. \tag{17}$$

where $(i, j) = \{1, 2, \ldots, r\}^2$ and $k \in \{1, 2, \ldots, \rho\}$. Additionally, the solution $x(t, \phi)$ of (1) satisfies the exponential estimates:

$$\|x(t, \phi)\| \leq \sqrt{\frac{c_2}{c_1}} e^{-\alpha t} \|\phi\|_\tau, \tag{18}$$

with $c_1 = \lambda_{\min}(P_1)$ and $c_2 = \lambda_{\max}(P_1) + \sum_{h=1}^{d} \tau_h \lambda_{\max}(Q_h)$, $h \in \{1, 2, \ldots, d\}$.

Proof. The time derivative of (14) along the trajectories of (11) is $\dot{V}(x_\tau) = V_1 + V_2$ with

$$V_1 = \overline{x}^T(t) \overline{P}_{\mathbf{w}}^T \overline{E} \dot{\overline{x}}(t) + \dot{\overline{x}}^T(t) \overline{E}^T \overline{P}_{\mathbf{w}} \overline{x}(t),$$
$$V_2 = \sum_{h=1}^{m} \frac{d}{\mathrm{d}t} \int_{-\tau_h}^{0} \overline{x}^T(t+\theta) \overline{E}^T \overline{Q}_h e^{2\alpha\theta} \overline{x}(t+\theta) \mathrm{d}\theta, \tag{19}$$

which once the dynamics of (11) are substituted and using Leibniz's rule yield

$$V_1 = \bar{x}^T(t) \overline{P}_{\mathbf{w}}^T \left(\overline{A}_{\mathbf{w}\omega} \bar{x}(t) + \sum_{h=1}^{d} \bar{A}_{\tau_h \mathbf{w}} \bar{x}(t - \tau_h) \right) + \left(\bar{A}_{\mathbf{w}\omega} \bar{x}(t) + \sum_{h=1}^{d} \bar{A}_{\tau_h \mathbf{w}} \bar{x}(t - \tau_h) \right)^T \bar{P}_{\mathbf{w}} \bar{x}(t),$$
$$V_2 = \sum_{h=1}^{d} \left\{ \bar{x}^T(t) \bar{E}^T \bar{Q}_h \bar{x}(t) - \bar{x}^T(t - \tau_h) e^{-2\alpha\tau_h} \bar{E}^T \bar{Q}_h \bar{x}(t - \tau_h) \right\} - 2\alpha \int_{-\tau_h}^{0} \bar{x}^T(t+\theta) \bar{E}^T \bar{Q}_h e^{2\alpha\theta} \bar{x}(t+\theta) \mathrm{d}\theta \Bigg\}. \tag{20}$$

From the latter, we have that $\dot{V}(x_t) + 2\alpha V(x_t)$ is equal to

$$\begin{bmatrix} \overline{x}(t) \\ \overline{x}(t-\tau_1) \\ \vdots \\ \overline{x}(t-\tau_d) \end{bmatrix}^T \begin{bmatrix} \overline{P}_{\mathbf{w}}^T \overline{A}_{\mathbf{w}\omega} + \overline{A}_{\mathbf{w}\omega}^T \overline{P}_{\mathbf{w}} + 2\alpha \overline{E}^T \overline{P}_{\mathbf{w}} + \sum_{h=1}^{d} \overline{E}^T \overline{Q}_h & (*) & \cdots & (*) \\ \overline{A}_{\tau_1 \mathbf{w}}^T \overline{P}_{\mathbf{w}} & -e^{-2\alpha\tau_1} \overline{E}\,\overline{Q}_1 & \cdots & (*) \\ \vdots & \vdots & \ddots & (*) \\ \overline{A}_{\tau_d \mathbf{w}}^T \overline{P}_{\mathbf{w}} & 0 & \cdots & -e^{-2\alpha\tau_d} \overline{E}\,\overline{Q}_d \end{bmatrix} \begin{bmatrix} \overline{x}(t) \\ \overline{x}(t-\tau_1) \\ \vdots \\ \overline{x}(t-\tau_d) \end{bmatrix}. \tag{21}$$

Thus, in order to fulfill condition (2) in Lemma 2, $\dot{V}(x_t) + 2\alpha V(x_t) < 0$ can be established after some algebraic manipulations when developing vectors $\overline{x}(t)$ and $\overline{x}(t-\tau_h), h \in \{1, 2, \ldots, d\}$, by the following inequality:

$$\begin{bmatrix} P_{2\mathbf{w}}^T A_{\mathbf{w}} + A_{\mathbf{w}}^T P_{2\mathbf{w}} + 2\alpha P_1 + \sum_{h=1}^{d} Q_h & (*) & (*) & (*) & (*) \\ P_1 - E_{\boldsymbol{\omega}}^T P_{2\mathbf{w}} + P_{3\mathbf{w}}^T A_{\mathbf{w}} & -E_{\boldsymbol{\omega}}^T P_{3\mathbf{w}} - P_{3\mathbf{w}}^T E_{\boldsymbol{\omega}} & \cdots & (*) & (*) \\ P_{2\mathbf{w}}^T A_{\tau_1 \mathbf{w}} & A_{\tau_1 \mathbf{w}}^T P_{3\mathbf{w}} & -e^{-2\alpha\tau_1} Q_1 & \cdots & (*) \\ \vdots & \vdots & \cdots & \ddots & (*) \\ P_{2\mathbf{w}}^T A_{\tau_d \mathbf{w}} & A_{\tau_d \mathbf{w}}^T P_{3\mathbf{w}} & 0 & \cdots & -e^{-2\alpha\tau_d} Q_d \end{bmatrix} < 0. \tag{22}$$

Finally, in order to drop off the scheduling functions $\mathbf{w}$ and ω via the relaxation scheme in Lemma 1, the proof is concluded.

Let us consider system (1). Now, the task is to design a multiple delayed PDC control law of the following form:

$$u = K_{\mathbf{w}\boldsymbol{\omega}} x(t) + \sum_{h=1}^{d} F_{h\mathbf{w}\boldsymbol{\omega}} x(t-\tau_h), \tag{23}$$

where $K_{\mathbf{w}\omega} = \sum_{j=1}^{r} \sum_{k=1}^{\rho} \mathbf{w}_j(z(x)) \omega_k(\zeta(x)) K_{jk}$ and $F_{h\mathbf{w}\omega} = \sum_{j=1}^{r} \sum_{k=1}^{\rho} \mathbf{w}_j(z(x)) \omega_k(\zeta(x)) F_{hjk}, h \in \{1, 2, \ldots, d\}$ are nonlinear gains to be designed via the augmented system (11); thus, (23) can be expressed as $u(t) = \overline{K}_{\mathbf{w}\omega} \overline{x}(t) + \sum_{h=1}^{d} \overline{F}_{h\mathbf{w}\omega} \overline{x}(t-\tau_h)$ with $\overline{K}_{\mathbf{w}\omega} = [\, K_{\mathbf{w}\omega} \;\; 0 \,]$ and $\overline{F}_{h\mathbf{w}\omega} = [\, F_{h\mathbf{w}\omega} \;\; 0 \,]$. The following result provides LMI conditions for the design of the control law (23). It is based on a slightly modification of the L-K functional candidate (14), that is,

$$\begin{aligned} V(x_\tau) &= \overline{x}^T(t) \overline{E}^T \overline{P}_{\mathbf{w}}^{-1} \overline{x}(t) \\ &\quad + \sum_{h=1}^{d} \int_{-\tau_h}^{0} \overline{x}^T(t+\theta) \overline{E}^T \overline{Q}_h e^{2\alpha\theta} \overline{x}(t+\theta) \mathrm{d}\theta, \end{aligned} \tag{24}$$

with

$$\begin{aligned} &\overline{E}^T \overline{P}_{\mathbf{w}}^{-1} = \overline{P}_{\mathbf{w}}^{-T} \overline{E} \geq 0, \\ &\overline{P}_{\mathbf{w}}^{-1} = \begin{bmatrix} P_1 & 0 \\ P_{2\mathbf{w}} & P_{3\mathbf{w}} \end{bmatrix}^{-1}, \\ &\overline{Q}_h = \begin{bmatrix} Q_h & 0 \\ 0 & 0 \end{bmatrix}, \quad P_1 > 0, Q_h > 0, \alpha > 0, h \in \{1, 2, \ldots, d\}. \end{aligned} \tag{25}$$

□

Theorem 2. *The origin of system (1) with an exact convex representation (6), under the law of control (23), is exponentially stable if existing matrices $P_1 > 0$, P_{2j}, P_{3j}, $R_h > 0$, M_{jk}, $N_{hjk}, h \in \{1, 2, \ldots, d\}$, $j \in \{1, 2, \ldots, r\}$, and a scalar $\alpha > 0$ if the LMIs (9) hold with the following:*

$$\Upsilon_{ijk} := \begin{bmatrix} P_{2j}^T + P_{2j} + 2\alpha P_1 + \sum_{h=1}^{d} R_h & (*) & (*) & (*) & (*) \\ A_i P_1 + B_i M_{jk} - E_k P_{2j} + P_{3j}^T & -E_k P_{3j} - P_{3j}^T E_k^T & \cdots & (*) & (*) \\ 0 & P_1 A_{\tau_1 i}^T + N_{1jk}^T B_i^T & -e^{-2\alpha\tau_1} R_1 & \cdots & (*) \\ \vdots & \vdots & \cdots & \ddots & (*) \\ 0 & P_1 A_{\tau_d i}^T + N_{djk}^T B_i^T & 0 & \cdots & -e^{-2\alpha\tau_d} R_d \end{bmatrix}. \tag{26}$$

Then, the vertex control gains are computed as $K_{jk} = M_{jk}P_1^{-1}$ and $F_{hjk} = N_{hjk}P_1^{-1}$, $j \in \{1, 2 \ldots, r\}$, $k \in \{1, 2, \ldots, \rho\}$, and $h \in \{1, 2, \ldots, d\}$. Moreover, $Q_h = P_1^{-1}R_hP_1^{-1}, h \in \{1, 2, \ldots, d\}$ and the solution satisfies the following exponential estimates:

$$\|x(t, \phi)\| \leq \sqrt{\frac{c_2}{c_1}} e^{-\alpha t} \|\phi\|_\tau, \tag{27}$$

where $c_1 = \lambda_{\min}(P_1^{-1})$ and $c_2 = \lambda_{\max}(P_1^{-1}) + \sum_{h=1}^{d} \tau_h \lambda_{\max}(Q_h)$.

Proof. Using the augmented system (11) and its corresponding control law, the closed-loop system is

$$\overline{E}\dot{\overline{x}}(t) = (\overline{A}_{\mathbf{w}\boldsymbol{\omega}} + \overline{B}_{\mathbf{w}}\overline{K}_{\mathbf{w}\boldsymbol{\omega}})\overline{x}(t) + \sum_{h=1}^{d} \left(\overline{A}_{\mathbf{w}\tau_h} + \overline{B}_{\mathbf{w}}\overline{F}_{h\mathbf{w}\boldsymbol{\omega}}\right)\overline{x}(t - \tau_h). \tag{28}$$

Similar to the proof of Theorem 1, consider the functional (24) and its time derivative $\dot{V}(x_t) = V_1 + V_2$ with

$$\begin{aligned} V_1 &= \dot{\overline{x}}^T(t)\overline{E}^T\overline{P}_{\mathbf{w}}^{-1}\overline{x}(t) + \overline{x}^T(t)\overline{P}_{\mathbf{w}}^{-T}\overline{E}\dot{\overline{x}}(t), \\ V_2 &= \sum_{h=1}^{d} \frac{d}{dt} \int_{-\tau_h}^{0} \overline{x}^T(t + \theta)\overline{E}^T\overline{Q}_h e^{2\alpha\theta}\overline{x}(t + \theta)\mathrm{d}\theta. \end{aligned} \tag{29}$$

Substituting the dynamics of (28) in V_1 while using Leibniz's rule in V_2, we have

$$\begin{aligned} \dot{V}_1 &= \left((\overline{A}_{\mathbf{w}\boldsymbol{\omega}} + \overline{B}_{\mathbf{w}}\overline{K}_{\mathbf{w}\boldsymbol{\omega}})\overline{x}(t) + \sum_{h=1}^{d}\left(\overline{A}_{\mathbf{w}\tau_h} + \overline{B}_{\mathbf{w}}\overline{F}_{h\mathbf{w}\boldsymbol{\omega}}\right)\overline{x}(t - \tau_h)\right)^T \overline{P}_{\mathbf{w}}^{-1}\overline{x}(t) + \overline{x}^T(t)\overline{P}_{\mathbf{w}}^{-T} \\ &\quad \cdot \left((\overline{A}_{\mathbf{w}\boldsymbol{\omega}} + \overline{B}_{\mathbf{w}}\overline{K}_{\mathbf{w}\boldsymbol{\omega}})\overline{x}(t) + \sum_{h=1}^{d}\left(\overline{A}_{\mathbf{w}\tau_h} + \overline{B}_{\mathbf{w}}\overline{F}_{h\mathbf{w}\boldsymbol{\omega}}\right)\overline{x}(t - \tau_h)\right), \\ V_2 &= \sum_{h=1}^{d}\left\{\overline{x}^T(t)\overline{E}^T\overline{Q}_h\overline{x}(t) - \overline{x}^T(t - \tau_h)e^{-2\alpha\tau_h}\overline{E}^T\overline{Q}_h\overline{x}(t - \tau_h) - 2\alpha\int_{-\tau_h}^{0}\overline{x}^T(t + \theta)\overline{E}^T\overline{Q}_h e^{2\alpha\theta}\overline{x}(t + \theta)\mathrm{d}\theta\right\}. \end{aligned} \tag{30}$$

Therefore, $\dot{V}(x_t) + 2\alpha V(x_t)$ is equivalent to

$$\begin{bmatrix} \overline{x}(t) \\ \overline{x}(t - \tau_1) \\ \vdots \\ \overline{x}(t - \tau_d) \end{bmatrix}^T \begin{bmatrix} \overline{P}_{\mathbf{w}}^{-T}(\overline{A}_{\mathbf{w}\boldsymbol{\omega}} + \overline{B}_{\mathbf{w}}\overline{K}_{\mathbf{w}\boldsymbol{\omega}}) + (*) + 2\alpha\overline{E}^T\overline{P}_{\mathbf{w}}^{-1} + \sum_{h=1}^{d}\overline{E}^T\overline{Q}_h & (*) & \cdots & (*) \\ \left(\overline{A}_{\tau_1\mathbf{w}} + \overline{B}_{\mathbf{w}}\overline{F}_{1\mathbf{w}\boldsymbol{\omega}}\right)^T\overline{P}_{\mathbf{w}}^{-1} & -e^{-2\alpha\tau_1}\overline{E}^T\overline{Q}_1 & \cdots & (*) \\ \vdots & \cdots & \ddots & (*) \\ \left(\overline{A}_{\tau_d\mathbf{w}} + \overline{B}_{\mathbf{w}}F_{d\mathbf{w}\boldsymbol{\omega}}\right)^T\overline{P}_{\mathbf{w}}^{-1} & 0 & \cdots & -e^{-2\alpha\tau_d}\overline{E}^T\overline{Q}_d \end{bmatrix} \begin{bmatrix} \overline{x}(t) \\ \overline{x}(t - \tau_1) \\ \vdots \\ \overline{x}(t - \tau_d) \end{bmatrix}. \tag{31}$$

After some simplifications, $\dot{V}(x_t) + 2\alpha V(x_t) < 0$ (condition (2) in Lemma 2 holds if

$$\begin{bmatrix} -P_1^{-T}P_{2\mathbf{w}}P_{3\mathbf{w}}^{-T}(A_{\mathbf{w}} + B_{\mathbf{w}}K_{\mathbf{w}\boldsymbol{\omega}}) + (*) + 2\alpha P_1^{-1} + \sum_{h=1}^{d} Q_h & (*) & (*) & (*) & (*) \\ P_{3\mathbf{w}}^{-T}(A_{\mathbf{w}} + B_{\mathbf{w}}K_{\mathbf{w}\boldsymbol{\omega}}) + P_i^{-1} + E_{\boldsymbol{\omega}}^T P_{3\mathbf{w}}^{-1}P_1^{-1} & -E_{\boldsymbol{\omega}}^T P_{3\mathbf{w}}^{-1} - P_{3\mathbf{w}}^{-T}E_{\boldsymbol{\omega}} & \cdots & (*) & (*) \\ -\left(A_{\tau_1\mathbf{w}}^T + F_{1\mathbf{w}\boldsymbol{\omega}}^T B_W^T\right)P_{3\mathbf{w}}^{-1}P_{2\mathbf{w}}P_1^{-1} & \left(A_{\tau_1\mathbf{w}}^T + F_{1\mathbf{w}\boldsymbol{\omega}}^T\right)P_{3\mathbf{w}}^{-1} & -e^{-2\alpha\tau_1}Q_1 & \cdots & (*) \\ \vdots & \vdots & \cdots & \ddots & (*) \\ -\left(A_{\tau_d\mathbf{w}}^T + F_{d\mathbf{w}\boldsymbol{\omega}}^T B_W^T\right)P_{3\mathbf{w}}^{-1}P_{2\mathbf{w}}P_1^{-1} & \left(A_{\tau_d\mathbf{w}}^T + F_{d\mathbf{w}\boldsymbol{\omega}}^T B_W^T\right)P_{3\mathbf{w}}^{-1} & 0 & \cdots & -e^{-2\alpha\tau_d}Q_d \end{bmatrix} < 0, \tag{32}$$

holds too; however, from the previous inequality, one cannot directly obtain LMI conditions. Thus, by means of the congruence property, that is, pre- and postmultiplying by the matrix block $-\operatorname{diag}\left[\begin{bmatrix} P_1 & 0 \\ P_{2\mathbf{w}} & P_{3\mathbf{w}} \end{bmatrix}, \underbrace{P_1, \ldots, P_1}_{d}\right]$ gives

$$\Upsilon_{ww\omega} := \begin{bmatrix} P_{2\mathbf{w}}^T + P_{2\mathbf{w}} + 2\alpha P_1 + \sum_{h=1}^{d} R_h & (*) & (*) & (*) & (*) \\ A_{\mathbf{w}}P_1 + B_{\mathbf{w}}M_{\mathbf{w}\boldsymbol{\omega}} - E_{\boldsymbol{\omega}}P_{2\mathbf{w}} + P_{3\mathbf{w}}^T & -E_{\boldsymbol{\omega}}P_{3\mathbf{w}} - P_{3\mathbf{w}}^T E_{\boldsymbol{\omega}}^T & \cdots & (*) & (*) \\ 0 & P_1 A_{\tau_1\mathbf{w}}^T + N_{1\mathbf{w}\boldsymbol{\omega}}^T B_{\mathbf{w}}^T & -e^{-2\alpha\tau_1}R_1 & \cdots & (*) \\ \vdots & \vdots & \cdots & \ddots & (*) \\ 0 & P_1 A_{\tau_d\mathbf{w}}^T + N_{d\mathbf{w}\boldsymbol{\omega}}^T B_{\mathbf{w}}^T & 0 & \cdots & -e^{-2\alpha\tau_d}R_d \end{bmatrix} < 0, \tag{33}$$

with the definitions $M_{\mathbf{w}\omega} = K_{\mathbf{w}\omega}P_1$ and $N_{h\mathbf{w}\omega} = F_{h\mathbf{w}\omega}P_1$, $h \in \{1, 2, \ldots, d\}$. Now, the previous inequality can be translated into the LMI conditions in the theorem once the relaxation scheme in Lemma 1 is applied.

Recall that, by hypothesis matrix, $E(x)$ in (1) is invertible in a region around the origin; thus, it is always possible to calculate a standard state-space form as follows:

$$\dot{x}(t) = \widetilde{A}(x)x(t) + \sum_{h=1}^{d} \widetilde{A}_{\tau_h}(x)x(t-\tau_h) + \widetilde{B}(x)u, \tag{34}$$

where $\widetilde{A}(x) = E^{-1}(x)A(x)$, $\widetilde{B}(x) = E^{-1}(x)B(x)$, and $\widetilde{A}_{\tau_h}(x) = E^{-1}(x)A_{\tau_h}(x)$, $h \in \{1, 2, \ldots, d\}$. Naturally, it is possible to obtain a convex representation of system (34), that is,

$$\dot{x}(t) = \widetilde{A}_{\mathbf{w}}(x)x(t) + \sum_{h=1}^{d} \widetilde{A}_{\tau_h\mathbf{w}}(x)x(t-\tau_h) + \widetilde{B}_{\mathbf{w}}(x)u, \tag{35}$$

with $\widetilde{A}_{\mathbf{w}} = \sum_{i=1}^{\widetilde{r}} \mathbf{w}_i(z)\widetilde{A}_i$, $\widetilde{A}_{\tau_h\mathbf{w}} = \sum_{i=1}^{\widetilde{r}} \mathbf{w}_i(z)\widetilde{A}_{\tau_h i}$, and $\widetilde{B}_{\mathbf{w}} = \sum_{i=1}^{\widetilde{r}} \mathbf{w}_i(z)\widetilde{B}_i$, where $\widetilde{r}$ is the number of vertex models, $h \in \{1, 2, \ldots, d\}$. Even though nonlinear systems (34) and (1) and their convex forms are equivalent, establishing exponential stability of them via LMIs may lead to different feasibility set solution. Keeping the original descriptor form (1) results in a convex representation with less vertex matrices; this, in general, yields less conservative results [64].

Thus, the following result provides stability and stabilization conditions for systems of the form (34) by means of the L-K functional (14) (for stability) and (24) (for stabilization), respectively.

Corollary 1. *Stability: the origin of system (1), with $u = 0$ and an exact convex representation (35), is exponentially stable if the exist matrices $P_1 > 0$, P_{2j}, P_{3j}, and $Q_h > 0$ with $h \in \{1, 2, \ldots, d\}$, $j \in \{1, 2, \ldots, \widetilde{r}\}$, and a scalar $\alpha > 0$ such that LMIs,*

$$\frac{2}{\widetilde{r}-1}\Upsilon_{ii} + \Upsilon_{ij} + \Upsilon_{ji} < 0, \quad \forall (i, j) = \{1, 2, \ldots, \widetilde{r}\}^2, \tag{36}$$

hold with

$$\Upsilon_{ij} := \begin{bmatrix} P_{2j}^T\widetilde{A}_i + \widetilde{A}_i^T P_{2j} + 2\alpha P_1 + \sum_{h=1}^{d} Q_h & (*) & (*) & (*) & (*) \\ P_1 - P_{2j} + P_{3j}^T\widetilde{A}_i & -P_{3j} - P_{3j}^T & \cdots & (*) & (*) \\ P_{2j}^T\widetilde{A}_{\tau_1 i} & \widetilde{A}_{\tau_1 i}^T P_{3j} & -e^{-2\alpha\tau_1}Q_1 & \cdots & (*) \\ \vdots & \vdots & \cdots & \ddots & (*) \\ P_{2j}^T\widetilde{A}_{\tau_d i} & \widetilde{A}_{\tau_d i}^T P_{3j} & 0 & \cdots & -e^{-2\alpha\tau_d}Q_d \end{bmatrix}. \tag{37}$$

Moreover, the solution $x(t, \phi)$ satisfies the following exponential estimates:

$$\|x(t, \phi)\| \leq \sqrt{\frac{c_2}{c_1}}e^{-\alpha t}\|\phi\|_\tau. \tag{38}$$

Stabilization: the origin of system (1) with an exact convex representation (35), under the law of control $u = \widetilde{K}_{\mathbf{w}\omega}x(t) + \sum_{h=1}^{d} \widetilde{F}_{h\mathbf{w}\omega}x(t-\tau_h)$, is exponentially stable if existing matrices $P_1 > 0$, P_{2j}, P_{3j}, $R_h > 0$, $\widetilde{M}_j$, $\widetilde{N}_{hj}$, $h \in \{1, 2, \ldots, d\}$, $j \in \{1, 2, \ldots, \widetilde{r}\}$, and a scalar $\alpha > 0$ if the LMIs (36) hold with

$$\Upsilon_{ij} \coloneqq \begin{bmatrix} P_{2j}^T + P_{2j} + 2\alpha P_1 + \sum_{h=1}^{d} R_h & (*) & (*) & (*) & (*) \\ \widetilde{A}_i P_1 + \widetilde{B}_i \widetilde{M}_j - P_{2j} + P_{3j}^T & -P_{3j} - P_{3j}^T & \dots & (*) & (*) \\ 0 & P_1 \widetilde{A}_{\tau_1 i}^T + \widetilde{N}_{1j}^T \widetilde{B}_i^T & -e^{-2\alpha\tau_1} R_1 & \dots & (*) \\ \vdots & \vdots & \dots & \ddots & (*) \\ 0 & P_1 \widetilde{A}_{\tau_d i}^T + \widetilde{N}_{dj}^T \widetilde{B}_i^T & 0 & \dots & -e^{-2\alpha\tau_d} R_d \end{bmatrix}. \tag{39}$$

Then, the vertex control gains are computed as $\widetilde{K}_j = \widetilde{M}_j P_1^{-1}$ and $\widetilde{F}_{hj} = \widetilde{N}_{hj} P_1^{-1}$, $\widetilde{F}_{hj} = \widetilde{N}_{hj} P_1^{-1}$, $j \in \{1, 2 \dots, \widetilde{r}\}, h \in \{1, 2, \dots, d\}$. Then, the solution satisfies the following exponential estimates:

$$\|x(t, \phi)\| \leq \sqrt{\frac{c_2}{c_1}} e^{-\alpha t} \|\phi\|_\tau. \tag{40}$$

Proof. It follows a similar path than results in Theorems 1 and 2, respectively.

The result above employs the same L-K functional of the descriptor approach, and thus the slack matrices $P_{2\mathbf{w}}$ and $P_{3\mathbf{w}}$ are also considered into the LMI conditions. Another set of LMI conditions for establishing the exponential estimates of systems in standard form (34) and its convex representation (35) can be done via a L-K functional without slack matrices, namely,

$$V(x_\tau) = x^T(t) P x(t) + \sum_{h=1}^{d} \int_{-\tau_h}^{0} x^T(t+\theta) Q_h e^{2\alpha\theta} x(t+\theta) \mathrm{d}\theta, \tag{41}$$

whose positiveness is inferred by $P > 0$, $Q_h > 0$, $h \in \{1, 2, \dots, d\}$ and its boundedness $c_1 \|x\|^2 \leq V(x_t) \leq c_2 \|x_t\|_\tau^2$, with $c_1 = \lambda_{\min}(P)$ and $c_2 = \lambda_{\max}(P) + \sum_{h=1}^{d} \tau_h \lambda_{\max}(Q_h)$. This is summarized in the following result. □

Corollary 2. *The origin of the system (1) with an exact convex representation (35) and $u(t) = 0$ is exponentially stable if there exists matrices $P > 0$, $Q_h > 0$ with $h \in \{1, 2, \dots, d\}$ and a scalar $\alpha > 0$ such that,*

$$\begin{bmatrix} P\widetilde{A}_i + \widetilde{A}_i^T P + 2\alpha P + \sum_{h=1}^{d} Q_h & (*) & \cdots & (*) \\ \widetilde{A}_{\tau_1 i}^T P & -e^{-2\alpha\tau_1} Q_1 & \cdots & (*) \\ \vdots & \vdots & \ddots & (*) \\ \widetilde{A}_{\tau_d i}^T P & \cdots & \cdots & -e^{-2\alpha\tau_d} Q_d \end{bmatrix} < 0, \tag{42}$$

holds for $i \in \{1, 2, \dots, \widetilde{r}\}$. Then, the solution satisfies the following exponential estimates:

$$\|x(t, \phi)\| \leq \sqrt{\frac{c_2}{c_1}} e^{-\alpha t} \|\phi\|_\tau, \tag{43}$$

with $c_1 = \lambda_{\min}(P)$ and $c_2 = \lambda_{\max}(P) + \sum_{h=1}^{d} \tau_h Q_h$.

Proof. It follows a similar path than previous results. □

Remark 1. Theorem 1 establishes LMI conditions for the exponential estimates for the origin of system (1), these conditions include results in [66, Theorem 1] are always included when $d = 1$ (system (1) with only one delay). Moreover, conditions in Corollary 2 always include those for linear systems in [4, Theorem 2], to see this set $r = 1$.

Remark 2. The numerical complexity of the LMI problems in the above results can be approximated by $\log_{10} = (n_d^3 n_l)$, where n_l is the number of total LMI rows and n_d is the number of scalar decision variables [70]. For Theorem 1 we have $n_l = n(d+2)r^2\ \rho + n(d+1)$ and $n_d = 0.5n(n+1)(1+d) + 2rn^2$; as for Theorem 2, $n_l = n(d+2)r^2\rho + n(d+1)$ and $n_d = 0.5n(n+1)(1+d) + 2rn^2 + nmr\rho(1+d)$; as for standard systems, Corollary 1 (stability) is $n_l = n(d+2)\widetilde{r}^2 + n(d+1)$ and $n_d = 0.5n(n+1)(1+d) + 2\widetilde{r}n^2$; Corollary 1 (stabilization) is $n_l = n(d+2)\widetilde{r}^2 + n(d+1)$ and $n_d = 0.5n(n+1)(1+d) + 2\widetilde{r}n^2 + nm\widetilde{r}(1+d)$; while Corollary 2 is $n_l = n(d+1)\widetilde{r} + n(d+1)$ and $n_d = 0.5n(n+1)(1+d)$.

Results in Theorem 2 can be directly applied for real-world setups; nevertheless, the LMIs might render controller gains whose magnitude cannot be applied in practice. To alleviate this issue as well as to avoid damages in the actuators, the following result provides conditions for bounding the control input (23); they can be combined with those of Theorem 2.

Theorem 3. *Consider the delayed nonlinear controller given in (23); then, this controller satisfies that $\|u\| < \mu$, for any $\mu > 0$, if the following inequalities hold:*

$$\begin{bmatrix} P_1 & M_{\mathbf{w\omega}}^T \\ M_{\mathbf{w\omega}} & \dfrac{\mu^2}{2} I \end{bmatrix} > 0, \tag{44}$$

$$\begin{bmatrix} e^{-2\alpha\tau_h} R_h & N_{h\mathbf{w\omega}}^T \\ N_{h\mathbf{w\omega}} & \dfrac{\mu^2}{2} I \end{bmatrix} > 0, \quad h \in \{1, 2, \ldots, d\}, \tag{45}$$

$$\begin{bmatrix} \tau^{-1} & \phi^T(\theta) & \phi^T(\theta) & \cdots & \phi^T(\theta) \\ \phi(\theta) & P_1 & 0 & \cdots & 0 \\ \phi(\theta) & 0 & R_1 & \cdots & 0 \\ \vdots & \vdots & \vdots & \ddots & 0 \\ \phi(\theta) & 0 & 0 & \cdots & R_d \end{bmatrix} > 0, \quad \forall \theta \in [-\tau, 0]. \tag{46}$$

Proof. Observe that $\|u\|^2 = u^T u$ with the delayed PDC (23) yields

$$\begin{aligned} \|u\|^2 &= \left(K_{\mathbf{w\omega}} x(t) + \sum_{h=1}^{d} F_{h\mathbf{w\omega}} x(t - \tau_h) \right)^T \left(K_{\mathbf{w\omega}} x(t) + \sum_{h=1}^{d} F_{h\mathbf{w}\omega} x(t - \tau_h) \right) \\ &= x^T(t) K_{\mathbf{w\omega}}^T K_{\mathbf{w\omega}} x(t) + 2 \sum_{h=1}^{d} x^T(t) K_{\mathbf{w\omega}}^T F_{h\mathbf{w\omega}} x(t - \tau_h) + \sum_{h=1}^{d} x^T(t - \tau_h) F_{h\mathbf{w\omega}}^T F_{h\mathbf{w\omega}} x(t - \tau_h) \\ &\le 2 \left(x^T(t) K_{\mathbf{w\omega}}^T K_{\mathbf{w\omega}} x(t) + \sum_{h=1}^{d} x^T(t - \tau_h) F_{h\mathbf{w\omega}}^T F_{h\mathbf{w\omega}} x(t - \tau_h) \right) \\ &\le 2 \left(x^T(t) K_{\mathbf{w\omega}}^T K_{\mathbf{w\omega}} x(t) + \sum_{h=1}^{d} \int_{-\tau_h}^{0} x^T(t + \theta) F_{h\mathbf{w\omega}}^T F_{h\mathbf{w\omega}} x(t + \theta) \mathrm{d}\theta \right) \le \mu^2, \end{aligned} \tag{47}$$

which is satisfied if the following holds:

$$\begin{aligned} &x^T(t) K_{\mathbf{w\omega}}^T 2\mu^{-2} K_{\mathbf{w\omega}} x(t) \\ &\quad + \sum_{h=1}^{d} \int_{-\tau_h}^{0} x^T(t + \theta) F_{h\mathbf{w\omega}}^T 2\mu^{-2} F_{h\mathbf{w\omega}} x(t + \theta) \mathrm{d}\theta \le 1. \end{aligned} \tag{48}$$

On the other hand, let us consider the following inequality on functional (14):

$$\begin{aligned} V(x_t) &= x^T(t) P_1^{-1} x(t) + \sum_{h=1}^{d} \int_{-\tau_h}^{0} x^T(t + \theta) e^{2\alpha\theta} Q_h x(t + \theta) \mathrm{d}\theta \\ &\le \phi^T(0) P_1^{-1} \phi(0) + \sum_{h=1}^{d} \int_{-\tau_h}^{0} \phi^T(\theta) e^{2\alpha\theta} Q_h \phi(\theta) \mathrm{d}\theta \le \phi^T(0) P_1^{-1} \phi(0) + \sum_{h=1}^{d} \int_{-\tau}^{0} \phi^T(\theta) e^{2\alpha\theta} Q_h \phi(\theta) \mathrm{d}\theta \le 1. \end{aligned} \tag{49}$$

Now, combining (48) and (49), it follows that

$$\begin{aligned} 0 &< x^T(t) K_{\mathbf{w\omega}}^T 2\mu^{-2} K_{\mathbf{w\omega}} x(t) + \sum_{h=1}^{d} \int_{-\tau_h}^{0} x^T(t + \theta) F_{h\mathbf{w\omega}}^T 2\mu^{-2} F_{h\mathbf{w\omega}} x(t + \theta) \mathrm{d}\theta \\ &\le x^T(t) P_1^{-1} x(t) + \sum_{h=1}^{d} \int_{-\tau_h}^{0} x^T(t + \theta) e^{2\alpha\theta} Q_h x(t + \theta) \mathrm{d}\theta \\ &\le \phi^T(0) P_1^{-1} \phi(0) + \sum_{h=1}^{d} \int_{-\tau_h}^{0} \phi^T(\theta) e^{2\alpha\theta} Q_h \phi(\theta) \mathrm{d}\theta \\ &< \phi^T(0) P_1^{-1} \phi(0) + \sum_{h=1}^{d} \int_{-\tau}^{0} \phi^T(\theta) \left(P_1^{-1} Q_h^{-1} \right) Q_h \left(Q_h^{-1} P_1^{-1} \right) \phi(\theta) \mathrm{d}\theta \le 1, \end{aligned} \tag{50}$$

or equivalently

$$x^T(t)\left(P_1^{-1} - K_{\mathbf{w\omega}}^T 2\mu^{-2} K_{\mathbf{w\omega}}\right)x(t) + \sum_{h=1}^{d}\int_{-\tau_h}^{0} x^T(t+\theta)\left(e^{2\alpha\theta}Q_h - F_{h\mathbf{w\omega}}^T 2\mu^{-2} F_{h\mathbf{w\omega}}\right)x(t+\theta)\mathrm{d}\theta > 0, \tag{51}$$

$$\int_{-\tau}^{0}\left(\tau^{-1} - \phi^T(\theta)P_1^{-1}\phi(\theta) - \sum_{h=1}^{d}\phi^T(\theta)X_1 Q_h^{-1} X_1\phi(\theta)\right)\mathrm{d}\theta > 0. \tag{52}$$

Thus, (51) is satisfied if

$$\begin{aligned} &P_1^{-1} - K_{\mathbf{w\omega}}^T 2\mu^{-2} K_{\mathbf{w\omega}} > 0, \\ &e^{-2\alpha\tau_h}Q_h - F_{h\mathbf{w\omega}}^T 2\mu^{-2} F_{h\mathbf{w\omega}} > 0, \quad h \in \{1,\ldots,d\} \end{aligned} \tag{53}$$

hold too. From the latter inequalities and using the Schur complement together with congruence property with block – diag$[P_1, I]$, conditions (44) and (45) follow with $M_{\mathbf{w}\omega} = K_{\mathbf{w}\omega}P_1^{-1}$, $N_{h\mathbf{w}\omega} = F_{h\mathbf{w}\omega}P_1^{-1}$, and $R_h = P_1 Q_h P_1$, $h \in \{1,2,\ldots,d\}$. Once again, employing the Schur complement on (52) gives

$$\begin{bmatrix} \tau^{-1} & \phi^T(\theta) & \phi^T(\theta) & \cdots & \phi^T(\theta) \\ \phi(\theta) & P_1 & 0 & \cdots & 0 \\ \phi(\theta) & 0 & P_1Q_1P_1 & \cdots & 0 \\ \vdots & \vdots & \vdots & \ddots & 0 \\ \phi(\theta) & 0 & 0 & \cdots & P_1Q_dP_1 \end{bmatrix} > 0, \quad \forall\theta \in [-\tau, 0], \tag{54}$$

which yields (46) after the substitution of $R_h = P_1 Q_h P_1, h \in \{1,2,\ldots,d\}$.

4. Examples

Next, a numerical example as well as the well-known inverted pendulum on a car is employed in order to illustrate the effectiveness of the proposed results. The LMI conditions have been checked with the LMIToolbox [6] within MATLAB 2109a.

4.1. Systems in Standard Form versus Descriptor Form. The following numerical example illustrates the advantages of the descriptor structure over standard state-space representations. Firstly, it compares stability at the origin via the LMIs in Theorem 1 and those in Corollary 2 by means of their feasibility sets. Secondly, a delayed nonlinear control law is designed via Theorem 2.

Consider a nonlinear system with two delays ($d = 2$) in the descriptor form (1):

$$\begin{aligned} E(x)\dot{x}(t) &= A(x)x(t) + A_{\tau_1}(x)x(t-\tau_1) \\ &\quad + A_{\tau_2}(x)x(t-\tau_2) + Bu, \\ x(\theta) &= \phi(\theta), \quad \theta \in [-\tau, 0], \end{aligned} \tag{55}$$

where the time delays are $\tau_1 = 0.1$ *y* $\tau_2 = 0.3 = \tau$, and matrices are as follows:

$$\begin{aligned} E(x) &= \begin{bmatrix} 0.8 & 0.1 - \dfrac{3}{5x_2^2 + 5} \\ 0.08 & 0.97 \end{bmatrix}, \\ A(x) &= \begin{bmatrix} -0.5\cos x_2 - 7.5 & -1 \\ \dfrac{0.083(7x_1 - 7\sin x_1)}{x_1} + a & -5.5 \end{bmatrix}, \\ B &= \begin{bmatrix} 0 \\ 1 \end{bmatrix}, \\ A_{\tau_1}(x) &= \begin{bmatrix} 9.5 + b & 14 \\ -6.6 & -\dfrac{0.067(155x_1 - 10\sin x_1)}{x_1} \end{bmatrix}, \\ A_{\tau_2}(x) &= \begin{bmatrix} \cos x_2 - 4.2 & -6.2 \\ 3.6 & 5.1 \end{bmatrix}. \end{aligned} \tag{56}$$

Descriptor form: following the sector nonlinearity approach, the following nonlinear terms have been identified: $\zeta_1 = (x_2^2 + 1)^{-1} \in [0,1]$, $z_1 = \cos x_2 \in [-1,1]$, and $z_2 = (\sin(x_1)/x_1) \in [-0.2, 1]$; their bounds have been calculated in the region $\Omega_x = \mathbb{R}^2$. Thus the vertex matrices are

$$\begin{aligned} A_1 &= \begin{bmatrix} -7 & -1 \\ 0.5 + a & -5.5 \end{bmatrix}, \\ A_2 &= \begin{bmatrix} -7 & -1 \\ -0.2 + a & -5.5 \end{bmatrix}, \\ A_3 &= \begin{bmatrix} -8 & -1 \\ 0.5 + a & -5.5 \end{bmatrix}, \\ A_4 &= \begin{bmatrix} -8 & -1 \\ -0.2 + a & -5.5 \end{bmatrix}, \\ A_{\tau_1 1} &= \begin{bmatrix} 9.4 + b & 14.2 \\ -6.6 & -10.2 \end{bmatrix}, \\ A_{\tau_1 2} &= \begin{bmatrix} 9.4 + b & 14.2 \\ -6.6 & -9.4 \end{bmatrix}, \\ A_{\tau_1 3} &= \begin{bmatrix} 9.4 + b & 14.2 \\ -6.6 & -10.2 \end{bmatrix}, \\ A_{\tau_1 4} &= \begin{bmatrix} 9.4 + b & 14.2 \\ -6.6 & -9.4 \end{bmatrix}, \\ A_{\tau_2 1} &= \begin{bmatrix} -5.2 & -6.2 \\ 3.6 & 5.1 \end{bmatrix}, \end{aligned}$$

$$
\begin{aligned}
A_{\tau_2 2} &= \begin{bmatrix} -5.2 & -6.2 \\ 3.6 & 5.1 \end{bmatrix}, \\
A_{\tau_2 3} &= \begin{bmatrix} -3.2 & -6.2 \\ 3.6 & 5.1 \end{bmatrix}, \\
A_{\tau_2 4} &= \begin{bmatrix} -3.2 & -6.2 \\ 3.6 & 5.1 \end{bmatrix}, \\
B_1 = B_2 = B_3 = B_4 &= \begin{bmatrix} 0 \\ 1 \end{bmatrix}, \\
E_1 &= \begin{bmatrix} 0.8 & 0.1 \\ 0.08 & 0.97 \end{bmatrix}, \\
E_2 &= \begin{bmatrix} 0.8 & -0.5 \\ 0.08 & 0.97 \end{bmatrix}.
\end{aligned}
\tag{57}
$$

Commonly, systems of the form (55) are analyzed in the following standard form:

$$
\dot{x} = \widetilde{A}(x)x(t) + \widetilde{A}_{\tau_1}(x)x\left(t-\tau_1\right) + \widetilde{A}_{\tau_2}(x)x\left(t-\tau_2\right) + \widetilde{B}(x)u,
\tag{58}
$$

where

$$
\begin{aligned}
\widetilde{A}(x) &= E^{-1}(x)A(x) = \frac{x_2^2+1}{0.768x_2^2+0.816}\begin{bmatrix} 0.97 & -0.1+\dfrac{3}{5x_2^2+5} \\ -0.08 & 0.8 \end{bmatrix}\begin{bmatrix} -0.5\cos x_2 - 7.5 & -1 \\ \dfrac{0.083\left(7x_1 - 7\sin x_1\right)}{x_1} + a & -5.5 \end{bmatrix}, \\
\widetilde{A}_{\tau_1}(x) &= E^{-1}(x)A_{\tau_1}(x) = \frac{x_2^2+1}{0.768x_2^2+0.816}\begin{bmatrix} 0.97 & -0.1+\dfrac{3}{5x_2^2+5} \\ -0.08 & 0.8 \end{bmatrix}\begin{bmatrix} 9.5+b & 14 \\ -6.6 & -\dfrac{0.067\left(155x_1 - 10\sin x_1\right)}{x_1} \end{bmatrix}, \\
\widetilde{A}_{\tau_2}(x) &= E^{-1}(x)A_{\tau_2}(x) = \frac{x_2^2+1}{0.768x_2^2+0.816}\begin{bmatrix} 0.97 & -0.1+\dfrac{3}{5x_2^2+5} \\ -0.08 & 0.8 \end{bmatrix}\begin{bmatrix} \cos x_2 - 4.2 & -6.2 \\ 3.6 & 5.1 \end{bmatrix}, \\
\widetilde{B}(x) &= E^{-1}(x)B = \frac{x_2^2+1}{0.768x_2^2+0.816}\begin{bmatrix} 0.97 & -0.1+\dfrac{3}{5x_2^2+5} \\ -0.08 & 0.8 \end{bmatrix}\begin{bmatrix} 0 \\ 1 \end{bmatrix}.
\end{aligned}
\tag{59}
$$

In this case, four nonlinear terms are defined as follows: $z_1 = \cos x_2 \in [-1, 1]$, $z_2 = \sin x_1/x_1 \in [-0.2, 1]$, $z_3 = (x_2^2 + 1)^{-1} \in [0, 1]$, and $z_4 = (x_2^2 + 1)/(0.768x_2^2 + 0.816) \in [1.2255, 1.3021]$; their bounds hold within Ω_x. Some of the vertex matrices are given below:

$$\widetilde{A}_1 = \begin{bmatrix} -8.3824 & -0.5147 \\ 1.1765 & -5.2942 \end{bmatrix},$$

$$\widetilde{A}_{10} = \begin{bmatrix} -10.1694 & -0.5469 \\ 1.3542 & -5.6251 \end{bmatrix},$$

$$\widetilde{A}_{15} = \begin{bmatrix} -9.6324 & -4.5589 \\ 0.5882 & -5.2942 \end{bmatrix},$$

$$\widetilde{A}_{\tau_1 1} = \begin{bmatrix} 11.9829 & 18.13 \\ -7.3922 & -11.3922 \end{bmatrix},$$

$$\widetilde{A}_{\tau_1 10} = \begin{bmatrix} 12.732 & 19.263 \\ -7.8543 & -12.104 \end{bmatrix},$$

$$\widetilde{A}_{\tau_1 15} = \begin{bmatrix} 7.13 & 11.12 \\ -7.3922 & -10.608 \end{bmatrix},$$

$$\widetilde{A}_{\tau_2 1} = \begin{bmatrix} -6.6226 & -7.9952 \\ 4.0392 & 5.6079 \end{bmatrix},$$

$$\widetilde{A}_{\tau_2 10} = \begin{bmatrix} -4.5105 & -8.4949 \\ 4.0834 & 5.9584 \end{bmatrix},$$

$$\widetilde{A}_{\tau_2 15} = \begin{bmatrix} -1.5981 & -4.2451 \\ 3.8432 & 5.6079 \end{bmatrix},$$

$$\widetilde{B}_1 = \begin{bmatrix} -0.12255 \\ 0.9804 \end{bmatrix},$$

$$\widetilde{B}_{10} = \begin{bmatrix} -0.13021 \\ 1.0417 \end{bmatrix},$$

$$\widetilde{B}_{15} = \begin{bmatrix} 0.61275 \\ 0.9804 \end{bmatrix}. \tag{60}$$

Note that for this example, we have the following:

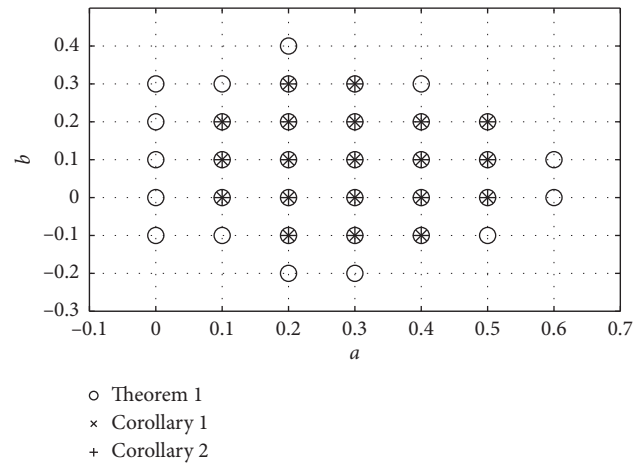

Figure 1: Feasibility sets for Theorem 1, Corollary 1, and Corollary 2 are applied to the example given in Subsection 4.1.

(i) With respect to its exact convex representation, the descriptor one has $(E_k, A_i, A_{\tau_i}, B), k = 1, 2, i = 1, 2, 3, 4$, i.e., 8 vertexes, while the standard has $(\widetilde{A}_i, \widetilde{A}_{\tau_i}, \widetilde{B}_i), i = 1, 2, \ldots, 2^4$, i.e., 16 vertexes. Additionally, the descriptor keeps a constant matrix B; thus, descriptor form requires less computational resources [64]. Indeed, in this case with $n = 2, m = 1$, $r = 4$, $\rho = 2$, $\widetilde{r} = 16$, and $d = 2$, the computational complexity using Theorem 1 is 7.2567 with 35 LMIs, using Corollary 1 is 9.7228 with 35 LMIs, and using Corollary 2 is 4.8713 with 19 LMIs.

(ii) With respect to feasibility sets for Theorem 1, and Corollaries 1 and 2, when $u = 0$ and parameter values as $a \in [0, 0.8]$, $b \in [-0.2, 0.5]$ for convex representations of systems (55) and (58), respectively. In Figure 1, the regions marked with a circle ($\circ$) correspond to the feasibility sets using Theorem 1, while the regions marked by ($\times$) and ($+$) are the feasibility sets obtained using Corollaries 1 and 2, respectively. It can be seen that by using the descriptor form the feasibility set is larger, i.e., the descriptor approach provides more relaxed results than the standard approach.

Thus, results given in Theorem 1 improve the previously classic results found in the literature.

On the other hand, Figure 2 shows that the system response (55) does not converge to the trivial equilibrium point when $a = -2.5$, $b = 6.2$, $u = 0$, $\tau_1 = 0.1$, $\tau_2 = 0.3$, and $\phi(\theta) = \begin{bmatrix} -5 & 5 \end{bmatrix}^T$, $\theta \in [-0.3, 0]$.

Next, a delayed nonlinear controller of the form (23) is given by

$$u = K_{\mathbf{w}\boldsymbol{\omega}} x(t) + \sum_{h=1}^{2} F_{h\mathbf{w}\boldsymbol{\omega}} x(t - \tau_h), \tag{61}$$

which is employed to stabilize this system. To this end, LMI conditions in Theorem 2 with an exponential decay $\alpha = 0.5$ together with those from in Theorem 3 for $u < 48 = \mu$ render feasible solution providing the following values:

$$P_1^{-1} = \begin{bmatrix} 0.20603 & 0.19458 \\ 0.19458 & 0.21717 \end{bmatrix},$$

$$Q_1 = \begin{bmatrix} 3.5866 & 3.3247 \\ 3.3247 & 3.1135 \end{bmatrix},$$

$$Q_2 = \begin{bmatrix} 1.0972 & 1.215 \\ 1.215 & 1.4539 \end{bmatrix},$$

$$\begin{aligned}
K_{11} &= [\,-11.0453 \quad -13.9169\,], \\
F_{111} &= [\,-11.7060 \quad -6.5843\,], \\
F_{211} &= [\,2.5606 \quad 2.2870\,], \\
K_{12} &= [\,-7.3722 \quad -12.1755\,], \\
F_{112} &= [\,-13.9524 \quad -8.5677\,], \\
F_{212} &= [\,3.2894 \quad 3.1315\,], \\
K_{21} &= [\,-10.4266 \quad -13.6762\,], \\
F_{121} &= [\,-10.9789 \quad -6.6378\,], \\
F_{221} &= [\,2.2735 \quad 1.9269\,], \\
K_{22} &= [\,-6.7172 \quad -11.7399\,], \\
F_{122} &= [\,-13.2816 \quad -8.7126\,], \\
F_{222} &= [\,3.0448 \quad 2.8193\,], \\
K_{31} &= [\,-9.8536 \quad -13.3457\,], \\
F_{131} &= [\,-9.7933 \quad -4.8426\,], \\
F_{231} &= [\,-0.2040 \quad 1.5048\,], \\
K_{32} &= [\,-6.7529 \quad -11.8054\,], \\
F_{132} &= [\,-13.8964 \quad -8.4844\,], \\
F_{232} &= [\,0.6296 \quad 3.0749\,], \\
K_{41} &= [\,-9.0894 \quad -12.9706\,], \\
F_{141} &= [\,-9.2846 \quad -5.0947\,], \\
F_{241} &= [\,-0.3599 \quad 1.2441\,], \\
K_{42} &= [\,-5.7661 \quad -11.1366\,], \\
F_{142} &= [\,-13.6875 \quad -9.0667\,], \\
F_{242} &= [\,0.5619 \quad 2.9637\,].
\end{aligned} \tag{62}$$

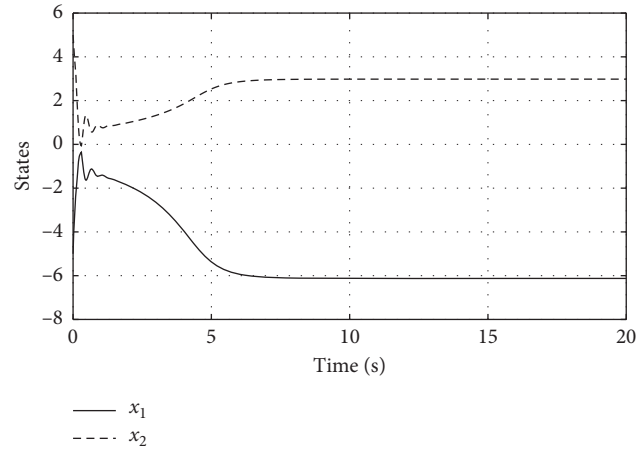

Figure 2: System response of the example given in Subsection 4.1 (descriptor form) when $a = -2.5$, $b = 6.2$, and $u = 0$.

Effectively, system (55) is stabilized at the origin as shown in Figure 3. The evolution in time of the system state is shown in Figure 3(a), while the guaranteed exponential decay in the system response is depicted in Figure 3(b).

4.2. Nonlinear Controller versus Delayed Nonlinear Controller. The following example is to illustrate the advantages of the use of artificial delays in controllers when there is the presence of noise, as mentioned in the introduction and its corroboration by various results found in the literature.

Consider the system known as the car-pendulum, whose scheme is shown in Figure 4, a mathematical model is given by

$$\begin{bmatrix} M_1 + M_2 & -M_2 l \cos\theta \\ -M_2 l \cos\theta & J + M_2 l^2 \end{bmatrix} \begin{bmatrix} \ddot{\tilde{x}}(t) \\ \ddot{\theta}(t) \end{bmatrix} + \begin{bmatrix} c\dot{\tilde{x}} + M_2 l \dot{\theta}^2 \sin\theta \\ \gamma\dot{\theta} - M_2 g l \sin\theta \end{bmatrix} = \begin{bmatrix} F \\ 0 \end{bmatrix}. \tag{63}$$

For illustrative purposes, a delayed measurement $\tau > 0$ in the positions of the car and pendulum are intentionally added. Also, we define $x_1 = \tilde{x}$, $x_2 = \dot{\tilde{x}}$, $x_3 = \theta$, $x_4 = \dot{\theta}$, and $u = F$. Thus, for $g = 9.81\,\mathrm{m/s^2}$, $l = 0.304\,\mathrm{m}$, $M_2 = 0.2\,\mathrm{kg}$, $M_1 = 1.3282\,\mathrm{kg}$, $J = (M_2 l^2)/3$, $c = 0.001$, $\gamma = 0.001$, and $\tau = 0.05$, the system (63) can be rewritten as

$$E(x)\dot{x}(t) = A(x)x(t) + A_\tau(x)x(t-\tau) + Bu(t). \tag{64}$$

where

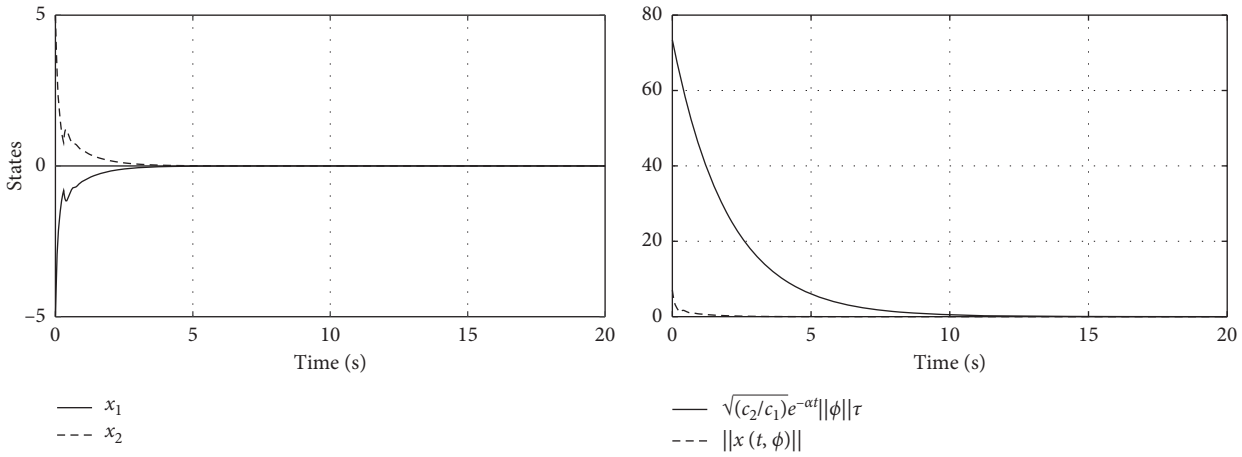

Figure 3: System response of the example given in Section 4.1 (descriptor form) using delayed controller (61). (a) Time evolution of the closed-loop system. (b) Guaranteed exponential decay $\alpha = 0.5$ for the closed-loop system.

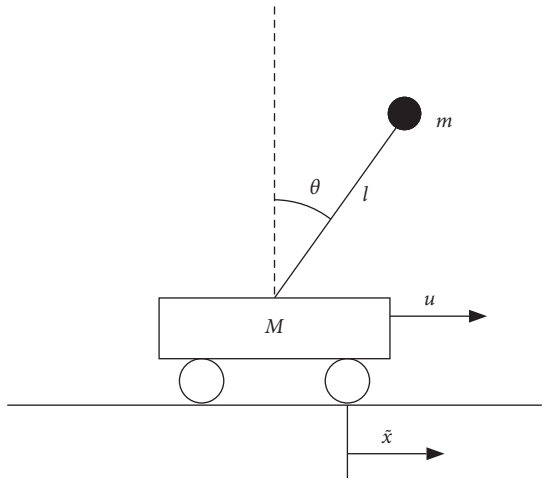

Figure 4: Schematic of the inverted pendulum system.

$$E(x) = \begin{bmatrix} 1 & 0 & 0 & 0 \\ 0 & 1.5482 & 0 & -0.0669\cos x_3 \\ 0 & 0 & 1 & 0 \\ 0 & -0.0669\cos x_3 & 0 & 0.0271 \end{bmatrix},$$

$$A(x) = \begin{bmatrix} 0 & 1 & 0 & 0 \\ 0 & -0.001 & 0 & -0.0669x_4 \sin x_3 \\ 0 & 0 & 0 & 1 \\ 0 & 0 & \dfrac{0.6561 \sin x_3}{x_3} & -0.001 \end{bmatrix},$$

$$A_\tau(x) = \begin{bmatrix} 0 & 0 & 0 & 0 \\ 0.1 & 0 & 0 & 0 \\ 0 & 0 & 0 & 0 \\ 0 & 0 & 0.2 & 0 \end{bmatrix},$$

$$B = \begin{bmatrix} 0 \\ 1 \\ 0 \\ 0 \end{bmatrix}. \tag{65}$$

Considering the region $\Omega_x = \{x: |x_1| \le 2\,\text{m}, |x_2| \le 3\,\text{m/s}, |x_3| \le \pi/3\,\text{rad}, |x_4| \le 4\,\text{rad/s}\}$, the nonconstant terms and their bounds are $\zeta_1 = \cos x_3 \in [0.5, 1]$, $z_1 = x_4 \sin x_3 \in [-0.4238, 0.4238]$, and $z_2 = \sin x_3/x_3 \in [0.827, 1]$; the vertex matrices are

$$A_1 = \begin{bmatrix} 0 & 1.0 & 0 & 0 \\ 0 & -0.001 & 0 & -0.0258 \\ 0 & 0 & 0 & 1.0 \\ 0 & 0 & -0.4933 & -0.001 \end{bmatrix},$$

$$A_2 = \begin{bmatrix} 0 & 1 & 0 & 0 \\ 0 & -0.001 & 0 & -0.025 \\ 0 & 0 & 0 & 1 \\ 0 & 0 & -0.596 & -0.001 \end{bmatrix},$$

$$A_3 = \begin{bmatrix} 0 & 1 & 0 & 0 \\ 0 & -0.001 & 0 & 0.0258 \\ 0 & 0 & 0 & 1 \\ 0 & 0 & -0.4933 & -0.001 \end{bmatrix},$$

$$A_4 = \begin{bmatrix} 0 & 1 & 0 & 0 \\ 0 & -0.001 & 0 & 0.0258 \\ 0 & 0 & 0 & 1 \\ 0 & 0 & -0.5964 & -0.001 \end{bmatrix},$$

$$A_{\tau 1} = A_{\tau 2} = A_{\tau 3} = A_{\tau 4} = \begin{bmatrix} 0 & 0 & 0 & 0 \\ 0.1 & 0 & 0 & 0 \\ 0 & 0 & 0 & 0 \\ 0 & 0 & 0.2 & 0 \end{bmatrix},$$

$$B_1 = B_2 = B_3 = B_4 = \begin{bmatrix} 0 \\ 1 \\ 0 \\ 0 \end{bmatrix},$$

$$E_1 = \begin{bmatrix} 1 & 0 & 0 & 0 \\ 0 & 1.5282 & 0 & -0.0304 \\ 0 & 0 & 1 & 0 \\ 0 & -0.0304 & 0 & 0.0370 \end{bmatrix},$$

$$E_2 = \begin{bmatrix} 1.0 & 0 & 0 & 0 \\ 0 & 1.5482 & 0 & -0.0608 \\ 0 & 0 & 1 & 0 \\ 0 & -0.0608 & 0 & 0.0370 \end{bmatrix}. \tag{66}$$

As mentioned above, with the purpose of showing the advantages of using a controller with delayed action in the presence of noise; for this example, two controllers are used: a nonlinear controller of the following form is

$$u = K_{\mathbf{w}\omega} x(t), \tag{67}$$

and a delayed nonlinear controller of the form (23) is given by

$$u = K_{\mathbf{w}\omega} x(t) + F_{\mathbf{w}\omega} x(t - \tau). \tag{68}$$

To illustrate the effectiveness of Theorem 3, the controllers (68) are conditioned to satisfy that $\|u(t)\| < 12$. For the controller (67), the same condition is requested, for which Theorem 3 can be used, after some simple adjustments when considering free-delays controller. For the controller (67), the corresponding LMI conditions in Theorem 2 with an exponential decay $\alpha = 0.003$ are found feasible with the following values:

$$P_1 = \begin{bmatrix} 0.02024 & 0.04411 & 0.1428 & -0.005929 \\ 0.04411 & 0.1874 & 0.6166 & -0.02698 \\ 0.1428 & 0.6166 & 6.036 & 0.1574 \\ -0.005929 & -0.02698 & 0.1574 & 0.2537 \end{bmatrix},$$

$$Q_1 = \begin{bmatrix} 0.0077 & 0.0225 & 0.1455 & 0.00005 \\ 0.02258 & 0.09603 & 0.4836 & 0.0042 \\ 0.1455 & 0.4836 & 7.879 & 0.0778 \\ 0.00005 & 0.0042 & 0.0778 & 0.1026 \end{bmatrix},$$

$$K_{11} = \begin{bmatrix} -0.3685 & -1.71 & -8.965 & -3.468 \end{bmatrix},$$

$$K_{12} = \begin{bmatrix} -0.4382 & -1.979 & -8.867 & -2.879 \end{bmatrix},$$

$$K_{21} = \begin{bmatrix} -0.3567 & -1.626 & -5.913 & -3.452 \end{bmatrix},$$

$$K_{22} = \begin{bmatrix} -0.4368 & -1.95 & -6.884 & -2.852 \end{bmatrix},$$

$$K_{31} = \begin{bmatrix} -0.3619 & -1.668 & -8.823 & -3.516 \end{bmatrix},$$

$$K_{32} = \begin{bmatrix} -0.435 & -1.955 & -8.748 & -2.915 \end{bmatrix},$$

$$K_{41} = \begin{bmatrix} -0.3483 & -1.573 & -5.728 & -3.505 \end{bmatrix},$$

$$K_{42} = \begin{bmatrix} -0.4333 & -1.924 & -6.765 & -2.889 \end{bmatrix}. \tag{69}$$

On the other hand, for the delayed controller (68), LMI conditions in Theorem 2 with an exponential decay $\alpha = 0.003$ are also feasible with the following values:

$$P_1^{-1} = \begin{bmatrix} 0.0020 & 0.0062 & 0.02261 & -0.0005 \\ 0.0062 & 0.0422 & 0.1531 & -0.003 \\ 0.0226 & 0.1531 & 2.366 & 0.07454 \\ -0.0005 & -0.0030 & 0.0745 & 0.1213 \end{bmatrix},$$

$$Q_1 = \begin{bmatrix} 0.0003 & 0.0016 & 0.0134 & 0.0002 \\ 0.0016 & 0.0114 & 0.0789 & 0.002 \\ 0.0134 & 0.0789 & 2.284 & 0.031 \\ 0.0002 & 0.002 & 0.031 & 0.0418 \end{bmatrix},$$

$$\begin{aligned} K_{11} &= [\,-0.1389 \;\; -0.9876 \;\; -4.926 \;\; -2.323\,], \\ F_{11} &= [\,-0.092 \;\; -0.0006 \;\; -5.691 \;\; 0.0014\,], \\ K_{12} &= [\,-0.1457 \;\; -0.99 \;\; -4.341 \;\; -2.052\,], \\ F_{12} &= [\,-0.0867 \;\; -0.0001 \;\; -3.54 \;\; 0.0004\,], \\ K_{21} &= [\,-0.1368 \;\; -0.9425 \;\; -2.012 \;\; -2.263\,], \\ F_{21} &= [\,-0.0932 \;\; -0.001 \;\; -5.956 \;\; 0.0011\,], \\ K_{22} &= [\,-0.1479 \;\; -0.9792 \;\; -2.502 \;\; -2.001\,], \\ F_{22} &= [\,-0.0870 \;\; -0.0001 \;\; -3.634 \;\; 0.0004\,], \\ K_{31} &= [\,-0.1394 \;\; -0.9793 \;\; -4.867 \;\; -2.345\,], \\ F_{31} &= [\,-0.0928 \;\; -0.0008 \;\; -5.829 \;\; 0.0017\,], \\ K_{32} &= [\,-0.1459 \;\; -0.9801 \;\; -4.278 \;\; -2.078\,], \\ F_{32} &= [\,-0.0870 \;\; -0.0001 \;\; -3.628 \;\; 0.0004\,], \\ K_{41} &= [\,-0.1373 \;\; -0.9317 \;\; -1.924 \;\; -2.284\,], \\ F_{41} &= [\,-0.0944 \;\; -0.00135 \;\; -6.136 \;\; 0.0019\,], \\ K_{42} &= [\,-0.1485 \;\; -0.9693 \;\; -2.432 \;\; -2.025\,], \\ F_{42} &= [\,-0.0873 \;\; -0.0002 \;\; -3.74 \;\; 0.0005\,]. \end{aligned} \tag{70}$$

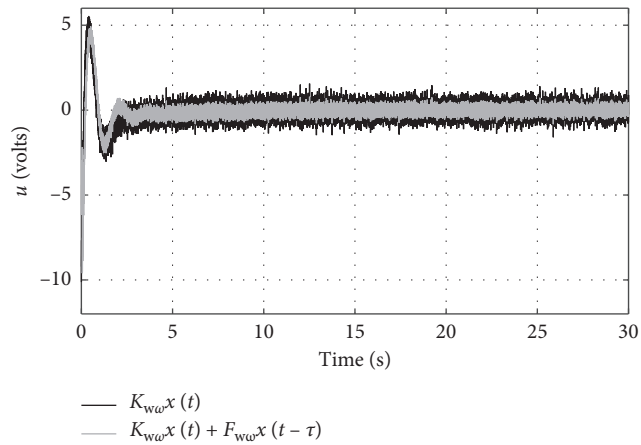

Figure 5: Time evolution of control laws (67) and (68).

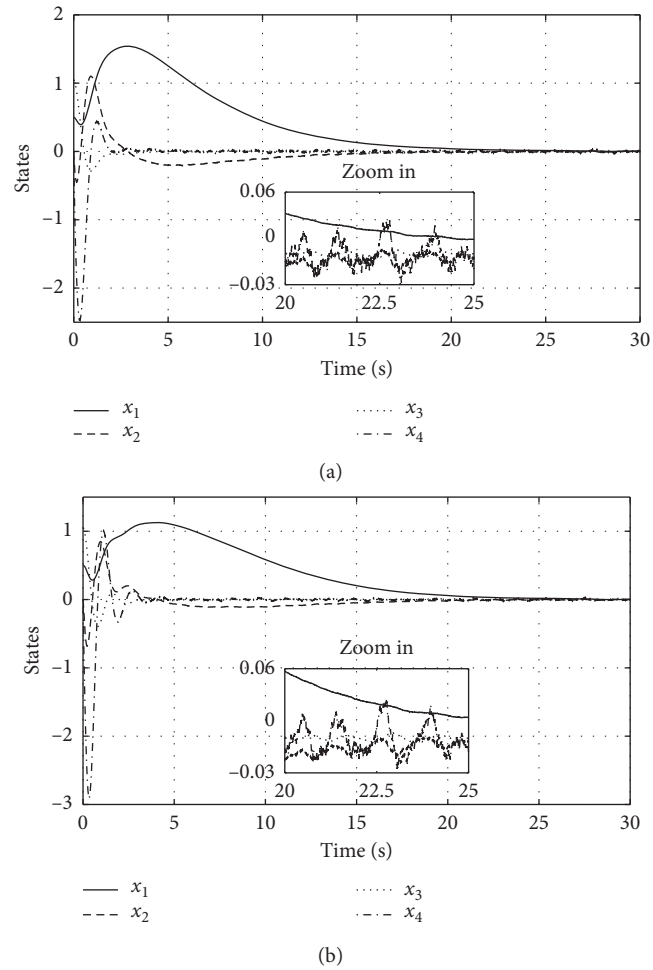

Figure 6: System response of the example given in Section 4.2. Time evolution of the closed-loop system with (a) (28) and (b) (68).

To simulate the noise present in the sensors, a random signal with variance 0.001 and a step 0.001 is introduced at the system input. In Figure 5, the applied control signals are plotted, and it can be seen that the control signal presents less noisy when using the delayed controller than the other.

In Figure 6, the evolution in time of the state of the system (64), with $\phi(\theta) = \begin{bmatrix} 0.5 & 0 & \pi/3 & 0 \end{bmatrix}^T$, $\theta \in [-0.05, 0]$, under the control laws (67) and (68), is shown. It can be seen that the overshoot is greater when using a controller without a delayed action.

Remark 3. Systems of the form (63) can be stabilized by a free-delay controller of the form (67). However, using delayed controllers of the form (68) or (23) to stabilize this system class may be a better option when systems have inherent noise.

5. Conclusions

In this paper, analysis and design using a convex approach for nonlinear descriptor systems with multiple delays have been presented. This analysis allows synthesizing delayed nonlinear controllers to ensure convergence of the system trajectories with a guaranteed exponential decay; moreover, conditions for bounding the control input avoid possible saturation in the actuators have been provided. It also has been shown that keeping the descriptor form increases the possibility of obtaining feasibility in the LMI conditions, unlike the use of standard forms. Also, it is observed that including deliberately delays in the controller can reduce noise in the control signal, thus avoiding mechanical wear of the actuators. As future work, an extension of the proposed results in nonlinear descriptor systems with multiple time-varying delays is in course, since it will allow the synthesis of controllers for a larger class of systems.

Data Availability

No data were used to support this study.

Conflicts of Interest

The authors declare that there are no conflicts of interests regarding the publication of this paper.

Acknowledgments

This work was partially supported by the CONACYT scholarship 998399 (J. A. Romero-Vega).

References

[1] H. K. Khalil, *Nonlinear Systems*, Prentice Hall, New Jersey, NJ, USA, 3 edition, 2002.

[2] S. Boyd, L. E. Ghaoui, E. Feron, and V. Belakrishnan, "Linear matrix inequalities in system and control theory," *SIAM: Studies in Applied Mathematics*, vol. 15, 1994.

[3] P. Apkarian and P. Gahinet, "A convex characterization of gain-scheduled H/sub ∞/controllers," *IEEE Transactions on Automatic Control*, vol. 40, no. 5, pp. 853–864, 1995.

[4] S. Mondie and V. L. Kharitonov, "Exponential estimates for retarded time-delay systems: an LMI approach," *IEEE Transactions on Automatic Control*, vol. 50, no. 2, pp. 268–273, 2005.

[5] C. Scherer, *Linear Matrix Inequalities in Control Theory*, Delf University, Delf, Netherlands, 2004.

[6] P. Gahinet, A. Nemirovski, A. J. Laub, and M. Chilali, *LMI Control Toolbox*, Math Works, Natick, MA, USA, 1995.

[7] N. N. Krasovskii, "On the application of the second method of Lyapunov for equations with time delays," *Prikladnaya Matematika Mekh*, vol. 20, no. 3, pp. 315–327, 1956.

[8] B. S. Razumikhin, "Stability of delay systems," *Prikladnaya Matematika Mekh*, vol. 20, no. 4, pp. 500–512, 1956.

[9] L. Dugard and I. V. Erik, *Stability and Control of Time-Delay Systems*, Springer, Berlin, Germany, 1998.

[10] K. Gu, "An integral inequality in the stability problem of time-delay systems," in *Proceedings of the 39th IEEE Conference on Decision and Control (Cat. No. 00CH37187)*, pp. 2805–2810, IEEE, Sydney, Australia, December 2000.

[11] E. Fridman and U. Shaked, "An improved stabilization method for linear time-delay systems," *IEEE Transactions on Automatic Control*, vol. 47, no. 11, pp. 1931–1937, 2002.

[12] E. Fridman, A. Seuret, and J.-P. Richard, "Robust sampled-data stabilization of linear systems: an input delay approach," *Automatica*, vol. 40, no. 8, pp. 1441–1446, 2004.

[13] S. Xu and J. Lam, *Robust Control and Filtering of Singular Systems*, Springer, Berlin, Germany, 2006.

[14] X. Li and C. E. De Souza, "Criteria for robust stability and stabilization of uncertain linear systems with state delay," *Automatica*, vol. 33, no. 9, pp. 1657–1662, 1997.

[15] K. Gu, "Discretized LMI set in the stability problem of linear uncertain time-delay systems," *International Journal of Control*, vol. 68, no. 4, pp. 923–934, 1997.

[16] S. M. Young, P. Park, W. H. Kwon, and S. L. Young, "Delay-dependent robust stabilization of uncertain state-delayed systems," *International Journal of Control*, vol. 74, no. 14, pp. 1447–1455, 2001.

[17] E. Fridman, "New Lyapunov-Krasovskii functionals for stability of linear retarded and neutral type systems," *Systems & Control Letters*, vol. 43, no. 4, pp. 309–319, 2001.

[18] S.-I. Niculescu, "On delay-dependent stability under model transformations of some neutral linear systems," *International Journal of Control*, vol. 74, no. 6, pp. 609–617, 2001.

[19] Q.-L. Han, "Robust stability of uncertain delay-differential systems of neutral type," *Automatica*, vol. 38, no. 4, pp. 719–723, 2002.

[20] M. Wu, Y. He, and J.-H. She, "New delay-dependent stability criteria and stabilizing method for neutral systems," *IEEE Transactions on Automatic Control*, vol. 49, no. 12, pp. 2266–2271, 2004.

[21] P.G. Park, "A delay-dependent stability criterion for systems with uncertain time-invariant delays," *IEEE Transactions on Automatic Control*, vol. 44, no. 4, pp. 876-877, 1999.

[22] E. Fridman and U. Shaked, "A descriptor system approach to H/sub ∞/control of linear time-delay systems," *IEEE Transactions on Automatic Control*, vol. 47, no. 2, pp. 253–270, 2002.

[23] X. Zhang, P. Tsiotras, and C. Knospe, "Stability analysis of LPV time-delayed systems," *International Journal of Control*, vol. 75, no. 7, pp. 538–558, 2002.

[24] E. Fridman and U. Shaked, "Delay-dependent stability and H ∞ control: constant and time-varying delays," *International Journal of Control*, vol. 76, no. 1, pp. 48–60, 2003.

[25] X. Jiang and Q.-L. Han, "Delay-dependent robust stability for uncertain linear systems with interval time-varying delay," *Automatica*, vol. 42, no. 6, pp. 1059–1065, 2006.

[26] Y. He, Q.-G. Wang, C. Lin, and M. Wu, "Delay-range-dependent stability for systems with time-varying delay," *Automatica*, vol. 43, no. 2, pp. 371–376, 2007.

[27] H. Shao, "New delay-dependent stability criteria for systems with interval delay," *Automatica*, vol. 45, no. 3, pp. 744–749, 2009.

[28] J. Sun, G. P. Liu, J. Chen, and D. Rees, "Improved delay-range-dependent stability criteria for linear systems with time-varying delays," *Automatica*, vol. 46, no. 2, pp. 466–470, 2010.

[29] H.-B. Zeng, Y. He, M. Wu, and J. She, "Free-matrix-based integral inequality for stability analysis of systems with time-varying delay," *IEEE Transactions on Automatic Control*, vol. 60, no. 10, pp. 2768–2772, 2015.

[30] V. L. Kharitonov and D. Hinrichsen, "Exponential estimates for time delay systems," *Systems & Control Letters*, vol. 53, no. 5, pp. 395–405, 2004.

[31] S. Xu, J. Lam, and M. Zhong, "New exponential estimates for time-delay systems," *IEEE Transactions on Automatic Control*, vol. 51, no. 9, pp. 1501–1505, 2006.

[32] Y. He, M. Wu, J.-H. She, and G.-P. Liu, "Parameter-dependent Lyapunov functional for stability of time-delay systems with polytopic-type uncertainties," *IEEE Transactions on Automatic Control*, vol. 49, no. 5, pp. 828–832, 2004.

[33] S. Xu and J. Lam, "Improved delay-dependent stability criteria for time-delay systems," *IEEE Transactions on Automatic Control*, vol. 50, no. 3, pp. 384–387, 2005.

[34] R. S. Kumar, G. Sugumaran, R. Raja, Q. Zhu, and U. K. Raja, "New stability criterion of neural networks with leakage delays and impulses: a piecewise delay method," *Cognitive Neurodynamics*, vol. 10, no. 1, pp. 85–98, 2016.

[35] G. Rajchakit, P. Chanthorn, M. Niezabitowski, R. Raja, D. Baleanu, and A. Pratap, "Impulsive effects on stability and passivity analysis of memristor-based fractional-order competitive neural networks," *Neurocomputing*, vol. 417, pp. 290–301, 2020.

[36] S. Pandiselvi, R. Raja, J. Cao, X. Li, and G. Rajchakit, "Impulsive discrete-time GRNs with probabilistic time delays, distributed and leakage delays: an asymptotic stability issue," *IMA Journal of Mathematical Control and Information*, vol. 36, no. 1, pp. 79–100, 2019.

[37] S. Angulo, R. Márquez, and M. Bernal, "Quasi-polynomial-based robust stability of time-delay systems can be less conservative than Lyapunov–Krasovskii approaches," *IEEE Transactions on Automatic Control*, vol. 65, no. 7, pp. 3164–3169, 2019.

[38] C. Abdallah, D. Peter, J. Benites-Read, and R. Byrne, "Delayed positive feedback can stabilize oscillatory systems," in *Proceedings of the American Control Conference, 1993*, pp. 3106-3107, IEEE, San Francisco, CA, USA, June 1993.

[39] A. G. Ulsoy, "Time-delayed control of SISO systems for improved stability margins," *Journal of Dynamic Systems, Measurement, and Control*, vol. 137, no. 4, Article ID 041014, 2015.

[40] H. Suh and Z. Bien, "Use of time-delay actions in the controller design," *IEEE Transactions on Automatic Control*, vol. 25, no. 3, pp. 600–603, 1980.

[41] I. Suh and Z. Bien, "Proportional minus delay controller," *IEEE Transactions on Automatic Control*, vol. 24, no. 2, pp. 370–372, 1979.

[42] S. Mondié, R. Villafuerte, and R. Garrido, "Tuning and noise attenuation of a second order system using Proportional Retarded control," *IFAC Proceedings Volumes*, vol. 44, no. 1, pp. 10337–10342, 2011.

[43] K. Pyragas, "Continuous control of chaos by self-controlling feedback," *Physics Letters A*, vol. 170, no. 6, pp. 421–428, 1992.

[44] M. E. Bleich and E. S. Joshua, "Stability of periodic orbits controlled by time-delay feedback," *Physics Letters A*, vol. 210, no. 1-2, pp. 87–94, 1996.

[45] W. Just, T. Bernard, M. Ostheimer, E. Reibold, and H. Benner, "Mechanism of time-delayed feedback control," *Physical Review Letters*, vol. 78, no. 2, p. 203, 1997.

[46] M. de Sousa Vieira and A. J. Lichtenberg, "Controlling chaos using nonlinear feedback with delay," *Physical Review E*, vol. 54, no. 2, p. 1200, 1996.

[47] M. S. George and S. Tenqchen, "Design of proportional-minus-delay action feedback controllers for second-and third-order systems," in *Proceedings of the American Control Conference, 1988*, pp. 254–260, IEEE, Atlanta, GA, USA, June 1988.

[48] N. Olgac and R. Sipahi, "The cluster treatment of characteristic roots and the neutral type time-delayed systems," in *Proceedings of the ASME 2004 International Mechanical Engineering Congress and Exposition*, pp. 1359–1368, Anaheim, CA, USA, November 2004.

[49] C.-I. Morarescu and S. Niculescu, "Stability crossing curves of SISO systems controlled by delayed output feedback," *Dynamics of Continuous, Discrete and Impulsive Systems Serires B*, vol. 14, no. 5, p. 659, 2007.

[50] R. Sipahi, H. Fazelinia, and N. Olgac, "Generalization of cluster treatment of characteristic roots for robust stability of multiple time-delayed systems," *International Journal of Robust and Nonlinear Control*, vol. 18, no. 14, pp. 1430–1449, 2008.

[51] R. Villafuerte, S. Mondié, and R. Garrido, "Tuning of proportional retarded controllers: theory and experiments," *IEEE Transactions on Control Systems Technology*, vol. 21, no. 3, pp. 983–990, 2013.

[52] A. Ramirez, S. Mondié, R. Garrido, and R. Sipahi, "Design of proportional-integral-retarded (PIR) controllers for second-order LTI systems," *IEEE Transactions on Automatic Control*, vol. 61, no. 6, pp. 1688–1693, 2016.

[53] J.-E. Hernández-Díez, C.-F. Méndez-Barrios, S. Mondié, S.-I. Niculescu, and E. J. González-Galván, "Proportional-delayed controllers design for LTI-systems: a geometric approach," *International Journal of Control*, vol. 91, no. 4, pp. 907–925, 2018.

[54] F. Medina-Dorantes, R. Villafuerte-Segura, and B. Aguirre-Hernández, "Controller with time-delay to stabilize first-order processes with dead-time," *Journal of Control Engineering and Applied Informatics*, vol. 20, no. 2, pp. 42–50, 2018.

[55] R. Villafuerte, F. Medina, L. Vite, and B. Aguirre, "Tuning of a time-delayed controller for a general class of second-order LTI systems with dead-time," *IET Control Theory & Applications*, vol. 13, no. 3, 2018.

[56] T. Takagi and M. Sugeno, "Fuzzy identification of systems and its applications to modeling and control," *IEEE Transactions on Systems, Man, and Cybernetics*, vol. SMC-15, no. 1, pp. 116–132, 1985.

[57] T. Taniguchi, K. Tanaka, and H. O. Wang, "Model construction, rule reduction and robust compensation for generalized form of Takagi-Sugeno fuzzy systems," *IEEE Transactions on Fuzzy Systems*, vol. 9, no. 2, pp. 525–537, 2001.

[58] Y.-Y. Cao and P. M. Frank, "Stability analysis and synthesis of nonlinear time-delay systems via linear Takagi-Sugeno fuzzy models," *Fuzzy Sets and Systems*, vol. 124, no. 2, pp. 213–229, 2001.

[59] B. Chen, C. Lin, X. Liu, and S. Tong, "Guaranteed cost control of T-S fuzzy systems with input delay," *International Journal*

of Robust and Nonlinear Control, vol. 18, no. 12, pp. 1230–1256, 2008.

[60] B. Zhang, J. Lam, S. Xu, and Z. Shu, "Robust stabilization of uncertain T-S fuzzy time-delay systems with exponential estimates," *Fuzzy Sets and Systems*, vol. 160, no. 12, pp. 1720–1737, 2009.

[61] M. Ramírez, R. Villafuerte, T. González, and M. Bernal, "Exponential estimates of a class of time-delay nonlinear systems with convex representations," *International Journal of Applied Mathematics and Computer Science*, vol. 25, no. 4, pp. 815–826, 2015.

[62] S. Angulo, David Vazquez, R. Márquez, and M. Bernal, "Stability of Takagi-Sugeno fuzzy systems with time-delay: a non-quadratic functional approach," in *Proceedings of the 2017 IEEE International Conference on Fuzzy Systems (FUZZ-IEEE)*, pp. 1–6, Naples, Italy, July 2017.

[63] F. L. Lewis, D. M. Dawson, and C. T. Abdallah, *Robot Manipulator Control: Theory and Practice*, CRC Press, Boca Raton, FL, USA, 2003.

[64] V. Estrada-Manzo, Z. Lendek, T. M. Guerra, and P. Pudlo, "Controller design for discrete-time descriptor models: a systematic LMI approach," *IEEE Transactions on Fuzzy Systems*, vol. 23, no. 5, pp. 1608–1621, 2015.

[65] T. M. Guerra, V. Estrada-Manzo, and Zs. Lendek, "Observer design for Takagi–Sugeno descriptor models: an LMI approach," *Automatica*, vol. 52, pp. 154–159, 2015.

[66] J. C. Arceo, R. Villafuerte, V. Estrada-Manzo, and M. Bernal, "Lmi-based controller design for time-delay nonlinear descriptor systems with guaranteed exponential estimates," *IFAC-PapersOnLine*, vol. 51, no. 13, pp. 585–590, 2018.

[67] B. Aguiar, T. González, and M. Bernal, "A way to exploit the fractional stability domain for robust chaos suppression and synchronization via LMIs," *IEEE Transactions on Automatic Control*, vol. 61, no. 10, pp. 2796–2807, 2015.

[68] H. D. Tuan, P. Apkarian, T. Narikiyo, and M. Kanota, "New fuzzy control model and dynamic output feedback parallel distributed compensation," *IEEE Transactions on Fuzzy Systems*, vol. 12, no. 1, pp. 13–21, 2004.

[69] T. Taniguchi, K. Tanaka, K. Yamafuji, and H. O. Wang, "Fuzzy descriptor systems: stability analysis and design via LMIs," *Proceedings of the 1999 American Control Conference*, vol. 3, pp. 1827–1831, 1999.

[70] C. Armenta, M. Bernal, V. Estrada-Manzo, and A. Sala, "Exact Takagi-Sugeno descriptor models of recurrent high-order neural networks for control applications," *Computational and Applied Mathematics*, vol. 39, no. 1, p. 29, 2020.

Hindawi
Mathematical Problems in Engineering
Volume 2021, Article ID 8871603, 17 pages
https://doi.org/10.1155/2021/8871603

Research Article

M-Matrix-Based Robust Stability and Stabilization Criteria for Uncertain Switched Nonlinear Systems with Multiple Time-Varying Delays

Marwen Kermani [1,2] **and Anis Sakly** [1]

[1] *Laboratory of Automation, Electrical Systems and Environment (LAESE) National Engineering School of Monastir (ENIM), Ibn El Jazzar, Skaness 5019, University of Monastir, Monastir, Tunisia*
[2] *National School of Advanced Science and Technology of Borj Cedria, BP 122 Hammam-Chott 1164, Tunisia University of Carthage, Tunis, Tunisia*

Correspondence should be addressed to Marwen Kermani; kermanimarwen@gmail.com

Received 15 September 2020; Revised 29 December 2020; Accepted 15 January 2021; Published 30 January 2021

Academic Editor: Rosalba Galván-Guerra

This paper focuses on the robust stability and the memory feedback stabilization problems for a class of uncertain switched nonlinear systems with multiple time-varying delays. Especially, the considered time delays depend on the subsystem number. Based on a novel common Lyapunov functional, the aggregation techniques, and the Borne and Gentina criterion, new sufficient robust stability and stabilization conditions under arbitrary switching are established. Compared with existing results, the proposed criteria are explicit, simple to use, and obtained without finding a common Lyapunov function for all subsystems through linear matrix inequalities, considered very difficult in this situation. Moreover, compared with the memoryless one, the developed controller guarantees the robust stability of the corresponding closed-loop system with more performance by minimizing the effect of the delays in the system dynamics. Finally, two numerical simulation examples are shown to prove the practical utility and the effectiveness of the proposed theories.

1. Introduction

Switched systems constitute an important class of hybrid systems, which can be described by a family of subsystems and a rule that orchestrates the switching amongst them [1].

Recently, switched systems have attracted considerable attention, and some valuable results have been achieved [1–33]. Among these research topics, stability analysis, stabilization, and control design of switched systems under arbitrary switching are fundamental issues in the design and the analysis of such systems. This kind of switching strategy lies in the fact that the stability of each autonomous or closed-loop subsystem does not necessarily imply the stability of the corresponding switched system. In this framework, it is well known that the existence of a common Lyapunov function (CLF) for all the subsystems through the linear matrix inequalities (LMIs) is a sufficient condition for such systems to be asymptotically stable under arbitrary switching [3]. However, this function is very difficult to find even for switched linear systems [3]. Therefore, this task becomes more and more compiled when switched nonlinear systems are involved [5].

Frequently, to avoid the conservatism related to the existence of a CLF, some attention has been devoted to considering switched systems under restricted switching. Although many interesting results have been proposed for this alternative, such as the dwell time approach [7] and the multiple Lyapunov function [6], stability under arbitrary switching remains more suitable for real systems. In fact, it offers more effectiveness for control design along with stability preserved.

As is well known, time-delay is usually often encountered in many engineering processes, which is considered in many recent studies [4, 13–20, 25–31, 33–37]. Thus, the presence of this phenomenon can affect the dynamic characteristics of systems, and it leads to the degradation of the system performance. Besides, when practical systems with errors or external disturbances are modeling, uncertainties parameters are frequently included. In this context, two types of uncertainties exist in the literature, which are mainly polytopic uncertainties and norm bounded. Indeed, one of the most significant exigencies for a control system is robustness [38, 39]. Therefore, from a practical viewpoint, it is necessary to investigate switched time-varying delay systems with extra uncertain parameters. In this regard, many of the uncertain systems can be approximated by systems with polytopic uncertainties.

In recent years, switched nonlinear time-varying delay systems have received a major interest, and many significant results have been established [4, 13–20, 25–31, 33]. Thus, from the switching strategies, the existing results can be classified into two categories, which are, respectively, restrictive switching and arbitrary switching. In fact, stability analysis and stabilization under restrictive switching have been investigated mainly based on the Lyapunov–Krasovskii functional (LKF) and the average dwell time approach [15]. For example, in [15], the robust stability and the control design problems for switched nonlinear systems have been investigated by using the average dwell time approach. The work in [34] addresses state feedback controllers design for switched nonlinear time-delay systems. Furthermore, the stability analysis of switched nonlinear systems has been investigated in [17] by employing the trajectory-based comparison method.

On the other side, the stability analysis and stabilization of switched time-delay systems under arbitrary switching have been studied based on the common Lyapunov–Krasovskii functional (CLKF) [14] for all the subsystems. Despite the difficulty related to the application of this method for switched nonlinear systems, some results exist for this framework. For instance, in [18], the adaptive control problem for switched nonlinear systems has been presented based on the adaptive backstepping technique and the CLF approach. In addition, in [20], the stabilization problem for switched nonlinear systems has been investigated based on the Metzler matrices. Moreover, the work in [19] deals with the stability analysis of switched nonlinear interconnected systems based on the vector Lyapunov approach and M-matrix theory. The authors in [25, 28] have focused on the stability analysis of switched nonlinear systems by using the aggregation techniques and the M-matrix theory. Furthermore, by including the Takagi–Sugeno (TS) fuzzy model as a powerful approximation tool of the initial nonlinear system, based on the aggregation techniques, algebraic stability criterion for TS Fuzzy switched systems were proposed in [30, 31].

It should be noted that all the aforementioned works for feedback stabilization have considered memoryless state feedback controllers. However, this kind of controllers cannot have an effect on the time-delay systems, since it does not introduce the past state information of the systems. In [26], a memory state feedback controller for time-varying delay switched systems has been considered. Indeed, it has been verified that this kind of controller had better immunity to reduce the influence of delay in system dynamics.

From a practical point of view, switched dynamical systems can be affected by mode depending time-varying delays. However, due to its complexities, this kind of systems is less considered [20, 40].

To the best of our knowledge, the robust stability analysis and the memory state feedback controller design for uncertain switched nonlinear systems with mode depending multiple time-varying delays under arbitrary switching have not been studied yet, which are the subject of this work.

Motivated by this consideration, in this paper, new robust stability criteria and memory feedback controller design under random switching for a class of uncertain switched nonlinear systems with multiple time-varying delays have been established. Indeed, based on a CLF, the aggregation techniques [41], and the Borne–Gentina criterion [41], new robust stability conditions for the considered autonomous systems are given. Besides, the obtained results are extended to develop a memory state feedback controller through the pole assignment control for the closed-loop corresponding switched systems.

The main contributions of this paper are emphasized as follows:

(1) There are no results to address switched nonlinear systems with uncertain parameters and mode-dependent multiple time-varying delays. Out of research interest, novel stability analysis and feedback controller design under arbitrary switching for more general kinds of switched nonlinear systems will be presented.

(2) Compared to the existing criterion for switched systems under arbitrary switching, by using the aggregation techniques the difficulty related to the existence of a CLF through the LMIs approach can be avoided.

(3) Contrary to searching a CLF through the LMIs approach considering a hard task in this investigation, the developed stability and stabilization criteria are explicit and simple to use.

(4) Although there are some studies on memory state feedback control, the memory state feedback controller has not been involved for switched nonlinear systems with multiple time-varying delays. In addition, the developed controller has an explicit form, and it allows stabilizing the resulting closed-loop systems under arbitrary switching without any computations over LMIs constraints.

The rest of the paper is organized as follows: Section 2 gives the problem statement and some definitions. In Section 3, the main results are presented. Section 4 focuses on the application of the main results to switched nonlinear systems modeled by differential equations. In Section 5, some simulation examples are provided to illustrate the

effectiveness of the proposed approach. Finally, some conclusions are addressed in Section 6.

Notations. Throughout this paper, I_n is an identity matrix, $\Re^n$ denotes the n-column vectors, and $\|.\|$ denotes the Euclidean norm. In addition, for any given vectors $v = (v_l)_{1\le l\le n}$, $w = (w_l)_{1\le l\le n} \in \Re^n$, the scalar product of vectors u and v is defined as $\langle v, w\rangle = \sum_{l=1}^{n} v_l w_l$. The sign function is defined as $sgn(\varphi) = 1$ (resp. $sgn(\varphi) = -1$) if $\varphi \in \mathbb{R}_+^*$(resp. $\varphi \in \mathbb{R}_-^*$) and $sgn(\varphi) = 0$ if $\varphi = 0$. For a given matrix A, $\lambda(A)$ denotes the set of its eigenvalues and $A^T$and A^{-1} denote its transpose and inverse, respectively. We denote $A^* = (a_{il}^*)_{1\le i,l\le n}$with $a_{il}^* = a_{il}$ if $i = l$ and $a_{il}^* = |a_{il}|$ if $i \ne l$. Finally, the representation $(.)$ denotes $(x(t), t)$.

2. Problem Statement and Preliminaries

2.1. Problem Statement. Consider the following switched nonlinear system with multiple time-varying delays given by

$$\begin{cases} \dot{x}(t) = A_{\sigma(t)}(\cdot)x(t) + \sum_{l=1}^{L} D_{l,\sigma(t)}(\cdot)x\left(t - r_{l,\sigma(t)}(t)\right) + B_{\sigma(t)}(\cdot)u(t), \\ x(\theta) = \phi(\theta), \quad \theta \in \left[-\max_{l\in\underline{L}}\left(r_{l,\sigma(t)}\right) 0\right], \end{cases} \tag{1}$$

where $x(t) \in \Re^n$ is the state vector at time t, $u(t)$ is the control input, $\sigma(t)$: $\Re_+ \longrightarrow \underline{N} = \{1, \ldots, N\}$ is the switching signal, and $\sigma(t) = i \in \underline{N}$ means that the i^{th} subsystem is active with N being the number of subsystems. $A_i(.)$, $D_{l,i}(.)$, and $B_i(.)$ are matrices which have nonlinear elements with appropriate dimensions, and $\phi(t)$ is the continuous vector valued function specifying the initial state of the system. $r_{l,i}(t)$ denotes the time-varying delay functions which satisfy

$$0 \le r_{l,i}(t) \le \tau, \tag{2}$$

$$\left|\dot{r}_{l,i}(t)\right| \le d < 1, \tag{3}$$

where τ and d are two constant scalars.

Assume that all subsystems are uncertain of polytopic type, which are represented as

$$A_i(.) = \sum_{p=1}^{P} \mu_{ip}(t) A_{ip}(.), \quad i \in \underline{N}, \tag{4}$$

$$D_{l,i}(.) = \sum_{q=1}^{Q} \lambda_{l,iq}(t) D_{l,iq}(.), \tag{5}$$

where $A_{ip}(.)$, $p \in \underline{P}$, and $D_{l,iq}(.)$ $q \in \underline{Q}$ are, respectively, the vertex matrices denoting the extreme points of the polytopes $A_i(.)$ and $D_i(.)$. $P$is the number of the vertex matrices $A_i(.)$, Q is the number of the vertex matrices $D_{l,i}(.)$ and the weighting factors $\mu_{ip}(t)$, $\lambda_{l,iq}(t)$ are polytopic uncertainties parameters belonging to$\mu_{ip}(t)$: $\sum_{p=1}^{P} \mu_{ip}(t) = 1$ $\mu_{ip}(t)$: $\sum_{p=1}^{P} \mu_{ip}(t) = 1$, $\mu_{ip}(t) \ge 0$, and $\lambda_{l,iq}(t)$: $\sum_{q=1}^{Q} \lambda_{l,iq}(t) = 1$, $\lambda_{l,iq}(t) \ge 0$.

2.2. Preliminaries. In the sequel, we introduce some lemmas, definitions, and criteria, which play important roles in deducing our main results.

Lemma 1 (see [40]). *The matrix $A = (a_{ij})_{1\le i,j\le n}$ is called an M − matrix if the following conditions are satisfied:*

(i) $a_{ii} > 0\,(i = 1, \ldots, n)$, $a_{ij} \le 0\,(i \ne j, i, j = 1, \ldots, n)$.

(ii) All the successive principal minors of A are positive:

$$\det\begin{pmatrix} a_{11} & \cdots & a_{1i} \\ \vdots & \ddots & \vdots \\ a_{i1} & \cdots & a_{ii} \end{pmatrix} > 0, \quad (i = 1, \ldots, n). \tag{6}$$

(iii) For any positive vector $x = (x_1, \ldots, x_n)^T$, the system of equations $A(.)x$ has a positive solution $x = (x_1, \ldots, x_n)^T$.

Definition 1. (see [41]). The matrix $T_{mc}(.)$ is said to be the pseudo-overvaluing matrix of the system given by $\dot{x} = A(.)x$, respectively, to the vector norm $p(x) = [|x_1|, \ldots, |x_i|, \ldots, |x_n|]^T$, with $x = [x_1, x_2, \ldots, x_n]^T$, if the next inequality is satisfied:

$$D^+ p(x) \le T_{mc}(.)p(x), \tag{7}$$

where D^+ denotes the right-hand derivative operator.

Assumption 1. In what follows, we assumed that all the nonlinear elements $T_{mc}(.)$ are separated in the last row.

Lemma 2 (see [41]). *If $T_{mc}(.)$is the pseudo-overvaluing matrix of the system: $\dot{x} = A(.)x$, then it verifies the following properties:*

(i) All the off-diagonal elements of $T_{mc}(.)$ are nonnegative

(ii) If the eigenvalues of $T_{mc}(.)$ have negative real parts, then $T_{mc}(.)$ is the opposite of an M − matrix

(iii) The main eigenvector $v(t, x(t))$ is related to the main eigenvalue λ_m such that reel(λ_m)= max $(\lambda \in \lambda M_C(.))$ is a constant vector

Lemma 3 (see [41]). *The application of the Kotelyanski lemma [42] to the pseudo-overvaluing matrix $T_{mc}(.)$is relative to the system: $\dot{x} = A(.)x$; $A(.) = (a_{ij}(.))_{1\le i,j\le n}$ allows deducing the stability of the corresponding system, if $T_{mc}(.)$ is the opposite of an M − matrix, which implies that all the successive principal minors have alternated signs with the first being negative:*

$$a_{1,1} < 0,$$

$$\begin{vmatrix} a_{1,1} & |a_{1,2}| \\ |a_{2,1}| & a_{2,2} \end{vmatrix} > 0, \ldots, (-1)^n \begin{vmatrix} a_{1,1} & |a_{1,2}| & \cdots & |a_{1,n}| \\ |a_{2,1}| & a_{2,2} & \cdots & |a_{2,n}| \\ \vdots & \vdots & \cdots & \vdots \\ |a_{n,1}(.)| & |a_{n,2}(.)| & \cdots & a_{n,n}(.) \end{vmatrix} > 0. \tag{8}$$

3. Main Results

3.1. Stability Analysis. In this section, we investigate sufficient delay-dependent stability conditions for the autonomous system (1).

Theorem 1. *The autonomous system (1) is robustly asymptotically stable under $\sigma(t) = i \in \underline{N}$, if $T_{mc}(.)$ is the opposite of an $M-$ matrix, where*

$$T_{mc}(.) = \max_{\substack{i\in\underline{N}\\ p\in\underline{P}}} \left(A_{ip}(.)\right)^{*} + (1-d)\max_{\substack{i\in\underline{N}\\ q\in\underline{Q}}}\left(\sup_{[.]}\left(\left|\sum_{l=1}^{L} D_{l,iq}(.)\right|\right)\right), \tag{9}$$

and d is given in (3).

Proof. Let $\nu \in \mathfrak{R}^n$ with components $(\nu_h > 0, \forall h = 1, \ldots, n)$ and $x(t) \in \mathfrak{R}^n$.

Define the following Lyapunov functional for the autonomous system (1):

$$V(t) = V_1(t) + V_2(t), \tag{10}$$

with

$$\begin{aligned} V_1(t) &= (1-d)^2\langle |x(t)|, \nu\rangle, \\ V_2(t) &= (1-d)\langle \sum_{l=1}^{L} D_{l,M} \int_{t-r_{l,\sigma(t)}(t)}^{t} |x(s)|\mathrm{d}s, \nu\rangle, \end{aligned} \tag{11}$$

where

$$D_{l,M} = \max_{\substack{i\in\underline{N}\\ q\in\underline{Q}}}\left(\sup_{[.]}\left(\left|\sum_{l=1}^{L} D_{l,iq}(.)\right|\right)\right). \tag{12}$$

The right derivative of $V(t)$ along the trajectory of system (1) yields to

$$\frac{\mathrm{d}^{+}V(t)}{\mathrm{d}t^{+}} = \frac{\mathrm{d}^{+}V_1(t)}{\mathrm{d}t^{+}} + \frac{\mathrm{d}^{+}V_2(t)}{\mathrm{d}t^{+}}, \tag{13}$$

where

$$\begin{aligned} \frac{\mathrm{d}^{+}V_1(t)}{\mathrm{d}t^{+}} &= (1-d)^2\langle \frac{\mathrm{d}^{+}|x(t)|}{\mathrm{d}t^{+}}, \nu\rangle \\ &= (1-d)^2\langle \mathrm{sgn}(x(t))\frac{\mathrm{d}^{+}x(t)}{\mathrm{d}t^{+}}, \nu\rangle, \\ \mathrm{sgn}(x(t)) &= \begin{pmatrix} \mathrm{sgn}(x_1(t)) & & \\ & \ddots & \\ & & \mathrm{sgn}(x_n(t)) \end{pmatrix}. \end{aligned} \tag{14}$$

Then,

$$\begin{aligned} \frac{\mathrm{d}^{+}V_1(x(t),t)}{\mathrm{d}t^{+}} &= (1-d)^2\left\langle\left\langle \mathrm{sgn}(x(t))\left(A_{\sigma(t)}(.)x(t) + \sum_{l=1}^{L} D_{l,\sigma(t)}(.)x\left(t - r_{l,\sigma(t)}(t)\right)\right), \nu\right\rangle, \\ &\le (1-d)^2\left\langle\left((A_{mc}(.))^{*}|x(t)| + \left|\sum_{l=1}^{L} D_{l,mc}\right|\left|x\left(t - r_{l,\sigma(t)}(t)\right)\right|\right), \nu, \right\rangle \end{aligned} \tag{15}$$

where $A_{mc}(.) = \max_{\substack{i\in\underline{N}\\ p\in\underline{P}}} ((A_{ip}(.))^{*})$.

On the other side, $((\mathrm{d}^{+}V_2(t))/\mathrm{d}t^{+}) = (1-d)\langle|\sum_{l=1}^{L} D_{l,mc}|(|x(t)|), \nu\rangle - (1-d)\,(1-\dot{r}_{l,\sigma(t)}(t))\,\langle|\sum_{l=1}^{L} D_{l,mc}|(|x(t - r_{l,\sigma(t)}(t))|), \nu\rangle$. Therefore, it is easy to see that

$$\begin{aligned} \left(\dot{r}_{l,\sigma(t)}(t) - 1\right)\left\langle\left|\sum_{l=1}^{L} D_{l,mc}\right|\left(\left|x\left(t - r_{l,\sigma(t)}(t)\right)\right|\right), \nu\right\rangle &\le \left(|\dot{r}_{l,\sigma(t)}(t)| - 1\right)\left\langle\left|\sum_{l=1}^{L} D_{l,mc}\right|\left(\left|x\left(t - r_{l,\sigma(t)}(t)\right)\right|\right), \nu\right\rangle, \\ &\le (d-1)\left\langle\left|\sum_{l=1}^{L} D_{l,mc}\right|\left(\left|x\left(t - r_{l,\sigma(t)}(t)\right)\right|\right), \nu\right\rangle, \end{aligned} \tag{16}$$

which implies

$$\frac{\mathrm{d}^{+}V_2(x(t),t)}{\mathrm{d}t^{+}} \le (1-d)\left\langle\left|\sum_{l=1}^{L} D_{l,mc}\right|(|x(t)|), \nu\right\rangle - (1-d)^2\left\langle\left|\sum_{l=1}^{L} D_{l,mc}\right|\left(\left|x\left(t - r_{l,\sigma(t)}(t)\right)\right|\right), \nu\right\rangle. \tag{17}$$

From (15) and (17), we obtain

$$\begin{aligned}\frac{\mathrm{d}^{+}V(t)}{\mathrm{d}t^{+}} &< (1-d)^{2}\left\langle \left(\left(A_{mc}(.)\right)^{*}|x(t)|\right), \nu \right\rangle + (1-d)^{2}\left\langle \left(\left| \sum_{l=1}^{L} D_{l,mc} \right| \left| x\left(t - r_{l,\sigma(t)}(t)\right)\right| \right), \nu \right\rangle \\ &+ (1-d)\left\langle \left| \sum_{l=1}^{L} D_{l,mc} \right| \left(|x(t)|\right), \nu \right\rangle - (1-d)^{2}\left\langle \left| \sum_{l=1}^{L} D_{l,mc} \right| \left(\left| x\left(t - r_{l,\sigma(t)}(t)\right)\right| \right), \nu \right\rangle, \\ &= (1-d)^{2}\left\langle \left(\left(A_{mc}(.)\right)^{*}|x(t)|\right), \nu \right\rangle + (1-d)\left\langle \left(\left| \sum_{l=1}^{L} D_{l,mc} \right| |x(t)| \right), \nu \right\rangle.\end{aligned} \tag{18}$$

Since $0 < (1-d) \leq 1$, it becomes

$$\begin{aligned}&\left\langle \left(\left(A_{mc}(.)\right)^{*}|x(t)|\right), \nu \right\rangle + (1-d)\left\langle \left(\left| \sum_{l=1}^{L} D_{l,mc} \right| |x(t)| \right), \nu \right\rangle \\ &= \left\langle \left(\left(A_{mc}(.)\right)^{*} + (1-d)\left| \sum_{l=1}^{L} D_{l,mc} \right| \right) |x(t)|, \nu \right\rangle \\ &= \left\langle \left| T_{mc}(.) \right| |x(t)|, \nu \right\rangle,\end{aligned} \tag{19}$$

where is $T_{mc}(.)$ given in (9), knowing that

$$\langle T_{mc}(.)|x(t)|, \nu\rangle = \langle T_{mc}(.)^{T}\nu, |x(t)|\rangle. \tag{20}$$

The main eigenvector $\nu(t, x(t))$of $T_{mc}(.)$ relative to the main eigenvalue λ_m is constant. We assume that $T_{mc}(.)$ is the opposite of an $M-$ matrix. Therefore, we can find a vector $\omega \in \Re_{+}^{*n}(\omega_h \in \Re_{+}^{*} h = 1, \ldots, n)$ satisfying the following relation $(-T_{mc}(.))^{T}\nu = \omega, \forall \nu \in \Re_{+}^{*n}$.

Thus, it easy to follow that

$$\langle (T_{mc}(.))|x(t)|\rangle, \nu = \langle \left(T_{mc}(.)\right)^{T}\nu, |x(t)|\rangle = -\langle \omega, |x(t)|\rangle. \tag{21}$$

Substituting (21) into (19) leads to

$$\frac{\mathrm{d}^{+}V(t)}{\mathrm{d}t^{+}} \leq -\langle \omega, |x(t)|\rangle = -\sum_{h=1}^{n} \omega_h \left| x_h(t) \right|. \tag{22}$$

Therefore, it can be established that $((\mathrm{d}^{+}V(t))/\mathrm{d}t^{+}) < 0$ for all $x(t) \neq 0$.

This completes the proof of Theorem 1. □

Remark 1. Theorem 1 gives the main results of the stability analysis for the autonomous system (1) under $\sigma(t) = i \in \underline{N}$ and all admissible uncertainties (4) and (5). The conditions presented in Theorem 1 will be simplified by applying the Borne–Gentina criterion in Theorem 3 and Corollary 1.

3.2. Memory State Feedback Design. In this section, we consider the following memory state feedback controller:

$$u(t) = -K_{\sigma(t)}(.)x(t) - \sum_{l=1}^{L} L_{l,\sigma(t)}(.)x\left(t - r_{l,\sigma(t)}(t)\right), \tag{23}$$

where $K_i(.)$ and $L_{l,i}(.), i \in \underline{N}$, are nonlinear controller gains to be determined.

The resulting closed-loop switched system composed from (1) and (23) is represented by

$$\begin{cases} \dot{x}(t) = \overline{A}_{\sigma(t)}(.)x(t) + \sum_{l=1}^{L} \overline{D}_{l,\sigma(t)}(.)x\left(t - r_{l,\sigma(t)}(t)\right), \\ x(\theta) = \phi(\theta), \quad \theta \in \left[-\max_{1 \leq l \leq L}(\tau_l) 0 \right], \end{cases} \tag{24}$$

where $\overline{A}_{\sigma(t)}(.) = A_{\sigma(t)}(.) - B_{\sigma(t)}(.)K_{\sigma(t)}(.)$ and $\overline{D}_{l,\sigma(t)}(.) = D_{l,\sigma(t)}(.) - B_{\sigma(t)}(.)L_{l,\sigma(t)}(.)$.

In what follows, we present our result for the memory state feedback control of system (1).

Theorem 2. *System (1) is robustly stabilizable via controller (23) under $\sigma(t) = i \in \underline{N}$, for all admissible uncertainly parameters $\mu_{ip}(t)$ and $\lambda_{iq}(t)$ for each $p \in \underline{P}$ and $q \in \underline{Q}$, such that the closed-loop switched system (5) is robustly asymptotically globally stable, if there exist matrices $K_{ip}(.)$ and $L_{l,iq}(.)$, $l \in \underline{L}$, with appropriate dimensions, satisfying that $T_{mc}(.)$ is the opposite of an $M-$ matrix,where*

$$T_{mc}(.) = \max_{\substack{i \in \underline{N} \\ p \in \underline{P}}} \left(\overline{A}_i(.)\right)^{*} + (1-d) \max_{\substack{i \in \underline{N} \\ q \in \underline{Q}}} \left(\sum_{l=1}^{L} \sup_{[.]} \left(\left| \overline{D}_{l,i}(.) \right| \right) \right), \tag{25}$$

and d is introduced in (3).

Proof. We assume that there exist matrices $K_{ip}(.)$ and $L_{l,iq}(.)$, $\forall i \in \underline{N}$, $p \in \underline{P}$, $q \in \underline{Q}$, and $l \in \underline{L}$ satisfying that $T_{mc}(.)$ is the opposite of an $M-$ matrix. According to the proof of Theorem (1), system (1) is robustly asymptotically stabilizable via controller (23) under $\sigma(t) = i \in \underline{N}$ and all admissible uncertainties (4) and (5).

The proof of Theorem 2 is completed. □

Remark 2. Theorem 2 gives the main results for the stabilization of the control system (1) via controller (23). In the sequel, by applying the Borne–Gentina criterion, this result will be applied in Theorem 4 to develop a memory feedback controller via the pole assignment control to stabilize the corresponding closed-loop system under $\sigma(t) = i \in \underline{N}$ and all admissible uncertainties (4) and (5).

4. Application to Switched Systems Modeling via Differential Equations

In this subsection, we apply the previously reached results for a class of switched nonlinear systems modeled by a set of differential equations.

Considering a class of uncertain switched nonlinear systems with multiple time-varying delays formed by N subsystems, each subsystem $S_i, i \in \underline{N}$ is given by the following differential equation:

$$\begin{cases} y^{n}(t) + \left(\left(\sum_{p=1}^{P} \mu_{ip}(t) \sum_{h=0}^{n-1} \widetilde{a}_{ip}^{h}(.) y^{(h)}(t) \right) + \sum_{l=1}^{L} \sum_{q=1}^{Q} \lambda_{iq,l}(t) \sum_{h=0}^{n-1} \widetilde{d}_{l,iq}^{h}(.) y^{(h)}\left(t - r_{i,l}(t)\right) \right) = \widetilde{b}_i(.) u(t), \quad 0 \le r_{i,l}(t) \le \tau, \\ y^{(j)}(s) = \phi_h(s), \quad s \in [-\tau\ 0], h = 1, \ldots, n-1, \end{cases} \tag{26}$$

where $y(t) \in \mathfrak{R}^n$, $\widetilde{a}_{ip}^{h}(.)$, and $\widetilde{d}_{i,q,l}^{h}(.)$ are nonlinear coefficients, $\forall i \in \underline{N}$, $p \in \underline{P}$, $q \in \underline{Q}$, $l \in \underline{L}$, and $(h = 1, \ldots, n-1)$. $u(t) \in \mathfrak{R}$ is the control input. $r_{i,l}(t)$ denotes the time-varying delays satisfying that $0 \le r_{i,l}(t) \le \tau$ and $|\dot{r}_{i,l}(t)| \le d < 1$ where τ and d are given, respectively, in (2) and (3). $\phi_j(s)(h = 1, \ldots, n-1)$ are the initial conditions on $[-\tau\ 0]$.

Consider the following change of variable:

$$x_{h+1}(t) = \frac{\mathrm{d}y^{(h)}}{\mathrm{d}t^{(h)}}, \quad h = 0, \ldots, n-1. \tag{27}$$

Due to (27), relation (26) becomes

$$\begin{cases} \dot{x}_h(t) = x_{h+1}(t), \\ \dot{x}_n(t) = -\left(\sum_{p=1}^{P} \mu_{ip}(t) \sum_{h=0}^{n-1} \widetilde{a}_{ip}^{h}(.) x_{h+1}(t) + \sum_{l=1}^{L} \sum_{q=1}^{Q} \lambda_{iq,l}(t) \sum_{h=0}^{n-1} \widetilde{d}_{iq,l}^{j}(.) x_{h+1}\left(t - r_{i,l}(t)\right) \right) + \widetilde{B}_i(.) u(t), \quad i \in \underline{N}, \end{cases} \tag{28}$$

or under matrix form, we obtain the following state representation:

$$\begin{cases} \dot{x}(t) = \sum_{p=1}^{P} \mu_{ip}(t) \widetilde{A}_{ip}(.) x(k) + \sum_{l=0}^{L} \sum_{q=1}^{Q} \lambda_{iq,l}(t) \widetilde{D}_{l,iq}(.) x\left(t - r_{l,\sigma(t)}(t)\right) + \widetilde{B}_i(.) u(t), \\ x(s) = \phi(s), \ s \in \left[-\max_{1 \le l \le L}(\tau_l)\ 0 \right], \quad i \in \underline{N}, \end{cases} \tag{29}$$

where $x(t)$ is the state vector, whose components are $x_h(t)$, $h = 1, \ldots, n$.

The vertex matrices $\widetilde{A}_{ip}(.)$, $\widetilde{D}_{l,iq}(.)$, and $\widetilde{B}_i(.)$ are given as follows:

$$\widetilde{A}_{ip}(.)=\begin{bmatrix}0 & 1 & \dots & 0\\ 0 & 0 & \ddots & \vdots\\ \vdots & \vdots & \ddots & 1\\ -\widetilde{a}_{ip}^{0}(.) & -\widetilde{a}_{ip}^{1}(.) & \dots & -\widetilde{a}_{ip}^{n-1}(.)\end{bmatrix},\quad i\in \underline{N},$$

$$\widetilde{B}_{i}(.)=\begin{bmatrix}0\\ \vdots\\ 0\\ \widetilde{b}_{i}(.)\end{bmatrix},\quad i\in \underline{N},$$

$$\widetilde{D}_{l,iq}(.)=\begin{bmatrix}0 & 0 & \dots & 0\\ 0 & 0 & \ddots & \vdots\\ \vdots & \vdots & \ddots & 0\\ -\widetilde{d}_{l,iq}^{0}(.) & -\widetilde{d}_{l,iq}^{1}(.) & \dots & -\widetilde{d}_{l,iq}^{n-1}(.)\end{bmatrix},\quad i\in \underline{N},\tag{30}$$

where $\widetilde{a}_{ip}^{h}(.)$ is a coefficient of the instantaneous characteristic polynomial $G_{\widetilde{A}_{ip}(.)}(s)$ of matrix $\widetilde{A}_{ip}(.)$ given by

$$G_{\widetilde{A}_{ip}(.)}(s)=s^{n}+\sum_{h=0}^{n-1}\widetilde{a}_{ip}^{h}(.)s^{h},\tag{31}$$

and $\widetilde{d}_{l,iq}^{h}(.)$ is a coefficient of the instantaneous characteristic polynomial $N_{\widetilde{D}_{l,iq}(.)}(s)$ of matrix $\widetilde{D}_{l,iq}(.)$ defined by

$$N_{\widetilde{D}_{l,iq}(.)}(s)=\sum_{h=0}^{n-1}\widetilde{d}_{i}^{h}(.)s^{h}.\tag{32}$$

Assume that all subsystems are uncertain of polytopic type, which can be described as

$$\begin{aligned}\widetilde{A}_{i}(.)&=\sum_{p=1}^{P}\mu_{ip}(t)\widetilde{A}_{ip}(.),\quad p\in \underline{P}, i\in \underline{N},\\ \widetilde{D}_{l,i}(.)&=\sum_{q=1}^{Q}\lambda_{l,iq}(t)\widetilde{D}_{l,iq}(.),\quad q\in \underline{Q}, l\in \underline{L}, i\in \underline{N}.\end{aligned}\tag{33}$$

Considering the switched rule given in (1), the switched control system will be represented as

$$\begin{cases}\dot{x}(t)=\widetilde{A}_{\sigma(t)}(.)x(t)+\sum_{l=1}^{L}\widetilde{D}_{l,\sigma(t)}(.)x\left(t-r_{l,\sigma(t)}(t)\right)+\widetilde{B}_{\sigma(t)}(.)u(t),\\ x(\theta)=\phi(\theta),\quad \theta\in[-\tau,0], \sigma(t)=i\in \underline{N}.\end{cases}\tag{34}$$

Finally, according to the controller (23), the closed-loop system will be represented by

$$\begin{cases}\dot{x}(t)=\overline{\widetilde{A}}_{\sigma(t)}(.)x(t)+\sum_{l=1}^{L}\overline{\widetilde{D}}_{l,\sigma(t)}(.)x\left(t-r_{l,\sigma(t)}(t)\right),\\ x(s)=\phi(s),\quad s\in[-\tau,0], \sigma(t)=i\in \underline{N},\end{cases}\tag{35}$$

with $\overline{\widetilde{A}}_{i}(.)=\widetilde{A}_{i}(.)-\widetilde{B}_{i}(.)K_{i}(.)$ and $\overline{\widetilde{D}}_{l,i}(.)=\widetilde{D}_{l,i}(.)-\widetilde{B}_{i}(.)L_{l,i}(.)$.

A change of base for system (35) into the arrow matrix form [31] allows that

$$\begin{cases}\dot{z}(t)=\sum_{p=1}^{P}\mu_{ip}(t)E_{ip}(.)z(t)+\sum_{l=1}^{L}\sum_{q=1}^{Q}\lambda_{l,iq}(t)F_{l,iq}(.)z\left(t-r_{l,i}(t)\right),\\ z(s)=P\phi(s),\quad s\in[-\tau,0], i\in \underline{N},\end{cases}\tag{36}$$

where $z(t)=Px(t)$ is the new state vector and P is the corresponding passage matrix given by

$$P=\begin{bmatrix}1 & 1 & \dots & 1 & 0\\ \alpha_{1} & \alpha_{2} & \dots & \alpha_{n-1} & 0\\ (\alpha_{1})^{2} & (\alpha_{2})^{2} & \dots & (\alpha_{n-1})^{2} & \vdots\\ \vdots & \vdots & \dots & \vdots & 0\\ (\alpha_{1})^{n-1} & (\alpha_{2})^{n-1} & \dots & (\alpha_{n-1})^{n-1} & 1\end{bmatrix},\tag{37}$$

with α_{j}, $j=1,\dots,n-1$ being distinct arbitrary constant parameters.

The vertex matrices in the arrow form $E_{ip}(.)$ and $F_{l,iq}(.)$ are given by

$$E_{ip}(.)=P^{-1}\overline{\widetilde{A}}_{ip}(.)P=\begin{bmatrix}\alpha_{1} & 0 & \dots & 0 & \beta_{1}\\ 0 & \ddots & \ddots & \vdots & \vdots\\ \vdots & \ddots & \ddots & 0 & \vdots\\ 0 & \dots & 0 & \alpha_{n-1} & \beta_{n-1}\\ \gamma_{ip}^{1}(.) & \dots & \dots & \gamma_{ip}^{n-1}(.) & \gamma_{ip}^{n}(.)\end{bmatrix},\quad i\in \underline{N}, p\in \underline{P},$$

$$F_{l,iq}(.)=P^{-1}\overline{\widetilde{D}}_{l,iq}(.)P=\begin{bmatrix}0_{n-1,n-1},\dots,0_{n-1,1}\\ \delta_{l,iq}^{1}(.),\dots,\delta_{l,iq}^{n-1}(.)\ \delta_{l,iq}^{n}(.)\end{bmatrix},\quad i\in \underline{N}, l\in \underline{L}, q\in \underline{Q},\tag{38}$$

with

$$\beta_h = \prod_{\substack{q=1 \\ q\neq h}}^{n-1} \left(\alpha_h - \alpha_q\right)^{-1}, \quad \forall h = 1, \ldots, n-1. \tag{39}$$

The elements of $E_{ip}(.)$ are given as follows:

$$\begin{cases} \gamma_{ip}^{h}(.) = -G_{\widetilde{\overline{A}}_{ip}(.)}(\alpha_h), & \forall h = 1, \ldots, n-1, \\ \gamma_{ip}^{n}(.) = -\overline{\overline{a}}_{ip}^{n-1}(.) - \sum_{h=1}^{n-1} \alpha_h,, & i \in \underline{N}, p \in \underline{P}, \end{cases} \tag{40}$$

and the elements of $F_{l,iq}(.)$ are

$$\begin{cases} \delta_{l,iq}^{h}(.) = -N_{\widetilde{\overline{D}}_{l,iq}(.)}(\alpha_h), & \forall h = 1, \ldots, n-1, \\ \delta_{l,iq}^{n}(.) = -\overline{\overline{d}}_{l,iq}^{n-1}(.) & \end{cases} , i \in \underline{N}, l \in \underline{L}, q \in \underline{Q}. \tag{41}$$

Taking into account the previous relations, the matrix $T_{l,ipq}(.)$ is given by

$$T_{l,ipq}(.) = \begin{bmatrix} \alpha_1 & 0 & \ldots & 0 & |\beta_1| \\ 0 & \ddots & \ddots & \vdots & \vdots \\ \vdots & \ddots & \ddots & 0 & \vdots \\ 0 & \ldots & 0 & \alpha_{n-1} & |\beta_{n-1}| \\ t_{l,ipq}^{1}(.) & \ldots & \ldots & t_{l,ipq}^{n-1}(.) & t_{l,ipq}^{n}(.) \end{bmatrix}, \quad i \in \underline{N}, l \in \underline{L}, q \in \underline{Q}, \tag{42}$$

with

$$\begin{cases} t_{l,ipq}^{h}(.) = \left|\gamma_{ip}^{h}(.)\right| + (1-d) \sup_{[.]} \left(\sum_{l=1}^{L} \left|\delta_{l,iq}^{h}(.)\right| \right), & h = 1, \ldots, n-1, \\ t_{l,ipq}^{n}(.) = \gamma_{ip}^{n}(.) + (1-d) \sup_{[.]} \left(\left(\sum_{l=1}^{L} \left|\delta_{l,iq}^{n}(.)\right| \right) \right). \end{cases} \tag{43}$$

Finally, the common pseudo-overvaluing matrix $T_{mc}(.)$ of system (35) can be deduced such as

$$T_{mc}(.) = \begin{bmatrix} \alpha_1 & 0 & \ldots & 0 & |\beta_1| \\ 0 & \ddots & \ddots & \vdots & \vdots \\ \vdots & \ddots & \ddots & 0 & \vdots \\ 0 & \ldots & 0 & \alpha_{n-1} & |\beta_{n-1}| \\ \overline{t}^{1}(.) & \ldots & \ldots & \overline{t}^{n-1}(.) & \overline{t}^{n}(.) \end{bmatrix}, \tag{44}$$

where

$$\overline{t}^{h}(.) = \max_{\substack{i \in \underline{N} \\ p \in \underline{P} \\ q \in \underline{Q}}} \left(t_{l,ipq}^{h}(.) \right), \quad \forall h = 1, \ldots, n. \tag{45}$$

4.1. Stability Conditions for Continuous-Time Uncertain Switched Nonlinear Systems with Multiple Time-Varying Delays. In this subsection, we give some sufficient stability conditions for the autonomous system (34).

Theorem 3. *The autonomous system (34) is robustly globally asymptotically stable under $\sigma(t) = i \in \underline{N}$ and admissible uncertainties (4) and (5), if there exist $\alpha_h < 0$ $(h = 1, \ldots, n-1)$, $\alpha_h \neq \alpha_q, \forall h \neq q$, such that the following condition is satisfied:*

$$-\overline{t}^{n}(.) + \sum_{h=1}^{n-1} \overline{t}^{h}(.) \left|\beta_h\right| \alpha_h^{-1} > 0. \tag{46}$$

Proof. The application of the Borne–Gentina criterion to $T_{mc}(.)$ yields to the following stability conditions for the autonomous system (34):

$$(-1)^h \Delta_h > 0, \quad h = 1, \ldots, n-1, \tag{47}$$

where Δ_h is the h^{th} principal minor of $T_{mc}(.)$.

Therefore, for $h = 1, \ldots, n-1$, the first condition in Theorem 3 is verified such that $\alpha_h \in \mathfrak{R}_{-}^{*}$.

Finally, for $h = n$, the last condition is verified as follows:

$$(-1)^n \det\left(T_{mc}(.)\right) = (-1)^n \begin{vmatrix} \alpha_1 & 0 & \ldots & 0 & |\beta_1| \\ 0 & \ddots & \ddots & \vdots & \vdots \\ \vdots & \ddots & \ddots & 0 & \vdots \\ 0 & \ldots & 0 & \alpha_{n-1} & |\beta_{n-1}| \\ \overline{t}^{1}(.) & \ldots & \ldots & \overline{t}^{n-1}(.) & \overline{t}^{n}(.) \end{vmatrix}, \tag{48}$$

That is,

$$= (-1)^n \left[\overline{t}^{n}(.) \prod_{q=1}^{n-1} \alpha_q - \sum_{h=1}^{n-1} \left(|\overline{t}^{h}(.)| |\beta_h| \prod_{\substack{h=1 \\ h\neq q}}^{n-1} \alpha_h \right) \right] > 0. \tag{49}$$

The division of this previous condition by $((-1)^{n-1} \prod_{q=1}^{n-1} \alpha_q)$ yields to $-\overline{t}^{n}(.) + \sum_{h=1}^{n-1} \overline{t}^{h}(.) |\beta_h| \alpha_h^{-1} > 0$.

The proof of Theorem 3 is complete. □

Remark 3. If there exist parameters $\alpha_h (h = 1, \ldots, n-1)$ satisfying that

$$\begin{aligned} &\beta_h \left(G_{\widetilde{A}_{ip}(.)}(\alpha_h) + (1-d) \sup_{[.]} \left(\sum_{l=1}^{L} N_{\widetilde{D}_{l,iq}(.)}(\alpha_h) \right) \right) \\ &= -\beta_h \left(\gamma_{ip}^{n}(.) + (1-d) \sup_{[.]} \left(\sum_{l=1}^{L} \delta_{l,iq}^{n}(.) \right) \right) < 0, \end{aligned} \tag{50}$$

Theorem 3 can be simplified to Corollary 1.

Corollary 1. *The autonomous system (35) is robustly globally asymptotically stable under $\sigma(t) = i \in \underline{N}$ and admissible uncertainties (4) and (5), if there exist α_h $(h = 1, \ldots, n-1) < 0$ such that $\alpha_h \neq \alpha_q$, $\forall h \neq q$, and the inequalities below are satisfied:*

$$\begin{aligned}
&\beta_h\left(G_{\widetilde{A}_{ip}(.)}(s=\alpha_h) + (1-d)\sup_{[.]}\left(\sum_{l=1}^{L} N_{\widetilde{D}_{l,iq}(.)}(s=\alpha_h)\right)\right) < 0,\\
&\beta_h\left(G_{\widetilde{A}_{ip}(.)}(s=0) + (1-d)\sup_{[.]}\left(\sum_{l=1}^{L} N_{\widetilde{D}_{l,iq}(.)}(s=0)\right)\right) > 0.
\end{aligned} \tag{51}$$

Proof. If there exist α_h $(h = 1, \ldots, n-1) < 0$ such that

$$\begin{aligned}
&\beta_h\left(G_{\widetilde{A}_{ip}(.)}(\alpha_h) + (1-d)\sup_{[.]}\left(\sum_{l=1}^{L} N_{\widetilde{D}_{l,iq}(.)}(\alpha_h)\right)\right)\\
&\quad = -\beta_h\left(\gamma_{ip}^{n}(.) + (1-d)\sup_{[.]}\left(\sum_{l=1}^{L}\delta_{l,iq}^{n}(.)\right)\right) < 0,
\end{aligned} \tag{52}$$

$T_{mc}(.)$ will be given by $T_{mc}(.) = \begin{bmatrix} \alpha_1 & 0 & \ldots & 0 & \beta_1 \\ 0 & \ddots & \ddots & \vdots & \vdots \\ \vdots & \ddots & \ddots & 0 & \vdots \\ 0 & \ldots & 0 & \alpha_{n-1} & \beta_{n-1} \\ t_{l,ipq}^{1}(.) & \ldots & \ldots & t_{l,ipq}^{n-1}(.) & t_{l,ipq}^{n}(.) \end{bmatrix}$, where $\overline{t}_{l,ipq}^{h}(.) = (\gamma_{ip}^{h}(.) + (1-d)\sup_{[.]}(\sum_{l=1}^{L}\delta_{l,iq}^{h}(.)))$, $\forall h = 1, \ldots, n$.

Therefore, the n^{th} principal minor of $T_{mc}(.)$ is calculated as follows:

$$\begin{aligned}
\Delta_n &= -\left(\gamma_{ip}^{n}(.) + (1-d)\sup_{[.]}\left(\sum_{l=1}^{L}\delta_{l,iq}^{n}(.)\right)\right)\\
&\quad + \sum_{h=1}^{n-1}(\alpha_h)^{-1}\left(\gamma_{ip}^{h}(.) + (1-d)\sup_{[.]}\left(\sum_{l=1}^{L}\delta_{l,iq}^{h}(.)\right)\right)\beta_h,\\
&= \prod_{h=1}^{n-1}(\alpha_h)^{-1}\left(G_{\widetilde{A}_{ip}(.)}(0) + (1-d)\sup_{[.]}\left(\sum_{l=1}^{L} N_{\widetilde{D}_{l,iq}(.)}(0)\right)\right).
\end{aligned} \tag{53}$$

This implies that $G_{\widetilde{A}_{ip}(.)}(0) + (1-d)\sup_{[.]}(\sum_{l=1}^{L} N_{\widetilde{D}_{l,iq}(.)}(0)) > 0$.

This proof is complete. □

4.2. Memory Feedback Stabilization for Uncertain Switched Nonlinear Systems with Time-Varying Delays. In this subsection, a new memory feedback stabilization for the control system (34) via the pole assignment control is given in Theorem 4.

Theorem 4. *Let all n poles $\{p_1, \ldots, p_n\}$ of system (34) be imposed as real, distinct, and negative. Then, the control system (34) is stabilizing via control law (23), such that the corresponding closed-loop, switched system is robustly globally asymptotically stable under $\sigma(t) = i \in \underline{N}$ and admissible uncertainties (4) and (5), if the following conditions are satisfied:*

$$\begin{cases}
\overline{t}^{h}(.) = \max\limits_{\substack{i\in\underline{N}\\ p\in\underline{P}\\ q\in\underline{Q}}}\left(\left|\gamma_{ip}^{h}(.)\right| + (1-d)\sup\limits_{[.]}\left(\sum\limits_{l=1}^{L}\left|\delta_{l,iq}^{h}(.)\right|\right)\right) = 0, \quad \forall h = 1, \ldots, n,\\
\overline{t}^{n}(.) = \max\limits_{\substack{i\in\underline{N}\\ p\in\underline{P}\\ q\in\underline{Q}}}\left(\gamma_{ip}^{n}(.) + (1-d)\sup\limits_{[.]}\left(\sum\limits_{l=1}^{L}\left|\delta_{l,iq}^{n}(.)\right|\right)\right) = p_n,
\end{cases} \tag{54}$$

where

$$\begin{cases}
\beta_h = \prod\limits_{\substack{q=1\\ q\neq h}}^{n-1}\left(p_h - p_q\right)^{-1}, \quad \forall h = 1, \ldots, n-1,\\
\gamma_{ip}^{h}(.) = -G_{\overline{\overline{A}}_{ip}}(p_h), \quad \forall h = 1, \ldots, n-1,\\
\gamma_{ip}^{n}(.) = -\overline{\overline{a}}_{ip}^{(1)}(.) - \sum\limits_{h=1}^{n-1} p_h,
\end{cases} \tag{55}$$

$$\begin{cases}
\delta_{l,iq}^{h}(.) = -N_{\overline{\overline{D}}_{l,iq}(.)}(p_h), \quad \forall h = 1, \ldots, n-1,\\
\delta_{l,iq}^{n}(.) = -\overline{\overline{d}}_{l,iq}^{n-1}(.)
\end{cases} \tag{56}$$

Proof. For $p_h = \alpha_h$ are real and negative $h = 1, \ldots, n-1$, the Borne–Gentina criterion yields to the following stabilization conditions:

$$(-1)^n\begin{vmatrix} p_1 & 0 & \ldots & 0 & |\beta_1| \\ 0 & \ddots & \ddots & \vdots & \vdots \\ \vdots & \ddots & \ddots & 0 & \vdots \\ 0 & \ldots & 0 & p_{n-1} & |\beta_{n-1}| \\ \overline{t}^{1}(.) & \ldots & \ldots & \overline{t}^{n-1}(.) & \overline{t}^{n}(.) \end{vmatrix} > 0. \tag{57}$$

Since the new dynamic of the system permits concluding that overall $\overline{t}^{j}(.) = 0$ for $j = 1, \ldots, n-1$ and $\overline{t}^{n}(.) = p_n \overline{t}^{n}(.) = p_n$, thus (55) becomes

$$T_{mc}(.)=\begin{bmatrix} p_1 & 0 & \dots & 0 & |\beta_1| \\ 0 & \ddots & \ddots & \vdots & \vdots \\ \vdots & \ddots & \ddots & 0 & \vdots \\ 0 & \dots & 0 & p_{n-1} & |\beta_{n-1}| \\ 0 & \dots & \dots & 0 & p_n \end{bmatrix}, \tag{58}$$

and the system is stable since $p_h < 0$ $h = 1, \dots, n$. □

5. Illustrative Examples

In this section, two numerical examples are introduced to demonstrate the theoretical results.

Example 1. Let us consider system (34) with three subsystems, where the randomly switched model is given as

$$A_{11}(.)=\begin{bmatrix} 0 & 1 \\ -1.5f(.) & 1-\Phi(.) \end{bmatrix},$$
$$A_{12}(.)=\begin{bmatrix} 0 & 1 \\ 1-f(.) & -2\Phi(.) \end{bmatrix},$$
$$A_{21}(.)=\begin{bmatrix} 0 & 1 \\ -f(.) & 1-\Phi(.) \end{bmatrix},$$
$$A_{22}(.)=\begin{bmatrix} 0 & 1 \\ -2f(.) & -3\Phi(.) \end{bmatrix},$$
$$A_{31}(.)=\begin{bmatrix} 0 & 1 \end{bmatrix}\begin{bmatrix} 0 & 1 \\ -2f(.) & -\Phi(.) \end{bmatrix},$$
$$A_{32}(.)=\begin{bmatrix} 0 & 1 \\ 1-2f(.) & -\Phi(.) \end{bmatrix},$$
$$D_{1,11}(.)=\begin{bmatrix} 0 & 0 \\ -4.5\psi(.) & -3\psi(.) \end{bmatrix},$$
$$D_{2,11}(.)=\begin{bmatrix} 0 & 0 \\ 3.8\psi(.) & -2.7\psi(.) \end{bmatrix},$$
$$D_{1,12}(.)=\begin{bmatrix} 0 & 0 \\ -4\psi(.) & 1.5\psi(.) \end{bmatrix},$$
$$D_{12,2}(.)=\begin{bmatrix} 0 & 0 \\ 2\psi(.) & -3.5\psi(.) \end{bmatrix},$$
$$D_{1,21}(.)=\begin{bmatrix} 0 & 0 \\ -1.3\psi(.) & 0.9\psi(.) \end{bmatrix},$$
$$D_{2,21}(.)=\begin{bmatrix} 0 & 0 \\ -0.4\psi(.) & -1.2\psi(.) \end{bmatrix},$$
$$D_{1,22}(.)=\begin{bmatrix} 0 & 0 \\ -1.8\psi(.) & 1.2\psi(.) \end{bmatrix},$$
$$D_{2,22}(.)=\begin{bmatrix} 0 & 0 \\ -0.7\psi(.) & -2\psi(.) \end{bmatrix},$$
$$D_{1,31}(.)=\begin{bmatrix} 0 & 0 \\ -3\psi(.) & -2.2\psi(.) \end{bmatrix},$$
$$D_{2,31}(.)=\begin{bmatrix} 0 & 0 \\ 0 & -0.4\psi(.) \end{bmatrix},$$
$$D_{1,32}(.)=\begin{bmatrix} 0 & 0 \\ -3\psi(.) & -3\psi(.) \end{bmatrix},$$
$$D_{2,32}(.)=\begin{bmatrix} 0 & 0 \\ 0 & 0.7\psi(.) \end{bmatrix}, \tag{59}$$

with $f(.)$, $\Phi(.)$, and $\psi(.)$ are general nonlinear functions.

Hence, we suppose that $\psi(.) \in E([-1, 0.2, 0.5])$ and the corresponding delay functions are listed as follows: $r_{1,1}(t) = 0.8 + (1/5)\cos^2(t)$, $r_{2,1}(t) = 1 + (1/5)\cos^2(t)$, $r_{1,2}(t) = 1.2 + (1/8)\cos^2(t)$, $r_{2,2}(t) = 0.5 + (1/8)\cos^2(t)$, $r_{1,3}(t) = 0.6 + (1/6)\cos^2(t)$, and $r_{2,3}(t) = 1 + (1/6)\cos^2(t)$.

From Corollary 1, with $\alpha = -1$, we obtain the following robust stability conditions:

$$\begin{cases} f(.) < -2.39 + \Phi(.) \\ f(.) < -0.65 + 0.5\Phi(.) \\ f(.) > 0.5. \end{cases} \tag{60}$$

The stability domain given by the nonlinear $f(.)$ relative to the nonlinear $\Phi(.)$ is illustrated in Figure 1. For choice $f(.) = 2$, $\Phi(.) = 5.3$, and $\psi(.) = 0.2$, the uncertain parameters

$$\begin{aligned} &\mu_{11} = \mu_{21} = \mu_{31} = 0.6, \\ &\mu_{12} = \mu_{22} = \mu_{32} = 0.4, \\ &\lambda_{1,11} = \lambda_{2,11} = \lambda_{1,21} = \lambda_{2,21} = \lambda_{1,31} = \lambda_{2,31} = 0.6, \\ &\lambda_{1,12} = \lambda_{2,12} = \lambda_{1,22} = \lambda_{2,22} = \lambda_{1,32} = \lambda_{2,32} = 0.4. \end{aligned} \tag{61}$$

The initial state vector $\phi(t) = [1 \ -4]^T$ and the simulation results are illustrated in Figures 2–4 where the switched signal given in Figure 5 is randomly generated.

Remark 4. From Figures 2 and 3, we observe that the considered system is robustly asymptotically stable under randomly switching and any admissible uncertainties (4) and (5), which proves the effectiveness of the result given in Corollary 1.

Remark 5. The considered system in Example 1 is subject to uncertain complex nonlinear dynamics and mode depending on multiple time-varying delays. However, it is very difficult to find a CLF for the system under consideration in Example 1.

Remark 6. The result given in Corollary 1 can construct an alternative to searching a CLF through the LMIs approach for studying robust stability under arbitrary switching.

Indeed, in [32], the authors introduced a simple linear example without time-delay and uncertainty for which a CLF does not exist.

Example 2. (see [43]). Consider the following switched system given by a set of differential equations represented as

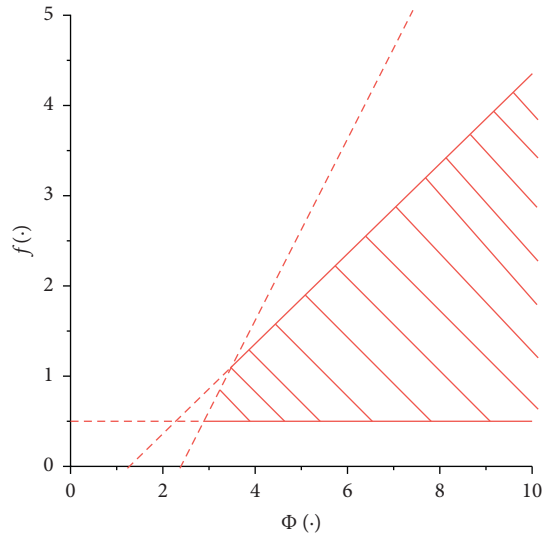

Figure 1: Stability domain for the system in Example 1.

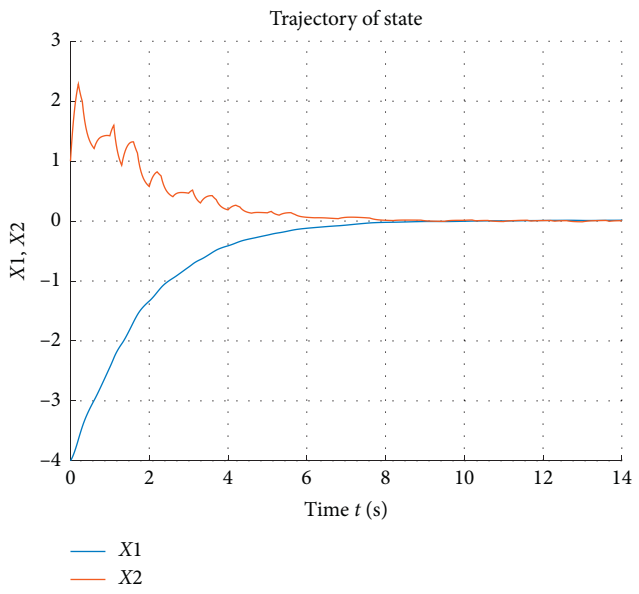

Figure 2: The state responses of the system in Example 1.

$$\ddot{x}(t) + \sum_{p=1}^{2} \mu_{ip}(t) a_{ip}(.) \dot{x}(t) + \sum_{p=1}^{2} \mu_{ip}(t) \frac{\varphi_{ip}(x(t))}{x(t)} x(t) + \sum_{l=1}^{2}\sum_{q=1}^{2} \lambda_{l,iq}(t) b_{l,iq}(.) \dot{x}\left(t - r_{l,i}(t)\right) + \sum_{l=1}^{2}\sum_{q=1}^{2} \lambda_{l,iq}(t) c_{l,iq}(.) x\left(t - r_{l,i}(t)\right) + u(t) = 0, \tag{62}$$

where $a_{ip}(.)$, $b_{l,iq}(.)$, and $c_{l,iq}(.)$ are nonlinear parameters for each $i \in \{1, 2, 3\} p \in \{1, 2\}$, $q \in \{1, 2\}$, and $l \in \{1, 2\}$.

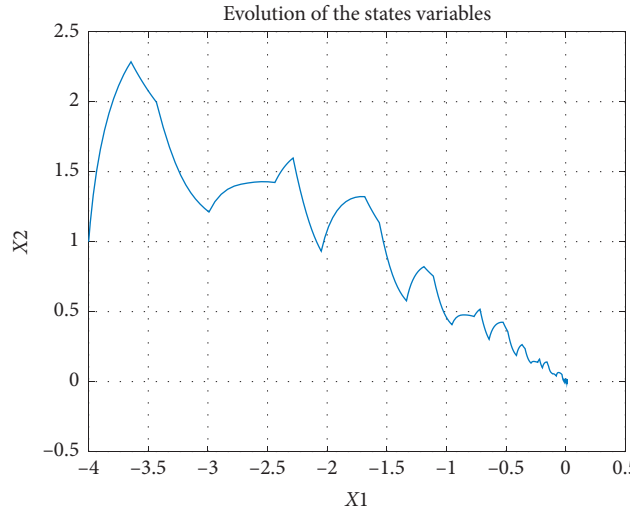

Figure 3: State space of the system in Example 1.

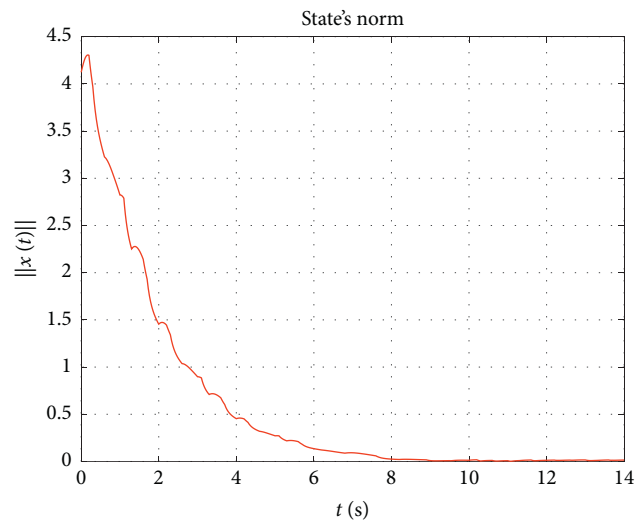

Figure 4: State's norm of the system in Example 1.

All the subsystems can be represented under matrix representation such as

$$\dot{x}(t) = \sum_{p=1}^{2} \mu_{ip}(t) A_{ip}(.) x(t) + \sum_{l=1}^{2}\sum_{q=1}^{2} \lambda_{l,iq}(t) D_{l,iq}(.) x \cdot \left(t - r_{l,i}(t)\right) + B_i u(t). \tag{63}$$

Consider the following controller:

$$u(t) = -\sum_{p=1}^{2} \mu_{ip}(t) K_{ip}(.) x(t) - \sum_{l=1}^{2}\sum_{p=1}^{2} \lambda_{l,iq}(t) L_{l,iq}(.) x\left(t - r_{l,iq}(t)\right), \tag{64}$$

where the gains are $K_{ip}(.) = [K_{ip}^{1}(.)\, K_{ip}^{2}(.)]$ and $L_{l,iq}(.) = [L_{l,iq}^{1}(.)\, L_{l,iq}^{2}(.)]$, for each $i \in \{1, 2, 3\} p \in \{1, 2\}$, $q \in \{1, 2\}$, and $l \in \{1, 2\}$.

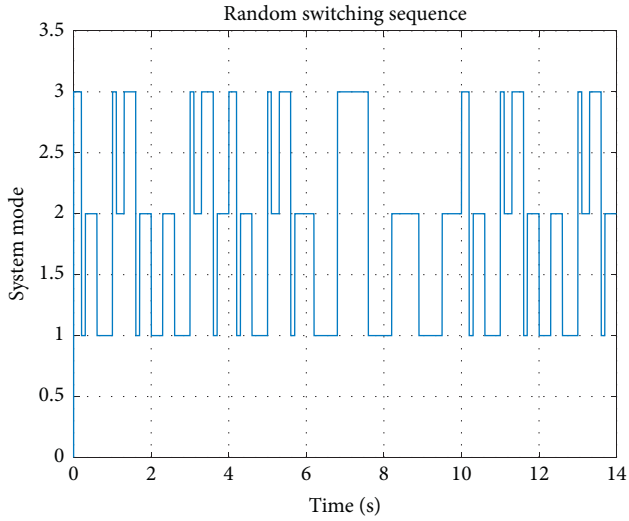

FIGURE 5: Random switching sequence for the system given in Example 1.

All the closed-loop subsystems will be represented as follows:

$$\dot{x}(t) = \sum_{p=1}^{2} \mu_{ip}(t)\overline{\widetilde{A}}_{ip}(.)x(t) + \sum_{l=1}^{2}\sum_{p=1}^{2} \lambda_{l,iq}(t)\overline{\widetilde{D}}_{l,iq}(.)x\left(t - r_{l,i}(t)\right), \tag{65}$$

where

$$\overline{\widetilde{A}}_{ip}(.) = \begin{pmatrix} 0 & 1 \\ -\dfrac{\varphi_{ip}(x)}{x} - K_{ip}^{1}(.) & -a_{ip}(.) - K_{ip}^{2}(.) \end{pmatrix}, \tag{66}$$

$$\overline{\widetilde{D}}_{l,iq}(.) = \begin{pmatrix} 0 & 0 \\ -c_{l,iq}(.) - L_{l,iq}^{1}(.) & -b_{l,iq}(.) - L_{l,iq}^{2}(.) \end{pmatrix}.$$

The time-varying delay functions are

$$\begin{aligned} r_{1,1}(t) &= 0.8 + \frac{1}{5}\cos^2(t), \\ r_{1,2}(t) &= 0.4 + \frac{1}{8}\cos^2(t), \\ r_{2,1}(t) &= 1 + \frac{1}{5}\cos^2(t), \\ r_{2,2}(t) &= 0.5 + \frac{1}{8}\cos^2(t), \\ r_{1,3}(t) &= 0.6 + \frac{1}{6}\cos^2(t), \\ r_{2,3}(t) &= 0.5 + \frac{1}{6}\cos^2(t). \end{aligned} \tag{67}$$

All the vertex matrices will be represented under the arrow form such as

where

$$\begin{aligned} E_{11}(.) &= \begin{bmatrix} \alpha & 1 \\ \gamma_{11}^{1}(.) & \gamma_{11}^{2}(.) \end{bmatrix}, \\ E_{12}(.) &= \begin{bmatrix} \alpha & 1 \\ \gamma_{12}^{1}(.) & \gamma_{12}^{2}(.) \end{bmatrix}, \\ E_{21}(.) &= \begin{bmatrix} \alpha & 1 \\ \gamma_{21}^{1}(.) & \gamma_{21}^{2}(.) \end{bmatrix}, \\ E_{22}(.) &= \begin{bmatrix} \alpha & 1 \\ \gamma_{22}^{1}(.) & \gamma_{22}^{2}(.) \end{bmatrix}, \\ E_{31}(.) &= \begin{bmatrix} \alpha & 1 \\ \gamma_{31}^{1}(.) & \gamma_{31}^{2}(.) \end{bmatrix}, \\ E_{32}(.) &= \begin{bmatrix} \alpha & 1 \\ \gamma_{32}^{1}(.) & \gamma_{32}^{2}(.) \end{bmatrix}, \\ F_{1,11}(.) &= \begin{bmatrix} 0 & 0 \\ \delta_{1,11}^{1}(.) & \delta_{1,11}^{2}(.) \end{bmatrix}, \\ F_{2,11}(.) &= \begin{bmatrix} 0 & 0 \\ \delta_{2,11}^{1}(.) & \delta_{2,11}^{2}(.) \end{bmatrix}, \\ F_{1,12}(.) &= \begin{bmatrix} 0 & 0 \\ \delta_{1,12}^{1}(.) & \delta_{1,12}^{2}(.) \end{bmatrix}, \\ F_{2,21}(.) &= \begin{bmatrix} 0 & 0 \\ \delta_{2,21}^{1}(.) & \delta_{2,21}^{2}(.) \end{bmatrix}, \\ F_{1,21}(.) &= \begin{bmatrix} 0 & 0 \\ \delta_{1,21}^{1}(.) & \delta_{1,21}^{2}(.) \end{bmatrix}, \\ F_{2,21}(.) &= \begin{bmatrix} 0 & 0 \\ \delta_{2,21}^{1}(.) & \delta_{2,21}^{2}(.) \end{bmatrix}, \\ F_{1,22}(.) &= \begin{bmatrix} 0 & 0 \\ \delta_{1,22}^{1}(.) & \delta_{1,22}^{2}(.) \end{bmatrix}, \\ F_{2,22}(.) &= \begin{bmatrix} 0 & 0 \\ \delta_{2,22}^{1}(.) & \delta_{2,22}^{2}(.) \end{bmatrix}, \\ F_{1,31}(.) &= \begin{bmatrix} 0 & 0 \\ \delta_{1,31}^{1}(.) & \delta_{1,31}^{2}(.) \end{bmatrix}, \\ F_{2,31}(.) &= \begin{bmatrix} 0 & 0 \\ \delta_{2,31}^{1}(.) & \delta_{2,31}^{2}(.) \end{bmatrix}, \\ F_{1,32}(.) &= \begin{bmatrix} 0 & 0 \\ \delta_{1,32}^{1}(.) & \delta_{1,32}^{2}(.) \end{bmatrix}, \\ F_{2,32}(.) &= \begin{bmatrix} 0 & 0 \\ \delta_{2,32}^{1}(.) & \delta_{2,32}^{2}(.) \end{bmatrix}, \end{aligned} \tag{68}$$

$$\begin{cases} \gamma_{11}^{1}(.) = -G_{\overline{A}_{11}(.)}(\alpha) = -\left[\alpha^2 + \alpha\left(a_{11}(.) + K_{11}^{2}(.)\right) + K_{11}^{1}(.) + \dfrac{\varphi_{11}(x)}{x}\right], \\ \gamma_{11}^{2}(.) = \left(-a_{11}(.) - K_{11}^{2}(.) - \alpha\right), \end{cases}$$

$$\begin{cases} \gamma_{12}^{1}(.) = -G_{\overline{A}_{12}(.)}(\alpha) = -\left[\alpha^2 + \alpha\left(a_{12}(.) + K_{12}^{2}(.)\right) + K_{12}^{1}(.) + \dfrac{\varphi_{12}(x)}{x}\right], \\ \gamma_{12}^{2}(.) = \left(-a_{12}(.) - K_{12}^{2}(.) - \alpha\right), \end{cases}$$

$$\begin{cases} \gamma_{21}^{1}(.) = -G_{\overline{A}_{21}(.)}(\alpha) = -\left[\alpha^2 + \alpha\left(a_{21}(.) + K_{21}^{2}(.)\right) + K_{21}^{1}(.) + \dfrac{\varphi_{21}(x)}{x}\right], \\ \gamma_{21}^{2}(.) = \left(-a_{21}(.) - K_{21}^{2}(.) - \alpha\right), \end{cases}$$

$$\begin{cases} \gamma_{22}^{1}(.) = -G_{\overline{A}_{22}(.)}(\alpha) = -\left[\alpha^2 + \alpha\left(a_{22}(.) + K_{22}^{2}(.)\right) + K_{22}^{1}(.) + \dfrac{\varphi_{22}(x)}{x}\right], \\ \gamma_{22}^{2}(.) = \left(-a_{22}(.) - K_{22}^{2}(.) - \alpha\right), \end{cases}$$

$$\begin{cases} \gamma_{31}^{1}(.) = -G_{\overline{A}_{31}(.)}(\alpha) = -\left[\alpha^2 + \alpha\left(a_{31}(.) + K_{31}^{2}(.)\right) + K_{31}^{1}(.) + \dfrac{\varphi_{31}(x)}{x}\right], \\ \gamma_{31}^{2}(.) = \left(-a_{31}(.) - K_{31}^{2}(.) - \alpha\right), \end{cases}$$

$$\begin{cases} \gamma_{32}^{1}(.) = -G_{\overline{A}_{32}(.)}(\alpha) = -\left[\alpha^2 + \alpha\left(a_{32}(.) + K_{32}^{2}(.)\right) + K_{32}^{1}(.) + \dfrac{\varphi_{32}(x)}{x}\right], \\ \gamma_{32}^{2}(.) = \left(-a_{32}(.) - K_{32}^{2}(.) - \alpha\right), \end{cases}$$

$$\begin{cases} \delta_{1,11}^{1}(.) = -N_{\overline{D}_{1,11}(.)}(\alpha) = -\left[\left(b_{1,11}(.) + L_{1,11}^{2}(.)\right)\alpha + c_{1,11}(.) + L_{1,11}^{1}(.)\right], \\ \delta_{1,11}^{2}(.) = -\left[b_{1,11}(.) + L_{1,11}^{2}(.)\right], \end{cases}$$

$$\begin{cases} \delta_{2,11}^{1}(.) = -N_{\overline{D}_{2,11}(.)}(\alpha) = -\left[\left(b_{2,11}(.) + L_{2,11}^{2}(.)\right)\alpha + c_{2,11}(.) + L_{2,11}^{1}(.)\right], \\ \delta_{2,11}^{2}(.) = -\left[b_{2,11}(.) + L_{2,11}^{2}(.)\right], \end{cases}$$

$$\begin{cases} \delta_{1,12}^{1}(.) = -N_{\overline{D}_{1,12}(.)}(\alpha) = -\left[\left(b_{1,12}(.) + L_{1,12}^{2}(.)\right)\alpha + c_{1,12}(.) + L_{1,12}^{1}(.)\right], \\ \delta_{1,12}^{2}(.) = -\left[b_{1,12}(.) + L_{1,12}^{2}(.)\right], \end{cases}$$

$$
\begin{cases}
\delta_{2,12}^{1}(.) = -N_{\overline{D}_{2,12}(.)}(\alpha) = -\left[\left(b_{2,12}(.) + L_{2,12}^{2}(.)\right)\alpha + c_{2,12}(.) + L_{2,12}^{1}(.)\right], \\
\delta_{2,12}^{2}(.) = -\left[b_{2,12}(.) + L_{2,12}^{2}(.)\right],
\end{cases}
$$

$$
\begin{cases}
\delta_{1,21}^{1}(.) = -N_{\overline{D}_{1,21}(.)}(\alpha) = -\left[\left(b_{1,21}(.) + L_{1,21}^{2}(.)\right)\alpha + c_{1,21}(.) + L_{1,21}^{1}(.)\right], \\
\delta_{1,21}^{2}(.) = -\left[b_{1,21}(.) + L_{1,21}^{2}(.)\right],
\end{cases}
$$

$$
\begin{cases}
\delta_{2,21}^{1}(.) = -N_{\overline{D}_{2,21}(.)}(\alpha) = -\left[\left(b_{2,21}(.) + L_{2,21}^{2}(.)\right)\alpha + c_{2,21}(.) + L_{2,21}^{1}(.)\right], \\
\delta_{2,21}^{2}(.) = -\left[b_{2,21}(.) + L_{2,21}^{2}(.)\right], \\
\delta_{1,22}^{1}(.) = -N_{\overline{D}_{1,22}(.)}(\alpha) = -\left[\left(b_{1,22}(.) + L_{1,22}^{2}(.)\right)\alpha + c_{1,22}(.) + L_{1,22}^{1}(.)\right], \\
\delta_{1,22}^{2}(.) = -\left[b_{1,22}(.) + L_{1,22}^{2}(.)\right],
\end{cases}
$$

$$
\begin{cases}
\delta_{2,21}^{1}(.) = -N_{\overline{D}_{2,21}(.)}(\alpha) = -\left[\left(b_{2,21}(.) + L_{2,21}^{2}(.)\right)\alpha + c_{2,21}(.) + L_{2,21}^{1}(.)\right], \\
\delta_{2,21}^{2}(.) = -\left[b_{2,21}(.) + L_{2,21}^{2}(.)\right],
\end{cases}
$$

$$
\begin{cases}
\delta_{1,22}^{1}(.) = -N_{\overline{D}_{1,22}(.)}(\alpha) = -\left[\left(b_{1,22}(.) + L_{1,22}^{2}(.)\right)\alpha + c_{1,22}(.) + L_{1,22}^{1}(.)\right], \\
\delta_{1,22}^{2}(.) = -\left[b_{1,22}(.) + L_{1,22}^{2}(.)\right],
\end{cases}
$$

$$
\begin{cases}
\delta_{2,22}^{1}(.) = -N_{\overline{D}_{2,22}(.)}(\alpha) = -\left[\left(b_{2,22}(.) + L_{2,22}^{2}(.)\right)\alpha + c_{2,22}(.) + L_{2,22}^{1}(.)\right], \\
\delta_{2,22}^{2}(.) = -\left[b_{2,22}(.) + L_{2,22}^{2}(.)\right],
\end{cases}
$$

$$
\begin{cases}
\delta_{1,31}^{1}(.) = -N_{\overline{D}_{1,31}(.)}(\alpha) = -\left[\left(b_{1,31}(.) + L_{1,31}^{2}(.)\right)\alpha + c_{1,31}(.) + L_{1,31}^{1}(.)\right], \\
\delta_{1,31}^{2}(.) = -\left[b_{1,31}(.) + L_{1,31}^{2}(.)\right],
\end{cases}
$$

$$
\begin{cases}
\delta_{2,31}^{1}(.) = -N_{\overline{D}_{2,31}(.)}(\alpha) = -\left[\left(b_{2,31}(.) + L_{2,31}^{2}(.)\right)\alpha + c_{2,31}(.) + L_{2,31}^{1}(.)\right], \\
\delta_{2,31}^{2}(.) = -\left[b_{2,31}(.) + L_{2,31}^{2}(.)\right],
\end{cases}
$$

$$
\begin{cases}
\delta_{1,32}^{1}(.) = -N_{\overline{D}_{1,32}(.)}(\alpha) = -\left[\left(b_{1,32}(.) + L_{1,32}^{2}(.)\right)\alpha + c_{1,32}(.) + L_{1,32}^{1}(.)\right], \\
\delta_{1,32}^{2}(.) = -\left[b_{1,32}(.) + L_{1,32}^{2}(.)\right],
\end{cases}
$$

$$
\begin{cases}
\delta_{2,32}^{1}(.) = -N_{\overline{D}_{2,32}(.)}(\alpha) = -\left[\left(b_{2,32}(.) + L_{2,32}^{2}(.)\right)\alpha + c_{2,32}(.) + L_{2,32}^{1}(.)\right], \\
\delta_{2,32}^{2}(.) = -\left[b_{2,32}(.) + L_{2,32}^{2}(.)\right].
\end{cases}
\tag{69}
$$

For the following pole placement $p_1 = -1$ and $p_2 = -2$, by Theorem 4, we obtain the following robust stabilization conditions:

(i) $\alpha = p_1 = -1 < 0$

(ii) $t_{11}^{1}(.) = t_{21}^{1}(.) = t_{31}^{1}(.) = t_{12}^{1}(.) = t_{22}^{1}(.) = t_{32}^{1}(.) = 0$

(iii) $\max\left(t_{11}^{2}(.), t_{21}^{2}(.), t_{31}^{2}(.), t_{12}^{2}(.), t_{22}^{2}(.), t_{32}^{2}(.)\right) = p_2 = -2 < 0$

Condition (iii), when we choose $t_{11}^{2}(.) = p_2$, $t_{21}^{2}(.) = -3$, $t_{12}^{2}(.) = -3.5$, $t_{22}^{2}(.) = -4$, $t_{31}^{2}(.) = -4.5$ and $t_{32}^{2}(.) = -5$ yields to following controller gains:

$$K_{11}(.) = \left[2 - \frac{\varphi_{11}(x)}{x}3 - a_{11}(.)\right],$$

$$K_{12}(.) = \left[2 - \frac{\varphi_{12}(x)}{x}3 - a_{12}(.)\right],$$

$$K_{21}(.) = \left[2 - \frac{\varphi_{21}(x)}{x}3 - a_{21}(.)\right],$$

$$K_{22}(.) = \left[2 - \frac{\varphi_{22}(x)}{x}3 - a_{22}(.)\right],$$

$$K_{31}(.) = \left[2 - \frac{\varphi_{31}(x)}{x}3 - a_{31}(.)\right],$$

$$K_{32}(.) = \left[2 - \frac{\varphi_{32}(x)}{x}3 - a_{32}(.)\right],$$

$$L_{1,11}(.) = \left[-c_{1,11}(.) - b_{1,11}(.)\right],$$

$$L_{2,11}(.) = \left[-c_{2,11}(.) - b_{2,11}(.)\right], \quad (70)$$

$$L_{1,12}(.) = \left[-c_{1,12}(.) - b_{1,12}(.)\right],$$

$$L_{2,12}(.) = \left[-c_{2,12}(.) - b_{2,12}(.)\right],$$

$$L_{1,21}(.) = \left[-c_{1,21}(.) - b_{1,21}(.)\right],$$

$$L_{2,21}(.) = \left[-c_{2,21}(.) - b_{2,21}(.)\right],$$

$$L_{1,22}(.) = \left[-c_{1,22}(.) - b_{1,22}(.)\right],$$

$$L_{2,22}(.) = \left[-c_{2,22}(.) - b_{2,22}(.)\right],$$

$$L_{1,31}(.) = \left[-c_{1,31}(.) - b_{1,31}(.)\right],$$

$$L_{2,31}(.) = \left[-c_{2,21}(.) - b_{2,31}(.)\right],$$

$$L_{1,32}(.) = \left[-c_{1,32}(.) - b_{1,32}(.)\right],$$

$$L_{2,32}(.) = \left[-c_{2,22}(.) - b_{2,32}(.)\right].$$

The simulation results for fixed initial points $\phi(t) = [2 - 1]^T$ are given in Figures 6 –8, respectively, which show the state responses, the state trajectory, and the state's norm of the system given in Example 1 where the switching mode given in Figure 9 is randomly generated.

The simulation results reveal that the state trajectories closed-loop system controlled by the memory state feedback controller are converging to zero, and the closed-loop system is robustly asymptotically stable where the switching signal is randomly generated.

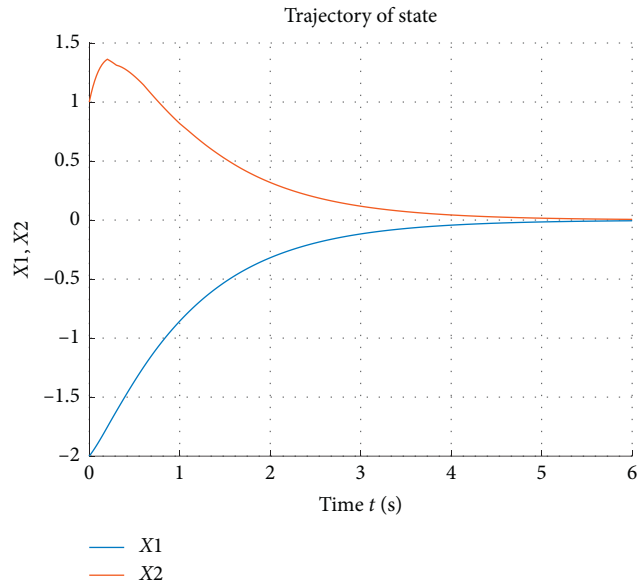

Figure 6: State responses of the closed-loop system in Example 2.

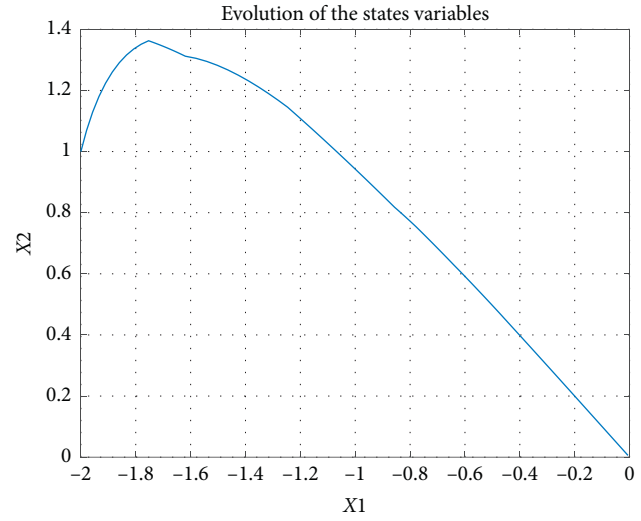

Figure 7: Evaluation of the state's variables of the closed-loop system in Example 2.

Remark 7. The developed memory state feedback controller given in Theorem 4 can reduce the effect of the delays especially for switched systems with multiple time-varying delays and it guaranteed to the considering system more performance and immunity to the delays as well as the uncertainties compared with the memoryless controller.

Remark 8. Form Theorem 4, we obtain the robust stability of a closed-loop system given in Example 2 where the switching signal is randomly generated and for any admissible uncertainties (4) and (5). In fact, the result given in Theorem 4 can be an alternative to find a CLF through the LMI approach.

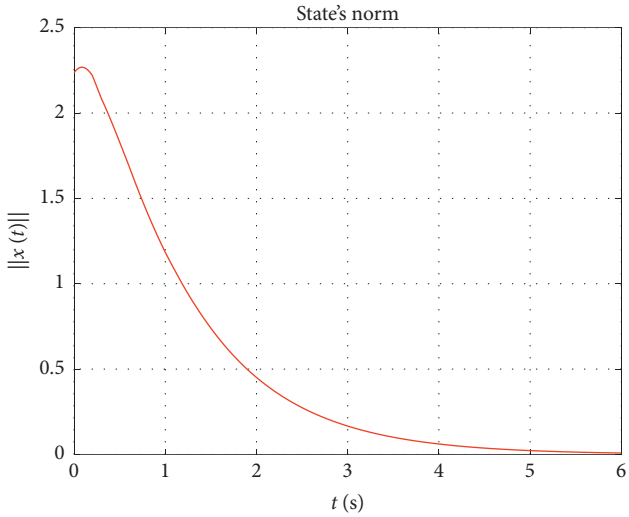

Figure 8: State's norm of the closed-loop system in Example 2.

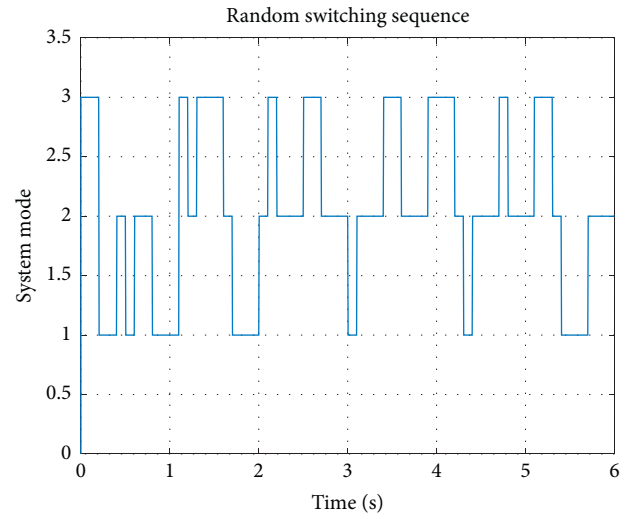

Figure 9: Random switching sequence for the system in Example 2.

6. Conclusion

This paper has investigated new robust stability and stabilization criteria under arbitrary switching for a class of uncertain switched nonlinear systems. The systems under consideration are subject to multiple time-varying delays and polytopic-type parameter uncertainty. The proposed results are obtained by using a novel CLF, the Borne–Gentina criterion, and the aggregation techniques. Compared to the existing results in this area, the developed criteria are explicit, are simple to use, and can construct an interesting alternative to find a CLF through the LMI approach, considered a hard task in this case.

Future research will extend the results of this paper to switched stochastic systems with time-varying delays and actuator saturation.

Data Availability

No data were used to support this study.

Conflicts of Interest

The authors declare no potential conflicts of interest with respect to the research, authorship, and/or publication of this article.

References

[1] D. Liberzon and A.-S. Morse, "Basic problems in stability and design of switched systems," *IEEE Trans. Control System Magazine*, vol. 19, no. 5, pp. 59–70, 1999.

[2] Z. Sun and S.-S. Ge, *Stability Theory of Switched Dynamical Systems*, Springer-Verlag London, London, UK, 2011.

[3] D. Liberzon and R. Tempo, "Common Lyapunov functions and gradient algorithms," *IEEE Transactions on Automatic Control*, vol. 49, no. 6, pp. 990–994, 2004.

[4] Y. G. Sun, L. Wang, and G. Xie, "Stability of switched systems with time-varying delays: delay-dependent common Lyapunov functional approach," in *Proceedings of the of the American Control Conference*, pp. 1544–1549, Minneapois, USA, June 2006.

[5] L. Vu and D. Liberzon, "Common Lyapunov functions for families of commuting nonlinear systems," *Systems and Control Letters*, vol. 54, no. 5, pp. 405–416, 2005.

[6] M. S. Branicky, "Multiple Lyapunov functions and other analysis tools for switched and hybrid systems," *IEEE Transactions on Automatic Control*, vol. 43, no. 4, pp. 475–482, 1998.

[7] H. Ishii and B. A. Francis, "Stabilizing a linear system by switching control with dwell time," *IEEE Transactions on Automatic Control*, vol. 47, no. 12, pp. 1962–1973, 2002.

[8] W. P. Dayawansa and C. F. Martin, "Dynamical systems which undergo switching," *IEEE Transactions on Automatic Control*, vol. 44, no. 4, pp. 751–760, 1999.

[9] D. Liberzon, *Switching in Systems and Control*, Birkhäuser Boston, Boston, USA, 2003.

[10] R. Shorten, F. Wirth, O. Mason, K. Wulff, and C. King, "Stability criteria for switched and hybrid systems," *Siam Review*, vol. 49, no. 4, pp. 545–592, 2007.

[11] P. Colaneri, J. C. Geromel, and A. Astolfi, "Stabilization of continuous-time switched nonlinear systems," *Systems & Control Letters*, vol. 57, no. 1, pp. 95–103, 2008.

[12] D. Yali, L. Jinying, M. Shengwei, and L. Mingliang, "Stabilization for switched nonlinear time-delay systems," *Nonlinear Analysis-Hybrid Systems*, vol. 5, no. 1, pp. 78–88, 2011.

[13] L. Shilong, X. Zhengrong, and C. Qingwei, "Stability and stabilization of a class of switched nonlinear systems with time-varying delay," *Applied Mathematics and Computation*, vol. 218, no. 23, pp. 11534–11546, 2012.

[14] Y.-E. Wang, X.-M. Sun, Z. Wang, and J. Zhao, "Construction of Lyapunov-Krasovskii functionals for switched nonlinear systems with input delay," *Automatica*, vol. 50, no. 4, pp. 1249–1253, 2014.

[15] S. Pezeshki, M. A. Badamchizadeh, A. R. Ghiasi, and S. Ghaemi, "Stability analysis and robust tracking control for a class of switched nonlinear systems with uncertain input delay," *Transactions of the Institute of Measurement and Control*, vol. 41, no. 7, pp. 2053–2063, 2019.

[16] W. Qi, X. Yang, X. Gao, J. Cheng, Y. Wei, and W. Yunliang, "Stability for delayed switched systems with Markov jump parameters and generally incomplete transition rates," *Applied Mathematics and Computation*, vol. 365, p. 124718, 2020.

[17] X. Liu, Q. Zhao, and S. Zhong, "Stability analysis of a class of switched nonlinear systems with delays: a trajectory-based comparison method," *Automatica*, vol. 91, pp. 36–42, 2018.

[18] H. Li and X. Wang, "Adaptive tracking control for a class of uncertain switched nonlinear systems with time-delay," *Transactions of the Institute of Measurement and Control*, vol. 40, no. 4, pp. 1102–1108, 2018.

[19] H. Xue and J. Zhang, "Robust exponential stability of switched delay interconnected systems under arbitrary switching," *Acta Mathematica Scientia*, vol. 38, no. 6, pp. 1921–1938, 2018.

[20] Y. Li, Y. Sun, and F. Meng, "New criteria for exponential stability of switched time-varying systems with delays and nonlinear disturbances," *Nonlinear Analysis: Hybrid Systems*, vol. 26, pp. 284–291, 2017.

[21] M. Kermani and A. Sakly, "A new robust pole placement stabilization for a class of time varying polytopic uncertain switched nonlinear systems under arbitrary switching," *Control Engineering and Applied Informatics*, vol. 17, no. 2, pp. 21–30, 2015.

[22] Y. Chang, Y. Wang, F. E. Alsaadi, and G. Zong, "Adaptive fuzzy output-feedback tracking control for switched stochastic pure-feedback nonlinear systems," *International Journal of Adaptive Control and Signal Processing*, vol. 33, no. 10, pp. 1567–1582, 2019.

[23] L. Ma, X. Huo, X. Zhao, and G. Zong, "Adaptive fuzzy tracking control for a class of uncertain switched nonlinear systems with multiple constraints: a small-gain approach," *International Journal of Fuzzy Systems*, vol. 21, no. 8, pp. 2609–2624, 2019.

[24] L. Ma, N. Xu, X. Huo, and X. Zhao, "Adaptive finite-time output-feedback control design for switched pure-feedback nonlinear systems with average dwell time," *Nonlinear Analysis: Hybrid Systems*, vol. 37, p. 100908, 2020.

[25] M. Kermani and A. Sakly, "On the stability analysis of switched nonlinear systems with time varying delay under arbitrary switching," *Journal of Systems Science and Complexity*, vol. 30, no. 2, pp. 329–346, 2017.

[26] Z. Le, J. Meiyu, Y. Hong, and W. Gang, "Memory state feedback control for time-varying delay switched fuzzy systems," *Advances in Fuzzy Systems*, vol. 2019, p. 14, Article ID 4787925, 2019.

[27] A. Sakly and M. Kermani, "Stability and stabilization studies for a class of switched nonlinear systems via vector norms approach," *ISA Transactions*, vol. 57, pp. 144–161, 2015.

[28] M. Kermani and A. Sakly, "Delay-independent stability criteria under arbitrary switching of a class of switched nonlinear time-delay systems," *Advances in Difference Equations*, pp. 1–20, 2015.

[29] D. Yali D, H. Jing, Y. Yonghong, and W. Huimin, "Robust stabilization of discrete-time switched periodic systems with time delays," *Complexity*, vol. 2019, p. 13, Article ID 3950848, 2019.

[30] N. Aoun, M. Kermani, and A. Sakly, "Delay-dependent stability analysis of TS fuzzy switched time-delay systems," *Mathematical Problems in Engineering*, vol. 2017, Article ID 8123830, 16 pages, 2017.

[31] N. Aoun, M. Kermani, and A. Sakly, "Simple algebraic criteria for asymptotic stability of a class of TS fuzzy time-delay switched systems," *Mathematical Problems in Engineering*, vol. 2018, Article ID 1265359, 13 pages, 2018.

[32] V. T. Minh, "Stability for switched dynamic hybrid systems," *Mathematical and Computer Modelling*, vol. 57, no. 1-2, pp. 78–83, 2013.

[33] H. Ye, B. Jiang, H. Yang, and G.-H. Zhao, "Global state-feedback control for switched nonlinear time-delay systems via dynamic gains," *Mathematical Problems in Engineering*, vol. 2020, p. 11, Article ID 7626931, 2020.

[34] A. Pratap, R. Raja, J. Cao, G. Rajchakit, and F. E. Alsaadi, "Further synchronization in finite time analysis for time-varying delayed fractional order memristive competitive neural networks with leakage delay," *Neurocomputing*, vol. 317, no. 23, pp. 110–126, 2018.

[35] P. Anbalagan, R. Ramachandran, J. Cao, G. Rajchakit, and C. P. Lim, "Global robust synchronization of fractional order complex valued neural networks with mixed time varying delays and impulses," *International Journal of Control, Automation and Systems*, vol. 17, no. 2, pp. 509–520, 2019.

[36] P. Chanthorn, G. Rajchakit, U. Humphries, P. Kaewmesri, R. Sriraman, and C. Pe-Lim, "A delay-dividing approach to robust stability of uncertain stochastic complex-valued hopfield delayed neural networks," *Symmetry*, vol. 12, no. 5, pp. 1–19, 2020.

[37] S. Mobayen and G. Pujol-Vázquez, "A robust LMI approach on nonlinear feedback stabilization of continuous state-delay systems with lipschitzian nonlinearities: rimental validation," *expe Iranian Journal of Science and Technology, Transactions of Mechanical Engineering*, vol. 43, no. 3, pp. 549–558, 2019.

[38] K. Zhao, F. Doyle, and K. Glover, *Robust and Optimal Control*, Upper Saddle River, NJ, USA, 1996.

[39] M. Jafari and S. Mobayen, "Second-order sliding set design for a class of uncertain nonlinear systems with disturbances: an LMI approach," *Mathematics and Computers in Simulation*, vol. 156, pp. 110–125, 2019.

[40] F. Robert, "Recherche d'une M-matrice parmi les minorantes d'un opérateur liéaire," *Numerische Mathematik*, vol. 9, no. 2, pp. 188–199, 1966.

[41] L. T. Grujic, J. C. Gentina, and P. Borne, "General aggregation of large-scale systems by vector Lyapunov functions and vector norms," *International Journal of Control*, vol. 24, no. 4, pp. 529–550, 1976.

[42] D. M. Kotelyanski, "Some properties of matrices with positive elements," *Matematicheskii Sbornik*, vol. 31, pp. 497–505, 1952.

[43] D. A. Altshuller, "A partial solution of the Aizerman problem for second-order systems with delays," *IEEE Trans. Automatic Control*, vol. 53, no. 9, pp. 2058–2060, 2008.

Hindawi
Mathematical Problems in Engineering
Volume 2021, Article ID 6647273, 13 pages
https://doi.org/10.1155/2021/6647273

Research Article

Congestion Prediction Based on Dissipative Structure Theory: A Case Study of Chengdu, China

Xiaoke Sun,[1] **Hong Chen**,[1] **Yahao Wen**,[2] **Zhizhen Liu**,[1] **and Hengrui Chen**[1]

[1]*College of Transportation Engineering, Chang'an University, Xi'an, China*
[2]*Guangdong Communication Planning & Design Institute Co., Ltd., Guangzhou, China*

Correspondence should be addressed to Hong Chen; hongchen8233@163.com

Received 3 December 2020; Revised 29 December 2020; Accepted 5 January 2021; Published 19 January 2021

Academic Editor: Víctor Estrada-Manzo

With the continuous growth of traffic demand and the mismatch of urban transportation facilities, urban traffic congestion has been caused, leading to various related problems, such as environmental pollution, traffic accidents, and slow economic development. Many cities have implemented relevant measures to improve traffic congestion, but fewer are ideal. This study used the hidden Markov model combined with the dissipative structure theory and entropy theory to predict the congestion more accurately. The temporal and spatial distributions of the online ride-hailing Didi data in Chengdu were analyzed. There are morning peaks, noon peaks, and evening peaks during workdays. During the noon peak and evening peak, travel demand in the city's central area is relatively stable. It is found that the prediction model has a higher accuracy after combining the dissipative structure theory and entropy theory, which could be used to propose methods to prevent congestion.

1. Introduction

Due to the rapid increase in urban expansion, traffic demand has also increased rapidly in recent years. Under such circumstances, traffic congestion has become a common problem in large cities, resulting in increased pollution emissions, traffic time, and casualties and slowing down the economy [1]. Traffic congestion is caused by various factors, such as the backwardness of transportation infrastructure, public transportation inability to meet general travel needs, and improper traffic control. Accurate traffic jam prediction can improve travelers' satisfaction with traffic services and reduce related travel costs. There have been many methods used to predict traffic congestion in the current research process, including qualitative research, quantitative prediction, and various statistical techniques. However, most of the methods previously studied by scholars are still based on traditional transportation research methods. In the spatio-temporal analysis, some scholars used GPS data to compare the temporal and spatial patterns of taxi travel in Shanghai and New York City and established a regression model to study the relationship between urban land use, a permanent population, employment, and car ownership [2]. There are also studies using geographically weighted regression to model the spatial heterogeneity of taxi passenger capacity and visualize parameter estimates' spatial distribution [3]. A visual analysis system of urban functions based on time-space taxi travel is proposed [4]. Some scholars have researched the interactive relationship between the taxi travel trajectory network's topological structure and the spatial differentiation, revealing the spatial characteristics and movement laws of urban residents' activities and interaction between the spatial layout of urban functions and residents' activities. Provide a reference for optimizing the taxi transportation network and taxi operation management [5].

In terms of travel patterns, some scholars have studied how the travel pattern variables extracted from large-scale taxi GPS data can lead to the collapse of spatial agglomeration in urban areas and proposed a data-driven modelling method based on potential Dirichlet allocation of 50 travel modes [6]. Using the massive dataset of Didi Travel, including Didi Express and Didi Taxi services, some scholars analyzed the fluctuations in the number of orders in different urban areas after implementing travel restrictions in Shanghai in 2016 [7]. Some scholars analyzed Beijing taxis' GPS trajectory data and found that taxi travel

patterns have similar characteristics to individual travel patterns [8]. Massive car-hailing data have become a popular source for analyzing traffic operation and road congestion status [9]. Some studies have used clustering methods to detect different passenger distribution patterns in subways and taxis, examine the difference between passenger distribution patterns and cluster spatial distribution, and perform a two-step classification analysis to determine the factors affecting passenger patterns [10]. Some scholars have proposed a new model based on the hidden Markov model and contrast to define the traffic state during peak time in two-dimensional space. This model uses average speed and contrast to capture traffic patterns [11]. Other studies have proposed an expert system that detects traffic jams and accidents from real-time GPS data collected by GPS trackers or driver's smartphones. The system will assign a traffic state to each section of the map according to the vehicle [12].

In terms of research methods, some scholars decompose the datasets of subway station entry and exit, weekdays, and weekends to obtain principal components and feature vectors [13]. Some studies have proposed a three-stage framework to explore the congestion correlation between road segments from multiple real-world data and found that the traffic congestion correlation has obvious directionality and transmission [14]. Some scholars have proposed a new method based on the entropy maximization theory, which uses the large-scale taxi GPS trajectory to model the OD distribution of Harbin city to verify the OD distribution of the taxi GPS data in the urban system [15].

In terms of congestion prediction, some scholars have proposed a method to detect traffic congestion from the taxi's GPS trajectory at the turning level. Based on the analysis of GPS trajectory characteristics and identification of active trajectory segments, three congestion trajectories of different intensities are detected [16]. Some scholars have proposed a probabilistic model for predicting driving journey paths based on hidden Markov models. The prediction results show that this method is an accurate and feasible potential method [17]. Some scholars have proposed mining mixed temporal association rules to predict traffic congestion, apply the Dbscan algorithm to find the traffic environment, and generate qualified rules for predicting road network traffic congestion [18].

Nowadays, there is a new direction for studying traffic congestion. With the advent of the "big data" era, modern technology combined with traditional traffic management methods to effectively and timely obtain traffic demand information and identify road traffic conditions is an important idea to alleviate traffic congestion. With the rapid development of the mobile Internet, online car-hailing travels have been rapidly developed. It is also one of the supplementary travel modes of urban public transportation. A large amount of GPS data is generated in the daily operation process, attracting many scholars to develop big traffic data: analysis, mining, and application research. The famous physicist Prigogine introduced open systems to the second law of thermodynamics in 1969 and developed it to establish the dissipative structure theory. Dissipative structure theory explains how an open system changes from disorder to order, an extension of entropy theory. At present, dissipative structure theory has significantly impacted many fields of natural sciences and social sciences, such as physics, astronomy, biology, economics, and philosophy [19]. However, research of dissipative structure theory on the diffusion of pollutants is rarely studied.

This research uses dissipative structure and entropy theory, combined with the hidden Markov model, based on previous studies. Based on analyzing the temporal and spatial distribution of Chengdu, it predicts congestion in a part of Chengdu's downtown area. It carries out verification, and the result shows that the prediction result is much better.

The rest of this article is organized as follows: after the Introduction, Section 2 introduces materials and methods, including data and the theory; Section 3 presents result analysis and discussion; Section 4 presents conclusion.

2. Materials and Methods

2.1. Data

2.1.1. Didi GPS Track Data. The data source used in this article is the Didi Gaia Data Open Platform, the data location is Chengdu City, the data time is November 2016, a total of 30 days, and the data scope is the trajectory data of the second ring road in Chengdu, so the research scope is divided. It is designated as the five central districts of Chengdu: Jinniu District, Chenghua District, Jinjiang District, Wuhou District, and Qingyang District. The data are stored in CSV file format and divided into GPS track data and travel OD data (recording the OD point information of each track data). The average order data from Sunday to Thursday is about 220,000 pieces a day and from Friday to Saturday is about 250,000 pieces a day. GPS track data record the operating status of each vehicle and records, and the interval is 3 s. The amount of data per day is about 3 GB, and the amount of track point data generated in one day is about 36 million. The formats of GPS track data and order data in the original data are shown in Table 1.

2.1.2. Road Network Data and POI Data. The road network data used are downloaded from the BIGEMAP mapper. The road network includes highways and urban roads (express roads, main roads, secondary roads, and branch roads). The coordinate system used WGS84 coordinates.

The POI data source is from BIGEMAP mapper, and the coordinate system adopted WGS84 coordinates. POI data include hotels, restaurants, roads, real estate communities, companies, enterprises, shopping, transportation facilities, finance, tourist attractions, car services, commercial buildings, life services, leisure and entertainment, medical care, and government agencies. POI data information includes longitude, latitude, address, and name.

2.2. Principal Component Analysis. Generally, in the study of multivariate research, we tend to use as few variables as possible to get more information. When the number of variables increases, the computational complexity will

Table 1: GPS track and order data structure description.

Attribute name	Example	Attribute description
CAR_ID	0531a086baf4ffa55f648202bd6fea25	Vehicle number
ORDER_ID	072a331f7399614626d2f73698c495b1	Track number
TIME	1478482828	GPS timestamp
O_TIME	1478482826	Boarding time
D_TIME	1478483238	Get-off time
O_LONGITUDE	104.1251	Longitude of boarding position
O_LATITUDE	30.67288	Latitude of boarding position
D_LONGITUDE	104.11075	Longitude of drop-off position
D_LATITUDE	30.65962	Latitude of drop-off position

increase geometrically. Similarly, in studying road traffic status, it is unnecessary to use all variables to analyze the traffic status. At the same time, it is impossible to check all variables. Therefore, it is essential to filter the variables. Thus, the principal component of the statistical method is used. Analysis can reduce the dimensionality of the data and transform a group of potentially correlated variables into linearly uncorrelated variables through orthogonal transformation. The changed group of variables is called the principal component. It can be used to analyze the variables to determine the more significant variables on traffic status and traffic congestion prediction, a standard method for dimensionality reduction. Typical steps for dimensionality reduction include the following: (1) standardize raw data; (2) calculate the covariance matrix and its eigenvalues and eigenvectors; (3) sort eigenvalues; and (4) keep the eigenvectors corresponding to the first N eigenvalues and construct them into the new space.

2.3. Hidden Markov Model. Hidden Markov model (HMM) is a dynamic Bayesian network with a simple structure, a directed graph model. In this system, the state of the system at the next moment is determined only by the current state and does not depend on any previous state. It is a directed graph model, which is widely used in many fields. As shown in Figure 1, there are two types of variables in the hidden Markov model: hidden variables (Y_1, Y_2, Y_3, . . ., Y_n) and observed variables (X_1, X_2, X_3, . . ., X_n). Y_n and X_n represent the system status and observations of the nth time.

2.4. Entropy Theory and Dissipative Structure Theory. Entropy was used to describe the second law of thermodynamics. As a state parameter, entropy represents the uniformity of any kind of energy distribution in space.

$$S = K * lnN. \quad (1)$$

The entropy S of the material system is equal to the Bosch coefficient K product and the number N of states' logarithm. The entropy value of the system directly reflects the degree of uniformity of the state. The smaller the entropy value of the system is, the more orderly and unevenly the state is. The more significant the system's entropy value is, the more disordered and uniform it is. The system always tries to spontaneously change from a state with a small entropy value to a state with a significant entropy value (from order to disorder).

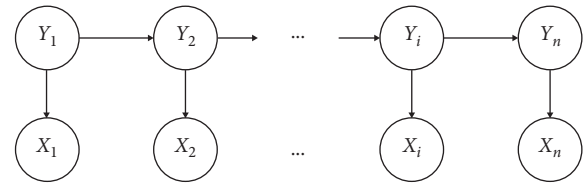

Figure 1: Structure of the hidden Markov model.

The entropy principle mainly studies the ideal isolated system, while the dissipative structure theory extends the system to open systems. The generalized dissipative structure can refer to a series of open systems far from equilibrium, physical, chemical, socioeconomic, and biological systems, which focuses on explaining how the open system moves from disorder to order [20].

3. Result Analysis and Discussion

3.1. Spatial and Temporal Distribution of Congestion in Chengdu

3.1.1. Time Distribution Characteristics. By counting the daily travel frequency within a month, as shown in Figure 2, it can be seen that the daily travel frequency is approximately a one-week cycle, with the highest travel frequency on Friday and Saturday. After the workweek, on Friday afternoon and Saturday, the frequency of people going out for entertainment and leisure will increase.

To understand the travel frequency at different times of the day, take an hour as a unit to count the frequency of pickup and drop-off points at various times during working days and nonworking days, as shown in Figures 3 and 4.

As can be seen from the distribution diagram of the time of getting on and off the bus, there is a morning peak (8 : 00–10 : 00), noon peak (12 : 00–14 : 00), and evening peak (17 : 00–19 : 00) during work, while on rest days, there are only noon peaks and evening peaks. On Friday, the morning, afternoon, and evening peaks are similar to Monday to Thursday. Still, in the evening peak until midnight, the number of trips on Friday is higher than that on Monday to Thursday. There are some similarities and differences in travel time's frequency distribution on Saturdays and Sundays on weekends. The difference is manifested in the apparent peak periods at noon (13 : 00–14 : 00) and evening

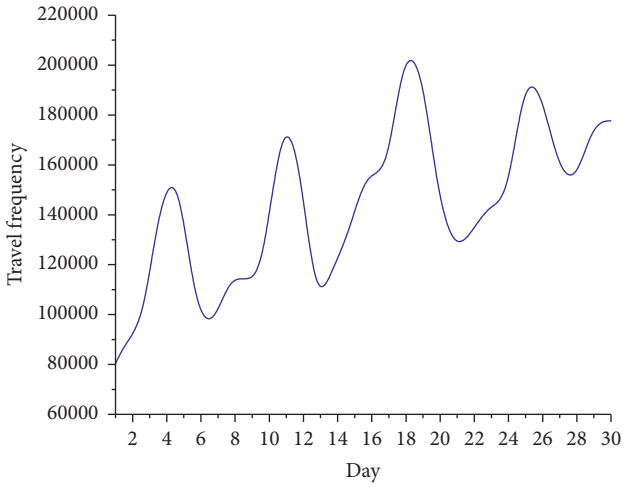

Figure 2: Travel frequency in November.

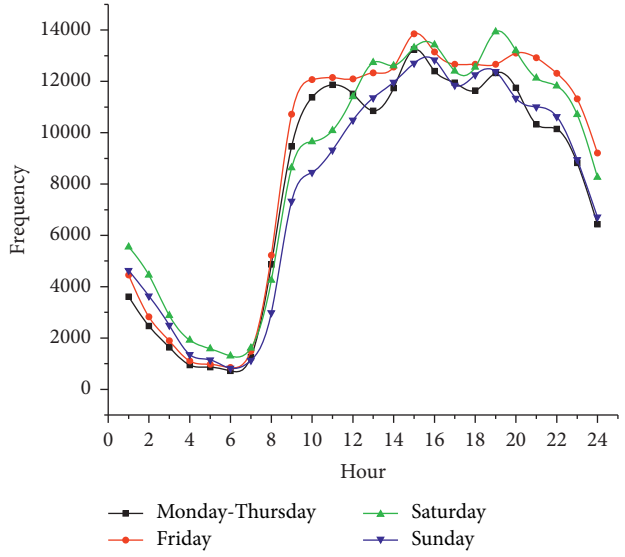

Figure 3: Distribution of boarding time.

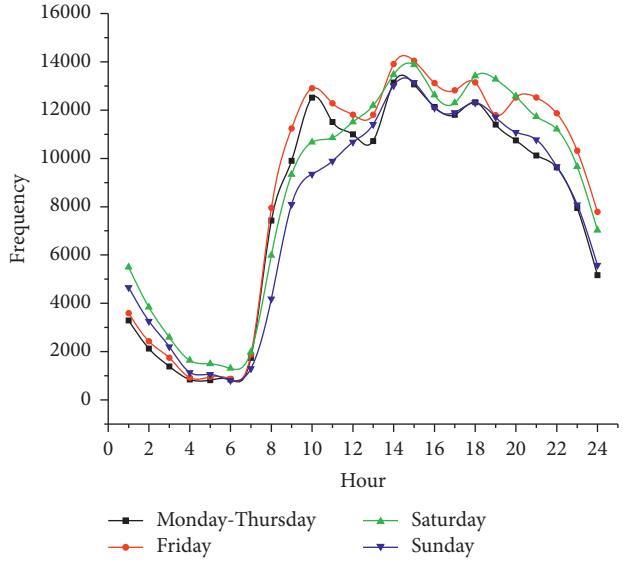

Figure 4: Distribution of drop-off time.

(17 : 00–18 : 00). Besides, since the next day is a working day, people are more inclined to end the day's itinerary earlier on Sunday evening. The overall travel frequency during the evening rush hour on Sunday is less than that on Saturday.

3.1.2. Spatial Distribution Characteristics Based on the Kernel Density Algorithm. The grid surface is generated based on the kernel density algorithm to establish the hot spot detection model. The parameter selection of the kernel density algorithm affects the clustering effect and effectiveness of the model. The larger the research scale and the larger the bandwidth, the smoother the result presented by the heat map; the smaller the research scale and the smaller the bandwidth, the more detailed the heat map's effect in Table 2. Using multiple parameter selection and comparative analysis, selecting different parameters to produce clustering effect and hot spot detection, the hot spot area's location can be preliminarily judged. Select the date of November 11 (Friday) as the representative days, visualize the data, analyze the trajectory data's spatial characteristics, and display it in a heat map. The heat map in different parameter combinations is shown in Figure 5.

It can be known from the heat map that the demand for travel in the central area of the city is relatively stable. As the city center's various supporting facilities are relatively complete, the population is much more. Hotels, restaurants, commercial buildings, shopping centers, residential areas, and other buildings are densely distributed. These places can generate a lot of transportation demand.

3.2. Analysis of Didi GPS Data Features. Due to Didi's ride-hailing rules, some data need to be cleared. In collecting trajectory data, the sampling interval is 3 s, and the sampling frequency is relatively high. More redundant data are generated, which take up massive storage space and higher computer performance requirements, which significantly increases the processing runtime of the calculation. Therefore, it is necessary to compress the taxi trajectory data [21].

Calculate the length of the trajectory according to the compressed trajectory. Under the premise of ensuring accuracy, the travel distance statistics of 140,000 passenger trajectories extracted are made. The travel distance (a) and time (b) distribution are shown in Figure 6. The travel distance is mostly concentrated within 3–10 km, and this travel distance segment accounts for about 75% of the total travel ratio. The travel time is mainly focused on 6–26 minutes, accounting for about 75% of the total travel ratio.

After the invalid trajectory data are further eliminated and filtered, the travel speed diagram in the main urban area within one day by time intervals is obtained, as shown in Figure 7.

It can be seen from Figure 7 that, by calculating the average speed of the vehicles in each period, it can be found that the speed of the vehicles is slower in the morning peak and evening peak on working days. At night, the speed of the vehicle is faster.

Based on calculating the average travel speed of the entire road network by period, a single trajectory's speed is calculated. The speed characteristics of the trajectory are further feature mined and analyzed based on different road sections. For a single trajectory, calculate the travel speed according to different sampling frequencies, and calculate the speed of different road sections in one travel. Take a trajectory on November 7 as an example, combined with the trajectory data points matched on the map, as shown in Figure 8. Vehicles drive from Fenglin Road near Zhongfang Hongfengling and then pass through Shengdeng Road, Jianshe South Road, Hongguang Road, Xinhong North Branch Road, and Xiaolongqiao Road to reach the destination. Figure 9 shows the travel speed graph with sampling intervals of 3 s, 6 s, 15 s, and 30 s. When the sampling interval is 3 s, and the sampling frequency is dense, the speed-time image obtained can be regarded as an instantaneous speed graph. It can be seen that the rapid speed fluctuates wildly. It cannot reflect the road operation well. When the sampling interval is 15 s or 30 s, the effect of the displayed map is better.

After map matching, combining the road segment trajectory map, divide the trajectory into seven road segments, as shown in Figure 8, and calculate the seven road segments' travel speed, respectively.

After adjusting and improving the instantaneous speed map, the road section speed map divided by road section is obtained, as shown in Figure 10. It can be seen from Figure 10 that the vehicle speed is low at the beginning of the start, and the vehicle is driving on road sections 5 and 6 with faster speed, and the overall driving speed is relatively smooth and unobstructed.

3.3. Analysis of Influencing Factors of Congestion in Chengdu

3.3.1. Extraction of Factors Affecting Traffic State. In the BIGEMAP map downloader, the downloaded POI data have the following 15 categories. The POI categories are readjusted and divided into six categories, namely, commercial, residential, office, transportation, leisure class, and life class. The classification situation and the proportion of each type are shown in Figure 11.

Due to the dense flow of people and the high demand for online car-hailing in the city's central area, various regions have different degrees of influence on the pickup point. It is of considerable significance to analyze the possible impact of different POI types on the road state. Calculate the distance between the pickup point and the different POI types nearby, find the connection between the pickup point and the POI type, and further determine the impact on the road traffic state and traffic congestion the follow-up work [22].

Based on the principal component analysis method, this paper calculates the distance from the OD points of the trajectory data to various POI points. The Euclidean distance from each OD point to different POI points is calculated to facilitate statistics and classification.

After categorizing the POI data, combine the trajectory data's spatial characteristics and the distance from the OD point

Table 2: Influence of different parameters on the clustering effect.

Group	Order	Bandwidth (unit: m)	Pixel size	Number of hotspots (unit: number)
1	1	108.8	10	2104
2	2	317.0	10	623

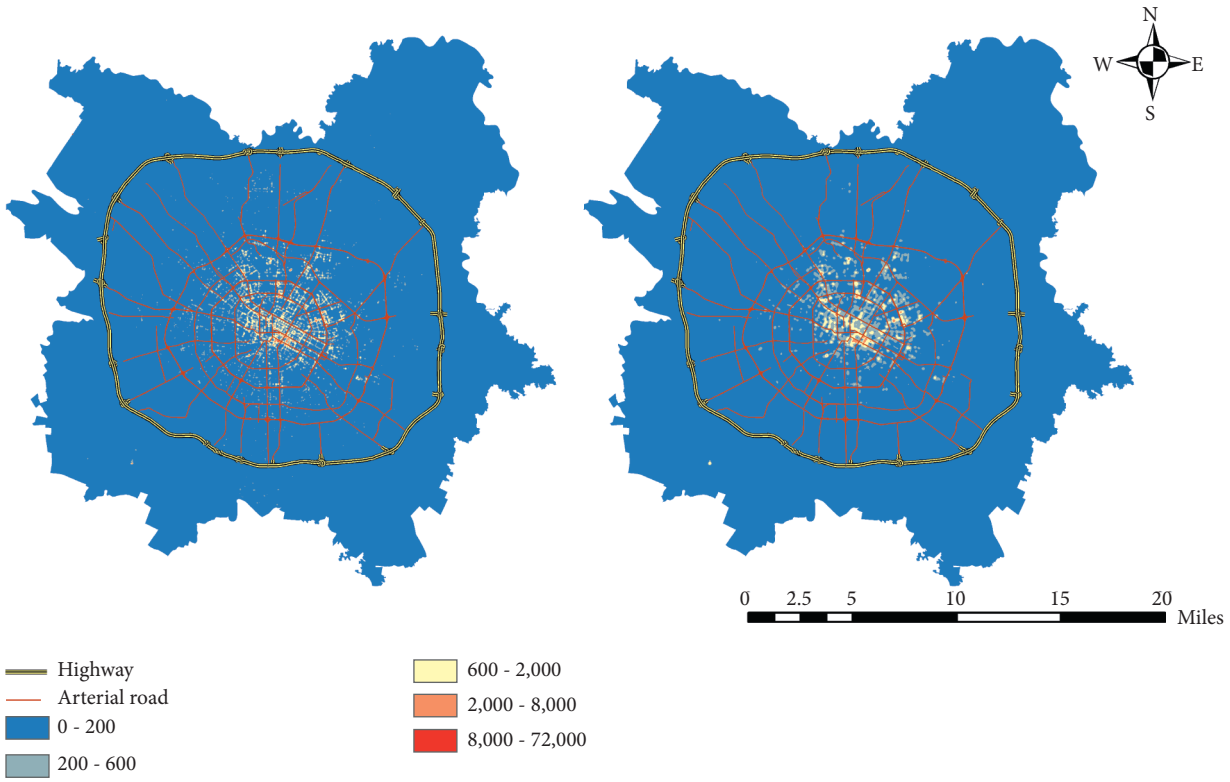

Figure 5: Heat diagram in different parameter combinations.

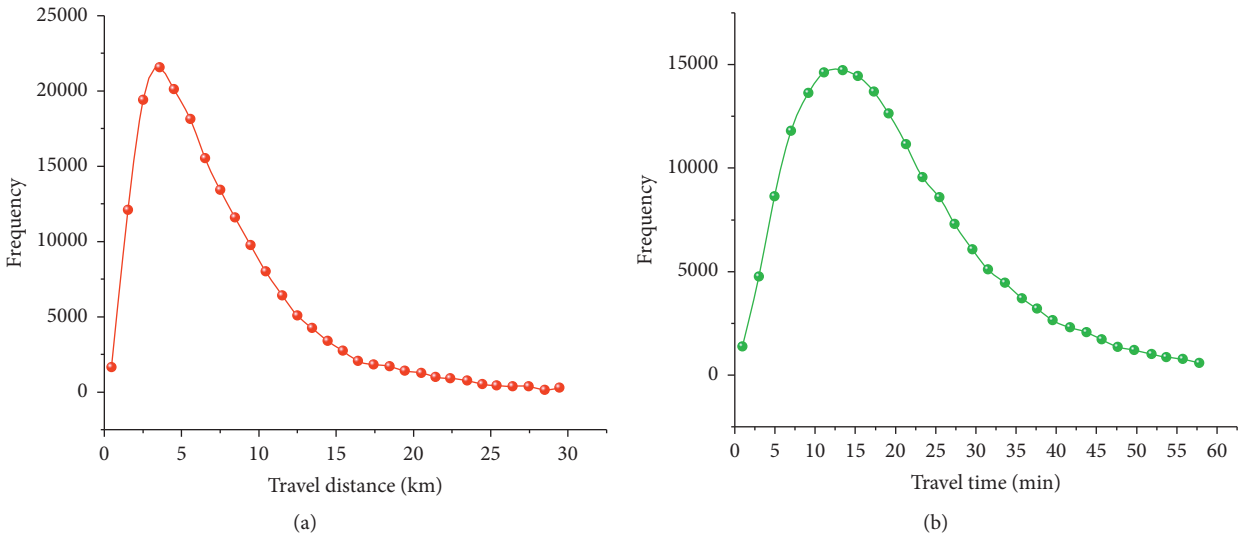

Figure 6: Distance (a) and time (b) distribution.

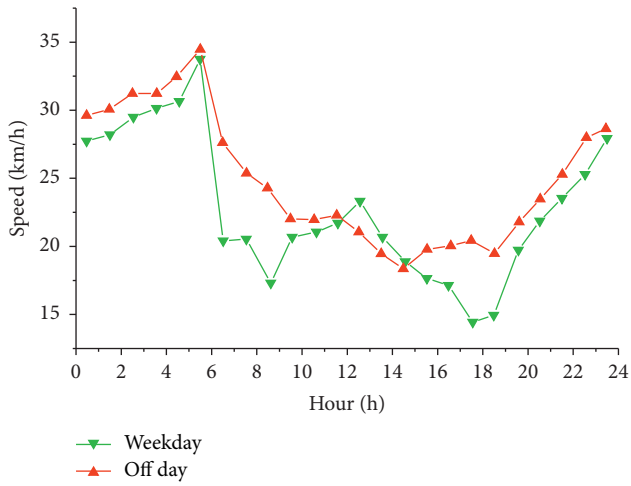

Figure 7: Daily hourly average speed.

Figure 8: Divide the trajectory map based on road sections.

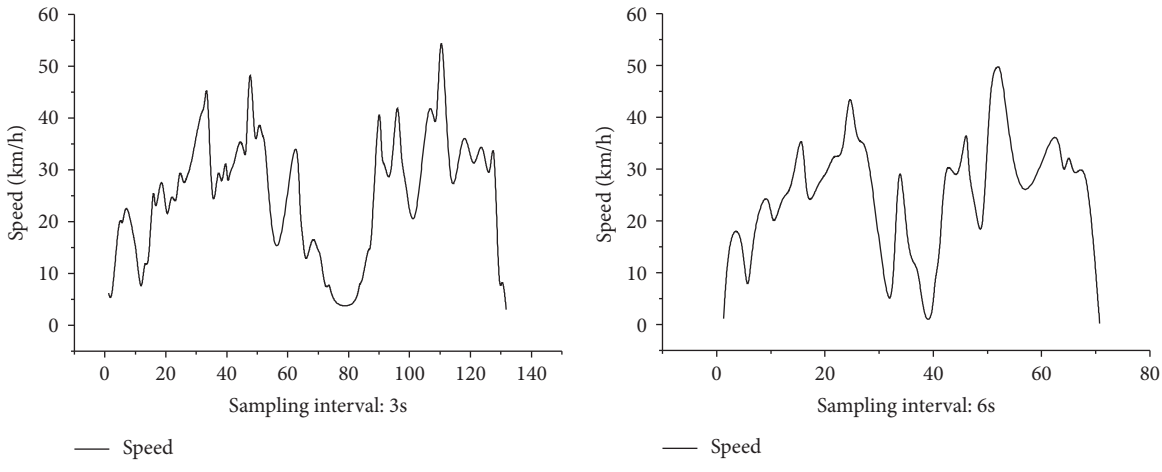

(a) (b)

Figure 9: Continued.

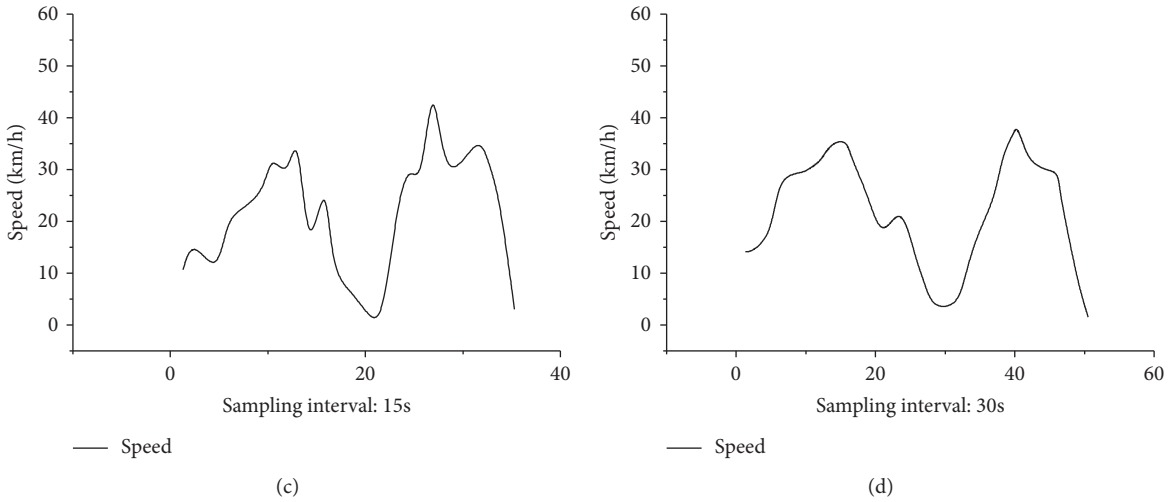

Figure 9: Speed time of different time intervals.

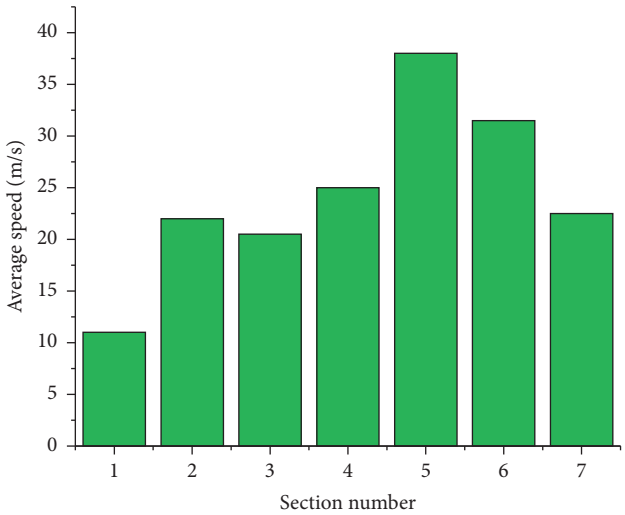

Figure 10: Travel speed based on road segment division.

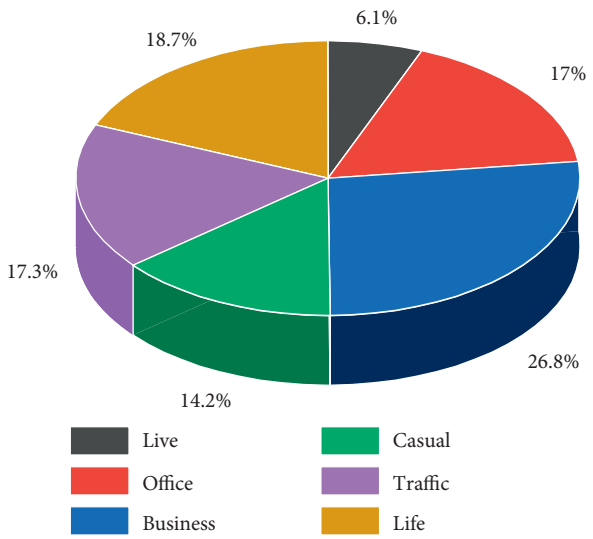

Figure 11: Percentage of POI classification.

of the order data to various POIs, perform a correlation test, and express it in a matrix.

From Table 3, the commercial and residential categories have a more significant impact on the frequency of getting on and off the bus.

In the city's central area, travel demand is relatively strong near commercial buildings, shopping centers, and large residential areas. The distance between OD points and the commercial regions and residences is closer than other types. The relationship between OD points and commercial and residential areas is relatively close, so that it can be considered an influencing factor.

3.3.2. Construction of an Influencing Factor Set. This paper selects the area around the east section of the second ring road in Chengdu as the research area and divides the road sections and time periods. There are 4 road types in the divided road sections, and the time period and the road sections are both the influencing factors. The average travel time and the average speed of the road section are the main manifestations of whether the road is congested, and the road traffic state is the direct manifestation of whether the road is congested. Therefore, both are used as influencing factors. This paper uses principal component analysis to extract the types of POI that have a greater impact on the boarding point: the distance from the boarding point to the subway station, commercial area, and residential area, which are used as an influencing factor. The set of influencing factors selected in this paper is moderate. Too few would lead to unsatisfactory prediction results, and too many would easily lead to "overfitting," and the error of the model will increase. Therefore, the influencing factors F1–F8 are finally determined.

The types and descriptions of each factor are as follows:

F1: type of road.

The type of road has a significant influence on the vehicle's speed and determines the upper limit of Table 4.

The speed is influencing the road traffic conditions and congestion. The corresponding relationship of road types is shown in Table 4. The road segments are classified and numbered according to the relationship table, which is represented by S_{aa}.

F2: average travel time of the road section (s).

The road segment's average travel time is obtained according to the order data and is counted in seconds.

F3: average travel speed of the road section (km/h).

Based on the road segment division and speed calculation in front of the article.

F4: period.

According to the trajectory data's temporal and spatial distribution characteristics, boarding at different times in a day is counted. On weekdays, the frequency of boarding at 8–10 am is relatively high. Simultaneously, considering the regularity of commuting passenger flow, this period is selected as the counter, divided into shorter periods. Choose 10 minutes as the time segment, divided into 12 time segments, respectively, represented by 1–12 ($a-l$).

F5: road traffic status.

According to the road section, it is divided into five statuses, which are unblocked, basically unblocked, slightly congested, moderately congested, and severely congested, represented by 1–5.

F6: the distance to the subway station (m).

The subway can efficiently carry many passengers, which affects the travel mode of nearby shuttle vehicles and nearby people. The Euclidean distance is used here by calculating the distance from the boarding point to the nearest subway station.

The distance of F6–F8 is obtained through the distance calculation tool in the ArcGIS software. The distance is divided into three categories: 0–500 m, 500–1000 m, and distances higher than 1000 m, represented by 1, 2, and 3, respectively.

F7: distance to the business district (m).

By calculating the distance from the pickup point to the nearest commercial area, the commercial area's judgment is obtained by dividing POI data. The Euclidean distance is used here.

F8: distance to a residential area (m).

By calculating the Euclidean distance from the pickup point to the nearest residential area, the residential area's determination is obtained through the POI data division. The Euclidean distance is used for calculation.

By dividing the influencing factor set, the final main parameter table is shown in Table 5.

3.4. Congestion Prediction Based on the Dissipative Structure

3.4.1. Dissipative Structure Condition. According to the dissipative structure theory established by Prigokin, the following four necessary conditions must be met to produce a dissipative structure.

The system must be open. The system must exchange material, energy, and information with the outside world and obtain negative entropy from the outside world to offset the increase in its extraction. The system can evolve from disorder to order and from simple to complex.

The system is far from equilibrium. The open system under the combined action of internal and external factors may destroy the original structure and form a new orderly structure when it is far from the equilibrium state.

Nonlinear interaction: there is a nonlinear mechanism in the interaction between the subsystems that make up the system, prompting the emergence of new properties in the system, leading to the system's complexity and diversity. When a linear system changes, it is often carried out gradually; when a nonlinear system changes, there are often qualitative transformations and jumps. When affected by the outside world, a linear system will respond progressively, while a nonlinear

Table 3: Correlation analysis based on POI data classification.

	Live	Office	Business	Casual	Traffic	Life
Live	10.000	−0.011	**0.682**	0.565	0.535	−0.373
Office	−0.011	10.000	0.366	0.377	0.302	0.388
Business	**0.682**	0.366	10.000	0.597	0.355	−0.112
Casual	0.565	0.377	0.597	10.000	0.212	−0.421
Traffic	0.535	0.302	0.355	0.212	10.000	−0.092
Life	−0.373	0.388	−0.112	−0.421	−0.092	10.000

Table 4: Type of road and numbers.

Type of road	Number
Urban expressway	1
Urban arterial road	2
Urban secondary road	3
Branch road	4

Table 5: Parameter.

Variable	Abbreviated representation	Min	Average	Max
Road type	R_t	—	—	—
Average travel time (s)	T_{ij}	—	—	—
Average travel speed (km/h)	V_{ij}	—	—	70
Period	T_n	—	—	—
Traffic status	S_{sta}	—	—	—
Distance to the subway station (m)	D_{me}	8.46	746.9	2875.41
Distance to the commercial area (m)	D_{com}	14.57	1379.06	5383
Distance to a residential area (m)	D_{res}	7.42	456.78	1348.95

system is very complicated. Sometimes it ignores external signals, and sometimes it reacts fiercely. A linear system changes continuously and changes state over time, while a nonlinear system can maintain its stability for a long time.

There are huge random fluctuations. For a nonequilibrium system far from the equilibrium state, the small random changes may rapidly amplify and form huge volatility, making the system transition from an unstable state to a new ordered state, thus creating a dissipative structure [20].

Chengdu has met the four necessary conditions for a dissipative structure.

Chengdu is an open system. Chengdu's road traffic system is an open system that can carry vehicles both inside and outside Chengdu.

The road traffic system of Chengdu is far from equilibrium. Traffic flow is the leading cause of traffic congestion. Moreover, traffic flow is always in an unbalanced stage, affected by many factors, such as weather, holidays, and traffic control.

The road traffic system of Chengdu is in a nonlinear interaction. As mentioned above, many factors affect traffic flow, and congestion forecasting is a very complicated process, which cannot be forecasted solely by linear models.

There are substantial random fluctuations in the road traffic system of Chengdu. Since Chengdu is a tourist-oriented city, a large amount of traffic will be generated during holidays. Due to the impact of other uncontrollable factors such as traffic accidents, the traffic system will have substantial random fluctuations in traffic volume.

In Chengdu's road system, a specific type of state in the congestion state can be used as a critical point 3: slightly congested), a certain threshold reached when the system leaves the equilibrium state. When the threshold is reached, self-organization can be used to relieve the congestion state. As a part of the road system, human intervention belongs to the road system's self-organization phenomenon. Social self-organization will transform the system from a disordered state to an orderly state.

3.4.2. Entropy Analysis. According to the dissipative structure theory and entropy theory, the influencing factors are divided into the primary deterministic entropy value and the uncertainty entropy value, affecting the total entropy value of the road traffic system. The deterministic entropy value consists of the influence of road type, period, distance to the subway station, distance to commercial area, and distance to the residential area on the degree of congestion. The uncertainty entropy value is composed of the road section's average travel time, the average travel speed of the road section, and the road traffic conditions on the degree of congestion. Among them, the deterministic entropy value is fixed. This study will discuss the surrounding facilities when the surrounding facilities are relatively stable, without considering the impact of environmental factors and construction facilities changes.

$$S_d = -\sum_{i}^{d} K_i P_i ln P_i, \tag{2}$$

$$S_n = -\sum_{i}^{n} K_i P_i ln P_i, \tag{3}$$

$$S_c = S_d + S_n, \tag{4}$$

where S_d is the deterministic entropy value and d represents the type of deterministic entropy factors. S_n is the uncertainty entropy value and n represents the type of uncertainty entropy factors. S_c is the total entropy. The congestion state changes as the total entropy value changes. When the total entropy value reaches a specific amount, when the system leaves the equilibrium state to reach a certain threshold (3: slightly congested), the system changes simultaneously, from state 1 or 2 changes to 3 or other states. At this time, human intervention is required for traffic, which is the phenomenon of systematic self-organization.

3.4.3. Congestion Prediction. This paper used Python language scipy, scikit-learn, hmmlearn, and other libraries, combined with the dissipative structure theory and the hidden Markov model for prediction.

We display the traffic congestion information of a trajectory in a congestion matrix. Each row represents various information of a road section. The first column to the eighth column represents F1–F8, representing the entropy's influencing factors and its initial observation matrix. The representation is as follows:

$$X_{ij} = \begin{bmatrix} 4 & 42 & 11 & 10 & 4 & 813 & 623 & 21 \\ 3 & 27 & 22 & 10 & 1 & 997 & 764 & 53 \\ 2 & 183 & 21 & 10 & 3 & 1123 & 536 & 163 \\ 2 & 51 & 25 & 10 & 2 & 1387 & 123 & 178 \\ 4 & 36 & 38 & 10 & 1 & 1523 & 96 & 231 \\ 4 & 18 & 32 & 10 & 1 & 1459 & 321 & 93 \\ 3 & 42 & 22 & 10 & 2 & 1203 & 413 & 46 \end{bmatrix}. \quad (5)$$

Use linear changes to standardize the matrix to obtain a standardized matrix of screening indicators:

$$X_{ij} = \begin{bmatrix} 1.000 & 0.230 & 0.289 & 1.000 & 1.000 & 0.534 & 0.815 & 0.091 \\ 0.750 & 0.148 & 0.579 & 1.000 & 0.250 & 0.656 & 1.000 & 0.229 \\ 0.500 & 1.000 & 0.553 & 1.000 & 0.750 & 0.737 & 0.702 & 0.706 \\ 0.500 & 0.279 & 0.658 & 1.000 & 0.500 & 0.911 & 0.161 & 0.771 \\ 1.000 & 0.197 & 1.000 & 1.000 & 0.250 & 1.000 & 0.126 & 1.000 \\ 1.000 & 0.098 & 0.842 & 1.000 & 0.250 & 0.958 & 0.420 & 0.402 \\ 0.750 & 0.230 & 0.579 & 1.000 & 0.500 & 0.790 & 0.541 & 0.199 \end{bmatrix}. \quad (6)$$

Similarly, use Python language programming for batch processing and summarize all trajectories' observation matrix to obtain the initial observation matrix X_{ij}:

$$X_{ij} = \begin{bmatrix} x_{ij} & \cdots & x_{mj} \\ \vdots & \ddots & \vdots \\ x_{in} & \cdots & x_{mn} \end{bmatrix}. \quad (7)$$

$P(S_t|S_{t-1})$ is the current state transition probability, that is, the transition between the five traffic states of the road section; the steps to calculate the state transition matrix are as follows:

(a) Group the original data

(b) According to the previous period division, suppose the time series is $S = \{S_a, S_b, \ldots, S_l\}$

There are N observations, divided into five states, expressed as $C = \{C_1, C_2, C_3, C_4, C_5\}$.

After dividing the data in the training set based on different periods and road sections, a matrix of periods and road section sets is obtained. Each row represents the road congestion state of a road section in a different period. The state transition matrix form is as follows:

$$A_S = \begin{bmatrix} S_{11a} & \cdots & S_{11l} \\ \vdots & \ddots & \vdots \\ S_{85a} & \cdots & S_{85l} \end{bmatrix}. \quad (8)$$

Among them, a, b, c, ..., l are represented as 12 time periods, and 11–85 are designated as the division numbers of road sections.

3.4.4. Model Check. After the model training is over, output the fitted model, and compare it with the test value data (November 24th–November 30th).

Figure 12 shows the prediction results from 9 : 30 to 9 : 40. The second section of the East Section of the First Ring Road, Jianshe South Road, Xinhong Road, and the East Section of the Erxian Bridge of the Middle Ring Road are slightly congested. Some sections of the road are moderately congested, and the remaining routes are unblocked or basically unblocked. From 9 : 30 to 9 : 40, except for Xinhong Road and the second section of the East Section of the First Ring Road, which is slightly different from the predicted value, the remaining road sections' actual congestion index is the same as the predicted value.

The congestion state 3 (light congestion) is set as the congestion threshold, the congestion is greater than or equal to 4, and the acceptable state is 1–3. When the predicted value reaches 3, the congestion threshold is reached, indicating that the dissipative structure's critical state has been reached. The influencing factors have reached the critical state of the dissipative structure. However, since the hidden Markov model's hidden variables are not visible, the hidden variables affect the predicted value. The influence is not visible, and only the dissipative structure can be used to analyze the influencing factors listed in this study. In terms of energy research, the dissipative structure can be formed or maintained only when the open system supports exchanging information, material, and energy with the outside world. In the system of this study, the exchange of traffic is the main form of energy exchange, and the increase in traffic flow is the formation of congestion. The main factors of traffic flow will affect the road section's average travel time and the average travel speed of the road section and ultimately affect the road section's traffic state. In terms of entropy research, due to the dissipative structure theory, when an open system undergoes a sudden change, it will transform from its original disordered state to a new state of order in time, space, or function. Entropy is a sign of order. It is a measure of system stability. In this study, the entropy value is combined with eight influencing factors: road type, average travel time of the road section, and hidden influencing factors. The most important influencing factors are the average travel time of the road section and the road section's average travel speed influence to act.

To quantitatively test the prediction effect of the model, three indicators, mean square error (MSE), mean absolute error (MAE), and mean fundamental percentage error (MAPE), are introduced.

It can be seen from the above results that when taking the area near the Second Ring East Road in Chengdu as the research object, consider F1–F5 (road type, average travel time of road segment, the average travel speed of road segment, period, and traffic state of road segment). Hidden Markov model prediction has good accuracy when other influencing factors are used. If the POI-based influencing factors F6–F8 (distance to the subway station, distance to commercial area, and distance to residential area) are considered, the accuracy of prediction can be further

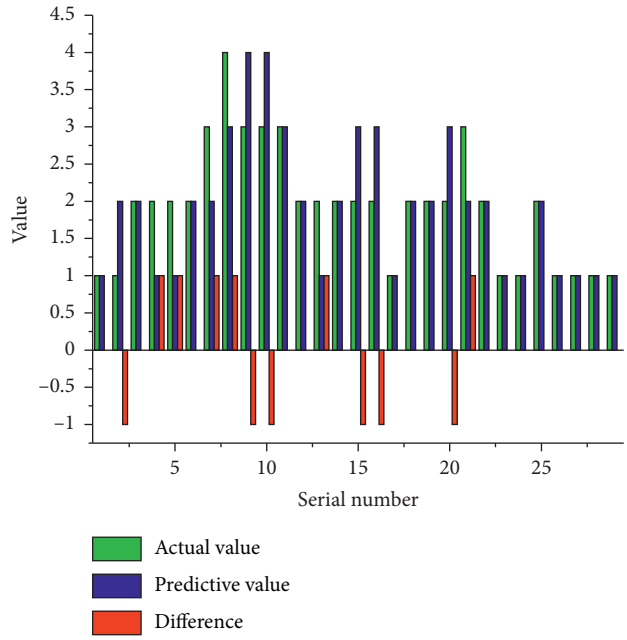

Figure 12: Difference between the actual value and predictive value.

Table 6: Error comparison of prediction methods.

	MSE	MAE	MAPE
Forecast model error	54187.05	167.63	6.54
Model error based on POI	31958.61	128.19	4.51

improved. The model's accuracy can be further verified with the visualized road network traffic status, as shown in Table 6.

In summary, the prediction results of different evaluation index models are not the same. If the mean square error, average absolute error, and average fundamental percentage error are used as evaluation indicators, the model considers factors such as POI having higher accuracy. Within the region, there is better effectiveness and scope of application.

4. Conclusions

In this study, Chengdu was selected as the research object, using Didi car-hailing data to perform data cleaning, coordinate conversion, and map matching on approximately 6 million order data and about 90 GB of trajectory data. After completing the preprocessing of the trajectory data, the characteristic analysis of the trajectory data found that there were morning peaks (8 : 00–10 : 00), noon peaks (12 : 00–14 : 00), and evening peaks (17 : 00–19 : 00), while on rest days, there were only noon peak and evening peak. The demand for travel in the city's central area is relatively stable in terms of spatial distribution. This paper also extracted the road sections' speed characteristics based on the road sections' division and divided the congested road sections according to the speed. Based on the principal component analysis of the POI data, the "principal components" that have the most significant impact on the road traffic state of the POI data are found to provide a basis for further research, such as subsequent predictions. According to the principal component analysis of spatial distribution characteristics, commercial and residential areas significantly impact pickup points. In this study, the area around the east section of the Second Ring Road in Chengdu was selected as the study area, and the road segment and period were divided. Simultaneously, road types, average travel time, and road speed were considered influencing factors. When considering the set of influencing factors of POI, the distance from the boarding point to the subway station, commercial area, and residential area is considered. The initial observation matrix is constructed for the two situations, and the state transition matrix is established according to various influencing factors. Finally, combine the hidden Markov model and the dissipative structure theory, using Python to transform and solve the matrix, and verify the training set's results and the test set. The results show that the model has a certain degree of prediction accuracy. The accuracy of the prediction model based on the GPS data of car-hailing and considering the impact of POI is higher than that without considering its impact. As commercial and residential areas have a more significant effect on pickup points, public transportation should be vigorously developed to reduce passengers' travel demand in private cars and taxis in commercial and residential areas. Traffic organization should be strengthened near congestion points to promote traffic flow circulation and reduce congestion entropy, like intersection signal timing.

Data Availability

All data are collected from the websites http://outreach.didichuxing.com/research/opendata/ and http://www.bigemap.com/.

Conflicts of Interest

The authors declare that they have no known competing financial interests or personal relationships that could have appeared to influence the work reported in this paper.

Authors' Contributions

Xiaoke Sun wrote the paper, Hong Chen provided the research ideas, Yahao Wen and Zhizhen Liu processed the data, and Hengrui Chen revised the paper.

Acknowledgments

This work was supported by the 111 Project of Sustainable Transportation for Urban Agglomeration in Western China under Grant number B20035, the National Natural Science Foundation of China under Grant number 51878062, and Xi'an Science and Technology Bureau under Grant number SZJJ2019-22.

References

[1] Z. Bouyahia, H. Haddad, N. Jabeur, and A. Yasar, "A two-stage road traffic congestion prediction and resource dispatching toward a self-organizing traffic control system," *Personal and Ubiquitous Computing*, vol. 23, no. 5-6, pp. 909–920, 2019.

[2] W. Ge, D. Shao, M. Xue, H. Zhu, X. Zhao, and J. Cheng, "Urban taxi ridership analysis in the emerging metropolis: case study in Shanghai," *Case Studies on Transport Policy*, vol. 8, no. 1, pp. 173–179, 2020.

[3] X. Qian and S. V. Ukkusuri, "Spatial variation of the urban taxi ridership using GPS data," *Applied Geography*, vol. 59, pp. 31–42, 2015.

[4] Z. Zhou, J. Yu, Z. Guo, and Y. Liu, "Visual exploration of urban functions via spatio-temporal taxi OD data," *Journal of Visual Languages & Computing*, vol. 48, pp. 169–177, 2018.

[5] Y. Yang, Z. He, Z. Song, X. Fu, and J. Wang, "Investigation on structural and spatial characteristics of taxi trip trajectory network in Xi'an, China," *Physica A: Statistical Mechanics and Its Applications*, vol. 506, pp. 755–766, 2018.

[6] J. Bao, P. Liu, X. Qin, and H. Zhou, "Understanding the effects of trip patterns on spatially aggregated crashes with large-scale taxi GPS data," *Accident Analysis & Prevention*, vol. 120, pp. 281–294, 2018.

[7] D. Sun and X. Ding, "Spatiotemporal evolution of ridesourcing markets under the new restriction policy: a case study in Shanghai," *Transportation Research Part A: Policy and Practice*, vol. 130, pp. 227–239, 2019.

[8] H. Cai, X. Zhan, J. Zhu, X. Jia, A. S. F. Chiu, and M. Xu, "Understanding taxi travel patterns," *Physica A: Statistical Mechanics and Its Applications*, vol. 457, pp. 590–597, 2016.

[9] D. Sun, K. Zhang, and S. Shen, "Analyzing spatiotemporal traffic line source emissions based on massive didi online car-hailing service data," *Transportation Research Part D: Transport and Environment*, vol. 62, pp. 699–714, 2018.

[10] K. Kim, "Exploring the difference between ridership patterns of subway and taxi: case study in Seoul," *Journal of Transport Geography*, vol. 66, pp. 213–223, 2018.

[11] J. F. Zaki, A. Ali-Eldin, S. E. Hussein, S. F. Saraya, and F. F. Areed, "Traffic congestion prediction based on Hidden Markov Models and contrast measure," *Ain Shams Engineering Journal*, vol. 11, no. 3, p. 535, 2020.

[12] E. D'Andrea and F. Marcelloni, "Detection of traffic congestion and incidents from GPS trace analysis," *Expert Systems with Applications*, vol. 73, pp. 43–56, 2017.

[13] Y. Gong, Y. Lin, and Z. Duan, "Exploring the spatiotemporal structure of dynamic urban space using metro smart card records," *Computers, Environment and Urban Systems*, vol. 64, pp. 169–183, 2017.

[14] Y. Wang, J. Cao, W. Li, T. Gu, and W. Shi, "Exploring traffic congestion correlation from multiple data sources," *Pervasive and Mobile Computing*, vol. 41, pp. 470–483, 2017.

[15] J. Tang, J. Liang, S. Zhang, H. Huang, and F. Liu, "Inferring driving trajectories based on probabilistic model from large scale taxi GPS data," *Physica A: Statistical Mechanics and Its Applications*, vol. 506, pp. 566–577, 2018.

[16] Z. Kan, L. Tang, M.-P. Kwan, C. Ren, D. Liu, and Q. Li, "Traffic congestion analysis at the turn level using Taxis' GPS trajectory data," *Computers, Environment and Urban Systems*, vol. 74, pp. 229–243, 2019.

[17] J. Tang, S. Zhang, X. Chen, F. Liu, and Y. Zou, "Taxi trips distribution modeling based on Entropy-Maximizing theory: a case study in Harbin city-China," *Physica A: Statistical Mechanics and Its Applications*, vol. 493, pp. 430–443, 2018.

[18] F. Wen, G. Zhang, L. Sun, X. Wang, and X. Xu, "A hybrid temporal association rules mining method for traffic congestion prediction," *Computers & Industrial Engineering*, vol. 130, pp. 779–787, 2019.

[19] L. A. Segel and J. L. Jackson, "Dissipative structure: an explanation and an ecological example," *Journal of Theoretical Biology*, vol. 37, no. 3, pp. 545–559, 1972.

[20] X. Sun, H. Chen, Z. Liu, and H. Chen, "Research on PM2.5 concentration based on dissipative structure theory: a case study of Xi'an, China," *Scientific Reports*, vol. 10, no. 1, p. 16435, 2020.

[21] L. Zheng, D. Xia, X. Zhao et al., "Spatial-temporal travel pattern mining using massive taxi trajectory data," *Physica A: Statistical Mechanics and Its Applications*, vol. 501, pp. 24–41, 2018.

[22] S. Zhang, J. Tang, H. Wang, Y. Wang, and S. An, "Revealing intra-urban travel patterns and service ranges from taxi trajectories," *Journal Of Transport Geography*, vol. 61, pp. 72–86, 2017.

Hindawi
Mathematical Problems in Engineering
Volume 2021, Article ID 8856571, 13 pages
https://doi.org/10.1155/2021/8856571

Research Article

Fault-Tolerant Control for Three-Tank System in Case of Sensor Faults

Mondher Amor, Taoufik Ladhari, Salim Hadj Said, and Faouzi M'Sahli

Industrial Systems Study and Renewable Energy Unit, National Engineering School of Monastir, University of Monastir, Ibn El Jazzar Street, Monastir 5019, Tunisia

Correspondence should be addressed to Mondher Amor; mondheramor@yahoo.fr

Received 4 September 2020; Revised 17 December 2020; Accepted 2 January 2021; Published 18 January 2021

Academic Editor: José Antonio Rosales Martínez

This research paper would be devoted to the application of a fault-tolerant control (FTC) for a benchmark system composed of three interconnected tanks in case of sensor faults. The control scheme includes two blocks: fault detection and isolation (FDI) block and a control law reconfiguration block. The strategy of the FDI method is based on a bank of high gain observers; each of them is constructed to estimate the system state vector. Thus, the diagnostic signal-residuals are generated by the comparison of measured and estimated outputs and the faulty sensor is isolated. The reconfiguration block performs an update of the controller parameters according to the operating mode. The application of this method to a pilot plant demonstrates that the hydrographic system maintains quite performances after sensor faults occurrence.

1. Introduction

Any automation of a process aims at reaching an almost perfect solution to obtain a final product of good quality and health of all faults. The automated system control theory has been widely developed and applied to the industrial process. These techniques ensure the stability of the closed-loop system and yield a predefined performance in the case where all system components operate safely. However, the more automated the process is, the more it is subject to fault occurrence. Hence, the need for a control method that is able to ensure nominal performance within highly automated systems where immediate maintenance is out of reach. This control is referred to as fault-tolerant control (FTC) which becomes extremely important in the last few decades. There are two approaches to the synthesis of an FTC. One approach, known as passive FTC, aims at designing a robust controller against some given faults. Another approach, known as active FTC, requires a fast fault detection and isolation (FDI) algorithm followed by a control law adjustment that allows maintaining high performances in the controlled system.

The detection and isolation of faults is an important research area in process control due to the improvements that can be reached in terms of the safety and reliability of the plant. This can be traced from some valuable survey papers [1–3] and books [4, 5]. Different methods have been developed and implemented in different directions and for several systems [6–11] such as model-based method [12, 13], observer method [14–16], parameter estimation method [17], parity space method [18], and a combination of these methods with artificial intelligent [8, 19].

The three-tank system (3TS) is considered an important and effective prototype of many applications in industrial processes, such as water treatment, food industry, chemical and petrochemical plants, oil, and gas systems. It is widely used in water conditioning systems, which provide the user with an abundant supply of luxuriously conditioned water and in craft brewing systems. In spite of the fact that many fault detection and isolation methods have already been applied to three-tank system systems, a few fault accommodation techniques have been considered. In [20], a feedback linearization approach for fault-tolerant control in a 3TS benchmark is investigated. Noura et al. proposed an

approach based on the online estimation for the fault and the computation of additive control law is able to compensate for the fault effect on the system [21]. Mendoca et al. have used predictive control and fuzzy logic to design a fault-tolerant control for a 3TS [22]. Orani et al. presented a global observer based on a second-order sliding mode control algorithm for the simultaneous fault detection, isolation, and reconstruction for hydraulic vertical 3TS [23]. Other researchers have focused on fault diagnosis and accommodation for both sensor and actuator faults; they have proposed an analytical redundancy method to solve the drawbacks of the hardware redundancy such as cost and space [24]. It should be noted that all these previous works have developed FTC solutions based on the linearized model of the 3TS. This means that these approaches are valid only around an operating area. To overcome the previous drawbacks, some papers have focused on the application of actuator fault magnitude estimation [25] or fault-tolerant control [26–28] by using a nonlinear model of the 3TS.

In this paper, we focus on the online sensor fault detection and isolation by adopting high gain observers' bank. A reconfiguration of the controller is then performed by adjusting the design parameters to compensate for the sensor fault effects. Compared to previous works, the proposed approach has the feature to potentially mitigate the required time of the FDI process as well as the ability to reach the reference trajectory after the fault occurrence. The other purpose of this paper is to show the experimental performance of the proposed FTC method on a real plant. Moreover, it is important to mention that the proposed FTC approach is valid for several working areas and not only locally around the operating point.

The paper is organized as follows. Section 2 presents the 3TS model to illustrate sensor faults and accommodation methods. The next section is devoted to the strategy of fault diagnosis based on high gain observers bank used to detect, isolate, and estimate the faults. In section four, the full fault-tolerant control scheme is exposed. In this context, a new adjusted control law that aims to reduce the fault effect on the system outputs is discussed. Experimental results are given and presented in section 5. Finally, a conclusion and some perspectives are given in the sixth section.

2. Three-Tank System Presentation

2.1. Plant Description. The 3TS plant consists of three identical cubes with the same cross section area S. These tanks are coupled serially to each other via cylindrical pipes of the same cross section area S_n. The complete structure of the plant is shown in Figure 1.

Two pumps P_1 and P_2, driven by DC-motors, represent, respectively, the input flows Q_1 and Q_2 of tanks T_1 and T_3. The plant is a closed system, in which the liquid that enters the reservoir from the tanks returns to the tanks thanks to two pumps.

Besides the outflow valve on T_3, the system includes five additional valves. Two of them are used to join each pair of neighboring tanks and can be manually tuned to close the connection between the two consecutive tanks. The other three valves V_{l1}, V_{l2}, and V_{l3} are at the bottom of each tank.

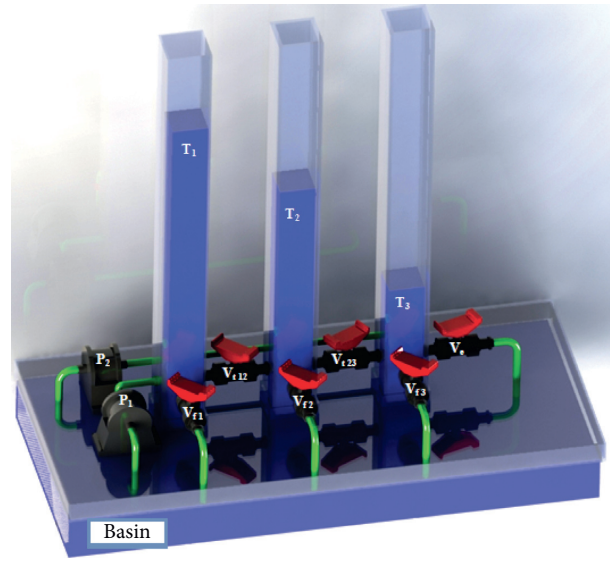

Figure 1: Full structure of the computer design plant.

These leak valves can be used to manually drain each tank [29]. A piezoresistive differential pressure sensor, associated with each tank, delivers an analog voltage signal to measure the three liquid levels denoted by h_1, h_2, and h_3.

2.2. Mathematical Model. The analytic model can be easily derived from the principle of mass conservation and the Torricelli law. In fact, the change of water volume in tank i ($i = 1{:}3$) is determined by the following equation:

$$\dot{V}_i = S_i \cdot \frac{dh_i}{dt} = \sum Q_{\text{in},i} - \sum Q_{\text{out},i}, \tag{1}$$

where $\sum Q_{\text{in},i}$ and $\sum Q_{\text{out},i}$ represent the total liquid inflows and outflows in tank i, respectively. Then, the mathematical model is specified by the following mass balance equations:

$$\begin{cases} \dot{h}_1(t) = \dfrac{1}{S}\left(Q_1(t) - Q_{12}(t) - Q_{l1}(t)\right), \\ \dot{h}_2(t) = \dfrac{1}{S}\left(Q_{12}(t) - Q_{23}(t) - Q_{l2}(t)\right), \\ \dot{h}_3(t) = \dfrac{1}{S}\left(Q_2(t) + Q_{23}(t) - Q_e(t) - Q_{l3}(t)\right), \end{cases} \tag{2}$$

where t represents the time; h_1, h_2, and h_3 represent the liquid levels in each tank; S represents the cross section of the tanks; Q_1 and Q_2 designate respectively the flow rates of pumps P_1 and P_2; Q_{ij} denotes the flow rates between tank T_i and T_j; and Q_{li} represents the output flow of the corresponding tank when its leak valve is open. Q_e is the leakage valve. The flows Q_{ij} and Q_e in (2) are given by Torricelli's law as follows:

$$\begin{aligned} Q_{ij}(t) &= a_{zi} S_n \operatorname{sgn}\left(h_i - h_j\right)\sqrt{2g\left|h_i - h_j\right|}, \\ Q_e(t) &= a_{z3} S_n \sqrt{2gh_3}, \end{aligned} \tag{3}$$

where a_{zi} is the outflow coefficient, sgn(.) is the sign of the argument, and g is the acceleration of gravity. Consequently, the nonlinear 3T model is given as follows:

$$\begin{cases} \dfrac{dh_1}{dt} = -a_1 \operatorname{sign}(h_1 - h_2)\sqrt{|h_1 - h_2|} + \dfrac{Q_1}{S}, \\ \dfrac{dh_2}{dt} = a_1 \operatorname{sign}(h_1 - h_2)\sqrt{|h_1 - h_2|} - a_2 \operatorname{sign}(h_2 - h_3)\sqrt{|h_2 - h_3|}, \\ \dfrac{dh_3}{dt} = a_2 \operatorname{sign}(h_2 - h_3)\sqrt{|h_2 - h_3|} - a_3\sqrt{h_3} + \dfrac{Q_2}{S}, \end{cases} \tag{4}$$

where a_i represents the system parameter given by

$$a_i = \frac{1}{S} a_{zi} S_n \sqrt{2g}; \quad i = 1, \ldots, 3. \tag{5}$$

2.3. Three-Tank System Faults Representation. The 3TS laboratory system is considered as a rich ground to serve as a test environment for the FTC. It is used as a benchmark system that can be affected by various additive and/or multiplicative faults:

(i) Faults actuator: an actuator fault can be represented by

$$u_i^f(k) = \alpha_i u_i(k) + u_{i0}; \quad i = 1, 2, \tag{6}$$

(i) where u_i^f and u_i represent the faulty and the normal control action of the ith pump, respectively. The constant offset is denoted by u_{i0} and $0 \le \alpha_i \le 1$ denotes a gain degradation of the i^{th} actuator.

(ii) Faults sensor: similar to the actuator fault representation, a faulty output can be written as

$$y_j^f(k) = \beta_j y_j(k) + y_{j0}; \quad j = 1, 2, 3, \tag{7}$$

where y_j^f and y_j represent the faulty and the normal level of the j^{th} sensor, respectively. The constant offset is denoted by y_{j0} and $0 \le \beta_j \le 1$ denotes a gain degradation of the jth sensor.

3. Fault Detection and Isolation FDI Strategy

3.1. Problem Statement. It is important to be able to carry out the fault detection and isolation before that the faults induce a drastic effect on the system performance. Even in the case of system changes, faults should be detected and isolated. The observer-based approach is used to generate residual signals corresponding to the difference between measured and estimated signals. It is straightforward to think that if the system is faulty, the residual signal will be different to zero. However, the resultant residual will be equal to zero in case of an unfaulty system. The residual signal is compared to a fixed threshold; this comparison is followed by a decision block. To handle all possible sensor faults, we use an observer's bank composed of three high gain observers. Each observer uses the information of two sensors to estimate the third state as it is shown in Figure 2.

The three estimated liquid levels $\widehat{y}_1$, $\widehat{y}_2$, and $\widehat{y}_3$ provided by the observers' bank allow to calculate the three residuals as follows:

$$r_j = y_j - \widehat{y}_j, \quad \text{for } j = 1, \ldots, 3. \tag{8}$$

Considering these following notations, Table 1 can be established:

$$\begin{aligned} \text{sensor}_j &= \begin{cases} 0, & \text{fault in the } j^{\text{th}} \text{ sensor}, \\ 1, & \text{no fault in the } j^{\text{th}} \text{ sensor}, \end{cases} \\ r_j &= \begin{cases} \neq 0, & \text{fault in the } j^{\text{th}} \text{ sensor}, \\ 0, & \text{no fault in the } j^{\text{th}} \text{ sensor}. \end{cases} \end{aligned} \tag{9}$$

Consequently, the novel output vector used to implement the control law is given by

$$y_c = \begin{pmatrix} y_{c1} \\ y_{c2} \\ y_{c3} \end{pmatrix}; \quad \text{where } y_{cj} = \overline{F_j}.y_j + F_j.\widehat{y}_j, \tag{10}$$

with y_j and $\widehat{y}_j$ are, respectively, the measured and the estimated output. F_j is a binary variable such as

$$F_j = \begin{cases} 1, & \text{fault in the } j\text{th sensor}, \\ 0, & \text{no fault in the } j\text{th sensor}. \end{cases} \tag{11}$$

Once the FDI is performed, the faulty sensor S_i is identified and the binary variable F_i is set to 1. As a result, the control output y_{ci} switches from measured to the estimated output provided by the i^{th} observer (see Figure 3).

3.2. Observer Design

3.2.1. Basic Concepts. Consider nonlinear systems of the form:

$$\begin{cases} \dot{x} = f(x, u), \\ y = p(x), \end{cases} \tag{12}$$

where the vectors x and u are, respectively, the state and control defined on the subsets M and U and the vector-valued functions f (.) and p (.) are sufficiently differentiable with respect to their arguments.

Firstly, assume y is a single output. Suppose an injective map $\zeta = q(x)$ exists, which has a continuous inverse and brings system (12) into the bitriangular form:

$$\begin{aligned} \begin{bmatrix} \dot{\zeta} \\ \vdots \\ \dot{\zeta}_{k-1} \\ \dot{\zeta}_k \end{bmatrix} &= \begin{bmatrix} \zeta_2 + \psi(\zeta_1, u) \\ \vdots \\ \zeta_k + \psi_{k-1}(\zeta_1, \ldots, \zeta_{k-1}, u) \\ \psi_k(\zeta_1, \ldots, \zeta_k, u) \end{bmatrix}, \\ y &= \zeta_1. \end{aligned} \tag{13}$$

Denote the system in the ζ-coordinate as

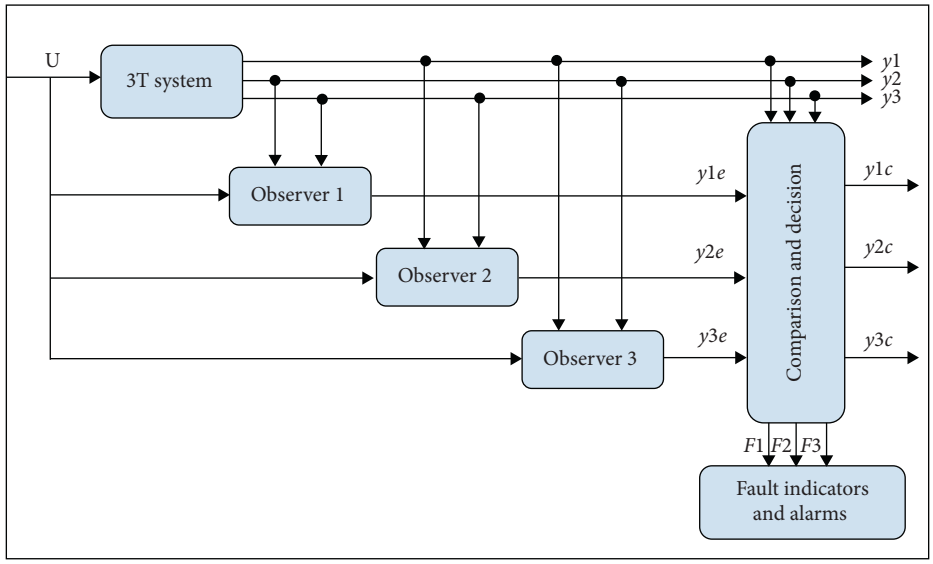

Figure 2: Synoptic scheme of FDI applied to 3-tank system.

Table 1: Faults signature for the three residuals.

Sensor 1	Sensor 2	Sensor 3	r_1	r_2	r_3	F_1	F_2	F_3
1	1	1	0	0	0	0	0	0
0	1	1	$\neq 0$	0	0	1	0	0
1	0	1	0	$\neq 0$	0	0	1	0
1	1	0	0	0	$\neq 0$	0	0	1
0	0	1	$\neq 0$	$\neq 0$	0	1	1	0
1	0	0	0	$\neq 0$	$\neq 0$	0	1	1
0	1	0	$\neq 0$	0	$\neq 0$	1	0	1
0	0	0	$\neq 0$	$\neq 0$	$\neq 0$	1	1	1

$$\dot{\zeta} = A\zeta + \psi(\zeta, u), \quad y = C\zeta, \tag{14}$$

with

$$A = \begin{bmatrix} 0 & 1 & & & \\ & \ddots & \ddots & & \\ & & \ddots & \ddots & \\ & & & \ddots & 1 \\ & & & & 0 \end{bmatrix},$$
$$C = \begin{bmatrix} 1 & 0 & \cdots & 0 \end{bmatrix}, \tag{15}$$
$$\psi(.) = \begin{bmatrix} \psi(\zeta_1, u) \\ \vdots \\ \psi_{k-1}(\zeta_1, \ldots, \zeta_{k-1}, u) \\ \psi_k(\zeta_1, \ldots, \zeta_k, u) \end{bmatrix}.$$

Assume in the coordinate change $\dim[\zeta] = \dim[x]$ and the Jacobian $(\partial q(x)/\partial x)$ is nonsingular. According to [30], for (12) an asymptotic observer is

$$\dot{\hat{x}} = f(\hat{x}, u) + \left(\frac{\partial q(x)}{\partial x}\bigg|_{x=\hat{x}} \right)^{-1} L_\theta (y_i - p(\hat{x})), \tag{16}$$

where $L_\theta = \begin{bmatrix} \theta L_1 \\ \vdots \\ \theta^k L_k \end{bmatrix}$ and $\theta > 0$ is a scalar; the size of L_i is equal to the dimension of ζ_i.

In a practical design, L is firstly chosen such that A-LC is stable. Then, an arbitrary $\theta \geq 1$may be chosen. A large value of θ involved relatively a fast convergence in the estimation error, but, at the same time, it can induce an amplification of the noise measurement.

3.2.2. HGO Design for the 3TS Model. The nonlinear model (4) of the three-tank system can be written as follows:

$$\dot{h} = f(h) + gQ, \tag{17}$$

where

$$h = \begin{bmatrix} h_1 \\ h_2 \\ h_3 \end{bmatrix},$$
$$Q = \begin{bmatrix} Q_1 \\ Q_2 \end{bmatrix},$$
$$g = \begin{bmatrix} \frac{1}{S} & 0 \\ 0 & 0 \\ 0 & \frac{1}{S} \end{bmatrix},$$
$$f(h) = \begin{bmatrix} -a_1 \operatorname{sgn}(h_1 - h_2)\sqrt{|h_1 - h_2|} \\ a_1 \operatorname{sgn}(h_1 - h_2)\sqrt{|h_1 - h_2|} - a_2 \operatorname{sgn}(h_2 - h_3)\sqrt{|h_2 - h_3|} \\ a_2 \operatorname{sgn}(h_2 - h_3)\sqrt{|h_2 - h_3|} - a_3\sqrt{h_3} \end{bmatrix}. \tag{18}$$

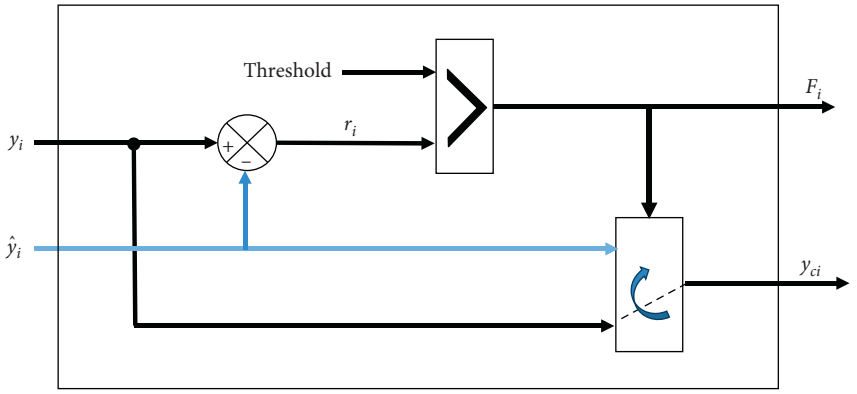

Figure 3: Internal diagram of comparison and decision unit.

Typical values of the 3T system are given in Table 2. These values are later used in observer and controller implementation.

(1) Observer Form with a Single Output Measurement. If only a single measurement is available during operating, according to (16), the observer for the 3TS model takes the form

$$\dot{\hat{h}} = f(\hat{h}) + g(Q) + \left(\frac{\partial q_{ij}(h)}{\partial h}\bigg|_{h=\hat{h}}\right)^{-1} L_\theta (y_i - \hat{h}_i), \quad (19)$$

where

$$L_\theta = \begin{bmatrix} \theta l_1 \\ \theta^2 l_2 \\ \theta^3 l_3 \end{bmatrix}, \quad \theta \geq 1,$$
$$L = \begin{bmatrix} L_1 \\ L_2 \\ L_3 \end{bmatrix}, \quad (20)$$

ensuring that the matrix A-LC is Hurwitz:

$$A = \begin{bmatrix} 0 & 1 & 0 \\ 0 & 0 & 1 \\ 0 & 0 & 0 \end{bmatrix},$$
$$C = \begin{bmatrix} 1 & 0 & 0 \end{bmatrix}. \quad (21)$$

For instance, suppose only $y_1 = h_1$ is available. Then, $\zeta = q_1(h)$ with

$$q_1(h) = \begin{bmatrix} h_1 \\ L_f h_1 \\ L_f^2 h_1 \end{bmatrix} = \begin{bmatrix} h_1 \\ -a_1 \operatorname{sign}(h_1 - h_2)\sqrt{|h_1 - h_2|} \\ a_1^2 \operatorname{sign}(h_1 - h_2)\sqrt{|h_1 - h_2|} - \dfrac{a_1 a_2 \operatorname{sign}(h_2 - h_3)\sqrt{|h_2 - h_3|}}{2\sqrt{h_1 - h_2}} \end{bmatrix}, \quad (22)$$

Table 2: Physical parameters of the three-tank system.

Tank cross section areas	S_1=S_2=S_3=S=0.01 m^2
Pipe cross section areas	S_N = 0.0000786 m^2
Coefficients	$a_1 = 0.1$; $a_2 = 0.086$; $a_3 = 0.099$
Maximum in-flow rate	$Q_{max} = 6.66.\ 10^{-5}$ m^3/s

where $L_f^j h(x)$ is the jth Lie derivative of the function h by f; for example, $h(x)$ and $f(x)$ are differentiable functions of x up to the order n.

So, we have

$$\frac{\partial q_1}{\partial h} = \begin{bmatrix} 1 & 0 & 0 \\ -a & a & 0 \\ b & -c-b & c \end{bmatrix}, \quad (23)$$

with

$$a = \frac{a_1}{2\sqrt{|h_1 - h_2|}};$$
$$b = \frac{a_1 a_2 \operatorname{sgn}(h_2 - h_3)\sqrt{|h_1 - h_2|}}{4\sqrt{|h_1 - h_2||h_1 - h_2|}}; \quad (24)$$
$$c = \frac{a_1 a_2}{4\sqrt{|h_1 - h_2|.|h_2 - h_3|}},$$

and hence

$$\left(\frac{\partial q_1}{\partial h}\right)^{-1} = \begin{pmatrix} 1 & 0 & 0 \\ 1 & \dfrac{1}{a} & 0 \\ 1 & \dfrac{1}{a} + \dfrac{b}{ca} & \dfrac{1}{c} \end{pmatrix}. \quad (25)$$

(2) Observer Form with Both State Measurements. To detect and isolate several sensor faults in the whole operating area, we use in FDI block a bank of nonlinear observers. According to [30] and using the assumption cited in [31] if

two measurements *yi* and *yj* are available, the HGO is given by

$$\dot{\hat{h}} = f(\hat{h}) + g(Q) + \left(\frac{\partial q_{ij}(h)}{\partial h}\Big|_{h=\hat{h}}\right)^{-1} L_\theta (y_{i,j} - \hat{h}_{i,j}), \tag{26}$$

where

$$L_\theta = \begin{bmatrix} L_1\theta \\ L_2\theta^2 \end{bmatrix}, \quad \theta \geq 1,$$
$$L = \begin{bmatrix} L_1 \\ L_2 \end{bmatrix}, \tag{27}$$
$$L = \begin{bmatrix} L_1 \\ L_2 \end{bmatrix},$$

where $L1$ and $L2$ are, respectively, $2x2$ and $1x2$ constant matrix, which can be easily determined such that *A-LC* has merely stable eigenvalues (26).

(i) b.1-*Observer* 1. Suppose $y_2 = h_2$ and $y_3 = h_3$ are the two available measurements. Let $\varepsilon_1 = \begin{bmatrix} h_2 \\ h_3 \end{bmatrix}$ and $\varepsilon_2 = L_f h_2$ is the Lie derivative of *h2* by *f*:

$$\varepsilon = \begin{bmatrix} \varepsilon_1 \\ \varepsilon_2 \end{bmatrix} = q_{23}(h) = \begin{bmatrix} h_2 \\ h_3 \\ L_f h_2 \end{bmatrix},$$

$$y_{2,3} - \hat{h}_{2,3} = \begin{bmatrix} y_2 \\ y_3 \end{bmatrix} - \begin{bmatrix} \hat{h}_2 \\ \hat{h}_3 \end{bmatrix}, \tag{28}$$

$$\left(\frac{\partial q_{23}}{\partial h}\right)^{-1} = \begin{bmatrix} 1 + \dfrac{b}{a} & -\dfrac{b}{a} & \dfrac{1}{a} \\ 1 & 0 & 0 \\ 0 & 1 & 0 \end{bmatrix},$$

(ii) with

$$a = \frac{a_1}{2\sqrt{|h_1 - h_2|}};$$
$$b = \frac{a_2}{2\sqrt{|h_2 - h_3|}}; \tag{29}$$
$$L = \begin{bmatrix} L_1 \\ L_2 \end{bmatrix},$$

(iii) where the dimensions of *L1* and *L2* are, respectively, *2x2* and *1x2* constant matrix, which can be easily determined such that *A-LC* has merely stable eigenvalues. In this case, we have

$$A = \begin{bmatrix} 0 & 0 & 1 \\ 0 & 0 & 0 \\ 0 & 0 & 0 \end{bmatrix};$$
$$C = \begin{bmatrix} 1 & 0 & 0 \\ 0 & 1 & 0 \end{bmatrix}; \tag{30}$$
$$L_\theta = \begin{bmatrix} L_1\theta \\ L_2\theta^2 \end{bmatrix}.$$

(iv) b.2-*Observer* 2. Suppose $y1 = h1$ and $y3 = h3$ are the two available measurements; $\varepsilon_1' = \begin{bmatrix} h_1 \\ h_3 \end{bmatrix}$; and $\varepsilon_2' = L_f h_1$ is the Lie derivative of *h1* by *f*:

$$\varepsilon' = \begin{bmatrix} \varepsilon_1' \\ \varepsilon_2' \end{bmatrix} = q_{21}(h) = \begin{bmatrix} h_1 \\ h_3 \\ L_f h_1 \end{bmatrix},$$

$$y_{2,1} - \hat{h}_{2,1} = \begin{bmatrix} y_1 \\ y_3 \end{bmatrix} - \begin{bmatrix} \hat{h}_1 \\ \hat{h}_3 \end{bmatrix}, \tag{31}$$

$$\left(\frac{\partial q_{13}}{\partial h}\right)^{-1} = \begin{bmatrix} 1 & 1 & 0 \\ 0 & 0 & 1 \\ 0 & \dfrac{1}{a} & 0 \end{bmatrix},$$

(v) with a and b as given below, and $L\theta$ is the same as given in observer 1.

(vi) b.3-*Observer* 3. Suppose $y_1 = h_1$ and $y_2 = h_2$ are available. Let $\varepsilon_1'' = \begin{bmatrix} h_2 \\ h_1 \end{bmatrix}$ and $\varepsilon_2'' = L_f h_2$ is the Lie derivative of *h2* by *f*:

$$\varepsilon'' = \begin{bmatrix} \varepsilon_1'' \\ \varepsilon_2'' \end{bmatrix} = q_{21}(h) = \begin{bmatrix} h_2 \\ h_1 \\ L_f h_2 \end{bmatrix},$$

$$y_{2,1} - \hat{h}_{2,1} = \begin{bmatrix} y_2 \\ y_1 \end{bmatrix} - \begin{bmatrix} \hat{h}_2 \\ \hat{h}_1 \end{bmatrix}, \tag{32}$$

$$\left(\frac{\partial q_{21}}{\partial h}\right)^{-1} = \begin{bmatrix} 0 & 1 & 0 \\ 1 & 0 & 0 \\ 1 + \dfrac{a}{b} & -\dfrac{a}{b} & \dfrac{1}{b} \end{bmatrix},$$

Where $L\theta$ is the same as given in observer 1.

The proof of convergence of this observer is detailed in [31].

4. FTC Design

The main objective is to establish a closed-loop regulation to track two reference liquid levels. For this reason, two PI controllers are installed. Each one controls one liquid level. In safety mode, these controllers can successfully accomplish this task. However, in the case of a faulty sensor, nominal performances are affected in the best case, and it can lead to instability in the worst case. To avoid such behavior, we should use the FTC that allows reconfiguring the controller when a fault occurs. As is shown in Figure 4, the role of the FTC unit can be divided into two main tasks: the first one is the FDI detailed in Section 3 and the second one concerns the control law reconfiguration which performs the design parameters adjustment. In the case of faulty sensor *Si*, the binary variable *Fi* is set to 1. As a result, the control output yci switches from measured to the estimated output provided by the *i*th observer. To reduce the sensor fault effect and to maintain the closed-loop performance, the control output yci is used for the feedback and then compared with the input reference.

The sensor fault accommodation allows reducing the fault effect, and so the system still operates in the degraded mode. To alleviate this degradation, we suggest adjusting the parameters of the PI controller (k_p, k_i), from the normal mode parameters (k_{pin}, k_{iin}) to faulty mode parameters (k_{pf}, k_{if}) using a switcher block.

5. FTC Application

To prove the validity of the FTC strategy proposed in paragraphs 3 and 4, we apply it to the hydrographic system described in the second section. The main aim is to accomplish a closed-loop regulation of two levels h_1 and h_3. As is shown in Figure 5, the test setup is composed by the following:

(i) Three liquid tanks with 1-meter height and one evacuation reservoir.

(ii) Two 36 W water-pumps (12 V/3 A) with a 4 Lpm liquid flow.

(iii) Three piezoresistive transducers MPX-5010 with sensitivity equal to 450 mV/kPa; everyone equips each tank. These transducers provide accurate analog output signals that are proportional to the pressure variation due to the liquid injection. The accepted range of pressure is from 0 to 10 kPa and the output signal is between 0.2 and 4.7 v. The main feature of this sensor is the possibility to connect it directly to a microcontroller without using a conditioning card.

(iv) An STM32Fio card is used as an I/O interface to establish a connection, via USB port, between the control desk using MATLAB/Simulink environment and the I/O peripheries (the three piezoresistive differential pressure sensors as input and the motopump drive board as output).

(v) A control desk with MATLAB/Simulink environment.

(vi) Power supply of two variable voltage sources 30 V/4A.

The control law is implemented in real time using a sampling period of 0.1s.

The experimental setup is in the laboratory "Study of Industrial Systems and Renewable Energies" "ESIER" at the National Engineers School of Monastir, Tunisia.

5.1. Fault Free Case. In a faulty free case, the PI controllers successfully ensure this task since these outputs track well the desired trajectory as is shown in Figure 6.

To ensure good tracking of the level references h_1 and h_3, we used two PI controllers, one for each level with identical parameters $K_{pn} = 20$ and $K_{in} = 15$.

5.2. Faulty Cases

5.2.1. Fault Scenarios

(i) At $t1 = 300$s, a constant offset of -8 cm is added to liquid level h_1 ($\beta 1 = 1$, $y_{10} = -8$ cm).

(ii) At $t2 = 500$s, a constant offset of -6 cm is added to liquid level h_3 ($\beta 3 = 1$, $y_{30} = -6$ cm).

5.2.2. Sensor Fault Effect without FTC. The consequence of the fault scenario in the feedback performance is illustrated in Figure 7. From the instant $t1 = 300$s, the measured level h_1 has a bias of -8 cm compared to its real value; that is why the control law tries to cancel the static error created by the faulty measurement which appears clearly in the sudden magnitude change of u_1. Consequently, the real output is different from the reference and it is equal to the value of reference plus the bias value ($37.5 + 8 = 43.5$ cm). Since $t = 450$**s**, the control law u_1 has been almost constant and greater than the nominal value in the fault-free case. Similar to level 1 fault consequence, Figure 8 shows the effect of the fault in sensor 3 which arises at a real level different from the reference, and after $t = 720$s, a control law u_2 which has almost a constant value greater than the nominal one.

5.2.3. FTC without Controller Adjustment. The application of the previous FDI method to the same fault scenario sited in subsection 5.2.1 requires the use of observers' bank in order to generate residual and to identify the faulty sensor. After a transient time, this residual is compared to a fixed threshold which allows setting the binary variable *Fi* to 1 or 0.

(i) At $t = t1 = 300$s, a bias of -8 cm is added to the liquid level 1; this sudden change induces a rocking of the control output y_{c1} from the measured y_1 to the estimated $\widehat{y}_1$ generated by the observer 1 (see Figures 2 and 3).

(ii) At $t = t2 = 500$s, similar to level 1, a bias of -6 cm is added to the third level and, consequently, the feedback is ensured by the estimated output $\widehat{y}_3$.

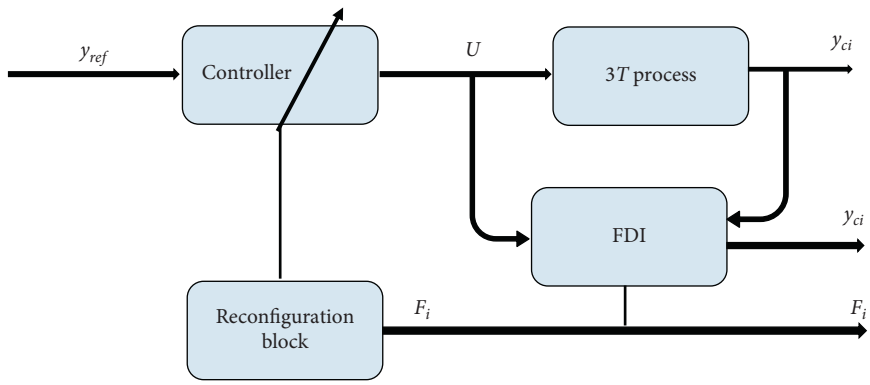

Figure 4: Synoptic scheme of an FTC including FDI module.

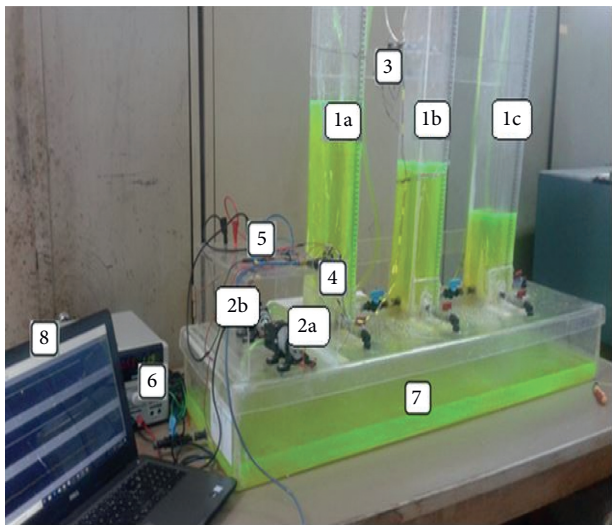

Figure 5: Experimental plant: (1a, 1b, 1c) 3 cubic tanks; (2a, 2b) 2 DC motopumps; (3) liquid level sensors; (4) Fio std STM32 board; (5) motor driver board; (6) power supply; (7) basin; and (8) control desk.

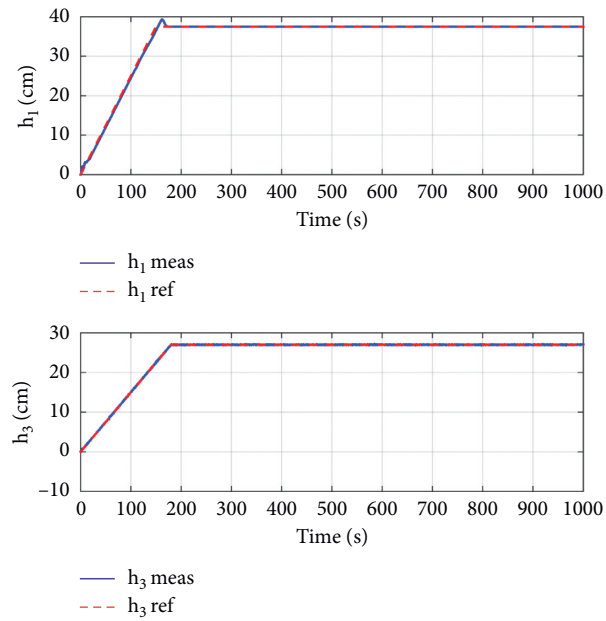

Figure 6: Tracking performances of liquid levels 1 and 3 in the fault-free case.

In a practical design, L is firstly chosen such that A-LC is Hurwitz. Then, an arbitrary $\theta \geq 1$ may be chosen. Normally, a large value of θ allows a fast estimation error convergence. But, in the same way, it can generate excessive peaks during the transient, beside inducing an amplification of the noise measurement in the state estimation. To achieve a compromise, we have chosen the observers' parameters as $\theta_1 = \theta_2 = \theta_3 = 2$.

As is shown in Figures 9 and 10, levels 1 and 3 try to suitably track the liquid reference trajectories. But, since the comparison of the input reference is done with an estimated value of the real measurement, large oscillations appear after the fault occurrence.

5.2.4. FTC with Controller Adjustment. To improve the performance of the closed-loop sited lastly, we suggest the adjustment of the controller parameters from the nominal one ($K_{pn} = 20$, $K_in = 15$) to the faulty one ($K_{pf} = 70$, $K_{if} = 50$) using a switcher block in which the switching condition is the error between the estimated and the measured signals. As is shown in Figure 11, in a healthy case, the error is less than the threshold; then $K_p = K_{pn}$, after fault occurrence, the error is greater than the threshold and K_p switch to K_{pf}.

The result of this adjustment is shown in Figures 12 and 13. Compared to Figures 9 and 10, the quality of regulation is improved.

5.2.5. Result Discussion. The proposed active fault-tolerant control ensures typically quite performances for the closed-loop system. Indeed, after sensor fault accommodation a controller reconfiguration is performed to improve the tracking performances. The tracking errors $e_1 = y_1 - y_{1\text{ref}}$ and $e_3 = y_3 - y_{3\text{ref}}$ are depicted, respectively, in Figures 14 and 15 for three cases: fault-free case (a), FTC without control law adjustment (b), and FTC with control law adjustment (c).

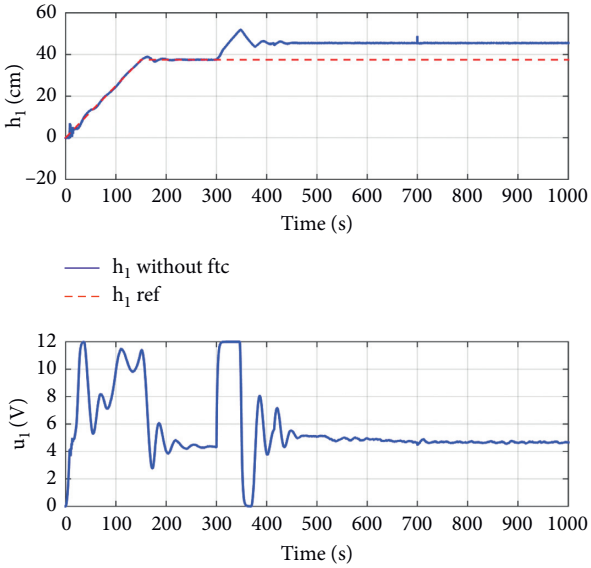

Figure 7: Dynamic response of level 1 without FTC and its control law u_1.

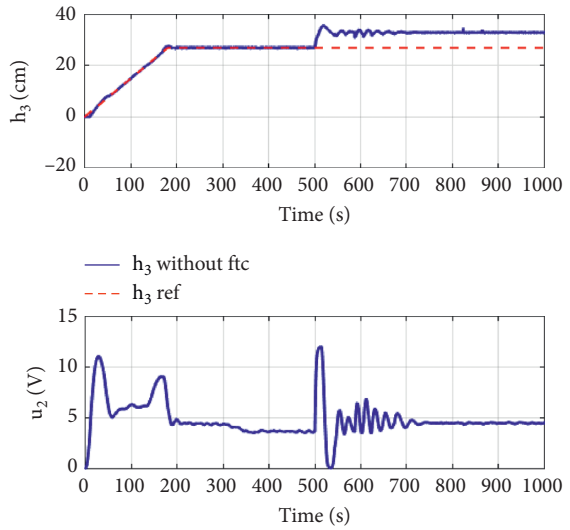

Figure 8: Dynamic response of level 3 without FTC and its control law u_2.

To evaluate the control performance, we use the mean square error MSE criterion defined by

$$\text{MSE} = \frac{1}{n}\sum_{k=1}^{n}\left(y_{\text{ref}}(k) - y(k)\right)^2, \tag{33}$$

where n is the number of measurements, $y_{\text{ref}}(k)$ is the desired output, and $y(k)$ is the system output. The computation of the MSE for outputs y_1 and y_3 in cases a, b, and c is illustrated by Table 3, when $n = 10000$.

As seen in Table 3, the MSE values arising from the proposed approach are a little bigger than the fault-free case, but it is still widely smaller than the case of FTC without control law parameters adjustment. This also is confirmed by the dynamic behavior of the output levels y1 and y3 after sensor fault occurrence.

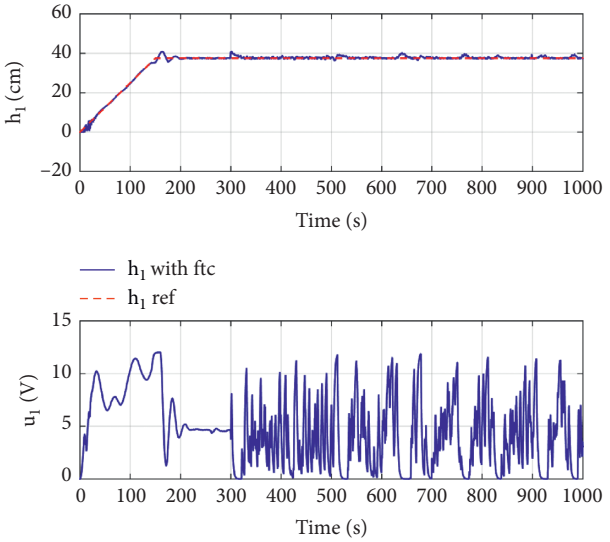

Figure 9: Tracking performance of level 1 with FTC and its control law u_1.

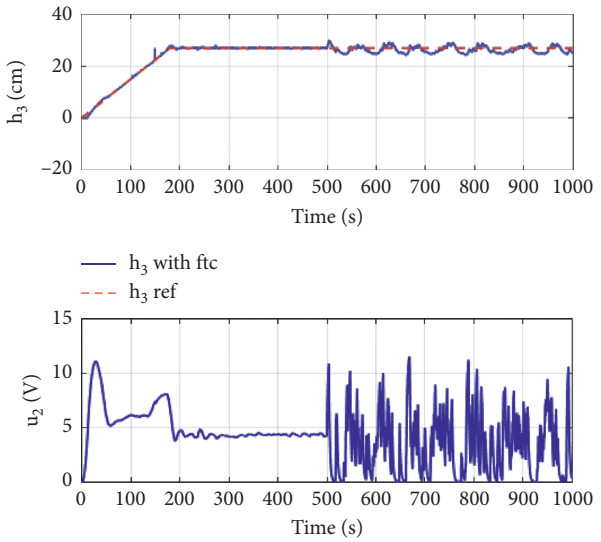

Figure 10: Tracking performance of level 3 with FTC and its control law u_2.

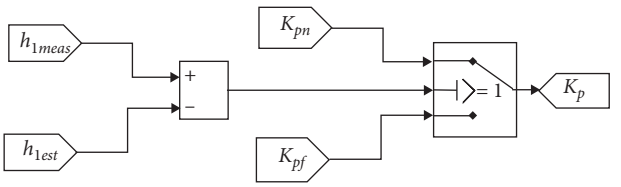

Figure 11: Schematic diagram of the controller parameters switching.

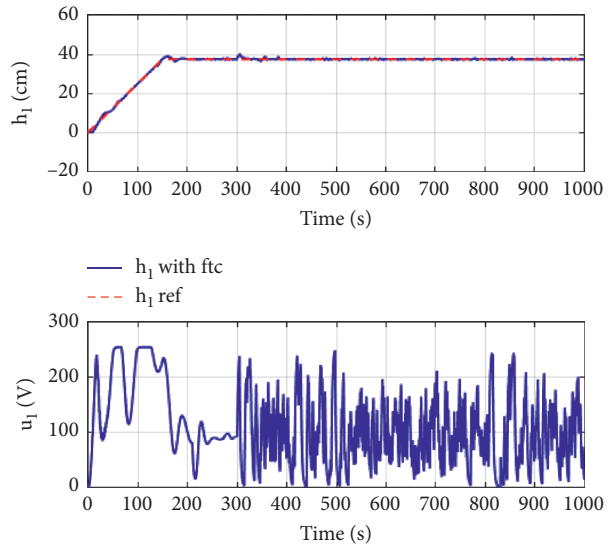

Figure 12: Dynamic response of level 1 with FTC and its adjusted control law u_1.

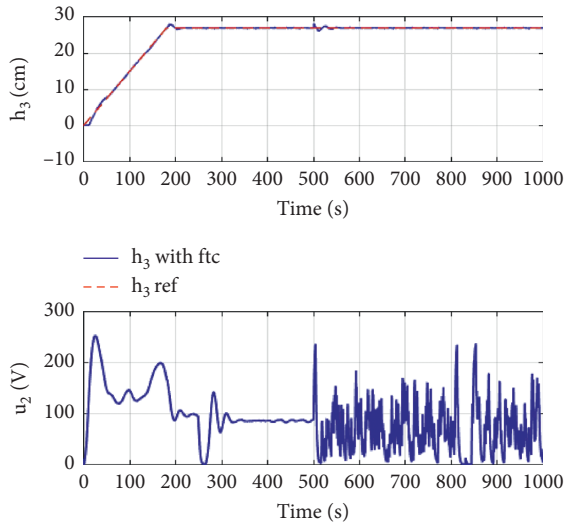

Figure 13: Dynamic response of level 3 with FTC and its adjusted control law u_2.

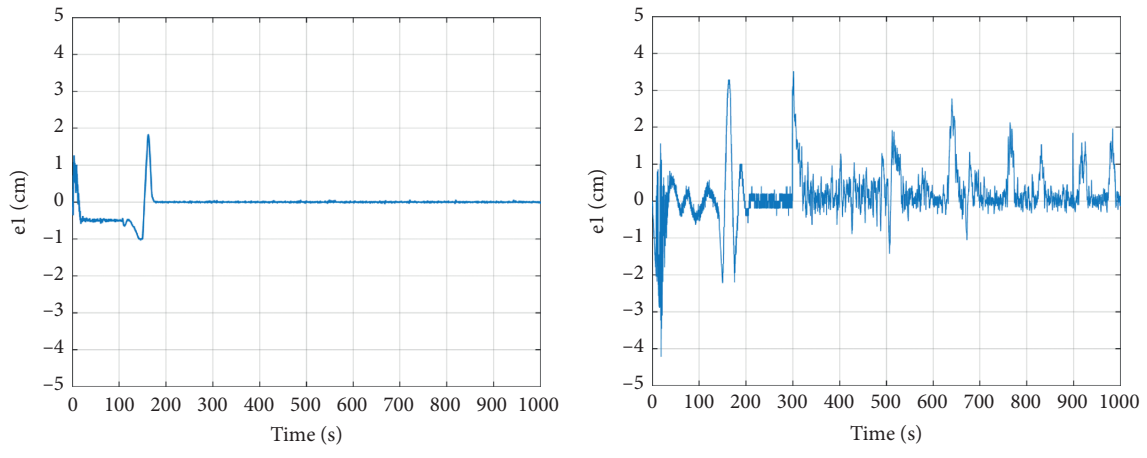

Figure 14: Continued.

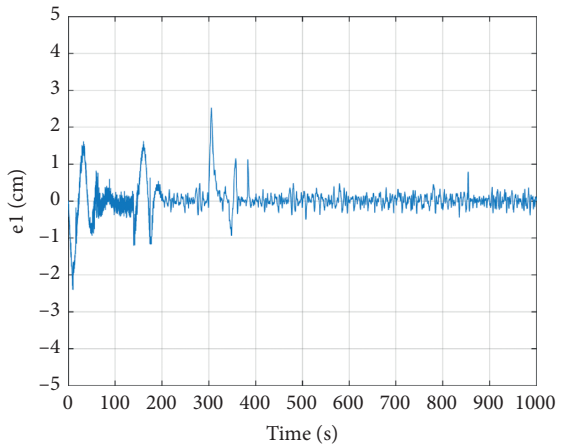

(c)

Figure 14: Tracking error e1.

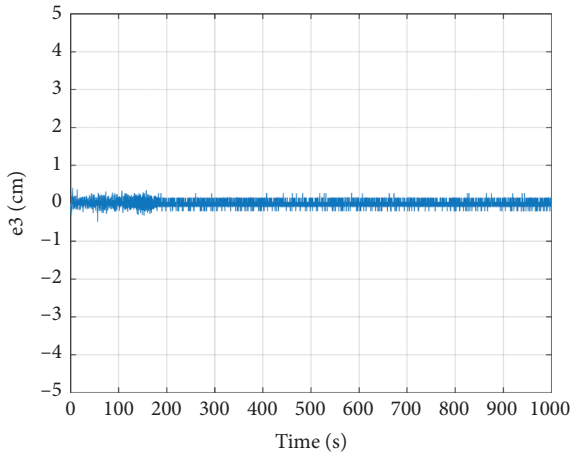

(a)

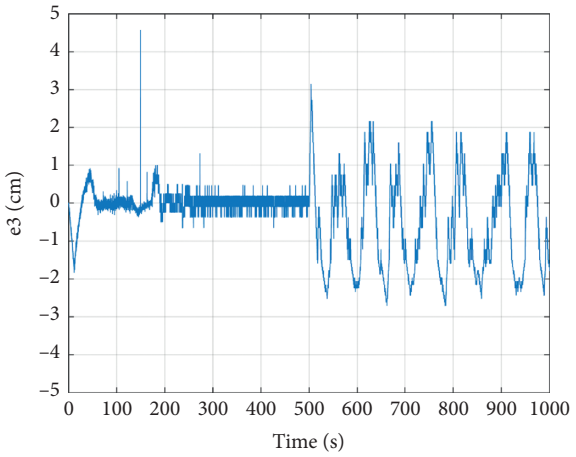

(b)

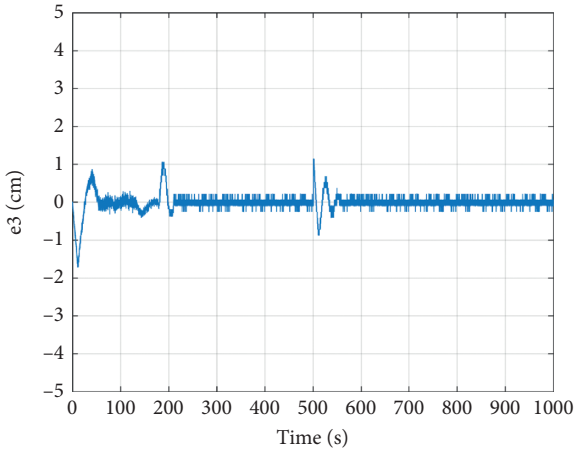

(c)

Figure 15: Tracking error e3.

Table 3: Performance tracking comparison.

	Fault-free case	FTC without parameters adjustment	FTC with parameters adjustment
e1	0.1266	0.5183	0.1422
e3	0.1002	1.0762	0.1491

6. Conclusion

In this study, a bank of high gain observers has been considered for FDI application in a 3TS. After sensor detection and isolation, fault accommodation is applied to ensure the reference tracking aim. For preserving the same performance as the safe mode, a controller parameters adjustment is also proposed. Experimental results are given for the validation of our approach.

This work can be extended to reach simultaneous sensor and actuator faults by using unknown input observers. The performance of the controller feedback can be improved using a filtered high gain observer, which ensures a good state estimation, even in the case of noisy measurements.

Data Availability

The data used to support the findings of this study are available from the corresponding author upon request.

Conflicts of Interest

The authors declare that they have no conflicts of interest.

References

[1] R. J. Patton, "Fault tolerant control": the 1997 situation survey," in *Proceedings of the IFAC SAFEPROCESS'97*, vol. 2, pp. 1033–1055, Hull, UK, August 1997.

[2] R. Isermann, "Model-based fault detection and diagnosis – status and applications," *Annual Review of Control*, vol. 29, pp. 71–85, 2005.

[3] M. Kordestani, M. Saif, M. E. Orchard, R. Razavi-Far, and K. Khorasani, "Failure prognosis and applications-A survey of recent literature," *IEEE Transactions on Reliability*, vol. 99, pp. 1–21, 2019.

[4] J. Chen and R. J. Patton, *Robust Model-Based Fault Diagnosis for Dynamic Systems*, Kluwer Academic Publisher, London, UK, 1999.

[5] S. Simani, C. Fantuzzi, and R. J. Patton, *Model-based Fault Diagnosis in Dynamic Systems Using Identification Techniques*, Springer, London, UK, 2003.

[6] W. Yan-Feng, W. Pei-Liang, L. Zu-Xin, and C. Hui-Ying, "Fault-tolerant control for networked control systems with limited information in case of actuator fault," *Mathematical Problems in Engineering*, vol. 2015, Article ID 785289, 7 pages, 2015.

[7] W. Yan-feng, "Robust fault detection for networked control systems with markov time-delays and data packet loss in both S/C and C/A channels," *Mathematical Problems in Engineering*, vol. 2019, Article ID 4672862, 11 pages, 2019.

[8] M. Kordestani, K. Salahshoor, A. A. Safavi, and M. Saif, "An adaptive passive fault tolerant control system for a steam turbine using a PCA based inverse neural network control strategy," in *Proceedings of the 2018 World Automation Congress (WAC)*, vol. 40–45, IEEE, Washington, USA, June 2018.

[9] M. Kordestani, A. A. Safavi, N. Sharafi, and M. Saif, "Fault tolerant control of rhine-meuse delta water system: a performance assessment based approach," in *Proceedings of the 5th International Conference on Power Generation Systems and Renewable Energy Technologies (PGSRET)*, Istanbul, Turkey, August 2019.

[10] F. Kimmich, A. Schwarte, and R. Isermann, "Fault detection for mordern diesel engines using signal-and process modelbased methods," *Control Enginerering Practice*, vol. 13, pp. 189–203, 2005.

[11] L. Min, Z. Zuo, H. Liu, C. Liuand, and B. Zhu, "Adaptive fault tolerant control for trajectory tracking of a quadrotor helicopter," *Transactions of the Institute of Measurement and Control*, vol. 40, no. 12, pp. 3560–3569, 2018.

[12] F. Boem, A. J. Gallo, D. M. Raimondo, and T. Parisini, "Distributed fault-tolerant control of large-scale systems: an active fault diagnosis approach," *IEEE Transactions on Control of Network Systems*, vol. 7, no. 1, 2020.

[13] Z. Zhao, Y. Yang, S. X. Ding, and L. Li, "Fault-tolerant control for systems with model uncertainty and multiplicative faults," *IEEE Transactions on Systems, Man, and Cybernetics: Systems*, vol. 50, no. 2, 2020.

[14] H. Qian, Y. Peng, and M. Cui, "Adaptive observer-based fault-tolerant control design for uncertain systems," *Mathematical Problems in Engineering*, vol. 2015, Article ID 429361, 16 pages, 2015.

[15] F. Chen and M. Dunnigan, "Comparative study of a sliding-mode observer and kalman filters for full state estimation in an induction machine," in *IEE Proceedings Electric Power Applications*vol. 149, pp. 53–64, IET, 2002.

[16] A. Mesbah, A. E. M. Huesman, H. J. M. Kramer, and P. M. J. Van Den Hof, "A comparison of nonlinear observers for output feedback model-based control of seeded batch crystallization processes," *Journal of Process Control*, vol. 21, no. 4, pp. 652–666, 2011.

[17] E. M. Cimpoesu, B. D. Ciubotaru, and D. Stefanoiu, "fault detection and diagnosis using parameter estimation with recursive least squares," in *Proceedings of the 2013 19th International Conference on Control Systems and Computer Science*, pp. 18–23, Bucharest, Romania, May 2013.

[18] M. Zhong, T. Xue, Y. Song, S. X. Ding, and E. L. Ding, "Parity space vector machine approach to robust fault detection for linear discrete-time systems," *IEEE Transactions on Systems, Man, and Cybernetics: Systems*, vol. 51, 2018.

[19] Y. Li and G. Yang, "Fuzzy adaptive output feedback fault-tolerant tracking control of a class of uncertain nonlinear systems with nonaffine nonlinear faults," *IEEE Transactions on Fuzzy Systems*, vol. 24, 2016.

[20] V. Dardinier-Maron, F. Hamelin, and H. Noura, "A fault-tolerant control design against major actuator failures: application to a three- tank system," in *Proceedings of the 38 th Conference on Decision and Control*, Phoenix, AZ, USA, August 1999.

[21] H. Noura, D. Theilliol, and D. Sauter, "Actuator fault-tolerant control design: demonstration on a three-tank-system," *International Journal of Systems Science*, vol. 31, no. 9, pp. 1143–1155, 2000.

[22] L. F. Mendoca, J. M. C Sousa, and J. M. G. Sa Da Costa, "Fault tolerant control of a three tank Benchmark using weigted predictive control," in *Proceedings of the Foundations of Fuzzy Logic and Soft Computing, 12th International Fuzzy Systems Association World Congress, IFSA 2007*, vol. 4529, pp. 732–742, Cancun, Mexico, June 2007.

[23] N. Orani, A. Pisano, and E. Usai, "Fault detection and reconstruction for a three-tank system via high-order sliding-mode observer," in *Proceedings of the 18th IEEE International Conference on Control Applications Parts of 2009 IEEE Multi-Conference on Systems and Control Saint Petersburg*, pp. 1714–1719, Saint Petersburg, Russia, July 2009.

[24] D. Theilliol, H. Noura, and J.-C. Ponsart, "Fault diagnosis and accommodation of a three-tank system based on analytical redundancy," *ISA Transactions*, vol. 41, no. 3, pp. 365–382, 2002.

[25] M. Amor, T. Ladhari, S. Hadj Said, and F. M'Sahli, "Hardware implementation of actuator fault estimation applied to a hydrographic plant," in *Proceedings of the 19th International Conference on Sciences and Techniques of Automatic Control and Computer Engineering (STA)*, Sousse, Tunisia, March 2019.

[26] M. Amor, T. Ladhari, S. Hadj Said, and F. M'Sahli, "Actuator fault-tolerant control applied to three-tank system," *Mathematical Problems in Engineering*, vol. 2020, Article ID 8514049, 9 pages, 2020.

[27] D. H. Zhou, G. Z. Wang, and S. X. Ding, "Sensor fault tolerant control of nonlinear systems with application to a three-tank-system," *IFAC Proceedings Volumes*, vol. 33, no. 11, pp. 789–794, 2000.

[28] Y. Yang, L. Li, and S. X Ding, "A control-theoretic study on Runge-Kutta methods with application to real-time fault-tolerant control of nonlinear systems," *IEEE Transactions on Industrial Electronics*, vol. 62, no. 6, pp. 3914–3922, 2015.

[29] M. Amor, T. Ladhari, S. Hadj Said, and F. M'Sahli, "On-line continuous-discrete time observer for three-tank system," in *Proceedings of the 15th International Multi-Conference on Systems, Signals & Devices (SSD)*, Hammamet, Tunisia, March 2018.

[30] M. Hou, Y. S. Xiong, and R. J. Patton, "Observing a three-tank system," *IEEE Transactions on Control Systems Technology*, vol. 13, no. 3, pp. 478–484, 2005.

[31] M. Hou, Y. S. Xiong, and R. J. Patton, *Observer Design for a Three Tank System*, The 15thTriennial Word Congress, Barcelona, Spain, 2002.

Hindawi
Mathematical Problems in Engineering
Volume 2021, Article ID 8853441, 15 pages
https://doi.org/10.1155/2021/8853441

Research Article

Adaptive Observer-Based Sliding Mode Control for a Two-Wheeled Self-Balancing Robot under Terrain Inclination and Disturbances

Ines Jmel,[1] Habib Dimassi ,[1,2] Salim Hadj-Said,[1] and Faouzi M'Sahli[1]

[1]*University of Monastir, Ecole Nationale d'Ingénieurs de Monastir, LAS2E, Monastir 5019, Tunisia*
[2]*University of Sousse, Institut Supérieur des Sciences Appliquées et de Technologie de Sousse, Sousse, Tunisia*

Correspondence should be addressed to Habib Dimassi; dimassihabib2013@gmail.com

Received 3 September 2020; Revised 28 November 2020; Accepted 24 December 2020; Published 7 January 2021

Academic Editor: Raúl Villafuerte-Segura

This paper investigates an output feedback sliding mode control scheme for a two-wheeled self-balancing robot under terrain inclination and disturbances. First of all, an adaptive high-gain observer is designed for the robot to estimate, simultaneously, the unmeasured states and the unknown terrain inclination angle which appears nonlinearly in the dynamics of the wheeled robot, using the only measured linear and angular positions. Then, the estimated states and the reconstructed unknown inclination angle are used by an appropriate continuously implemented sliding mode controller whose the design is based on the boundary layer approximation approach to reduce the chattering phenomenon. The objective of the proposed robust controller is to ensure the tracking control of the two-wheeled robot despite the unknown terrain inclination and the presence of friction disturbances. The stability of the adaptive observer-based output feedback system is established through a Lyapunov analysis, and it is inspired from sliding modes theory. Numerical simulations results highlight the effectiveness of the proposed tracking control scheme applied on two-wheeled self-balancing robot subject to terrain inclination even in the presence of unavailable disturbances.

1. Introduction

The two-wheeled self-balancing robot is an exceptional type of wheeled mobile robots which has been broadly applied in many areas such as hostile terrain, agriculture, and industry. The hard nonlinearity and the underactuation of these systems make the trajectory tracking control a challenging research problem [1, 2]. Some classical control strategies such as backstepping [3, 4] and adaptive controllers [5] are treated by several researchers to control the movement of the wheeled inverted pendulum. In [6, 7], the backstepping technique is combined with an adaptive controller to ensure the stabilization and the convergence of the tracking error. The authors in [8] represented a combination between H_∞ and backstepping techniques to stabilize tracking errors under bounded disturbances. In [9], a Kalman filter-based optimal (H-infinity) controller was proposed for the linearized model of the wheeled pendulum. Moreover, Fuzzy systems had attested their effectiveness as a rigorous method in robotics and control applications. In [10], a fuzzy control scheme was proposed for a two-wheeled inverted pendulum. Also, in [11], a nonsingleton general type-2 fuzzy logic controller was designed for an underactuated mobile two-wheeled self-balancing robot. In [12, 13], an adaptive fuzzy control design was performed for dynamic balance and stable tracking of desired trajectories for wheeled inverted pendulum in the presence of uncertainties.

In addition, a PD-PI controller based on Kalman filter algorithm was designed in [14] to stabilize a two-wheeled self-balancing robot while avoiding acute and dynamic obstacles in the sensed environment. Furthermore, common networked control strategies have been implemented in [15] for stabilizing a two-wheeled inverted pendulum robot over a wireless channel despite time-varying delays and paket loss. Also, a new feedback reinforcement learning method was proposed in [16] to solve the LQR control problem for the two-wheeled self-balancing robot. The suggested method

scheme was completely online and did not require any knowledge of the system parameters.

In any formulation of a control problem, the mathematical model developed to establish the control law does not reflect the actual process exactly. These differences may be due to, for example, the direct approximation of complex process behaviors and the variations of system parameters or unmodeled dynamics, especially for systems which are characterized by an inherent instability, nonlinearity, and underactuation like the two-wheeled self-balancing robots. Nevertheless, it must be ensured that, despite all these uncertainties, the resulting control should reach the predefined objectives. For this reason, it is necessary to synthesize a robust controller able to overcome this problem. Sliding mode control is an efficient robust control method which has the advantage to be insensitive to disturbances and characterized by the finite-time convergence property and the simplicity of its implementation [17]. In this context, a sliding mode controller was developed, in [18, 19], for the control of underactuated systems. In [20], the authors discussed the control problem and gave design technology of the sliding mode controller for the two-wheeled mobile robot with lower center of gravity. The validity of the proposed controller was analyzed through numerical simulations. Likewise, the authors in [21, 22] developed a sliding mode controller for nonholonomic mobile robot in order to realize a tracking trajectory in the presence of model uncertainties, frictional disturbances, and measurement noise. Moreover, a novel LMI-based sliding mode controller has been proposed in [23] for the control of a class of underactuated systems which are featured as in cascade form with external disturbances. In [24], an optimization-based nonlinear controller was designed for trajectory tracking for nonholonomic wheeled mobile robots. In the same context, a fast terminal sliding mode strategy has been designed in [25] for finite-time tracking control of nonholonomic systems. The efficiency of this method was illustrated to apply on a wheeled mobile robot as a benchmark of a nonholonomic system. Besides, two sliding mode controllers were designed in [26] to control the balancing and the steering movement of a two-wheeled inverted pendulum robot with friction compensation. In addition a sliding mode control was designed in [27] to track the smooth curved welding path. In [28], a sliding mode velocity control was proposed for mobile wheeled inverted pendulum systems. More recently, in [29], the authors proposed a sliding mode controller (SMC) associated to a high-order disturbance observer (HODO) for mobile wheeled inverted pendulum (MWIP) systems. The stability of the closed loop system and the convergence of the estimation errors have been proved with a Lyapunov analysis, and theoretical results have been also validated experimentally. Motivated by the incontestable advantages of the latter robust control method, we propose, in this paper, a continuously implemented sliding mode controller for the two-wheeled self-balancing robot where the boundary layer approximation method is adopted in the designed controller to reduce the well-known chattering phenomenon often linked to the use of discontinuous controllers.

For outdoor applications, mobile robots have to face more challenges such as uneven, sloped, or rough terrain surface. This invites researchers to design controllers in order to control the stability of the two-wheeled self-balancing robot moving on an inclined terrain [30–33]. In [34], the authors had shown the effect of terrain inclination on the performance and stability region of two-wheeled mobile robots. Moreover, they established and analyzed the dynamic model on slope of the treated robot. The linear quadratic regulation (LQR) method was used to design a linear controller whose efficiency was presented through simulation results. In [35], a disturbance observer was used to estimate the handling force and the slope angle when getting on and off a human-riding wheeled inverted pendulum vehicle. A sliding mode control was used in [33] for a two-wheeled inverted pendulum mobile robot driving on uniform slopes. Also, to eliminate the influence of the inclined plane considered as external disturbances, the authors had developed, in [36], an active disturbance rejection control scheme for two-wheeled self-balancing robots which achieved control aims even in the presence of a slope. However, most of mentioned works had resorted to linearization in order to design controller. To deal with problems related to rough terrain, wheeled robots should consistently recognize the current situation of the surface in order to preserve wheel traction and battery energy. The solution that we adopt is to develop an adaptive observer to estimate unmeasured states and the unknown terrain inclination angle.

In fact, specific attention has been booked to the design of adaptive observers in order to ensure, under specific condition, a joint estimation of unmeasured states and system parameters with exponential convergence. Various works had focused to design an observer for a linear system as it was improved in [37]. Others were interested in nonlinear systems with linear parameterization as in [38, 39] and nonlinear parameterization as in [40], where the authors had developed an adaptive observer for the nonlinearly parameterized class of nonlinear systems. The exponential convergence is achieved under certain persistent condition by the adjustment of the gain observer. Simulation results highlighted the effectiveness of the developed observer. More recently, the robustness of the latter adaptive observer has been improved in [41] by adding a sliding mode term. The proposed adaptive observer in [41] was also combined with an auxiliary high gain observer to satisfy the so-called observer matching condition and applied for the inverted pendulum system to solve the problem of simultaneous estimation of states, unknown parameter (mass variation parameter), and friction disturbances with experimental validation.

In this context, since the inclination parameter appears nonlinearly in the dynamics of the self-balancing robot, we adopt the adaptive estimation approach developed in [40] to deal with terrain inclination.

Then, the estimated states and parameters are combined with the continuously implemented sliding mode control law in order to provide a robust adaptive observer-based sliding mode controller. The convergence of the estimated tracking error is established through the Lyapunov analysis.

In summary, the two-wheeled self-balancing robot is a benchmark of underactuated system. The hard nonlinearity of this system makes its control an interesting issue.

For outdoor application, the two-wheeled self-balancing robot is always faced to several phenomenons such as

sloping and skidding that can cause a loss of system stability. Hence, motivated by the advantages of the sliding mode control as a robust controller and to deal with the variation of terrain inclination, we suggest, in this paper, an adaptive observer-based sliding mode controller for a two-wheeled self-balancing robot subject to terrain inclination. From a theoretical viewpoint, the demonstration of the convergence of the adaptive observer with nonlinear parameterization and in the presence of bounded disturbance will be firstly established based on a Lyapunov analysis; then, the analysis of the stability of the output feedback tracking control system composed of the adaptive observer and the continuously implemented sliding mode controller will be carried out based on sliding modes theory. In summary, the main contributions of this paper from both theoretical and application viewpoints are given as follows:

(i) Adaptive estimation of the unmeasured states and the unknown terrain inclination parameter which appears nonlinearly in the dynamics of the two-wheeled self-balancing robot in the presence of disturbances

(ii) Design of the robust adaptive output feedback controller (adaptive observer + sliding mode controller) for the tracking control of the two-wheeled robot despite the unknown terrain inclination and friction disturbances

(iii) Proof of the convergence of the designed adaptive observer and stability analysis of the closed-loop system based on the Lyapunov analysis

The remainder of the paper is organized as follows. The next section presents the problem statement and preliminaries. A robust adaptive observer-based sliding mode control, as well as the convergence of the tracking control scheme, is analyzed in Section 3. Simulation results through *Matlab/Simulink* assert the performance of the proposed method in Section 4. Finally, we conclude the paper with conclusive remarks in Section 5.

1.1. Notations. $|\cdot|$ represents the euclidean norm for vectors and induced norm for matrices. I_n is an identity matrix with $n \times n$ dimension. $0_{n\times m}$ is a null matrix with n rows and m columns. $\lambda_{\max}(M)$ and $\lambda_{\min}(M)$ denote, respectively, the maximum and the minimum eigenvalue of M. $\operatorname{diag}(M_1, \ldots, M_n)$ represents the block-diagonal matrix $= \begin{pmatrix} M_1 & 0 & \cdots & 0 \\ 0 & \ddots & \ddots & \vdots \\ \vdots & \ddots & \ddots & \vdots \\ 0 & \cdots & 0 & M_n \end{pmatrix}$, where $M_1, \ldots, M_n$ are square matrices. $R^+ \in \mathbb{R}^{n\times m}$ denotes the pseudoinverse (generalized inverse) of a matrix $R \in \mathbb{R}^{m\times n}$. That is, R^+ is a matrix such that $RR^+R = R$ and $R^+RR^+ = R^+$.

2. Context and Problem Statement

2.1. Model of a Two-Wheeled Self-Balancing Robot. The two-wheeled self-balancing robot is an underactuated system, and it has fewer actuators (2 actuators) than degrees of freedom (3 degree of freedom). The dynamics of this robot is similar to that of a pendulum cart. In fact, the two-wheeled torques C_L and C_R are transformed, using a decoupling unit, into two torques C_δ and C_ψ. The torque C_ψ supervises both the robot position and the pitch angle. It ensures the translation along the x-axis while preserving the upright position, whereas the torque C_δ controls the right and left rotation of the robot which ensures the desired yaw trajectory.

Referring to [42–44], the model of the two-wheeled self-balancing robot is as follows:

$$\begin{aligned} \dot{x}_1 &= x_2, \\ \dot{x}_2 &= F(x,\rho) + G(x,\rho)u + d(t), \end{aligned} \tag{1}$$

where $x_1 = [x, \psi, \delta]^T$, $x_2 = [\dot{x}, t\dot{\psi}n, q\dot{\delta}]^T$, and $x = [x_1, x_2]^T$. $u = [C_\psi, C_\delta]^T$ is the control input vector. x, ψ, and δ represent, respectively, the linear displacement of the chassis, the pitch angle, and the yaw angle. $d(t) = [d_1(t), d_2(t), d_3(t)]^T$ represents the disturbance vector. $d(t)$ is assumed to be bounded and differentiable with respect to time. For each $t \geq 0$, $|d(t)| \leq \zeta$, where ζ is a positive number.

$G(x,\rho) = [g_{11}(x,\rho), 0; g_{21}(x,\rho), 0; 0, g_{32}(x,\rho)]$ and $F(x,\rho) = [f_1(x,\rho), f_2(x,\rho), 0]^T$, where

$$\begin{aligned} f_1(x,\rho) &= \frac{1}{\overline{B}}\left[M_p^2L^2R^2g\sin(\psi)\cos(\psi+\alpha) + \left(M_pL^2 + J_p\right)\left(M_p + 2M_r\right)gR^2\sin(\alpha) - \left(M_pL^2 + J_p\right)M_pLR^2\dot{\psi}^2\sin(\psi+\alpha)\right]f_2(x,\rho) \\ &= \frac{1}{\overline{B}}\left[M_p^2L^2R^2\dot{\psi}^2\sin(\psi+\alpha)\cos(\psi+\alpha) - \left(2M_rR^2 + M_pR^2 + 2J_r\right)M_pgL\sin(\psi) + M_p\left(M_p + 2Mr\right)LR^2g\sin(\alpha)\cos(\psi+\alpha)\right], \\ g_{11}(x,\rho) &= \frac{-2}{\overline{B}}\left[\left(M_pL^2 + J_p\right)R + M_pLR^2\cos(\psi+\alpha)\right], \\ g_{21}(x,\rho) &= \frac{-2}{R\overline{B}}\left[M_pLR\cos(\psi+\alpha) + \left(2M_rR^2 + M_pR^2 + 2J_r\right)\right], \\ g_{32}(x,\rho) &= \frac{2D}{\left[\left(M_rR + (J_r/R)\right)D^2 + 2J_\delta R\right]} \text{ with } \overline{B} = M_p^2L^2R^2\cos^2(\psi+\alpha) - \left(2M_rR^2 + M_pR^2 + 2J_r\right)\left(MpL^2 + Jp\right). \end{aligned} \tag{2}$$

J_p is the moment of inertia of the chassis with respect to the z-axis, J_δ is the moment of inertia of the chassis with respect to the y-axis, and J_r is the moment of inertia of the wheel. M_p is the total mass of the robot. D is the lateral distance between the contact patches of the wheels, R is the radius of the wheels, and M_r is its mass.

$\rho = \alpha$ is the angle of terrain inclination, which is assumed unknown and which will be estimated later through an adaptive observer.

2.2. Problem formulation. The two-wheeled self-balancing robot is a nonlinear MIMO underactuated system; thus, it is very challenging to keep balance when it climbs or descends on a slope and, especially, in the presence of nonmeasurable disturbances. In this work, the considered problem consists in designing an output feedback sliding mode controller for the self-balanced robot model subject to unknown disturbances, to generate a robust command for going up and down the slope. In case of going up the slope, the controller generates an acceleration of the gear-motor driving the wheels, whereas in the going down case, a deceleration is performed for the safety of the vehicle. Such behavior is required for ensuring the global engine stability. Despite the importance of the studied issue, according to our knowledge, theoretical developments dealing with the terrain inclination and the disturbances simultaneously for the nonlinear model of the two-wheeled self-balancing robot are infrequent.

In addition, it is well known that the dynamics of underactuated systems such as the two-wheeled self-balancing robot may contain hard nonlinearities and nonholonomic constraints which make the control of these systems an open and interesting issue. These features should be considered during control design in order to establish a robust controller which guarantees the system performance even under different operating conditions. Sliding mode control is an efficient robust controller, thanks to its effectiveness for dealing with uncertain and disturbed systems. Persuaded by its advantages, we adopt this popular technique to ensure the tracking objectives.

Furthermore, when a mobile robot moves on a trajectory, several phenomenons such as sloping and skidding can cause a loss of wheel traction and battery energy, as well as system stability. Thus, having an instantaneous knowledge of the terrain inclination angle could be lucrative to keep the performance of the adopted control law.

The solution to deal with this problem is to design an adaptive observer to estimate conjointly unmeasured states $(\dot{x}, \dot{\psi}, \dot{\delta})$ and the angle of terrain inclination which represents the unknown parameter $\rho = \alpha$. That is,

$$\begin{aligned} \lim_{t\longrightarrow\infty} |x(t) - \widehat{x}(t)| &= 0, \\ \lim_{t\longrightarrow\infty} |\rho(t) - \widehat{\rho}(t)| &= 0. \end{aligned} \tag{3}$$

Then, the estimated states $\widehat{x}(t)$ and the reconstructed unknown parameter $\widehat{\rho}(t)$ generated by the adaptive observer are to be injected into the sliding mode control law in order to perform the following trajectory tracking aims:

$$\lim_{t\longrightarrow\infty} \left|x(t) - x_r(t)\right| = 0, \tag{4}$$

where $x_r(t)$ is the reference trajectory.

3. Adaptive Observer-Based Sliding Mode Control for the Two-Wheeled Self-Balancing Robot

In this section, we present first the adaptive observer design method for the wheeled robot, and then, we combine it with the sliding mode controller whose objective is to ensure tracking control despite the presence of unknown terrain inclination and disturbances. Before describing the adaptive observer-based sliding mode control system, the following assumption must be taken into account.

Assumption 1. For any bounded control input u, the state x is assumed bounded. Moreover, the unknown parameter ρ is also assumed to be bounded and slowly varying, that is, $\dot{\rho}(t) = 0$, almost everywhere.

It is to be noticed that some physical autonomous systems such as chaotic systems verify the boundedness assumption of the trajectories naturally (Assumption 1). In the case of controlled systems (nonautonomous systems) which include the two-wheeled self-balancing robot considered in this paper, the boundedness of the states may be guaranteed by synthesizing an appropriate bounded control input. We notice also that assuming the unknown angle inclination parameter $\rho(t) = \alpha(t)$ is usually satisfied in practice in the self-balancing robot system under terrain inclination, which is trivially reasoning from a physical viewpoint.

By considering Assumption 1, let $(u, x, \rho) \in (U, X, \Theta)$, where $U \subset \mathbb{R}^2$, $X \subset \mathbb{R}^6$, and $\Theta \subset \mathbb{R}$ are three compact sets.

For the two-wheeled self-balancing robot system, the nonlinearities $F(x, \rho)$ and $G(x, \rho)$ are just once continuously differentiable but not globally Lipschitz. In such a case, we use, under Assumption 1, the Lipschitz prolongation approach in order to build prolongations $\widetilde{F}$ and $\widetilde{G}$ of the nonlinearities F and G using saturation functions [40, 45], where $\widetilde{F}$ and $\widetilde{G}$ are globally Lipschitz and defined as $\widetilde{F}(x, \rho) = F(\sigma(x), \sigma^\rho(\rho))$ and $\widetilde{G}(x, \rho) = G(\sigma(x), \sigma^\rho(\rho))$, where $\sigma\colon \mathbb{R}^n \longrightarrow X, x \mapsto \sigma(x)$ and $\sigma^\rho\colon \mathbb{R} \longrightarrow \Theta, \rho \mapsto \sigma^\rho(\rho)$ are smooth bounded saturation functions such that $\sigma(x) = x$ and $\sigma^\rho(\rho) = \rho$ for all $x \in X$ and $\rho \in \Theta$.

In this way, the trajectories of the wheeled robot system (46) coincide with those of the following system:

$$\begin{aligned} \dot{x}_1 &= x_2, \\ \dot{x}_2 &= \widetilde{F}(x, \rho) + \widetilde{G}(x, \rho)u + d(t), \end{aligned} \tag{5}$$

where $\widetilde{G}(x, \rho) = [\widetilde{g}_{11}(x, \rho), 0; \widetilde{g}_{21}(x, \rho), 0; 0, \widetilde{g}_{32}(x, \rho)]$ and $\widetilde{F}(x, \rho) = [\widetilde{f}_1(x, \rho), \widetilde{f}_2(x, \rho), 0]^T$ are the Lipschitz extension functions of $G(x, \rho)$ and $F(x, \rho)$, respectively.

In the rest of the paper, we will rather focus on system (5) for the design of our proposed adaptive observer-based tracking control approach for the considered two-wheeled self-balancing robot.

3.1. Adaptive Observer for States and Terrain Inclination Angle Estimation. Adaptive observer design represents a popular method for states and unknown parameter estimation. Since the unknown terrain inclination angle appears nonlinearly in the dynamic of the two-wheeled self-balancing robot and given the triangular structure of our system, we adopt the adaptive observer treated in [40] and we recall, in this section, the main features of this estimation approach.

Actually, the two-wheeled self-balancing robot system (5) is included in the class of systems considered in [40] and may be written in the following form:

$$\begin{cases} \dot{x} = Ax + \widetilde{f}(x,\rho) + \widetilde{g}(x,\rho)u + B\,d(t), \\ y = Cx = x_1, \end{cases} \tag{6}$$

where $A = \begin{bmatrix} 0_3 & I_3 \\ 0_3 & 0_3 \end{bmatrix}$, $B = \begin{bmatrix} 0_3 \\ I_3 \end{bmatrix}$, and $C = [\, I_3, 0_3 \,]$. $\widetilde{g}(x,\rho) = \begin{bmatrix} 0_{3\times 2} \\ \widetilde{G}(x,\rho) \end{bmatrix}$, $\widetilde{f}(x,\rho) = \begin{bmatrix} 0_{3\times 1} \\ \widetilde{F}(x,\rho) \end{bmatrix}$, and $x = \begin{bmatrix} x_1 \\ x_2 \end{bmatrix}$.

Conforming to [40], the adaptive observer developed for system (6) is given by

$$\begin{cases} \dot{\widehat{x}} = A\widehat{x} + \widetilde{g}(\widehat{x},\widehat{\rho})u + \widetilde{f}(\widehat{x},\widehat{\rho}) - \theta\Delta_\theta^{-1}\left(\overline{S}^{-1} + Y(t)P(t)Y^T(t)\right)C^TK(C\widetilde{x}), \\ \dot{\widehat{\rho}}(t) = -\theta P(t)Y^T(t)C^TK(C\widetilde{x}), \\ \dot{Y}(t) = \theta\left(A - \overline{S}^{-1}C^TC\right)Y(t) + \Delta_\theta\dfrac{\partial\widetilde{f}}{\partial\rho}(\widehat{x},\widehat{\rho}) + \Delta_\theta\dfrac{\partial\widetilde{g}}{\partial\rho}(\widehat{x},\widehat{\rho})u, \quad \text{with } Y(0) = 0, \\ \dot{P}(t) = -\theta P(t)Y^T(t)C^TCY(t)P(t) + \theta P(t), \quad \text{with } P(0) = P^T(0) > 0, \end{cases} \tag{7}$$

where $\widehat{x} = \begin{bmatrix} \widehat{x}_1 \\ \widehat{x}_2 \end{bmatrix}$; $\Delta_\theta = \mathrm{diag}[I_3, 1/\theta I_3]$, where $\theta > 0$ is a real number, $\widetilde{x} = \widehat{x} - x$, and $\overline{S}$ is the unique solution of the following algebraic Lyapunov equation:

$$\overline{S} + A^T\overline{S} + \overline{S}A - C^TC = 0, \tag{8}$$

where $\overline{S}$ is the symmetric positive definite (SPD) and the matrix $(A - \overline{S}^{-1}C^TC)$ is Hurwitz. K is a design matrix of appropriate dimensions to be determined later.

For the convergence of the unknown parameters estimation errors, the following assumption is required.

Assumption 2. For any trajectory $(\widehat{x}, t\widehat{\rho}) \in X \times \Omega$, the matrix $CY(t)$ must satisfy the condition of persistent excitation, and it means: $\exists\delta_1, \delta_2 > 0; \exists T > 0; \forall t \geq 0$: $\delta_1 I_m \leq \int_t^{t+T} Y^T(t)C^TCY(\tau)\mathrm{d}\tau \leq \delta_2 I_m$.

The persistency of excitation is a classical condition usually adopted in the literature of adaptive estimation. It is behind the asymptotic stability and parametric convergence, and it signifies that the studied system is sufficiently rich in frequencies.

Proposition 1. *Consider the system (6) subject to the unknown parameter $\rho(t)$ and the disturbance $d(t)$, together with the adaptive observer (7), under Assumptions 1 and 2. Then, the state estimation error $\widetilde{x} = \widehat{x} - x$ and the adaption error $\widetilde{\rho} = \widehat{\rho} - \rho$ converge to a small compact set whose radius may be reduced by choosing sufficiently high values of the design parameter θ.*

Proof. The proof of Proposition 1 is mainly based on the proof of Theorem 3.1 in [40] while taking into account the presence of the disturbance $d(t)$. We consider the Lyapunov function

$$W(t) = \Omega(t)^T\overline{S}\Omega(t) + \widetilde{\rho}^T(t)P^{-1}\widetilde{\rho}(t), \tag{9}$$

where

$$\begin{cases} \Omega(t) = \overline{x}(t) - Y(t)\widetilde{\rho}(t), \\ \overline{x}(t) = \Delta_\theta(\widehat{x} - x). \end{cases} \tag{10}$$

Proceeding as in Theorem 3.1 in [40] and taking into account the presence of the perturbation term $d(t)$, one may obtain

$$\begin{aligned} \dot{W} &\leq -2\mu W - 2\Omega^T\overline{S}\Delta_\theta B\,d(t) \\ &\leq -2\mu W + 2|B|\zeta\sqrt{\lambda_{\max}(\overline{S})}\theta^{-1}\sqrt{W(\Omega)} \\ &\leq -\mu W - \mu\sqrt{W(\Omega)}\left[\sqrt{W(\Omega)} - 2|B|\zeta\mu^{-1}\sqrt{\lambda_{\max}(\overline{S})}\,\theta^{-1}\right], \end{aligned} \tag{11}$$

where we recall that ζ is a positive constant such that, for all $t \geq 0$, $|d(t)| \leq \zeta$ and

$$\mu = \frac{1}{2}(\theta - c_1)\left(1 - \frac{c_2}{2\sqrt{\theta(\theta - c_1)}}\right), \tag{12}$$

where c_1 and c_2 are positive constants which depend on the upper bounds of the different bounded signals and on the minimal and maximal eigenvalues of the matrices $\overline{S}$ and P (see the proof of Theorem 3.1 in [40]).

Next, from the last inequality (11), we deduce that as long as $\sqrt{W(t)} \geq 2|B|\zeta\mu^{-1}\sqrt{\lambda_{\max}(\overline{S})}\theta^{-1}$, one has

$$\dot{W}(t) \leq -\mu W(t). \tag{13}$$

If $\sqrt{W(0)} \geq 2|B|\zeta\mu^{-1}\sqrt{\lambda_{\max}(\overline{S})}\theta^{-1}$, $\Omega(t)$ and $\tilde{\rho}(t)$ will decrease exponentially such that

$$W(t) \leq W(0)e^{-\mu t}. \tag{14}$$

Consequently, there exists a finite time T_a such that for all $t \geq T_a$,

$$\sqrt{W(t)} \leq 2|B|\zeta\mu^{-1}\sqrt{\lambda_{\max}(\overline{S})}\theta^{-1}. \tag{15}$$

We have

$$\frac{1}{\sqrt{2}}\sqrt{\lambda_{\min}(\overline{S})}|\Omega(t)| + \frac{1}{\sqrt{2}}\sqrt{\lambda_{\min}\left(P^{-1}\right)}|\tilde{\rho}(t)| \leq \sqrt{W(t)}. \tag{16}$$

Next, combining inequalities (15) and (16) and using (10), it may be deduced that the estimation error $\tilde{x}(t)$ and the adaptation error $\tilde{\rho}(t)$ converge to a compact set whose radius may be reduced by choosing a sufficiently large value of the design parameter θ.

Once the unmeasured states and the unknown parameter are reconstructed by the adaptive observer (6), the estimated signals are employed, in the next section, by the sliding mode control law in order to build an adaptive sliding mode controller. □

3.2. Adaptive Observer-Based Sliding Mode Control for the Two-Wheeled Self-Balancing Robot. In this section, we apply the sliding mode control on the two-wheeled self-balancing robot and we replace the unknown parameter $\rho = \alpha$ and the speed states $(\dot{x}, \dot{\phi}, \dot{\delta})$, which are not accessible to measurement by their estimates obtained from the proposed adaptive observer as it is denoted in Figure 1.

The problem of trajectory tracking consists to determine the control law u which insures the convergence of the state vector $x_1 = [x \ \psi \ \delta]^T$ to the reference vector $x_r = [x_r \ \psi_r \ \delta_r]^T$ with a tracking error on the first component of the state vector:

$$e = x_r - x_1. \tag{17}$$

Affected by the influence of terrain inclination α, the pitch angle ψ_r will not be identical to zero when the two-wheeled self-balancing robot becomes stable on the slope. In fact, ψ_r will become a constant ψ_{eq} which depends on α, and it is defined as [31]

$$\psi_{\text{eq}} = \arccos\left(\frac{-M_r R\sin(\alpha)}{M_p}\right) - \arccos\left(\frac{R\sin(\alpha)}{\sqrt{R^2\sin^2(\alpha) + L^2}}\right). \tag{18}$$

We select the sliding variables vector as follows:

$$\begin{aligned} S &= \lambda(x_r - x_1) + (\dot{x}_r - \hat{x}_2) \\ &= \lambda(x_r - x_1) + (\dot{x}_r - x_2) + x_2 - \hat{x}_2 \\ &= \lambda(x_r - x_1) + (\dot{x}_r - x_2) + \tilde{x}_2, \end{aligned} \tag{19}$$

where λ is a positive constant.

Inspired from sliding modes theory, we propose the following sliding mode controller incorporating the estimated states generated by the adaptive observer (7):

$$u = [\widetilde{G}(\hat{x}, t\hat{\rho})]^+ \left[\ddot{x}_r - \widetilde{F}(\hat{x}, t\hat{\rho}) + \lambda(\dot{x}_r - \hat{x}_2) - k\frac{S}{|S|}\right], \tag{20}$$

where k is a positive constant.

However, the presence of the discontinuous function, in the sliding mode control, gives rise to the well-known *chattering* phenomenon which represents the main disadvantage of sliding modes controllers. To overcome this problem, it is lucrative to transform the discontinuous function by a continuous one using the boundary layer approximation approach to eliminate the chattering phenomenon [46]. Then, we rather consider the following "continuously implemented sliding mode controller" instead of (20):

$$u = [\widetilde{G}(\hat{x}, t\hat{\rho})]^+ \left[\ddot{x}_r - \widetilde{F}(\hat{x}, t\hat{\rho}) + \lambda(\dot{x}_r - \hat{x}_2) + \frac{kS}{|S| + \varepsilon} + \beta S\right], \tag{21}$$

where $[\widetilde{G}(\hat{x}, t\hat{\rho})]^+$ represents the pseudoinverse matrix of $\widetilde{G}(\hat{x}, t\hat{\rho})$. β and ε are positive constants.

Before proving the convergence of the tracking error of the closed loop system, we show first, in the proof of the following theorem, that $S(t)$ converges to a compact set whose radius may be made as small as possible by adjusting the design parameters ε and β.

Theorem 1. *We consider the system (6) under the continuously implemented sliding mode control input (21) and incorporate the adaptive observer (7) such that Assumptions 1 and 2 are satisfied. Then, $S(t)$ is uniformly bounded with an upper bound which may be made arbitrarily small by reducing the design parameter ε and increasing the design parameter β.*

Proof. Let us start with an appropriate Lyapunov function:

$$V = \frac{1}{2}S^T S. \tag{22}$$

Differentiating this function and referring to (19), one obtains

$$\begin{aligned} \dot{V} &= S\dot{S} = S\left[\lambda(\dot{x}_r - x_2) + (\ddot{x}_r - \dot{x}_2) + \dot{\tilde{x}}_2\right] \\ &= S\left[\lambda(\dot{x}_r - x_2) + (\ddot{x}_r - \widetilde{F}(x,\rho) - G(x,\rho)u - d(t)) + \dot{\tilde{x}}_2\right] \\ &= S[\lambda(\dot{x}_r - x_2) + (\ddot{x}_r - \widetilde{F}(\hat{x}, t\hat{\rho}) - G(\hat{x}, t\hat{\rho})u - d(t)) + \dot{\tilde{x}}_2 \\ &\quad - \widetilde{F}(x,\rho) - \widetilde{G}(x,\rho)u + \widetilde{F}(\hat{x},\hat{\rho}) + \widetilde{G}(\hat{x},\hat{\rho})u]. \end{aligned} \tag{23}$$

Let

$$\eta(x, \hat{x}, \rho, \hat{\rho}) = -\widetilde{F}(x,\rho) - \widetilde{G}(x,\rho)u + \widetilde{F}(\hat{x},\hat{\rho}) + \widetilde{G}(\hat{x},\hat{\rho})u. \tag{24}$$

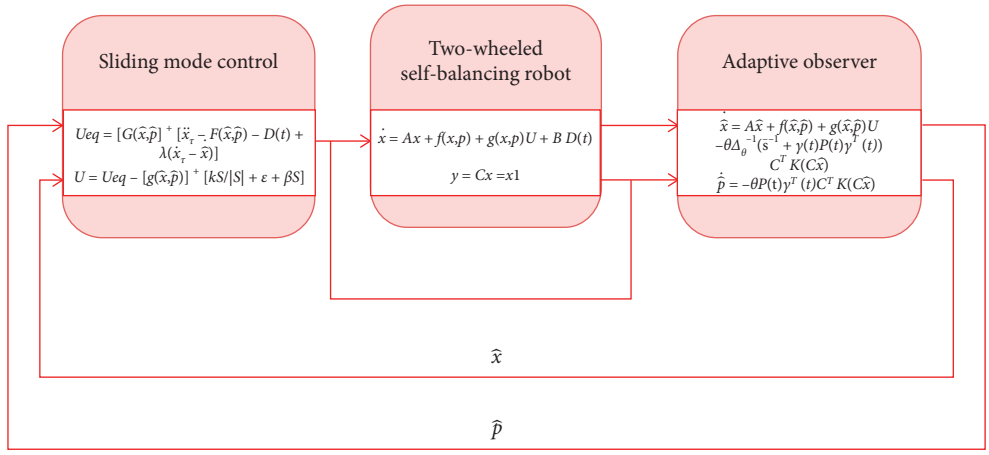

Figure 1: Synoptic diagram of the proposed control method.

Now, replacing the control input vector u by its expression described in (21), one has

$$\dot{V} = S\left[\eta(x,\hat{x},\rho,\hat{\rho}) - d(t) + \dot{\hat{x}}_2 - \lambda\tilde{x}_2 - \frac{kS}{|S|+\varepsilon} + \beta S\right]$$

$$= -\beta S^2 - \frac{k|S|^2}{|S|+\varepsilon} + \left[\dot{\tilde{x}}_2 - \lambda\tilde{x}_2 + \eta(x,\hat{x},\rho,\hat{\rho}) - d(t)\right]. \tag{25}$$

At this stage, it is needful to prove the boundedness of $\eta(x,\hat{x},\rho,\hat{\rho})$ and $\dot{\tilde{x}}_2$ in order to admit the convergence $S(t)$.

Let us first prove the boundedness of $\eta(x,\hat{x},\rho,\hat{\rho})$. We have

$$\eta(x,\hat{x},\rho,\hat{\rho}) = -\tilde{F}(x,\rho) - \tilde{G}(x,\rho)u + \tilde{F}(\hat{x},\hat{\rho}) + \tilde{G}(\hat{x},\hat{\rho})u. \tag{26}$$

This can be written as

$$\begin{aligned}\eta(x,\hat{x},\rho,\hat{\rho}) &= -\tilde{F}(x,\rho) + \tilde{F}(\hat{x},\rho) - \tilde{F}(\hat{x},\rho) - \tilde{G}(x,\rho)u \\ &\quad + \tilde{G}(\hat{x},\rho)u - \tilde{G}(\hat{x},\rho)u + \tilde{F}(\hat{x},\hat{\rho}) + \tilde{G}(\hat{x},\hat{\rho})u \\ &= -(\tilde{F}(x,\rho) - \tilde{F}(\hat{x},\rho)) - (\tilde{G}(x,\rho) - \tilde{G}(\hat{x},\rho))u \\ &\quad - (\tilde{F}(\hat{x},\rho) - \tilde{F}(\hat{x},\hat{\rho})) - (\tilde{G}(\hat{x},\rho) - \tilde{G}(\hat{x},\hat{\rho}))u.\end{aligned} \tag{27}$$

Tacking into account that $\tilde{F}(x,\rho)$ and $\tilde{G}(x,\rho)$ are Lipschitz with respect to x uniformly in ρ and $\tilde{F}(\hat{x},t\rho)$ and $\tilde{G}(\hat{x},t\rho)$ are Lipschitz with respect to ρ uniformly in $\hat{x}$, we can write that

$$\begin{aligned}|\eta(x,\hat{x},\rho,\hat{\rho})| &\le k_F|x-\hat{x}| + k_G|u||x-\hat{x}| \\ &\quad + k_{\rho 1}|\rho-\hat{\rho}| + k_{\rho 2}|u||\rho-\hat{\rho}| \\ &\le (k_F + k_u k_G)|\tilde{x}| + \left(k_{\rho 1} + k_{\rho 2}k_u\right)|\tilde{\rho}|,\end{aligned} \tag{28}$$

where k_F, k_G, k_u, $k_{\rho 1}$, and $k_{\rho 2}$ are a positive constants.

From the convergence of the adaptive observer [40], it follows that there exists a positive constant $k_\eta > 0$ such that

$$|\eta(x,\hat{x},\rho,\hat{\rho})| \le k_\eta. \tag{29}$$

Next, we need to show the boundedness of $\dot{\tilde{x}}_2$. To that end, conforming to [40], taking into account the presence of the disturbance term $d(t)$ and using (7), we have

$$\begin{aligned}\dot{\tilde{x}} &= A\tilde{x} + \tilde{f}(\hat{x},\hat{\rho}) + \tilde{g}(\hat{x},\hat{\rho})u - (\tilde{f}(x,\rho) + \tilde{g}(x,\rho)u) \\ &\quad - \theta\Delta_\theta^{-1}\bar{S}^{-1}C^T K(C\tilde{x}) + \Delta_\theta^{-1}Y\dot{\tilde{\rho}} - Bd(t).\end{aligned} \tag{30}$$

We set $\bar{x}_c = \Delta_c\tilde{x}$ and $\Delta_c = \begin{bmatrix}\theta I_3 & 0_3 \\ 0_3 & I_3\end{bmatrix}$. Referring to (30) and tacking into account that $\Delta_c A\Delta_c^{-1} = \theta A$ and $C\Delta_c = C$, we get

$$\begin{aligned}\dot{\bar{x}}_c &= \theta\left(A - \theta K_o S^{-1}C^T C\right)\bar{x}_c + \theta Y\dot{\tilde{\rho}} + \Delta_c(\tilde{f}(\hat{x},\hat{\rho}) + \tilde{g}(\hat{x},\hat{\rho})u \\ &\quad - (\tilde{f}(x,\rho) + \tilde{g}(x,\rho)u) - B\,d(t)).\end{aligned} \tag{31}$$

Hence,

$$\dot{\bar{x}}_c = \theta\bar{A}\bar{x}_c + W(u,\hat{x},\hat{\rho}), \tag{32}$$

where $W(u,\hat{x},\hat{\rho}) = \tilde{f}(\hat{x},\hat{\rho}) + \tilde{g}(\hat{x},\hat{\rho})u - (\tilde{f}(x,\rho) + \tilde{g}(x,\rho)u) - B\,d(t) + \theta Y\dot{\tilde{\rho}}$ and $\bar{A} = A - \theta K_o S^{-1}C^T C$. $\bar{A}$ is Hurwitz, and $\dot{W}$ is bounded. In fact, we recall that $x(t)$, $u(t)$, $d(t)$, and $\rho(t)$ are assumed to be bounded. Furthermore, $\partial\tilde{g}/\partial x$ and $\partial\tilde{f}/\partial x$ are bounded because $\tilde{f}$ and $\tilde{g}$ are assumed continuously differentiable.

Therefore, according to Theorem 1 of [47], we can conclude that $\lim_{\theta\longrightarrow+\infty}\bar{x}_c = 0$. As a result, $\lim_{\theta\longrightarrow+\infty}\dot{\tilde{x}}_1 = 0$ and $\lim_{\theta\longrightarrow+\infty}\dot{\tilde{x}}_2 = 0$.

Now, let $k_2 > 0$ and $\tilde{k}_2 > 0$ such that $|\tilde{x}_2(t)| \le k_2$ and $|\dot{\tilde{x}}_2(t)| \le \tilde{k}_2$.

Returning to (25) and using (29), we deduce that

$$\dot{V} \le -\beta S^2 - \frac{k|S|^2}{|S|+\varepsilon} + \left(\tilde{k}_2 + \lambda k_2 + k_\eta + \zeta\right)|S|. \tag{33}$$

Table 1: Two-wheeled self-balancing robot parameters.

Symbol	Name	Value (unit)
M_p	Body weight including the loads	20.82 (kg)
M_r	Mass of the wheel	0.420 (kg)
D	Distance between the contact patches of the wheels	0.438 (m)
L	Distance between the chassis and the center	0.4 (m)
R	Radius of the wheel	0.106 (m)
g	Gravity constant	9.8 (ms^{-2})
J_p	The moment of inertia of the chassis with respect to the z-axis	0.28 ($kg{\cdot}m^2$)
J_δ	The moment of inertia of the chassis with respect to the y-axis	1.12 ($kg{\cdot}m^2$)
J_r	Moment of inertia of the wheel	0.1 ($kg{\cdot}m^2$)

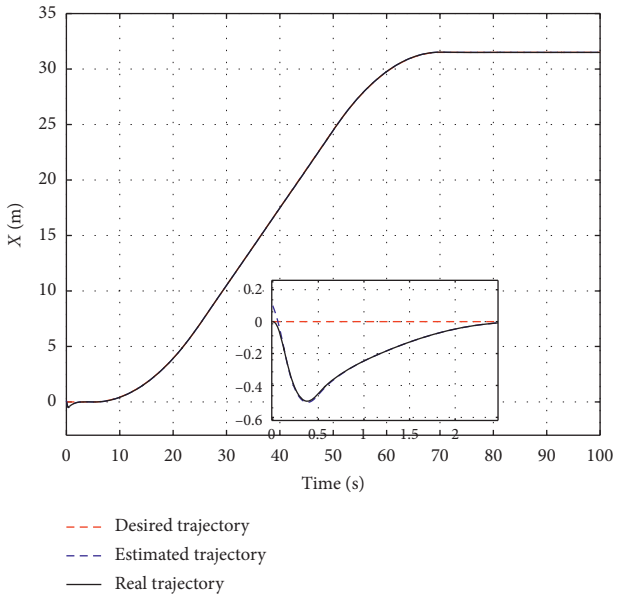

Figure 2: Linear displacement x.

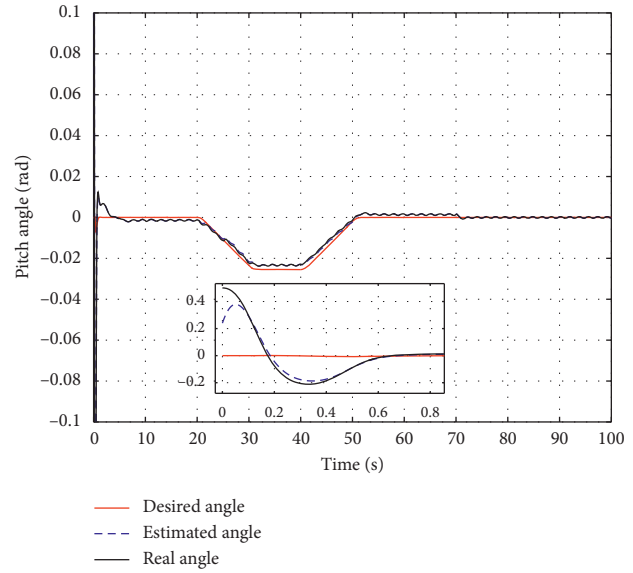

Figure 3: Response of the pitch angle ψ according to terrain inclination.

Supposing $k_s = \tilde{k}_2 + \lambda k_2 + k_\eta + \zeta$, one obtains

$$\begin{aligned}\dot{V} &\le -\beta S^2 - \frac{k|S|^2}{|S|+\varepsilon} + \frac{k_s(|S|+\varepsilon)|S|}{|S|+\varepsilon} \\ &\le -\beta S^2 - \frac{k|S|^2}{|S|+\varepsilon} + \frac{k_s|S|^2}{|S|+\varepsilon} + \frac{k_s\varepsilon|S|}{|S|+\varepsilon} \\ &\le -\beta S^2 - (k-k_s)\frac{|S|^2}{|S|+\varepsilon} + k_s\varepsilon, \quad \text{since } \frac{|S|}{|S|+\varepsilon} < 1.\end{aligned} \tag{34}$$

Choosing k sufficiently large such that $k > k_s$, we have

$$\begin{aligned}\dot{V}(S(t)) &\le -\beta S^2(t) + k_s\varepsilon \\ &\le -\beta V(S(t)) - (\beta V(S(t)) - k_s\varepsilon).\end{aligned} \tag{35}$$

As long as $\beta V(S(t)) \ge k_s\varepsilon$, i.e, $V(S(t)) \ge k_s\varepsilon/\beta$, we have $\dot{V}(S(t)) \le -\beta V(S(t))$. Then, if $V(S(t)) \ge k_s\varepsilon/\beta$, $S(t)$ will be exponentially decreasing, and there exists a finite time T_s such that, for all $t \ge T_s$, $(V(S(t)) \le) k_s\varepsilon/\beta$, which means that, for all $t \ge T_s$, we have

$$|S(t)| \le \left(\frac{2k_s\varepsilon}{\beta}\right)^{1/2}, \tag{36}$$

which means that $S(t)$ is uniformly bounded and its upper bound $(2k_s\varepsilon/\beta)^{1/2}$ may be made small by reducing the design parameter ε and increasing the design parameter β.

Now, it remains to show the convergence of the tracking error of the closed-loop system. □

Corollary 1. *We consider the system (6) with control input (21) and incorporate the adaptive observer (7) such that Assumptions 1 and 2 are satisfied. Then, the tracking errors of the closed-loop system converge to a compact set whose radius may be reduced by choosing small values of the design parameter ε and by increasing the design parameter β.*

Proof. Referring to (17), the derivative of the tracking error becomes

$$\dot{e} = S - \lambda e - \tilde{x}_2. \tag{37}$$

Let us consider the Lyapunov function $V_1 = e^T P_1 e$; its derivative is given by

$$\dot{V}_1 = 2e^T P_1 \dot{e}. \tag{38}$$

Using (37), this allows to obtain

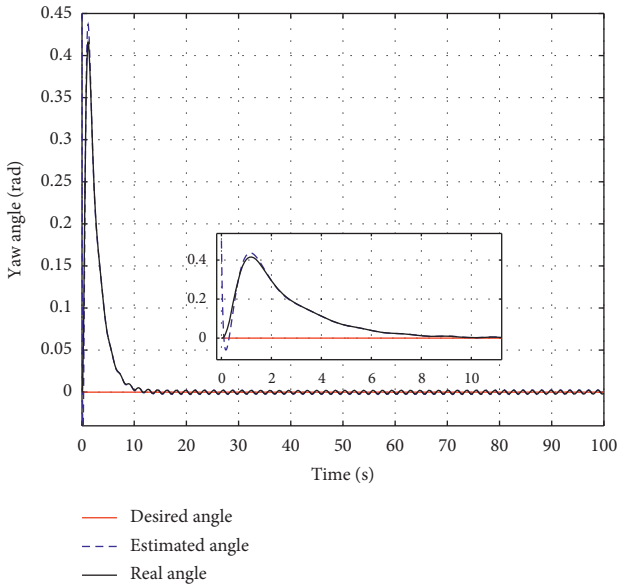

Figure 4: Response of the yaw angle δ.

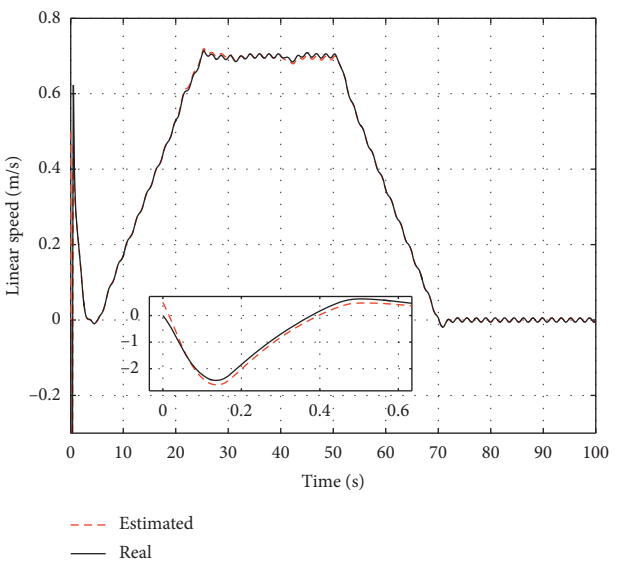

Figure 5: State estimation of linear speed.

$$\begin{aligned}\dot{V}_1 &= 2e^T P_1 (S - \lambda e - \tilde{x}_2) \\ &= -2\lambda e^T P_1 e + 2e^T P_1 S - 2e^T P_1 \tilde{x}_2.\end{aligned} \tag{39}$$

Reminding that $|\tilde{x}_2(t)| \le k_2$ and using (36), one obtains

$$\begin{aligned}\dot{V}_1 &\le -2\lambda V_1 + 2|e|\lambda_{\max}(P_1)\left(\left(\frac{2k_s\varepsilon}{\beta}\right)^{1/2} + k_2\right) \\ &\le -2\lambda V_1 + c_3\sqrt{V_1},\end{aligned} \tag{40}$$

where

$$c_3 = 2\sqrt{\lambda_{\min}(P_1)}\,(\lambda_{\max}(P_1))\left(\left(\frac{2k_s\varepsilon}{\beta}\right)^{1/2} + k_2\right), \tag{41}$$

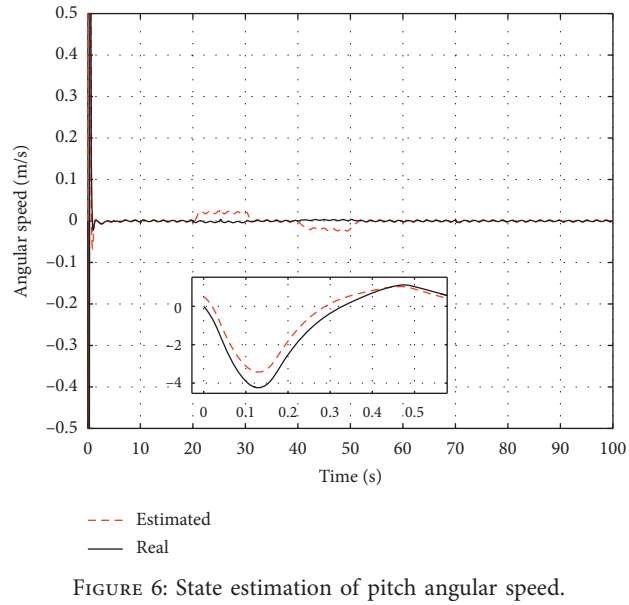

Figure 6: State estimation of pitch angular speed.

and (40) can be written as

$$\dot{V}_1 \le -\sqrt{V_1}\,(\lambda\sqrt{V_1} - c_3) - \lambda V_1. \tag{42}$$

Hence, as long as $\lambda\sqrt{V_1} - c_3 \ge 0$, i.e, $V_1 \ge (c_3/\lambda)^2$, we have $\dot{V}_1(e(t)) \le -\lambda V_1(e(t))$, which means that $V_1(e(t))$ will be decreasing exponentially fast until $V_1(e(t)) < (c_3/\lambda)^2$ after a finite time T_{f2}.

Since $\lambda_{\min}(P_1)|e(t)|^2 \le V_1(e(t))$, we have

$$|e(t)| \le \frac{\lambda c_3}{\sqrt{\lambda_{\min}(P_1)}}, \quad \forall t \ge T_{f2}. \tag{43}$$

By considering the expression (41) of the constant c_3, we deduce, from inequality (43), that the tracking errors of the closed-loop system converge to a compact set whose radius may be made as small as possible by reducing the design parameter ε and increasing the design parameter β. □

Remark 1. Based on the different abovementioned demonstrations and using the different assumptions considered in this paper, we summarize the following algorithm to describe how the different design parameters are selected and the steps of the implementation process:

Step 1: we compute the matrix $\overline{S}$ and the solution of the algebraic Lyapunov equation (8). The latter equation (8) is solvable for $\overline{S}$ as long as the pair (A, C) is observable, which is the case for the two-wheeled self-balancing robot considered in this paper. For the choice of $\overline{S}$, we solve the equation $\overline{S} + A^T\overline{S} + \overline{S}A - C^TC = 0$ using the pole placement method and the Matlab function place.

Step 2: the choice of θ should ensure a compromise between fast convergence of the state estimation and the satisfactory dealing with noise rejection (with $\theta > 1$).

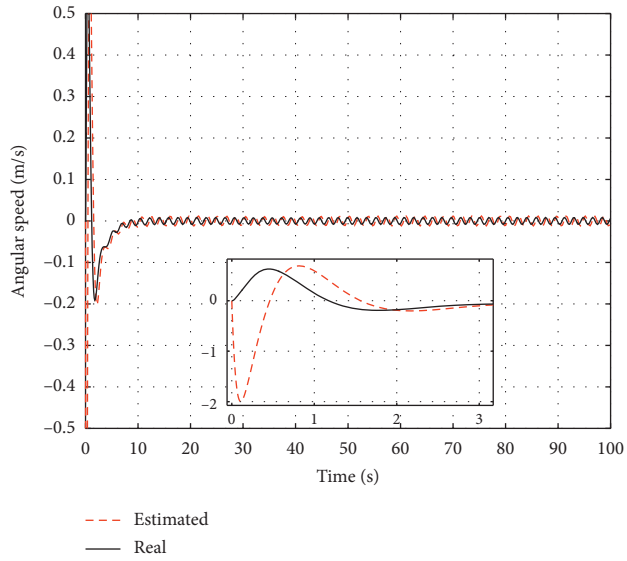

Figure 7: State estimation of yaw angular speed.

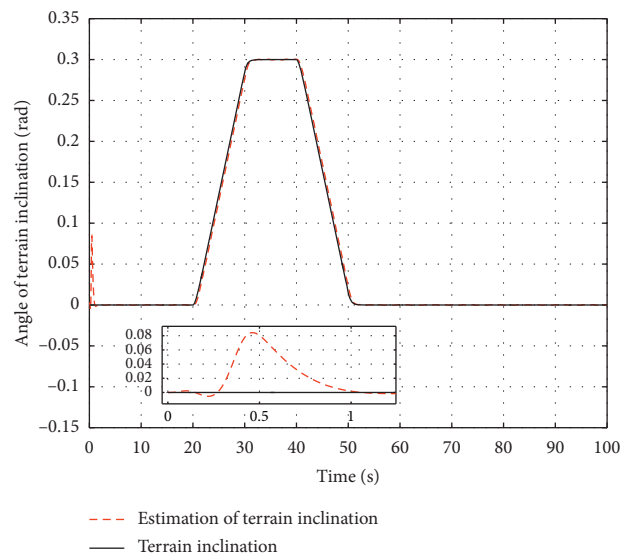

Figure 8: Estimation of terrain inclination α under the proposed observer.

Step 3: we choose a large value of the design parameter β and a small value of the parameter ε such that

$$\beta \gg 1$$
$$0 < \varepsilon \ll 1. \tag{44}$$

Step 4: we select a positive parameter λ according to the reference tracking priority that we should to give to the state x_1 or x_2.

Step 5: we choose a sufficiently large parameter k such that $k > k_s$ with $k_s = \widetilde{k}_2 + \lambda k_2 + k_\eta + \zeta$, where ζ, k_2, and $\widetilde{k}_2$ are, respectively, the upper bounds of the disturbance $d(t)$, the state $\widetilde{x}_2(t)$, and its derivative $\dot{\widetilde{x}}_2(t)$; k_η is the upper-bound of the signal $\eta(x, \widehat{x}, \rho, \widehat{\rho})$ given by equation (29).

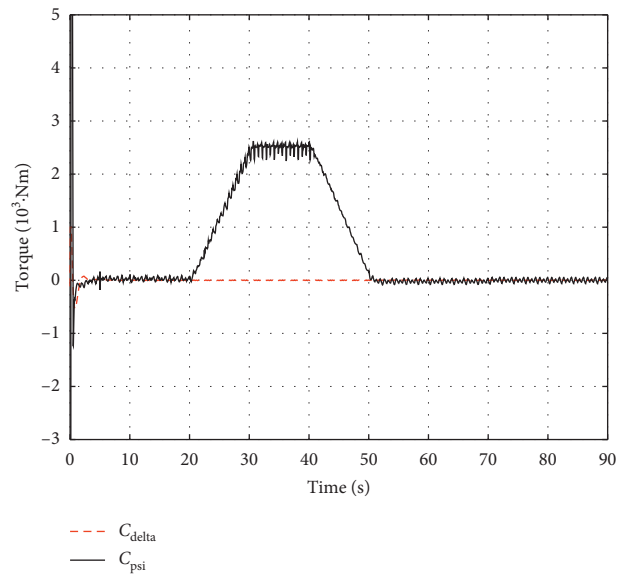

Figure 9: The control input u under the adaptive sliding mode controller in the presence of a slope.

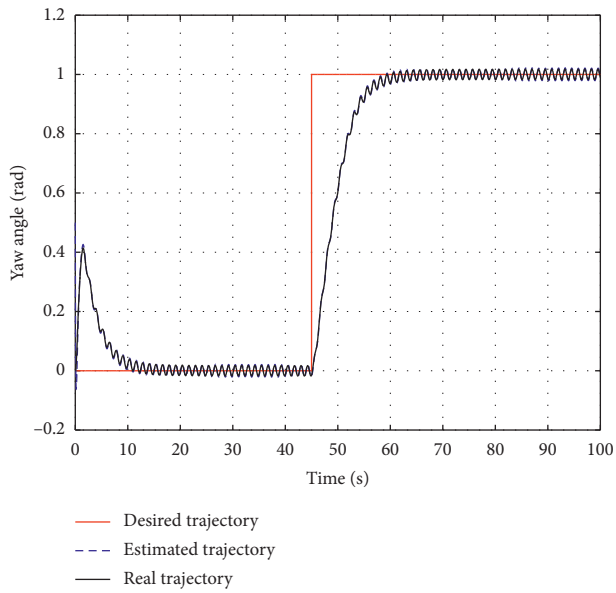

Figure 10: Response of the yaw angle δ.

Step 6: we compute the pseudoinverse $[\widetilde{G}(\widehat{x}, \widehat{\rho})]^+$ of the matrix function $\widetilde{G}(\widehat{x}, \widehat{\rho})$ (see the definition of the pseudoinverse of a matrix at the end of Section 1).

Remark 2. Terminal sliding mode control is an efficient robust control approach that has proved interesting advantages compared to conventional sliding mode control: we report, for instance, its fast convergence rate and its high tracking accuracy [25]. In this context, an adaptive nonsingular integral terminal sliding mode control approach has been proposed in [17]. The convergence rate of the latter control approach was recently improved in [17] with application to the trajectory tracking control of autonomous

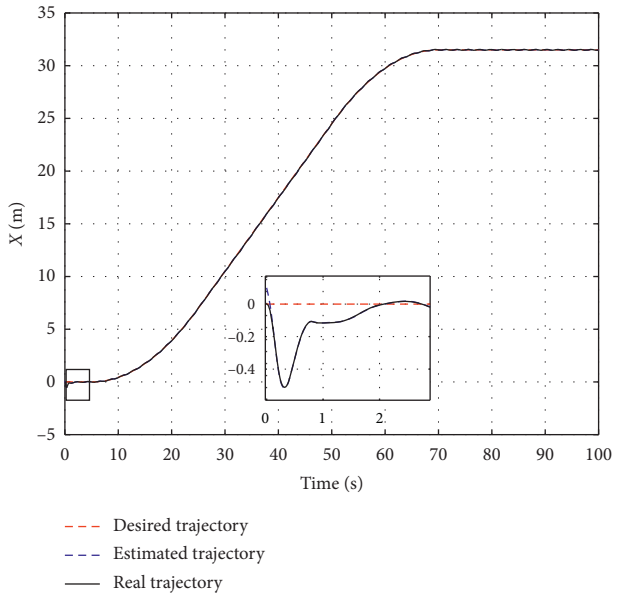

Figure 11: Linear displacement x.

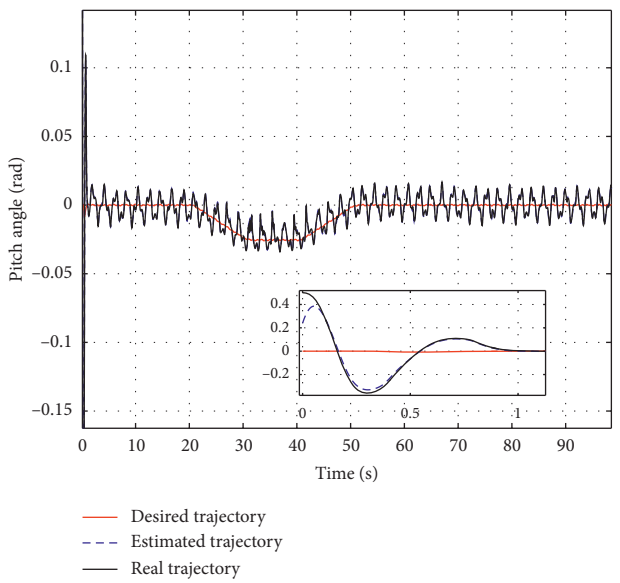

Figure 12: Response of the pitch angle ψ according to terrain inclination.

underwater vehicles. Terminal sliding mode control may be investigated in future works for the two-wheeled self-balancing robot to design a more efficient tracking control scheme with improved convergence properties.

4. Numerical Simulations

In this section, the numerical simulations carried out using *Matlab/Simulink* software, applied on the two-wheeled self-balancing robot, are performed to highlight the effectiveness of the proposed adaptive sliding mode controller.

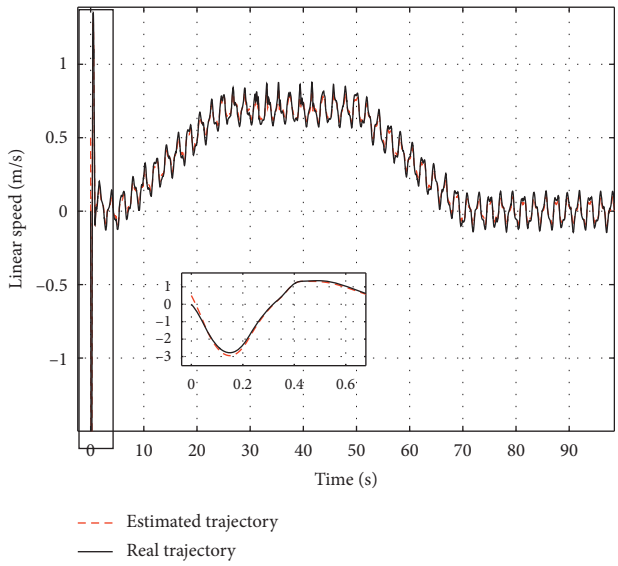

Figure 13: State estimation of linear speed.

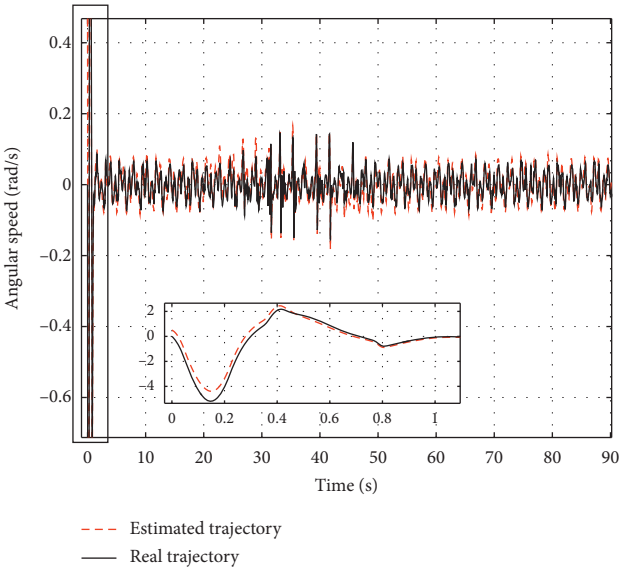

Figure 14: State estimation of pitch angular speed.

The robot parameters are summarized in Table 1.

The initial conditions for the position states are fixed as $x = 0$ m; $\psi = 0.5$ rad; and $\delta = 0$ rad, and all the speed states are fixed to zero ($\dot{x} = 0$ m/s, $\dot{\psi} = 0$ rad/s, and $\dot{\delta} = 0$ rad/s).

The disturbance vector $d(t)$ is chosen such that $d_1(t) = -0.3\sin(3\pi t)Nm$, $d_2(t) = -0.02\sin(2\pi t + \pi)Nm$, and $d_3(t) = -0.2\sin(5\pi t)Nm$.

Firstly, we apply the adaptive observer (7) to estimate unmeasured states and the terrain inclination with the following initial condition: $\hat{x}(0) = 0.1$ m, $\hat{\psi}(0) = 0.24$ rad, $\hat{\delta}(0) = 0.5$ rad, $\hat{\dot{x}}(0) = 0.5$ m/s, $\hat{\dot{\psi}}(0) = 0.5$ rad/s, $\hat{\dot{\delta}}(0) = 0$ rad/s, and $\hat{\alpha}(0) = 0$ rad.

The design parameters of the adaptive observer are selected as $\theta = 10$, $P(0) = 1$ and $Y(0) = [0\,0\,0\,0\,0\,0]^T$.

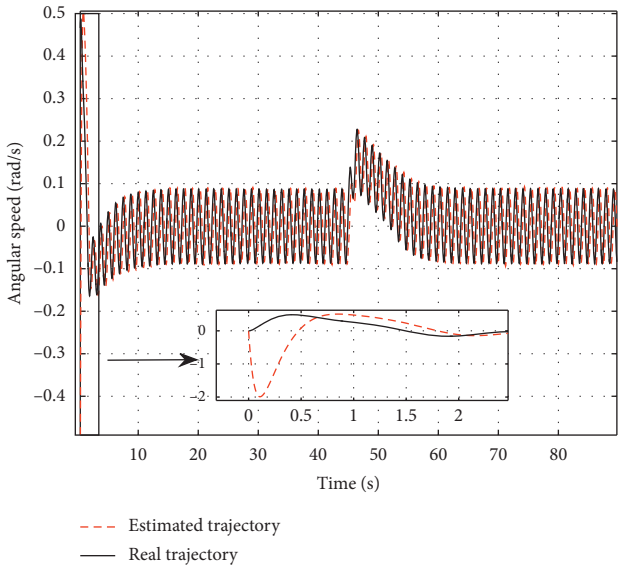

Figure 15: State estimation of yaw angular speed.

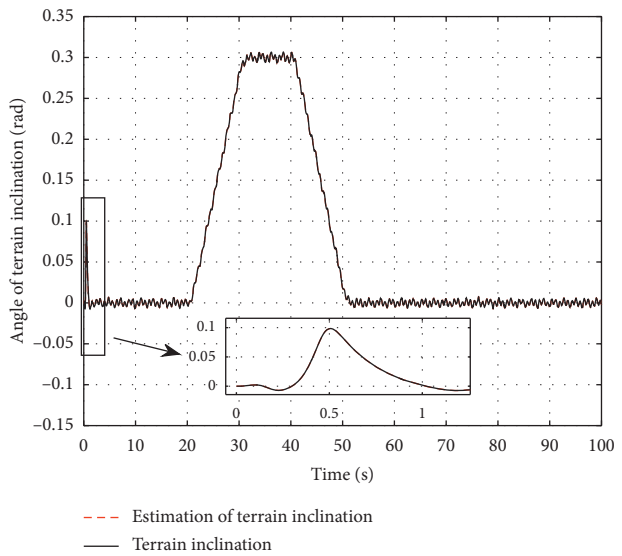

Figure 16: Estimation of terrain inclination α under the proposed observer.

The design matrix $\overline{S}^{-1}C^T$ is chosen such that

$$\overline{S}^{-1}C^T = \begin{bmatrix} 2 & 0 & 0 \\ 0 & 2 & 0 \\ 0 & 0 & 2 \\ 1 & 0 & 0 \\ 0 & 1 & 0 \\ 0 & 0 & 1 \end{bmatrix}.$$

Once the terrain inclination and the unmeasured states are available, we apply the continuously implemented sliding mode controller given by (21) to the two-wheeled self-balancing robot, where $S(t)$ is defined by equation (19) such that pseudoinverse $[\widetilde{G}(\widehat{x}, t\widehat{\rho})]^+$ is computed as follows:

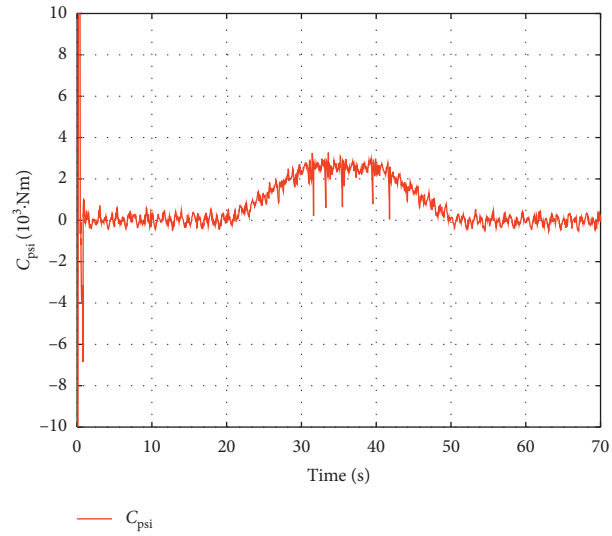

Figure 17: The torque $C_{\psi 26}$ under the adaptive sliding mode controller in the presence of a slope.

$$[\widetilde{G}(\widehat{x}, t\widehat{\rho})]^+ = \begin{bmatrix} \dfrac{1}{2\widetilde{g}_{11}(\widehat{x}, \widehat{\rho})} & \dfrac{1}{2\widetilde{g}_{21}(\widehat{x}, \widehat{\rho})} & 0 \\ 0 & 0 & \dfrac{1}{\widetilde{g}_{32}(\widehat{x}, \widehat{\rho})} \end{bmatrix}, \quad (45)$$

where $x_r(t)$, $\psi_{eq}(t)$, and $\delta_r(t)$ are the desired reference trajectories suitably planned as depicted in Figures 2–4.

The design parameters are chosen as follows: $\varepsilon = 0.1$, $k = 16$, $\lambda = 10$, and $\beta = 10$.

The simulation results are illustrated through Figures 2–9.

The tracking problem studied in this paper consists to maintain the pitch angle equilibrium even in the presence of a slope and disturbances and to impose the linear displacement to track a reference trajectory. Figures 2–4 attest that the tracking objective of displacement is achieved.

Indeed, the two-wheeled self-balancing robot tracks well the desired trajectories (Figures 2 and 4) although keeping the equilibrium of the pitch angle despite the presence of a slope (Figure 3).

Figure 5 shows that the linear speed traces a trapezoidal profile. Figures 6 and 7 reveal a right harmony between angular velocities and their estimates.

The performance of the proposed adaptive observer to estimate the angle of terrain inclination is outstanding from Figure 8. The control input vector u is on view in Figure 9 where small oscillations are recorded. It may be observed in Figure 9 that the couple C_δ is increasing after the instant 20 s which corresponds to the beginning of terrain inclination. Thus, the wheeled robot continues to follow its reference trajectory despite the presence of the terrain inclination.

In a more sophisticated and realistic scenario, we have added a variation of the yaw angle as it is represented in Figure 10. We have also added a white noise $\omega(t)$ of power equal to 10^{-9}. In addition, we have modified the external

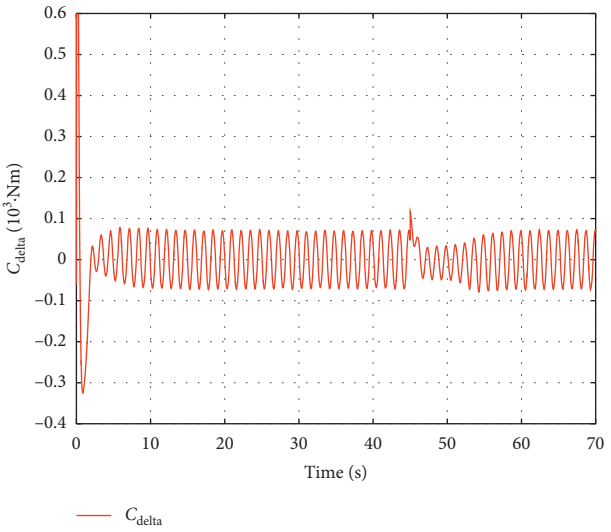

FIGURE 18: The torque $C_{\delta 26}$ under the adaptive sliding mode controller in the presence of a slope.

disturbances as $d_1(t) = -0.2\sin(3t)Nm$, $d_2(t) = -0.2\cos(2t)Nm$, and $d_3(t) = -0.3\sin(5t)Nm$.

The simulation results are illustrated through Figures 11–18.

Figures 10–12 attest that the tracking objective of displacement is obtained. Indeed, the two-wheeled self-balancing robot tracks well the desired trajectories (Figures 10 and 11) although keeping the equilibrium of the pitch angle despite the presence of a slope (Figure 12). Figure 13 shows that the linear speed traces a trapezoidal profile. Figures 14 and 15 reveal a right harmony between angular velocities and their estimates.

The performance of the proposed adaptive observer to estimate the angle of terrain inclination is shown from Figure 16. Figure 17 represents the torque $C_{\psi 26}$ which ensures the translation along the x-axis while preserving the upright position. It seems clear from Figure 18 that the couple $C_{\delta 26}$ increases at the instant 45 s which corresponds to the beginning of the yaw angle variation. Thus, the wheeled robot continues to follow its reference trajectory despite the presence of the terrain inclination and the presence of disturbances and measurement noise.

5. Conclusions

In this paper, a robust adaptive observer-based sliding mode control has been proposed for the two-wheeled self-balancing robot subject to terrain inclination and disturbances. The application of the adaptive observer guarantees the simultaneous estimation of unmeasured states and the terrain inclination angle which is assumed unknown. The convergence of the proposed controller was illustrated through a Lyapunov analysis and inspired from sliding modes theory. Numerical simulations emphasize the performance of the designed control method applied to the two-wheeled self-balancing robot. In future work, we will enhance our control algorithm by using the terminal sliding mode in order to improve the convergence properties of the controller. Also, we will focus on the problem of observer based-fault tolerant control for the considered system.

Data Availability

The data used to support the findings of this study are included within the article.

Conflicts of Interest

The authors declare that they have no conflicts of interest.

Acknowledgments

This work was supported by the University of Monastir, the National Engineering School of Monastir, and the University of Sousse.

References

[1] Y. Ning, M. Yue, and Z. Lin, "Time-optimal control of underactuated wheeled inverted pendulum vehicles along specified paths," in *Proceedings of the 2020 5th International Conference on Advanced Robotics and Mechatronics (ICARM)*, Shenzhen, China, 2020.

[2] S. Kim and S. Kwon, "Robust transition control of underactuated two-wheeled self-balancing vehicle with semi-online dynamic trajectory planning," *Mechatronics*, vol. 68, Article ID 102366, 2020.

[3] C. Acar and T. Murakami, "Underactuated two-wheeled mobile manipulator control using nonlinear backstepping method," in *Proceedings of the 34th Annual Conference of IEEE Industrial Electronics*, Orlando, FL, USA, November 2008.

[4] C.-H. Chiu, Y.-F. Peng, and Y.-W. Lin, "Intelligent backstepping control for wheeled inverted pendulum," *Expert Systems with Applications*, vol. 38, no. 4, pp. 3364–3371, 2011.

[5] A. Benaskeur and A. Desbiens, "Application of adaptive backstepping to the stabilization of the inverted pendulum," in *Proceedings of the IEEE Canadian Conference on Electrical and Computer Engineering*, Waterloo, Canada, 1998.

[6] T. Nomura, Y. Kitsuka, H. Suemitsu, and T. Matsuo, "Adaptive backstepping control for a two-wheeled autonomous robot," in *Proceedings of the 2009 ICCAS-SICE*, Fukuoka, Japan, 2009.

[7] R. Cui, J. Guo, and Z. Mao, "Adaptive backstepping control of wheeled inverted pendulums models," *Nonlinear Dynamics*, vol. 79, no. 1, pp. 501–511, 2015.

[8] N. T. Binh, N. M. Hung, N. A. Tung, D. P. Nam, and N. T. Long, "Robust H-infinity backstepping control design of a wheeled inverted pendulum system," in *Proceedings of the 2017 International Conference on System Science and Engineering*, Ho Chi Minh City, Vietnam, 2017.

[9] G. Rigatos, K. Busawon, J. Pomares, and M. Abbaszadeh, "Nonlinear optimal control for the wheeled inverted pendulum system," *Robotica*, vol. 38, no. 1, pp. 29–47, 2019.

[10] C. H. Huang, W. J. Wang, and C. H. Chiu, "Design and implementation of fuzzy control on a two-wheel inverted pendulum," *IEEE Transaction on Industrial Electronics*, vol. 58, no. 7, pp. 2988–3001, 2010.

[11] T. Zhao, Q. Yu, S. Dian, R. Guo, and S. Li, "Non-singleton general type-2 fuzzy control for a two-wheeled self-balancing robot," *International Journal of Fuzzy Systems*, vol. 21, no. 6, pp. 1724–1737, 2019.

[12] Z. Li, "Adaptive fuzzy output feedback motion/force control for wheeled inverted pendulums," *IET Control Theory & Applications*, vol. 5, no. 10, pp. 1176–1188, 2011.

[13] Y. J. Liu, S. Tong, and C. P. Chen, "Adaptive fuzzy control via observer design for uncertain nonlinear systems with unmodeled dynamics," *IEEE Transactions on Fuzzy Systems*, vol. 21, no. 2, pp. 275–288, 2012.

[14] C. Iwendi, M. A. Alqarni, J. H. Anajemba, A. S. Alfakeeh, Z. Zhang, and A. K. Bashir, "Robust navigational control of a two-wheeled self-balancing robot in a sensed environment," *IEEE Access*, vol. 7, pp. 82337–82348, 2019.

[15] Z. Music, F. Molinari, S. Gallenmüller et al., "Design of a networked controller for a two-wheeled inverted pendulum robot," *IFAC-PapersOnLine*, vol. 52, no. 20, pp. 169–174, 2019.

[16] L. Guo, S. A. A. Rizvi, and Z. Lin, "Optimal control of a two-wheeled self-balancing robot by reinforcement learning," *International Journal of Robust and Nonlinear Control*, 2020.

[17] L. Qiao and W. Zhang, "Trajectory tracking control of AUVs via adaptive fast nonsingular integral terminal sliding mode control," *IEEE Transactions on Industrial Informatics*, vol. 16, no. 2, pp. 1248–1258, 2019.

[18] W. Wang, X. D. Liu, and J. Q. Yi, "Structure design of two types of sliding-mode controllers for a class of under-actuated mechanical systems," *IET Control Theory & Applications*, vol. 1, no. 1, pp. 163–172, 2007.

[19] S. Mahjoub, F. Mnif, and N. Derbel, "Second-order sliding mode approaches for the control of a class of underactuated systems," *International Journal of Automation and Computing*, vol. 12, no. 2, pp. 134–141, 2015.

[20] M. Yue, W. Sun, and P. Hu, "Sliding mode robust control for two-wheeled mobile robot with lower center of gravity," *International Journal of Innovative Computing, Information and Control*, vol. 7, no. 2, pp. 637–646, 2011.

[21] H. T. Yau, C. C. Wang, N. S. Pai, and M. J. Jang, "Robust control method applied in self-balancing two-wheeled robot," in *Proceedings of the 2nd International Symposium on Knowledge Acquisition and Modeling*, Wuhan, China, 2009.

[22] N. K. Goswami and P. K. Padhy, "Sliding mode controller design for trajectory tracking of a non-holonomic mobile robot with disturbance," *Computers & Electrical Engineering*, vol. 72, pp. 307–323, 2018.

[23] S. Mobayen, "Design of LMI-based sliding mode controller with an exponential policy for a class of underactuated systems," *Complexity*, vol. 21, no. 5, pp. 117–124, 2019.

[24] H. Mirzaeinejad, "Optimization-based nonlinear control laws with increased robustness for trajectory tracking of non-holonomic wheeled mobile robots," *Transportation Research Part C: Emerging Technologies*, vol. 101, pp. 1–17, 2019.

[25] S. Mobayen, M. J. Yazdanpanah, and V. J. Majd, "A finite-time tracker for nonholonomic systems using recursive singularity-free FTSM," in *Proceedings of the 2011 IEEE American Control Conference*, San Francisco, CA, USA, 2011.

[26] F. Dai, X. Gao, S. Jiang, W. Guo, and Y. Liu, "A two-wheeled inverted pendulum robot with friction compensation," *Mechatronics*, vol. 30, pp. 116–125, 2015.

[27] T. L. Chung, T. H. Bui, T. T. Nguyen, and S. B. Kim, "Sliding mode control of two-wheeled welding mobile robot for tracking smooth curved welding path," *KSME International Journal*, vol. 18, no. 7, pp. 1094–1106, 2004.

[28] J. Huang, Z. H. Guan, T. Matsuno, T. Fukuda, and K. Sekiyama, "Sliding-mode velocity control of mobile-wheeled inverted-pendulum systems," *IEEE Transactions on Robotics*, vol. 26, no. 4, pp. 750–758, 2010.

[29] J. Huang, Z. Guan, T. Matsuno, T. Fukuda, and K. Sekiyama, "High-order disturbance observer based sliding mode control for mobile wheeled inverted pendulum systems," *IEEE Transactions on Industrial Electronics*, vol. 67, no. 3, pp. 2030–2041, 2019.

[30] D. S. Nasrallah, H. Michalska, and J. Angeles, "Controllability and posture control of a wheeled pendulum moving on an inclined plane," *IEEE Transactions on Robotics*, vol. 23, no. 3, pp. 564–577, 2007.

[31] F. Dai F, X. Gao, S. Jiang, Y. Liu, and J. Li, "A multi-DOF two wheeled inverted pendulum robot climbing on a slope," in *Proceedings of the IEEE International Conference on Robotics and Biomimetics*, vol. 201, Bali, Indonesia, December 2014.

[32] K. Hirata, M. Kamatani, and T. Murakami, "Advanced motion control of two-wheel wheelchair for slope environment," in *Proceedings of the IECON 2013-39th Annual Conference of the IEEE Industrial Electronics Society*, Vienna, Austria, 2013.

[33] M. S. Key, C. G. Jeon, and D. S. Yoo, "Sliding mode control for a two-wheeled inverted pendulum mobile robot driving on uniform slopes," in *Proceedings of the 12th International Conference on Control, Automation and Systems*, Jeju Island, Republic of Korea, 2012.

[34] Z. Kausar, K. Stol, and N. Patel, "The effect of terrain inclination on performance and the stability region of two-wheeled mobile robots," *International Journal of Advanced Robotic Systems*, vol. 9, no. 5, p. 218, 2012.

[35] T. Takei, O. Matsumoto, and K. Komoriya, "Simultaneous estimation of slope angle and handling force when getting on and off a human-riding wheeled inverted pendulum vehicle," in *Proceedings of the IEEE/RSJ International Conference on Intelligent Robots and Systems*, St. Louis, MO, USA, 2009.

[36] D. Liang, N. Sun, Y. Wu, and Y. Fang, "Differential flatness-based robust control of self-balanced robots," *IFAC-PapersOnLine*, vol. 51, no. 31, pp. 949–954, 2018.

[37] Q. Zhang, "Adaptive observer for multiple-input-multiple-output (MIMO) linear time-varying systems," *IEEE Transactions on Automatic Control*, vol. 47, no. 3, pp. 525–529, 2002.

[38] A. Xu and Q. Zhang, "State and parameter estimation for nonlinear systems," in *Proceedings of the 2002 IFAC World Congress*, vol. 35, no. 1, Barcelona, Spain, 2002.

[39] G. Besançon, "Remarks on nonlinear adaptive observer design," *Systems & Control Letters*, vol. 41, no. 4, pp. 271–280, 2000.

[40] M. Farza, M. M'Saad, T. Maatoug, and M. Kamoun, "Adaptive observers for nonlinearly parameterized class of nonlinear systems," *Automatica*, vol. 45, no. 10, pp. 2292–2299, 2009.

[41] I. Jmel, H. Dimassi, S. Hadj-Said, and F. M'Sahli, "An adaptive sliding mode observer for inverted pendulum under mass variation and disturbances with experimental validation," *ISA Transactions*, vol. 102, pp. 264–279, 2020.

[42] F. Grasser, A. D'Arrigo, S. Colombi, and A. C. Rufer, "JOE: a mobile, inverted pendulum," *IEEE Transactions on Industrial Electronics*, vol. 49, no. 1, pp. 107–114, 2002.

[43] M. Chen, "Robust tracking control for self-balancing mobile robots using disturbance observer," *IEEE/CAA Journal of Automatica Sinica*, vol. 4, no. 3, pp. 458–465, 2017.

[44] D. Liang, N. Sun, Y. Wu, and Y. Fang, "Modeling and motion control of self-balance robots on the slope," in *Proceedings of*

the 31st Youth Academic Annual Conference of Chinese Association of Automation, Wuhan, China, 2016.

[45] H. Dimassi, S. Hadj-Said, A. Loria, and F. M'Sahli, "An adaptive observer for a class of nonlinear systems with a high gain approach. Application to the twin-rotor system," *International Journal of Control*, 2019.

[46] J. J. E. Slotine and W. Li, *Applied Nonlinear Control*, Prentice Hall, Englewood Cliffs, NJ, USA, 1991.

[47] K. Kalsi, J. Lian, S. Hui, and S. H. Żak, "Sliding-mode observers for systems with unknown inputs: a high-gain approach," *Automatica*, vol. 46, no. 2, pp. 347–353, 2010.

Hindawi
Mathematical Problems in Engineering
Volume 2020, Article ID 8840890, 13 pages
https://doi.org/10.1155/2020/8840890

Research Article

Robust State Estimation for a Nonlinear Hybrid Model of the Alternating Activated Sludge Process Using Filtered High-Gain Observers

Afef Boudagga,[1] Habib Dimassi ,[1,2] Salim Hadj-Said,[1] and Faouzi M'Sahli[1]

[1]*University of Monastir, National Engineering School of Monastir, LAS2E, 5019, Monastir, Tunisia*
[2]*University of Sousse, Institut Supérieur des Sciences Appliquées et de Technologie de Sousse, Sousse, Tunisia*

Correspondence should be addressed to Habib Dimassi; dimassihabib2013@gmail.com

Received 18 September 2020; Revised 23 November 2020; Accepted 25 November 2020; Published 12 December 2020

Academic Editor: Baltazar Aguirre Hernandez

In this paper, a robust state estimation method based on a filtered high-gain observer is developed for the alternating activated sludge process (AASP) considered as a nonlinear hybrid system. Indeed, we assume that the biodegradable substrate and the ammonia concentrations in the AASP model are unmeasured due to the high cost of their sensors whose maintenance is also very expensive. The observer design is based on the association of the classical high-gain observer and the idea of the application of linear filters on the observation error to deal with measurement noise. It is shown through a Lyapunov analysis that the designed observer ensures the estimation of the unmeasured states (the biodegradable substrate and the ammonia concentrations) based on the measured dissolved oxygen and nitrate concentrations subject to noise. A comparison with the classical high-gain observer is performed via numerical simulations in order to show the robustness of the suggested estimation approach against Gaussian measurement noise.

1. Introduction

Safe water is a fundamental human need to ensure good health and hygiene. Many wastewater treatment technologies are required to provide environmental protection and ecosystem preservation. The alternating activated sludge process (AASP) [1] represents a famous biological wastewater treatment process. This process consists of two separate phases: the aeration phase where the ammonium is converted into nitrate and the anoxic phase where the nitrate is used for organic carbon removal. In order to preserve the effluent quality of water as specified by the NPDES (National Pollutant Discharge Elimination System) [2], modeling the alternating activated sludge process has attracted many scientific research studies. Indeed, different models have been proposed [3–6]. To reduce the complexity of previous models, the authors have presented, in [7], a new reduced model for the activated sludge process which can be considered as a nonlinear hybrid system. Motivated by the advantages of the latter model, we consider in this paper the problem of high-gain observer (HGO) design for a nonlinear hybrid model of the alternating activated sludge process subject to measurement noise.

Hybrid systems are characterized by the combination of both continuous and discrete dynamics and have recently attracted several research studies in both control and observation problems. Switched systems represent a special class of hybrid systems which are defined by a collection of subsystems connected by a switching rule: see reference [8] in which an overview on switched systems is developed. Moreover, in [9], various issues on the stability and design of switched systems have been presented. To analyze the stability of switched and hybrid systems, multiple Lyapunov functions have been introduced in [10]. In particular, the problem of observation of hybrid and switched systems has been investigated in the last decade. Indeed, many control and observation techniques from the literature of automatic controls such as high-gain techniques [11], sliding-mode

techniques [12], and linear matrix inequality (LMI) techniques [13] have been extended and exploited to solve the problem of estimation of hybrid and switched systems. For instance, in [14], the authors have given sufficient and necessary conditions to ensure the observability of hybrid systems. In [11], a high-gain observer (HGO) is designed for a class of uniformly observable nonlinear hybrid systems. In [15], a high-order sliding-mode observer is proposed for a class of nonlinear switched systems. Moreover, the authors have proposed, in [16], a sliding-mode observer for robust fault diagnosis of switched systems with application to a DC-DC power electronic converter, through linear matrix inequalities. In [17], a sliding-mode observer is synthesized for a switched system based on the switched Lyapunov function approach with application to fault detection and reconstruction of switched power electronics systems. In addition, in [18], an unknown input observer has been developed and applied to an activated sludge process modeled as a hybrid nonlinear system. A hybrid observer has been also proposed in [19] to provide a robust fault detection approach for a linear switched system. Moreover, in [20], a hybrid sliding-mode observer has been designed to estimate conjointly states and unknown inputs for a switched system. Recently, in [21], the authors have designed an observer-based adaptive finite-time tracking control for a class of nonlinear switched systems with unmodeled dynamics. In addition, the authors [22] have developed a fuzzy logic system-based switched observer to approximate unmeasured states for a switched pure-feedback nonlinear system with average dwell time. However, the observation of nonlinear switched systems is still yet an open issue, and many problems which have been solved for classical nonlinear systems may be generalized and extended to the hybrid case, and many existing estimation methods may be extended to switched systems. One of the most important observation methods which have been well developed in the literature for a class of continuous nonlinear systems is the high-gain observer-based estimation approach characterized by the easiness of its implementation and its good estimation performance. High-gain observers are designed under particular assumptions such as the triangular canonical form as well as the Lipschitz condition, and several high-gain observer structures are available in the literature. Indeed, a high-gain observer has been proposed for a large class of MIMO nonlinear systems, in [23]. In [24], the unmeasured states and the unknown inputs have been estimated by designing cascaded high-gain observers. Recently, in [25], an adaptive nonlinear high-gain observer is proposed to estimate the speed of an induction motor.

Despite the several advantages which characterize high-gain observers, the main drawback of these observers consists in their high sensitivity to measurement noise. Many alternative solutions have been proposed in the literature to deal with this problem. Indeed, in order to provide good state estimation in the presence of measurement noise, authors have proposed to modify the observer gain structure by switching between high and low gain values, in [26]. A gain parameter adaptation process has been suggested in [27] to improve the performance of the high-gain observer in the presence of noise.

Recently, a robust high-gain observer including a linear filter has been suggested in [28, 29]. The latter observer consists of a filtered high-gain observer (FHGO) characterized by a simple structure.

Motivated by its good estimation performances and its robustness against measurement noise, we adopt, in this paper, the filtered high-gain observer developed in [29], and we extend the procedure design to a class of nonlinear switched systems which include the activated sludge process model. Indeed, in the alternating activated sludge process, some concentrations are hardly measured in practice, due to the high cost of concentration sensors whose maintenance is also expensive. Moreover, concentration sensors are always subject to measurement noise. In this paper, we propose a filtered high-gain observer for a class of nonlinear hybrid systems subject to measurement noise and its application to the alternating activated sludge process. A Lyapunov analysis is provided to establish the convergence of the estimation errors in each mode despite the presence of measurement noise. Numerical simulations using Matlab/Simulink software are carried out with a comparative study between the proposed filtered high-gain observer adopted in this work and the classical high-gain observer in order to validate our theoretical results and illustrate the good performances of the proposed observer in terms of state estimation and robustness against measurement noise.

This paper is organized as follows: in the second section, a description of the alternating activated sludge process (AASP) and its model are presented, and then, the problem of state estimation is formulated. In Section 3, a filtered high-gain observer is designed for a class of switched systems and applied to the AASP. Numerical simulations are devoted, in Section 4, to highlight the robustness and the estimation performances of the proposed observer compared to the classical high-gain observer. Finally, we conclude with some remarks.

2. Context and Problem Formulation

2.1. Presentation of the Alternating Activated Sludge Process

2.1.1. Description of the Process. Overabundance of nitrogen (N) can cause various health and ecological issues. The activated sludge process presented in Figure 1 can ensure biological nitrogen removal which is very necessary to preserve the environment. The purpose of this process is to eliminate polluting components existing in the water by the action of bacteria whose activity is related to the presence of oxygen. Indeed, activated sludge is defined by sludge particles reacting with organisms (bacteria) that need oxygen to grow in aeration tanks.

The alternating activated sludge process (AASP) is identified by three main components. The unique aeration tank (Vae = 0.03 m^3) represents the first component that is composed of an aeration surface whose role is to inject oxygen in the reactor which is very necessary to provide an aerobic phase ($S_{O2} \neq 0$ and KLa $\neq 0$) and an anoxic phase

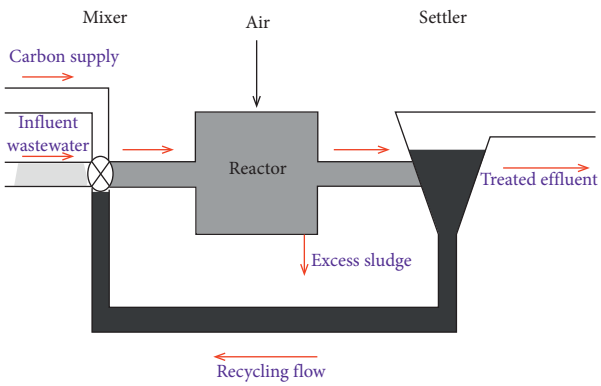

FIGURE 1: The alternating activated sludge process diagram [7].

($S_{O2} \simeq 0$ and KLa = 0). The settler which represents the second component allows the separation of activated sludge (AS) and treats wastewater. The majority of AS must be returned to the aeration tank to guarantee a high number of organisms. This function is provided by the return activated sludge which represents the third component. It is to be noticed that the waste activated sludge must be eliminated from the system and the purified water should be delivered to natural water.

The AASP is characterized by two phases: firstly, an aerobic phase (aeration period) is active, where a high quantity of air is added in the reactor to provide oxygen and convert ammonium to nitrate. When the oxygen is exhausted and the aerobic phase (nitrification) is finished, the anoxic phase (denitrification) is started. During the anoxic phase, a source of carbon is added to convert nitrate into nitrogen. At the moment when aeration is restarted, the oxygen concentration is different to zero, and a new aerobic phase is started.

2.1.2. Model of the Alternating Activated Sludge Process. The reduced state model of the activated sludge process suggested by [7] is constituted by four states: S_s is the biodegradable substrate, S_{NO3} is the nitrate concentration, S_{NH4} is the ammonia concentration, and S_{O2} is the dissolved oxygen concentration. The latter model is given by the following equations:

$$\begin{cases} \dot{S}_s = D_s S_{\text{sin}} + D_c S_{\text{sc}} - (D_s + D_c) S_s - \dfrac{1}{Y_H}\left(\tilde{\Upsilon}_1 + \tilde{\Upsilon}_2\right) + \tilde{\Upsilon}_5, \\ \dot{S}_{NO3} = -(D_s + D_c) S_{NO3} - \dfrac{1 - \Upsilon_H}{2.86 \Upsilon_H} \tilde{\Upsilon}_2 + \tilde{\Upsilon}_3, \\ \dot{S}_{NH4} = D_s S_{NH4in} - (D_s + D_c) S_{NH4} - i_{NBM}\left(\tilde{\Upsilon}_1 + \tilde{\Upsilon}_2\right) - \tilde{\Upsilon}_3 + \tilde{\Upsilon}_4, \\ \dot{S}_{O2} = -(D_s + D_c) S_{O2} + KLa\left(S_{O2sat} - S_{O2}\right) - \dfrac{1 - \Upsilon_H}{\Upsilon_H} \tilde{\Upsilon}_1 - 4.57 \tilde{\Upsilon}_3. \end{cases} \tag{1}$$

This model is characterized by the following input variables: the concentration of substrate soluble in water S_{sin} and the ammonia input concentration S_{NH4in}. The alternating phase operation is ensured by the oxygen transfer coefficient KLa which is characterized by a high value during the aerobic phase and a near zero value during the anoxic phase. S_{sc} is the concentration of the external source of carbon.

The mathematical expressions of $\tilde{\Upsilon}_1, \tilde{\Upsilon}_2, \ldots, \tilde{\Upsilon}_5$ are presented in the following equations:

$$\begin{cases} \tilde{\Upsilon}_1 = \lambda_1 S_s \dfrac{S_{O2}}{S_{O2} + K_{O2H}}, \\ \tilde{\Upsilon}_2 = \lambda_1 S_s \dfrac{S_{NO3}}{S_{NO3} + K_{NO3}} \dfrac{K_{O2H}}{S_{O2} + K_{O2H}}, \\ \tilde{\Upsilon}_3 = \lambda_2 \dfrac{S_{NH4}}{S_{NH4} + K_{NH4AUT}} \dfrac{S_{O2}}{S_{O2} + K_{O2AUT}}, \\ \tilde{\Upsilon}_4 = \lambda_3, \\ \tilde{\Upsilon}_5 = \lambda_4 \left(\dfrac{S_{O2}}{S_{O2} + K_{O2H}} + \eta_{NO3h} \dfrac{S_{NO3}}{S_{NO3} + K_{NO3}} \dfrac{K_{O2H}}{S_{O2} + K_{O2H}} \right). \end{cases} \tag{2}$$

The parameter values of the considered activated sludge process model are provided in Table 1 in Section 4.

2.2. Problem Statement. In this paper, we investigate the problem of estimation of the unmeasured states of the alternating activated sludge process model despite the presence of measurement noise. To that end, we present first a general class of nonlinear hybrid systems subject to measurement noise for which the problem of robust estimation will be addressed, and then, we show that the considered class of hybrid systems includes the considered activated sludge process with its two modes (the aerobic phase and the anoxic phase).

2.2.1. A General Class of Nonlinear Hybrid Systems. We consider the following class of nonlinear hybrid systems which constitutes an extension of the class of nonlinear continuous systems considered in reference [30] to the hybrid case:

$$\begin{cases} \dot{x}^r(t) = g^r(u, x^r) + B^r \varepsilon(t), \\ y^r = h^r(x^r) = \overline{C}^r x^r(t) + \overline{w}(t) = x_1^r + \overline{w}(t), \end{cases} \tag{3}$$

where $r \in \pi = \{1, 2, \ldots, M\}$ represents the index of the activated mode, M is an integer, $\overline{C}^r = (I_{n_1^r}, 0_{n_1^r \times n_2^r}, \ldots, 0_{n_1^r \times n_{q_r}^r})$,

$$x^r(t) = \begin{pmatrix} x_1^r \\ \vdots \\ x_{n^{r-1}}^r \\ x_{n^r}^r \end{pmatrix}, \quad g^r(u, x^r) = \begin{pmatrix} g_1^r(u, x_1^r, x_2^r) \\ g_2^r(u, x_1^r, x_2^r, \ldots, x_3^r) \\ \vdots \\ g_{q_r-1}^r(u, x^r) \\ g_{q_r}^r(u, x^r) \end{pmatrix},$$

and $B^r = \begin{pmatrix} 0 \\ \vdots \\ 0 \\ I_{n^r} \end{pmatrix}$. $x^r \in \mathbb{R}^{n^r}$ is the state vector with $x_k^r \in \mathbb{R}^{n_k^r}$, $k = 1, \ldots, q_r$ and $p^r = n_1^r \geq n_2^r \cdots \geq n_{q_r}^r$, $\sum_{k=1}^{q_r} n_k^r = n^r$, $y^r \in \mathbb{R}^{p^r}$ is the output, the input $u \in U$ a compact subset of $\mathbb{R}^n$, $g^r(u, x^r) \in \mathbb{R}^{n^r}$ with $g_k^r \in \mathbb{R}^{n_k^r}$, and $\overline{w}(t)$ is the output noise.

The piecewise constant function is designed to characterize switched systems: σ: $R^+ \longrightarrow \pi = \{1, 2, \ldots, M\}$, with $\sigma = r \in \pi$. If $t \in [[\tau_i, \tau_{i+1}$, the subsystem $\sigma(\tau_i)$ is active, where τ_i is a monotone nondecreasing finite sequence of time points. We assume that each subsystem is uniformly observable. In addition, it is assumed that there exists a diffeomorphism on the interval $[[\tau_i, \tau_i + 1$ defined by $x^r \longrightarrow z^r = \Phi^r(x^r) = [h^r(x^r), L_{g_r}(x^r), \ldots, L_{g_r}^{n^r-1}(x^r)]$ that transforms system (3) into the following form which represents an extension of a similar form presented in [30] to the hybrid case:

$$\begin{cases} \dot{z}^r = A^r z^r + \varphi^r(z^r, u) + \dfrac{\partial \phi^r}{\partial x^r} B^r \varepsilon(t), \\ y^r = C^r z^r + \overline{w}(t) = z_1^r + \overline{w}(t), \end{cases} \tag{4}$$

where $L_{g_r}(x^r)$ is the Lie derivative of $h^r(x^r)$ in the direction of $g^r(x^r)$ and $z^r \in \mathbb{R}^{n^r}$ is the state. The matrices A^r and C^r are as follows:

$$A^r = \begin{pmatrix} 0 & I_{n_1^r} & 0 & & 0 \\ \vdots & \ddots & I_{n_1^r} & \ddots & 0 \\ 0 & & \ddots & \ddots & I_{n_1^r} \\ 0 & \cdots & & 0 & 0 \end{pmatrix}, \tag{5}$$

$$C^r = \left(I_{n_1^r}, 0_{n_1^r}, \ldots, 0_{n_1^r} \right). \tag{6}$$

For the high-gain observer design in the presence of measurement noise, we make the following assumptions:

Assumption 1: the state $x^r(t)$ and the input $u(t)$ are uniformly bounded.

Assumption 2: the unknown function ε is uniformly bounded and $\exists \delta_\varepsilon > 0$; $\mathrm{Sup}_{t \geq 0} \mathrm{Ess} \|\overline{\varepsilon}(t)\| \leq \delta_\varepsilon$.

Assumption 3: $\overline{w}$ is a bounded noise signal and $\exists \delta_w > 0$; $\mathrm{Sup}_{t \geq 0} \mathrm{Ess} \|\overline{w}(t)\| \leq \delta_w$.

Assumption 4: $\forall k \in \{1, \ldots, q_r - 1\}$, $\forall x^r \in \mathbb{R}^{n^r}$, $\forall u \in U$: $\exists \alpha, \beta > 0$ such that

$$\alpha^2 I_{n_{k+1}^r} \leq \left(\frac{\mathrm{d}g_k^r}{\mathrm{d}x_{k+1}^r} \right)^T \frac{\mathrm{d}g_k^r}{\mathrm{d}x_{k+1}^r} \leq \beta^2 I_{n_{k+1}^r}. \tag{7}$$

Assumption 5: the evolution duration of each subsystem of system (3) is known.

Assumption 6: the dwell time $(\tau_{i+1} - \tau_i) > \tau_{\min}$ with $\tau_{\min}$ is a positive real and $i \in \pi = \{1, 2, \ldots, M\}$.

Remark 1. Note that Assumption 5 means that we do not consider systems with the Zeno phenomenon. Furthermore, when the duration of evolution τ_i of each system is measurable, the instability due to τ_i is excluded. On the other hand, it is to be noticed that Assumption 6 means that the dwell time which represents the duration between two switches should be sufficient to ensure the perfect convergence of the synthesized observer to the real system before a new switch [11].

2.2.2. The Alternating Activated Sludge Process Modeled as a Nonlinear Hybrid System. In this section, we show that the AASP (2) may be written in the form of the nonlinear hybrid system (3). Indeed, the studied process is composed by two subsystems: $r \in \{1, 2\}$. In fact, when $\mathrm{KLa} \neq 0$ and $S_{\mathrm{O2}} \neq 0$, $r = 1$: the aerobic phase is active. When $\mathrm{KLa} = 0$ and S_{O2} near zero, $r = 2$: the anoxic phase is active. Refer to reference [31] where we have also considered a nonlinear hybrid model of the alternating activated sludge process.

(1) Aerobic Phase. During this phase $r = 1$, the state vector is $x^1 = ((x_1^1)^T, (x_2^1)^T)^T$ such that

Table 1: Parameters of the activated sludge process model.

Parameters	Values	Designation
S_{O2sat}	$9.5\,g\cdot m^{-3}$	Dissolved oxygen saturation concentration
KLa	225 or $0\,day^{-1}$	Coefficient of oxygen transfer
λ_1	$62.59\,day^{-1}$	Heterotrophic biomass growth rate
λ_2	$187.37\,g\cdot m^{-3}\cdot day^{-1}$	Speed of production of nitrate by the autotrophic activity
λ_3	$52.63\,g\cdot m^{-3}\cdot day^{-1}$	Speed of hydrolysis of slowly biodegradable substrate by the heterotrophic activity
λ_4	$987.2\,g\cdot m^{-3}\cdot day^{-1}$	Soluble organic nitrogen ammonification
K_{O2H}	$0.2\,g\cdot m^{-3}$	Average saturation coefficient of oxygen for the heterotrophic biomass
K_{NO3}	$0.5\,g\cdot m^{-3}$	Average saturation coefficient of nitrate
K_{NH4AUT}	$0.98\,g\cdot m^{-3}$	Average saturation coefficient of ammonia for the autotrophic biomass
K_{O2AUT}	$0.4\,g\cdot m^{-3}$	Average saturation coefficient of oxygen for the autotrophic biomass
Y_H	$0.64\,g\cdot g^{-1}$	Performance coefficient of heterotrophic biomass
i_{NBM}	$0.086\,g\cdot g^{-1}$	Mass of nitrogen in the heterotrophic and autotrophic biomass concentration
η_{NO3h}	0.31	Hydrolysis correction factor in the anoxic phase
D_s	$1.14\,day^{-1}$	The dilution rate
D_c	$0.016\,day^{-1}$	The dilution rate

$$x_1^1 = \begin{pmatrix} S_{NO3} \\ S_{O2} \end{pmatrix}, \quad x_2^1 = \begin{pmatrix} S_s \\ S_{NH4} \end{pmatrix}, \quad g^1\left(u, x^1\right) = \begin{pmatrix} g_1^1\left(u, x_1^1, x_2^1\right) \\ g_2^1\left(u, x_1^1, x_2^1\right) \end{pmatrix}, \tag{8}$$

where $g_1^1(u, x_1^1, x_2^1) = \begin{pmatrix} g_{1,1}^1(\cdot) \\ g_{1,2}^1(\cdot) \end{pmatrix}$ and $g_2^1(u, x_1^1, x_2^1) = \begin{pmatrix} g_{2,1}^1(\cdot) \\ g_{2,2}^1(\cdot) \end{pmatrix}$ with

$$\begin{aligned} g_{1,1}^1\left(u, x_1^1, x_2^1\right) &= -(D_s + D_c)S_{NO3} - \frac{1 - Y_H}{2.86Y_H}\widetilde{\Upsilon}_2 + \widetilde{\Upsilon}_3, \\ g_{1,2}^1\left(u, x_1^1, x_2^1\right) &= -(D_s + D_c)S_{O2} + KLa\left(S_{O2sat} - S_{O2}\right) - \frac{1 - Y_H}{Y_H}\widetilde{\Upsilon}_1 - 4.57\widetilde{\Upsilon}_3, \\ g_{2,1}^1\left(u, x_1^1, x_2^1\right) &= D_{Sin} + D_c S_{sc} - (D_s + D_c)S_s - \frac{1}{Y_H}\left(\widetilde{\Upsilon}_1 + \widetilde{\Upsilon}_2\right) + \widetilde{\Upsilon}_5, \\ g_{2,2}^1\left(u, x_1^1, x_2^1\right) &= D_s S_{NH4in} - (D_s + D_c)S_{NH4} - i_{NBM}\left(\widetilde{\Upsilon}_1 + \widetilde{\Upsilon}_2\right) - \widetilde{\Upsilon}_3 + \widetilde{\Upsilon}_4. \end{aligned} \tag{9}$$

The output vector, $y^1 = \overline{C}^1 x^1 + \overline{w}(t) = x_1^1 + \overline{w}(t)$, with $\overline{C}^1 = \begin{pmatrix} 1 & 0 & 0 & 0 \\ 0 & 1 & 0 & 0 \end{pmatrix}$.

(2) Anoxic Phase. During anoxic phase $r = 2$, the state vector is $x^2 = (x_1^2, x_2^2, x_3^2)^T$ with

$$x_1^2 = S_{NO3}, \quad x_2^2 = S_{NH4}, \quad x_3^2 = S_s, \quad g^2\left(u, x^2\right) = \begin{pmatrix} g_1^2(\cdot) \\ g_2^2(\cdot) \\ g_2^2(\cdot) \end{pmatrix}, \tag{10}$$

where $g_1^2(u, x_1^2, x_2^2, x_3^2) = g_{1,1}^1(\cdot)$, $g_2^2(u, x_1^2, x_2^2, x_3^2) = g_{2,2}^1(\cdot)$, and $g_3^2(u, x_1^2, x_2^2, x_3^2) = g_{2,1}^1(\cdot)$

The output vector, $y^2 = \overline{C}^2 x^2 + \overline{w}(t) = x_1^2 + \overline{w}(t)$, with $\overline{C}^2 = (1 \;\; 0 \;\; 0)$.

3. A Filtered High-Gain Observer (FHGO)

In this section, we propose a filtered high-gain observer for the general nonlinear hybrid system (3), and we apply it to the considered alternating activated sludge process (2) considered in this work. To that end, we anticipate our procedure design by applying an appropriate state transformation to the considered nonlinear hybrid system (3) similar to that used in reference [29].

3.1. State Transformation. Proceeding as in [29], the change of coordinates is given by $x^r \longrightarrow z^r = \Phi^r(x^r) = [z_1^r, \ldots, z_{q_r}^r]^T$, $z_k^r \in \mathbb{R}^{n_1^r}, k = 1, \ldots, q_r$, where

$$\Phi^r(x^r,u)=\begin{pmatrix} g_1^r(u,x_1^r,x_2^r) \\ \dfrac{\partial g_1^r(u,x_1^r,x_2^r)}{\partial x^r} g_2^r(u,x_1^r,x_2^r,x_3^r) \\ \vdots \\ \left(\prod_{k=1}^{q-2}\dfrac{\partial g_k^r}{\partial x_{k+1}^r}(u,x^r)\right) g_{q_r-1}^r(u,x^r) \end{pmatrix}. \quad (11)$$

As shown in [30], it may be established that the transformation Φ^r transforms system (3) in the following structure:

$$\begin{cases} \dot{z}^r = A^r z^r + \varphi^r(z^r,u) + \dfrac{\partial \phi^r}{\partial x^r} B^r \varepsilon(t), \\ y^r = C^r z^r + w(t) = z_1^r + \overline{w}(t), \end{cases} \quad (12)$$

where

$$\varphi^r(z^r,u)=\begin{pmatrix} \varphi_1^r(u,z_1^r) \\ \varphi_2^r(u,z_1^r,z_2^r) \\ \vdots \\ \varphi_k^r(u,z_1^r,\ldots,z_k^r) \\ \varphi_{q_r}^r(u,z^r) \end{pmatrix}, \quad (13)$$

with $\varphi_k^r(u,z^r)\in\mathbb{R}^{n_1^r}, k=1,\ldots,q_r, A^r$ and C^r are given, respectively, by (5) and (6). In the sequel, we rather focus on the transformed nonlinear hybrid system described by equation (12).

3.2. A Filtered High-Gain Observer for Nonlinear Hybrid Systems. A filtered high-gain observer for the obtained class of nonlinear hybrid systems given by (12) is now introduced. The observer design is based on the combination of the high-gain observer design procedure in the measurement-free noise case developed in [30] for a class of nonlinear continuous systems in the triangular canonical form and the design procedure of FHGO in the presence of noisy measurements proposed in [29]. In addition, we suggest an extension of the above design procedures to the class of nonlinear hybrid systems (3) which include the alternated activated sludge process (2) considered in this paper. The filtered high-gain observer that we propose provides the estimation of unmeasured states in each mode despite the presence of measurement noise.

For the observer design, we require the following additional assumption:

> Assumption 7: $\phi^r(u,\phi^c(z^r))$ and $\varphi^r(z^r,u)$ are globally Lipschitz with respect to z^r uniformly in u. $\phi^c(z^r)$ is the converse of ϕ^r.

Before defining the candidate observer, we introduce the following notations:

$\Lambda^r(\widehat{x}^r,u)$ is the bloc diagonal matrix defined by

$$\Lambda^r=\operatorname{diag}\left(I_{n_1^r},\frac{dg^r(u,x^r)}{dx_2^r},\ldots,\prod_{k=1}^{q_r}\frac{dg^r(u,x^r)}{dx_{k+1}^r}\right). \quad (14)$$

$(\Lambda^r)^+$ represents the left inverse of Λ^r, and

$$K^r=\operatorname{diag}\left(\mathscr{C}_{n^r}^1,\ldots,\mathscr{C}_{n^r}^{n^r}\right), \quad (15)$$

with $\mathscr{C}_{n^r}^k=((n^r!)/((n^r-k)!k!)), k=1,\ldots,n^r$. Let

$$\Gamma^r=\frac{\partial \phi^r}{\partial x^r}(u,\phi^c(\widehat{z}^r)) \cdot\left((\Lambda^r)^+(u,\phi^c(\widehat{z})^r)-\left(\frac{\partial \phi^r}{\partial x^r}(u,\phi^r(\widehat{z})^r\right)^+\right), \quad (16)$$

$$\Delta^r=\operatorname{diag}\left(I_{n_1^r},\frac{1}{\theta}I_{n_1^r},\ldots,\frac{1}{\theta^{q_r-1}}I_{n_1^r}\right),$$

where θ is a positive real.

$$M^r=\begin{pmatrix} A^r & -K^r \\ (C^r)^T C^r & -2I_{n^r}+(A^r)^T \end{pmatrix}. \quad (17)$$

The filtered high-gain observer that we proposed for system (12) is given by

$$\begin{cases} \dot{\widehat{z}}^r(t)=A^r\widehat{z}^r+\varphi^r(\widehat{z}^r,u)-\theta K^r e^r(t)-\theta\Gamma^r K^r e^r(t), \\ \dot{e}^r(t)=-2\theta e^r(t)+\theta^2(A^r)^T e^r(t)+\theta(C^r)^T(C^r\widehat{z}^r(t)-y^r(t)). \end{cases} \quad (18)$$

Noting that M^r is Hurwitz (see Lemma 1 in [28]), there exists a symmetric positive definite (SPD) matrix $P=P^T$ and a positive real $\mu>0$ such that

$$(M^r)^T P+PM^r\le -2\mu I_{2n^r}. \quad (19)$$

Proposition 1. *We suppose that system (12) satisfies Assumptions 1–7. Then, $\forall\rho>0$; $\exists\theta_0>0$; $\forall\theta\ge\theta_0, \forall u$ such that $\|u\|_\infty\le\rho$; $\forall\widehat{z}^r(0)\in\mathbb{R}^{n^r}$, we have*

$$\left\|\widehat{z}^r(t)-z^r(t)\right\|\le\sigma\theta^{n^r-1}e^{\left(-\mu\theta/2\lambda_M\right)t}\left\|z^r(0)\right\| + 2\frac{\lambda_M\sigma}{\mu}\left(\theta^{n^r-1}\delta_w+\beta^{n^r-1}\frac{\delta_\varepsilon}{\theta}\right), \quad (20)$$

with $Z^r(0)=\begin{pmatrix}\widehat{z}^r(0)-z^r(0))\\ e^r(0)\end{pmatrix}$, $\theta_0=\max(1,((2\lambda_M(\Upsilon\prod_{i=1}^{n^r}K_i+\sqrt{n^r}\sqrt{L_\varphi}))/\mu))$, *and* $\sigma=\sqrt{\lambda_M/\lambda_m}$ *is the conditioning number of the matrix P.*

Proof. Set $\widetilde{z}^r=\widehat{z}^r-z^r$, $\widetilde{\varphi}^r(u,\widehat{z}^r,z^r)=\varphi^r(u,\widehat{z}^r)-\varphi^r(u,z^r)$, and $\overline{z}^r=\theta^{n^r-1}\Delta_\theta\widetilde{z}^r$, with $\Delta_\theta=\operatorname{diag}[I_{n_1^r},(1/\theta)I_{n_1^r},\ldots,(1/(\theta^{n^r-1}I_{n_1^r}))]$. Using (12) and (18), one has

$$\dot{\widehat{z}}^r = A^r\widehat{z}^r + \widetilde{\varphi}^r\left(u,\widehat{z}^r,z^r\right) - \left(\frac{\partial\phi^r}{\partial x^r}\left(u,\phi^c\left(z^r\right)\right)\right)B\varepsilon(t) - \theta K^r e^r(t) - \theta\Gamma^r K^r e^r(t). \tag{21}$$

It is easy to check that

$$\begin{aligned}\Delta_\theta A^r\Delta_\theta^{-1} &= \theta A^r,\\ C^r\Delta_\theta^{-1} &= C^r.\end{aligned} \tag{22}$$

From (22) and seeing the commutation of K^r and Δ_θ with each other, one has

$$\begin{aligned}\dot{\overline{z}}^r &= \Delta_\theta A^r\Delta_\theta^{-1}\overline{z}^r + \theta^{n^r-1}\Delta_\theta\widetilde{\varphi}^r\left(u,\widehat{z}^r,z^r\right)\\ &\quad - \theta^{n^r-1}\Delta_\theta\left(\frac{\partial\phi^r}{\partial x^r}(u,\phi^c(z^r))B\varepsilon(t) - \theta^{n^r}\Delta_\theta K^r e^r(t) - \theta^{n^r}\Delta_\theta\Gamma^r K^r e^r(t)\right.\\ &= \theta A^r\overline{z}^r + \theta^{n^r-1}\Delta_\theta\widetilde{\varphi}^r\left(u,\widehat{z}^r,z^r\right)\\ &\quad - \theta^{n^r-1}\Delta_\theta\left(\frac{\partial\phi^r}{\partial x^r}(u,\phi^c(z^r))B\varepsilon(t) - \theta K^r\overline{e}^r(t) - \theta^{n^r}\Delta_\theta\Gamma^r K^r\theta^{1-n^r}\Delta_\theta^{-1}\overline{e}^r(t)\right.\\ &= \theta A^r\overline{z}^r + \theta^{n^r-1}\Delta_\theta\widetilde{\varphi}^r\left(u,\widehat{z}^r,z^r\right)\\ &\quad - \theta^{n^r-1}\Delta_\theta\left(\frac{\partial\phi^r}{\partial x^r}(u,\phi^c(z^r))B\varepsilon(t) - \theta K^r\overline{e}^r(t) - \theta\Delta_\theta\Gamma^r\Delta_\theta^{-1}K^r\overline{e}^r(t),\right.\end{aligned} \tag{23}$$

where $\overline{e}^r(t) = \theta^{n^r-1}\Delta_\theta e^r(t)$. Furthermore, using (22), one gets

$$\begin{aligned}\dot{\overline{e}}^r &= -2\theta\overline{e}^r(t) + \theta^2\Delta_\theta\left(A^r\right)^T\Delta_\theta^{-1}\overline{e}^r(t)\\ &\quad + \theta\left(C^r\right)^T C^r\overline{z}^r - \theta^{n^r}\left(C^r\right)^T\overline{w}(t)\\ &= -2\theta\overline{e}^r(t) + \theta\left(A^r\right)^T\overline{e}^r(t) + \theta\left(C^r\right)^T C^r\overline{z}^r - \theta^{n^r}\left(C^r\right)^T\overline{w}(t).\end{aligned} \tag{24}$$

Now, equations (23) and (24) can be assembled in a compact form as follows:

$$\begin{aligned}\dot{\overline{Z}}^r &= \theta M^r\overline{Z}^r + \begin{pmatrix}\theta^{n^r-1}\Delta_\theta\widetilde{\varphi}^r\left(u,\widehat{z}^r,z^r\right)\\ 0_{n^r,1}\end{pmatrix}\\ &\quad - \begin{pmatrix}\theta^{n^r-1}\Delta_\theta\left(\dfrac{\partial\phi^r}{\partial x^r}(u,\phi^c(z^r))B\varepsilon(t)\right)\\ \theta^{n^r}\left(C^r\right)^T\overline{w}(t)\end{pmatrix}\\ &\quad - \begin{pmatrix}\theta\Delta_\theta\Gamma^r\Delta_\theta^{-1}K^r\overline{e}^r(t)\\ 0_{n^r,1}\end{pmatrix},\end{aligned} \tag{25}$$

where $\overline{Z}^r = \begin{pmatrix}\overline{z}^r\\ \overline{e}^r\end{pmatrix}$. Let $V^r(\overline{Z}^r) = (\overline{Z}^r)^T P\overline{Z}^r$ be the Lyapunov function with P being symmetric positive definite matrix. One gets

$$\begin{aligned}\dot{V}^r &= 2\left(\overline{Z}^r\right)^T P\overline{Z}^r\\ &= 2\left(\overline{Z}^r\right)^T P\theta M^r\overline{Z}^r + 2\left(\overline{Z}^r\right)^T P\begin{pmatrix}\theta^{n^r-1}\Delta_\theta\widetilde{\varphi}^r\left(u,\widehat{z}^r,z^r\right)\\ 0_{n^r,1}\end{pmatrix}\\ &\quad - 2\left(\overline{Z}^r\right)^T P\begin{pmatrix}\theta^{n^r-1}\Delta_\theta\left(\dfrac{\partial\phi^r}{\partial x^r}(u,\phi^c(z^r))B\varepsilon(t)\right)\\ \theta^{n^r}\left(C^r\right)^T\overline{w}(t)\end{pmatrix}\\ &\quad - 2\left(\overline{Z}^r\right)^T P\begin{pmatrix}\theta\Delta_\theta\Gamma^r\Delta_\theta^{-1}K^r\overline{e}^r(t)\\ 0_{n^r,1}\end{pmatrix}\\ &\le -2\mu\theta\left\|\overline{Z}^r\right\|^2 + 2\left\|P\overline{Z}^r\right\|\left(\left\|\theta^{n^r-1}\Delta_\theta\widetilde{\varphi}^r\left(u,\widehat{z}^r,z^r\right)\right\| + \left\|\theta^{n^r-1}\Delta_\theta\left(\frac{\partial\phi^r}{\partial x^r}(u,\phi^c(z^r))B\varepsilon(t)\right)\right\|\right.\end{aligned}$$

$$+\left\|\theta^{n^r}\left(C^r\right)^T\overline{w}(t)\right\|+\left\|\theta\Gamma^rK^r\overline{e}^r(t)\right\|\Big)$$
$$\leq -2\mu\theta\left\|\overline{Z}^r\right\|^2+2\lambda_M\left\|\overline{Z}^r\right\|\Big(\left\|\theta^{n^r-1}\Delta_\theta\widetilde{\varphi}^r\left(u,\widehat{z}^r,z^r\right)\right\|+\left\|\theta\Gamma^rK^r\overline{e}^r(t)\right\|\Big)$$
$$+2\sqrt{\lambda_M}\sqrt{V^r\left(\overline{z}^r\right)}\Big(\left\|\theta^{n^r-1}\Delta_\theta\left(\frac{\partial\phi^r}{\partial x^r}\left(u,\phi^c\left(z^r\right)\right)B\varepsilon(t)\right\|+\left\|\theta^{n^r}\overline{w}(t)\right\|\right). \tag{26}$$

We note that thanks to the triangular structure of φ^r, we have

$$\left\|\theta^{n^r-1}\Delta_\theta\widetilde{\varphi}^r\left(u,\widehat{z}^r,z^r\right)\right\|\leq\sqrt{n^r}L_\varphi\left\|Z^r\right\|\leq\sqrt{n^r}\sqrt{L_\varphi}\left\|\overline{Z}^r\right\|. \tag{27}$$

Similarly, taking into consideration the triangular structure of $(\partial\phi^r/\partial x^r)(u,\phi^c(z^r))$, we can show that

$$\left\|\theta^{n^r-1}\Delta_\theta\left(\frac{\partial\phi^r}{\partial x^r}(u,\phi^c(z^r))B\varepsilon(t)\right\|\leq\beta^{n^r-1}\delta_\varepsilon. \tag{28}$$

Finally, Γ^r is lower triangular with zeros on the main diagonal; then, one obtains

$$\left\|\theta\Delta_\theta\Gamma^r\Delta_\theta^{-1}K^r\overline{e}^r(t)|\leq\Upsilon\prod_{i=1}^{n^r}K_i\right\|\overline{e}^r(t)\left\|\leq\Upsilon\prod_{i=1}^{n^r}K_i|\overline{Z}^r\right\|, \tag{29}$$

with $K_i=C_{n^r}^k=((n^r!)/((n^r-k)!k!)), k=1,\ldots,n^r$ and $\|\overline{e}^r(t)\|\leq\|\overline{Z}^r\|$. Using (27)–(29), we have

$$\dot{V}^r\leq\left(-2\mu\theta+2\lambda_M\left(\Upsilon\prod_{i=1}^{n^r}K_i+\sqrt{n^r}\sqrt{L_\varphi}\right)\right)\left\|\overline{Z}^r\right\|^2$$
$$+2\sqrt{\lambda_M}\sqrt{V^r\left(\overline{Z}^r\right)}\left(\beta^{n^r-1}\delta_\varepsilon+\theta^{n^r}\|\overline{w}(t)\|\right). \tag{30}$$

Now, we choose θ such that $-2\mu\theta+2\lambda_M(\Upsilon\prod_{i=1}^{n^r}K_i+\sqrt{n^r}\sqrt{L_\varphi})<-\mu\theta$. So, it arises from each $\theta>\theta_0=((2\lambda_M(\Upsilon\prod_{i=1}^{n^r}K_i+\sqrt{n^r}\sqrt{L_\varphi}))/\mu)$ that

$$\dot{V}^r\left(\overline{Z}^r\right)\leq-\mu\theta\left\|\overline{Z}^r\right\|^2+2\sqrt{\lambda_M}\sqrt{V^r\left(\overline{Z}^r\right)}\left(\beta^{n^r-1}\delta_\varepsilon+\theta^{n^r}\|\overline{w}(t)\|\right)$$
$$\leq\frac{-\mu\theta}{\lambda_M}V^r\left(\overline{Z}^r\right)+2\sqrt{\lambda_M}\sqrt{V^r\left(\overline{Z}^r\right)}\left(\beta^{n^r-1}\delta_\varepsilon+\theta^{n^r}\|\overline{w}(t)\|\right), \tag{31}$$

or equivalently,

$$\frac{\mathrm{d}}{\mathrm{d}t}\sqrt{V^r\left(\overline{Z}^r(t)\right)}\leq\frac{-\mu\theta}{2\lambda_M}\sqrt{V^r\left(\overline{Z}^r(t)\right)}$$
$$+\sqrt{\lambda_M}\left(\beta^{n^r-1}\delta_\varepsilon+\theta^{n^r}\|\overline{w}(t)\|\right). \tag{32}$$

Using the comparison lemma, it arises that

$$\sqrt{V^r\left(\overline{Z}^r(t)\right)}\leq e^{\left((-\mu\theta)/\left(2\lambda_M\right)\right)t}\sqrt{V^r\left(\overline{Z}^r(0)\right)}$$
$$+2\frac{\lambda_M^{3/2}}{\mu}\left(\theta^{n^r-1}\delta_w+\beta^{n^r-1}\frac{\delta_\varepsilon}{\theta}\right). \tag{33}$$

This yields to

$$\left\|\left(\overline{Z}^r(t)\right)\right\|\leq\sigma e^{\left((-\mu\theta)/\left(2\lambda_M\right)\right)t}\left\|\overline{Z}^r(0)\right\|$$
$$+2\frac{\lambda_M\sigma}{\mu}\left(\theta^{n^r-1}\delta_w+\beta^{n^r-1}\frac{\delta_\varepsilon}{\theta}\right). \tag{34}$$

Next, set $Z^r(t)=\begin{pmatrix}\widetilde{z}^r\\ e^r\end{pmatrix}$. One has for $\theta\geq1$ and for all $t\geq0\|Z^r(t))\|\leq\|(\overline{Z}^r(t))\|\leq\theta^{n^r-1}\|Z^r(t))\|$. So we have

$$\left\|Z^r(t))\right\|\leq\sigma\theta^{n^r-1}e^{\left((-\mu\theta)/\left(2\lambda_M\right)\right)t}\left\|Z^r(0)\right\|$$
$$+2\frac{\lambda_M\sigma}{\mu}\left(\theta^{n^r-1}\delta_w+\beta^{n^r-1}\frac{\delta_\varepsilon}{\theta}\right), \tag{35}$$

which completes the proof. □

Remark 2. The designed filtered high-gain observer (FHGO) for a class of switched systems represents an extension of the FHGO which has been recently developed in references [28, 29] for a class of nonlinear systems in the canonical form of observability and having a triangular structure. Indeed, we rather consider in our paper a more general class of nonlinear switched systems subject to measurement noise, which enlarges the applicability of our proposed robust estimation approach.

The main disadvantage of the FHGO scheme consists in the fact that it requires the resolution of $(n+m)$ ordinary differential equations (ODE) instead of only n ODE for the standard HGO. Such drawback can restrict the application of the FHGO to the relatively fast plants which need a high sampling rate. The filtered high-gain observer used in this paper may be compared with the work in [29] where a FHGO has been designed for a class of uncertain nonlinear systems with sampled outputs to overcome the latter hindrance. Extending our work to the case of filtered continuous-discrete high-gain observer design when a weak and a variable sampling of the output measurement can be used is one of our main interests in the future works.

3.3. Observer Design in the Original Coordinates. Proceeding as in references [29, 30], the proposed observer (18) can be written in the original coordinates x^r as follows:

$$\begin{cases}\dot{\widehat{x}}^r(t)=g^r\left(\widehat{x}^r,u\right)-\theta\left(\Lambda^r\right)^+\left(\widehat{x}^r,u\right)\left(\Delta^r\right)^{-1}K^rE^r(t),\\ \dot{E}^r(t)=-2\theta E^r(t)+\theta^2\left(A^r\right)^TE^r(t)+\theta\left(C^r\right)^T\left(C^r\widehat{x}^r(t)-y^r(t)\right).\end{cases} \tag{36}$$

Now, our main objective is to apply the proposed filtered high-gain observer to the considered alternating activated sludge process (2). According to the corresponding model (1), the whole observer is composed by two-alternated-FHGO scheme as follows:

For $r = 1$ (aerobic phase), $x_1^1 = \begin{pmatrix} S_{NO3} \\ S_{O2} \end{pmatrix} \in \mathbb{R}^2$ is the measured states vector and $x_2^1 = \begin{pmatrix} S_s \\ S_{NH4} \end{pmatrix} \in \mathbb{R}^2$ is unmeasured states vector. In this case, we have

$$\left(\Delta^1\right)^{-1} = \operatorname{diag}\left(I_2, \theta I_2\right),$$

$$K^1 = \operatorname{diag}\left(2I_2, I_2\right),$$

$$\Lambda^1 = \begin{pmatrix} 1 & 0 & 0 & 0 \\ 0 & 1 & 0 & 0 \\ 0 & 0 & \dfrac{\mathrm{d}g_{1,1}^1\left(u, x_1^1, x_2^1\right)}{\mathrm{d}S_s} & \dfrac{\mathrm{d}g_{1,1}^1\left(u, x_1^1, x_2^1\right)}{\mathrm{d}S_{NH4}} \\ 0 & 0 & \dfrac{\mathrm{d}g_{1,2}^1\left(u, x_1^1, x_2^1\right)}{\mathrm{d}S_s} & \dfrac{\mathrm{d}g_{1,2}^1\left(u, x_1^1, x_2^1\right)}{\mathrm{d}S_{NH4}} \end{pmatrix}, \tag{37}$$

with

$$\frac{\mathrm{d}g_{1,1}^1\left(u, x_1^1, x_2^1\right)}{\mathrm{d}S_s} = -\lambda_1 \frac{1 - Y_H}{2.86 Y_H}\left(\frac{S_{NO3}}{\left(S_{NO3} + K_{NO3}\right)}\right)\left(\frac{KO2H}{\left(S_{O2} + K_{O2H}\right)}\right),$$

$$\frac{\mathrm{d}g_{1,2}^1\left(u, x_1^1, x_2^1\right)}{\mathrm{d}S_s} = -\lambda_1\left(\frac{\left(1 - Y_H\right)}{Y_H}\right)\left(\frac{S_{O2}}{\left(S_{O2} + K_{O_2H}\right)}\right),$$

$$\frac{\mathrm{d}g_{1,1}^1\left(u, x_1^1, x_2^1\right)}{\mathrm{d}S_{NH4}} = \lambda_2\left(\frac{S_{O2}}{\left(S_{O2} + K_{O2_AUT}\right)}\right)\left(\frac{K_{NH4AUT}}{\left(S_{NH4} + \left(K_{NH_4AUT}\right)^2\right)}\right), \tag{38}$$

$$\frac{\mathrm{d}g_{1,2}^1\left(u, x_1^1, x_2^1\right)}{\mathrm{d}S_{NH4}} = -4.57\lambda_2\left(\frac{S_{O2}}{\left(S_{O2} + K_{O_2AUT}\right)}\right)\left(\frac{K_{NH_4AUT}}{\left(S_{NH4} + \left(K_{NH_4AUT}\right)^2\right)}\right).$$

On the other hand, for $r = 2$ (anoxic phase), $x_1^2 = S_{NO3} \in \mathbb{R}$ is the measured state. $x_2^2 = S_{NH4}$ and $x_3^2 = S_s$ are the unmeasured states. So, one obtains

$$\left(\Delta^2\right)^{-1} = \operatorname{diag}\left(1, \theta, \theta^2\right),$$

$$K^2 = \operatorname{diag}\left(3, 3, 1\right),$$

$$\Lambda^2 = \begin{pmatrix} 1 & 0 & 0 \\ 0 & \dfrac{\mathrm{d}g_1^2\left(u, x_1^2, x_2^2, x_3^2\right)}{\mathrm{d}S_{NH4}} & 0 \\ 0 & 0 & \dfrac{\mathrm{d}g_1^2\left(u, x_1^2, x_2^2, x_3^2\right)}{\mathrm{d}S_{NH4}} \quad \dfrac{\mathrm{d}g_2^2\left(u, x_1^2, x_2^2, x_3^2\right)}{\mathrm{d}S_s} \end{pmatrix}, \tag{39}$$

with

$$\frac{\mathrm{d}g_1^2\left(u, x_1^2, x_2^2, x_3^2\right)}{\mathrm{d}S_{\mathrm{NH4}}} = \lambda_2\left(\frac{S_{\mathrm{O2}}}{\left(S_{\mathrm{O2}} + K_{\mathrm{O_2AUT}}\right)}\right) \cdot \left(\frac{K_{\mathrm{NH_4AUT}}}{\left(S_{\mathrm{NH4}} + K_{\mathrm{NH_4AUT}}\right)^2}\right), \quad (40)$$

$$\frac{\mathrm{d}g_2^2\left(u, x_1^2, x_2^2, x_3^2\right)}{\mathrm{d}S_s} = -i_{\mathrm{NBM}}\left(\left(\frac{\widetilde{\Upsilon}_1}{S_s}\right) + \left(\frac{\widetilde{\Upsilon}_2}{S_s}\right)\right).$$

We recall that, for $r = 1$ ($\mathrm{KLa} \neq 0$, $S_{\mathrm{O2}} \neq 0$), the aerobic phase is active, and for $r = 2$ ($\mathrm{KLa} = 0$, $S_{\mathrm{O2}} \simeq 0$), the anoxic phase is active.

Remark 3. The problem of adaptive and robust observer design for switched systems remains an open research field to be explored. Indeed, many existing estimation methods which have been designed in the literature for classical continuous linear and nonlinear systems may be extended and generalized for hybrid systems and in particular for switched system. For instance, the robust and efficient estimation approach based on terminal sliding-mode observers may be extended to switched systems. Indeed, terminal sliding-mode observers have very interesting finite-time convergence properties. We report for instance the recent reference [32] in which the authors have designed an adaptive terminal sliding-mode observer to compensate for mismatched uncertainties of a class of nonlinear systems.

4. Numerical Simulations

Numerical simulations are dedicated to highlight the good state estimation performances and the robustness of the proposed observer against measurement noise compared to the classical high-gain observer. For both phases, the input signal $u(t) = (S_{\mathrm{sc}}, S_{\mathrm{sin}}, S_{\mathrm{NH4in}})^T = (1600, 200, 70)^T$. The initial value of the activated sludge process state is fixed as $x(0) = \begin{pmatrix} 0.3 & 0 & 10 & 5.3 \end{pmatrix}^T$. The initial estimated states for the classical high-gain observer and the proposed filtered high-gain observer are chosen as $\widehat{x}(0) = \begin{pmatrix} 0.3 & 0 & 12 & 5.7 \end{pmatrix}^T$. θ is set to 12. The outputs are corrupted by a Gaussian noise with a 0.02 variance value. The different parameters of the ASP model are defined in Table 1.

Numerical simulations are carried out using Matlab/Simulink software. The state estimation provided by the classical HGO and the proposed FHGO observers is illustrated in Figures 2–5. It is shown that the proposed filtered high-gain observer provides better performances in terms of state estimation and robustness against measurement noise compared to the classical one. Indeed, Figures 2 and 3 prove that the biodegradable substrate S_s and the ammonia concentration S_{NH4} are quite estimated by the filtered high-gain observer despite the presence of measurement noise, whereas the estimation performances are degraded when using the classical high-gain observer.

In order to further illustrate the robustness properties of the adopted FHGO in this paper, additional simulations are carried out in a more realistic scenario where the considered AASP system is simultaneously corrupted by an unknown input $\varepsilon(t)$ in its dynamics and measurement noise $\overline{w}(t)$ in the output equations. We notice that the unknown input $\varepsilon(t)$ may include disturbances and modeling uncertainties. For simulations, we assume that the unknown input consists of a disturbance signal $\varepsilon(t) = 50\sin(20\pi t)$, and the measurement noise $\overline{w}(t)$ is a Gaussian noise with a 0.02 variance value. In addition, we select the high-gain design parameter as $\theta = 12$. To emphasize the robustness properties of the adopted estimation approach, we simulate simultaneously the proposed FHGO and the classical HGO for the AASP system. The simulation results are given in Figures 6 and 7.

It is shown in Figures 6 and 7 that the adopted FHGO is able to estimate perfectly the unmeasured biodegradable

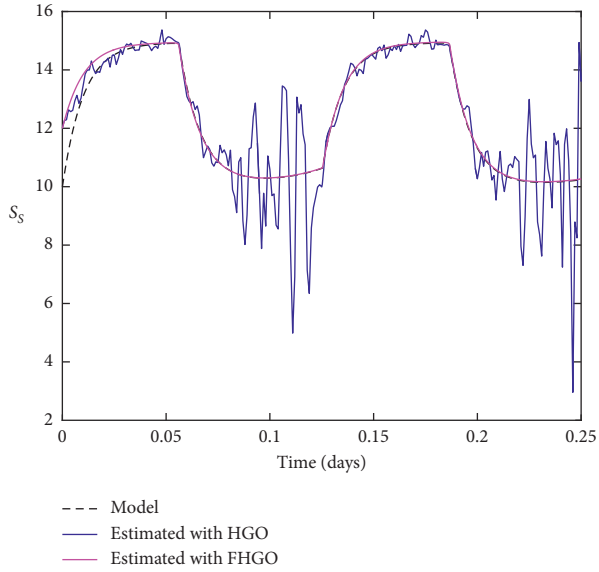

Figure 2: S_s estimation.

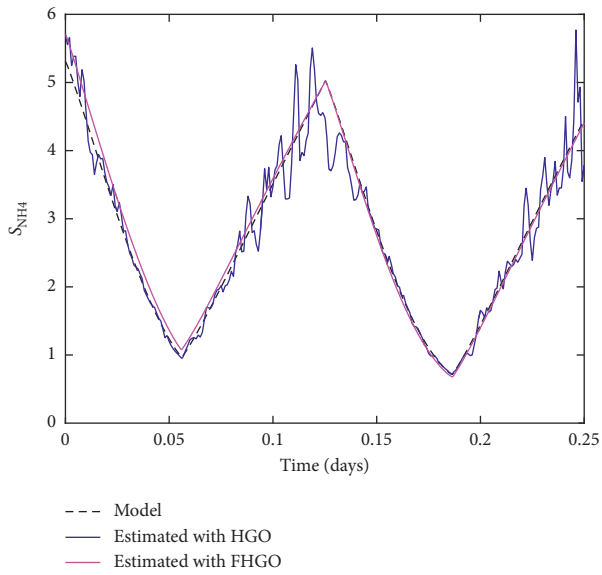

Figure 3: S_{NH4} estimation.

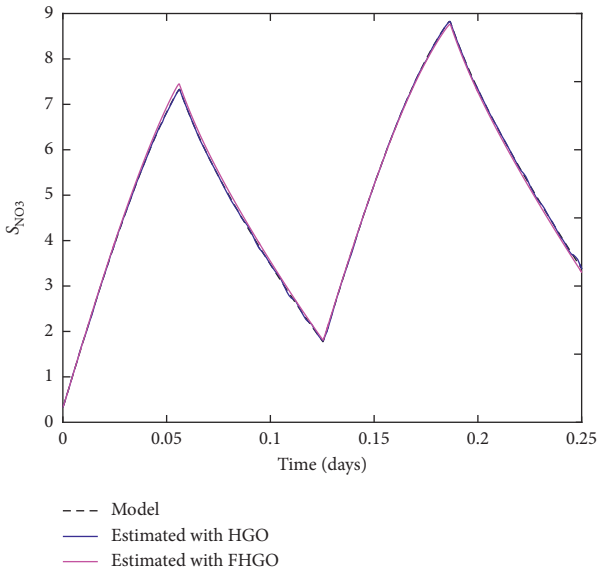

Figure 4: S_{NO3} estimation.

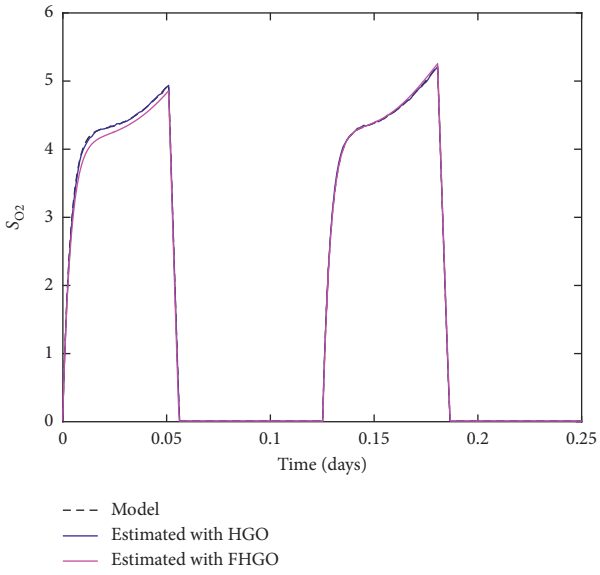

Figure 5: S_{O2} estimation.

concentration S_s and the unmeasured ammonia concentration S_{NH4} despite the presence of disturbances in the dynamics and the presence of Gaussian measurement noise, contrary to the case of the classical HGO where we observe a degradation on the estimation performances as illustrated in Figures 6 and 7. Indeed, it is well known that the main disadvantage of the classical HGO consists in its high sensitivity to measurement noise. Moreover, it is to be noticed that when designing a classical HGO, in practice, it is very difficult to find an optimal choice of the design parameter θ to reject simultaneously the effect of the disturbance $\varepsilon(t)$ and the measurement noise $\overline{w}(t)$. To overcome the drawbacks of the classical HGO, the proposed FHGO in this paper allows to reduce the sensitivity

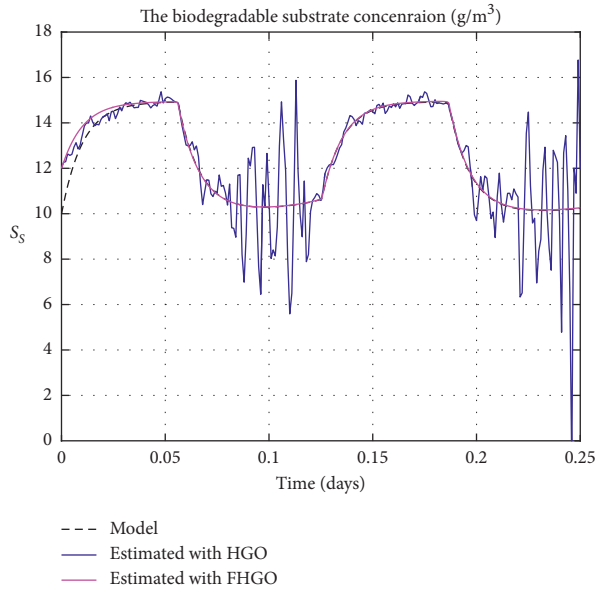

Figure 6: Estimation of the biodegradable concentration S_s in the presence of a disturbance $\varepsilon(t)$ and measurement noise $\overline{w}(t)$ by the proposed FHGO and classical HGO.

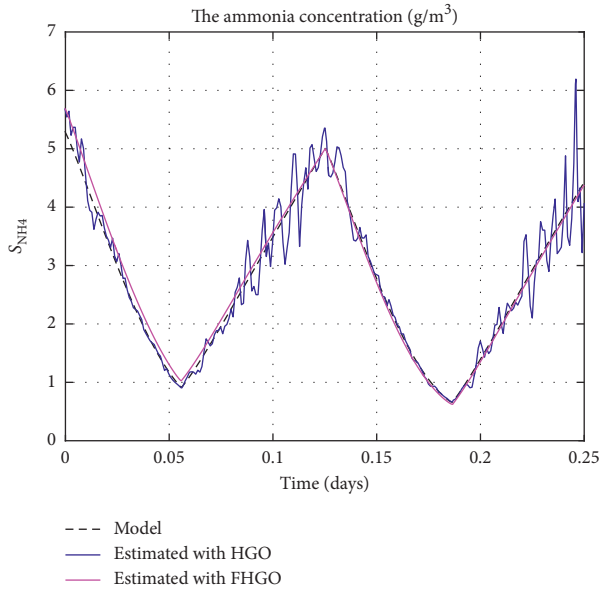

Figure 7: Estimation of the ammonia concentration S_{NH4} in the presence of a disturbance $\varepsilon(t)$ and measurement noise $\overline{w}(t)$ by the proposed FHGO and classical HGO.

to measurement noise thanks to the idea of applying linear filters on the observation error while keeping its ability to compensate for disturbances present in the dynamics of the nonlinear system by choosing sufficiently high values of the design parameter θ. The latter properties have been clearly shown in Figures 6 and 7 where we illustrate the superiority of the proposed FHGO compared to the classical HGO in terms of robustness against disturbances and measurement noise.

5. Conclusion

In this paper, we have designed a filtered high-gain observer (FHGO) for a class of nonlinear hybrid systems in order to solve simultaneously the problems of the high cost of reliable sensors and the high sensitivity to measurement noise. The proposed estimation method was applied to the alternating activated sludge plant model where we have shown that a quite estimation of the ammonia concentration and the biodegradable substrate is achieved when only the noisy dissolved oxygen and nitrate concentrations are used. The simulation results show clearly the filtering capabilities of the FHGO that inhibits the noise amplification in the estimation of unavailable state variable (such aspect is known as the main hindrance for the standard HGO). Extending our work to the case of continuous-discrete HGO where outputs are only available at the sampling time represents one of our main interests in the future works.

Notation

$\|\cdot\|$: Euclidean norm
$0_{j\times k}$: Null matrix with j rows and k columns
$I_{n_1^r}$: Identity matrix with $n_1^r \times n_1^r$ dimension
$0_{n_1^r}$: $n_1^r \times n_1^r$ null matrix
$I_{n_{k+1}^r}$: $n_{k+1}^r \times n_{k+1}^r$ identity matrix.

Data Availability

The data used to support the findings of this study are included within the article.

Conflicts of Interest

The authors declare that they have no conflicts of interest.

Acknowledgments

This work was supported by the University of Monastir, the National Engineering School of Monastir, and the University of Sousse.

References

[1] M. Scholz, *Activated Sludge Processes. Wetlands for Water Pollution Control*, Elsevier, Amsterdam, Netherlands, Chapter 15, 2016.

[2] M. C. Ozturk, F. Martin Serrat, and F. Teymour, "Optimization of aeration profiles in the activated sludge process," *Chemical Engineering Science*, vol. 139, pp. 1–14, 2016.

[3] M. Henze, C. P. L. Grady, W. Gujer, G. R. Marais, and T. Matsuo, "Activated sludge model no. 1," Scientific and Technical Report 1, IAWQ, London, UK, 1987.

[4] M. Henze, W. Gujer, T. Mino, T. Matsuo, M. C. Wentzel, and G. V. R. Marais, "Activated sludge model no. 2," Scientific and Technical Reports, IAWQ, London, UK, 1995.

[5] M. Henze, W. Gujer, T. Mino et al., "Activated sludge model no. 2D, ASM2D," *Water Science and Technology*, vol. 39, no. 1, pp. 165–182, 1999.

[6] W. Gujer, M. Henze, T. Mino, and M. Van Loosdrecht, "Activated sludge model no. 3," *Water Science and Technology*, vol. 39, no. 1, pp. 183–193, 1999.

[7] R. Marquez, M. Belandria-Carvajal, C. Ríos-Bolívar, and M. Rios-Bolivar, "Average modeling of an alternating aerated activated sludge process for nitrogen removal," *IFAC Proceedings Volumes*, vol. 44, no. 1, pp. 14195–14200, 2011.

[8] P. J. Antsaklis and A. Nerode, "Hybrid control systems: an introductory discussion to the special issue," *IEEE Transactions on Automatic Control*, vol. 43, no. 4, pp. 457–460, 1998.

[9] D. Liberzon and A. S. Morse, "Basic problems in stability and design of switched systems," *IEEE Control Systems*, vol. 19, no. 5, pp. 59–70, 1999.

[10] M. S. Branicky, "Stability of switched and hybrid systems," in *Proceedings of the 33rd IEEE Conference on Decision and Control*, pp. 3498–3503, Lake Buena Vista, FL, USA, December 1994.

[11] N. Barhoumi, F. Msahli, M. Djemaï, and K. Busawon, "Observer design for some classes of uniformly observable nonlinear hybrid systems," *Nonlinear Analysis: Hybrid Systems*, vol. 6, no. 4, pp. 917–929, 2012.

[12] M. Jafari and S. Mobayen, "Second-order sliding set design for a class of uncertain nonlinear systems with disturbances: an LMI approach," *Mathematics and Computers in Simulation*, vol. 156, pp. 110–125, 2019.

[13] S. Mobayen and G. Pujol-Vazquez, "A robust LMI approach on nonlinear feedback stabilization of continuous state-delay systems with Lipschitzian nonlinearities: experimental validation," *Iranian Journal of Science and Technology, Transactions of Mechanical Engineering*, vol. 43, pp. 54–558, 2019.

[14] D. Boutat, A. Benali, and J.-P. Barbot, "About the observability of piecewise dynamical systems," *IFAC Proceedings Volumes*, vol. 37, no. 13, pp. 1183–1188, 2004.

[15] J. Vila, A. Pisano, and E. Usai, "Continuous and discrete state reconstruction for nonlinear switched systems via high-order sliding-mode observers," *International Journal of Systems Science*, vol. 42, no. 5, pp. 725–735, 2011.

[16] J. Li, X. Guo, C. Chen, and Q. Su, "Robust fault diagnosis for switched systems based on sliding mode observer," *Applied Mathematics and Computation*, vol. 341, pp. 193–203, 2019.

[17] J. Li, K. Pan, and Q. Su, "Sensor fault detection and estimation for switched power electronics systems based on sliding mode observer," *Applied Mathematics and Computation*, vol. 353, pp. 282–294, 2019.

[18] F. Smida, T. Ladhari, S. Hadj Said, and F. M'Sahli, "Unknown inputs nonlinear observer for an activated sludge process," *Mathematical Problems in Engineering*, vol. 2018, Article ID 1382914, 12 pages, 2018.

[19] D. E. C. Belkhiat, N. Messai, and N. Manamanni, "Robust fault detection based-observer for linear switched systems," *IFAC Proceedings Volumes*, vol. 42, no. 17, pp. 392–397, 2009.

[20] J. Van Gorp, M. Defoort, K. C. Veluvolu, and M. Djemai, "Hybrid sliding mode observer for switched linear systems with unknown inputs," *Journal of the Franklin Institute*, vol. 351, no. 7, pp. 3987–4008, 2014.

[21] Y. Chang, S. Zhang, N. D. Alotaibi, and A. F. Alkhateeb, "Observer-based adaptive finite-time tracking control for a class of switched nonlinear systems with unmodeled dynamics," *IEEE Access*, vol. 8, pp. 204782–204790, 2020.

[22] L. Ma, N. Xu, X. Huo, and X. Zhao, "Adaptive finite-time output-feedback control design for switched pure-feedback nonlinear systems with average dwell time," *Nonlinear Analysis: Hybrid Systems*, vol. 37, pp. 1–23, 2020.

[23] M. Farza, M. M'Saad, and L. Rossignol, "Observer design for a class of MIMO nonlinear systems," *Automatica*, vol. 40, no. 1, pp. 135–143, 2004.
[24] S. H. Saïd, F. M'Sahli, and M. Farza, "Simultaneous state and unknown input reconstruction using cascaded high-gain observers," *International Journal of Systems Science*, vol. 48, no. 15, pp. 3346–3354, 2017.
[25] A. Kadrine, Z. Tir, O. P. Malik, M. A. Hamida, A. Reatti, and A. Houari, "Adaptive non-linear high gain observer based sensorless speed estimation of an induction motor," *Journal of the Franklin Institute*, vol. 357, no. 13, pp. 8995–9024, 2020.
[26] J. H. Ahrens and H. K. Khalil, "High-gain observers in the presence of measurement noise: a switched-gain approach," *Automatica*, vol. 45, no. 4, pp. 936–943, 2009.
[27] M. Oueder, M. Farza, R. M'Saad, and M. M'Saad, "A high gain observer with updated gain for a class of MIMO non-triangular systems," *Systems & Control Letters*, vol. 61, no. 2, pp. 298–308, 2012.
[28] C. Tréangle, M. Farza, and M. M'Saad, "A simple filtered high gain observer for a class of uncertain nonlinear systems," in *Proceedings of the 18th IEEE Conference on Sciences and Techniques of Automatic Control and Computer Engineering (STA)*, pp. 396–401, Monastir, Tunisia, December 2017.
[29] C. Tréangle, M. Farza, and M. M'Saad, "Filtered high gain observer for a class of uncertain nonlinear systems with sampled outputs," *Automatica*, vol. 101, pp. 197–206, 2019.
[30] M. Farza, M. M'Saad, and M. Sekher, "A set of observers for a class of nonlinear systems," in *Proceedings of the IFAC World Congress*, Prague, Czech Republic, July 2005.
[31] A. Boudagga, H. Dimassi, S. Hadj-Said, and F. M'Sahli, "A filtered high gain observer for a nonlinear hybrid system: the alternating activated sludge process," in *Proceedings of The19th International Conference on Sciences and Techniques of Automatic Control and Computer Engineering (STA)*, pp. 13–18, Sousse, Tunisia, March 2019.
[32] G. Gurumurthy and D. K. Das, "Terminal sliding mode disturbance observer based adaptive super twisting sliding mode controller design for a class of nonlinear systems," *European Journal of Control*, 2020.

Hindawi
Mathematical Problems in Engineering
Volume 2020, Article ID 8868234, 11 pages
https://doi.org/10.1155/2020/8868234

Research Article

$\mathscr{H}_2$ Control of Markovian Jump Systems with Input Saturation and Incomplete Knowledge of Transition Probabilities

Bum Yong Park

The Division of Electrical Engineering and Department of IT Convergence Engineering, Kumoh National Institute of Technology, Gumi-si, Gyeongsangbuk-do, Republic of Korea

Correspondence should be addressed to Bum Yong Park; bumyong.park@kumoh.ac.kr

Received 3 September 2020; Revised 11 November 2020; Accepted 24 November 2020; Published 10 December 2020

Academic Editor: Rosalba Galván-Guerra

This paper proposes an $\mathscr{H}_2$ state-feedback controller for Markovian jump systems with input saturation and incomplete knowledge of transition probabilities. The proposed controller is developed using second-order matrix polynomials of an incomplete transition rate to derive less conservative stabilization conditions. The proposed controller not only guarantees $\mathscr{H}_2$ performance but also rejects matched disturbances. The effectiveness of the proposed method is demonstrated using three numerical examples.

1. Introduction

Over the last few decades, Markovian jump systems (MJSs) have been recognized as one of the most effective models for the representation of dynamic systems subjected to random and abrupt variations. Thus, numerous studies have been conducted to analyze and synthesize MJSs [1–7]. The findings of these studies have been applied in various practical systems, such as networked control systems [8], manufacturing systems [8], economic systems [9], power systems [10], and actuator saturation [11]. In particular, studies have focused on the analysis and synthesis of ideal MJSs having exact values of transition probabilities [12].

However, such MJSs with exactly known transition probabilities have limited scope for application in practical systems because it is difficult to obtain complete knowledge of transition probabilities. Thus, recent studies on controller synthesis have focused on MJSs with incomplete knowledge of transition probabilities. Such studies have employed the free-connection weighting method and linear matrix inequalities (LMIs) [13–16].

However, several practical systems suffer from input saturation because of the physical limitations of the control system [17–19]. It is well known that input saturation generally degrades control system performance and system stability [20].

Thus, the control synthesis problem should be considered with input saturation in practical systems. In particular, the stochastic stabilization problem for MJSs subjected to actuator saturation was studied based on exactly known transition probabilities [21, 22]. Furthermore, the stabilization of saturated MJSs with incomplete knowledge of transition probabilities was studied using the free-connection weighting matrix approach [11]. In addition, the stabilization condition for MJSs in the presence of both partially unknown transition rates and input saturation was proposed [23].

To the best of the author's knowledge, intensive studies on the $\mathscr{H}_2$ control of MJSs with input saturation and incomplete knowledge of transition probabilities have not been conducted thus far. A previous study stabilized nonhomogeneous MJSs with input saturation [24]; however, the findings are not applicable to practical systems because disturbances were not considered.

Thus, an $\mathscr{H}_2$ stabilization condition for MJSs with input saturation and incomplete knowledge of transition probabilities is proposed herein. The main contributions of this study are as follows:

This is the first proposal to propose a stabilization condition to accomplish stochastic stability and guarantee $\mathscr{H}_2$ performance for MJSs with input saturation and incomplete knowledge of transition probabilities.

The proposed controller consists of two parts: a linear control part to guarantee $\mathscr{H}_2$ performance and a nonlinear control part to reject the matched disturbances.

Based on the proposed relaxation method using the second-order matrix polynomials of the incomplete transition rate, this paper presents less conservative stabilization conditions for estimating the domain of attraction.

The effectiveness of the proposed controller is demonstrated using two numerical examples and a practical example.

The remainder of this paper is organized as follows. Section 2 provides a description of the system and some preliminary results. Section 3 introduces the proposed $\mathscr{H}_2$ controller for MJSs with input saturation and incomplete knowledge of transition probabilities. Section 4 presents the simulations of three examples for verifying the proposed controller. Section 5 concludes the paper.

Notation. The notations $X \geq Y$ and $X > Y$ indicate that $X - Y$ is positive semidefinite and positive definite, respectively. In symmetric block matrices, $(*)$ is used as an ellipsis for terms that are induced by symmetry. Furthermore, $\mathbf{He}(X) = X + X^T$ stands for any matrix X, and $\mathbf{E}[\cdot]$ denotes the mathematical expectation. For any matrices S_i and S_{ij},

$$\begin{aligned}\left[S_i\right]_{i\in\{1,2,\ldots,N\}} &= \left[S_{11}, S_{12}, \ldots, S_{1N}\right],\\ \left[S_{ij}\right]_{i,j\in\{1,2,\ldots,N\}} &= \begin{bmatrix} S_{11} & S_{12} & \cdots & S_{1N}\\ S_{21} & S_{22} & \ddots & \vdots\\ \vdots & \ddots & \ddots & \vdots\\ S_{N1} & \cdots & \cdots & S_{NN}\end{bmatrix}.\end{aligned} \tag{1}$$

We also use $\|x\|_p$ to indicate the p-norm of x, i.e., $\|x\|_p \triangleq (|x_1|^p + \cdots + |x_n|^p)^{(1/p)}$, $p \geq 1$. $\lambda_{\min}(X)$ and $\lambda_{\max}(X)$ denote a minimum eigenvalue and a maximum eigenvalue of X, respectively. The notation e_k indicates a unit vector with a single nonzero entry at the kth position, i.e., $e_k \triangleq [0 \ldots \underbrace{1}_{k^{\text{th}}} \ldots 0]^T$.

2. System Description and Preliminaries

Consider the following continuous-time MJS with input saturation and a matched disturbance:

$$\dot{x}(t) = A(r_t)x(t) + B(r_t)\{\text{sat}(u(t)) + d(t)\}, \tag{2}$$

$$z(t) = C(r_t)x(t), \tag{3}$$

where $x(t) \in \mathfrak{R}^n$ is the state, $u(t) \in \mathfrak{R}^m$ is the control input, $d(t) \in \mathfrak{R}^m$ is the matched disturbance, and $z(t) \in \mathfrak{R}^q$ is the controlled output. The matched disturbance $d(t)$ is assumed to be $|e_k^T d(t)| < \varepsilon$. Here, $\{r_t, t \geq 0\}$ is a continuous-time Markov jumping process in a finite set $D = \{1, 2, 3, \ldots, N\}$ with mode transition probabilities:

$$P(r_{t+\delta t} = j \mid r_t = i) = \begin{cases} \pi_{ij}\delta t + o(\delta t), & \text{if } i \neq j,\\ 1 + \pi_{ij}\delta t + o(\delta t), & \text{if } i = j,\end{cases} \tag{4}$$

where $\delta t > 0$, $\lim_{\delta t \longrightarrow 0}(o(\delta t)/\delta t) = 0$, and π_{ij} is the transition rate from mode i to j at time $t + \delta t$. For $r_t = i \in D$, to simplify the notation, $A(r_t) = A_i$, $B(r_t) = B_i$, $D(r_t) = D_i$, and $C(r_t) = C_i$. Further, $\text{sat}(\cdot)$ denotes a saturation operator, which is defined as

$$[\text{sat}(u)]_i \triangleq \begin{cases} [u]_i, & \left|[u]_i\right| < \mu,\\ \mu, & \left|[u]_i\right| \geq \mu,\\ -\mu, & \left|[u]_i\right| \leq \mu,\end{cases} \tag{5}$$

where $\mu(> \varepsilon)$ is the saturation level. Furthermore, the transition rate matrix Π belongs to

$$S_\Pi \triangleq \left\{ \left[\pi_{ij}\right]_{i,j\in D} | 0 \leq \pi_{ij}, \quad \text{for } i \neq j, \pi_{ii} = -\sum_{j=1, i\neq j}^{N} \pi_{ij} \right\}. \tag{6}$$

In view of the aforementioned relations, π_{ij} accords with the following relationships, for all $i, j \in D$:

$$\nu_{ij}\pi_{ij} \geq 0, \sum_{j=1}^{N} \pi_{ij} = 0, -\nu_{ij}\pi_{ij}\left(\pi_{ij} + \pi_{ii}\right) \geq 0, \tag{7}$$

where

$$\nu_{ij} = \begin{cases} 1, & i \neq j,\\ -1, & i = j.\end{cases} \tag{8}$$

For future convenience, two sets are defined with respect to the measurability of the transition rate for $i, j \in D$:

$$\begin{aligned} D_i^+ &\triangleq \left\{ j | \pi_{ij} \text{ is known for } i \right\},\\ D_i^- &\triangleq \left\{ j | \pi_{ij} \text{ is unknown for } i \right\}.\end{aligned} \tag{9}$$

The following lemma and definitions are introduced as preliminaries required to prove the theorems presented in the subsequent sections.

Lemma 1 (see [25]). *Let* $u, v \in \mathfrak{R}^m$,

$$\begin{aligned} u &= \begin{bmatrix} u_1 & u_2 & \ldots & u_m \end{bmatrix}^T,\\ v &= \begin{bmatrix} v_1 & v_2 & \ldots & v_m \end{bmatrix}^T.\end{aligned} \tag{10}$$

Assume that $|e_k^T v| \leq \mu$ for all $k \in [1, m]$, and then

$$\text{sat}(u) \in \mathbf{Co}\{E_s u + E_s^- v |, s \in \left[1, 2^m\right]\}, \tag{11}$$

where E_s denotes a diagonal matrix with all possible combinations of 1 and 0 diagonal entries, $E_s^- \triangleq I - E_s$, and **Co** is the convex hull.

Definition 1 (see [21]). A set $\mathcal{S} \in \mathfrak{R}^n$ is called the domain of attraction in the mean square sense of (2), if for any initial mode $r_0 \in D$ and initial state $x(0) \in \mathcal{S}$, the state $x(t)$ of (2) satisfies

$$\lim_{T\longrightarrow\infty}\left(\int_0^T \mathbf{E}\left[\|x(\tau)\|^2\right]\mathrm{d}\tau|x(0),r_0\right) < x^T(0)\Psi x(0), \quad (12)$$

where $\Psi > 0$.

3. Main Results

This section considers the design problem of the $\mathscr{H}_2$ state-feedback controller.

A controller is proposed for system (2) as follows:

$$u(t) = K(r_t)x(t) + \overline{u}(r_t, x(t)), \quad (13)$$

where $K(r_t)$ is the linear controller part to guarantee the $\mathscr{H}_2$ performance and $\overline{u}(r_t, x(t))$ is the nonlinear controller part to reject the matched disturbance $B(r_t)d(t)$. Thus, the proposed controller is designed to stochastically stabilize and minimize the upper bound of the following linear quadratic cost:

$$J(t) = \mathbf{E}\left[\int_t^\infty x^T(\tau)Q(r_t)x(\tau)\mathrm{d}\tau\right], \quad (14)$$

where $Q(r_t) = Q_i \geq 0$. Here, for $r_t = i \in D$, $K(r_t) = K_i$ and $\overline{u}(r_t, x(t)) = \overline{u}_i(x(t))$. Using system (2) and the proposed controller (13), the resultant closed-loop system is expressed as follows:

$$\dot{x}(t) = A_i x(t) + B_i\{\mathrm{sat}(K_i x(t) + \overline{u}_i(x(t))) + d(t)\}. \quad (15)$$

Theorem 1. *Consider system (15) with input saturation and incomplete knowledge of the transition rate. For $i, j \in D$, $s \in [1, 2^m]$, and $k \in [1, m]$, suppose that there exist symmetric matrices $\overline{P}_i$ and R_{ij}, matrices $\overline{K}_i$, $\overline{H}_i$, Λ_{ij}, Y_{ij}, S_{i0}, and S_{ij}, and a scalar γ such that*

$$\overline{P}_i > 0, \quad (16)$$

$$\Lambda_{ij} + \Lambda_{ij}^T > 0, Y_{ij} + Y_{ij}^T > 0, \quad (17)$$

$$\begin{bmatrix} R_{ij} & \overline{P}_i \\ (*) & \overline{P}_j \end{bmatrix} > 0, \quad i \neq j, \quad (18)$$

$$\begin{bmatrix} \overline{\Gamma}_s^i & \left[\Gamma_j^i\right]_{j\in D_i^-} \\ (*) & \left[\Gamma_{jl}^i\right]_{j,l\in D_i^-} \end{bmatrix} < 0, \quad (19)$$

$$\begin{bmatrix} \gamma & x^T(0) \\ x(0) & \overline{P}_0 \end{bmatrix} > 0, \quad (20)$$

$$\begin{bmatrix} \overline{P}_i & \overline{H}_i^T e_k \\ e_k^T \overline{H}_i & (\mu - \varepsilon)^2 \end{bmatrix} > 0, \quad (21)$$

$$\begin{bmatrix} 1 & x^T(0) \\ x(0) & \overline{P}_i \end{bmatrix} > 0, \quad (22)$$

where

$i \in D_i^+$

$$\begin{aligned}
\overline{\Gamma}_s^i &= \overline{\Omega}_s^i + \Pi_i^+ E^T \mathbf{He}(S_{i0})E + \sum_{j\in D_i^+} \nu_{ij}\pi_{ij}E^T\mathbf{He}(\Lambda_{ij})E \\
&\quad - \sum_{j\in D_i^+} \nu_{ij}\pi_{ij}(\pi_{ij} + \pi_{ii})E^T\mathbf{He}(Y_{ij})E, \\
\Gamma_j^i &= \frac{1}{2}E^T G_{ij} + E^T(S_{i0} + \Pi_i^+ S_{ij}) + \nu_{ij}E^T\Lambda_{ij} - \nu_{ij}\pi_{ii}E^T Y_{ij}, \\
\Gamma_{jj}^i &= \mathbf{He}(S_{ij}) - \nu_{ij}\mathbf{He}(Y_{ij}), \\
\Gamma_{jl}^i &= S_{il} + S_{ij},
\end{aligned} \quad (23)$$

$i \in D_i^-$

$$\begin{aligned}
\overline{\Gamma}_s^i &= \overline{\Omega}_s^i + \Pi_i^+ E^T \mathbf{He}(S_{i0})E + \sum_{j\in D_i^+} \nu_{ij}\pi_{ij}E^T\mathbf{He}(\Lambda_{ij})E \\
&\quad - \sum_{j\in D_i^+} \nu_{ij}\pi_{ij}^2 E^T\mathbf{He}(Y_{ij})E, \\
\Gamma_j^i &= \frac{1}{2}E^T G_{ij} + E^T S_{i0} + \Pi_i^+ E^T S_{ij} + \nu_{ij}E^T\Lambda_{ij} \\
&\quad - \sum_{j\in D_i^+} c_{ij}\nu_{ij}\pi_{ij}E^T Y_{ij}, \\
\Gamma_{jj}^i &= \mathbf{He}(S_{ij}) - 2\nu_{ij}\mathbf{He}(Y_{ij}), \\
\Gamma_{jl}^i &= \begin{cases} S_{il} + S_{ij}, & i \neq l, \\ S_{il} + S_{ij} - \nu_{ij}Y_{ij}, & i = l, \end{cases} \\
\Pi_i^+ &= \sum_{j\in D^+} \pi_{ij}, \\
\overline{\Omega}_s^i &\triangleq \begin{bmatrix} \mathbf{He}(A_i\overline{P}_i + B_i E_s \overline{K}_i + B_i E_s^- \overline{H}_i) + \sum_{j\in D_i^+} \pi_{ij}G_{ij} & \overline{P}_i \\ \overline{P}_i & -Q_i^{-1} \end{bmatrix}, \\
G_{ij} &\triangleq \kappa_{ij}R_{ij} + (1 - \kappa_{ij})\overline{P}_i, \\
\kappa_{ij} &= \begin{cases} 1, & i \neq j, \\ 0, & i = j, \end{cases} \\
E &= [\, I \;\; 0 \,] \in \mathfrak{R}^{n\times 2n}.
\end{aligned} \quad (24)$$

Then, the set $\cap_{i=1}^N \Omega(P_i)$ is contained in the domain of attraction, and the proposed system (15) is stochastically stable with the $\mathscr{H}_2$ cost in (14) guaranteed by γ. Furthermore, the proposed controller is constructed as $u(t) = K_i x(t) + \overline{u}_i(x(t))$ for mode i, where $K_i = \overline{K}_i\overline{P}_i^{-1}$ and each component of $\overline{u}_i(x(t))$ is defined as

$$[\overline{u}_i(x(t))]_k = -\varepsilon\mathrm{sgn}(e_k^T B_i^T P_i x(t)). \quad (25)$$

Proof. Consider the following mode-dependent control input $u(t)$ and the auxiliary input $v(t)$:

$$\begin{aligned} u(t) &= K(r_t)x(t) + \overline{u}_i(x(t)), \\ v(t) &= H(r_t)x(t) + \overline{u}_i(x(t)), \end{aligned} \tag{26}$$

where $v(t)$ is used to handle the input saturation in Lemma 1. For the representation method (10) in Lemma 1, the following condition should be satisfied:

$$\left|e_k^T H(r_t)x(t) + e_k^T \overline{u}_i(x(t))\right| \le \mu. \tag{27}$$

From the definition of $\overline{u}_i(x(t))$ in (25), the left side of (27) can be derived as follows:

$$\begin{aligned} &\left|e_k^T H(r_t)x(t) + e_k^T \overline{u}_i(x(t))\right| \\ &\quad \le \left|e_k^T H(r_t)x(t)\right| + \left|e_k^T \overline{u}_i(x(t))\right| \\ &\quad = \left|e_k^T H(r_t)x(t)\right| + \varepsilon. \end{aligned} \tag{28}$$

Then, the sufficient condition for (27) is given as follows:

$$\left|e_k^T H(r_t)x(t)\right| \le \mu - \varepsilon. \tag{29}$$

Therefore, the representation method in Lemma 1 can be used if $x(t) \in L(H(r_t))$ for $k \in [1, m]$, where

$$L(H(r_t)) = \left\{x(t) \in \mathfrak{R}^n \middle| \left|e_k^T H(r_t)x(t)\right| \le \mu - \varepsilon\right\}. \tag{30}$$

To establish a set invariance condition [25], the ellipsoid $\Omega(P(r_t)) \triangleq \left\{x(t) \in \mathfrak{R}^n | xt(t)^T nPq(r_t)hx_(t)x \le 71\right\}$ is in the linear region $L(H(r_t))$, that is, for $k \in [1, m]$,

$$x^T(t)P_i x(t) > x^T(t)H_i^T e_k \frac{1}{(\mu - \varepsilon)^2} e_k^T H_i x(t), \tag{31}$$

or equivalently,

$$\begin{bmatrix} P_i & H_i^T e_k \\ e_k^T H_i & (\mu - \varepsilon)^2 \end{bmatrix} > 0. \tag{32}$$

Then, multiplying both sides of the above equation by $\mathrm{diag}\{P_i^{-1}, I\}$ yields (20), where $\overline{P}_i = P_i^{-1}$ and $\overline{H}_i = H_i \overline{P}_i$.

Let us choose $V(x(t)) = x^T(t)P(r_t)x(t)$ as a Lyapunov function, where $P(r_t)$ is a positive definite matrix. Then, from the weak infinitesimal operator ∇ of the Markov process, $\nabla V(x(t))$ is given by

$$\begin{aligned} \nabla V &= \lim_{\delta t \longrightarrow 0} \frac{1}{\delta t}\left(\mathbf{E}\left[V(x(t+\delta t), r_{t+\delta t} = j) | x(t), r_t = i\right]\right. \\ &\quad \left. - V(x(t), r_t = i)\right) \\ &= \frac{\mathrm{d}V(x(t), i)}{\mathrm{d}t} + \sum_{j=1}^{N} \pi_{ij} V(x(t), j) \\ &= 2x^T(t)P_i \dot{x}(t) + x^T(t)\sum_{j=1}^{N} \pi_{ij} P_j x(t). \end{aligned} \tag{33}$$

According to the convex property and condition (21), there exist variables η_s such that

$$\begin{aligned} \mathrm{sat}(u(t)) &= \sum_{s=1}^{2^m} \eta_s \{E_s u(t) + E_s^- v(t)\} \\ &= \sum_{s=1}^{2^m} \eta_s \{E_s K(r_t)x(t) + E_s^- H(r_t)x(t) + \overline{u}_i(x(t))\} \\ &= \sum_{s=1}^{2^m} \eta_s \{E_s K(r_t)x(t) + E_s^- H(r_t)x(t)\} + \overline{u}_i(x(t)), \end{aligned} \tag{34}$$

where $\sum_{s=1}^{2^m} \eta_s = 1$.

Then, $\nabla V(x(t))$ can be rewritten as

$$\begin{aligned} \nabla V(x(t)) &= 2x^T(t)\left\{P_i A_i + \sum_{s=1}^{2^m} \eta_s P_i B_i (E_s K_i + E_s^- H_i)\right\} x(t) \\ &\quad + 2x^T(t)P_i B_i \left(\sum_{s=1}^{2^m} \eta_s \overline{u}_i(x(t)) + d(t)\right) + x^T(t)\sum_{j=1}^{N} \pi_{ij} P_j x(t) \\ &= \sum_{s=1}^{2^m} \eta_s \left[2x^T(t)\{P_i A_i + P_i B_i (E_s K_i + E_s^- H_i)\} + 2x^T(t)P_i B_i (\overline{u}_i(x(t)) + d(t)) + x^T(t)\sum_{j=1}^{N} \pi_{ij} P_j x(t)\right]. \end{aligned} \tag{35}$$

Furthermore, from (25) and $|e_k^T d(t)| < \varepsilon$, we have

$$2x^T(t)P_i B_i (\overline{u}_i(x(t)) + d(t)) \le 0. \tag{36}$$

Thus, if the following condition holds, for $i \in D$ and $s \in [1, 2^m]$,

$$\mathbf{He}(P_i A_i + P_i B_i E_s K_i + P_i B_i E_s^- H_i) + Q_i + \sum_{j=1}^{N} \pi_{ij} P_j < 0, \tag{37}$$

then, from (36) and (35), $\nabla V(x(t))$ can be expressed as the following relation:

$$\nabla V(x(t)) \le 2\sum_{s=1}^{2^m} \eta_s x^T(t)\{P_iA_i + P_iB_i(E_sK_i + E_s^-H_i)\} + x^T(t)\sum_{j=1}^{N}\pi_{ij}P_jx(t) < -x^T(t)Q_ix(t). \tag{38}$$

Using the generalized Dynkin's formula [26], the above relation allows

$$\begin{aligned}&\mathbf{E}[V(t)] - V(0)\\ &= \mathbf{E}\left[\int_0^t \nabla V(\tau)\mathrm{d}\tau|x(0), r_0\right]\\ &< -\mathbf{E}\left[\int_0^t x^T(\tau)Q(r_\tau)x(\tau)\mathrm{d}\tau|x(0), r_0\right]\\ &\le -\min_{i\in D}(\lambda_{\min}(Q_i))\mathbf{E}\left[\int_0^t \|x(\tau)\|^2\mathrm{d}\tau|x(0), r_0\right],\end{aligned} \tag{39}$$

which leads to

$$\begin{aligned}&\min_{i\in D}(\lambda_{\min}(Q_i))\mathbf{E}\left[\int_0^t \|x(\tau)\|^2\mathrm{d}\tau|x(0), r_0\right]\\ &< V(0) - \mathbf{E}[V(t)]\\ &\le V(0),\end{aligned} \tag{40}$$

because the following equation is valid:

$$\mathbf{E}\left[\int_0^t \|x(\tau)\|^2\mathrm{d}\tau|x(0), r_0\right] < \frac{V(0)}{\min_{i\in D}(\lambda_{\min}(Q_i))}. \tag{41}$$

From (41), it is allowed that

$$\lim_{T\longrightarrow\infty} \mathbf{E}\left[\int_0^t \|x(\tau)\|^2\mathrm{d}\tau|x(0), r_0\right] \le x^T(0)\Psi x(0), \tag{42}$$

where

$$\Psi = \frac{\max_{r_0\in D}(\lambda_{\max}(P_{r_0}))}{\min_{i\in D}(\lambda_{\min}(Q_i))} > 0. \tag{43}$$

Furthermore, from (39), we have

$$J(0) < V(0) = x^T(0)P(r_0)x(0), \tag{44}$$

which guarantees the $\mathscr{H}_2$ cost through (20), indicating that $x^T(0)P(r_0)x(0) < \gamma$ using the Schur complement.

Subsequently, by pre- and postmultiplying (37) with P_i^{-1}, we have

$$\mathbf{He}(\mathscr{A}_s^i) + \overline{P}_iQ_i\overline{P}_i + \sum_{j=1}^{N}\pi_{ij}\overline{P}_iP_j\overline{P}_i < 0, \tag{45}$$

where $\mathscr{A}_s^i = A_i\overline{P}_i + B_iE_s\overline{K}_i + B_iE_s^-\overline{H}_i$, $\overline{P}_i = P_i^{-1}$, and $\overline{K}_i = K_i\overline{P}_i$.

Note that for $i = j$, $\overline{P}_iP_j\overline{P}_i = \overline{P}_i$, and for $i \ne j$, (18) leads to $\overline{P}_iP_j\overline{P}_i \le R_{ij}$. Equation (45) holds because of the following condition:

$$\mathbf{He}(\mathscr{A}_s^i) + \overline{P}_iQ_i\overline{P}_i + \sum_{j=1}^{N}\pi_{ij}G_{ij} < 0, \tag{46}$$

where $G_{ij} \triangleq \kappa_{ij}R_{ij} + (1-\kappa_{ij})\overline{P}_i$.

Applying the Schur complement to (46) yields

$$\begin{bmatrix}\mathbf{He}(\mathscr{A}_s^i) + \sum_{j=1}^{N}\pi_{ij}G_{ij} & \overline{P}_i\\ \overline{P}_i & -Q_i^{-1}\end{bmatrix} < 0. \tag{47}$$

To derive the LMI conditions, (47) can be written as follows:

$$\Omega_s^i \triangleq \overline{\Omega}_s^i + \sum_{j\in D_i^-}\pi_{ij}E^TG_{ij}E < 0. \tag{48}$$

In addition, according to condition (7), the following equations can be derived from (19):

$$C_i^1 \triangleq \mathbf{He}\left(\left(\Pi_i^+ + \sum_{j\in D_i^-}\pi_{ij}\right)E^T\left(S_{i0} + \sum_{j\in D_i^-}\pi_{ij}S_{ij}\right)E\right) = 0, \tag{49}$$

$$C_i^2 \triangleq \sum_{j=1}^{N}\nu_{ij}\pi_{ij}E^T\mathbf{He}(\Lambda_{ij})E \ge 0, \tag{50}$$

$$C_i^3 \triangleq -\sum_{j=1}^{N}\nu_{ij}\pi_{ij}(\pi_{ij} + \pi_{ii})E^T\mathbf{He}(Y_{ij})E \ge 0. \tag{51}$$

Then, the positive semidefinite matrix L^i is constructed using (49)–(51) in the following form:

$$\begin{aligned}L^i &\triangleq C_i^1 + C_i^2 + C_i^3\\ &= \overline{L}^i + \sum_{j\in D_i^-}\pi_{ij}\mathbf{He}(L_j^iE)\\ &\quad + \sum_{j\in D_i^-}\sum_{\substack{l\in D_i^-\\ l>j}}\pi_{ij}\pi_{il}E^T\mathbf{He}(L_{jl}^i)E\\ &\quad + \sum_{\substack{l\in D_i^-\\ l=j}}\pi_{ij}^2E^T\mathbf{He}(L_{jj}^i)E \ge 0,\end{aligned} \tag{52}$$

where

$$i \in D_i^+$$

$$\begin{aligned}
\overline{L}^i &= \Pi_i^+ E^T \mathbf{He}(S_{i0})E + \sum_{j\in D_i^+} \pi_{ij} E^T \mathbf{He}\left(\nu_{ij}\Lambda_{ij}\right)E \\
&\quad - \sum_{j\in D_i^+} \pi_{ij}^2 E^T \mathbf{He}\left(\nu_{ij}Y_{ij}\right)E \\
&\quad - \sum_{j\in D_i^+} \pi_{ij}\pi_{ii} E^T \mathbf{He}\left(\nu_{ij}Y_{ij}\right)E, \\
L_j^i &= E^T\left(S_{i0} + \Pi_i^+ S_{ij}\right) + E^T\nu_{ij}\Lambda_{ij} - E^T\nu_{ij}\pi_{ii}Y_{ij}, \\
L_{jl}^i &= S_{il} + S_{ij}, \\
L_{jj}^i &= S_{il} - \nu_{ij}Y_{ij}, \\
i &\in D_i^-
\end{aligned} \tag{53}$$

$$\begin{aligned}
\overline{L}^i &= \Pi_i^+ E^T \mathbf{He}(S_{i0})E + \sum_{j\in D_i^+} \pi_{ij} E^T \mathbf{He}\left(\nu_{ij}\Lambda_{ij}\right)E \\
&\quad - \sum_{j\in D_i^+} \pi_{ij}^2 E^T \mathbf{He}\left(\nu_{ij}Y_{ij}\right)E, \\
L_j^i &= E^T\left(S_{i0} + \Pi_i^+ S_{ij}\right) + E^T\left(\nu_{ij}\Lambda_{ij}\right) - \sum_{j\in D_i^+} c_{ij}\pi_{ij}E^T\left(\nu_{ij}Y_{ij}\right), \\
L_{jl}^i &= \begin{cases} S_{il} + S_{ij}, & i \neq l, \\ S_{il} + S_{ij} - \nu_{ij}Y_{ij}, & i = l, \end{cases} \\
L_{jj}^i &= S_{ij} - 2\nu_{ij}Y_{ij},
\end{aligned} \tag{54}$$

where

$$c_{ij} = \begin{cases} 1, & i = j, \\ 0, & i \neq j. \end{cases} \tag{55}$$

Based on the S-procedure, if $\Omega_s^i < 0$ whenever $L^i \geq 0$, the following sufficient condition is formulated:

$$L^i + \Omega_s^i < 0, \tag{56}$$

which can be converted to the following LMI condition:

$$\begin{bmatrix} I \\ \left[\pi_{ij}E\right]_{j\in D_i^-} \end{bmatrix}^T \begin{bmatrix} \overline{\Gamma}_s^i & \left[\Gamma_j^i\right]_{j\in D_i^-} \\ (*) & \left[\Gamma_{jl}\right]_{j,l\in D_i^-} \end{bmatrix} \begin{bmatrix} I \\ \left[\pi_{ij}E\right]_{j\in D_i^-} \end{bmatrix} < 0, \tag{57}$$

where

$$\begin{aligned}
\overline{\Gamma}_s^i &= \overline{\Omega}_s^i + \overline{L}^i, \\
\Gamma_j^i &= \frac{1}{2}E^T G_{ij} + L_j^i, \\
\Gamma_{jl}^i &= L_{jl}^i.
\end{aligned} \tag{58}$$

Then, (57) holds because of the LMI conditions (16)–(19). □

4. Numerical Examples

In this section, the $\mathscr{H}_2$ performance is investigated through numerical examples to verify the effectiveness of the proposed method.

4.1. Example 1. Consider an MJS with four modes ($N = 4$), whose system matrices are

$$\begin{aligned}
A_1 &= \begin{bmatrix} 0.35 & -7.30 \\ 1.48 & 0.81 \end{bmatrix}, \\
A_2 &= \begin{bmatrix} 0.89 & -3.11 \\ 1.48 & 0.21 \end{bmatrix}, \\
A_3 &= \begin{bmatrix} -0.11 & -0.85 \\ 2.31 & -0.10 \end{bmatrix}, \\
A_4 &= \begin{bmatrix} -0.17 & -1.48 \\ 1.59 & -0.27 \end{bmatrix}, \\
B_1 &= \begin{bmatrix} 0.57 \\ 1.23 \end{bmatrix}, \\
B_2 &= \begin{bmatrix} 0.78 \\ -0.49 \end{bmatrix}, \\
B_3 &= \begin{bmatrix} 1.34 \\ 0.39 \end{bmatrix}, \\
B_4 &= \begin{bmatrix} -0.38 \\ 1.07 \end{bmatrix}, \\
C_1 &= \begin{bmatrix} 0.0 & -0.1 \end{bmatrix}, \\
C_2 &= \begin{bmatrix} 0.1 & 0.0 \end{bmatrix}, \\
C_3 &= \begin{bmatrix} 0.0 & 0.1 \end{bmatrix}, \\
C_4 &= \begin{bmatrix} 0.1 & 0.0 \end{bmatrix}, \\
\Pi &= \begin{bmatrix} -1.3 & 0.2 & \pi_{13} & \pi_{14} \\ \pi_{21} & \pi_{22} & 0.3 & 0.3 \\ 0.6 & \pi_{32} & -1.5 & \pi_{34} \\ 0.4 & \pi_{42} & \pi_{43} & \pi_{44} \end{bmatrix}, \\
Q_1 &= Q_2 = Q_3 = Q_4 = \begin{bmatrix} 10 & 0 \\ 0 & 10 \end{bmatrix}, \\
\varepsilon &= 0.1, \mu = 1,
\end{aligned} \tag{59}$$

where π_{13}, π_{14}, π_{21}, π_{22}, π_{32}, π_{34}, π_{42}, π_{43}, and π_{44} are the unknown transition rates. The following sets can be obtained using the transition rate matrix Π:

$$\begin{aligned}
D_1^+ &= \{1,2\}, D_2^+ = \{3,4\}, D_3^+ = \{1,3\}, D_4^+ = \{1\}, \\
D_1^- &= \{3,4\}, D_2^- = \{1,2\}, D_3^- = \{2,4\}, D_4^- = \{2,3,4\}.
\end{aligned} \tag{60}$$

Considering the initial condition $x(0) = \begin{bmatrix} 0.2 & -0.15 \end{bmatrix}^T$, the state trajectories of the closed-loop system shown in Figure 1 are stochastically stable with incomplete knowledge of transition rates under the input saturation and matched

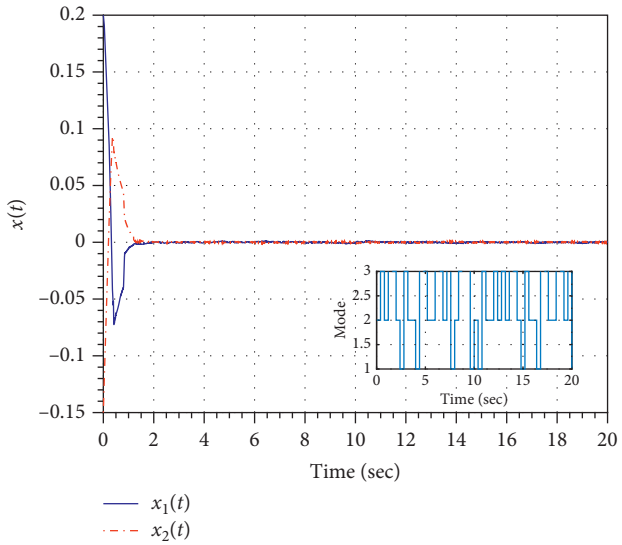

Figure 1: State trajectories for Example 1.

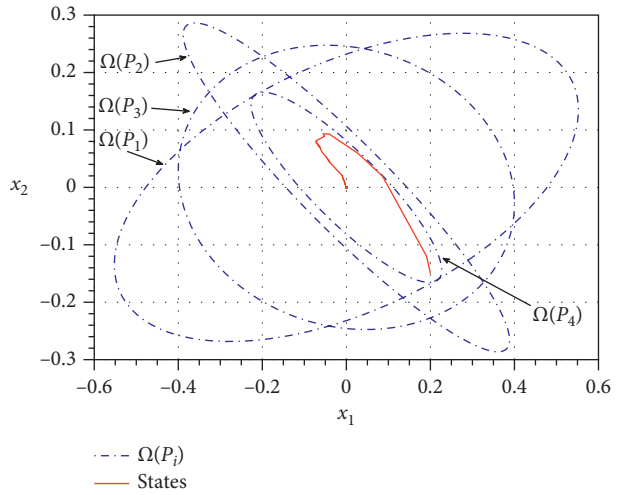

Figure 2: Domain of attraction for Example 1.

disturbances. Here, we set $r_0 = 2$ and $d(t) = 0.1\sin(2t^2 - 0.7)$.

According to Theorem 1, the $\mathscr{H}_2$ performance $\gamma = 0.2803$, and the proposed controller gains are obtained as follows:

$$
\begin{aligned}
K_1 &= \begin{bmatrix} 3.2384 \times 10^5 & -2.1342^6 \end{bmatrix},\\
K_2 &= \begin{bmatrix} -1.5913 \times 10^6 & -7.8766 \times 10^5 \end{bmatrix},\\
K_3 &= \begin{bmatrix} -8.9047 \times 10^5 & -8.0083 \times 10^5 \end{bmatrix},\\
K_4 &= \begin{bmatrix} -9.0151 \times 10^6 & -1.5631 \times 10^7 \end{bmatrix},\\
P_1 &= \begin{bmatrix} 4.3829 & -4.5290 \\ -4.5290 & 1.8561 \end{bmatrix},\\
P_2 &= \begin{bmatrix} 47.968 & 60.404 \\ 60.404 & 88.256 \end{bmatrix},\\
P_3 &= \begin{bmatrix} 6.3342 & 1.1945 \\ 1.1945 & 16.543 \end{bmatrix},\\
P_4 &= \begin{bmatrix} 480.521 & 96.073 \\ 96.073 & 151.11 \end{bmatrix}.
\end{aligned}
\tag{61}
$$

Figure 2 presents the domain of attraction for the proposed controller. As shown in the figure, the state trajectory of the closed-loop system (15) converges to the origin as time progresses, as long as the initial state is in $\cap_{i=1}^{4}\Omega(P_i)$.

4.2. Example 2. Consider the following multiinput system with three different modes ($N = 3$) [24]:

$$
\begin{aligned}
A_1 &= \begin{bmatrix} -2.5 & 0.3 & 0.8 \\ 1 & -3 & 0.2 \\ 0 & 0.5 & -2 \end{bmatrix},\\
A_2 &= \begin{bmatrix} -2.5 & 1.2 & 0.3 \\ -0.5 & 5 & -1 \\ 0.25 & 1.2 & 5 \end{bmatrix},\\
A_3 &= \begin{bmatrix} 2 & 1.5 & -0.4 \\ 2.2 & 3 & 0.7 \\ 1.1 & 0.9 & -2 \end{bmatrix},\\
B_1 &= \begin{bmatrix} 0.707 & 0 & 0 \\ 0 & 1 & 0 \\ 0 & 0 & 1 \end{bmatrix},\\
B_2 &= \begin{bmatrix} 0.707 & 0 & 0 \\ 0 & 1 & 0 \\ 0 & 0 & 0.707 \end{bmatrix},\\
B_3 &= \begin{bmatrix} 0.707 & 0 & 0 \\ 0 & 1 & 0 \\ 0 & 0 & 1 \end{bmatrix},\\
\Pi &= \begin{bmatrix} -3 & \pi_{12} & \pi_{13} \\ \pi_{21} & \pi_{22} & 1 \\ \pi_{31} & 0.3 & \pi_{33} \end{bmatrix},\\
Q_1 &= Q_2\\
\varepsilon &= 0.01, \mu
\end{aligned}
\tag{62}
$$

where π_{12}, π_{13}, π_{21}, π_{22}, π_{31}, and π_{33} are the unknown transition rates. The following sets can be obtained using the transition rate matrix Π:

$$
\begin{aligned}
D_1^+ &= \{1\}, D_2^+ = \{3\}, D_3^+ = \{2\},\\
D_1^- &= \{2, 3\}, D_2^- = \{1, 2\}, D_3^- = \{1, 3\}.
\end{aligned}
\tag{63}
$$

According to Theorem 1, the $\mathscr{H}_2$ performance $\gamma = 0.0803$, and the proposed controller gains are obtained as follows:

$$K_1 = \begin{bmatrix} -94.941 & -12.248 & -2.4019 \\ -8.6349 & -61.833 & -6.8275 \\ -1.7987 & -6.8828 & -76.698 \end{bmatrix},$$

$$K_2 = \begin{bmatrix} -24.110 & -3.7947 & -0.69917 \\ -2.7040 & -13.943 & -2.0031 \\ -0.69626 & -2.8494 & -26.380 \end{bmatrix},$$

$$K_3 = \begin{bmatrix} -93.208 & -25.607 & 18.331 \\ -18.085 & -67.048 & -14.084 \\ 12.952 & -14.079 & -76.181 \end{bmatrix},$$

$$P_1 = \begin{bmatrix} 1.8198 \times 10^{-1} & 2.3490 \times 10^{-2} & 3.0898 \times 10^{-3} \\ 2.3490 \times 10^{-2} & 1.6739 \times 10^{-1} & 1.8759 \times 10^{-2} \\ 3.0898 \times 10^{-3} & 1.8759 \times 10^{-2} & 2.0758 \times 10^{-1} \end{bmatrix},$$

$$P_2 = \begin{bmatrix} 3.3589 \times 10^{-1} & 5.3394 \times 10^{-2} & 9.2638 \times 10^{-3} \\ 5.3394 \times 10^{-2} & 2.7157 \times 10^{-1} & 4.0095 \times 10^{-2} \\ 9.2638 \times 10^{-3} & 4.0095 \times 10^{-2} & 3.6452 \times 10^{-1} \end{bmatrix},$$

$$P_3 = \begin{bmatrix} 2.5519 \times 10^{-1} & 7.0131 \times 10^{-2} & -5.1063 \times 10^{-2} \\ 7.0131 \times 10^{-2} & 2.5930 \times 10^{-1} & 5.4768 \times 10^{-2} \\ -5.1063 \times 10^{-2} & 5.4768 \times 10^{-2} & 2.9602 \times 10^{-1} \end{bmatrix}. \tag{64}$$

Figure 3 shows the state trajectories and the mode evolution obtained using the aforementioned controller gains. Figure 4 shows the saturated control input, where $x(0) = [\,0.5 \;\; -0.3 \;\; -0.4\,]^T$ and $r_0 = 3$. Here, we set $d(t) = 0.01 \sin(t^2 + 0.1)$. Figures 5 and 6 show the domains of attraction on the $x_1(t) - x_2(t)$ and $x_2(t) - x_3(t)$ planes, respectively. As shown in the figures, the state trajectory of the closed-loop system (15) converges to the origin as time progresses, as long as the initial state is in $\cap_{i=1}^{3} \Omega(P_i)$. These figures show that the proposed controller stabilizes the MJS with input saturation and incomplete knowledge of the transition rates under the matched disturbance.

4.3. Example 3. Consider the following inverted pendulum system controlled using a DC motor [27]:

$$\begin{aligned} \dot{x}_1(t) &= x_2(t), \\ \dot{x}_2(t) &= \frac{g}{l} \sin x_1(t) + \frac{NK_m}{ml^2} x_3(t), \\ L_a \dot{x}_3(t) &= K_b N x_2(t) - R(r_t) x_3(t) + \text{sat}(u(t)), \end{aligned} \tag{65}$$

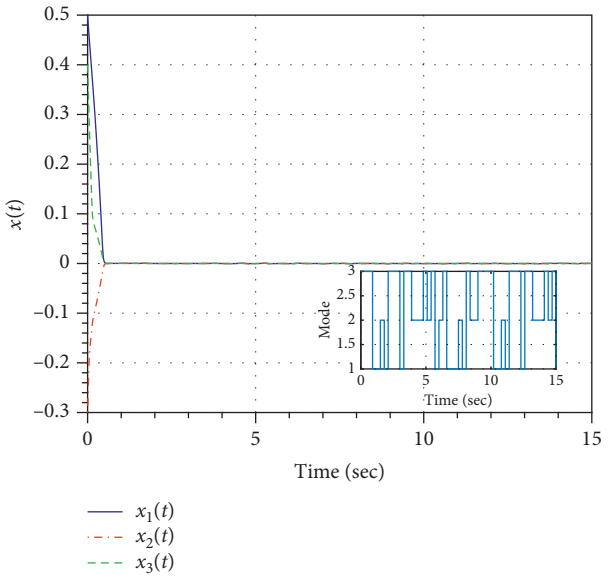

Figure 3: State trajectories for Example 2.

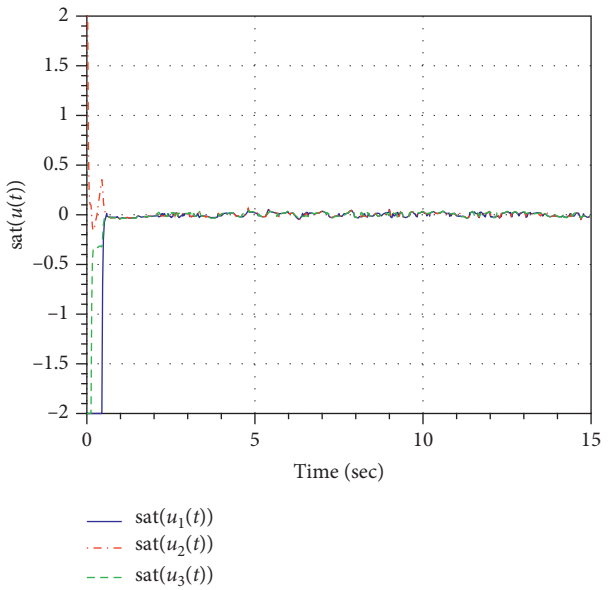

Figure 4: Control input for Example 2.

where $x_1(t)$ is the angle of the inverted pendulum, $x_2(t)$ is the angular velocity, $x_3(t)$ is the input current, $u(t)$ is the control input voltage, g is the acceleration of gravity, m and l are the mass and length of the inverted pendulum, respectively, K_b is the back-EMF constant, K_m is the motor torque constant, and N is the gear ratio. Here, $R(r_t)$ is the resistance in the DC motor, which is defined as

$$R(r_t) = \begin{cases} R_a, & \text{if } r_t = 1, \\ R_b, & \text{if } r_t = 2. \end{cases} \tag{66}$$

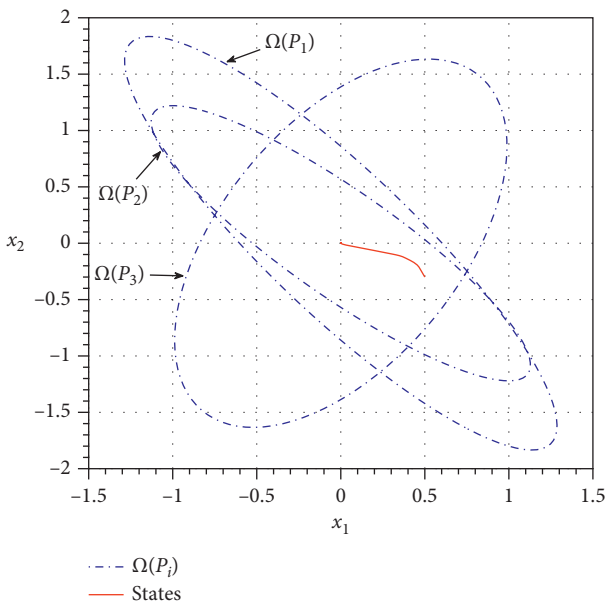

FIGURE 5: Domain of attraction ($x_1(t) - x_2(t)$ planes) for Example 2.

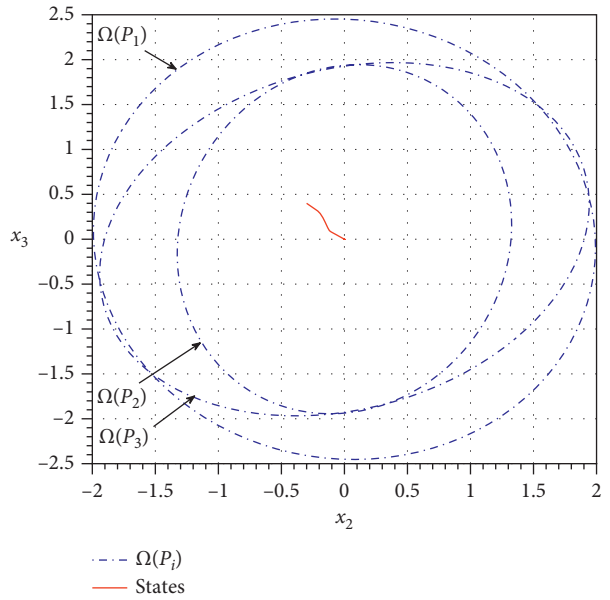

FIGURE 6: Domain of attraction ($x_2(t) - x_3(t)$ planes) for Example 2.

Let $L_a = 1$, $g = 9.8\,(\mathrm{m/s^2})$, $l = 1\,\mathrm{m}$, $m = 1\,\mathrm{kg}$, $N = 10$, $K_m = 0.1\,(\mathrm{Nm/A})$, $K_b = 0.1\,(\mathrm{Vs/rad})$, $R_a = 1\Omega$, and $R_b = 0.5\Omega$.

Using the aforementioned parameters, system (65) can be *linearized* as the following MJS with two modes:

$$\begin{aligned} \dot{x}(t) &= A(r_t)x(t) + B(r_t)\{\mathrm{sat}(u(t)) + d(t)\}, \\ z(t) &= C(r_t)x(t), \end{aligned} \tag{67}$$

where

$$\begin{aligned} x(t) &= \left[\, x_1(t) \;\; x_2(t) \;\; x_3(t) \,\right]^T, \\ A_1 &= \begin{bmatrix} 0 & 1 & 0 \\ 9.8 & 0 & 1 \\ 0 & 1 & -1 \end{bmatrix}, \\ A_2 &= \begin{bmatrix} 0 & 1 & 0 \\ 9.8 & 0 & 1 \\ 0 & 1 & -0.5 \end{bmatrix}, \\ B_1 &= B_2 = \begin{bmatrix} 0 \\ 0 \\ 1 \end{bmatrix}, \\ C_1 &= \left[\, 0.1 \;\; 0 \;\; 0 \,\right], \\ C_2 &= \left[\, 0.2 \;\; 0 \;\; 0 \,\right], \\ \Pi &= \begin{bmatrix} -0.6127 & 0.6127 \\ \pi_{21} & \pi_{22} \end{bmatrix}, \\ d(t) &= 0.01e^{-0.5t} \sin 10t^2, \\ \varepsilon &= 0.01,\ \mu = 12, \end{aligned} \tag{68}$$

where π_{21} and π_{22} are the unknown transition rates. Here, it is assumed that the matched disturbance $d(t)$ exists. Based on Theorem 1, the $\mathscr{H}_2$ performance $\gamma = 0.1399$, and the proposed controller gains are obtained as follows:

$$\begin{aligned} K_1 &= \left[\, -2.6199 \times 10^7 \;\; -8.6656 \times 10^6 \;\; -1.9736 \times 10^6 \,\right], \\ K_2 &= \left[\, -1.25 \times 10^7 \;\; -4.1531 \times 10^7 \;\; -1.0244 \times 10^7 \,\right], \\ P_1 &= \begin{bmatrix} 1.0289 \times 10^2 & 3.2962 \times 10^1 & 2.9323 \\ 3.2962 \times 10^1 & 1.0739 \times 10^1 & 9.6989 \times 10^{-1} \\ 2.9323 & 9.6989 \times 10^{-1} & 2.2090 \times 10^{-1} \end{bmatrix}, \\ P_2 &= \begin{bmatrix} 0.0698 \times 10^4 & 2.1904 \times 10^2 & 1.3991 \times 10^1 \\ 2.1904 \times 10^2 & 6.9178 \times 10^1 & 4.6483 \\ 1.3991 \times 10^1 & 4.6483 & 1.1465 \end{bmatrix}. \end{aligned} \tag{69}$$

Based on the aforementioned control gains, Figure 7 shows the state trajectories for $x(0) = \left[\, -0.1 \;\; 0.2 \;\; 0 \,\right]^T$ and the mode evolution r_t. As shown in the figure, the state trajectories of the closed-loop systems with the proposed controller converge to zero as time progresses.

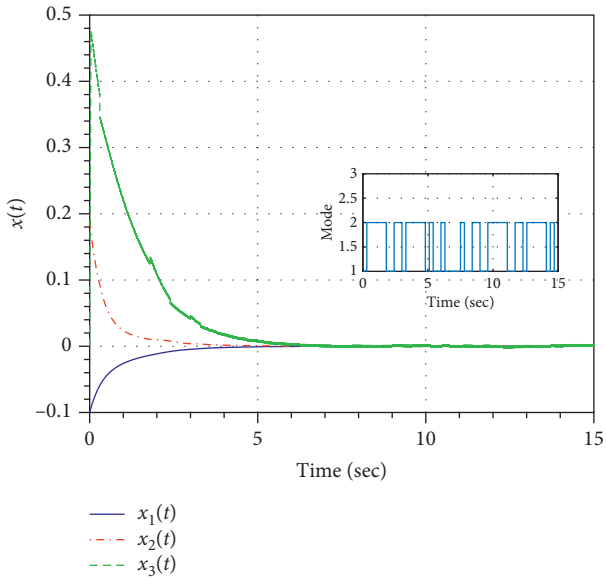

Figure 7: State trajectories for Example 3.

5. Conclusion

This paper proposed an $\mathscr{H}_2$ mode-dependent state-feedback controller for MJSs with input saturation and an incomplete knowledge of transition probabilities. Specifically, an invaluable relaxation method was developed into the second-order matrix polynomials of the unknown transition rate using all possible slack variables for the incomplete transition rates to obtain less conservative stabilization conditions. Consequently, the proposed controller guaranteed $\mathscr{H}_2$ performance and removed the matched disturbances. The effectiveness of the proposed controller was demonstrated using three examples.

Data Availability

The data used to support the findings of this study are available from the corresponding author upon request.

Conflicts of Interest

The author declares that there are no conflicts of interest regarding the publication of this paper.

Acknowledgments

This research was supported by the Grand Information Technology Research Center Program through the Institute of Information and Communications Technology and Planning and Evaluation (IITP) funded by the Ministry of Science and ICT (MSIT), Korea (IITP-2020-2020-0-01612).

References

[1] Y. Zhang, S. Xu, and J. Zhang, "Delay-dependent robust H_∞ control for uncertain fuzzy Markovian jump systems," *International Journal of Control, Automation and Systems*, vol. 7, no. 4, pp. 520–529, 2009.

[2] Y. Zhang, Y. He, M. Wu, and J. Zhang, "Stabilization for Markovian jump systems with partial information on transition probability based on free-connection weighting matrices," *Automatica*, vol. 47, no. 1, pp. 79–84, 2011.

[3] G.-L. Wang, "Robust stabilization of singular Markovian jump systems with uncertain switching," *International Journal of Control, Automation and Systems*, vol. 11, no. 1, pp. 188–193, 2013.

[4] L. Wu, X. Su, and P. Shi, "Output feedback control of Markovian jump repeated scalar nonlinear systems," *IEEE Transactions on Automatic Control*, vol. 59, no. 1, pp. 199–204, 2014.

[5] P. Shi and F. Li, "A survey on Markovian jump systems: modeling and design," *International Journal of Control, Automation and Systems*, vol. 13, no. 1, pp. 1–16, 2015.

[6] N. H. A. Nguyen, S. H. Kim, and J. Choi, "Stabilization of semi-Markovian jump systems with uncertain probability intensities and its extension to quantized control," *Mathematical Problems in Engineering*, vol. 2016, Article ID 8417475, , 2016.

[7] H. Chen, Z. Li, and W. Xia, "Event-triggered dissipative filter design for semi-markovian jump systems with time-varying delays," *Mathematical Problems in Engineering*, vol. 2020, Article ID 8983403, , 2020.

[8] F. Martinelli, "Optimality of a two-threshold feedback control for a manufacturing system with a production dependent failure rate," *IEEE Transactions on Automatic Control*, vol. 52, no. 10, pp. 1937–1942, 2007.

[9] L. Svensson and N. Williams, "Optimal monetary policy under uncertainty: a Markov jump-linear-quadratic approach," *Federal Reserve Bank St. Louis*, vol. 90, no. 4, pp. 275–294, 2008.

[10] V. Ugrinovskii and H. R. Pota, "Decentralized control of power systems via robust control of uncertain Markov jump parameter systems," *International Journal of Control*, vol. 78, no. 9, pp. 662–677, 2005.

[11] Y. Wang, C. Wang, and Z. Zuo, "Controller synthesis for Markovian jump systems with incomplete knowledge of transition probabilities and actuator saturation," *Journal of the Franklin Institute*, vol. 348, no. 4, pp. 2417–2429, 2011.

[12] S. H. Kim, "H2control of Markovian jump LPV systems with measurement noises: application to a DC-motor device with voltage fluctuations," *Journal of the Franklin Institute*, vol. 354, no. 4, pp. 1784–1800, 2017.

[13] S. H. Kim, "Less conservative stabilization conditions for Markovian jump systems with partly unknown transition probabilities," *Journal of the Franklin Institute*, vol. 351, no. 5, pp. 3042–3052, 2014.

[14] S. H. Kim, "Control synthesis of Markovian jump fuzzy systems based on a relaxation scheme for incomplete transition probability descriptions," *Nonlinear Dynamics*, vol. 78, no. 1, pp. 691–701, 2014.

[15] N. K. Kwon, B. Y. Park, P. Park, and I. S. Park, "Improved H_∞ state-feedback control for continuous-time Markovian jump fuzzy systems with incomplete knowledge of transition probabilities," *Journal of the Franklin Institute*, vol. 353, no. 15, pp. 3985–3998, 2016.

[16] J. Shin and B. Y. Park, "H_∞control of markovian jump systems with incomplete knowledge of transition probabilities," *International Journal of Control, Automation and Systems*, vol. 17, no. 10, pp. 2474–2481, 2019.

[17] B. Y. Park, S. W. Yun, and P. Park, "H_2state-feedback control for LPV systems with input saturation and matched disturbance," *Nonlinear Dynamics*, vol. 67, no. 2, pp. 1083–1096, 2017.

[18] B. Y. Park, S. W. Yun, Y. J. Choi, and P. Park, "Multistage γ-level $\mathscr{H}_\infty$control for input-saturated systems with disturbances," *Nonlinear Dynamics*, vol. 73, no. 3, pp. 1729–1739, 2017.

[19] S. H. Kim, "Reliable piecewise control design for systems with actuator saturation and fault," *International Journal of Systems Science*, vol. 46, no. 3, pp. 385–393, 2015.

[20] J. Zhang, W.-B. Xie, M.-Q. Shen, and L. Huang, "State augmented feedback controller design approach for T-S fuzzy system with complex actuator saturations," *International Journal of Control, Automation and Systems*, vol. 15, no. 5, pp. 2395–2405, 2017.

[21] H. Liu, E.-K. Boukas, F. Sun, and D. W. C. Ho, "Controller design for Markov jumping systems subject to actuator saturation," *Automatica*, vol. 42, no. 3, pp. 459–465, 2006.

[22] H. Yang, H. Li, F. Sun, and Y. Yuan, "Robust control for Markovian jump delta operator systems with actuator saturation," *European Journal of Control*, vol. 20, no. 4, pp. 207–215, 2014.

[23] Y. Wang, Z. Zuo, and Y. Cui, "Stochastic stabilization of Markovian jump systems with partial unknown transition probabilities and actuator saturation," *Circuits, Systems, and Signal Processing*, vol. 31, no. 1, pp. 371–383, 2012.

[24] N. H. A. Nguyen and S. H. Kim, "Relaxed robust stabilization conditions for nonhomogeneous markovian jump systems with actuator saturation and general switching policies," *International Journal of Control, Automation and Systems*, vol. 17, no. 3, pp. 586–596, 2019.

[25] Y.-Y. Cao, Z. Lin, and Y. Shamash, "Set invariance analysis and gain-scheduling control for LPV systems subject to actuator saturation," *Systems & Control Letters*, vol. 46, no. 2, pp. 137–151, 2002.

[26] A. Svishchuk, *Random Evolutions and Their Applications: New Trends*, Kluwer Academic Publishers, Norwell, MA, USA, 2000.

[27] Y.-Y. Cao and J. Lam, "Robust H_∞ control of uncertain Markovian jump systems with time-delay," *IEEE Transactions on Automatic Control*, vol. 45, no. 1, pp. 77–83, 2000.

Hindawi
Mathematical Problems in Engineering
Volume 2020, Article ID 9160592, 14 pages
https://doi.org/10.1155/2020/9160592

Research Article

Velocity-Free Adaptive Time Delay Control of Robotic System

Shini Chen[1,2] **and Xia Liu**[1,2]

[1]*School of Electrical Engineering and Electronic Information, Xihua University, Chengdu 610039, China*
[2]*Centre for Robotics Research, Xihua University, Chengdu 610039, China*

Correspondence should be addressed to Xia Liu; xliu_uestc@yahoo.com

Received 18 July 2020; Revised 22 October 2020; Accepted 11 November 2020; Published 24 November 2020

Academic Editor: Raúl Villafuerte-Segura

To improve the trajectory tracking performance of a complex nonlinear robotic system, a velocity-free adaptive time delay control is proposed. First, considering that conventional time delay control (TDC) may cause large time delay estimation (TDE) error under nonlinear friction, a TDC with gradient estimator is designed. Next, since it is complicated and time-consuming to adjust gains manually, an adaptive law is designed to estimate the gain of the gradient. Finally, in order to avoid the measurement of velocity and acceleration in the controller while enabling the robot to implement position tracking, an observer is designed. The proposed control can not only offset the nonlinear terms in the complex dynamics of the robotic system but also reduce the TDE error, estimate the gain of the gradient online, and avoid the measurement of velocity and acceleration. The stability of the system is analyzed via Lyapunov function. Simulations are conducted on a 2-DOF robot to verify the effectiveness of the proposed control.

1. Introduction

Robotic system is a nonlinear and strongly coupled system subject to various uncertainties, such as unmodeled dynamics and nonlinear friction [1]. These nonlinearity and uncertainties may degrade the tracking performance of the robotic system and even make the system unstable [2, 3].

In order to guarantee the tracking performance of robotic system with unknown dynamics, time delay control (TDC) which has a simple structure and good robustness was proposed; this was pioneered by Youcef-Toumi and Ito [4]. The main idea of TDC is to employ time delay estimation (TDE) technology. In TDE, the time delay of input torque and acceleration is employed to estimate the complex unknown dynamics and nonlinear terms which are difficult to handle. However, since the nonlinear terms are divided into soft nonlinearity and hard nonlinearity such as discontinuous Coulomb friction and static friction [5, 6], TDC has some inherent limitations. In fact, Coulomb friction accounts for 30% of the maximum control torque and cannot be ignored [7, 8], which results in large TDE error and greatly affects the system performance.

In order to compensate the TDE error caused by TDC, many auxiliary controllers have been designed. In [9], an adaptive gain sliding mode TDC method was designed for robot manipulators. The sliding mode control was used to reduce the TDE error, and the adaptive law was employed to reduce the chattering near the sliding mode surface. Based on the work in [9], a wide adaptive gain sliding mode TDC method was designed in [10]. The wide adaptive law was used to make the control gain range wider and suppress the adverse TDE error. The tracking performance and robustness of the system were improved. In [11], an adaptive TDC was designed for cable-driven manipulators to suppress the chattering and the TDE error. A fractional-order and nonsingular sliding mode surface was used to introduce the desired error dynamics. Moreover, the continuous and chatter-free adaptive gains were used to enhance the control performance under time-varying disturbances. In [12], a TDC method with ideal velocity feedback was designed for a robot manipulator with nonlinear friction. The ideal velocity feedback was used to cancel the hard nonlinearity which cannot be cancelled by TDC, suppressing the TDE error. The controller has a simple structure and yet provides good

online friction compensation. In [13], an inclusive enhanced TDC with nonlinear desired error dynamics was designed and the nonlinear sliding mode surface was used to reduce the TDE error and chattering. The approach inherits the advantages of TDC that is simple and model-free. In [14], a TDC method with internal model was designed for robot manipulators, where the internal model played a role in compensating for hard nonlinear friction and eliminating disturbance. The controller has a synergy effect coming from the complementary use of TDC and internal model. In [15], a fuzzy logic TDC was designed for a cable-driven robot. The TDC was used to estimate and cancel the soft nonlinearity while the fuzzy logic was used to cancel the hard nonlinearity. The fuzzy logic TDC not only has a simple structure but also can effectively track the desired trajectory. Although the TDE error can be offset effectively by the control methods in [9–15], several gains need to be adjusted and the velocity and acceleration need to be measured additionally. Since it is a time-consuming task to adjust gains, a TDC method based on gradient estimator was designed for robot manipulator in [16]. The TDE error can be effectively suppressed by the gradient estimator, and only one gain needs to be adjusted additionally. However, the gain of the gradient in [16] needs to be adjusted manually, and the velocity and acceleration in the controller still need to be measured, which may easily result in measurement noise.

Therefore, this paper presents a velocity-free adaptive TDC to improve the trajectory tracking performance of complex nonlinear robotic system. The main contributions of this paper are as follows: (1) a TDC with gradient estimator is designed to reduce the TDE error in the conventional TDC; (2) an adaptive law is designed to estimate the gain of the gradient online; and (3) an observer is designed to observe the velocity and acceleration in the controller, which can avoid the measurement of velocity and acceleration.

This paper is organized as follows. Section 2 states the problems of the conventional TDC. In Section 3, velocity-free adaptive TDC is presented. In Section 4, stability of the system is proved using Lyapunov stability synthesis. Comparative simulations are conducted to validate the proposed control in Section 5. Section 6 concludes the paper.

2. Problem Statement

The general dynamics of a n-DOF robot can be considered as follows [17]:

$$\boldsymbol{\tau} = \mathbf{M}(\mathbf{q})\ddot{q} + \mathbf{C}(\mathbf{q}, \dot{q})\dot{q} + \mathbf{G}(\mathbf{q}) + \mathbf{f}, \tag{1}$$

where $\tau \in \mathbf{R}^{n\times 1}$ is the input torque of the robot, $\mathbf{M}$ is the positive inertia matrix, $\mathbf{C}(\mathbf{q}, \dot{q}) \in \mathbf{R}^{n\times n}$ is the centripetal and Coriolis matrix, $\mathbf{G}(\mathbf{q}) \in \mathbf{R}^{n\times 1}$ is the gravity term, $\mathbf{f} \in \mathbf{R}^n$ is the friction torque, and $\mathbf{q} \in \mathbf{R}^{n\times 1}$, $\dot{q} \in \mathbf{R}^{n\times 1}$, and $\ddot{q} \in \mathbf{R}^{n\times 1}$ are the angular position, velocity, and acceleration of the robot, respectively.

Introducing a positive-definite diagonal constant matrix $\overline{M}$ into the general dynamics (1) of the robot, we can get

$$\overline{M}\ddot{q} + \mathbf{N}(\mathbf{q}, \dot{q}, \ddot{q}) = \boldsymbol{\tau}, \tag{2}$$

where $\mathbf{N}(\mathbf{q}, \dot{q}, \ddot{q}) \triangleq [\mathbf{M}(\mathbf{q}) - \overline{M}]\ddot{q} + \mathbf{C}(\mathbf{q}, \dot{q})\dot{q} + \mathbf{G}(\mathbf{q}) + \mathbf{f}$, which contains all the nonlinear terms in the complex dynamics of the robotic system. In practice, since $\mathbf{N}(\mathbf{q}, \dot{q}, \ddot{q})$ is very complicated and difficult to calculate, the main idea of conventional TDC is to employ TDE [18] to get its estimation $\widehat{N}(\mathbf{q}, \dot{q}, \ddot{q})$:

$$\mathbf{N}(\mathbf{q}, \dot{q}, \ddot{q}) \approx \mathbf{N}(\mathbf{q}, \dot{q}, \ddot{q})_{t-L} \triangleq \widehat{N}(\mathbf{q}, \dot{q}, \ddot{q}). \tag{3}$$

Notice that L represents the time delay. Obviously, when L is small enough, $\mathbf{N}(\mathbf{q}, \dot{q}, \ddot{q})$ can be accurately estimated by (3). The term $\mathbf{N}(\mathbf{q}, \dot{q}, \ddot{q})_{t-L}$ intentionally introduces the time delay L to estimate $\mathbf{N}(\mathbf{q}, \dot{q}, \ddot{q})$. According to (2), the complex dynamics of the robot can be estimated by $\mathbf{N}(\mathbf{q}, \dot{q}, \ddot{q})_{t-L}$ which is a simple structure.

Substituting (3) into (2), we can get the TDE as

$$\mathbf{N}(\mathbf{q}, \dot{q}, \ddot{q})_{t-L} = \boldsymbol{\tau}_{t-L} - \overline{M}\ddot{q}_{t-L}. \tag{4}$$

Let the desired error dynamics of the system be

$$\ddot{e} + \mathbf{K}_D\dot{e} + \mathbf{K}_p = 0, \tag{5}$$

where $\mathbf{e} = \mathbf{q}_d - \mathbf{q}$ is the position tracking error of the robot.

Rearranging (2)–(5), we can get the conventional TDC as

$$\boldsymbol{\tau} = \underbrace{\boldsymbol{\tau}_{t-L} - \overline{M}\ddot{q}_{t-L}}_{TDE} + \overline{M}\underbrace{\left[\ddot{q}_d + K_D\left(\dot{q}_d - \dot{q}\right) + K_P\left(q_d - q\right)\right]}_{\text{desired error dynamics}}, \tag{6}$$

where $\mathbf{q}_d$, $\dot{q}_d$, and $\ddot{q}_d$ denote the desired position, velocity, and acceleration of the robot and $\mathbf{K}_D$ and $\mathbf{K}_P$ represent the diagonal gain matrices of decoupled PD controllers. The first two terms $\tau_{t-L} - \overline{M}\ddot{q}_{t-L}$ consist of the TDE which offsets $\mathbf{N}(\mathbf{q}, \dot{q}, \ddot{q})$, and the other terms inject the desired error dynamics.

Remark 1. The term $\mathbf{N}(\mathbf{q}, \dot{q}, \ddot{q})$ in (2) contains all the nonlinear terms including uncertain parameters and friction of the robotic system. Since $\mathbf{N}(\mathbf{q}, \dot{q}, \ddot{q})$ can be offset by $\mathbf{N}(\mathbf{q}, \dot{q}, \ddot{q})_{t-L}$ in (3), the uncertain parameters and friction have no effect on the dynamic response of the control system.

From (3), we can see that when L is small enough, $\mathbf{N}(\mathbf{q}, \dot{q}, \ddot{q})$ can be accurately estimated. However, in practice, the minimum value of L can only be the sampling time. This limitation on L will cause TDE error. From (3), (4), and (6), we can get

$$\begin{aligned}\mathbf{N}(\mathbf{q}, \dot{q}, \ddot{q}) - \widehat{N}(\mathbf{q}, \dot{q}, \ddot{q}) &= \mathbf{N}(\mathbf{q}, \dot{q}, \ddot{q}) - \mathbf{N}(\mathbf{q}, \dot{q}, \ddot{q})_{t-L} \\ &= \overline{M}\left[\ddot{e} + \mathbf{K}_D\dot{e} + \mathbf{K}_P\mathbf{e}\right].\end{aligned} \tag{7}$$

From (5) and (7), we can obtain the TDE error ε:

$$\boldsymbol{\varepsilon} \triangleq \overline{M}^{-1}\left[N(\mathbf{q}, \dot{q}, \ddot{q}) - N(\mathbf{q}, \dot{q}, \ddot{q})_{t-L}\right] = \ddot{e} + \mathbf{K}_D\dot{e} + \mathbf{K}_P\mathbf{e}. \tag{8}$$

Obviously, there exits a deviation between ε and the desired error dynamics (5). Especially when there exists hard nonlinear friction such as Coulomb friction and static friction, the TDE error will become very large, affecting the tracking performance of the robotic system.

3. Velocity-Free Adaptive TDC

The idea of the proposed velocity-free adaptive TDC of robotic system is shown in Figure 1. TDC with gradient estimator τ is designed to reduce the TDE error ε. An adaptive law is designed to estimate the gain of the gradient and obtain its estimation $\widehat{K}_{\mathrm{GE}}$. An observer is designed to observe the velocity and acceleration and obtain the estimation of velocity $\widehat{\dot{x}}_1$ and the estimation of acceleration $\widehat{\ddot{x}}_2$, respectively. In this way, the real position $\mathbf{q}$ of the robot can track the desired position $\mathbf{q}_d$.

3.1. Design of TDC with Adaptive Gradient Estimator. Introducing the term $\widehat{\varepsilon}$ of gradient estimator into the TDC (6), we can get the TDC with gradient estimator as

$$\boldsymbol{\tau} = \boldsymbol{\tau}_{t-L} - \overline{M}\ddot{\mathbf{q}}_{t-L} + \overline{M}\left[\ddot{\mathbf{q}}_d + \mathbf{K}_D\left(\dot{\mathbf{q}}_d - \mathbf{q}\right) + \mathbf{K}_P\left(\mathbf{q}_d - \mathbf{q}\right)\right] + \overline{M}\widehat{\varepsilon}. \tag{9}$$

Substituting (9) into (2), we can obtain the closed-loop dynamics error of TDC with gradient estimator:

$$\ddot{e} + K_D\dot{e} + \mathbf{K}_P\mathbf{e} = -\widetilde{\varepsilon}, \tag{10}$$

where $\widetilde{\varepsilon} \triangleq \widehat{\varepsilon} - \varepsilon$ represents the estimation error of the TDE error. Define the cost function of the estimation error as

$$\mathbf{J}\left(\widetilde{\varepsilon}\right) = \frac{1}{2}\widetilde{\varepsilon}^T\widetilde{\varepsilon}. \tag{11}$$

Then, when the TDE error was slow-varying or constant, the gradient estimator can be designed as

$$\dot{\widehat{\varepsilon}} = -\mathbf{K}_{\mathbf{GE}}\frac{\partial \mathbf{J}}{\partial \widehat{\varepsilon}} = -\mathbf{K}_{\mathbf{GE}}\widetilde{\varepsilon} = \mathbf{K}_{\mathbf{GE}}\left(\ddot{e} + \mathbf{K}_D\dot{e} + \mathbf{K}_P\mathbf{e}\right), \tag{12}$$

where $\mathbf{K}_{\mathbf{GE}} \triangleq \mathbf{diag}\left(\mathbf{K}_{\mathrm{GE}_1}, \ldots, \mathbf{K}_{\mathrm{GE}_n}\right)$ is the positive gain matrix of the gradient estimator. Since the gradient estimator (12) always make the cost function surface negative, the gradient estimator can reduce the TDE error caused by TDC.

Therefore, (9) can be rewritten as

$$\boldsymbol{\tau} = \underbrace{\boldsymbol{\tau}_{t-L} - \overline{M}\ddot{\mathbf{q}}_{t-L}}_{\mathbf{TDE}} + \underbrace{\overline{M}\left[\ddot{\mathbf{q}}_d + \mathbf{K}_D\left(\dot{\mathbf{q}}_d - \dot{\mathbf{q}}\right) + \mathbf{K}_P\left(\mathbf{q}_d - \mathbf{q}\right)\right]}_{\text{desired error dynamics}} + \underbrace{\overline{M}\mathbf{K}_{\mathbf{GE}}\left(\dot{e} + \mathbf{K}_D\mathbf{e} + \mathbf{K}_P\int \mathbf{e}\mathbf{dt}\right)}_{\text{gradient estimator}}. \tag{13}$$

It can be seen from (13) that the TDC with gradient estimator does not need the nonlinear terms in the complex dynamics of the robotic system and can reduce the TDE error. In addition, the TDC with gradient estimator (13) only needs to adjust one gain, i.e., the gain of the gradient $\mathbf{K}_{\mathrm{GE}}$, assuming $\mathbf{K}_P = \beta\mathbf{K}_S$, $\mathbf{K}_D = \mathbf{K}_S + \beta\,(\beta > 0)$, $\mathbf{S} = \dot{e} + \mathbf{K}_S\mathbf{e}$, and $\mathbf{K}_S$ is a positive diagonal constant matrix. In order to estimate $\mathbf{K}_{\mathrm{GE}}$, the following adaptive law is designed:

$$\dot{\widehat{K}}_{\mathrm{GE}} = \frac{\psi}{\alpha}\|\mathbf{S}\| - \boldsymbol{\varepsilon}, \tag{14}$$

where α and ψ are positive parameters and $\varepsilon = \ddot{e} + \mathbf{K}_D\dot{e} + \mathbf{K}_P\mathbf{e}$.

According to (13) and (14), we can design the TDC with adaptive gradient estimator as

$$\boldsymbol{\tau} = \underbrace{\boldsymbol{\tau}_{t-L} - \overline{M}\ddot{\mathbf{q}}_{t-L}}_{\mathbf{TDE}} + \overline{M}\underbrace{\left[\ddot{\mathbf{q}}_d + \mathbf{K}_D\left(\dot{\mathbf{q}}_d - \dot{\mathbf{q}}\right) + \mathbf{K}_P\left(\mathbf{q}_d - \mathbf{q}\right)\right]}_{\text{desired error dynamics}} + \underbrace{\overline{M}\widehat{K}_{\mathrm{GE}}\left(\dot{e} + \mathbf{K}_D\mathbf{e} + \mathbf{K}_P\int \mathbf{e}\mathbf{dt}\right)}_{\text{adaptive gradient estimator}}. \tag{15}$$

where $\tau_{t-L} - \overline{M}\ddot{q}_{t-L}$ is the TDE which offsets $\mathbf{N}(\mathbf{q}, \dot{q}, \ddot{q})$, $\overline{M}\left[\ddot{\mathbf{q}}_d + \mathbf{K}_D\left(\dot{\mathbf{q}}_d - \dot{\mathbf{q}}\right) + \mathbf{K}_P\left(\mathbf{q}_d - \mathbf{q}\right)\right]$ is the desired error dynamics, and $\overline{M}\widehat{K}_{\mathrm{GE}}\left(\dot{e} + t\mathbf{K}_D neq + h\mathbf{K}_P\int \mathbf{e}\,\mathbf{dt}\right.$ is the adaptive gradient estimator to reduce the TDE error caused by TDC.

3.2. Design of the Observer. Let $\mathbf{x}_1 = \mathbf{q}$, $\overline{x}_2 = \dot{q}$. From (2) and (3), we can get the state-space equation of the dynamics of the robot (1):

$$\begin{cases} \dot{x}_1 = \overline{x}_2, \\ \dot{\overline{x}}_2 = -\overline{M}^{-1}\left[\mathbf{N}\left(\mathbf{x}_1, \overline{x}_2, \dot{\overline{x}}_2\right)_{t-L} - \boldsymbol{\tau}_{t-L}\right]. \end{cases} \tag{16}$$

Then, define a new variable $\mathbf{x}_2 = \overline{x}_2 - \mathbf{T}\mathbf{x}_1$, where $\mathbf{T} = \mathbf{diag}\left(t_1, t_2, \ldots, t_n\right)$, $t_i > 0$ $(i = 1, 2, \ldots, n)$. Substituting $\mathbf{x}_2$ into (16) gives

$$\begin{cases} \dot{x}_1 = \mathbf{T}\mathbf{x}_1 + \mathbf{x}_2, \\ \dot{x}_2 = -\overline{M}^{-1}\left[\mathbf{N}\left(\mathbf{x}_1, \overline{x}_2, \dot{\overline{x}}_2\right)_{t-L} - \boldsymbol{\tau}_{t-L}\right] - \mathbf{T}\mathbf{x}_2 - \mathbf{T}^2\mathbf{x}_1. \end{cases} \tag{17}$$

Suppose $\mathbf{L}_1 = \mathbf{diag}\left(l_{11}, l_{12}, \ldots, l_{1n}\right)$, $\mathbf{L}_2 = \mathbf{diag}\left(l_{21}, l_{22}, \ldots, l_{2n}\right)$, and $\mathbf{L}_1$ and $\mathbf{L}_2$ are positive-definite matrices. For simplicity, let $-\overline{M}^{-1}\left[\mathbf{N}\left(\mathbf{x}_1, \overline{x}_2, \dot{\overline{x}}_2\right)_{t-L} - \tau_{t-L}\right] = \mathbf{F}\left(\mathbf{x}_1, \mathbf{x}_2\right)$. Now, the observer of the robotic system can be designed as

$$\begin{cases} \dot{\widehat{x}}_1 = \mathbf{T}\widehat{x}_1 + \widehat{x}_2 - \mathbf{L}_1\mathbf{e}_{x1} + \mathbf{v}_1, \\ \dot{\widehat{x}}_2 = \mathbf{F}\left(\mathbf{x}_1, \widehat{x}_2\right) - \mathbf{T}\widehat{x}_2 - \mathbf{T}^2\widehat{x}_1 - \mathbf{L}_2\mathbf{e}_{x2} + \mathbf{v}_2 + \boldsymbol{\chi}\mathbf{sign}\left(\mathbf{v}_1\right), \end{cases} \tag{18}$$

where $\mathbf{v}_1 = -k_1\mathbf{sign}\left(\mathbf{e}_1\right)$, $\mathbf{v}_2 = k_2\mathbf{v}_1 + k_3|\mathbf{v}_1|^{\Upsilon}\mathbf{sign}\left(\mathbf{v}_1\right)$, k_1, k_2, $k_3 > 0$, $0 < \Upsilon < 1$, and χ is a positive-definite diagonal matrix. $\widehat{\mathbf{x}}_1$ and $\widehat{\mathbf{x}}_2$ are the estimations of $\mathbf{x}_1$ and $\mathbf{x}_2$, and $\mathbf{e}_{x1}$ and $\mathbf{e}_{x2}$ are the estimation errors of $\mathbf{x}_1$ and $\mathbf{x}_2$, respectively:

$$\begin{aligned} \mathbf{e}_{x1} &= \widehat{x}_1 - \mathbf{x}_1, \\ \mathbf{e}_{x2} &= \widehat{x}_2 - \mathbf{x}_2. \end{aligned} \tag{19}$$

From (18), it can be seen that the velocity $\dot{q}$ and acceleration $\ddot{q}$ of the robot system can be estimated by the observer. Consequently, the velocity and acceleration do not need to be measured.

Remark 2. In (19), $\mathbf{e}_{x2} = \widehat{x}_2 - \mathbf{x}_2$, where $\mathbf{x}_2$ is the velocity. Then, we can get $\dot{e}_{x2} = \dot{\widehat{x}}_2 - \dot{x}_2$, where $\dot{x}_2$ is the acceleration $\ddot{q}$. Moreover, from (2), we have $\ddot{q} = \overline{M}^{-1}\left[\tau - \mathbf{N}\left(\mathbf{q}, \dot{q}, \ddot{q}\right)\right]$.

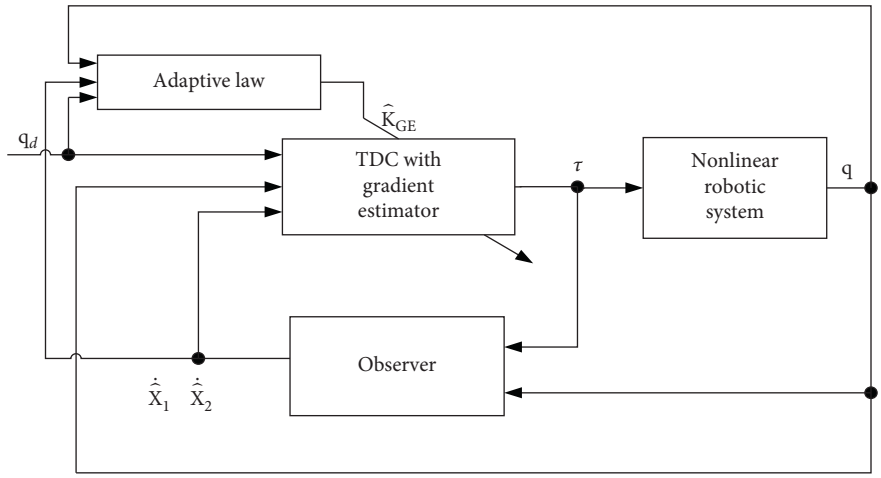

Figure 1: Block diagram of velocity-free adaptive TDC.

Therefore, we can avoid the direct measurement of the velocity in (18).

From (19), we can get the observer error as

$$\begin{cases} \dot{e}_{x1} = (\mathbf{T} - \mathbf{L}_1)\mathbf{e}_{x1} + \mathbf{e}_{x2} + \mathbf{v}_1, \\ \dot{e}_{x2} = -(\mathbf{T} + \mathbf{L}_2)\mathbf{e}_{x1} - \mathbf{T}\mathbf{e}_{x2} + \mathbf{v}_2 + \mathbf{F}(\mathbf{x}_1, \hat{x}_2) - \mathbf{F}(\mathbf{x}_1, \mathbf{x}_2) + \boldsymbol{\chi}\mathbf{sign}(\mathbf{v}_1). \end{cases} \tag{20}$$

Since the constant matrix $\mathbf{T}$ is easily adjusted in (18), the design is flexible. When the states $\hat{\dot{x}}_1$ and $\hat{\dot{x}}_2$ of the observer are far from the real states $\mathbf{x}_1$ and $\mathbf{x}_2$, the term $k_2\mathbf{v}_1$ can guarantee the rapid convergence of $\dot{e}_{x1}$ and $\dot{e}_{x2}$. Otherwise, the term $k_3|\mathbf{v}_1|^{\Upsilon}\mathbf{sign}(v_1)$ can guarantee the rapid convergence of $\dot{e}_{x1}$ and $\dot{e}_{x2}$.

Now, based on the TDC with adaptive gradient estimator and the observer, the velocity-free TDC with adaptive gradient estimator can be designed as

$$\boldsymbol{\tau} = \underbrace{\boldsymbol{\tau}_{t-L} - \overline{M}\dot{\hat{x}}_{2t-L}}_{\mathbf{TDE}} + \overline{M}\underbrace{\left[\ddot{q}_d + \mathbf{K}_D\left(\dot{q}_d - \hat{\dot{x}}_1\right) + \mathbf{K}_P\left(\mathbf{q}_d - \mathbf{q}\right)\right]}_{\text{desired error dynamics}} + \underbrace{\overline{M}\widehat{K}_{\mathbf{GE}}\left(\dot{e} + \mathbf{K}_D\mathbf{e} + \mathbf{K}_P\int\mathbf{e}\mathbf{dt}\right)}_{\text{adaptive gradient estimator}}. \tag{21}$$

The controller (21) adopts the TDE $\tau_{t-L} - \overline{M}\dot{\hat{x}}_{2t-L}$ which does not need the nonlinear terms in the complex dynamics of the robotic system. Meanwhile, $\overline{M}[\ddot{q}_d + \mathbf{K}_D(\dot{q}_d - \hat{\dot{x}}_1) + \mathbf{K}_P(\mathbf{q}_d - \mathbf{q})]$ injects the desired error dynamics and $\overline{M}\widehat{K}_{\mathrm{GE}}(\dot{e} + t\mathbf{K}_D neq + h\mathbf{K}_P\int\mathbf{e}\,\mathbf{dt}$ can reduce the TDE error caused by TDC using the adaptive gradient estimator. In addition, the use of observer can avoid the measurement noise of the velocity and acceleration in the robotic system.

Remark 3. In practice, there may still be the noise in the measurement of position. However, the influence of the noise caused by the measurement of position is far less than that of velocity and acceleration. The controller (21) can effectively avoid the measurement of velocity and acceleration.

4. Stability Analysis

4.1. Stability Analysis of the Observer. Let $\mathbf{F}(\mathbf{x}_1, \mathbf{x}_2)$, $\mathbf{F}(\mathbf{x}_1, \hat{x}_2)$ be the Lipschitz function [19], i.e., $\|\mathbf{F}(\mathbf{x}_1, \hat{x}_2) - \mathbf{F}(\mathbf{x}_1, \mathbf{x}_2)\| \le \overline{C}$, where $\overline{C}$ is a positive constant. Let us define $\mathbf{e}_x = [\mathbf{e}_{x1}, \mathbf{e}_{x2}]^T$. Then, from (5), we can get

$$\dot{e}_x = \mathbf{A}\mathbf{e}_x + \mathbf{F} + \overline{v}, \tag{22}$$

where $\mathbf{A} = \begin{bmatrix} \mathbf{T} - \mathbf{L}_1 & \mathbf{E} \\ -\mathbf{T}^2 - \mathbf{L}_2 & -\mathbf{T} \end{bmatrix}$, $\Delta\mathbf{F} = \begin{bmatrix} 0_{\mathbf{n}\times 1} \\ \mathbf{F}(\mathbf{x}_1, \hat{x}_2) - \mathbf{F}(\mathbf{x}_1, \mathbf{x}_2) \end{bmatrix}$, and $\overline{v} = \begin{bmatrix} \mathbf{v}_1 \\ \mathbf{v}_2 + \chi\mathbf{sign}(\mathbf{v}_1) \end{bmatrix}$.

Lemma 1 (see [20]). When the following equation holds, the observer error $\mathbf{e}_x$ will converge to zero in finite time:

$$\begin{cases} \mathbf{PA} + \mathbf{A}^T\mathbf{P} + \dfrac{\mathbf{PP}}{\sigma} + \varphi < 0, \\ l_{1i} > t_i, \\ k_1 - R = \eta > 0, \\ -2\mathbf{P}_2\mathbf{T} + \dfrac{\mathbf{P}_2\mathbf{P}_2}{\sigma} + \sigma\overline{C}_2\mathbf{E} < 0, \end{cases} \tag{23}$$

where $P = diag\{P_1, P_2\} > 0$, $\mathbf{P}_1 = \mathbf{diag}\{p_{11}, p_{12}, \ldots, p_{1n}\}$, $\mathbf{P}_2 = \mathbf{diag}\{p_{21}, p_{22}, \ldots, p_{2n}\}$, σ, η, $\overline{\mathbf{C}} > 0$, $\varphi = \mathbf{diag}\{0_{\mathbf{n}\times\mathbf{n}}, \sigma\overline{C}^2\mathbf{E}\}$, *and* $\mathbf{R}$ *is the boundary of* $\|\mathbf{e}_x\|$.

Consider a Lyapunov function:

$$\mathbf{V}_1 = \mathbf{e}_x^T\mathbf{P}\mathbf{e}_x. \tag{24}$$

Differentiating (24) with respect to time and substituting (22) and (23) into it yields

$$\dot{V}_1 \le \mathbf{e}_x^T\left(\mathbf{PA} + \mathbf{A}^T\mathbf{P}\right)\mathbf{e}_\mathbf{x} + 2\mathbf{e}_x^T\mathbf{PF} + 2\mathbf{e}_x^T\mathbf{P}\overline{v}. \tag{25}$$

According to (23) and (25), we have $2\mathbf{e}_x^T\mathbf{P}\Delta\mathbf{F} \le ((\mathbf{e}_x^T\mathbf{PP}\mathbf{e}_x)/\sigma) + \sigma\Delta\mathbf{F}^T\Delta\mathbf{F}$. Moreover, from (22), we know that $\mathbf{F}(\mathbf{x}_1, \widehat{x}_2)$, $\mathbf{F}(\mathbf{x}_1, \mathbf{x}_2)$ is the Lipschitz function. Thus, we have $|\Delta\mathbf{F}^T\Delta\mathbf{F} \le \overline{C}^2\|\mathbf{e}_{x2}\|^2$. Consequently, (25) can be rewritten into

$$\begin{aligned} \dot{V}_1 &\le \mathbf{e}_x^T\left(\mathbf{PA} + \mathbf{A}^T\mathbf{P}\right)\mathbf{e}_x + \frac{\mathbf{e}_x^T\mathbf{PP}\sigma}{\sigma} + \sigma\overline{C}^2\left\|\mathbf{e}_{x2}\right\|^2 + 2\mathbf{e}_x^T\mathbf{P}\overline{v} \\ &\le \mathbf{e}_x^T\left(\mathbf{PA} + \mathbf{A}^T\mathbf{P} + \frac{\mathbf{PP}}{\sigma} + \varphi\right)\mathbf{e}_x + 2\mathbf{e}_x^T\mathbf{P}\overline{v}. \end{aligned} \tag{26}$$

If $Q = \mathbf{PA} + \mathbf{A}^T\mathbf{P} + (\mathbf{PP}/\sigma) + \varphi < 0$ and $\Lambda = -\lambda_{\max}(\mathbf{Q})$, then we can get

$$\begin{aligned} \dot{V}_1 &\le -\Lambda\left\|\mathbf{e}_x\right\|^2 - 2k_1\sum_{i=1}^{n} p_{1i}\left|\mathbf{e}_{x1i}\right| - 2\mathbf{P}_{k1}\mathbf{e}_x - 2k_1\mathbf{P}_{k2}\mathbf{e}_x \\ &\quad - 2k_1^\gamma\mathbf{P}_{k3}\mathbf{e}_x \\ &\le -\left\|\mathbf{e}_x\right\|\begin{pmatrix} \Lambda\left\|\mathbf{e}_x\right\| - 2k_1\sqrt{\sum_{\mathbf{i}=\mathbf{1}}^{\mathbf{n}} k_2^2p_{2i}^2} \\ -2k_1^\gamma\sqrt{\sum_{\mathbf{i}=\mathbf{1}}^{\mathbf{n}} k_3^2p_{2i}^2} - 2\sqrt{\sum_{\mathbf{i}=\mathbf{1}}^{\mathbf{n}} p_{2i}^2\boldsymbol{\chi}_i^2} \end{pmatrix}, \end{aligned} \tag{27}$$

where

$$\begin{cases} \mathbf{P}_{k1} = [0_{1\times n}, p_{21}\chi_1\mathrm{sign}(e_{11}), \ldots, p_{2n}\chi_n\mathrm{sign}(e_{1n})], \\ \mathbf{P}_{k2} = [0_{1\times n}, p_{21}k_2\mathrm{sign}(e_{11}), \ldots, p_{2n}k_2\mathrm{sign}(e_{1n})], \\ \mathbf{P}_{k3} = [0_{1\times n}, p_{21}k_3\mathrm{sign}(e_{11}), \ldots, p_{2n}k_3\mathrm{sign}(e_{1n})]. \end{cases} \tag{28}$$

When $\|\mathbf{e}_x\| > R$,

$$R = \frac{2k_1\sqrt{\sum_{\mathbf{i}=\mathbf{1}}^{\mathbf{n}} k_2^2p_{2i}^2} + 2k_1^\gamma\sqrt{\sum_{\mathbf{i}=\mathbf{1}}^{\mathbf{n}} k_3^2p_{2i}^2} + 2\sqrt{\sum_{\mathbf{i}=\mathbf{1}}^{\mathbf{n}} p_{2i}^2\boldsymbol{\chi}_i^2}}{\Lambda}, \tag{29}$$

and we can get $\dot{V}_1 < 0$. Therefore, when $\|\mathbf{e}_x\|$ exceeds its bound R, $\dot{V}_1 < 0$, while when $\|\mathbf{e}_x\|$ decreases, $\|\mathbf{e}_x\|$ decreases to its bounds R within finite time.

Consider the second Lyapunov function as

$$V_2 = \frac{1}{2}\mathbf{e}_{x1\mathbf{i}}^T p_{1i}\mathbf{e}_{x1\mathbf{i}}. \tag{30}$$

Differentiating (30) with respect to time and substituting (23) into it yields

$$\dot{V}_2 \le -p_{1i}(l_{1i} - t_\mathbf{i})e_{x1\mathbf{i}}^2 - p_{1i}\left|\mathbf{e}_{x1\mathbf{i}}\right|\left(k_1 - \left|\mathbf{e}_{x2\mathbf{i}}\right|\right). \tag{31}$$

Let $l_{1i} > t_i$ *and* $k_1 - R = \eta > 0$, *(31) becomes*

$$\dot{V}_2 \le -p_{1i}\eta\left|\mathbf{e}_{x1i}\right| = -\sqrt{2p_{1i}}\eta\dot{V}_2^{1/2} < 0. \tag{32}$$

From (32), we can see that $\mathbf{e}_{x1}$ and $\dot{e}_{x1}$ can converge to zero in finite time.

When the sliding mode $\mathbf{e}_{x1} = \dot{e}_{x1} = 0$, we have $\mathbf{v}_1 = -\mathbf{e}_{x2}$ and $\mathbf{v}_2 = -k_2\mathbf{e}_{x2} - k_3|\mathbf{e}_{x2}|^\gamma\mathbf{sign}(e_{x2})$.

Take another Lyapunov function as

$$V_3 = \mathbf{e}_{x2}^T\mathbf{P}_2\mathbf{e}_{x2}. \tag{33}$$

Differentiating (33) with respect to time and substituting (23) into it yields

$$\begin{aligned} \dot{V}_3 &\le \mathbf{e}_2^T\left(-2\mathbf{P}_2\mathbf{T} + \frac{\mathbf{P}_2\mathbf{P}_2}{\sigma} + \mathbf{P}_2\overline{C}^2E\right)e_{x2} - 2\sum_{\mathbf{i}=\mathbf{1}}^{\mathbf{n}}\boldsymbol{\chi}_i p_{2i}\left|\mathbf{e}_{x2i}\right| \\ &\quad - 2\sum_{\mathbf{i}=\mathbf{1}}^{\mathbf{n}} k_2p_{2i}\mathbf{e}_{x2i}^2 - 2\sum_{\mathbf{i}=\mathbf{1}}^{\mathbf{n}} k_3p_{2i}\left|\mathbf{e}_{x2i}\right|^{1+\gamma}. \end{aligned} \tag{34}$$

Since we have $-2\mathbf{P}_2\mathbf{T} + (\mathbf{P}_2\mathbf{P}_2/\sigma) + \sigma\overline{C}^2\mathbf{E} < 0$ according to Lemma 1, we can further obtain

$$\begin{aligned} \dot{V}_3 &\le -2\sum_{\mathbf{i}=\mathbf{1}}^{\mathbf{n}} k_2p_{2i}\mathbf{e}_{x2i}^2 - 2\sum_{\mathbf{i}=\mathbf{1}}^{\mathbf{n}} k_2p_{2i}\left|\mathbf{e}_{x2\mathbf{i}}\right|^{1+\gamma} \\ &= -2k_2V_3 - 2k_3\sum_{\mathbf{i}=\mathbf{1}}^{\mathbf{n}} p_{2i}^{(1-\gamma)/2}V_3^{(1+\gamma)/2} < 0. \end{aligned} \tag{35}$$

From (35), we can see that $\mathbf{e}_{x2}$ can converge to zero in finite time.

4.2. Stability Analysis of the Closed-Loop System

Lemma 2 (see [21]). If the control gain $\overline{\mathbf{M}}$ in (9) is chosen to satisfy the condition $\|\mathbf{I} - \mathbf{M}^{-1}\mathbf{q}\overline{\mathbf{M}}\|_2 < 1$ for all $t \ge 0$, then $\|\ddot{q}_{t-L} - \ddot{q}\|_2 \longrightarrow 0$ as $L \longrightarrow 0$ and the error $\mathbf{H} - \widehat{\mathbf{H}}$ is bounded by a constant $H*$, i.e., $\|\mathbf{H} - \widehat{H}\| \le H^*$.

Lemma 3 (see [9]). For robotic system (1) controlled by the TDC with adaptive gradient estimators (14) and (15), the adaptive gain of the gradient $\widehat{K}_{\mathrm{GE}}$ has an upper bound:

$$\left\|\widehat{K}_{\mathrm{GE}}\right\| < \left\|\widehat{K}^{*}_{\mathrm{GE}}\right\|, \tag{36}$$

where $\widehat{K}^{*}_{GE}$ is a positive constant.

Theorem 1. *Consider the robotic system (1) which is controlled by the TDC with gradient estimator (13) and the adaptive law (14). Then, the closed-loop system (15) is stable and the position tracking error* $\mathbf{e}$ *of the robotic system is bounded.*

Proof. Define

$$\mathbf{H} \approx \mathbf{H}_{t-L} = \widehat{H} = \ddot{q}_{t-L} - \overline{M}^{-1}\boldsymbol{\tau}_{t-L}. \tag{37}$$

Now consider the Lyapunov function

$$V = \frac{1}{2}\mathbf{S}^{T}\mathbf{S} + \frac{1}{2}\frac{\alpha}{\psi}\left[H^{*} - \widehat{K}_{\mathrm{GE}}\left(\dot{e} + \mathbf{K}_{D}\mathbf{e} + \mathbf{K}_{P}\int \mathbf{e}\,\mathbf{dt}\right)\right]^{2}. \tag{38}$$

Let $\Delta = \dot{e} + \mathbf{K}_{D}\mathbf{e} + \mathbf{K}_{P}\int \mathbf{e}\,\mathbf{dt}$. Differentiating (38) and substituting Δ into it yields

$$\dot{V} = \mathbf{S}^{T}\dot{S} - \frac{\alpha}{\psi}\left(H^{*} - \widehat{K}_{\mathrm{GE}}\Delta\right)\left(\dot{\widehat{K}}_{\mathrm{GE}} + \dot{\Delta}\right). \tag{39}$$

From (8), we have $\dot{\Delta} = \varepsilon$. Now, substituting $\dot{S}$ and $\ddot{q}$ into (39), we can get

$$\dot{V} = \mathbf{S}^{T}\left(\ddot{q}_{d} - \mathbf{H} - \overline{M}^{-1}\boldsymbol{\tau} + \mathrm{K}_{S}\dot{e}\right) - \frac{\alpha}{\psi}\left(H^{*} - \widehat{K}_{\mathrm{GE}}\Delta\right)\left(\dot{\widehat{K}}_{\mathrm{GE}} + \varepsilon\right). \tag{40}$$

Substituting (15) and (37) into (39), we have

$$\dot{V} = \mathbf{S}^{T}\left(-\mathbf{R} - \widehat{H} + \delta\right) - \frac{\alpha}{\psi}\left(H^{*} - \widehat{K}_{\mathrm{GE}}\Delta\right)\left(\dot{\widehat{K}}_{\mathrm{GE}} + \varepsilon\right), \tag{41}$$

where $\mathbf{R} = \mathbf{H} - \widehat{H}$ and $\delta = -\overline{M}^{-1}\tau_{t-L} + \ddot{q}_{t-L} - \beta\mathbf{S} - \widehat{K}_{\mathrm{GE}}\Delta$.

Substituting (37) into (41), we can obtain

$$\begin{aligned}\dot{V} &= \mathbf{S}^{T}\left(-\mathbf{R} - \beta\mathbf{S} - \widehat{K}_{\mathrm{GE}}\Delta\right) - \frac{\alpha}{\psi}\left(H^{*} - \widehat{K}_{\mathrm{GE}}\Delta\right)\left(\dot{\widehat{K}}_{\mathrm{GE}} + \varepsilon\right)\\ &\le \|\mathbf{S}\|\|\mathbf{R}\| - \|\mathbf{S}\|\widehat{K}_{\mathrm{GE}}\Delta - \frac{\alpha}{\psi}\left(H^{*} - \widehat{K}_{\mathrm{GE}}\Delta\right)\left(\dot{\widehat{K}}_{\mathrm{GE}} + \varepsilon\right) - \beta\mathbf{S}^{2}\\ &= \left[\|\mathbf{S}\| - \frac{\alpha}{\psi}\left(\dot{\widehat{K}} + t\varepsilon\right)\right]\left(H^{*} - \widehat{K}_{\mathrm{GE}}\Delta\right) - \beta\mathbf{S}^{2}.\end{aligned} \tag{42}$$

Furthermore, Γ is taken as the upper bound of $\mathbf{S}$, and according to the adaptive law (14), we have

$$\dot{V} \le -\beta\mathbf{S}^{2} \le -\beta\Gamma^{2}. \tag{43}$$

From (43), we have $\dot{V} \le 0$.

According to (38), we can obtain

$$\frac{1}{2}\mathbf{S}^{2} \le V \le \frac{1}{2}\mathbf{S}^{2} + \frac{1}{2}\frac{\alpha}{\psi}\left[H^{*} - \widehat{K}_{\mathrm{GE}}\left(\dot{e} + \mathbf{K}_{D}\mathbf{e} + \mathbf{K}_{P}\int \mathbf{e}\,\mathbf{dt}\right)\right]^{2}. \tag{44}$$

Since H^{*} is a constant, from Lemma 2, it can be known that $\widehat{K}_{\mathrm{GE}}$ is bounded. Now let Z be the bound of $(1/2)(\alpha/\psi)[H^{*} - \widehat{K}_{\mathrm{GE}}(\dot{e} + t\mathbf{K}_{D}neq + h\mathbf{K}_{P}\int \mathbf{e}\,\mathbf{dt}]^{2}$ in (44) and we can get

$$V < \frac{1}{2}\Gamma^{2} + \frac{1}{2}\mathrm{Z}^{2}. \tag{45}$$

According to (44) and (45), we can obtain

$$\frac{1}{2}\mathbf{S}^{2} < \frac{1}{2}\Gamma^{2} + \frac{1}{2}\mathrm{Z}^{2}. \tag{46}$$

Thus, we can further get

$$\|\mathbf{S}\| < \sqrt{\Gamma^{2} + \mathrm{Z}^{2}}. \tag{47}$$

Equations (44) and (46) show that $\mathbf{S}$ has an upper bound and can be adjusted by α, ψ, and Γ. Since $\mathbf{S}$ is bounded and $\mathbf{S} = \dot{e} + \mathbf{K}_{S}\mathbf{e}$, $\dot{e} = -\mathbf{K}_{S}\mathbf{e}$ is asymptotically stable. The position tracking error $\mathbf{e}$ of the robotic system is bounded. This concludes the proof of Theorem 1. □

5. Simulation Studies

In order to verify the effectiveness of the velocity-free adaptive TDC, simulations are conducted on a 2-DOF robot and compared to the conventional TDC in Section 2 and the adaptive gain sliding mode TDC in [9].

The dynamics of the robot is as follows:

$$\begin{aligned}\mathbf{M} &= \begin{bmatrix}(m_1 + m_2)l_1^{2} + m_2 l_2^{2} + 2m_2 l_1 l_2 \cos\mathbf{q}_2 & m_2 l_2^{2}\cos\mathbf{q}_2\\ m_2 l_2^{2}\cos\mathbf{q}_2 & m_2 l_2^{2}\end{bmatrix},\\ \mathbf{C} &= \begin{bmatrix}-m_2 l_1 l_2 \dot{q}_2 \sin\mathbf{q}_2 & -m_2 l_1 l_2 \dot{q}_1 \dot{q}_2 \sin\mathbf{q}_2\\ m_2 l_1 l_2 \dot{q}_1 \sin\mathbf{q}_2 & 0\end{bmatrix},\\ \mathbf{G} &= \begin{bmatrix}[(m_1 + m_2)l_1\cos\mathbf{q}_2 + m_2 l_2\cos(\mathbf{q}_1 + \mathbf{q}_2)]g\\ m_2 l_2\cos(\mathbf{q}_1 + \mathbf{q}_2)g\end{bmatrix},\\ \mathbf{f} &= 0.02\mathrm{sign}(\dot{q}),\end{aligned} \tag{48}$$

where m_1 and m_2 represent the mass of links, l_1 and l_2 are the length of links, and g is the gravitational acceleration, respectively.

In the simulations, $m_1 = m_2 = 0.5$, $l_1 = 1$, $l_2 = 0.8$, and $g = 9.8$. The desired positions of joint 1 and joint 2 of the robot are $q_{d1} = q_{d2} = \sin 2\pi t$. The time delay is set to be the sampling time, i.e., $L = 0.001$ s.

When the conventional TDC (6) is employed, $\mathbf{K}_{D} = \mathbf{diag}\{80, 60\}$, $\mathbf{K}_{P} = \mathbf{diag}\{200, 180\}$, and $\overline{M} = \mathbf{diag}\{0.5, 0.4\}$. The simulation results of the conventional TDC are shown in Figures 2–4.

From Figure 2, it can be seen that, with the conventional TDC, the real position trajectory of joint 1 and joint 2 of the robot cannot track the desired position in a satisfactory way.

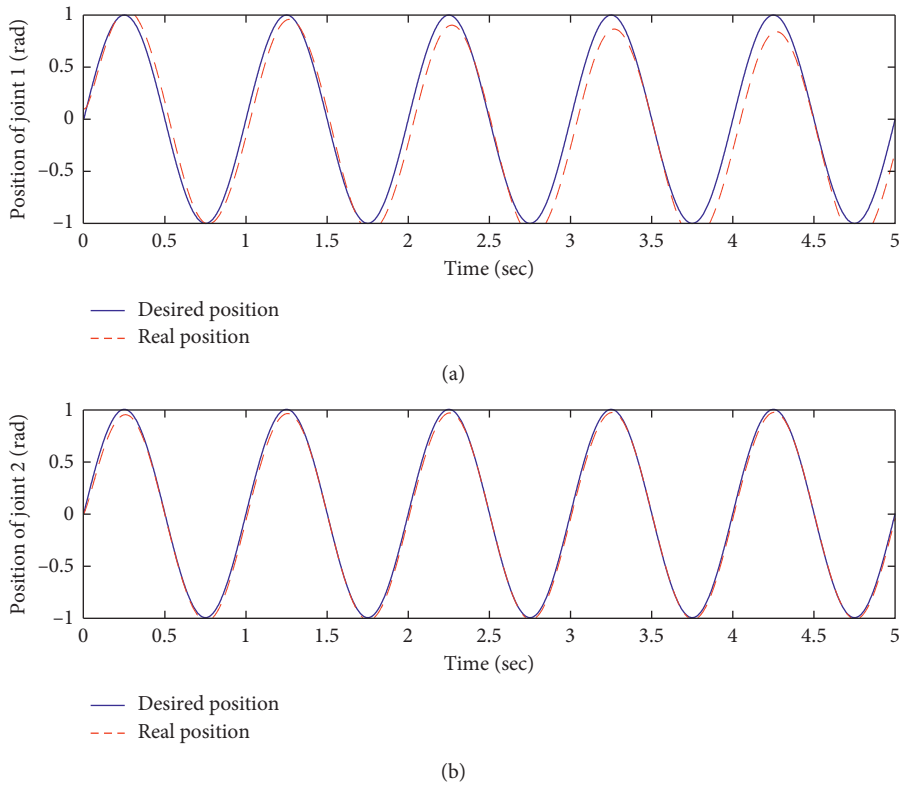

Figure 2: Position tracking of (a) joint 1 and (b) joint 2 (conventional TDC).

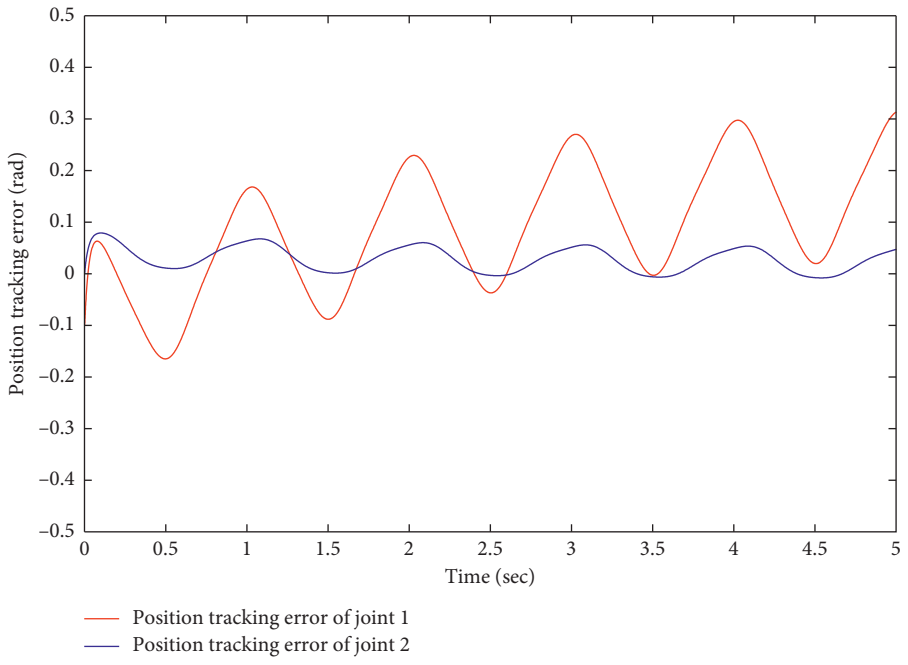

Figure 3: Position tracking error of joint 1 and joint 2 (conventional TDC).

There exists an obvious position error, especially for joint 1, as shown in Figure 3. Besides, as shown in Figure 4, the fluctuation of the input torque is obvious especially when it achieves the maximum value each time.

When the adaptive gain sliding mode TDC in [9] is employed, $\mathbf{K}_S = \mathbf{diag}\{5, 5\}$, $\beta = 85$, $\alpha = 20$, $\psi = 0.001$, and $\overline{M} = \mathbf{diag}\{1, 0.9\}$. The simulation results are shown in Figures 5–7.

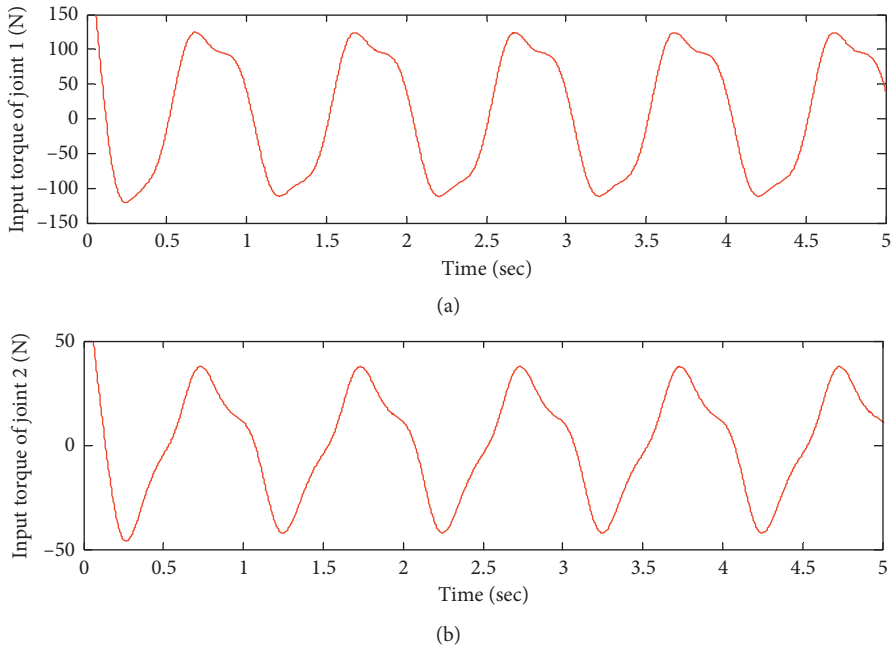

Figure 4: Input torque of (a) joint 1 and (b) joint 2 (conventional TDC).

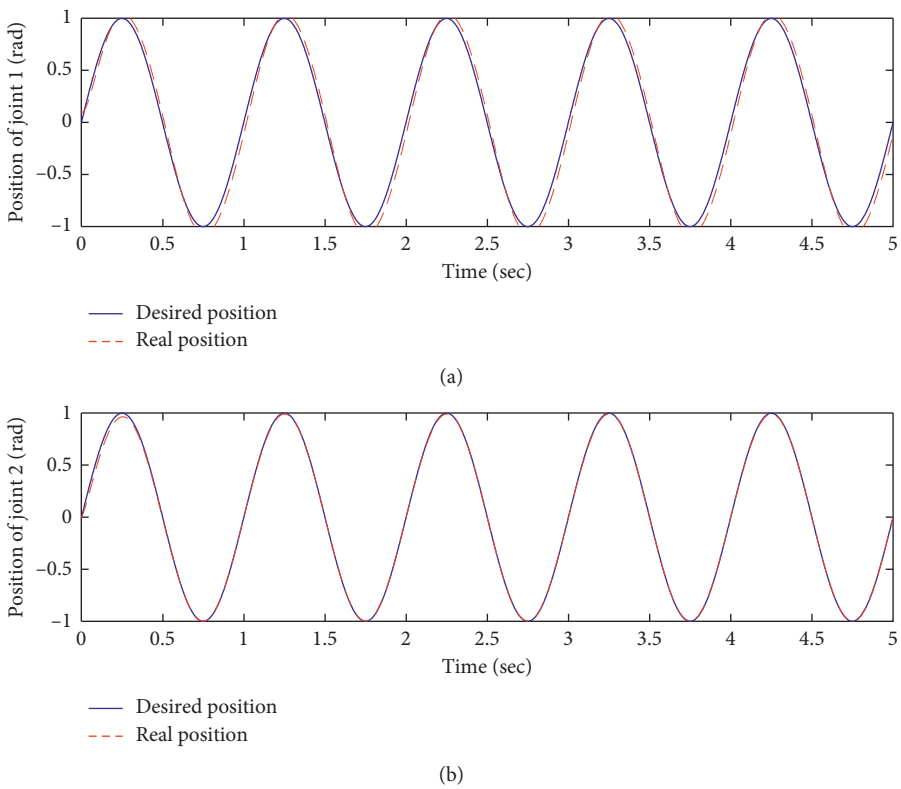

Figure 5: Position tracking of (a) joint 1 and (b) joint 2 (adaptive gain sliding mode TDC).

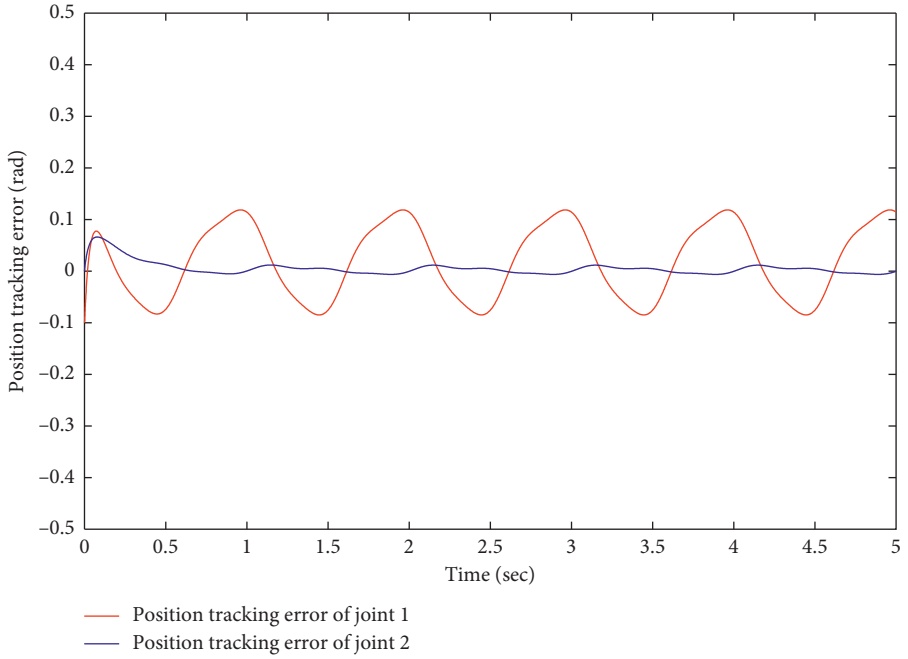

Figure 6: Position tracking error of joint 1 and joint 2 (adaptive gain sliding mode TDC).

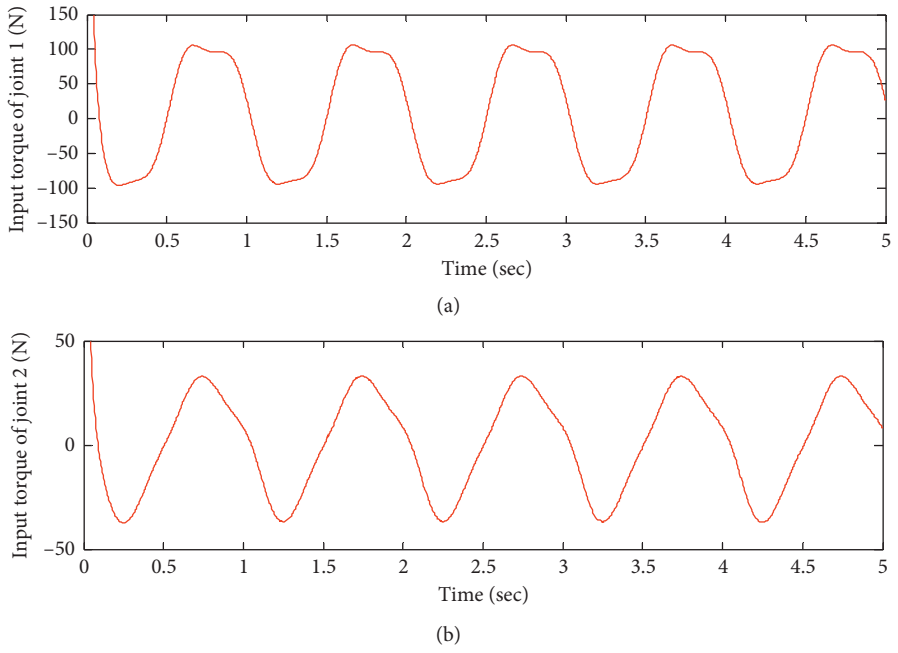

Figure 7: Input torque of (a) joint 1 and (b) joint 2 (adaptive gain sliding mode TDC).

From Figure 5, it can be seen that, with the adaptive gain sliding mode TDC, the position tracking of joint 1 has better tracking performance than that of the conventional TDC. However, the real position trajectory of joint 1 and joint 2 of the robot cannot track the desired position in a satisfying way either. There still exists obvious position error, especially for joint 1, as shown in Figure 6. In addition, the fluctuation of the input torque still exists, as shown in Figure 7, although it is smaller than that of the conventional TDC.

When the proposed control is employed, $\beta = 20$, $\mathbf{K}_S = \mathbf{diag}\{5, 10\}$, $\overline{M} = \mathbf{diag}\{0.05, 0.04\}$, $\alpha = 20$, and $\psi = 0.001$. The initial value of the gain of the gradient is $\widehat{K}_{\mathrm{GE}}(0) = \mathbf{diag}\{K_{\mathrm{GE}_1}(0), K_{\mathrm{GE}_2}(0)\}$, $K_{\mathrm{GE}_1}(0) = 0$, and $K_{\mathrm{GE}_2}(0) = 0$. For the observer, $\mathbf{T} = \mathbf{diag}\{0.01, 0.1\}$, $\mathbf{L}_1 = \mathbf{diag}\{1, 1\}$, $\mathbf{L}_2 = \mathbf{diag}\{0.001, 0.001\}$, $\boldsymbol{\chi} = \mathbf{diag}\{0.0001, 0.0001\}$, $k_1 = 0.0001$, $k_2 = 1$, $k_3 = 3$, and $\gamma = 0.5$. The simulation results of the proposed control are shown in Figures 8–13.

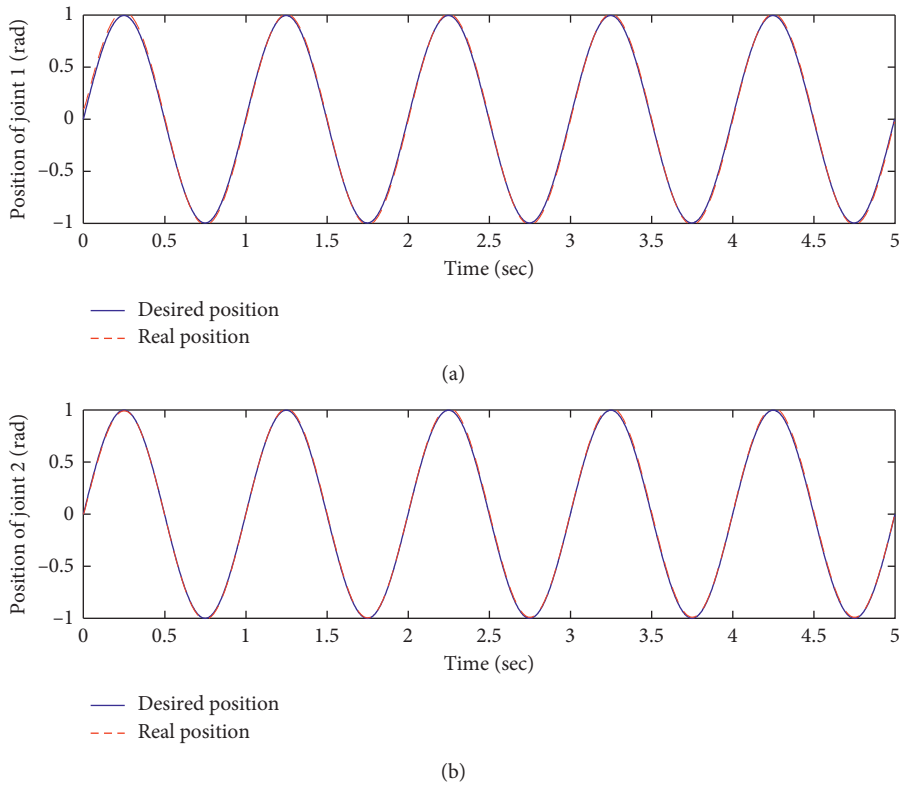

Figure 8: Position tracking of (a) joint 1 and (b) joint 2 (proposed control).

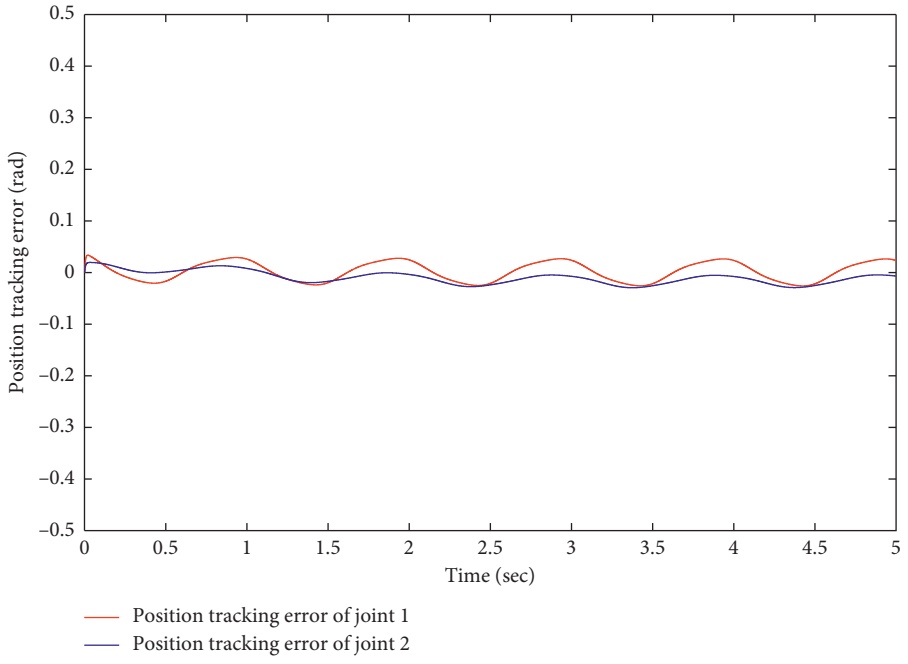

Figure 9: Position tracking error of joint 1 and joint 2 (proposed control).

From Figure 8, it can be seen that the real position trajectory of joint 1 and joint 2 of the robot can track the desired position in a satisfying way. The position tracking errors of both joints 1 and 2 are quite small, as shown in Figure 9. Moreover, from Figure 10, the fluctuation of the input torque is the smallest compared with that of the conventional TDC and the adaptive gain sliding mode TDC. Figure 11 shows that the gain of the gradient can be adjusted

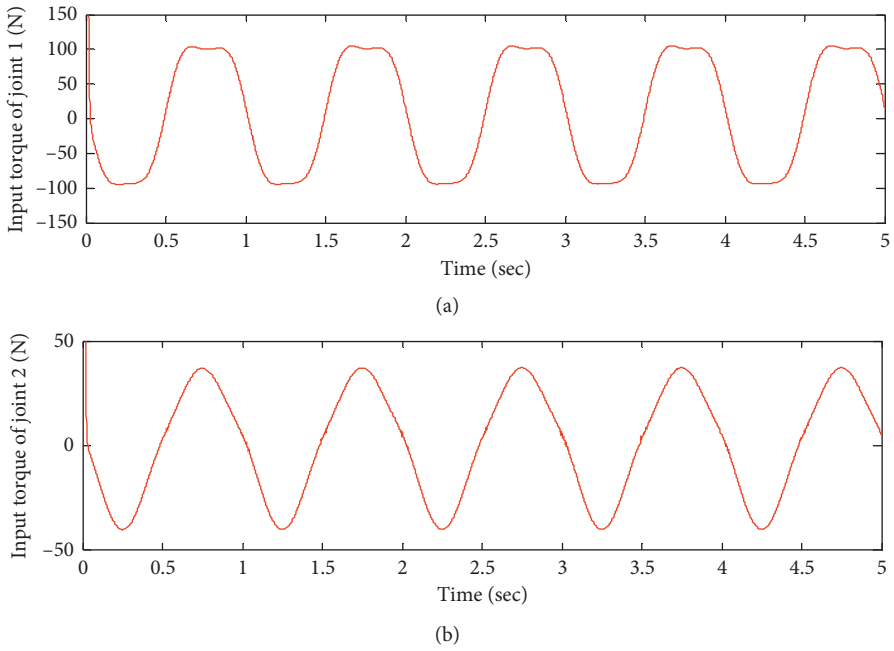

Figure 10: Input torque of (a) joint 1 and (b) joint 2 (proposed control).

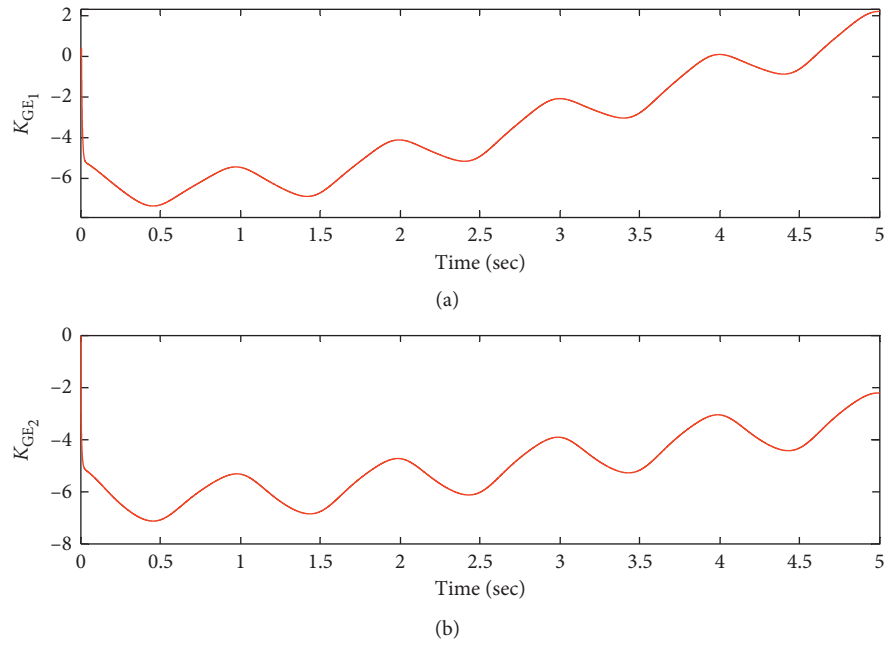

Figure 11: Adaptive gain of the gradient (a) K_{GE_1} and (b) K_{GE_2}(proposed control).

by the adaptive law. From Figures 12 and 13, it can be seen that the observer can effectively observe the velocity and acceleration of the robot.

In order to quantitatively compare the position tracking performance of the proposed method with the conventional TDC method and the adaptive gain sliding mode TDC in [9], the range of the position tracking error $e_{r_n} = |e_{\min_n}| \sim |e_{\max_n}|$ is calculated, where $n = 1, 2$ represents joint 1 and joint 2, respectively. The calculation results are shown in Table 1.

From Table 1, it can be seen that compared to the conventional TDC, the maximum position tracking error of joint 1 is 0.279362 rad smaller and that of joint 2 is 0.04987 rad smaller with the proposed control. In addition, compared to the adaptive gain sliding mode TDC, the maximum position tracking error of joint 1 is 0.08476 rad smaller and that of joint 2 is 0.03697 rad smaller with the proposed control.

Remark 4. There are three parameters to be chosen in the TDC with adaptive gradient estimator, i.e., α, β, and ψ. In

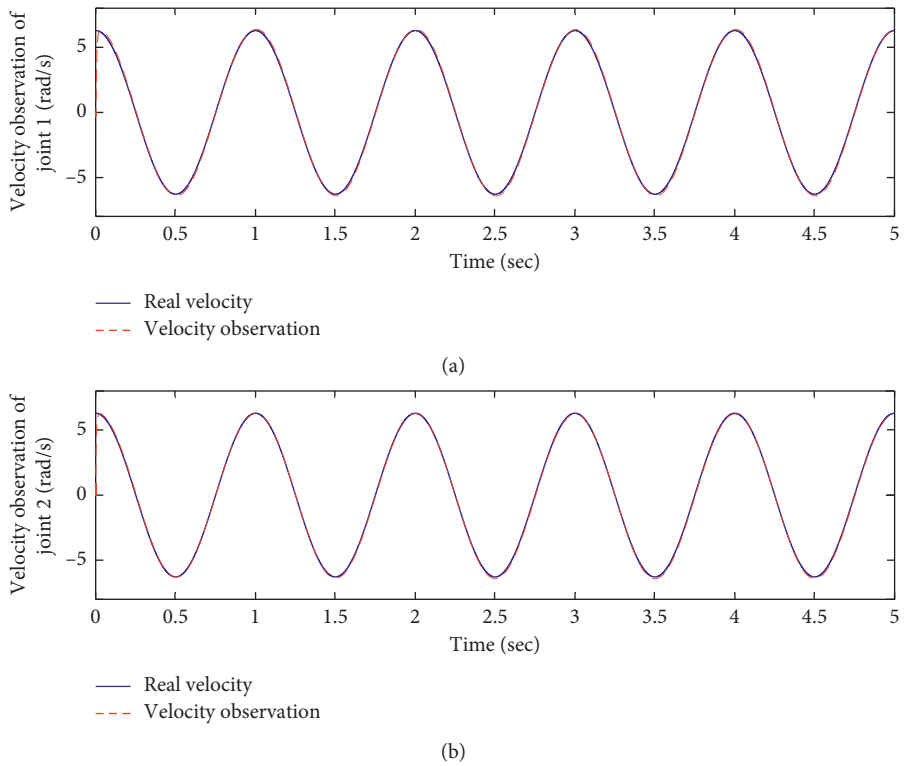

Figure 12: Velocity observation of (a) joint 1 and (b) joint 2 (proposed control).

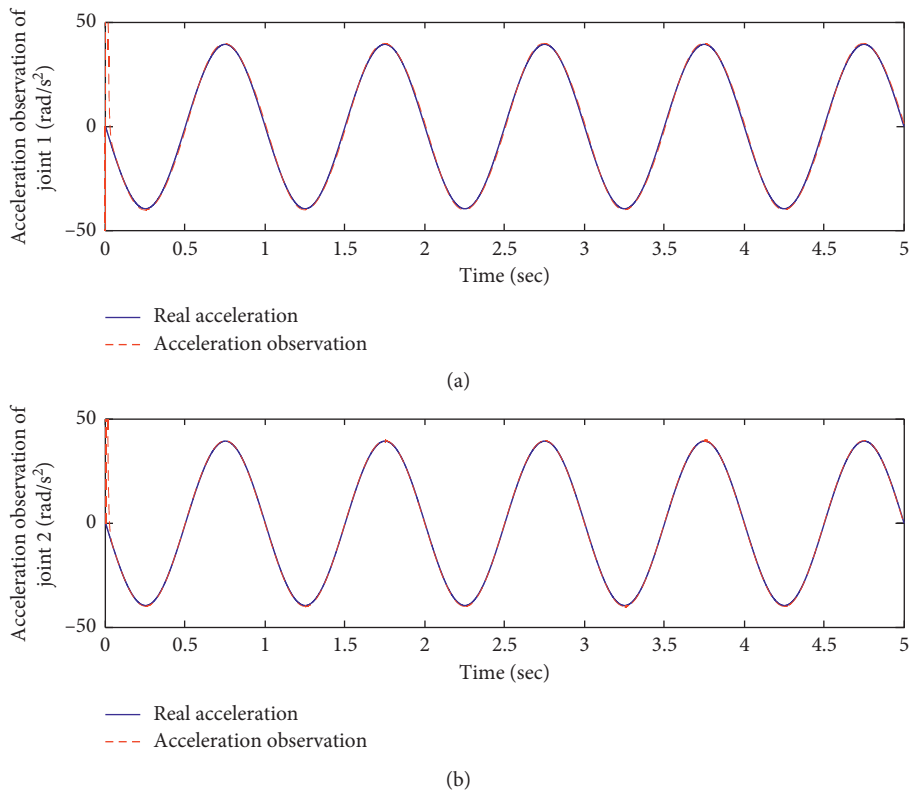

Figure 13: Acceleration observation of (a) joint 1 and (b) joint 2 (proposed control).

Table 1: Quantitative comparison of position tracking error.

	Conventional TDC	Adaptive gain sliding mode TDC	Proposed control
e_{r_1} (rad)	0–0.3133	0–0.1187	0–0.03394
e_{r_2} (rad)	0–0.0790	0–0.0661	0–0.02913

addition, there are four parameters to be chosen in the observer, i.e., k_1, k_2, k_3, and γ. When α, β, ψ, k_1, k_2, k_3, and γ increase to ten times of their values (or decrease to ten times of their values), the position tracking errors of joint 1 and joint 2 will become bigger.

6. Conclusions

To improve the trajectory tracking performance of complex nonlinear robotic system, this paper proposes a velocity-free adaptive TDC. A TDC with gradient estimator is designed considering that conventional TDC may cause large TDE error. Then, an adaptive law is designed to estimate the gain of the gradient. Next, an observer is designed to observe the velocity and acceleration in the controller. The proposed control can not only offset the nonlinear terms in the complex dynamics of the robotic system but also reduce the TDE error, estimate the gain of the gradient online, and avoid the measurement of velocity and acceleration. Experimental verification of the control proposed in this paper is quite necessary and remains as our work in the next step.

Data Availability

The data that supports our manuscript conclusions are some open access articles that have been properly cited, and the readers can easily obtain these articles to verify the conclusions.

Conflicts of Interest

The authors declare that they have no conflicts of interest regarding the publication of this paper.

Acknowledgments

This research was supported by the National Natural Science Foundation of China (Grant nos. 61973257, 61973331, and 61875166), Sichuan Science and Technology Program (Grant no. 2020YJ0367), and the Innovation Fund Project of Xihua University for Graduate Students (Grant no. YCJJ2020049).

References

[1] L. Zhang, Z. Li, and C. Yang, "Adaptive neural network based variable stiffness control of uncertain robotic systems using disturbance observer," *IEEE Transactions on Industrial Electronics*, vol. 64, no. 3, pp. 2236–2245, 2017.

[2] Z. Liu, G. Lai, Y. Zhang, and C. L. P. Chen, "Adaptive fuzzy tracking control of nonlinear time-delay systems with dead-zone output mechanism based on a novel smooth model," *IEEE Transactions on Fuzzy Systems*, vol. 23, no. 6, pp. 1998–2011, 2015.

[3] R. Babaghasabha, M. A. Khosravi, and H. D. Taghirad, "Adaptive robust control of fully-constrained cable driven parallel robots," *Mechatronics*, vol. 25, pp. 27–36, 2015.

[4] K. Youcef-Toumi and O. Ito, "A time delay controller for systems with unknown dynamics," in *Proceedings of the 1988 American Control Conference*, pp. 194–208, Atlanta, GA, USA, June 1990.

[5] M. Jin, Y. Jin, P. H. Chang, and C. Choi, "High-accuracy tracking control of robot manipulators using time delay estimation and terminal sliding mode," *International Journal of Advanced Robotic Systems*, vol. 8, pp. 65–78, 2011.

[6] Z. Yang, J. Peng, and Y. Liu, "Adaptive neural network force tracking impedance control for uncertain robotic manipulator based on nonlinear velocity observer," *Neurocomputing*, vol. 331, pp. 263–280, 2019.

[7] M. Rahmani and K. Behdinan, "Interaction of torque link free play and Coulomb friction nonlinearities in nose landing gear shimmy scenarios," *International Journal of Non-Linear Mechanics*, vol. 119, Article ID 103338, 2020.

[8] M. Ruderman and M. Iwasaki, "Observer of nonlinear friction dynamics for motion control," *IEEE Transactions on Industrial Electronics*, vol. 62, no. 9, pp. 5941–5949, 2015.

[9] J. Baek, M. Jin, and S. Han, "A new adaptive sliding-mode control scheme for application to robot manipulators," *IEEE Transactions on Industrial Electronics*, vol. 63, no. 6, pp. 3628–3637, 2016.

[10] J. Baek, W. Kwon, B. Kim, and S. Han, "A widely adaptive time-delayed control and its application to robot manipulators," *IEEE Transactions on Industrial Electronics*, vol. 66, no. 7, pp. 5332–5342, 2019.

[11] Y. Wang, F. Yan, J. Chen, F. Ju, and B. Chen, "A new adaptive time-delay control scheme for cable-driven manipulators," *IEEE Transactions on Industrial Informatics*, vol. 15, no. 6, pp. 3469–3481, 2019.

[12] M. Jin, S. H. Kang, and P. H. Chang, "Robust compliant motion control of robot with nonlinear friction using time-delay estimation," *IEEE Transaction on Industrial Electronics*, vol. 55, no. 1, pp. 258–269, 2008.

[13] M. Jin, S. H. Kang, P. H. Chang, and J. Lee, "Robust control of robot manipulators using inclusive and enhanced time delay control," *IEEE/ASME Transactions on Mechatronics*, vol. 22, no. 5, pp. 2141–2152, 2017.

[14] G. R. Cho, P. H. Chang, S. H. Park, and M. Jin, "Robust tracking under nonlinear friction using time-delay control with internal model," *IEEE Transactions on Control Systems Technology*, vol. 17, no. 6, pp. 1406–1414, 2009.

[15] S. R. Jiang, Y. Y. Wang, F. Ju, B. Chen, and H. T. Wu, "A new fuzzy time-delay control for cable-driven robot," *International Journal of Advanced Robotic Systems*, vol. 16, no. 2, pp. 1–10, 2019.

[16] D. K. Han and P.-h. Chang, "Robust tracking of robot manipulator with nonlinear friction using time delay control with gradient estimator," *Journal of Mechanical Science and Technology*, vol. 24, no. 8, pp. 1743–1752, 2010.

[17] H. Yan, C. Sun, and G. Hu, "Robust tracking control of an Euler-Lagrange system subject to uncertain friction and impact," in *Proceedings of the IEEE International Conference*

on Information and Automation, pp. 2227–2232, Lijiang, China, August 2015.

[18] H.-J. Bae, M. Jin, J. Suh, J. Y. Lee, P.-H. Chang, and D.-s. Ahn, "Control of robot manipulators using time-delay estimation and fuzzy logic systems," *Journal of Electrical Engineering and Technology*, vol. 12, no. 3, pp. 1271–1279, 2017.

[19] S. Ahmad, M. Rehan, and M. Iqbal, "Robust generalized filtering of uncertain Lipschitz nonlinear systems under measurement delays," *Nonlinear Dynamics*, vol. 92, no. 4, pp. 1567–1582, 2018.

[20] C. Hua, Y. Yang, and P. X. Liu, "Output-feedback adaptive control of networked teleoperation system with time-varying delay and bounded inputs," *IEEE/ASME Transactions on Mechatronics*, vol. 20, no. 5, pp. 2009–2020, 2015.

[21] M. Jin, J. Lee, P. H. Chang, and C. Choi, "Practical non-singular terminal sliding-mode control of robot manipulators for high-accuracy tracking control," *IEEE Transactions on Industrial Electronics*, vol. 56, no. 9, pp. 3593–3601, 2009.

Hindawi
Mathematical Problems in Engineering
Volume 2020, Article ID 5281904, 10 pages
https://doi.org/10.1155/2020/5281904

Research Article

A Novel Hybrid Robust Control Design Method for F-16 Aircraft Longitudinal Dynamics

Vi H. Nguyen and Thanh T. Tran

Faculty of Engineering, Vietnamese-German University, Le Lai, Thu Dau Mot, Binh Duong, Vietnam

Correspondence should be addressed to Thanh T. Tran; thanh.tt@vgu.edu.vn

Received 4 June 2020; Revised 20 August 2020; Accepted 10 September 2020; Published 22 September 2020

Academic Editor: Baltazar Aguirre Hernandez

This paper presents a hybrid robust control design method for a third-order lower-triangular model of nonlinear dynamic systems in the presence of disturbance. In this paper, a novel control design is presented systematically to synthesize a robust nonlinear feedback controller, called backstepping sliding mode control (BSMC), for the proposed system by a combined approach of backstepping design and sliding mode control. In this approach, a family of the "sliding surface" is introduced in state transformations. Then, a smooth switching function of the sliding surface is introduced and enforced to include in virtual feedbacks and a real control law from the control selection phrases of the backstepping design loop. The achieved control method proves a well-tracking command with asymptotic stability, provides a robustness in the presence of uncertainties, and eliminates completely a chattering phenomenon. The application of flight-path angle control corresponding to the longitudinal dynamics of a high-performance F-16 aircraft simulation model is implemented. Under some assumptions, full nonlinear longitudinal dynamics is reformed into a lower-triangular system for a direct application to formulate a control law. A closed-loop system is achieved for in-flight simulation with different flight profiles for a comparison of the existing methods. Also, an external disturbance on different loading/unloading conditions in flight is applied to verify and validate robustness of the proposed control method.

1. Introduction

A standard design method of the flight control system for nonlinear aircraft dynamic systems is based on gain scheduling from linear control system designs. In this method, a linearized model of the nonlinear flight dynamic system at key operating points within the flight envelope is achieved. From those selected points, linear controllers are designed and then combined continuously as the aircraft flies from one operating point to another. In [1], it is indicated that actual system performance and stability can be significantly different from design results due to linearized nonlinearities. Therefore, a direct application of a nonlinear flight system should be addressed for a new generation of flight control design [2–4]. However, these works neglected the effects of uncertainties that can lead to instability and poor performance of an aircraft system due to complex variations in aerodynamic models. Recently, robust control design methods for nonlinear aircraft flight dynamics have been addressed by many researchers [5–7]. Twenty-eight uncertain parameters are used to model aircraft motion in nonlinear longitudinal dynamics [5]. Then, a genetic algorithm is used to search a feasible design coefficient space that is evaluated by Monte Carlo for stability and performance robustness. A better approach in robust control methods [6, 7] is proposed to improve the handling qualities across the specified flight envelope without the use of gain scheduling. In this approach, the control parameters of dynamic inversion are designed to minimize the probability of violating design specifications and so provide a better design with good robustness in stability and performance subject to modeling uncertainties. However, mentioned control design methods are mostly focused on design of control parameters that are not fully able to adapt internal dynamics in order to ensure the stability and performance robustness. Thus, a new type of the robust controller, in

which a robust property for a nonlinear dynamic system must be included, is necessary to improve stability and performance of aircraft longitudinal dynamics.

In recent years, backstepping or recursive control design for a strict-feedback form of nonlinear dynamic systems is introduced firstly by authors [1] and is applied extensively for flight control of the nonlinear flight dynamic system [8–13]. In approaches [8–12], a full nonlinear dynamic system is transformed directly or indirectly into a strict-feedback form or a lower-triangular model for applicability via assumptions or state transformations. The achieved model will be divided into subsystems for control objectives. By considering each subsystem in relation with interconnected subsystems, a virtual feedback control is selected from satisfying the requirement of Lyapunov's theorem. After a series of control design for subsystems, a nonlinear feedback controller is obtained. By numerical simulation and experimental study, the backstepping control method can prove a very good performance and stability if system parameter modeling is accurate. On the other hand, the method might lead to a poor quality across the full flight envelope due to uncertain system parameters. Thus, a better approach [13] is proposed to improve the performance in this situation. In this design, an integrator with a tracking error is introduced and added into the control law via feedback selection. The achieved control system can improve robust performance and stability in the presence of disturbance, but time response of the flight-path angle or the attack angle is slower than that of the traditional methods. This behavior or robustness should be improved in designing the control system for a high-performance aircraft system.

Sliding mode control (SMC) was proposed firstly and applied by Slotine [14]. This method provides a robust control technique to deal with unmodeling dynamics or uncertain system parameters for nonlinear dynamic systems and has been widely used and extended for flight control design [15–21]. A linearized model for longitudinal dynamics is achieved for applying the sliding mode control design [17]. The achieved control method is simulated on the nonlinear flight longitudinal model of the F-16 aircraft. An extra controller of the integral sliding mode control allocation scheme [18], which is active if faults occurs, is built around a traditional controller. Although numerical simulation indicates that the proposed control shows good results for nominal and fault/failure conditions, a guideline on how it works or a stability proof is a concern in the paper. In order to solve for fuzzy stochastic systems subjected to matched/mismatched uncertainties, Wang et al. [20] propose a new method to remove these assumptions and present a new integral sliding mode control (ISMC) method. As discussed above, it is clear that each work has some advantage and some limitation, but mostly based on the traditional control design method. So, the question arises if there exists a systematic approach to formulate a robust nonlinear feedback controller that can inherit advances of the backstepping control and robust aspects of a sliding mode control design. This paper will provide a novel solution to deal with the proposed challenge by a combined design of the backstepping method and sliding mode control. In this proposal, a family of the "sliding surface" is introduced in state transformations. Then, the sliding surface and a smooth switching function are enforced to include in virtual feedbacks and a real control law from control selection phrases. Due to the inheritance of the properties of the backstepping control and sliding mode control, the achieved control method proves a well-tracking command with asymptotic stability, provides a robustness in the presence of uncertainties, and eliminates completely a chattering phenomenon. The application of flight-path angle control of a high-performance F-16 aircraft model is implemented to show advance of the proposed control method.

This paper is organized as follows: a hybrid controller formulation for a general class of a third-order lower-triangular model of a nonlinear dynamic system is presented in Section 2. Study of flight-path angle control of longitudinal dynamics of the F-16 aircraft mode is investigated to show applicability in Section 3. A numerical simulation of the full nonlinear F-16 aircraft model is implemented and compared to the integrator-backstepping control method; finally, conclusion and discussions are presented in the end of the paper.

2. A Hybrid Controller Formulation for a Single-Input Single-Output (SISO) Third-Order Lower-Triangular Model of Nonlinear Dynamic Systems

In this section, a problem formulation is considered firstly. Secondly, a new control design method is presented for formulating a backstepping sliding mode control (BSMC) law for the (SISO) third-order lower-triangular form of the nonlinear dynamic system. Some important remarks are given in the end of the section.

2.1. Problem Formulation. Consider an SISO third-order lower-triangular model [1] of nonlinear dynamics systems as

$$\dot{x}_1 = f_1(x_1) + g_1(x_1)x_2, \tag{1}$$

$$\dot{x}_2 = f_2(x_1, x_2) + g_2(x_1, x_2)x_3, \tag{2}$$

$$\dot{x}_2 = f_2(x_1, x_2, x_3) + g_2(x_1, x_2, x_3)u, \tag{3}$$

where the unknown valued functions $\widehat{f}_i\,(i = 1, 2, 3)$ and $\widehat{g}_i\,(i = 1, 2, 3)$ are approximated as known functions $f_i\,(i = 1, 2, 3)$ and $g_i\,(i = 1, 2, 3)$, respectively, in this paper. This approximation is based on working condition and experience for a specific system. $x_i\,(i = 1, 2, 3) \in R$ are the state variables, and the functions $f_i\,(i = 1, 2, 3) \in R$ are known real-valued, continuous, and differentiable. The functions $g_i\,(i = 1, 2, 3) \in R$ are known real-valued, continuous, differentiable, and invertible. The variable $u \in R$ is the control input.

The objective of this research is to synthesize a robust control law for systems (1)–(3) such that the outputs $y = h(x) = x_1$ track well the desired value or command, x_d,

asymptotically, where x_d is a triple-differentiable function in time. Also, a global asymptotic stability is achieved with no or acceptably small overshoot in the presence of the model parameter errors and external disturbances.

2.2. Formulation of Backstepping Sliding Mode Control Law

Theorem 1. *There exists coordinate transformations (4), (5), and (6) and virtual feedbacks α_1 and α_2 in (5) and (6), respectively, and real control u in (7):*

$$e_1(t) = x_1 - x_d, \tag{4}$$

$$e_2(t) = x_2 - \alpha_1(x_1, x_d, \dot{x}_d, p_1), \tag{5}$$

$$e_3(t) = x_3 - \alpha_2(x_1, x_2, x_d, \dot{x}_d, p_1, p_2), \tag{6}$$

$$u = K(x_1, x_2, x_3, x_d, \dot{x}_d, \ddot{x}_d, p_1, p_2, p_3). \tag{7}$$

Such that systems (1)–(3) can be transformed into a stable linear decoupling system in terms of a new set of state variables e_1, e_2, and e_3 as

$$\dot{e}_1(t) = -p_1 e_1(t)\tanh(\lambda e_1(t)), \tag{8}$$

$$\dot{e}_2(t) = -p_2 e_2(t)\tanh(\lambda e_2(t)), \tag{9}$$

$$\dot{e}_3(t) = -p_3 e_3(t)\tanh(\lambda e_3(t)), \tag{10}$$

where p_1, p_2, p_3, and λ are the strict positive values and $\tanh(\cdot)$ is a hyperbolic tangent function and defined as $\tanh(\sigma) = (e^{\sigma} - e^{-\sigma})/(e^{\sigma} + e^{-\sigma})$.

The following is a proof for Theorem 1.

The proof of Theorem 1 consists of three steps. Coordinate transformations are introduced firstly. Then, virtual feedbacks and real control can be selected in terms of recursive design approach [11]. By doing so, systems (1)–(3) can be reformed into systems (8)–(10).

Step 1. Taking derivative of equation (4) in association with equation (1) results in

$$\dot{e}_1(t) = f_1(x_1) + g_1(x_1)x_2 - \dot{x}_d. \tag{11}$$

In Lyapunov's approach, a virtual control law $\alpha_1(x_1, x_d, \dot{x}_d, p_1) := x_2$ can be selected such that the tracking error $e_1(t)$ in equation (11) converges asymptotically to zero with small or no overshoot. The virtual controller can be chosen from satisfying the condition in which time differentiation of a control Lyapunov function (CLF) [1], $L_1(e_1(t))$, is less than or equal to a negative definitive function, $w(e_1(t))$. In fact, a CLF is selected as

$$L_1(e_1(t)) = \frac{1}{2}e_1(t)^2. \tag{12}$$

Combining the result from time differentiation of the CLF, $L(e_1(t))$, and equation (11) achieves

$$\dot{L}_1(e_1(t)) = e_1(t)\dot{e}_1(t) = e_1(t)\{f_1(x_1) + g_1(x_1)x_2 - \dot{x}_d\}. \tag{13}$$

Then, the virtual control α_1 can be obtained from enforcing $\dot{L}_1(e_1(t))$ to be a negative definitive function, or

$$\begin{aligned} -p_1\tanh(\lambda e_1(t)) &= f_1(x_1) + g_1(x_1)x_2 - \dot{x}_d, \\ \alpha_1(x_1, x_d, \dot{x}_d, p_1) &= g_1^{-1}(x_1)\{-p_1\tanh(\lambda(x_1 - x_d)) \\ &\quad - f_1(x_1) + \dot{x}_d\}. \end{aligned} \tag{14}$$

Substituting equation (14) into equation (13) results in

$$\begin{aligned} \dot{L}_1(e_1(t)) &= -p_1 e_1(t)\tanh(\lambda e_1(t)) \\ &:= -w_1(e_1(t)) < 0 \forall e_1(t) \neq 0. \end{aligned} \tag{15}$$

Note that $w_1(e_1(t)) = p_1 e_1(t)\tanh(\lambda e_1(t))$ is a positive definitive function. Thus, $\dot{L}_1(e_1(t))$ is a negative definitive function. This means that an achieved virtual control $\alpha_1(x_1, x_d, \dot{x}_d, p_1)$ assures to make tracking error tend to zero.

Step 2. By choosing feedback (14) and state transformations (4) and (5), systems (1)–(2) are resynthesized in (e_1, e_2) coordinates as follows:

$$\dot{e}_1(t) = -p_1\tanh(\lambda e_1(t)), \tag{16}$$

$$\dot{e}_2(t) = f_2(e_1 + x_d, e_2 + \alpha_1) + g_2(e_1 + x_d, e_2 + \alpha_1)x_3 - \dot{\alpha}_1. \tag{17}$$

Noting that the functions f_1 and α_1 are only functions of states and command. Thus, the term $\dot{\alpha}_1$ can be represented explicitly in variables of $x_1, x_2, x_d, \dot{x}_d, \ddot{x}_d, p_1$, and λ, and $\dot{\alpha}_1$ is calculated in the following equation:

$$\dot{\alpha}_1 = \frac{\partial \alpha_1}{\partial x_1}f_1 + \frac{\partial \alpha_1}{\partial x_d}\dot{x}_d + \frac{\partial \alpha_1}{\partial \dot{x}_d}\ddot{x}_d. \tag{18}$$

As a similar approach, a virtual control $\alpha_2 := x_3$ and CLF $L_2(e_1(t), e_2(t))$ are selected to ensure that systems (16)–(17) are stabilized at origin, i.e.,

$$L_2(e_1(t), e_2(t)) = L_1(e_1(t)) + \frac{1}{2}e_2(t)^2. \tag{19}$$

By taking derivative of equation (19) in consideration with equations (15)–(17), one gets

$$\begin{aligned} \dot{L}_2(e_1(t), e_2(t)) &= -w_1(e_1(t)) + e_2(t)\{f_2(e_1 + x_d, e_2 + \alpha_1) \\ &\quad + g_2(e_1 + x_d, e_2 + \alpha_1)x_3 - \dot{\alpha}_1\}. \end{aligned} \tag{20}$$

Then, a virtual control α_2 can be obtained from enforcing $\dot{L}_2(e_1(t), e_2(t))$ to be a negative definitive function, or

$$-p_2\tanh(\lambda e_2(t)) = f_2(e_1 + x_d, e_2 + \alpha_1) + g_2(e_1 + x_d, e_2 + \alpha_1)x_3 - \dot{\alpha}_1,$$
$$\alpha_2(x_1, x_2, x_d, \dot{x}_d, \ddot{x}_d, p_1, p_2) = g_2^{-1}(x_1, x_2)\{-p_2\tanh(\lambda e_2(t)) - f_2(x_1, x_2) + \dot{\alpha}_1\}. \quad (21)$$

Substituting equation (21) into equation (20) results in

$$\dot{L}_2(e_1(t), e_2(t)) = -p_1 e_1(t)\tanh(\lambda e_1(t)) - p_2 e_2(t)\tanh(\lambda e_2(t)) := -w_2(e_1(t), e_2(t)) < 0 \forall e_1(t), e_2(t) \neq 0. \quad (22)$$

Note that $w_2(e_1(t), e_2(t)) = p_1 e_1(t)\tanh(\lambda e_1(t)) + p_2 e_2(t)\tanh(\lambda e_2(t))$ is a positive definitive function. Thus, $\dot{L}_2(e_1(t), e_2(t))$ is a negative definitive function. This means that an achieved virtual control α_2 assures to make tracking error, $e_2(t)$, tend to zero or the first subsystem and the second subsystem [1] are interconnected with the proposed method.

Step 3. By choosing feedbacks (14) and (21) and state transformations (4)–(6), systems (1)–(3) are reformed in (e_1, e_2, e_3) coordinates as follows:

$$\dot{e}_1(t) = -p_1\tanh(\lambda e_1(t)), \quad (23)$$

$$\dot{e}_2(t) = -p_2\tanh(\lambda e_2(t)), \quad (24)$$

$$\dot{e}_3(t) = f_3(e_1 + x_d, e_2 + \alpha_1, e_3 + \alpha_2) + g_3(e_1 + x_d, e_2 + \alpha_1, e_3 + \alpha_2)u - \dot{\alpha}_2. \quad (25)$$

Noting that the functions f_1, f_2 and α_1, α_2 are only functions of states and command. Thus, the term $\dot{\alpha}_2$ can be calculated and represented explicitly in variables of $x_1, x_2, x_3, x_d, \dot{x}_d, \ddot{x}_d, \dddot{x}_d, p_1, p_2,$ and λ.

As a similar approach in Step 2, a real nonlinear feedback control, called backstepping sliding mode control (BSMC) $u = K(x_1, x_2, x_3, x_d, \dot{x}_d, \ddot{x}_d, p_1, p_2, p_3)$ in (7), and a CLF $L_3(e_1(t), e_2(t), e_3(t))$ are selected to ensure that systems (26)–(28) are stabilized at origin $(0, 0, 0)$, i.e.,

$$L_3(e_1(t), e_2(t), e_3(t)) = L_2(e_1(t), e_2(t)) + \frac{1}{2}e_3(t)^2. \quad (26)$$

By taking derivative of equation (26) in consideration with equations (15), (23), (24), and (25), one gets

$$\dot{L}_3 = -w_2 + e_3(t)\{f_3(e_1 + x_d, e_2 + \alpha_1, e_3 + \alpha_2) + g_3(e_1 + x_d, e_2 + \alpha_1, e_3 + \alpha_2)u - \dot{\alpha}_2\}. \quad (27)$$

With the given assumption that the function $g_3(x_1, x_2, x_3)$ can be inverse, after some manipulations and return of original variables, a BSMC can be achieved as follows:

$$-p_3\tanh(\lambda e_3(t)) = f_3(e_1 + x_d, e_2 + \alpha_1, e_3 + \alpha_2) + g_3(e_1 + x_d, e_2 + \alpha_1, e_3 + \alpha_2)u - \dot{\alpha}_2,$$
$$u := K = g_3^{-1}(x_1, x_2, x_3)\{-p_3\tanh(\lambda e_3(t)) - f_3(x_1, x_2) + \dot{\alpha}_2\}. \quad (28)$$

Substituting equation (28) into equation (27) results in

$$\dot{L}_3 = -p_1 e_1(t)\tanh(\lambda e_1(t)) - p_2 e_2(t)\tanh(\lambda e_2(t)) - p_3 e_3(t)\tanh(\lambda e_3(t)), := -w_3(e_1(t), e_2(t), e_3(t)) < 0 \forall e_1(t), e_2(t), e_3(t) \neq 0. \quad (29)$$

Note that $w_3 = p_1 e_1(t)\tanh(\lambda e_1(t)) + p_2 e_2(t)\tanh(\lambda e_2(t)) + p_3 e_3(t)\tanh(\lambda e_3(t))$ is a positive definitive function. Thus, $\dot{L}_3(e_1(t), e_2(t), e_3(t))$ is a negative definitive function. This again ensures that the tracking error e_3 tends to origin.

Substituting (28) into (25), systems (1)–(3) in a new coordinate e_1, e_2, e_3 are rewritten as follows:

$$\dot{e}_1(t) = -p_1\tanh(\lambda e_1(t)), \quad (30)$$

$$\dot{e}_2(t) = -p_2\tanh(\lambda e_2(t)), \quad (31)$$

$$\dot{e}_3(t) = -p_3\tanh(\lambda e_3(t)), \quad (32)$$

where $p_1, p_2, p_3,$ and λ are the strict positive values.

Thus, there exists state transformations (4)–(6), virtual feedbacks (14) and (21), and real control law (28) such that systems (1)–(3) can be transformed into systems (8)–(10) or systems (30)–(32).

With the achieved control law in (28), substituting this control law into systems (1)–(3) results in a closed-loop system that is used to implement numerical simulation with different commands and initial conditions.

Remark 1. With positive values of $p_1, p_2, p_3,$ and λ, the solutions $e_1(t), e_2(t),$ and $e_3(t)$ of systems (30)–(32) are stabilized at origin $(0, 0, 0)$ at a certain time. This means that the BSMC will enforce the outputs $y = h(x) = x_1$ to have a well-tracking command x_d.

Remark 2. It is observed that the tracking errors $e_1(t), e_2(t),$ and $e_3(t)$ play a similar role as "sliding surfaces" in sliding mode control and the smooth switch function $\tanh(\lambda e_2) \approx \tanh(\lambda[x_2 + p_1(x_1 - x_d) + \cdots])$ plays a "similar" role as switch function $\text{sign}(\cdot)$ of the sliding surface in traditional SMC. This term will ensure the robustness of the proposed method as system parameter errors or external disturbance is present in the system.

Remark 3. If $f_1 = 0; g_1 = 1, f_2 = 0; g_2 = 1, f_3 = f; g_3 = 1;$ and $\tanh(\lambda e)$: $= e$, then the term $e_2 = x_2 - \alpha_1 = x_2 - \dot{x}_d + p_1(x_1 - x_d)$ is defined exactly as a sliding surface in the

traditional SMC [14] and the term $-p\tanh(e_2)$ is similar to the corrective input $-K\text{sign}(\sigma)$ in [14].

Remark 4. Noting that the hyperbolic tangent function $\tanh(\lambda\sigma)$ with a large value λ will reach to the discontinuous sign function $\text{sign}(\cdot)$. Thus, a very large value of λ might lead to a chattering problem. A suitable parameter of λ must be traded off for a good performance.

Remark 5. From equations (8)–(10), it is clear that the convergence speed of the proposed control algorithm will follow the exponential rule with gains p_1, p_2, and p_3. The greater the gains are, the faster the convergence rate is. Besides, the convergence speed of the proposed control algorithm also depends on the function $\tanh(e)$. If you would like to gain a faster response, you can increase λ, but a trade-off between λ and chattering issue must be considered for good performance.

3. Flight-Path Angle Control of F-16 Aircraft Model

In this section, the lower-triangular model of nonlinear longitudinal dynamics is introduced and explained for design suitability. An explicit BSMC law is presented by using the proposed theory in Section 2. Then, a numerical demonstration of flight-path angle control of the F-16 aircraft simulation model is implemented to show the advances, robustness, and applicability of the proposed method to flight dynamic systems as compared to the existing methods.

3.1. Problem Formulation. Consider longitudinal dynamics of the aircraft flight system as shown in Figure 1.

Assumptions on aerodynamic forces [10] and use of the relationship $\alpha = \theta - \gamma$ are applied to transform an original longitudinal motion into the lower-triangular systems (1)–(3):

$$\dot{\gamma} = -g_p \cos\gamma + \hat{L}_0 - \hat{L}_\alpha \gamma + \hat{L}_\alpha \theta, \tag{33}$$

$$\dot{\theta} = q, \tag{34}$$

$$\dot{q} = \hat{M}_0 + \hat{M}_\alpha(\theta - \gamma) + \hat{M}_q q + \hat{M}_{\delta_E}\delta_E, \tag{35}$$

where $g_p = (g/V_T)$, $\hat{L}_0 = (L_0/mV_T)$, $\hat{L}_\alpha = (L_\alpha/mV_T)$, $\hat{M}_0 = (M_0/I_y)$, $\hat{M}_\alpha = (M_\alpha/I_y)$, $\hat{M}_q = (M_q/I_y)$, and $\hat{M}_{\delta_E} = (M_{\delta_E}/I_y)$. Variables and parameters appearing include V_T: aircraft velocity, m: total mass of the aircraft, α: angle of attack, γ: flight-path angle, θ: pitch angle, q: pitch rate, δ_E: pitch control (elevator or horizontal vane), I_y: inertial moment about the y axis of the aircraft, g: gravity, $\hat{L}_0$: effective lift contribution from sources other than α, $\hat{L}_\alpha$: effective lift curve slope for α, $\hat{M}_0$: effective moment contributions from sources other than α, q, δ_E, $\hat{M}_\alpha$ and $\hat{M}_q$: effective moment contributions from sources α, q, and $\hat{M}_{\delta_E}$: effective pitch curve slope for δ_E.

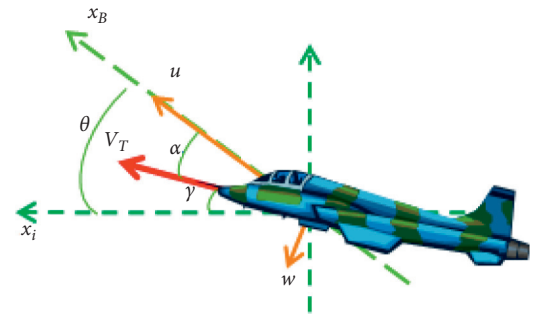

Figure 1: Model of longitudinal motion of the aircraft.

The objective is to design a backstepping sliding mode control law for the lower-triangular flight dynamics ((33)–(35) such that the flight-path angle (γ) tracks the command (γ_{ref}) with asymptotic stability. The performance specifications of the system should achieve well-behaved command tracking with zero or small acceptable overshoot.

3.2. Derivation of Backstepping Sliding Mode Control Law. With state variables (γ, θ, q) and control input δ_E, systems (33)–(35) are exactly the ones in (1)–(3) with $f_1(\gamma) = -(g/V_T)\cos\gamma + \hat{L}_0 - \hat{L}_\alpha\gamma$, $f_2(\gamma,\theta) = 0$, $f_3(\gamma,\theta,q) = \hat{M}_0 + \hat{M}_\alpha(\theta-\gamma) + \hat{M}_q q$, $g_1(\gamma) = \hat{L}_\alpha$, $g_2(\gamma,\theta) = 1$, and $g_3(\gamma,\theta,q) = \hat{M}_{\delta_E}$. It is clear that $f_i(i = 1,2,3)$ and $g_i(i = 1,2,3)$ are satisfying conditions in Section 2.2. Thus, there is a direct application of Theorem 1 in Section 2 or state transformations and feedbacks as

$$e_1(t) = \gamma - \gamma_{\text{ref}}, \tag{36}$$

$$e_2(t) = \theta - \alpha_1, \tag{37}$$

where a virtual feedback α_1 in equation (37) is determined as in the following equation:

$$\alpha_1 = \frac{1}{\hat{L}_\alpha}\left\{-p_1\tanh\left[\lambda(\gamma - \gamma_{\text{ref}})\right] + g_p\cos(\gamma) - \hat{L}_0 + \hat{L}_\alpha\gamma\right\}, \tag{38}$$

$$e_3(t) = q - \alpha_2, \tag{39}$$

where virtual feedback α_2 in equation (39) is determined as in the following equations:

$$\alpha_2 = -p_2\tanh\left(\lambda(\theta - \alpha_1)\right) + \dot{\alpha}_1, \tag{40}$$

$$\dot{\alpha}_1 = \frac{1}{\hat{L}_\alpha}\left\{-p_1\left(\text{sech}^2\left[\lambda(\gamma - \gamma_{\text{ref}})\right]\lambda F_\gamma - g_p\sin(\gamma)F_\gamma + \hat{L}_\alpha F_\gamma\right)\right\}, \tag{41}$$

$$F_\gamma = -g_p\cos\gamma + \hat{L}_0 - \hat{L}_\alpha\gamma + \hat{L}_\alpha\theta. \tag{42}$$

In addition, a BSMC law for systems (33)–(35) can be achieved in the following equation:

$$\delta_E = \delta_{E_0} + \frac{\pi}{180}\frac{1}{\widehat{M}_{\delta_E}}\{-p_3\tanh(\lambda(q-\alpha_2)) - \widehat{M}_0 - \widehat{M}_\alpha(\theta-\gamma) - \widehat{M}_q q + \dot{\alpha}_2\}, \tag{43}$$

where α_2 is determined in (40) and $\dot{\alpha}_2$ is determined in equations (44)–(46). The achieved BSMC law in equation (43) is used for further numerical study in the next section.

$$\dot{\alpha}_2 = -p_2\lambda(q-\dot{\alpha}_1)\mathrm{sech}^2(\lambda(\theta-\alpha_1)) + \ddot{\alpha}_1, \tag{44}$$

$$\ddot{\alpha}_1 = \frac{1}{\widehat{L}_\alpha}\{-p_1\mathrm{sech}^2(\lambda(\theta-\alpha_1))\lambda\dot{F}_\gamma - 2p_1\tanh(\lambda(\theta-\alpha_1)) \cdot \mathrm{sech}^2(\lambda(\theta-\alpha_1))\lambda^2F_\gamma^2 - g_p\sin(\gamma)\dot{F}_\gamma - g_p\cos(\gamma)F_\gamma^2 + \widehat{L}_\alpha\dot{F}_\gamma\}, \tag{45}$$

$$\dot{F}_\gamma = g_p\sin(\gamma)F_\gamma + \widehat{L}_\alpha(q-F_\gamma). \tag{46}$$

By substituting the BSMC in equation (43) into systems (33)–(35), a closed-loop system is achieved for numerical simulation. Figure 2 shows a control structure design for implementing a numerical simulation. A further explanation on this block diagram can be found in [13].

3.3. Numerical Simulation of Flight-Path Angle of F-16 Aircraft Model. For a further verification of advance and robustness of the proposed method, a full nonlinear F-16 aircraft model or a true model is used for numerical solutions. The aerodynamic data of the F-16 aircraft model are provided in [22] in which data are achieved from low-speed static and dynamic wind-tunnel tests at the NASA Langley Research Center. In this paper, the aircraft is assumed to be in level fight at Mach 0.5 and at an altitude of 25000 ft. Based on this assumption, control surfaces, aerodynamic coefficients, and other state variables at trim condition or level flight can be calculated for further simulation. For simplicity, those numbers are not listed in this paper. A closed-loop system with the BSMC law in equation (43) and a control structure in Figure 2 are used for four different flight-path command profiles away from the trim condition as follows.

Profile 1: a flight-path angle command of 10 (deg) is applied for 5 seconds; Profile 2: a multistep command is applied for the flight-path angle, in which γ_{ref} is put at 5 (deg) for the first 2.5 seconds, at 10 (deg) for the next 2.5 seconds, and then 5 (deg) in 5 seconds; Profile 3: a similar multistep command as in Profile 2 is applied for flight-path angle, but aircraft speed is varied from 600 ft/s to 500 ft/s during the simulation time; Profile 4: a doublet-step command is applied for flight-path angle for 10 seconds with change of aircraft center in which $\overline{x}_{\mathrm{cm}} = 0.3$ is used in control design, but $\overline{x}_{\mathrm{cm}} = 0.35$ will be used for this case for testing robustness. In the simulation, optimal positive gains of the BSMC in (43) $p_1 = 2.134$; $p_2 = 2.213$; $p_3 = 2.432$ are determined from the design model by using the modified genetic algorithm (MGA) [23]. The value $\lambda = 3$ is selected by the try and error technique to have a good performance. Numerical results are simulated both within and without the presence of disturbances. Also, numerical results from the BSMC-based method will be compared to the integrator-backstepping control (IBSC) method [13].

3.3.1. Profile 1: Single-Step Command of Flight-Path Angle. Solid line and dash line in Figure 3 show the time response of flight-path angle of the IBSC-based control and BSMC-based control methods, respectively. Both methods can provide a well-tracking command. Results show that the settling time $t_s = 2$ seconds of BSMC is shorter than that of the IBSC of $t_s = 3.5$ seconds. This has been predicted in [13] due to an introduction of an integrator of the tracking error. This is a limitation of the IBSC-based control system for a high-performance aircraft and is improved by the proposed BSMC-based method. Another advance of the proposed method is that control parameters are reduced from 4 (c_0, c_1, c_2, c_3)[13] to 3 (p_1, p_2, p_3). This will make MGA more robust as searching for optimal control parameters. Solid line and dash line in Figure 4 show the time response of the elevator surface of the IBSC-based control and BSMC-based control methods, respectively. Results indicate that the control signal from IBSC is saturated at an initial period, and this is a reason why there is a decrease in slope for rising time of time response after that. In a similar input signal of the BSMC, a saturation occurs at $t = 1.5$ seconds and leads to a decrease in magnitude of flight-path angle after that. However, saturation occurs in a short time, and thus the command tracking achieves quickly in this case. Also, results in Figures 3 and 4 indicate there is no chattering problem in the proposed control method. This is also an advance as compared to a traditional sliding mode control method [14].

3.3.2. Profile 2: Multistep Command of Flight-Path Angle. Figure 5 shows time response of flight-path angle with multistep command. The dot-dash line is the flight-path angle command, the dash line is associated with the IBSC-based control method, and the solid line is associated with the BSMC-based control methods. Results indicate the IBSC method results in a poor and less robust performance for a

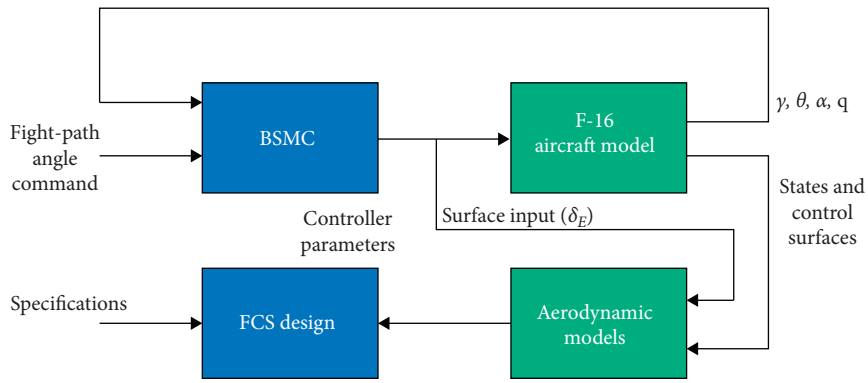

Figure 2: Block diagram of control architecture design.

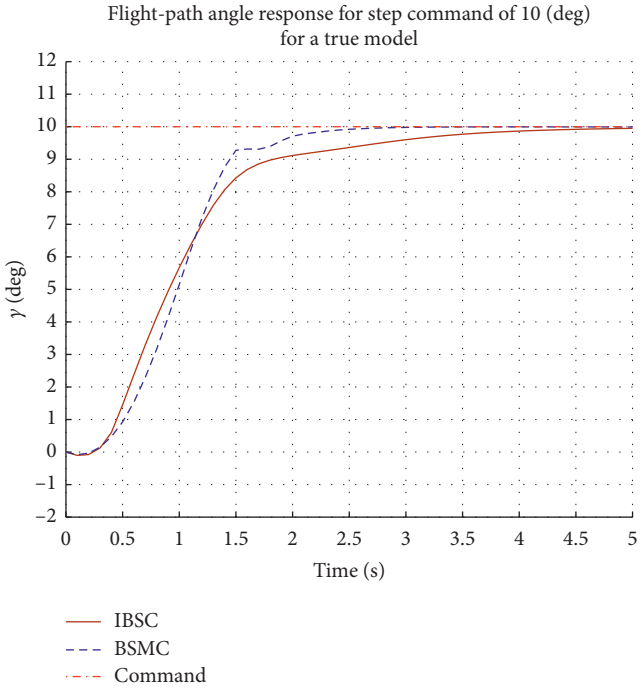

Figure 3: Time response of flight-path angle with step command 10 (deg).

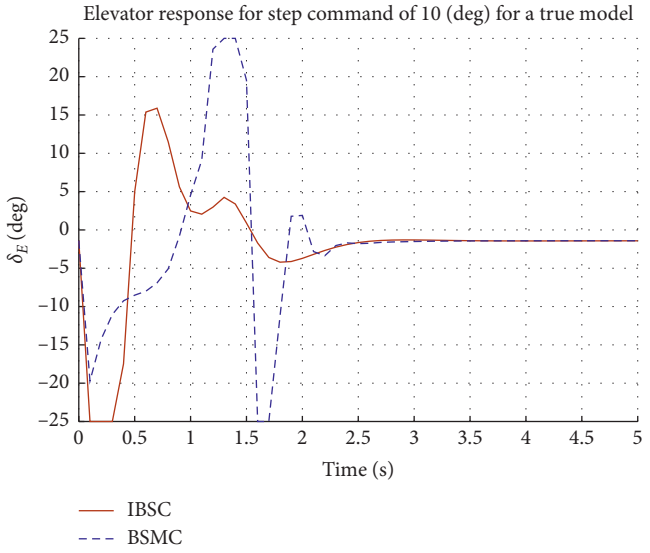

Figure 4: Time response of elevator surface with step command 10 (deg).

short period of time, but the BSMC can provide a much better performance than that of the IBSC. Solid line and dash line in Figure 6 show the time response of the elevator surface of the IBSC-based control and BSMC-based control methods, respectively. In order to meet demand of a given performance specification, the control signal of the IBSC tends to generate a high magnitude in the negative side, but the behavior of the BSMC is relatively different. We can see that BSMC-based response of the elevator surface is more effective and suitable to the practical observation. This is predicted in Section 1, in which a suitable control gain might not able to adapt with the change in internal dynamics of the system.

3.3.3. Profile 3: Multistep Command of Flight-Path Angle with a Varying Speed of Aircraft. In order to verify the robust performance, a multistep command is applied for flight-path angle with a change in aircraft speed that is varied from 600 ft/sec to 500 ft/sec during the 10 seconds in simulation. In this simulation condition, dash line in Figure 7 indicates the BSMC control method which can provide a good tracking for a short period. On the other hand, solid line in Figure 7 indicates the IBSC control method which can provide a good tracking for a phugoid (or longer) period of the aircraft system. This is due to a considerable effect of the integrator to improve the tracking as time increases.

3.3.4. Profile 4: Doublet Command of Flight-Path Angle with a Variation of Aircraft Mass Center, $\overline{x}_{cm}$. In previous simulations, the mass center of the aircraft $\overline{x}_{\text{cm}} = 0.3$ is used for designing control parameters and in-flight simulation. In reality, the mass center might be changed due to the unload of cargoes or other equipment. Thus, a variation of this parameter can further verify reliability and robustness of the control methods. In this simulation condition, the mass center is assigned to be $\overline{x}_{\text{cm}} = 0.35$. Figure 8 shows time response of flight-path angle for a doublet command in the presence of mass center change. The dash line again

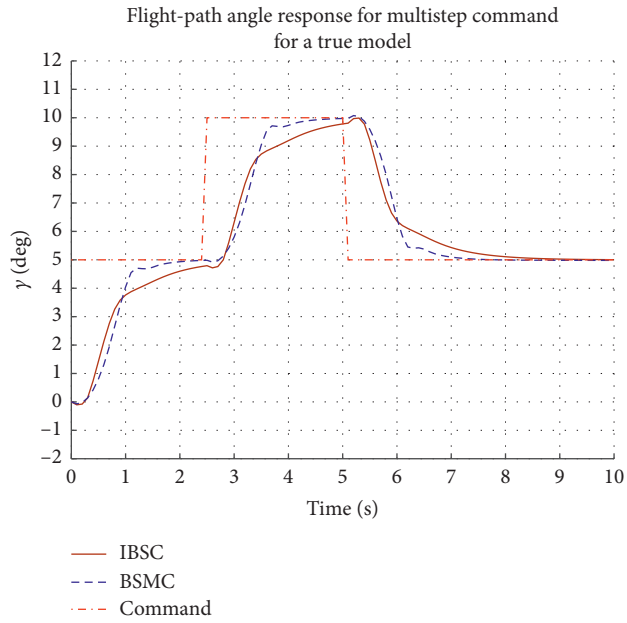

Figure 5: Time response of flight-path angle with multiple step command.

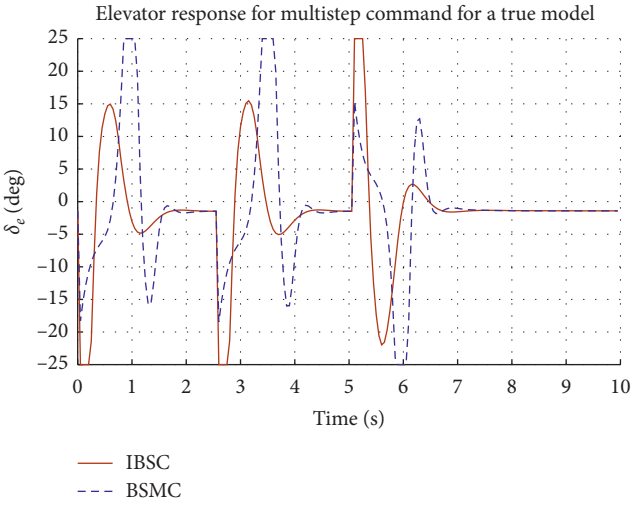

Figure 6: Time response of the elevator surface with multiple step command of flight-path angle.

indicates that the BSMC results in a well-behaved command tracking and fast response with no or small acceptable overshoot.

4. Conclusion and Future Work

A robust and fast-response control system plays an important role in designing and developing a high-performance aircraft. This requires an advanced control design method for nonlinear flight dynamic systems. In this paper, a hybrid robust control design method is proposed for a third-order SISO lower-triangular model of nonlinear dynamic systems in the presence of disturbances. Then, the application of flight-path angle control corresponding to the longitudinal dynamics of

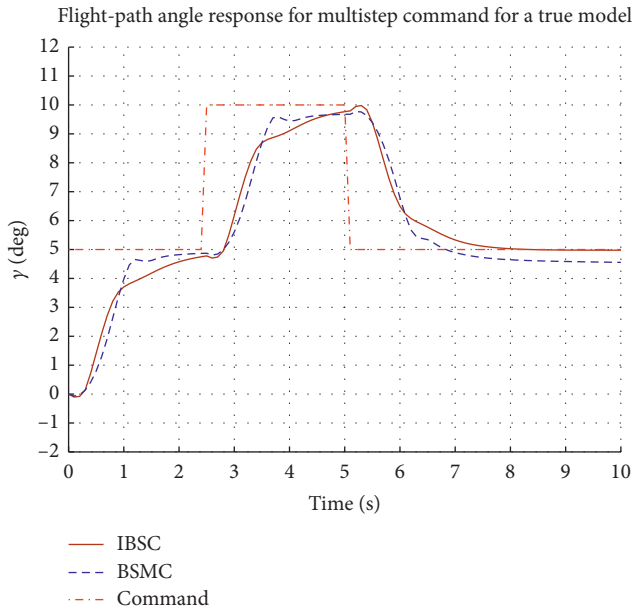

Figure 7: Time response of flight-path angle in time-varying change of speed of the aircraft.

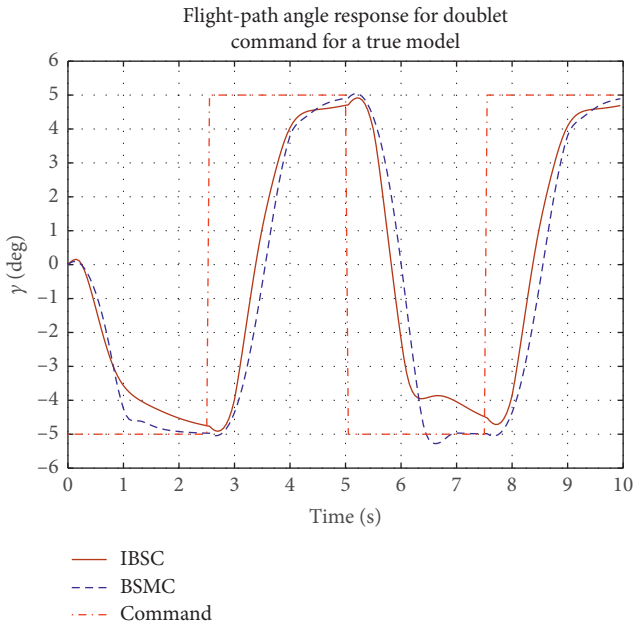

Figure 8: Time response of flight-path angle in doublet-step command in variation of aircraft mass center.

a high-performance F-16 aircraft simulation model is implemented. The contributions of this paper are as follows:

(i) The proposed control method also provides a diversity of nonlinear control design tools to a specific class of nonlinear dynamic systems and has a high potential for other application in engineering systems.

(ii) A novel controller synthesis method, called backstepping sliding mode control (BSMC) law, is presented systematically for a third-order SISO lower-triangular system. The BSMC-based control method results in an advanced control system which can provide an excellent and robust performance with asymptotic stability in the presence of uncertainties and eliminate completely a chattering phenomenon that is a drawback of a traditional SMC.

(iii) A successful application is implemented for the nonlinear flight dynamic system. In particular, a BSMC for flight-path angle control of the F-16 aircraft model is derived. Then, a control algorithm is provided for in-flight closed-loop simulation. Numerical results indicate the BSMC can provide a robust performance and stability with different flight profiles and presence of external disturbances.

With the development of high-performance digital computer, robust nonlinear control methods, and computational software, the nonlinear control system will result in a considerable role in improving accuracy, flexibility, and robustness in control systems.

The field of the research focuses only on a lower-triangular model of nonlinear dynamic systems. Therefore, an extended version of a generalized form of the nonlinear dynamic system can prove a better solution. Also, application is limited in aircraft motion in longitudinal axis and simulation results neglect effectiveness of lateral dynamics of the aircraft. Thus, investigation of full nonlinear aircraft fight dynamics should be considered to validate further the proposed method. In addition, this proposed control method can be applied to other engineering systems.

Data Availability

Readers can access the data supporting the conclusions in case readers would like to repeat the results, and data can be requested by sending an e-mail to the corresponding author.

Conflicts of Interest

The authors declare that there are no conflicts of interest regarding the publication of this paper.

Acknowledgments

This work was supported by Vietnamese-German University.

References

[1] M. Krstic, P. V. Kokotovic, and I. Kanellakopoulos, *Nonlinear and Adaptive Control Design*, John Wiley & Sons, Hoboken, NJ, USA, 1st edition, 1995.

[2] S. H. Lane and R. F. Stengel, "Flight control design using nonlinear inverse dynamics," *Automatica*, vol. 24, no. 4, pp. 471–483, 1988.

[3] L. Sonneveldt, Q. P. Chu, and J. A. Mulder, "Nonlinear flight control design using constrained adaptive backstepping," *Journal of Guidance, Control, and Dynamics*, vol. 30, no. 2, pp. 322–336, 2007.

[4] J. Farrell, M. Sharma, and M. Polycarpou, "Backstepping-based flight control with adaptive function approximation," *Journal of Guidance, Control, and Dynamics*, vol. 28, no. 6, pp. 1089–1102, 2005.

[5] C. I. Marrison and R. F. Stengel, "Design of robust control systems for a hypersonic aircraft," *Journal of Guidance, Control, and Dynamics*, vol. 21, no. 1, pp. 58–63, 1998.

[6] Q. Wang and R. F. Stengel, "Robust nonlinear control of a hypersonic aircraft," *Journal of Guidance, Control, and Dynamics*, vol. 23, no. 4, pp. 577–585, 2000.

[7] Q. Wang and R. F. Stengel, "Robust nonlinear flight control of a high-performance aircraft," *IEEE Transactions on Control Systems Technology*, vol. 13, no. 1, pp. 15–26, 2005.

[8] F. Giri, A. Rabeh, and F. Ikhouane, "Backstepping adaptive control of time-varying plants," *Systems & Control Letters*, vol. 36, no. 4, pp. 245–252, 1999.

[9] K.-H. Choi, T. Tran, and D.-S. Kim, "Back-stepping controller based web tension control for roll-to-roll web printed electronics system," *Journal of Advanced Mechanical Design, Systems, and Manufacturing*, vol. 5, no. 1, pp. 7–21, 2011.

[10] T. T. Tran, "Feedback linearization and backstepping: An equivalence in control design of strict-feedback form," *IMA Journal of Mathematical Control and Information*, 2019.

[11] T. T. Tran and B. Newman, "Back-stepping based flight path angle control algorithm for longitudinal dynamics," in *Proceedings of the AIAA Guidance, Navigation, and Control Conference*, Minneapolis, MN, USA, 2012.

[12] T. T. Tran and O. R. Gonzalez, "Backstepping-based control methodology for aircraft roll dynamics," *Proceedings of the Institution of Mechanical Engineers, Part I: Journal of Systems and Control Engineering*, vol. 234, no. 4, pp. 566–574, 2020.

[13] T. T. Tran and B. Newman, "Integrator-backstepping control design for nonlinear flight system dynamics," in *Proceedings of the AIAA Guidance, Navigation, and Control Conference*, Kissimmee, FL, USA, January 2015.

[14] J.-J. E. Slotine, "Sliding controller design for non-linear systems," *International Journal of Control*, vol. 40, no. 2, pp. 421–434, 1984.

[15] H. Xu, M. D. Mirmirani, and P. A. Ioannou, "Adaptive sliding mode control design for a hypersonic flight vehicle," *Journal of Guidance, Control, and Dynamics*, vol. 27, no. 5, pp. 829–838, 2004.

[16] B. Wu, D. Wang, and E. K. Poh, "Decentralized sliding-mode control for attitude synchronization in spacecraft formation," *International Journal of Robust and Nonlinear Control*, vol. 23, no. 11, pp. 1183–1197, 2013.

[17] S. Seshagiri and E. Promtun, "Sliding mode control of F-16 longitudinal dynamics," in *Proceedings of the American Control Conference*, pp. 1770–1775, Seattle, WA, USA, June 2008.

[18] H. Alwi, C. Edwards, and M. T. Hamayun, "Nonlinear integral sliding mode fault tolerant longitudinal aircraft control," in *Proceedings of the IEEE International Conference on Control Applications (CCA)*, pp. 970–975, Denver, CO, USA, September 2011.

[19] E. Promtun and S. Seshagiri, "Sliding mode control of pitch-rate of an F-16 aircraft," *IFAC Proceedings Volumes*, vol. 41, no. 2, pp. 1099–1104, 2008.

[20] Y. Wang, Y. Xia, H. Li, and P. Zhou, "A new integral sliding mode design method for nonlinear stochastic systems," *Automatica*, vol. 90, pp. 304–309, 2018.

[21] J. Fei and Z. Feng, "Fractional-order finite-time super-twisting sliding mode control of micro gyroscope based on double-loop fuzzy neural network," *IEEE Transactions on Systems, Man, and Cybernetics: Systems*, pp. 1–15, 2020.

[22] L. T. Nguyen, M. E. Ogburn, W. P. Gilbert, K. S. Kibler, P. W. Brown, and P. L. Deal, "Simulator study of stall/post-stall characteristics of a fighter airplane with relaxed longitudinal static stability," Techical Report L-12854, NASA, Washington, DC, USA, 1979.

[23] K. H. Choi, T. T. Thanh, Y. B. Su, and D. S. Kim, "An new approach for intelligent control system design using the modified genetic algorithm," *International Journal of Intelligent Systems Technologies and Applications*, vol. 9, no. 3/4, pp. 300–315, 2010.

Hindawi
Mathematical Problems in Engineering
Volume 2020, Article ID 9084369, 11 pages
https://doi.org/10.1155/2020/9084369

Research Article

Grasping Control of a UVMS Based on Fusion Visual Image Enhancement

Wei Chen,[1,2] **Lei Wang**,[1] **Yuhang Zhang**,[1] **Xu Li**,[1] **and Weiran Wang**[1]

[1]*School of Electronics and Information, Jiangsu University of Science and Technology, Zhenjiang 212003, China*
[2]*School of Automation, Southeast University, Nanjing 210096, China*

Correspondence should be addressed to Wei Chen; cw1@just.edu.cn

Received 25 May 2020; Revised 21 July 2020; Accepted 17 August 2020; Published 1 September 2020

Guest Editor: Raúl Villafuerte-Segura

The Underwater Vehicle Manipulator System (UVMS) is an essential equipment for underwater operations. However, it is difficult to control due to the constrained problems of weak illumination, multidisturbance, and large inertia in the underwater environment. After the UVMS mathematical model based on water flow disturbance is established, fusion image enhancement algorithm based on Retinex theory is proposed to achieve fine perception of the target. The control method based on redundant resolution algorithm is adopted to establish the anti-interference controller of the manipulator, which can compensate the internal and external uncertain interference. Finally, stable underwater operation is realized. The target ranging method is used to solve the angle of each joint of the manipulator to complete the tracking and grasping of the target. Underwater experiments show that the algorithm can improve the clarity of underwater images, ensure the accuracy of robot capture, and optimize the UVMS control performance.

1. Introduction

The Underwater Vehicle Manipulator System (UVMS) is an essential equipment for underwater operations, and it plays an important role in national defense construction, underwater engineering operations, underwater rescue, and marine exploration and development. At present, the UVMS has evolved from information-based operation to autonomous operation, which requires a precise control system. Underwater target detection and recognition are important prerequisites for the underwater operation of UVMS manipulators. The popular method is acoustic and optical perception. Currently, underwater optical sensing is mainly used, but underwater optical sensing faces many unfavorable factors such as the scattering and absorption of light by water, low contrast, and optical distortion. This makes the UVMS unable to achieve reliable identification of complex underwater environments. Therefore, enhancing the fine recognition capability of UVMS autonomous underwater targets is the basis for achieving accurate target information determination and manipulator capturing.

Underwater imaging technology is widely used in engineering applications and scientific experiments, such as underwater tracking and positioning and exploitation of marine resources [1]. The underwater target object is affected by water during the imaging process, and the light is partially absorbed, reflected, and scattered. The image is affected by the distance between the camera and the target object, and the intensity of the light decreases sharply as the distance increases [2]. Affected by this factor, the contrast of underwater images is reduced, and the sharpness of the target object in the image is poor. It is not conducive to further processing of underwater video images [3].

In the recent years, domestic and foreign scholars have studied a variety of underwater image enhancement methods, such as the adaptive histogram equalization based on contrast limitation, histogram method based on Rayleigh distribution stretching [4], transformation probability method [5], multiscale fusion method [6], image depth of field estimation method [7], optical property estimation method [8], and so on. These methods belong to the spatial domain enhancement method, which can remove the color

cast effect and increase the difference between the original similar pixels, thereby improving the contrast and sharpness of the image. But, the disadvantage of these methods is that it is easy to produce insufficient or excessive enhancement, thereby forming a false edge or texture. In addition, underwater image enhancement methods based on color constancy theory have also been applied, such as Retinex algorithm [9] and nonlinear image enhancement algorithm based on Retinex algorithm because Retinex algorithm itself has the function of constant color, which can significantly improve the local contrast of image enhancement. The algorithm can effectively improve the details and color information of the dark area of the artificial light source image; this is unmatched by other current image enhancement algorithms, so it is particularly suitable for UVMS. UVMS fusion image enhancement algorithm based on bilateral filtering and retinal algorithm is proposed in this paper. Firstly, the initial image is bilaterally filtered to obtain a coarse image. Secondly, the initial image is divided by the coarse image to obtain a detailed image. Thirdly, the rough image is improved by Retinex enhancement algorithm. Finally, the processed rough image and details are processed. Then, the image is fused to get a clear image.

The complexity and unpredictability of the real underwater environment make the design of UVMS precise controllers more difficult. Domestic and foreign scholars have also proposed a variety of control strategies. Londhe [10] used fuzzy logic control such as PID as the feedback part in order to enhance the overall closed-loop stability of the UVMS. Qiao and Zhang [11] adopted an adaptive nonsingular integral terminal sliding mode control. It predicts dynamic uncertainty and time-varying external interference to achieve trajectory tracking of autonomous underwater vehicles. Li [12] used adaptive antijamming control. Through real-time estimation and compensation of disturbance forces, higher control accuracy is achieved. Dai [13–15] presents an indirect adaptive control scheme which consists of three parts: an extended Kalman filter (EKF) estimation compensative system, a model-based computed torque controller (CTC), and an H∞ robust compensative tracking controller. Yan et al. [16] proposed a new trajectory tracking scheme for the constrained nonlinear UVMS. Zhan and Jin [17] adopted redundant resolution algorithm to predict local state dynamics as a fuzzy average of global state dynamics, and this is a discrete-time optimal control method. The response speed of the system disturbance adjustment is improved, and the anti-interference optimization of the control is realized. The dynamic stability of the system is improved.

Chen et al. [18] described the visual servo control method of the manipulator on land. With reference to this idea, the control process of the underwater manipulator is as follows.

First, stereo calibration of the underwater camera is performed, then underwater image enhancement technology is used to improve the quality of the original image, then hand-eye calibration algorithm is used to calculate the three-dimensional coordinates of the underwater target in the robot coordinates, and the robot is solved by inverse kinematics rotation angle of each joint. Finally, the servo motor is controlled to drive the joints of the manipulator to move, and the visual servo control experiment of the underwater manipulator is completed.

Retinex fusion visual enhancement algorithm effectively improves the details and color information of the dark area of the artificial light source image. This is unmatched by other current image enhancement algorithms

The redundant resolution can avoid the self-motion of the redundant system. At the same time, local key parameters are used to predict the characteristics of global parameters, which reduce the amount of control calculations compared to other control algorithms and improve the response speed of system disturbance adjustment.

This paper studies optimization algorithm for the abovementioned two points of image enhancement and manipulator control grabbing. Firstly, this paper uses Retinex theory to establish an image fusion enhancement algorithm to improve underwater image capture and analysis capabilities. From the perspective of fluid mechanics, various complex disturbance mechanisms are analyzed, such as complex underwater flow disturbance, uncertain disturbance of a system, and unstructured random disturbance. Secondly, a mathematical model of the UVMS in the actual water flow environment is also established. The redundant resolution algorithm is used to optimize the control performance of the manipulator and establish a performance index closer to the actual. The UVMS is used by our team to carry out sea cucumber model grabbing experiments, and it obtains the real-time angle of servo feedback of each joint of the UVMS. The analysis data shows that the UVMS manipulator accurately tracks the target trajectory while maintaining the stability of the UVMS, realizing the task of UVMS underwater operation under certain interference. This indirectly verifies the superiority of image fusion algorithms in underwater imaging and detail capture. Figure 1 is an UVMS control research roadmap based on fusion visual image enhancement. It is mainly divided into two parts: fusion image enhancement and redundancy resolution algorithm. The fusion image enhancement algorithm can get a clear image to observe the underwater environment, and the redundant resolution algorithm can get a stable dynamic system. Only combining fusion image enhancement algorithm and redundant resolution algorithm can be good for underwater target grabbing.

2. Establishment of the UVMS Mathematical Model Based on Disturbance

The UVMS movement mainly involves three coordinate systems: the earth coordinate system, the body coordinate system, and the manipulator coordinate system [19], as shown in Figure 2.

Set $I(x, y, z)$ as the geodetic coordinate system (configuration space), $B(x_b, y_b, z_b)$ as the UVMS body coordinate system, and $E(x_t, y_t, z_t)$ as the end effector coordinate system (task space). Vehicle dynamics are usually described by two coordinates: one is the fixed coordinate system and

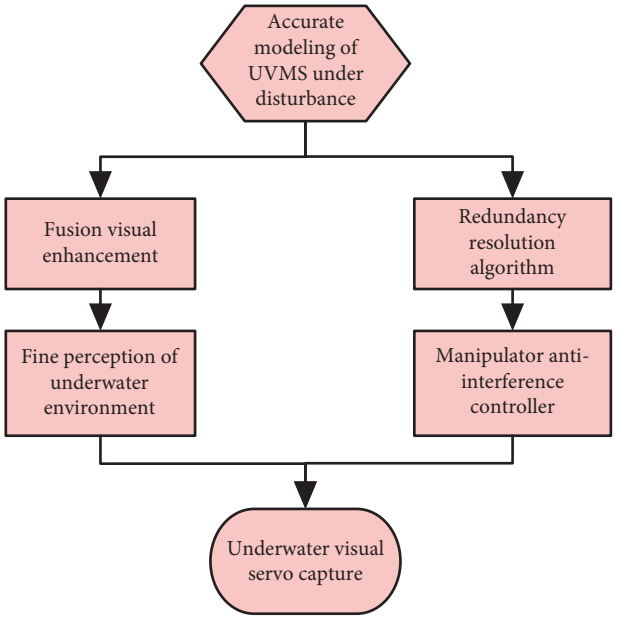

Figure 1: UVMS control research roadmap based on fusion visual image enhancement.

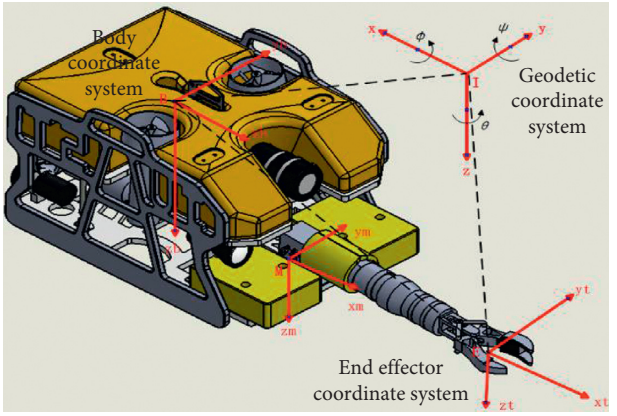

Figure 2: Coordinates of the underwater vehicle-manipulator system.

the other is the inertial frame of reference. The kinematic equation of the UVMS body can be expressed as follows:

$$\mathbf{M}\dot{\nu} + \mathbf{C}(\mathbf{v})\mathbf{v} + \mathbf{D}(\mathbf{v})\mathbf{v} + \mathbf{g}(\Theta) = \boldsymbol{\tau}_{\mathbf{ve}}, \tag{1}$$

$\mathbf{M}$ is the inertial force and system moment vector. $\mathbf{C}(\mathbf{v})$ is the Coriolis vector and centripetal effect, and $\mathbf{D}(\mathbf{v})$ is the hydrodynamic damping force vector. $\mathbf{g}(\Theta)$ is a recovery (gravity and buoyancy) vector. $\tau_{\mathbf{ve}}$ is the moment input vector of thruster and control plane forces.

$\mathbf{v} = [\ \mathbf{u}\ \mathbf{v}\ \mathbf{w}\ \mathbf{p}\ \mathbf{q}\ \mathbf{r}\ ]^{\mathbf{T}}$ is the linear velocity and angular velocity vector of the UVMS body. $\Theta = [\ \varphi\ \theta\ \psi\ ]^{\mathbf{T}}$ is a vector of Euler angles. The suffix **ve** indicates that it corresponds to the vehicle.

The relationship between the attitude of the underwater manipulator and the system configuration is as shown in (2):

$$\boldsymbol{\mu} = \mathbf{f}(\mathbf{q}), \tag{2}$$

where $\mu = [\ \mathbf{x_t}\ \mathbf{y_t}\ \mathbf{z_t}\ ]^{\mathbf{T}}$ is a vector containing the position and orientation of the underwater manipulator relative to the earth's fixed frame. $\mathbf{f}(\mathbf{q})$ represents the forward kinematics vector. Derivation of the abovementioned formula:

$$\dot{\mu} = \mathbf{J}(\mathbf{q})\dot{q}, \tag{3}$$

where $\mathbf{J}(\mathbf{q})$ is the Jacobian matrix which constitutes the speed mapping relationship between the configuration space and task space. Equation (1) is transformed into the dynamic equation of the manipulator in the task space:

$$\mathbf{M}_{\mu}\ddot{\mu} + \mathbf{C}_{\mu}\dot{\mu} + \mathbf{D}_{\mu}\dot{\mu} + \mathbf{G}_{\mu} + \mathbf{F}_{\mu} = \boldsymbol{\tau}_{\mathbf{in}}, \tag{4}$$

where $\mathbf{M}_{\mu}$ is the inertial matrix of the manipulator in the task space. $\mathbf{C}_{\mu}$ is the Coriolis force vector and centripetal force matrix of the manipulator. $\mathbf{D}_{\mu}$ is the vector of the hydrodynamic damping force of the manipulator. $\mathbf{G}_{\mu}$ is the vector of recovery effect of the manipulator. $\mathbf{F}_{\mu}$ is the vector of dynamic coupling of the manipulator. $\tau_{\mathbf{in}}$ is the vector that controls the input.

The dynamic model formulation of the underwater manipulator is established using the recursive Newton–Eulerian. The equation of motion dynamics of an underwater manipulator can be expressed as follows:

$$\mathbf{M}(q)\ddot{\mathbf{q}} + \mathbf{C}(q, \dot{\mathbf{q}}) + \mathbf{D}(q, \dot{\mathbf{q}}) + \mathbf{g}(q) + \mathbf{F}(q, \dot{\mathbf{q}}) = \boldsymbol{\tau} + \mathbf{d}, \tag{5}$$

$\mathbf{q} \in \mathbf{R}^{\mathbf{n}\times 1}$ is the vector of joint variables. d is an underwater disturbance vector.

Equation (5) is transformed into the dynamic equation of the underwater manipulator:

$$\mathbf{M}_{\mu}\ddot{\mu} + \mathbf{C}_{\mu}\dot{\mu} + \mathbf{D}_{\mu}\dot{\mu} + \mathbf{G}_{\mu} + \mathbf{F}_{\mu} = \boldsymbol{\tau}_{\mathbf{in}} + \boldsymbol{\tau}_{\mathbf{edis}}, \tag{6}$$

where $\tau_{\mathbf{edis}}$ is the external disturbance vector in the task space. For the water flow in the underwater environment, it can be regarded as the circulation system of the fluid in the horizontal and vertical directions. It is a process of slowly changing low frequency caused by changes in tidal wind, wind friction, and fluid density. External disturbance vector can be described as

$$\begin{aligned} \dot{\nu}_{\mathbf{c}} &= -\boldsymbol{\mu}\mathbf{v}_{\mathbf{c}} + \boldsymbol{\omega}, \\ \boldsymbol{\tau}_{\mathbf{edis}} &= \mathbf{C}_{\mathbf{A}}\mathbf{v}_{\mathbf{c}} + \mathbf{D}\mathbf{v}_{\mathbf{c}}, \end{aligned} \tag{7}$$

where $\mathbf{V_c} = [\ \mathbf{V_{cx}}\ \mathbf{V_{cy}}\ \mathbf{V_{cz}}\ 0\ 0\ 0\ ]$ is the current velocity vector. μ is a positive definite diagonal matrix. ω is a Gaussian white noise vector. Both $\mathbf{C_A}$ and $\mathbf{D}$ are constants. Taking into account the uncertainty of the parameters in the actual system, we add these factors to get

$$\begin{aligned} &(\mathbf{M}_{\mu} + \Delta\mathbf{M}_{\mu})\ddot{\mu} + (\mathbf{C}_{\mu} + \Delta\mathbf{C}_{\mu})\dot{\mu} + (\mathbf{D}_{\mu} + \Delta\mathbf{D}_{\mu})\dot{\mu} + (\mathbf{G}_{\mu} + \Delta\mathbf{G}_{\mu}) \\ &\quad + (\mathbf{F}_{\mu} + \Delta\mathbf{F}_{\mu}) = \boldsymbol{\tau}_{\mathbf{in}} + \boldsymbol{\tau}_{\mathbf{edis}}. \end{aligned} \tag{8}$$

Summarizing system uncertainty and external environmental interference as concentrated uncertainty [20], equation (9) is simplified to

$$\mathbf{M}_{\mu}\ddot{\mu} + \mathbf{C}_{\mu}\dot{\mu} + \mathbf{D}_{\mu}\dot{\mu} + \mathbf{G}_{\mu} + \mathbf{F}_{\mu} = \boldsymbol{\tau}_{\mathbf{in}} + \boldsymbol{\tau}_{\mathbf{dis}}. \quad (9)$$

Subtracting the abovementioned two formulas, we get

$$\boldsymbol{\tau}_{\mathbf{dis}} = \boldsymbol{\tau}_{\mathbf{edis}} - \Delta\mathbf{M}_{\mu}\ddot{\mu} - \Delta\mathbf{C}_{\mu}\dot{\mu} - \Delta\mathbf{D}_{\mu}\dot{\mu} - \Delta\mathbf{G}_{\mu}\Delta\mathbf{F}_{\mu}. \quad (10)$$

3. UVMS Fusion Image Enhancement Method

The basic characteristics of underwater imaging are mainly expressed as follows:

(1) The gray effect: with the attenuation of light signals underwater, the imaging effect of underwater targets is affected by flocs and underwater low-light environment

(2) Low contrast: because of the scattering of light in the underwater environment, the image contrast of the target taken by the underwater camera is poor

(3) The distinction is greater

(4) The image effect is worse

Due to the water flow disturbance and the near-surface disturbance caused by the underwater environment of the UVMS, the natural light source is prone to generate spots in the disturbed seawater, causing uneven illumination of the feedback image. In the deep sea, the UVMS relies on artificial light sources to obtain images and videos, which exacerbates the problem of uneven image illumination. This causes the decrease in the observation range of the UVMS, which brings greater difficulties to subsequent underwater operations.

Aiming at the abovementioned problems, UVMS fusion image enhancement algorithm based on bilateral filtering and Retinex algorithm is proposed. Figure 3 is a flowchart of UVMS fusion visual image enhancement algorithm. Firstly, the initial image is bilaterally filtered to obtain a coarse image. Secondly, the initial image is divided by the coarse image to obtain a detailed image. Thirdly, the rough image is improved by Retinex enhancement algorithm. Finally, the processed rough image and details are processed. The improved rough image and detailed image are fused to obtain the desired image.

The physical basis of the algorithm is that, in the process of observing the object to the final image, the visual system automatically removes the influence of illumination factors such as the intensity of the light source and the uneven illumination and only retains the properties of the object itself.

3.1. Bilateral Filtering. Figure 4 shows two typical underwater original images. As can be seen from the figure, the underwater image shows the characteristics of low contrast and poor clarity.

The bilateral filtering algorithm proves that using bilateral filtering to process images provides better edge retention than Gaussian filtering, effectively avoiding the occurrence of halo phenomenon. The bilateral filtering expression is as follows:

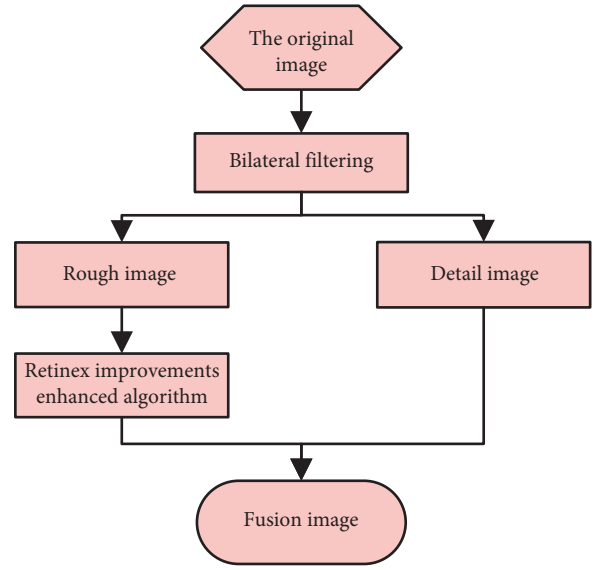

Figure 3: UVMS fusion image enhancement algorithm flow.

$$O(x, y) = \frac{\sum_{x_c, y_c} I(x_c, y_c) G(x, y, x_c, y)}{\sum_{x_c, y_c} G(x, y, x_c, y_c)}, \quad (11)$$

where $O(x, y)$ is the brightness of the output image at (x, y). $I(x_c, y_c)$ is the brightness of the input image at (x_c, y_c).

$$d^2(x, y) = (x - x_c)^2 + (y - y_c)^2. \quad (12)$$

In equation (12), $d^2(x, y)$ represents the square of the distance from each pixel to the center of the image (x_c, y_c).

$$p^2(x, y) = \left[f(x, y) - f(x_c - y_c)^2 \right], \quad (13)$$

In equation (13), $p^2(x, y)$ represents the square of the difference between the gray value $f(x, y)$ of each pixel and the center point $f(x_c, y_c)$.

The abovementioned two enhancement algorithms get two enhanced images, which are fused to enhance the image. The fusion formula is shown in follows:

$$R_i(x, y) = mR_{1i}(x, y) + (1 - m)R_{2i}(x, y), \quad i = R, G, B. \quad (14)$$

In (14), $R_i(x, y)$ is the values of R, G, and B of the merged image. $R_{1i}(x, y)$ is the R, G, and B values of the MSR multiscale Retinex- (MSR-) enhanced image. $R_{2i}(x, y)$ is the R, G, and B values of the enhanced image using bilateral filtering algorithm. m is the control coefficient and satisfies $0 < m < 1$.

3.2. Retinex-Improved Enhancement Algorithm. The rough image collected by the underwater camera is improved by Retinex enhancement algorithm.

Firstly, the input image is precorrected to reduce the dominant color. Secondly, the improved MSR algorithm is performed using the intensity channel to estimate the reflectance and illumination components. After that, the image is restored and the dynamics are compensated.

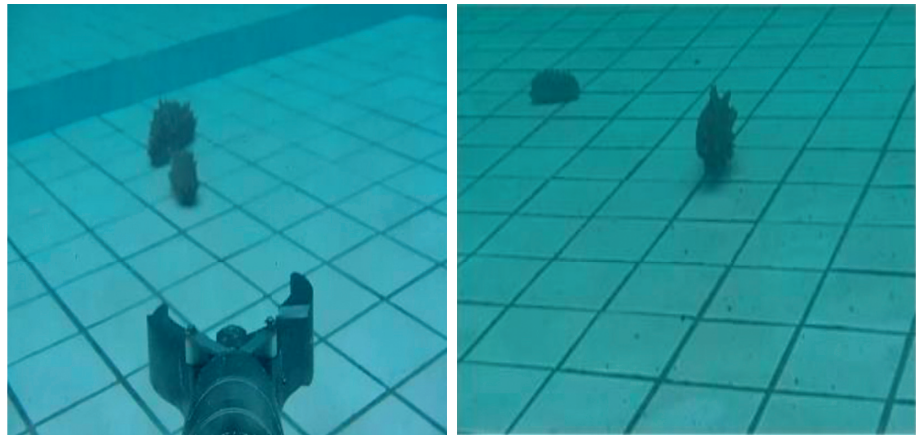

Figure 4: Underwater original images.

Finally, the color of the original image is alternately retained according to the requirements. Figure 5 is the Retinex-improved enhanced algorithm flow.

3.2.1. Color Precorrection. Since the density of water in seawater is much greater than that of air, water can absorb light energy. As the depth increases, the underwater image becomes darker and darker. The color will be unbalanced according to the decrease in the wavelength, and the underwater image will always be mainly green or blue. Therefore, color precorrection of underwater images is an indispensable step. Here, I_{mean} and I_{var} are introduced as the average and deviation values of the input image, and the maximum value $I_{\max}$ and the minimum value $I_{\min}$ of each channel can be obtained by

$$\begin{aligned} I(i)_{\max} &= I(i)_{\text{mean}} + \lambda\mu I(i)_{\text{var}}, \\ I(i)_{\min} &= I(i)_{\text{mean}} - \lambda\mu I(i)_{\text{var}}. \end{aligned} \tag{15}$$

In equation (14), $i \in \{R\ G\ B\}$,μ is the dynamics nominal, and λ is the color equalization scale.

The image after color precorrection can be expressed as follows:

$$I_{\text{cor}}(i) = \frac{I(i) - I(i)_{\min}}{I(i)\min_{\max} \times 255}. \tag{16}$$

3.2.2. MSR Algorithm with Intensity Channel. The color of an object observed by a person is not determined by the light intensity, but by the surface reflection ability of the object [21]. The image observed by the human eye can be expressed as a formula:

$$S(x, y) = L(x, y) \times R(x, y), \tag{17}$$

where $R(x, y)$ represents the reflected light image, which determines the intrinsic properties of the image. $L(x, y)$ represents the illuminance image. $S(x, y)$ represents the image obtained by the observer [22]. The reflection coefficient unique to an object is

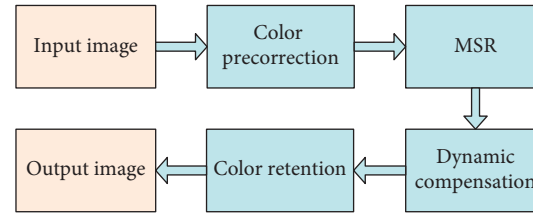

Figure 5: Retinex-improved enhancement algorithm flow.

$$R(x, y) = \frac{S(x, y)}{L(x, y)}. \tag{18}$$

Taking the logarithm of both sides at the same time, we can get

$$\log R(x, y) = \log S(x, y) - \log L(x, y). \tag{19}$$

The illumination component $L(x, y)$ of the image is removed from the original image, thereby obtaining the reflection component $R(x, y)$ of the image surface for the purpose of image enhancement.

Single-scale Retinex (SSR) is constructed by introducing a Gaussian surround function, but the SSR cannot provide dynamic range compression and color recovery at the same time [23]. The multiscale Retinex (MSR) compensates for the abovementioned shortcomings by weight superposition. The definition is as follows:

$$R(i)_{\text{MSR}} = \sum_{n=1}^{N} \omega_n \left(\log\left(S_{(i)}(x, y)\right) - \log\left(F(x, y, \sigma_n) \times S_{(i)}(x, y)\right) \right), \tag{20}$$

where N is the number of scales, ω_n is the weight of each scale, $\log(S^{(i)}(x, y)) - \log(F(x, y, \sigma_n) \times S^{(i)}(x, y))$ is the output image of the SSR, $\times$is the convolution operation, and $F(x, y, \sigma_n)$ is the Gaussian surround function for each scale. $i \in \{R\ G\ B\ S\}$, S is the intensity channel used to save the image color, and m is the number of image channels. The expression is as follows:

$$S = \frac{1}{m}\sum_{c=1}^{m} I_c. \tag{21}$$

3.2.3. Dynamic Compensation. As shown in (19), the MSR algorithm obtains an enhanced image from the logarithmic domain by linear transformation. Therefore, gains and deviations are often considered during the recovery process. These two feature quantities usually need to be adjusted for a given image, and it is difficult to apply to all underwater image enhancements. The effectiveness and practicability of the algorithm are greatly reduced.

In [24], the authors applied the adaptive stretching method in the CIE-Lab color model and established a stretching formula normalized to the brightness parameter and, finally, obtained a clear image with high contrast and saturation. We use the method of dynamic adaptive stretching to compensate image information. The compensation formula is as follows:

$$\begin{aligned} I(i)_{\mathrm{MSRMAX}} &= I(i)_{\mathrm{MSRMEAN}} + \mu I(i)_{\mathrm{MSRVAR}}, \\ I(i)_{\mathrm{MSRMIN}} &= I(i)_{\mathrm{MSRMEAN}} - \mu I(i)_{\mathrm{MSRVAR}}, \end{aligned} \tag{22}$$

where $I(i)_{\mathrm{MSRMAX}}$ and $I(i)_{\mathrm{MSRMIN}}$ are the maximum and minimum values of each channel after MSR processing, $I(i)_{\mathrm{MSRMEAN}}$ and $I(i)_{\mathrm{MSRVAR}}$ are the average and deviation values of the MSR output image, and μ is the dynamic range, $i \in \{R\ G\ B\}$.

The final compensated image is expressed as follows:

$I(i)_{\mathrm{DCMSR}}$ is the dynamically compensated MSR image.

$$I(i)_{\mathrm{DCMSR}} = \frac{R(i)_{\mathrm{MSR}} - I(i)_{\mathrm{MSRMIN}}}{I(i)\mathrm{MSRMAX}^{-I(i)\mathrm{MSRMIN}}} \times 255. \tag{23}$$

3.2.4. Color Retention. In MSR algorithm, color information is easily lost, which leads to a decrease in color saturation. With the emergence of Multiscale Retinex with Color Restoration (MSRCR), the abovementioned problem has been solved [25]. But, color gain and deviation face similar problems with image information. This limits the use of MSRCR. If we enlarge the original image chrominance information by a certain proportion, we can avoid the excessive color gain and deviation and generate an image closer to the original color.

$$I(i)_{\mathrm{DCMSRCP}} = \alpha \frac{I(i)_{\mathrm{mean}}}{I(S)_{\mathrm{DCMSRMEAN}}} I(i)_{\mathrm{DCMSR}}, \tag{24}$$

where $i \in \{R\ G\ B\}$, where α is the color retention coefficient, $I(i)_{\mathrm{mean}}$ is the average of the original image, $I(S)_{\mathrm{DCMSRMEAN}}$ is the intensity channel average of MSR algorithm after dynamic compensation, and $I(i)_{\mathrm{DCMSR}}$ is the dynamically compensated MSR image.

4. Underwater Manipulator Redundancy Resolution Algorithm

The precise model of the manipulator in the task space is established above. On this basis, this section will describe the servo antidisturbance control method of the underwater manipulator under visual enhancement.

The UVMS is a combined system of different speeds, and there is system self-motion. Redundancy can be used to determine the desired trajectory of the body and end effector without affecting its motion in the workspace.

$J(q)$ is the Jacobian matrix in this research, and n is the number of joints. When the velocity profile of the underwater manipulator is given, the joint speed of the robot and the speed of the UVMS can be determined by redundant resolution.

$$\dot{q} = J(q)^{\#}\dot{\mu} + \left(I_{n\times n} - J(q)^{\#}J(q)\right)\gamma, \tag{25}$$

where $J(q)^{\#}$ is the Moore–Penrose pseudoinverse matrix of the Jacobian matrix J. This can be calculated according to the following equation:

$$J(q)^{\#} = J(q)^{T}\left[J(q)J(q)^{J(q)^{\#}}\right]^{-1}, \tag{26}$$

where $J(q)^{\#}\dot{\mu}$ in equation (27) is a specific solution that is determined by the given speed of an underwater manipulator. $I_{n\times n} - J(q)^{\#}J(q)\gamma$ in equation (26) is the homogeneous solution obtained by projecting on the zero space of the Jacobian matrix J. It represents a self-motion that does not affect the motion of the task. Therefore, the vector J can be defined to obtain the optimal solution for the specified performance metric.

When a UVMS robot hovers over an underwater object, it will cause vibration or even instability of the UVMS body. The distance between the mass center position of the UVMS and the ZMP position is set as the performance index as in equation (27). In this paper, performance metrics are minimized along with redundancy analysis.

$$\begin{aligned} \Xi_1(\eta, \Theta) &= \frac{1}{2}W_{p1}\left\|r_{\mathrm{zmp}} - \Delta_{\mathrm{zmp}}\right\|^2, \\ &= \frac{1}{2}W_{p1}\left(x_{\mathrm{zmp}} - \Delta_x\right)^2, \end{aligned} \tag{27}$$

where W_{p1} is the weight matrix. UVMS manipulators are redundant so that the extra redundancy used in determining the zero moment point (ZMP) position can be used for other tasks, such as trajectory optimization. For this type of work, another performance metric can be used to create additional performance metrics for the angular trajectory of the manipulator joint, as shown in the following equation:

$$\Xi_2(\Theta) = \frac{1}{2}\sum_{i=1}^{n} W_{p2}\left[\frac{\theta_i - \theta_{i,\mathrm{mid}}}{\theta_{i,\mathrm{int}}}\right]^2, \theta_{i,\mathrm{mid}} = \frac{\theta_{i,\max} + \theta_{i,\min}}{2}, \theta_{i,\mathrm{int}} = \frac{\theta_{i,\max} - \theta_{i,\min}}{2}, \tag{28}$$

where $\theta_{i,\max}$ and $\theta_{i,\min}$ represent the maximum and minimum limit angles of the i-th chain and W_{p2} represents a weight matrix. In this paper, the limit angle of the node angle is set as a constraint considering the practical application of the manipulator. In order to satisfy these two constraints, a performance index that can establish the angular trajectory of the manipulator joint to improve stability is proposed. The performance of the entire UVMS over a limited range of manipulator joint angles is expressed as follows:

$$\Xi_2(\Theta) = \frac{1}{2}W_{p1}\left(x_{\text{zmp}} - \Delta_x\right)^2 + \frac{1}{2}\sum_{i=1}^{n} W_{p2}\left[\frac{\theta_i - \theta_{i,\text{mid}}}{\theta_{i,\text{int}}}\right]^2. \tag{29}$$

As shown in (30), the gradient analysis method (GAM) is used to perform redundancy analysis on the proposed performance index, and the solution in zero space can be obtained.

$$\begin{aligned} \gamma &= -\kappa \cdot \nabla\Xi, \\ \nabla\Xi &= \left[\frac{\partial g}{\partial\theta_1}, \frac{\partial g}{\partial\theta_2}, \cdots, \frac{\partial B}{\partial\theta_N}\right]^T. \end{aligned} \tag{30}$$

where κ and $\nabla\Xi$ represent the gradient vectors of the positive gradient constant and the performance index, respectively.

5. Experiment

The self-developed UVMS is used for underwater vision enhancement experiment and robot visual servo grasping experiment, respectively. The UVMS is equipped with a three-degree-of-freedom electric manipulator and a network camera, and it is equipped with 4 electric thrusters. The solid composite foam with a water absorption rate less than 1% (24 h) is selected on the UVMS, which can withstand the underwater environment of 2000 ft to 36000 ft. It has built-in environmental awareness systems such as inertial navigation, bathymetry, and thermal conductivity depth (CTD). The system is shown in Figure 6.

5.1. Image Enhancement Contrast Experiment. We carried out fusion image enhancement algorithm on underwater images. Then, it is compared with MSR algorithm and bilateral filtering algorithm for imaging effect and data analysis.

The imaging effect in Figure 7 shows that MSR algorithm compensates the detailed information of the dust at the bottom of the pool, and this enhances the color of the underwater image while maintaining the color constancy. Bilateral filtering algorithm considers the influence of the similarity between the pixel and the central pixel in the convolution kernel, and this eliminates noise while preserving the edges, enhancing the layering of the image. However, the enhanced image is obviously pale in color and distorted in color. In contrast, the fusion enhancement algorithm compensates for the imaging shortcomings of both, and it can better restore the shape of the sea cucumber model and the details of the experimental environment. The overall

Figure 6: Underwater vehicle-manipulator system.

picture is natural and closer to the actual underwater environment. Because the amount of image detail increases, this provides a wealth of reference data for subsequent underwater target recognition and ranging.

The data comparison in Table 1 shows that fusion enhancement algorithm has greatly improved the brightness, contrast, and clarity. The effectiveness of fusion algorithm in detail processing is confirmed by the improvement of information entropy. In the future, we will study 3D feature extraction and positioning technology of underwater targets based on point cloud data [26, 27].

5.2. UVMS Anti-Interference Grab Experiment. The overview of the visual servo anti-interference crawling experiment is as follows: First, inertial navigation, sounding, and other sensors are fused to detect the attitude of the system under the disturbance, and the control method based on redundant resolution algorithm is used to establish the anti-interference controller of the manipulator; it compensates the displacement of the UVMS body that has not been corrected or overcompensated in time. The vector data will be combined with the visually resolved data to obtain the final joint motor feedback angle.

Because the research object is the UVMS with 3 degrees of freedom control ability, the model parameters are shown in Table 2. The parameter selection of the controller is as follows:

$$\begin{aligned} \alpha &= 1.2/3, \\ \beta &= 0.5/3, \\ k_1 &= \begin{bmatrix} 2 & 0.5 & 0.5 \end{bmatrix}^T, \\ k_2 &= \begin{bmatrix} 0.5 & 1 & 0.5 \end{bmatrix}^T, \\ g &= 0. \end{aligned} \tag{31}$$

We simulated 1–3 sections of mixed water flow interference in the range of 5–15s:

$$\begin{aligned} t &= 0 - 5s\text{: } T = 0, \\ t &= 5 - 15s\text{: } T = A\sin\left(\frac{\pi}{2}(t-5)\right) + B\cos\left(\frac{\pi}{2}(t-5)\right). \end{aligned} \tag{32}$$

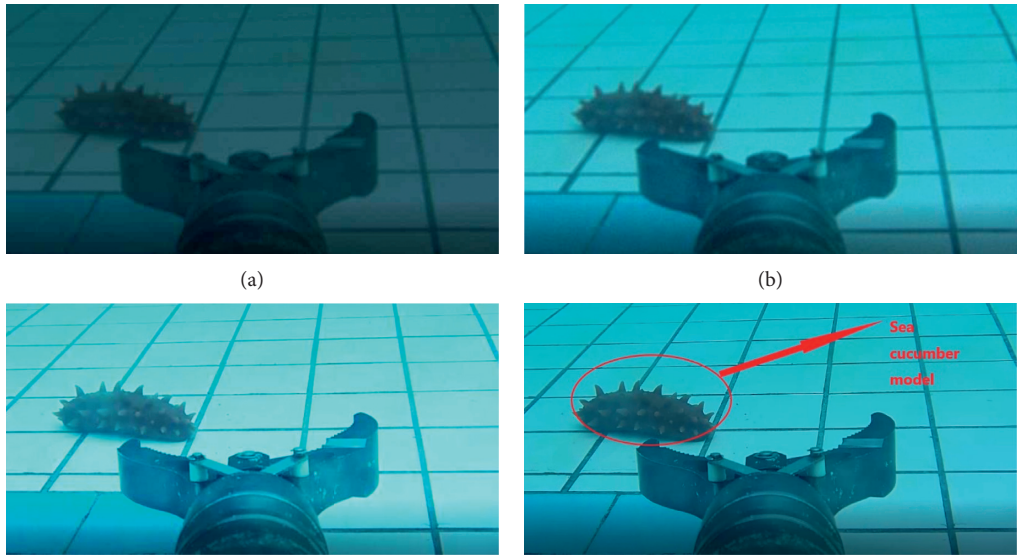

(a) (b) (c) (d)

Figure 7: (a) Original image. (b) MSR algorithm. (c) Bilateral filtering algorithm. (d) Fusion algorithm.

Table 1: Results of various algorithms in Figure 4.

Approach	Information entropy	Contrast	Brightness	Sharpness
Original image	2.6035	130.2151	60.6802	35.223
MSR	5.8231	206.3452	75.2635	45.3124
Bilateral filtering	6.211	230.2151	70.6351	50.3641
Fusion algorithm	6.423	263.2158	83.2012	53.2154

Table 2: UVMS model parameters.

Object	Model parameters	Numerical
UVMS body	Length, width, and height/quality	$500 \times 400 \times 300$ mm (25 kg)
Link 1	Link length/quality	0.30 m (3.5 kg)
Link 2	Link length/quality	0.32 m (2.7 kg)

We generate a three-dimensional trajectory diagram of the end effector of the UVMS underwater operation process (Figure 8).

The abovementioned simulation trajectory can be seen: The manipulator has a smooth transition during the interference period, there is no severe fluctuation and the servo control performance is excellent, and the underwater target is tracked accurately and quickly. As shown in Figure 8, the sudden disturbance brings displacement in the y-axis direction of the manipulator and antidisturbance controller makes the large-scale displacement caused by disturbance be compensated, and this allows the system to self-adjust in a shorter time. It is confirmed that the antidisturbance controller based on redundant resolution algorithm has an excellent balance control effect on the UVMS under the interference of water flow, and this improves the UVMS underwater control performance.

The turbulent boundary layer between the shallow water and the sea floor caused by the current has a great impact on underwater fishing operations. In order to achieve the effect of water flow turbulent layer, two horizontal and vertical 250 W aeration surge water cannons are set at the critical point of the water surface within 30 cubic meters centered on the UVMS operating point. We make the disturbance of the water flow under the fourth-level wind, and the reference velocity is 5 m/s.

We take the hovering UVMS centroid as the reference origin. The three-dimensional space point (unit: m) of the grab target in the task space obtained by visual ranging is 0.632, 0.643, −0.992. The reverse rotation angles of shoulder and elbow joints are 25.42° and 30.11, respectively. The relevant data during the movement of the manipulator is recorded in real time by feedback hardware such as underwater encoders and travel switches in each joint. Figure 9 is the experimental process of grabbing a sea cucumber model. Figure 10 shows the joint real-time feedback data. Data show that the final position of the shoulder joint of the underwater manipulator is 25.60°, and the final position of the elbow joint is 29.91°.

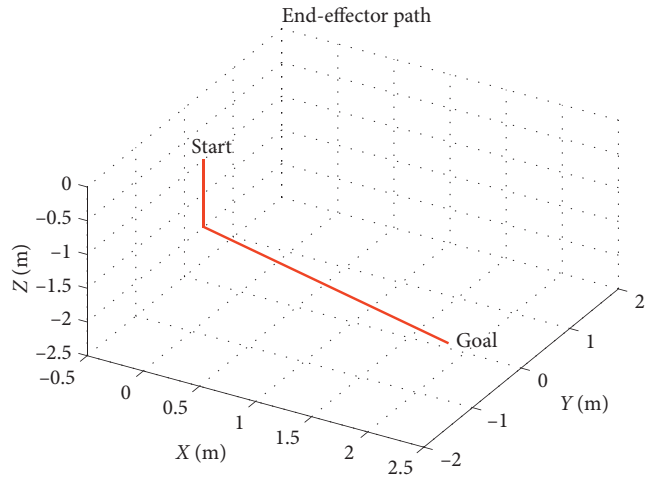

Figure 8: Underwater manipulator three-dimensional trajectory.

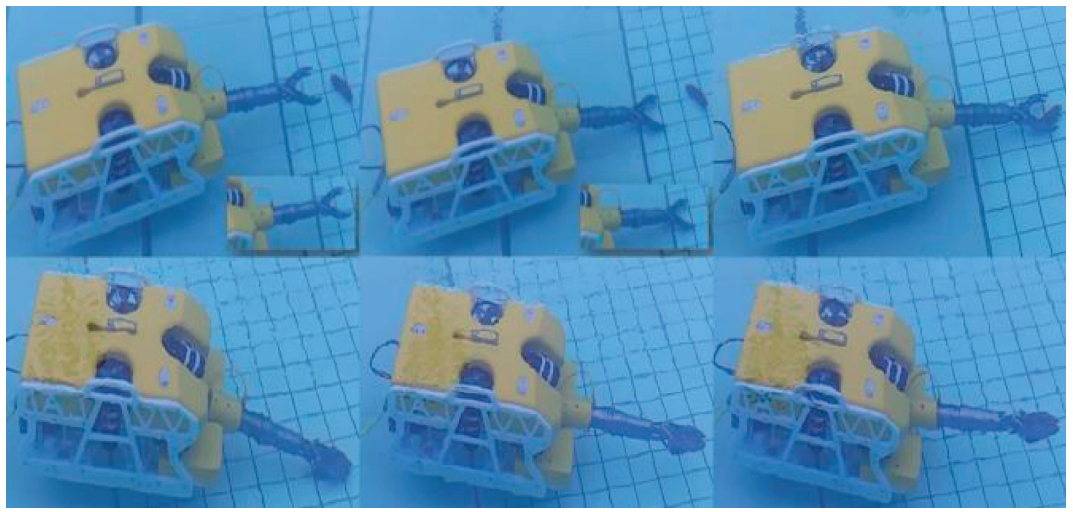

Figure 9: Underwater grab experiment process.

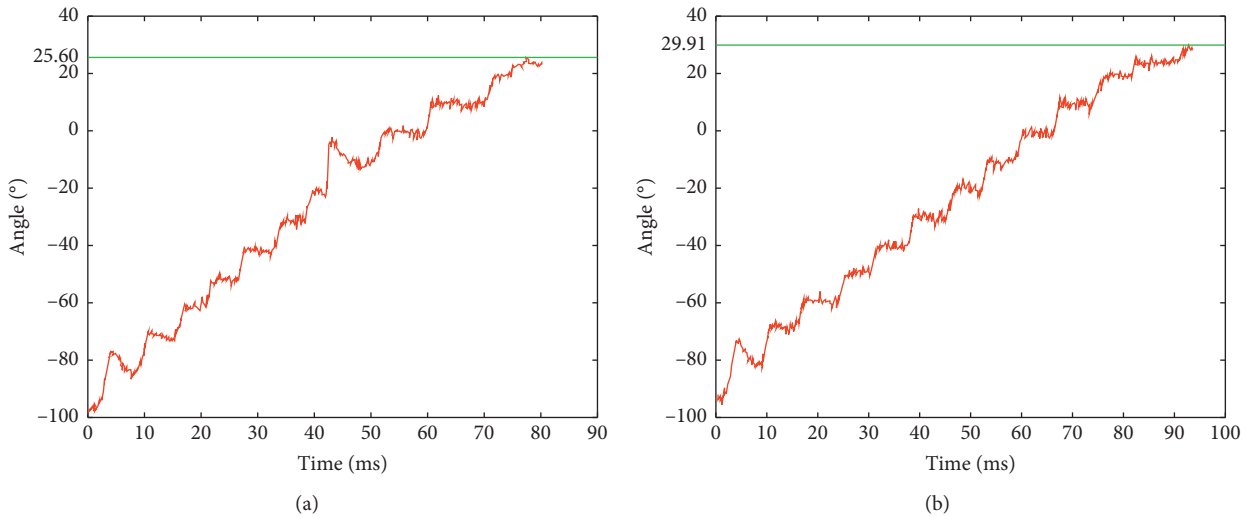

Figure 10: Real-time feedback angle of the shoulder joint and elbow joint. (a). Shoulder joint feedback angle. (b). Elbow joint feedback angle.

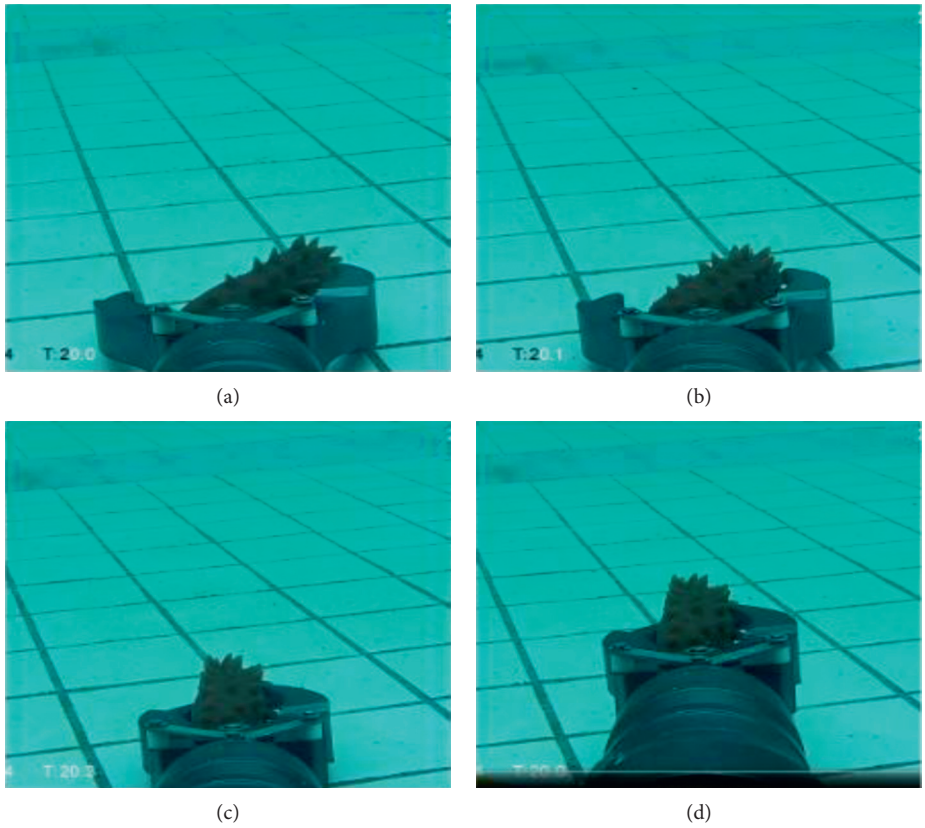

(a) (b) (c) (d)

Figure 11: Servo control capture process.

Experimental analysis shows that, under the interference of water flow, it is difficult for the manipulator to reach the ideal position, and the shoulder joint angle is too large. However, the angle error remains within ±2°, and this increases the success rate by 20% and the desired control effect is achieved.

Figure 11 shows the servo control capture process. The experimental results show that the grasping process is stable and the underwater manipulator reaches the target position to complete the designated task. At present, the optimal control methods of onshore industrial manipulator are relatively mature. In the next step, in order to obtain better underwater grasping effect and efficiency, we plan to use these methods in the acquisition of the underwater manipulator [28–30].

6. Conclusions

This paper proposes an optimized solution for the disadvantages of poor UVMS underwater image imaging quality and weak anti-interference ability. Fusion image enhancement algorithm is used to improve the underwater image capture and analysis capabilities. First, building an UVMS mathematical model with all the uncertainties, the model provides a basis for the design of antidisturbance controllers to obtain better UVMS antidisturbance parameters. In order to verify the performance of the anti-interference controller based on the redundant resolution algorithm and the enhancement effect of the image, we conducted an underwater sea cucumber model crawling experiment. The experiment measured the real-time angle of the servo feedback of each joint of the underwater mechanical arm and the three-dimensional trajectory of the manipulator. Analysis data show that the underwater manipulator accurately tracks the target trajectory while maintaining UVMS stability. This realizes the task of UVMS underwater operation under the disturbance of uncertainty. This verifies the effectiveness of the image fusion algorithm in underwater imaging and detail capture.

The research can be applied to the direction of aquaculture, and it can more clearly observe the growth of aquatic products and improve the grasping efficiency of underwater manipulator to improve the profit of aquaculture. Based on this article, the fusion enhancement algorithm under the artificial light source in the deep sea and the state prediction accuracy of the manipulator antidisturbance controller will be further developed in the future. The experimental study of the UVMS actual seafloor operation under the disturbance of ocean current is carried out to improve the comprehensive control performance of the closed-loop control system.

Data Availability

The data used to support the findings of this study are available from the corresponding author upon request.

Conflicts of Interest

The authors declare that they have no conflicts of interest.

Acknowledgments

This research was supported by Industrial Foresight Project of Zhenjiang City (GY2018018), Jiangsu Graduate Scientific Research and Practice Innovation Program (SJCX20 1474), and the National Natural Science Foundation of China (51809128).

References

[1] B. Wu, Y. Wang, and J. Yang, "Visibility restoration algorithm for single underwater image," *Journal of Henan Normal University (Natural Edition)*, vol. 41, no. 3, pp. 59–62, 2013.

[2] M. S. Hitam, T. Kuala, W. Yussof et al., "Mixture contrast limited adaptive histogram equalization for underwater image enhancement," in *Proceedings of the International Conference on Computer Applications Technology*, pp. 1–5, Sousse, Tunisia, January 2013.

[3] X. Y. Fu, P. X. Zhuang, Y. Huang et al., "A Retinex-based enhancing approach for single underwater image," in *Proceedings of the IEEE International Conference on Image Processing*, pp. 4572–4576, IEEE, Piscataway, NJ, USA, October 2014.

[4] Y. Y. Gao and H. M. Hu, "Dense fog image enhancement based on multi-subblock cooperative single-scale Retinex," *Journal of Beijing University of Aeronautics and Astronautics*, vol. 45, no. 5, pp. 101–108, 2019.

[5] M. S. Hitam, W. N. J. H. W. Yussof, E. A. Awalludin et al., "Mixture contrast limited adaptive histogram equalization for underwater image enhancement," in *Proceedings of the 2013 IEEE International Conference on Computer Applications Technology*, pp. 1–5, Sousse, Tunisia, January 2013.

[6] A. S. Abdul Ghani, N. A. Mat Isa, M. Isa et al., "Enhancement of low quality underwater image through integrated global and local contrast correction," *Applied Soft Computing*, vol. 37, pp. 332–344, 2015.

[7] X. Fu, Y. Liao, D. Zeng, Y. Huang, X.-P. Zhang, and X. Ding, "A probabilistic method for image enhancement with simultaneous illumination and reflectance estimation," *IEEE Transactions on Image Processing*, vol. 24, no. 12, pp. 4965–4977, 2015.

[8] N. D. Nguyen, H. S. Choi, N. H. Tran et al., "Simulation and experiment of underwater vehicle manipulator system using zero-moment point method," in *International Conference on Advanced Engineering Theory & Applications*, pp. 1–5, Springer, Berlin, Germany, 2017.

[9] Q. Tian, L. Wang, Y. Wang et al., "Research on vehicle detection algorithm based on Retinex," *Industrial Control Computer*, vol. 26, no. 12, pp. 1–13, 2019.

[10] P. S. Londhe, S. Mohan, and L. M. Waghmare, "Robust task-space control of an autonomous underwater vehicle-manipulator system by PID-like fuzzy control scheme with disturbance estimator," *Ocean Engineering*, vol. 139, no. 15, pp. 1–13, 2017.

[11] L. Qiao and W. Zhang, "Adaptive non-singular integral terminal sliding mode tracking control for autonomous underwater vehicles," *IET Control Theory & Applications*, vol. 11, no. 8, pp. 1293–1306, 2017.

[12] J. Li, L. Wan, H. Huang et al., "Adaptive anti-disturbance control method for underwater robot-manipulator system," *Journal of Tianjin University (Natural Science and Engineering Technology)*, vol. 51, no. 4, pp. 413–420, 2018.

[13] Y. Dai, S. Yu, Y. Yan, and X. Yu, "An EKF-based fast tube MPC scheme for moving target tracking of a redundant underwater vehicle-manipulator system," *IEEE/ASME Transactions on Mechatronics*, vol. 24, no. 6, pp. 2803–2814, 2019.

[14] Y. Dai and S. Yu, "Design of an indirect adaptive controller for the trajectory tracking of UVMS," *Ocean Engineering*, vol. 151, no. 1, pp. 234–245, 2018.

[15] Y. Dai, S. Yu, Y. Yan et al., "An adaptive EKF-FMPC for the trajectory tracking of UVMS," *Oceanic Engineering*, vol. 45, no. 3, pp. 699–713, 2020.

[16] Y. Yan, D. Wu, Y. Dai et al., "Robust control of underwater vehicle-manipulator system using grey wolf optimizer-based nonlinear disturbance observer and H-infinity controller," *Complexity*, vol. 2020, no. 2, 17 pages, Article ID 6549572, 2020.

[17] Y. Zhang and L. Jin, *Robot Manipulator Redundancy Resolution*, John Wiley & Sons, Ltd, Hoboken, NJ, USA, 2017.

[18] W. Chen, T. Xu, J. Liu, M. Wang, and D. Zhao, "Picking robot visual servo control based on modified fuzzy neural network sliding mode algorithms," *Electronics*, vol. 8, no. 6, p. 605, 2019.

[19] D. Huang, Y. Wang, W. Song et al., "Underwater image enhancement with adaptive histogram stretching under different color models," *Journal of Image and Graphics*, vol. 265, no. 5, pp. 28–39, 2018.

[20] W. Wang, L. Gu, B. Chen et al., "Underwater Robots -Non-singular terminal sliding mode control of manipulator system," *Zhejiang UniversityJournal (Engineering Edition)*, vol. 52, no. 337, pp. 121–129+166, 2018.

[21] Z. Tang, B. Zhou, X. Dai et al., "Vision enhancement of underwater robot based on improved," *DCP Algorithm*, vol. 40, no. 2, pp. 222–230, 2018.

[22] T. Xu, Y. Guan, J. Liu, and X. Wu, "Image-based visual servoing of helical microswimmers for planar path following," *IEEE Transactions on Automation Science and Engineering*, vol. 17, no. 1, pp. 325–333, 2020.

[23] C. Yu, X. Xiang, L. Lapierre, and Q. Zhang, "Robust magnetic tracking of subsea cable by AUV in the presence of sensor noise and ocean currents," *IEEE Journal of Oceanic Engineering*, vol. 43, no. 2, pp. 311–322, 2018.

[24] D. Huang, W. Wang, W. Song et al., "Underwater image enhancement of adaptive histogram stretching under different color models," *Chinese Journal of Image and Graphics*, vol. 23, no. 265, pp. 28–39, 2018.

[25] A. Zamuda and J. D. H. Sosa, "Success history applied to expert system for underwater glider path planning using differential evolution," *Expert Systems with Applications*, vol. 119, no. 4, pp. 155–170, 2019.

[26] W. Chen, X. Li, L. H. Ge, Y. Wang, and Y. Zhang, "Trajectory planning for spray painting robot based on point cloud slicing technique," *Electronics*, vol. 9, no. 6, p. 908, 2020.

[27] W. Chen, X. Wang, H. Liu, Y. Tang, and J. Liu, "Optimized combination of spray painting trajectory on 3D entities," *Electronics*, vol. 8, no. 1, p. 74, 2019.

[28] W. Chen, H. Liu, Y. Tang, and J. Liu, "Trajectory optimization of electrostatic spray painting robots on curved surface," *Coatings*, vol. 7, no. 10, p. 155, 2017.

[29] W. Chen, J. Liu, Y. Tang, J. Huan, and H. Liu, "Trajectory optimization of spray painting robot for complex curved surface based on exponential mean Bézier method," *Mathematical Problems in Engineering*, vol. 2017, no. 11, 10 pages, Article ID 4259869, 2017.

[30] W. Chen, J. Liu, Y. Tang, and H. Ge, "Automatic spray trajectory optimization on Bézier surface," *Electronics*, vol. 8, no. 2, p. 168, 2019.